THE UNIVERSITY OF QUEENSLAND

AUSTRALIA

ASPECTS OF INLET GEOMETRY AND DYNAMICS

VU THI THU THUY

B.E (WRU), ME (WRU), M.Sc. (IHE)

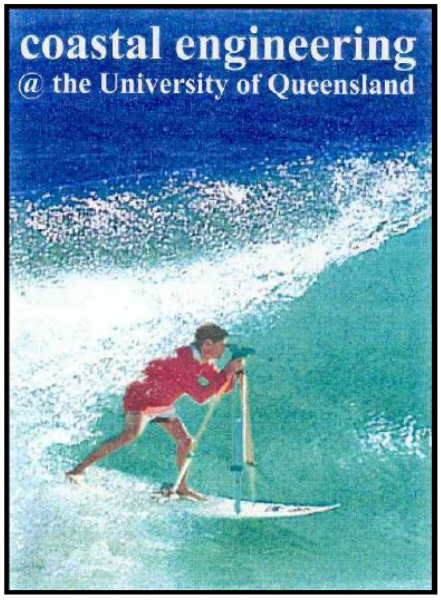

A thesis submitted for the degree of Doctor of Philosophy at

The University of Queensland in 2013

School of Civil Engineering

Abstract

This thesis contains new analytical approaches as well as laboratory- and field experiments conducted to understand the hydrodynamic and morphodynamic responses of tidal inlets to forcing from tides, river flow and waves on the time scales of closure, flood or storm events. The thesis outcome is effective new tools for authorities managing coastal zones balancing navigation-, shore protection- and socio-economic development purposes.

A new method of coastal inlet classification based on dimensionless parameters is presented. These parameters represent the relative strength of the three main forcing agents: tides, river flow and waves. This new classification is applied to 178 inlets along the NSW coast of Australia, and compared with other widely used classification schemes available in the literature.

The inlet hydraulic analysis is presented in Chapter 2 with given inlet geometry and wave climate with overwash discharge (Q_{over}) added into the usual governing equations. The hydraulic analysis of inlets in terms of the frequency response function for the linearised system is illustrated for cases of monochromatic and mixed diurnal/semi-diurnal tides. This analysis quantifies the influence of the entrance invert level, river flow and bay surface area. A case of inland flooding at Lake Conjola, Australia is used to test different methods resulting in a successful illustration of the importance of wave overwash as a driving force.

For each hydrodynamic condition, the inlet system and its elements have a corresponding morphological equilibrium state. New relationships for inlets in equilibrium were constructed based on dimensional analysis and tested on a data set of 36 natural inlets in the USA. These new relations depend not only on the tidal prism but also the tidal period, and mean annual significant wave height $\overline{H_s}$.

During unusual weather, the morphology of tidal inlets runs out of equilibrium. Subsequently, they may return to the previous equilibrium or move towards a new equilibrium or get closed. Inlet morphodynamics analysis is ideally carried out from topographical surveys. These are however costly and usually not available. Process based numerical models are still unreliable. A more economical and reliable new method, a 24.5hour moving window method, is introduced to infer hydraulic- and morpho-dynamic changes from tidal records. The morphological time scales are thus determined from time series of mean water levels, standard deviation, or the gain of the primary tidal components. This analytical method is successfully applied to inlet closure events and flood or storm events.

The morphological time scale, T_{morph} has been derived from the 24.5hour moving window analysis for many closure events with bay area (A_b<0.7km^2) in Australia. The results show a clear trend of T_{morph} decreasing with increasing relative wave strength – i.e., more rapid closure with

bigger waves. However, for larger inlets or inlets with training works the morphology changes, at the time scale of individual storms, are usually not significant enough to be measurable via the tidal records. The moving window analysis is an effective way to analyse surge- or flood events to clarify if the system gets higher hydraulic efficiency due to inlet scour or reduced gain due to non-linear friction effects and/or increased bay area due to elevated estuary water levels.

Regarding the non-seasonal opening/closing of inlets in NSW, the fraction of time the inlet is open and the average time it stays open, $\overline{T_{\text{open}}}$ are quantified in terms of the dimensionless relative tidal strength $\frac{\hat{Q}_{\text{potential}}}{\sqrt{g\overline{H_{\text{s}}}^{5}}}$.

The new relationships for inlet in equilibrium are applied to illustrate the use of a new, analytical inlet evolution equation based on the impulse response function for an inlet under the effects of variable waves and spring/neap tide variation.

An assessment of the state of the art of numerical, morphological modelling was made by applying the US Army Corps' CMS model to Pensacola Pass during and after Hurricane Katrina. The model underestimated the morphology changes observed and results did not reach an asymptote under steady, normal forcing after the event. Insignificant erosion of the ebb tidal delta in the model output, compared to observations, is attributed to (i) improper model assumptions on direction of sediment transport (ii) underestimation of role of waves in sediment transport and (iii) difficulties with numerical bed updating balancing stability versus accuracy.

Laboratory experiments on barrier development under waves and currents were carried out. Analysis of combinations of two wave cases with shorter period shows that the sediment transport direction is opposite to the net flow direction. The direction of sediment transport (q_{s}) is not consistent in the combinations including other two wave cases with the longer period. These cases show clearly that q_{s} cannot be generally assumed to be in the direction of the net flow as in the CMS model.

Based on the results of the laboratory experiments, the applicability of five existing state-of-the-art sediment transport (q_{s}) formulae to inlet morphodynamics has been assessed.

Declaration by author

This thesis is composed of my original work, and contains no material previously published or written by another person except where due reference has been made in the text. I have clearly stated the contribution by others to jointly-authored works that I have included in my thesis.

I have clearly stated the contribution of others to my thesis as a whole, including statistical assistance, survey design, data analysis, significant technical procedures, professional editorial advice, and any other original research work used or reported in my thesis. The content of my thesis is the result of work I have carried out since the commencement of my research higher degree candidature and does not include a substantial part of work that has been submitted to qualify for the award of any other degree or diploma in any university or other tertiary institution. I have clearly stated which parts of my thesis, if any, have been submitted to qualify for another award.

I acknowledge that an electronic copy of my thesis must be lodged with the University Library and, subject to the General Award Rules of The University of Queensland, immediately made available for research and study in accordance with the *Copyright Act 1968*.

I acknowledge that copyright of all material contained in my thesis resides with the copyright holder(s) of that material. Where appropriate I have obtained copyright permission from the copyright holder to reproduce material in this thesis.

Publications during candidature

Lam, N.T., Thanh, L.D., Cat, V.M. and Thuy, V.T.T., 2009. Sediment transport and morphodynamics of My A inlet, Vietnam, in the low flow season, The 5th International Conference on Asian and Pacific Coasts (APAC2009), 13-16 October 2009, Singapore, pp. 75-82.

Lam, N.T., Cat, V.M., Thanh, L.D. and Thuy, V.T.T., 2009. Modelling sediment transport at the Da Rang estuary, Phu Yen Province, Proceedings of the 50th Anniversary Workshop of Water Resources University, November 2009, pp. 72-79.

Thuy, T.T.V., Nielsen, P., Callaghan, D.P. and Hanslow, D.J., 2011. Application of the wave pump concept to simulate tidal anomalies in Lake Conjola, NSW, Australia, Proceedings of the 6th International Conference on APAC 2011. World Scientific, Singapore, HongKong, pp. 812-819.

Lam, N.T. and Thuy, T.T.V., 2012. Storm surge modeling for coastal structure design, International Conference on Coastal and Port Engineering in developing countries 2012- PIANC-COPEDEC VIII 2012, Chennai, India, pp. 205 - 214.

Thuy, T.T.V., Nielsen, P., Lam, T.N. and Selam, J.K., 2012. Sand barrier dynamics by waves and currents, International Conference on Coastal and Port Engineering in developing countries - PIANC-COPEDEC VIII 2012, Chennai, India, pp. 558 – 569.

Thuy, T.T.V., Nielsen, P., Callaghan, D.P. and Lam, T.N., 2012. Inferring inlet morphodynamics & hydraulic parameters from tidal records of Avoca Lake, NSW, Australia, The 4th International Conference on Estuaries and Coast (ICEC 2012), Hanoi, Vietnam, pp. 74-80.

Lam, N.T. and Thuy, V.T.T., 2012. Validation of near shore wave modeling for Cua Hoi estuary, The 4th International Conference on Estuaries and Coast (ICEC 2012), Hanoi, Vietnam, pp. 100-105.

Thuy, T.T.V., Nielsen, P. and Callaghan, D.P., 2013. Inferring inlet morphodynamics and hydraulic parameters from tidal records: A case study of four closure events of Avoca Lake, Australia. International Journal of Earth Sciences and Engineering, 6(2):225-231.

Thuy, T.T.V., Nielsen, P. and Callaghan, D.P., 2013. Inlet morpho-dynamics during a storm event inferred from tidal records: A case study of the Brunswick River, NSW, Australia. International Journal of Engineering Research, 2(2): 38-43.

Publications included in this thesis

Thuy, T.T.V., Nielsen, P., Callaghan, D.P. and Hanslow, D.J., 2011. Application of the wave pump concept to simulate tidal anomalies in Lake Conjola, NSW, Australia, Proceedings of the 6th International Conference on APAC 2011. World Scientific, Singapore, HongKong, pp. 812-819.

Nielsen, P., Callaghan, D.P. supervised the work; Callaghan, D.P helped one part of modelling and edited; Hanslow, D.J. provided data and related document. Thuy was responsible for analysis, drafting, writing and presentation of the work. It is partially incorporated as one section in Chapter 2.

Thuy, T.T.V., Nielsen, P., Lam, T.N. and Seelam, J.K., 2012. Sand barrier dynamics by waves and currents, International Conference on Coastal and Port Engineering in developing countries - PIANC-COPEDEC VIII 2012, Chennai, India, pp. 558 – 569.

- Nielsen, P. supervised the work, edited; Lam, T.N. help processed data, Seelam, J.K. helped doing experiments and edited; Thuy was responsible for doing experiment, processed data, analysis, drafting, writing and presentation of the work. It is partially incorporated in Chapter 8, Chapter 9.

Thuy, T.T.V., Nielsen, P., Callaghan, D.P. and Lam, T.N., 2012. Inferring inlet morphodynamics & hydraulic parameters from tidal records of Avoca Lake, NSW, Australia, The 4th International Conference on Estuaries and Coast (ICEC 2012), Hanoi, Vietnam, pp. 74-80.

- Nielsen, P., Callaghan, D.P. supervised the work; Callaghan, D.P edited; Lam, T.N. helped processing data. Thuy was responsible for analysis, drafting, writing and presentation of the work. It is partially incorporated as one section in Chapter 4.

Thuy, T.T.V., Nielsen, P. and Callaghan, D.P., 2013. Inferring inlet morphodynamics and hydraulic parameters from tidal records: A case study of four closure events of Avoca Lake, Australia. International Journal of Earth Sciences and Engineering, 6(2):225-231.

- Nielsen, P., Callaghan, D.P. supervised the work; Nielsen, P. edited. Thuy was responsible for analysis, drafting, writing the paper. It is revised and improved results of the paper in ICEC 2012, partially incorporated as one section in Chapter 4.

Thuy, T.T.V., Nielsen, P. and Callaghan, D.P., 2013. Inlet morpho-dynamics during a storm event inferred from tidal records: A case study of the Brunswick River, NSW, Australia. International Journal of Engineering Research, 2(2): 38-43.

- Nielsen, P., Callaghan, D.P. supervised the work; Nielsen, P. edited the work. Thuy was responsible for analysis, drafting, writing and finalising the paper. It is partially incorporated as one section in Chapter 4.

Contributions by others to the thesis

Peter Nielsen was the main supervisor introducing new concepts, guided, edited, provided financial support for field works and conferences and provided frequent encouragement.

David P. Callaghan: second supervisor guided, helped and supported with programming and modeling, edited.

Tom Baldock: co advisor commented and provided related document.

Lihwa, Lin: external supervisor, guided to use the CMS model, provided Pensacola pass model set up

Lam Tien Nghiem: support programming and data processing.

Jaya Kumar Seelam: helped during laboratory experiment, provided results of velocity from the SWASH model for sand bar dynamics (Section 9.4.1, 9.4.2), edited the first draft of thesis and manuscripts.

Dave Hanslow, NSW Office of Environment and Heritage's (OEH) provided data and related documents.

Statement of parts of the thesis submitted to qualify for the award of another degree

"None"

Acknowledgements

I highly appreciate and sincerely thank A/Prof. Peter Nielsen, my principal advisor, for closely guiding my research, introducing me to new ideas, bringing out the research insight and for supporting me for field works and conferences. I also profoundly thank him for his encouragement, patience, understanding, compassion and persistent support throughout my candidature to complete this thesis.

I would like to thank my co-supervisor Dr. David P. Callaghan for his help in guiding my work and supporting valuably in programming, modelling and editing papers and my thesis. I sincerely thank and appreciate my co advisor Prof. Tom Baldock for his valuable comments and support during my study.

I sincerely thank Dr. Lihwa Lin, my external supervisor in Coastal and Hydraulics Lab, US Army Corps of Engineers, for his guidance in using the CMS model and in setting up the Pensacola Pass model.

No words are sufficient to acknowledge and thank for the sacrifice and difficulties endured by my dearest husband Dr. Lam T. Nghiem and my beloved mom Mrs. Suu T. Ngo, who took care of my children while I was far away, shared my happiness and sadness, encouraged me frequently during my study. I sincerely appreciate their faith with me. My husband not only supported me spiritually but also technically with my programming, data processing and during many difficult times of my research, which enabled me to complete my thesis in time. My beloved mom, though unhealthy, sacrificed many things and took my burden and has always been with me. I hope she will be proud of my achievement and also proud of herself for being there to see her daughter succeed. I also thank my sons Dung and Minh for their spiritual support and their understanding towards their mom.

I sincerely appreciate and thank Dr. Jaya Kumar for his help during my laboratory experiments, discussions on modeling and for editing the first drafts of my thesis and publications.

I would like to thank Dr. Dean Patterson from BMT WBM Pty Ltd for his comments on my work and partly editing my thesis.

I acknowledge the continuous support of Mr. Dave Hanslow of the NSW Office of Environment and Heritage's (OEH) for providing data and related documents pertaining to inlets. Without their help it would be next to impossible to implement and check the new ideas presented in my thesis.

I acknowledge the financial support of my AUSAID Scholarship for my PhD tuition fee, Living Allowance and enclosed support. I also acknowledge the financial support of the University

of Queensland for International student (UQI) for the last research quarter tuition fee. I acknowledge the UQ-Post Grad school travel grant that enabled me to visit, interact and work with many experts on tidal inlets in the United States of America.

I appreciate the support of (Late) Dr. Nick Krauss, Dr. Julie Rosati, Dr. Lihwa Lin, Tanya Beck, Iren, Mitch, and others at the Coastal and Hydraulics Lab, US Army Corps of Engineers, for kindly providing and guiding me to complete the CMS model, as well as providing access to work with the US inlets data.

I place on record my gratitude to Mr. Graham Illidge, Mr. Clive Booth and Mr. Ahmed Ibrahim, former staff at hydraulics lab, for their technical assistance during my experiments. I acknowledge the intellectual fellowship of coastal engineers associated with UQ during my studies: Jaya Seelam, Damitha Peiris, Nimali, Tomoko Shimamoto, Dean Patterson, Pham Son, Ilya Khairanis and Mohammad Olfateh. I am thankful to my friends To Huu Duc and his wife, Cao Van Vui, Dao Linh, Prerna Jha, Dr. Vinh Dao, Nazanin Khezri, Chenming Zhang for their kind support and encouragement.

I thank the Director, Water Resources University, Hanoi, Vietnam for granting necessary leave for this study. I acknowledge the support of my supervisor and colleagues at the Structural Engineering Section who were there whenever I needed their help.

It is next to impossible to complete my thesis without the blessings of my dear father who from the heavens above has always been with me protecting me and encouraging me throughout my life.

Keywords

Tidal inlets, inlet morphodynamics, coastal system classification, wave overwash, wave pump, 24.5hour moving window, morphological time scales, morphodynamics infered from tidal records, inlet stability, seasonal opening/closure inlet, non-seasonal opening/closure inlet, CMS model, Pensacola Pass modelling, sand barrier dynamic, waves, currents, tides.

Australian and New Zealand Standard Research Classifications (ANZSRC)

090599 Civil Engineering 100%

Fields of Research (FoR) Classification

0905 Civil Engineering 100%

To my family

PREFACE

At the outset, the objective of this PhD project was to understand tidal inlets broadly in their steady or quasi-steady (~equilibrium) states and their hydrodynamic and morphodynamic behaviour under the main 'forces' of tides, river flow and waves.

Review of the literature and of available databases together with fieldwork in Vietnam and Australia focused this onto the development of a tide analysis procedure capable of resolving typical storm events of 2-5days duration, proper quantification of the tides as morphology drivers, issues related to the non-uniformity of shear stresses along the wetted perimeter at inlets and other problems related to the progression of numerical models of inlet morphodynamics. These more focused aims have been pursued as follows:

Chapter 1 reviews and updates previous studies by introducing new methods including a new quantification of tides as a morphodynamic driver and correspondingly a new quantitative weighting of waves versus tides and freshwater flow as morphodynamic drivers. The most important new insight is that the strength of the tide as a morphology driver must be quantified via the peak tidal discharge rather than the tide range.

Chapter 2 reviews classical inlet hydraulics with a special emphasis on simple harmonic forcing and the complex response function, which are later used extensively for illustrating estuary response to ocean tides. The hydraulics of lagoon flooding due to wave overwash of barriers is given a novel treatment using the wave pump concept.

In order to explore the impact on inlet hydraulics of morphological changes due to extreme waves and/or freshwater floods, which usually only last 2-5days, a new method of tidal analysis is pioneered in Chapter 3. In order to resolve these short events, a moving analysis window of 24.5hours is chosen and only two harmonic components of periods 24.5hour, and 12.25hours are used. This gives reasonably crisp results, at least for the dominant harmonic, while resolution of the main astronomical constituents requires much longer (~14days) windows and thus loses the ability to resolve typical storm events.

In Chapter 4, the 24.5hour window method is applied to closure events of small inlet systems on the coast of New South Wales, a flood in the Brunswick River, surges in the Limfjord (Denmark) and the Pensacola Pass inlet during Hurricane Katrina. On time scales of a few days, the new method captures morphological changes in the small inlets and temporarily improved response in the Limfjord inlet due to flushing after the surges. The Brunswick River entrance, which is hardened against erosion by rock walls, shows temporarily different hydraulic response due to increased estuary surface area and extra nonlinear friction during the flood but no significant morphological change. Similarly the large Pensacola Inlet system shows changed hydraulic

behaviour during the storm due to surge and barrier overwash but returns to the pre-storm response characteristics after the storm.

Chapter 5 reviews the literature on inlet stability and the extent to which inlet equilibriums can be understood on the basis of observations of real inlets which are never in true equilibrium since the forcing from tides, waves and fresh-water is constantly changing. The new material concerns quantification of the balance between waves versus tides as morphology drivers.

Methods for getting around the transience issue mentioned above are developed in Chapter 6 on inlet morphodynamics. Interpretative tools and an evolution equation are developed assuming a first order linear system.

An assessment of the state of the art of numerical morphological modeling is presented in Chapter 7. More specifically, the CMS model of the US Army Corps of Engineers, has been applied to Pensacola Inlet with forcing corresponding to Hurricane Katrina. The results give an idea about the reliability and predictive capability of today's leading morphodynamic software. Perhaps the most obvious short-coming of these models is their failing to reach equilibrium under steady forcing from waves and tides. Contributing to this problem is the inability of the underlying sediment transport models to predict morphological change even with measured flow parameters as input. This issue is explored in Chapter 8 through laboratory experiments on barrier development under waves and collinear currents in a wave flume at The University of Queensland. Based on the results of the laboratory experiments, the applicability of five existing state-of-the-art sediment transport (q_s) formulae on ripple bed has been assessed in Chapter 9.

Table of Contents

List of Tables xix
List of Figures xx
List of Symbols xxix
List of Abbreviations xxxiv

Chapter 1 DESCRIPTION AND CLASSIFICATION OF INLETS 1
1.1 Topographical definitions 1
1.2 Classification of coastal systems 3
1.2.1 Geo-morphological classification 3
1.2.2 Hydrodynamic classification of inlets 5
1.3 Application of new dimensionless parameters for classification of NSW estuaries, Australia 12
1.3.1 Data available and instructions for calculation 12
1.3.2 Summary of data and results of calculation for different coastal system groups 14

Chapter 2 INLET HYDRAULICS 17
2.1 Introduction 17
2.1.1 Tidal forcing 18
2.1.2 Bay response to tidal forcing 20
2.1.3 Phase relations between horizontal velocity u and surface elevation η 22
2.1.4 Fresh water flow 22
2.1.5 Overwash flow 23
2.2 Hydraulic models of inlet-bay systems 24
2.2.1 Weir models 25
2.2.2 Finite-channel-length models of inlet-bay systems 26
2.3 Simplified finite-channel-length systems 28
2.3.1 Simplifying assumptions 28
2.3.2 Integrated equation of motion 28
2.3.3 Linearization of the friction term 29
2.3.4 Influence of Q_f on $\eta_b(t)$ through $|u|u$: Fourier expansion of $|\cos \omega t+v|(\cos \omega t+v)$. 32
2.4 Frequency response function of the linearised system 35
2.4.1 Estuary response to monochromatic tides 39
2.4.2 Mixed diurnal and semi-diurnal ocean tides. 43
2.5 Lake Conjola tidal anomalies simulation 45

2.5.1 Introduction 45
2.5.2 Lake Conjola morphology and available data 46
2.5.3 Two node hydrodynamic model 48
2.5.4 Application, results and discussion 53
2.6 Conclusions 55

Chapter 3 LAGOON AND ESTUARINE TIDE ANALYSIS 57
3.1 Introduction 57
3.2 Window length 58
3.2.1 Traditional window length (1 year) 58
3.2.2 The Hinwood and McLean window (3-14 days) 59
3.2.3 24.5 hour moving window 60
3.2.4 Morphological time scale T_{morph} determined from 24.5 hour moving window analysis 61
3.2.5 Hydraulic time constants $T_1(t)$ and $T_2(t)$ from $G(t)$ and $\varphi(t)$ 63
3.3 Influence of record trend and method of detrending 65
3.3.1 Using 24.5h moving window for regular tides 65
3.3.2 Using 24.5h moving window for tides with trend 66
3.4 Different moving window length performance 71
3.5 Artefact of method on T_{morph} BY fitting different parameters 73
3.6 Nonlinear interactions of diurnal and semidiurnal tides 76

Chapter 4 MORPHODYNAMICS INFERRED FROM MEASURED TIDES 81
4.1 Two closure events of Lake Avoca 81
4.1.1 Description of Lake Avoca 81
4.1.2 Analysis of closure events 83
4.2 Storm event of May 2009 at Brunswick Heads 91
4.2.1 Description of Brunswick Heads and the storm event 91
4.2.2 Results of 24.5 hour moving window analysis 93
4.3 Overwash flood event in Lake Conjola 97
4.3.1 Recall Lake Conjola information 97
4.3.2 Results of 24.5 hour moving window analysis 99
4.4 Hurricane Katrina in Pensacola Pass, USA 105
4.4.1 Description of Pensacola pass, USA and Hurricane Katrina in 2005 105
4.4.2 Results of 24.5 hour moving window analysis 108

4.5 Summary of event analysis outcomes 113

Chapter 5 INLET STABILITY 116
5.1 Introduction 116
5.1.1 Historical equilibrium relationships 119
5.1.2 Cross-sectional stability 127
5.1.3 Sediment bypassing criteria 130
5.2 Why do sandy inlets not just grow wider and wider? 135
5.3 Dimensional analysis of inlets at equilibrium 138
5.4 Summary 142

Chapter 6 INLET MORPHODYNAMICS 144
6.1 Introduction to inlet morphodynamics 144
6.2 Evolution of tidal inlets review 145
6.3 Seasonal opening/closure cycles qualitatively 152
6.3.1 Seasonal opening/closure cycle of an inlet 152
6.3.2 A conceptual model for seasonal evolution an inlet 155
6.4 Non-seasonal opening and closure of sandy inlets 158
6.5 Determination of T_{morph} from transient inlet behaviour 163
6.5.1 Dynamic analysis based on $T_{morph}\frac{dy}{dt}+y(t)=x(t)$ 163
6.5.2 T_{morph} from 24.5 hour moving window analysis of tides 169
6.6 Conclusions on morphodynamics 174

Chapter 7 ASSESSMENT OF THE STATE OF THE ART OF NUMERICAL MORPHOLOGICAL MODELS OF INLETS 176
7.1 Introduction 176
7.1.1 Pensacola Pass 176
7.2 The CMS model 180
7.2.1 Governing equations for the water motion 180
7.2.2 The wave model 180
7.2.3 The sub-model coupling 181
7.2.4 Governing equations for sediment transport 182
7.3 Model set up, sub models, calibration and sensitivity testing 186
7.3.1 Sub model domains 186
7.3.2 Data sources for boundary and forcing conditions 187

7.3.3 Flow model calibration, wave and sediment sensitivity testing 188
7.3.4 Idealised normal condition for morphology model 196
7.3.5 Boundary conditions for morphology model and hydrodynamic model results 198
7.4 Morphodynamic model Results 199
7.4.1 Results of morphology change 199
7.4.2 Evolution of the throat area 205
7.4.3 Investigation on sediment transport 207
7.5 Conclusions for Pensacola Pass modelling 212

Chapter 8 LABORATORY EXPERIMENTS ON BARRIER SEDIMENT TRANSPORT. 213
8.1 Introduction 213
8.2 The experimental setup 213
8.2.1 The flume, the wave maker and the recording instruments 214
8.2.2 The sediment 216
8.3 Hydrodynamic data acquisition and data analysis 216
8.3.1 Water surface time series data and analysis 217
8.3.2 Horizontal velocity time series and analysis 222
8.3.3 Ripple dimension and prediction 226
8.4 Sediment transport data and analysis 229
8.4.1 Method of measurement and calculation 229
8.4.2 Sediment transport Results 231
8.5 Conclusions 235

Chapter 9 ASSESSEMENT OF EXISTING SEDIMENT TRANSPORT MODELS FOR SAND BARRIER DYNAMICS UNDER WAVES & CURRENTS 236
9.1 Introduction 236
9.2 existing sediment transport models FOR non breaking waves 236
9.2.1 Bed load transport models 237
9.2.2 Suspended load transport models 238
9.2.3 Total load transport 240
9.2.4 Selected transport models 240
9.3 Comparison between measurements & the chosen models at one cross section on top of sand barrier 245
9.4 Adopted results from SWASH model for sand barrier 249
9.4.1 Introduction of the SWASH model and model set up 249

9.4.2 Comparison model results and experiment data 250
9.4.3 Sediment transport rate along sand bar using model velocities in comparison with measured sediment transport rates 252
9.5 Conclusion of assessment of existing sediment transport models 254

Chapter 10 CONCLUSIONS AND RECOMMENDATIONS 256
10.1 New classification of coastal inlet systems 256
10.2 Inlet hydrodynamic analysis 257
10.3 Lagoon and estuarine tide analysis 257
10.4 Inlet stability 258
10.5 Inlet morphodynamics 258
10.6 Assessment of the state of the art of numerical morphological modelling 259
10.7 Experiments of sand barrier dynamics under waves & currents and assessment of existing sediment transport formulae 259
10.8 Recommendations 261
10.8.1 Application of research findings 261
10.8.2 Matters for further research 261
REFERENCES 262
APPENDICES 283
APPENDIX 1 Details of NSW estuaries in different groups presented using the classification of Roy et al. (2001) and Heap et al. (2001) and arranged from small to larger values of $Q_{tide}/\sqrt{gH^5}$ 284
APPENDIX 2 Details of the US estuaries from Powell (2006) and CIRP used for constructing equilibrium relationships in Figure 5.6, 5.7 and 5.19 293
APPENDIX 3 Available data during closure events and their fitting curves for T_{morph} presented in Table 6.1 (Avoca 1 and Avoca cf. Section 4.1) 296

List of tables

Page

Table 1.1: Classification of coastal lagoons based on the isolation level restricted by the barrier…3

Table 1.2. Three groups of NSW estuaries based on $\frac{\widehat{Q}_{\text{tide}}}{\sqrt{gH^5}}$ and $\frac{Q_{\text{f}}}{\sqrt{gH^5}}$ ……..14

Table 2.1. Results of $F(\omega)$ for different case of Q_f and A_b…… 41

Table 3.1. Comparison of initial and estimated timescales for three scenarios. ……73

Table 3.2. G_1, G_2 and phase lag φ_1, φ_2 for case φ_{o2}=0 andφ_{o2}=π …….....79

Table 5.1. Flood shoal volume and area versus spring tidal prism……... 126

Table 5.2. The overall criteria for inlet stability in terms of by-passing capacity …….131

Table 6.1. Summary external forces and T_{morph} for 13 closure events……... 170

Table 7.1: Summary of chosen model parameters…….....193

Table 7.2: The average sediment transport for 3 periods……...207

Table 8.1: Wave parameter for two period and two zones……... 217

Table 8.2: Summary current statistic parameters……...225

Table 8.3. Summary measured and calculated ripple dimension on top of the sand bar.....227

Table 9.1: Summary q_s by different model in compare with measured q_s at x=8.5m ($10^7 m^2/s$)....247

Table 9.2: Results of qs (107 m2/s) by different models along the sand barrier for case W1.....253

Appendix 1.1: Group of 35 Wave dominated estuaries (WDE) in NSW.....285

Appendix 1.2: Group of 16 Wave dominated delta (WDD) in NSW.....287

Appendix 1.3: Group of tide dominated estuaries (TDE) in NSW..... 288

Appendix 1.4: 100 ICOLLs in NSW..... 289

Appendix 2.1: Details of the US estuaries from Powell (2006).....294

Appendix 2.2: Details of the US estuaries from CIRP.....295

List of Figures

Page

Figure 1.1: Sand Cut inlet, Florida, USA (Google Earth image). 1

Figure 1.2: Morphological features of a tidal inlet system (Smith, 1984) 2

Figure 1.3: Classification of inlet shapes based on influence of waves, tide and river flow 5

Figure 1.4: Hydrodynamics based classification of tidal inlets (after Hayes, 1979). 6

Figure 1.5: Inlet classification in terms of relative wave strength to tide $\frac{\sqrt{gH^5}}{Q_{\text{tide}}}$ and relative freshwater to tide $\frac{Q_{\text{f}}}{Q_{\text{tide}}}$ 8

Figure 1.6: The Manning River mouth at Harrington, NSW, Australia. An example of high wave energy environment. 9

Figure 1.7: The Wadden Sea, NL. An example of mixed energy environment 10

Figure 1.8: Yangtze-Kiang, China: An example for highly tide-dominated coast with low wave energy and a large $\overline{Q_{tide}}$, tidal amplitude = 3.8m. 10

Figure 1.9: Three neighbouring inlets at 20°49'S 116°26'E in Western, Australia. In this area the spring tidal amplitude is around 2.2m and the tides are predominantly semi-diurnal. The mean significant wave height is of the order 0.7m. 11

Figure 1.10: Classification in terms of $\frac{\hat{Q}_{\text{tide}}}{\sqrt{gH^5}}$ and $\frac{Q_{\text{f}}}{\sqrt{gH^5}}$ for 178 estuaries in NSW, Australia. 15

Figure 2.1: A single inlet, single lake (node) - bay system. 17

Figure 2.2: Due to their different patterns of high tides, very different overwash potential results from tides of the fixed amplitudes (a_{o1}, a_{o2}) but different phase lag φ_{o2}. 19

Figure 2.3: Mixed tides resultant of two rotating vectors (diurnal, semi-diurnal) in the complex plane for the particular case of $\varphi_{o2} = 0$ 19

Figure 2.4: Complex vector illustration of the very different bichromatic tides with fixed (a_{o1}, a_{o2}) 20

Figure 2.5: The frequency response function $F(\omega)$ in the complex plane. 21

Figure 2.6: Tidal wave propagation in a tapering (converging) estuary. 21

Figure 2.7: Tidal range dampened significantly from 1.3m in the ocean to 0.2m inside Lake Conjola. 22

Figure 2.8: Phase difference between u and η for different wave 22

Figure 2.9: Lake Conjola, NSW, Australia where a significant flood event driven by wave overwash occurred in April 2006. 24

Figure 2.10: Wave overwashed at the entrance of Lake Conjola, flooding in Caravan Park 24

Figure 2.11: Two flow regime of Weir model applied for inlet. 25

Figure 2.12: $F(\omega)=f(a_o)$ based on Eq (2.36) with $0 < a_o < 2.2$m. 32

Figure 2.13: The influence of river flow velocity in non-linear friction term (2.37). 33

Figure 2.14: Comparison between the non-linear friction term $|u|u$ and the Fourier expansion in eq (2.38) and linearized in eq (2.42) with $v/\hat{u}$ =-1. 34

Figure 2.15: $F(\omega)$ corresponding to the friction free equation (2.47) and friction dominated (2.48). 36
Figure 2.16: $F(\omega)$ corresponding to T_1/T_2=0.33, T_1/T_2=1 calculated from Eq (2.44) and results from numerical solution of the non-linear Eq (2.18) with T_1/T_2= 8.8 37
Figure 2.17: Relation between T_1/T_2 and ωT_2 corresponding to different damping coefficient D of Walton and Escoffier (1981)..... 38
Figure 2.18: η_b calculated from two models: weir and finite-channel-length with L_c = 600m and z_{cr} = -0.3m from η_o 39
Figure 2.19: Results of $F(\omega)$ in comparison with the inertial free (2.48) with the numerical solution for the weir model and the finite-channel-length model solution..... 40
Figure 2.20: Different bay type results in change of A_b as the mean water level increases. 41
Figure 2.21: Different trend of $F(\omega)$ by changing Q_f and A_b (left), Q_f+A_b (right), eq (2.48). 42
Figure 2.22: Diurnal $F_1(\omega)$ for different cases of increasing z_{cr} from -2m to 0.1m,..... 43
Figure 2.23: Semi-diurnal $F_2(\omega)$ for z_{cr} increasing from -2m to 0.1m and 44
Figure 2.24: Results of $F_1(\omega)$ and $F_2(\omega)$ corresponding to Q_f increasing from 0 to 15m^3/s and z_{cr} reduce from 0 to -0.2m, Q_f reducing from 15 m^3/s to 0 z_{cr} increasing from -0.2m back to 0. 45
Figure 2.25: Location of Lake Conjola, NSW, Australia. 46
Figure 2.26: Closer view of Lake Conjola's entrance and location of tidal gauge. 47
Figure 2.27: Available data for the event from 6th to 11th April 2006. 48
Figure 2.28: Water levels at different locations at Lake Conjola in the event Dec 2008..... 48
Figure 2.29: Sketch of calculation scheme for two node model. 49
Figure 2.30: Notation and run-up scaling (L_R) for berm overwash..... 50
Figure 2.31: Results of overwash flow rate q_{over}(m^2/s) by different models 53
Figure 2.32: Results of water levels from different overtopping models..... 54
Figure 3.1: Example of moving 24.5 hour window for Avoca lake water levels 61
Figure 3.2: Example of exponential curves fitted to $\overline{\eta_{24.5}}(t)$ and $Stdv_{24.5}(t)$ for a closure event ... 62
Figure 3.3: Example of exponential fitting curves for $G_2(t)$ for Brunswick Heads, Au 63
Figure 3.4: $1/F_j(\omega)$ in the complex plane..... 64
Figure 3.5: Gain and phase difference without de-trending before harmonic analysis for Brunswick Head during flood event May 2009. 66
Figure 3.6: Linear de-trending in each window. 67
Figure 3.7: Results of Gain and phase difference with linear de-trending before harmonic analysis for Brunswick Head during flood event May 2009. 67
Figure 3.8: Harmonic analysis using 24.5 hour moving window for data series having exponential trend y=1-e$^{-t/T}$ with different values of the time constant T. 68
Figure 3.9: Comparison between results of amplitude and phase for diurnal and semi-diurnal by using 24.5 hour moving window with linear de-trending for data series having exponential trend with original data..... 69
Figure 3.10: Results from using 24.5 hour moving window with removing average de-trending method for data series having exponential trend. 70
Figure 3.11: Gains and phase differences obtained with de-trending by removing average before harmonic analysis for Brunswick Heads during the May 2009 flood event. ... 70

Figure 3.12: Gain and phase lag with de-trending by removing $\overline{\eta_{24}}(t)$ using 24 hour moving window for Brunswick Heads during flood event May 2009. 71
Figure 3.13: Gain and phase difference with de-trending by removing average using 25 hour moving window for Brunswick Heads during flood event May 2009. 72
Figure 3.14: Gain and phase difference with de-trending by remove average using 49 hour moving window for Brunswick Heads during flood event May 2009. 72
Figure 3.15: Case 1, input T_a=T_d=50 hours, output T_a=50 hours, T_d=48.7 hours. 74
Figure 3.16: Case 2, input T_a=70 hour s> T_d=50 hours, output T_a=70 hours, T_d=57 hours..... 75
Figure 3.17: Case 3, input T_a=50 hour s < T_d=70 hours, output T_a=50 hours, T_d=60 hours..... 75
Figure 3.18: G_1 and G_2 generated by the 24.5 hour window method for Avoca Closure Event 3 during Apr 2011 after de-trending η_b. 76
Figure 3.19: Response functions F_1 (left) and F_2 (right) after de-trending η_b for Avoca Closure Event 3. 77
Figure 3.20: Phase difference between ocean semi-diurnal and diurnal for Avoca Closure Event 3. 78
Figure 3.21: Ocean tides and bay tides generated by modified weir model with φ_{o2}=0. 78
Figure 3.22: Ocean tides and bay tides generated by modified weir model with φ_{o2}=π. 79
Figure 3.23: Response function F_1 with loop generated by changing φ_{o2}-φ_{o1} from 0 to 2π, z_{cr}=0 .. 79
Figure 3.24: Response function F_1 with loop size depending on z_{cr} in the complex plane. 80
Figure 4.1: Avoca Lake, NSW, Australia. 81
Figure 4.2: Lagoon tides showing four closure events in Avoca Lake during July 2010 to July 2011. 82
Figure 4.3: Data of closure Event 3 from 26 Apr 2011 to 3 May 2011: ocean tides, lake tides, significant wave height H_s, daily rain fall and run up calculated by Eq (2.56). 84
Figure 4.4: $\overline{\eta_{24.5}}(t)$ and $Stdv_{24.5}(t)$ of ocean tide, lake tide for Event 3 together with two exponential fitting curves of $\overline{\eta_{24.5}}(t)$ & $Stdv_{24.5}(t)$ for the lake. 84
Figure 4.5: Water levels, wave height, daily rain fall and wave run up for closure Event 1 (Jul 2010). 85
Figure 4.6: $\overline{\eta_{24.5}}(t)$ and $Stdv_{24.5}(t)$ with fitting curves for Event 1 (Jul 2010). 85
Figure 4.7: Gains and phase lags of the two 24.5-hour tide components for Closure Event 3..... 87
Figure 4.8: Tracks of F_1 (diurnal) and F_2 (semi-diurnal) in the complex plane for Closure Event 3. 87
Figure 4.9: Gains and phase lags of the two 24.5-hour harmonic components for 89
Figure 4.10: The tracks of F_1 (diurnal) and F_2 (semi-diurnal) in the complex plane for Avoca closure Event 1. 89
Figure 4.11: Amplitude of two tidal components for Avoca Closure Event 1 with the G_1>1-point indicated by the box. 90
Figure 4.12: The hydraulic time constant T_1, defined in Eq (3.14) for semi-diurnal for two closure events. 90
Figure 4.13: The Brunswick River entrance with the BHTG tide gauge about 630 m from the ends of the breakwaters. 91
Figure 4.14: Available H_{sig}, ocean water levels $\eta_O(t)$ at Coffs Harbour, tide levels at the BHTG $\eta_R(t)$ and tidal anomalies at the BHTG from 15/5 to 6/6/2009. 92

Figure 4.15: Daily rainfall [mm] at Myocum, May 2009..... 93
Figure 4.16: $\overline{\eta_O}(t)$, $\overline{\eta_R}(t)$, $Stdv_O(t)$, $Stdv_R(t)$ from 24.5 hour moving window analysis and mean super-elevation of the BHTG above the ocean: $\overline{\eta_R}(t)$ - $\overline{\eta_O}(t)$ for the May 2009 event at Brunswick Heads. 94
Figure 4.17: Ocean water levels at Coffs Harbour and at the BHTG after removal of the 24.5 hour means. 94
Figure 4.18: Gains and phase lags of the two tidal components obtained with a 24.5 hour moving window together with fitting exponential function for G_2 to obtain T_{morph}=76 hours..... 95
Figure 4.19: The tracks of F_1 and F_2 in the complex plane for the considered May 2009 event. ... 96
Figure 4.20: Amplitudes of the diurnal and semi diurnal tidal components at BHTG, and the ocean at Coffs Harbor 97
Figure 4.21: Oblique aerial photo of Lake Conjola – pre 1998 (MHL). 98
Figure 4.22: Available data for the event from 6th to 14 April 2006 at Lake Conjola: measured bay tides at gauge 1.3 km from the entrance, η_b at Jervis Bay and H_{rms} at Sydney. . 99
Figure 4.23: $\overline{\eta_{24.5}}(t)$ and $Stdv_{24.5}(t)$ for April 2006 event at Lake Conjola..... 100
Figure 4.24: Ocean and bay water levels before and after removal of the 24.5 hour means at Conjola. 101
Figure 4.25: Gain and phase lag for diurnal and semi-diurnal lake tides obtained with 24.5h moving window. 101
Figure 4.26: The tracks of F_1 and F_2 in the complex plane for the April 2006 event at Lake Conjola. 102
Figure 4.27: Amplitude of two components for ocean and bay tides for April 2006 event at Conjola..... 104
Figure 4.28: G_2 aid $\overline{\eta_b}(t)$ and $Stdv_b$ with exponential curves fitted, yielding T_{morph}= 33.6 hours by fitting $\overline{\eta_b}(t)$ and T_{morph}=16.7 hours by fitting G_2. ... 104
Figure 4.29: Pensacola pass, Florida, US image from Google Earth relative to the track of Hurricane Katrina (2005), the yellow point is Pensacola tidal station. 105
Figure 4.30: Ocean Water level at Dauphin station, Bay water level at Pensacola, and H_s at 21 m depth, from 21 July to 11:15 20 September 2005 including Hurricane Katrina from 28 August to 31 August 2005. 106
Figure 4.31: Ocean Water level at Dauphin station, Bay water level at Pensacola, Short period: 8:00 27 August to15:15 4 September 2005. 107
Figure 4.32: $\overline{\eta_{24.5}}(t)$ and $Stdv_{24.5}(t)$ of ocean and bay tides by 24.5 hour moving window..... 108
Figure 4.33: De-trended ocean and bay water level after removing $\overline{\eta_{24.5}}(t)$ 109
Figure 4.34: Gain and phase lag of the diurnal tide obtained by 24.5 hour moving window. 110
Figure 4.35: Amplitude of diurnal: a_{o1} for ocean tides, a_{b1} for bay tides..... 110
Figure 4.36: G_2 and φ_2 obtained by 24.5 hour moving window. 111
Figure 4.37: G_1 and φ_1 for the short period: 8:00 27 August to15:15 4 September 2005..... 111
Figure 4.38: The tracks of F_1 correspond to the dominant mode and is therefore less erratic than F_2 for short period: 8:00 27 August to15:15 4 September 2005..... 112

Figure 5.1: Top view of Wonboyn inlet from the rocks on the southern side, NSW, Au in December 2010, the inlet looks the same at every high water slack, reference to the star pickets. 116
Figure 5.2: Wonboyn inlet at low tide in December 2010. 117
Figure 5.3: Canh Duong inlet, Hue, Vietnam 117
Figure 5.4: Image of Pambula Lake from Google Earth 2006. 118
Figure 5.5: Concept of inlet stability. 119
Figure 5.6: V_{Ebb} versus the *relative tidal strength* $\frac{\hat{Q}_{tide}}{\sqrt{gH^5}}$ with 95% confidence limits for 22 natural inlets on the coast of Florida, USA 125
Figure 5.7: V_{Flood} versus tidal dominance measured by $\hat{Q}_{tide}/\sqrt{gH^5}$ with 95% confidence limits for 23 natural inlets on the coast of Florida, USA 126
Figure 5.8: Escoffier's diagram or "the inlet closure curve". 127
Figure 5.9: The dependence of equilibrium on forcing processes based on model results of Thuan An inlet, Hue, Vietnam (Stive et al., 2009) 129
Figure 5.10: Inlet by passing 130
Figure 5.11: Model of inlet bypassing for mixed energy coasts 132
Figure 5.12: Price Inlet, South Carolina, USA – an example of FitzGerald's stable inlet processes mechanism. 133
Figure 5.13: Breaches Inlet, South Carolina, USA – an example of FitzGerald's ebb tidal delta breaching mechanism 134
Figure 5.14: Flow pattern due to inlet geometry. 135
Figure 5.15: Locations for observations of water levels and currents at Canh Duong inlet 136
Figure 5.16: Observed water levels and currents obtained from the instruments. 137
Figure 5.17: Distribution of flow velocities at upstream transect S_1 and downstream transect S_2 measured at around 12:00 using FlowQuest 600 137
Figure 5.18: The relationship between $\frac{A}{\hat{Q}_{tide}}$ and $\frac{1}{w_s}$ for the data set 27 natural inlets without jetties on the coast of Florida, USA. 140
Figure 5.19: Relation between A versus $\frac{\hat{Q}_{tide}}{\sqrt{gH}}$ with 95% confidence limits for inlets at equilibrium. 142
Figure 6.1: Inlet opening and closing process. 146
Figure 6.2: The sketch of the Inlet reservoir model concept. 151
Figure 6.3: Seasonal variation of mean monthly rainfall in Hue province 152
Figure 6.4: Concepts of the seasonal opening/ closure cycle of an inlet 153
Figure 6.5: Escoffier diagram extended for seasonal variation of the closure curve 155
Figure 6.6: Escoffier diagram extended for seasonal variation of the equilibrium curve 157
Figure 6.7: Example of the basically non-seasonal variations of Ocean tides, offshore wave heights, and rainfall along the coast of NSW Australia. 159
Figure 6.8: Werri lagoon Estuary, surface area A_b= 0.142 km^2, catchment area 16.5 km^2 160
Figure 6.9: A year worth of tides recorded in Werri Lagoon 161

Figure 6.10: Fraction of time open and average time staying open plotted against the relative tidal dominance, based on tide potential. 162
Figure 6.11: According to (6.1) a morphological element adjusts in an exponential fashion towards its asymptotic form. 164
Figure 6.12: Convolution of $x(t)=\begin{cases}0 & for\, t<0\\ 500 & for\, t>0\end{cases}$ with T=10 hours ; 165
Figure 6.13: Convolution of $x(t)=\sin\omega t$ with $\omega T=1$. T= 1.9h. ω= 0.523rad/h. 166
Figure 6.14: $\hat{Q}_{tide}(t)$- thick line and $H(t)$-thin line with one large hurricane event. 167
Figure 6.15: Time series of $x_A(t)$ based on $H(t)$, $\hat{Q}_{tide}(t)$ and the corresponding $y_A(t)$ with T_{morph}=30 days =360 hours. 167
Figure 6.16: Time series of $x_{Vebb}(t)$ based on $H(t)$, $\hat{Q}_{tide}(t)$ and the corresponding $y_{Vebb}(t)$ with T_{morph}=30 days =360 hours. 169
Figure 6.17: T_{morph} vs $\frac{\sqrt{gH^5}}{\bar{Q}_{tide,pot}}$ with 95% confidence limits of 13 closure events corresponding to 7 NSW inlets with A_b<0.7 km^2. 171
Figure 6.18: The Limfjord estuary, Denmark is connected to the North Sea through the Thyborøn inlet. 173
Figure 6.19: Water levels in the North Sea (Ocean tides) and Thyborøen station. 173
Figure 6.20: Gain G_2 and phase lag φ_2 of the primary component, and $\overline{\eta_{24.5}}$ by 24.5 hour moving window at Thyborøen station. 174
Figure 7.1: Location of the study area and the Domain area for CMS-Flow and CMS-Wave for Pensacola Pass. 177
Figure 7.2: Average profiles of Fort Pickens units for May 2004 (Pre-Ivan), September 2004 (Post-Ivan) and July 2006 (recovery). 178
Figure 7.3: Pensacola inlet images before Katrina (2/2005) and after Katrina 1/3/2006 from Google Earth. 179
Figure 7.4: Flow chart of the CMS morphodynamics modeling process. 181
Figure 7.5: Sketch of the adaptation of q_s from non-equilibrium to equilibrium. 183
Figure 7.6: Flow domain, boundary and grid (196×190), size 10×15 m - 150×150 m, ... 186
Figure 7.7: Location of tidal gauses (WL) and wave buoys (W). 187
Figure 7.8: Observed and calculated water levels at Pensacola in March 2004. 189
Figure 7.9: Comparison among calculated and observed water levels at Pensacola station 189
Figure 7.10: Water levels and velocity field in the domain by wave and flow steering at peak storm time. 190
Figure 7.11: Significant wave height H_s, peak period T_p and wind speed during the storm. 191
Figure 7.12: Wave field by using Manning friction coefficient n=0.025 and n=0.07 corresponding to peak wave at boundary. 191
Figure 7.13: Results of wave field by Battjes & Janssen, (1978) wave breaking formulae corresponding to peak waves at the boundary. 192
Figure 7.14: Morphology change by total load equilibrium model with sediment transport Watanabe's formula and Lund-CIRP 194
Figure 7.15: Morphology change by A/D model with different concentration profile and 196

Figure 7.16: Representative tide (red color) in 28 days measured water levels 197
Figure 7.17: Wave roses for all incoming waves and waves range from $0.8\overline{H_s} < \overline{H_s} < 1.2\overline{H_s}$ from 2000 - 2010. 197
Figure 7.18: Boundary and calculated water levels; H_s for 1032 hours simulation including Hurricane Katrina..... 198
Figure 7.19: Calculated velocity at the middle point of the entrance. 199
Figure 7.20: Morphology change after simulation period of 1032 hours..... 200
Figure 7.21: Three most dynamic regions considered for further investigation..... 201
Figure 7.22: Comparison $Z_{change}(t)$ by 2 models for 4 areas of interest..... 202
Figure 7.23: Comparison of $Z_{cumchange}(t)$ by 2 models for 3 areas of interest. 203
Figure 7.24: Throat section at different times: (1) beginning of the simulation; (2) peak storm time, (3) 8 days after storm with A_{max} and (4) end of simulation 205
Figure 7.25: Throat area varying with time and 4 cross sections were shown in Figure 7.24. 206
Figure 7.26: Average sediment transport vector field for period 2. 208
Figure 7.27: Average sediment transport vector field for period 3. 209
Figure 7.28: Interested regions for calculation $\overline{q_s}$ during 3 periods. 210
Figure 7.29: $\overline{q_s}$ (10-3 m2/s) for different regions before, during and after storm. 210

Figure 8.1: View of the wave flume and the instruments (wave gauge and ADV). 214
Figure 8.2: Sketch of wave flume and locations of the wave gauges. 215
Figure 8.3: Grain size distribution of the sediment used in experiments. 216
Figure 8.4: Transformation of waves over the sand bar..... 218
Figure 8.5: Amplitude spectra at 5 locations of W1 and W4 219
Figure 8.6: H_{rms}/H_i for all wave cases with opposite currents. 221
Figure 8.7: H_{rms}/H_i for all combinations of 4 different wave cases and 6 different currents 221
Figure 8.8: U_{ave} -profiles at different locations along the sand bar..... 223
Figure 8.9: Phase average velocity at the point on center top of the barriers of W1 and W4 combined with strongest following and opposing current. 224
Figure 8.10: Ripple bed at top of the sand barrier for case W1 and W4..... 226
Figure 8.11: Calculated ripple height (η_r) by different formulae versus measurement. 228
Figure 8.12: Calculated ripple length (λ_r) by different formulae versus measurement. 228
Figure 8.13: Sampling lines for $Z_s(x,y)$. The transects (x_i) are chosen so that the sampling points along 'C' are alternately on ripple crests and troughs. 229
Figure 8.14: Sand bar profile before and after test for case W1+Q25 and W4+Q25. 230
Figure 8.15: Measured sediment transport rate along the sand barrier for W1 with two following currents Q = 10 L/s and Q=25 L/s 231
Figure 8.16: Measured sediment transport rate along the sand barrier for W1 with three opposing currents Q =-10, -20, -25 L/s. 232
Figure 8.17: Measured sediment transport rate along the sand barrier for W2 with three following currents Q=10, 20, 25 L/s. 233
Figure 8.18: Measured sediment transport rate along the sand barrier for W2 with three opposing currents Q =-10, -20, -25 L/s. 233

Figure 8.19: Measured sediment transport rate along the sand barrier for W4 with three following currents Q=10, 20, 25 L/s. 234
Figure 8.20: Measured sediment transport rate along the sand barrier for W4 with three opposing currents Q = -10, -20, -25 L/s. 234
Figure 9.1: Illustration of ripple migration of coarse sand and vortex ripple of fine sand. 237
Figure 9.2: Illustration of large pick-up function corresponding to large vertical velocity 244
Figure 9.3: Calculated sediment transport rate at x=8.5m by different models 246
Figure 9.4: Measured q_s versus velocity skewness R_u and acceleration skewness R_a. 248
Figure 9.5: Negative correlation with velocity skewness R_u in combinations of W1 249
Figure 9.6: Comparison between model results and measurements water levels and velocity for W1 250
Figure 9.7: Comparison between model results and measurements water levels and velocity for W4 with final bathymetry profile. 251
Figure 9.8: Comparision phase average velocity between measurement and model 251
Figure 9.9: Calculated q_s by different models along the sand barrier for case W1 252
Figure 9.10: Calculated q_s by different models along the sand barrier for case W4 254
Figure A3.1: Water levels, wave height, daily rain fall and wave run up for closure event 2 at Avoca Lake from 5/11/2010 to 28/11/2010. 297
Figure A3.2: Results of $\overline{\eta_{24.5}}(t)$ and $Stdv_{24.5}(t)$ with fitting curves for event 2. 297
Figure A3.3: Water levels, wave height, for closure event 5 at Avoca Lake from 24/04/2008 to 30/04/2008. 298
Figure A3.4: Results of $\overline{\eta_{24.5\,b}}(t)$, $Stdv_{24.5\text{-}b}(t)$ and $G_2$with fitting curves for event 5 298
Figure A3.5: Water levels and wave height for closure event at Wamberal from 29/04/2011 to 3/05/2011. 299
Figure A3.6: Results of $\overline{\eta_{24.5\,b}}(t)$, $Stdv_{24.5\text{-}b}(t)$ and $G_2$with fitting curves for G_2 T_{morph} =38.4h... 299
Figure A3.7: Water levels and wave height at Port Kembla for closure event1 at Werri from 07/11/2009 to 19/11/2009. 300
Figure A3.8: Results of $\overline{\eta_{24.5\,b}}(t)$, $Stdv_{24.5\text{-}b}(t)$ and $G_2$with fitting curves for G_2 T_{morph} =25h..... 300
Figure A3.9: Water levels and wave height at Port Kembla for closure event 2 at Werri from 01/04/2010 to 13/5/2010. 301
Figure A3.10:Results of $\overline{\eta_{24.5\,b}}(t)$, $Stdv_{24.5\text{-}b}(t)$ and $G_2$with fitting curves for G_2T_{morph} =54h 301
Figure A3.11:Water levels for closure event 1 at Dee Why lagoon 17/03/2012 to 16/4/2012. 302
Figure A3.12:Wave height and wave direction offshore Sydney for closure event 1 at Dee Why lagoon from 17/03/2012 to 16/4/2012. 302
Figure A3.13:Results of $\overline{\eta_{24.5\,b}}(t)$, $Stdv_{24.5\text{-}b}(t)$ and $G_2$with fitting curves for G_2 and $Stdv_{24.5\text{-}b}(t)$. 303
Figure A3.14:Results of G_2 and $Stdv_{24.5\text{-}b}(t)$ with fitting curves closer in closing process for event 1 at Dee Why lagoon 303
Figure A3.15:Water levels for closure event 1 at Dee Why lagoon from 18/4/2012 to 28/5/2012. 304
Figure A3.16:Wave height and wave direction offshore Sydney for closure event 2 at Dee Why lagoon from 18/4/2012 to 28/5/2012. 304

Figure A3.17:Results of $\overline{\eta_{24.5\,b}}(t)$, G_2 and $Stdv_{24.5\text{-b}}(t)$ with fitting curves for closure event 2 at Dee Why lagoon.. 305
Figure A3.18:Water levels and wave height at Sydney for closure event 1 at Terrigal from 18/1/2011 to 5/2/2011. 305
Figure A3.19:Results of $\overline{\eta_{24.5\,b}}(t)$, G_2 and $Stdv_{24.5\text{-b}}(t)$ with fitting curves for closure event 1 at Terrigal..... 306
Figure A3.20:Water levels for closure event 2 at Terrigal from 13/3/2012 to 24/3/2012. 306
Figure A3.21:Wave height and wave direction offshore Sydney for closure event 2 at Terrigal from 13/3/2012 to 24/3/2012. 307
Figure A3.22:Results of $\overline{\eta_{24.5\,b}}(t)$, G_2 and $Stdv_{24.5\text{-b}}(t)$ with fitting curves for closure event 2 at Terrigal. T_{morph} =120h from fitting $Stdv_{24.5\text{-b}}(t)$. 307
Figure A3.23:Water levels and wave height at Sydney for closure event at Cockrone from 21/6/2008-25/6/2008. 308
Figure A3.24:Results of $\overline{\eta_{24.5\,b}}(t)$, G_2 and $Stdv_{24.5\text{-b}}(t)$ with fitting curves for closure event at Cockrone 308
Figure A3.25:Water levels and wave height at Eden for closure event at Back lagoon from 14/12/2010-18/12/2010. 309
Figure A3.26:Results of $\overline{\eta_{24.5\,b}}(t)$, G_2 and $Stdv_{24.5\text{-b}}(t)$ with fitting curves for closure at Back lagoon. T_{morph} =99.3h from fitting $Stdv_{24.5\text{-b}}(t)$..... 309

List of Symbols

A	cross-sectional flow area (m²) or semi-excursion of wave orbital (m) in chapter 9
A_b	bay or lagoon surface area (m^2) or backward entrainment coefficient in chapter 9
A_c	inlet cross-sectional area (m^2)
A_{eq}	cross-sectional flow area at equilibrium state (m²)
A_f	forward entrainment coefficient in chapter 9
Arg	argument
a_b	tidal amplitude in the bay (m)
a_{b1}	tidal amplitude of diurnal component in the bay (m)
a_{b2}	tidal amplitude of semi-diurnal component in the bay (m)
a_o	tidal amplitude in the ocean (m)
a_{o1}	tidal amplitude of diurnal component in the ocean (m)
a_{o2}	tidal amplitude of semi-diurnal component in the ocean (m)
a_1	empirical coefficient of A-P relationships (a_1 dimension depends on the power n)
a	tidal amplitude in general (m)
B	surface width (m)
C	the Chézy roughness coefficient ($m^{0.5}/s$)
C_d	wind drag coefficient (dimensionless)
$C_{g,min}$	min group velocity (m/s)
C_o	reference concentration at the bed
C_{os}	C_o for sine wave of velocity amplitude U_1
c	sediment concentration [-]
D	dimensionless damping coefficient
D_E	dissipation energy (W/m)
D_s	ad-hoc bed slope coefficient
d	water depth below the reference level (datum) (m)
d_{50}	sediment median diameter (m)
E_f	energy flux (W/m)
e	Exponential function
F	dimensionless overall impedance of the inlet accounts for total the head loss:
f	Coriolis parameter (inertial frequency) (s^{-1}) or friction factor
$F(\omega)$	frequency response function
$F_1(\omega)$	frequency response function of diurnal component
$F_2(\omega)$	frequency response function of semi-diurnal component
F_x	friction components in x-direction (m/s²)
F_y	friction components in y-direction (m/s²)
G	gain of response function
G_1	gain of response function of diurnal component
G_2	gain of response function of semi-diurnal component
g	acceleration due to gravity (m/s²)
$\frac{\sqrt{gH^5}}{\bar{Q}_{tide}}$	dimensionless number of relative wave strength to tide [-]
H	wave height in general (m)
H_i	incoming wave height (m)
H_o	wave height in deep water (m)
$H_{o,rms}$	root mean square wave height in deep water (m)
H_s	significant wave height (m)
H_{ST}	significant wave height at toe of structure (m)
$\overline{H_s}$	average significant wave height (m)
h	total water depth, $h = d + \eta$ (m)
h_c	inlet channel depth (m)
h_{cri}	critical depth (m)

Im	imaginary part of complex number
i	imaginary unit, $i = \sqrt{-1}$
k	wave number
K_{en}	conveyance for inlet geometry in section 2.7
K_r	reflection coefficient
k_{en}	entrance loss
k_{ex}	exit loss
k_s	bottom roughness thickness [L]
L	length of sand hump (m)
L_b	adaptation length for bed load (m)
L_c	inlet length (m)
L_o	wave length in deep water (m)
L_R	run up vertical scales (m)
L_s	adaptation length for suspended load (m) chapter 7 or vertical scale of concentration distribution in chapter 9
L_t	total adaptation length (m)
l_m	mixing length [L]
n	empirical coefficient of A-P relationships or Manning's coefficient ($m^{-1/3}s$)
P	tidal prism (m³/tidal cycle) or sediment pick up function in chapter 7
P_a	atmospheric pressure (Pa, N/m²)
P_c	channel wetted perimeter (m)
P_{eq}	tidal prism at equilibrium state (m^3)
P_{x},P_{y}	atmospheric pressure (Pa)
p'_m	sediment porosity
Q	flow discharge in general or total flow rate through inlet including tides and river flows (m^3/s) in chapter 1
$\overline{Q}$	mean flow rate through inlet include tides and river flow (m^3/s)
$\hat{Q}$	maximum discharge (m^3/s)
Q_{en}	inlet entrance out flow in chapter 2 (m^3/s)
Q_f	river discharge (m^3/s)
$Q_{tide,actual}$	actual tidal flow (m^3/s)
$\frac{Q_{\text{f}}}{\hat{Q}_{tide}}$	dimensionless number of relative river strength to tide [-]
$\frac{Q_{\text{f}}}{\sqrt{gH^5}}$	dimensionless number of relative river strength to wave [-]
Q_g	gross longshore transport rate arriving in inlet [L^3T^{-1}]
Q_{over}	overwash flow across the berm by large waves (m^3/s)
Q_s	sediment transport rate (m^3/s)
$Q_{s,x}$	sediment transport rate in x direction (m^3/s)
$Q_{s,y}$	sediment transport rate in y direction (m^3/s)
$\overline{Q_{sy}}$	total annual littoral drift (m^3/year)
$\hat{Q}_{tide}$	peak tidal discharge (m^3/s)
$\overline{Q_{tide}}$	mean tidal discharge (m^3/s)
$\frac{\hat{Q}_{tide}}{\sqrt{gH^5}}$	dimensionless number of relative tide strength to wave [-]
$\hat{Q}_{tide,pot}$	maximum potential tidal flow (m^3/s)
q	flow rate per unit width (m^2/s)
q_b	bed load transport rate per unit width (m^2/s)
q_s	suspended load transport rate per unit width (m^2/s)
$q_{s,eq,}$	equilibrium sediment transport rate per unit width ($m^3/s/m$),

$q_{s,x,}$	sediment transport rate per unit width in x directions (cross shore) (m^3/s/m)
$q_{s,y,}$	sediment transport rate per unit width in y directions (long shore) (m^3/s/m),
q_{tot}	total load transport rate per unit width (m^2/s)
R	hydraulic radius (m)
R^2	squared of correlation coefficient
Re	real part of complex number
R_t	tidal range in general (m)
R_{tb}	bay tidal range (m)
R_{to}	tidal range in the ocean (m)
Ru	skewness number by Ribberink & AlSalem (1994)
r'	bypassing criteria [-] in chapter 5
r	hydraulic roughness [L] in chapter 9
r_s	fraction of suspended sediments
S_f	friction slope
$Stdv_{24.5}$	standard deviation calculated by 24.5hour moving window (m)
S_{wx}	component of acting force on unit mass water body caused by radiation stresses in x-directions (m/s²)
S_{wy}	component of acting force on unit mass water body caused by radiation stresses in y-directions (m/s²)
S_{xx}	radiation stress component transferring x-momentum through a plane x=constant (N/m)
S_{xy}	radiation stress component transferring y-momentum through a plane x=constant (N/m)
S_{yy}	radiation stress component transferring y-momentum through a plane y=constant (N/m)
s	sediment specific density (ρ_s/ρ)
$sign$	sign of function
T	time constance [T] in chapter 4
T	tidal period(s) in chapter 1, 3 or wave period in chapter 8, time constant chapter 2, 3, 6
T_1	time constant in chapter 2, describes the geometrical and frictional features of the system
T_2	time constant in chapter 2, period corresponding to Helmholtz frequency Ω_H
$T_{building}$	barrier building time scale [T]
T_{scour}	flood scour time scale [T]
T_{hyd}	hydraulic time scale [T]
T_{mean}	mean period of bound wave (s)
T_{morph}	morphodynamic time scale [T]
T_p	the wave period, e g, the peak spectral period (s)
$\overline{T_{open}}$	average length of time inlet stay open [T]
T_{tide}	tidal period [T]
t	time (s)
t_d	Time of u-zero-down-crossing (s)
t_u	Time of u- zero-up-crossing (s)
U	the magnitude of depth-averaged horizontal velocity vector, $U=\sqrt{u^2+v^2}$ (m/s)
U_1	amplitude of first sine wave velocity (m/s)
U_2	amplitude of second sine wave velocity (m/s)
U_{max}	maximum horizontal velocity (can be x or y direction) (cm/s)
U_{mean}	mean current velocity Q/A (cm/s)
U_{min}	minimum horizontal velocity (can be x or y direction) (cm/s)
U_n	amplitude of $u_n(t)$
U_x	transverse velocity component oriented normal to the flume side wall (cm/s)
U_x	horizontal velocity component, aligned longitudinally to the flow direction U_y (cm/s)
u	velocity (m/s)
$\hat{u}$	maximum velocity, velocity amplitude(m/s)
$\overline{u}$	mean tidal current or mean velocity in general (m/s)
$\tilde{u}$	periodic velocity driven by wave (m/s)
u_∞	free stream velocity (m/s)

u_*	friction velocity (m/s)
u, v	depth-averaged flow velocity in x-, y- directions (m/s)
u_s	horizontal velocity of sediment particle (m/s)
u_{wm}	maximum orbital wave velocity (m/s)
V	the wind speed at 10 m above the surface, $V = \sqrt{V_x^2 + V_y^2}$ (m/s)
V_x	component of wind speed in x-directions (m/s)
V_y	component of wind speed in y-directions (m/s)
$V_{c,eq}$	channel volume below MLW at equilibrium (m^3)
V_{change}	volume change of interested area between before and after simulation period or different time step (m^3)
V_{cr}	critical velocity (m/s)
V_{Ebb}	volume of ebb tidal delta (m^3)
V_{Flood}	volume of flood tidal delta (m^3)
V_{mm}	mean-maximum velocity through a stable inlet cross-section area (m/s)
$\overline{V}$	cross-section-averaged flow velocity
V_{morph}	mophodynamic volume [L^3]
v	constant run-off velocity of the river or overwash inflow (m/s)
var	variance
W	width of channel (m) (W_1, W_2 : width of cross section 1, 2 respectively)
W	width of inlet channel (m)
W_{eq}	width of the inlet at equilibrium [L]
w_m	mixing velocity (m/s)
w_s	sediment settling settling velocity (m/s)
X_{Ci},	x-coordinate of the crest of the ripple i in centre line (m).
X_{Ti}	x-coordinate of the trough of the ripple i in centre line (m).
$\overline{X_i}$	x-coordinate of mean profile (m)
x	Cartesian co-ordinate in the horizontal direction (m)
x	longitudal coordinate along channel axis (m)
y	Cartesian co-ordinate in the horizontal direction (m)
Z_b	bed elevation (m).
z_{berm}	berm elevation (m)
Z_c	elevation of point on the centre section corresponding to X_{Ci}(m)
Z_{change}	bed elevation change of interested area between before and after simulation period or different time step (m)
Z_T	elevation of point on the centre section corresponding to X_{Ti}(m)
$\overline{Z}_i$	z-coordinate of mean profile (m)
Z'_{Li}	elevation of point on the left of centre section corresponding to X_{Ti}(m)
Z'_{Ri}	z-coordinate of point right of the middle line corresponding to X_{Ti} (m)
z_{cr}	invert inlet level or weir level (m)
$Z_{cumchange}$	bed elevation change cumulative by time of interested area (m)
Z_{Li}	elevation of point on the left of centre section corresponding to X_{Ci}(m).
Z_{Ri}	z-coordinate of point right of the middle line corresponding to X_{Ci} (m)
α	transport related coefficient
α_c	empirical coefficient ($m^{-1.5}$)
β	beach slope (rad)
γ_r	reduction factor for turning model in section 2.7 [-]
Δ	pump height (m)
$\Delta\theta$	Shields parameter increase
ΔQ_s	gradient of sediment transport (m^3/s)
ε	horizontal eddy diffusion (m^2/s), or wave pump efficiency section 2.7 [-]
η	water surface elevation or water level with respect to the reference level (datum) (m)
η_o	ocean tidal water level (m)
$\overline{\eta_{24.5}}$	average water surface calculated by 24.5hour moving window (m)

η_b	bay tidal water level (m)
$\eta_{de\text{-}trended}$	de-trended water level after removed $\overline{\eta_{24.5}}$ from tidal records (m)
η_{finish}	water level at time inlet finish closing (m)
λ_{max}	maximum ripple length (m)
$\eta_{r,max}$	maximum ripple height (m)
η_{start}	water level at time inlet start closing (m)
η_t	wave set up (m)
Ω_H	Helmholtz frequency
θ	Shields mobility parameter or non-dimensional shear stress
$\theta_{2.5}$	Shields parameter corresponding to r=2.5d_{50}
$\widehat{\theta}_{2.5}$	Peak value of $\theta_{2.5}$
θ_c	critical Shields parameter
θ_I	inlet Shields mobility parameter
θ'	skin friction shields parameter
θ_r	Shields parameter account for ripple shape
κ	von Karman's constant, $\kappa \approx 0.4$
ν	kinematic fluid viscosity (m^2/s)
ξ_o	surf similarity parameter [-]
$\xi()$	impulse response function
ρ	water density (kg/m^3)
ρ_a	air density (kg/m^3)
ρ_s	sediment density (kg/m^3)
τ	shear stress (N/m^2)
τ_{bx}	bed shear stress in x direction (m^2/s)
τ_{by}	bed shear stress in y direction (m^2/s)
τ_{cr}	critical shear stress (N/m^2)
τ_{ix}	internal stress component in x -direction (m/s^2)
τ_{iy}	internal stress component in y-direction (m/s^2)
τ_{wx}	wind shear stress in x -direction ($kg/m/s^2$)
τ_{wy}	wind shear stress in y-direction ($kg/m/s^2$)
Φ	notation for a function
Φ_b	non-dimensional bed load
Φ	phase angle between near bed and free stream flow in chapter 9
φ_1	phase lag of diurnal component (rad)
φ_2	phase lag of semi-diurnal component (rad)
φ_{b1}	tidal phase of diurnal component in the bay (rad)
φ_{b2}	tidal phase of semi-diurnal component in the bay (rad)
φ_{o1}	tidal phase of diurnal component in the ocean (rad)
φ_{o2}	tidal phase of semi-diurnal component in the ocean (rad)
Ω	angular wave frequency (rad)
ω_{tide}	angular tide frequence (rad)
ω'	dimensionless tidal frequency

List of Abbreviations

ADV	Acoustic Doppler Velocimeter
AHD	Australian height datum
AL	Atlanta
AU	Australia
BHTG	Brunswick river tide gauge
CA	California
CERC	Coastal Engineering Research Centre
CIRP	Coastal inlets research program
CMS	Coastal modelling system
DHI	Danish Hydraulic Institute
GA	Georgia
HFT	high frequency terms
HT	high tide
ICOLL	Intermittently Closed and Opened Lakes and Lagoon
IHE	Institute for water education, Delft, The Netherlands
MHL	Manly Hydraulics Laboratory, NSW, Australia
MLLW	Mean lowest low water
MSL	Mean sea level
NAD83	North American datum of 1983
NAVD88	North American vertical datum of 1983
NC	North Columbia
NET	Non-equilibrium sediment transport
NJ	New Jersey
NLSE	Non-linear shallow water equations
NSW	New South Wales
NTC	National tide centre
OR	Oregon
RD	River dominated
RMSE	root mean squared error
SC	South Carolina
SWASH	Simulating Waves till Shore
SWL	still water level
TDE	Tide dominated estuaries
USACE	United States Army Corps of Engineers
VN	Vietnam
WA	Washington
WABED	Wave action balance equation diffraction
WDD	Wave Dominated deltas
WDE	Wave Dominated Estuaries
WRU	Water Resources University, Hanoi, Vietnam

Chapter 1

DESCRIPTION AND CLASSIFICATION OF INLETS

1.1 TOPOGRAPHICAL DEFINITIONS

A tidal inlet is, according to the definition in the Handbook of Coastal and Ocean Engineering (2010), a short, narrow waterway that connects an inland body of water such as a lagoon, bay, or estuary with a larger tidal body as a sea or ocean as shown in Figure 1.1.

Figure 1.1: Sand Cut inlet, Florida, USA (Google Earth image).

According to Bruun (1978), tidal inlets are normally divided into three main sections (cf. Figure 1.1):

a) the ocean section with $\tilde{u} \geq \bar{u}$ that may include outer shoals (ebb tidal delta) and bars and one or more channels, whose development is significantly influenced by the wave action with periodic velocity $\tilde{u}$ driven by waves, combined with weaker tidal currents $\bar{u}$.

b) the gorge with $0 \leq \frac{\tilde{u}}{\bar{u}} \leq 1$, which is the channel section having the minimum cross-sectional area and usually with less exposure to waves; and

c) the bay section ($\tilde{u} << \bar{u}$), which may include inner shoals (flood tidal delta) and channels, with dominant current influence and relatively little wave action.

Smith (1984) described comprehensively the morphological features of a tidal inlet system, with its longitudinal cross section X-Y as in Figure 1.2. Some elements may occur depending on the interaction amongst various factors such as tides, waves, river flows, sediment availability, topography and inlet geology in particular.

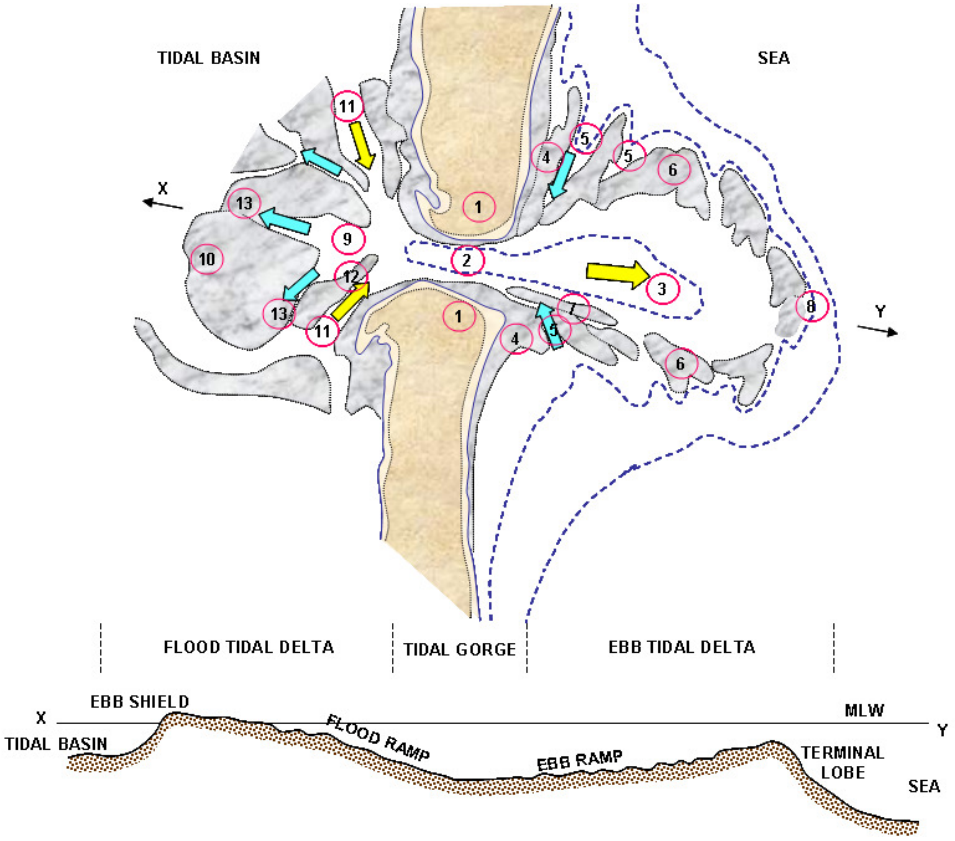

1) Coastal barrier or spit headland;
2) The tidal gorge;
3) The main ebb channel and ebb ramp;
4) Swash platforms;
5) Marginal flood channels;
6) Marginal shoals;
7) Ebb tidal levee;
8) Ebb delta terminal lobe;
9) The flood ramp;
10) The ebb shield;
11) Main ebb dominated inner channel;
12) Ebb spit;
13) Spill over channels

Figure 1.2. Morphological features of a tidal inlet system (Smith, 1984).

1.2 CLASSIFICATION OF COASTAL SYSTEMS

A tidal inlet works side by side with its associated inland water body in a united coastal system or estuary. They influence each other in several ways. It is not adequate to distinguish tidal inlets separately without considering the effects of the connected water body. Thus, classification of coastal systems in a broader view is necessary for management as well as research of tidal inlets. There are several methods to classify coastal systems based on different perspectives.

Burgess et al. (2004) records 25 different methods, which cover a large range of aspects to classify coastal systems in the USA. Barton et al. (2007) and Hale & Bucher (2008) reviewed comprehensively the classification for New South Wales (NSW) estuaries in Australia, mostly based on geomorphology, salinity and hydrology. Duck & Silva (2012) reviewed the classification of coastal lagoons in different perspectives, with an emphasis on hydro-morphology.

1.2.1 Geo-morphological classification

In geomorphological perspective, the classifications by Kierfve (1994) and Isla (1995) were based on the isolation level of coastal lagoons restricted by the coastal barrier. Each type presents its own hydro-morphological conditions and geo-morphological features (Table 1.1).

Table 1.1: Classification of coastal lagoons based on the isolation level restricted by the barrier.

Type of coastal lagoon	Dominant Hydro-morphological conditions	Dominant geo-morphological features
Coastal bay - no barrier	Macrotidal	Offshore sand ridges
Leaky lagoon- many wide tidal inlets	Mesotidal-tidal action similar to open ocean	Tidal flats dominate
Restricted lagoon- several tidal inlet	Mesotidal-tidal action through inlets restricted by wave action	Salt marshes dominated
Choked lagoon- narrow tidal inlets	Micro tidal- small tidal action through inlets; barrier washover by waves	Open water and intra-lagoon deltas

This classification is narrower and less quantitative compared to Hayes (1979), as shown in Figure 1.4.

Wright (1977) classified coastal systems first based on river dominance with three basic effluent behaviours:

1) outflow inertial with fully turbulent jets;

2) turbulent bed friction seaward of the mouth;

3) outflow buoyancy with effluent velocity near constant and strong outflow density stratification that govern the sediment deposition and morphologic pattern of the system.

Then the tide and wave forces modify the effluent and corresponding sediment transport and morphology for tidal dominated system and wave dominated system.

In the view of geologists and geomorphologists, the land-sea interface is the most important factor to classify coastal inlets which are lagoons, estuaries and deltas (Carter, 1989; Davies, 1980). This is quite similar to Figure 1.3 sketched by de Vriend et al. (1999).

With the same geomorphic view with biological criteria added, the Roy et al.'s (2001) scheme is widely used to classify estuaries within NSW. It comprises five groups of: 1) bays, 2) tide dominated estuaries, 3) wave dominated estuaries, 4) intermittent estuaries and 5) fresh water bodies with four states of sediment infilling of: A) youthful, B) intermediate, C) semi-mature and D) mature. Saintilan (2004) tested this scheme and assessed that it is an effective distinguishing method. Another scheme proposed by Heap et al. (2001) used the ratio of wave to tide energy at the entrance to classify 780 coastal systems around Australia. Their seven subclasses are quite similar to Roy et al. (2001) without sediment infilling states. Heap et al. (2001) did not separate intermittent systems in one class, but named a new class of 'strand plain'. Roper et al. (2011) compared two classification schemes in three main groups of lake, river, and lagoon with an associated conceptual model of the chlorophyll - a response to catchment load for 184 estuaries of NSW. Wave dominated estuaries is the main class within 130 estuaries based on the Heap et al. (2001) scheme, whereas small creeks and lagoon ICOLLs are the dominant group within 184 estuaries identified by Roy et al. (2001).

The decision of which classification scheme to be followed depends on the perspective and interest of managers or researchers. Nowadays, the classification based on hydro-morphological perspective related to ecological parameters has become a fashionable trend since the sustainability of the environment is given more attention. In the present study, the emphasis is on hydraulics and morphodynamics.

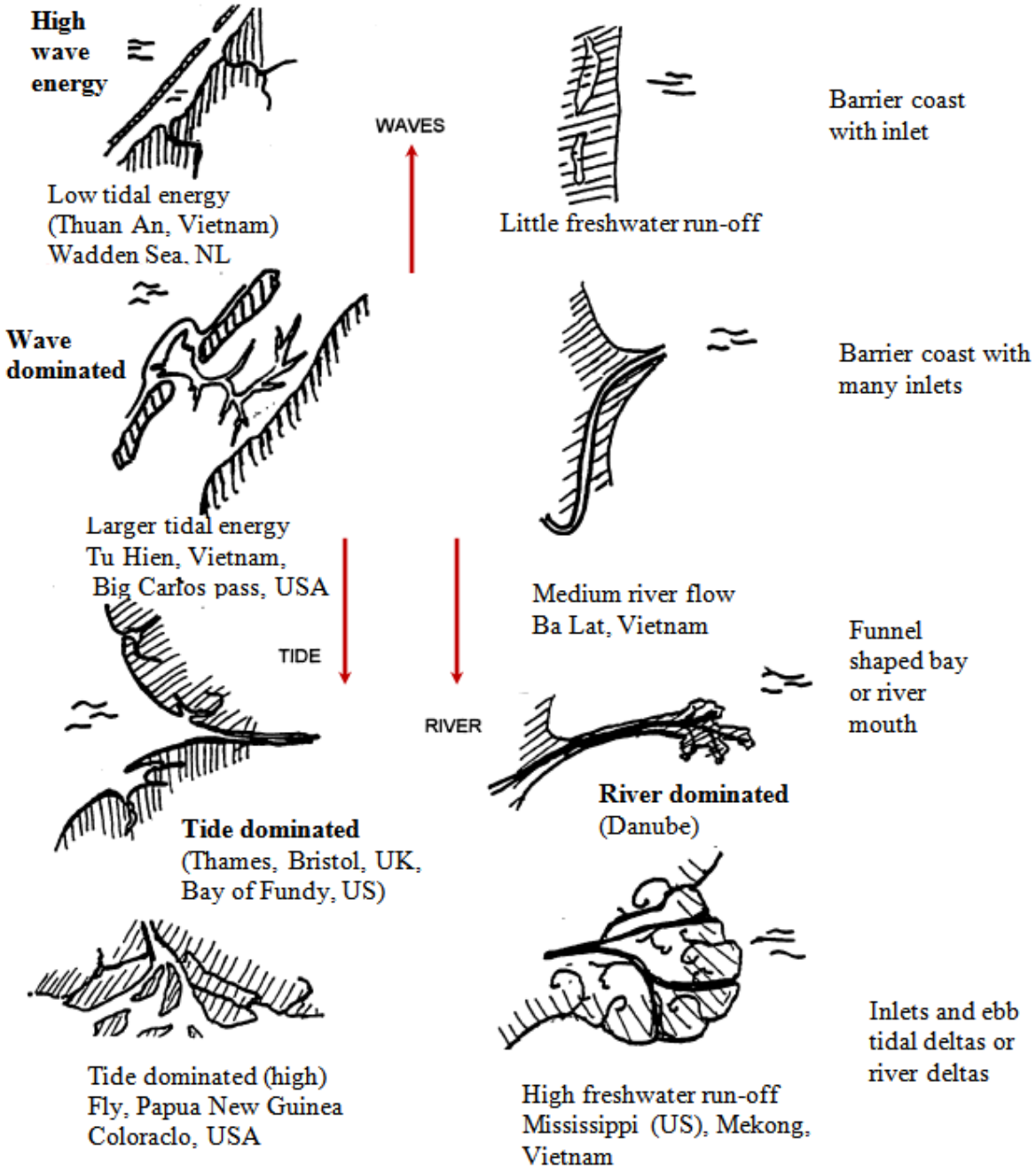

Figure 1.3: Classification of inlet shapes based on influence of waves, tide and river flow (De Vriend et al, 1999).

1.2.2 Hydrodynamic classification of inlets

The exchange of water through an inlet can be caused by the tide, wind, seiches, and by river flow, together with wind waves. Of the major three; tides, waves and freshwater, the tides are the most regular while waves and freshwater flow are more episodic or seasonal. Therefore, when searching

for a driver of the typical or perhaps the 'equilibrium' state of an inlet, the first candidate for 'the main driver' has been the tide. Hence, O'Brien (1931, 1969) correlated inlet throat area A with the volume P of the tidal prism and many subsequent studies have confirmed that there is indeed such a correlation.

It is however broadly agreed that the shaping of an inlet is, in general, the result of at least three significant drivers; tides, waves and freshwater as indicated by the conceptual map (Figure 1.3) of de Vriend et al. (1999). The question is then: How do we quantify the relative strength of these drivers?

The influence of the river discharge compared with the tidal flow is logically assessed by considering the ratio between the peak or mean tidal discharge ($\hat{Q}_{tide}$ or $\overline{Q}_{tide}$) and the river or freshwater discharge Q_f. When $\overline{Q_{tide}} / Q_f \geq 20$, the flow is said to be tide-dominated and the inlet is considered as a tidal inlet.

The hydrodynamic classification of inlets by Hayes (1979) (Figure 1.4) measures the relative strength of waves versus tides in terms of the wave height H and ocean tidal range R_{to}.

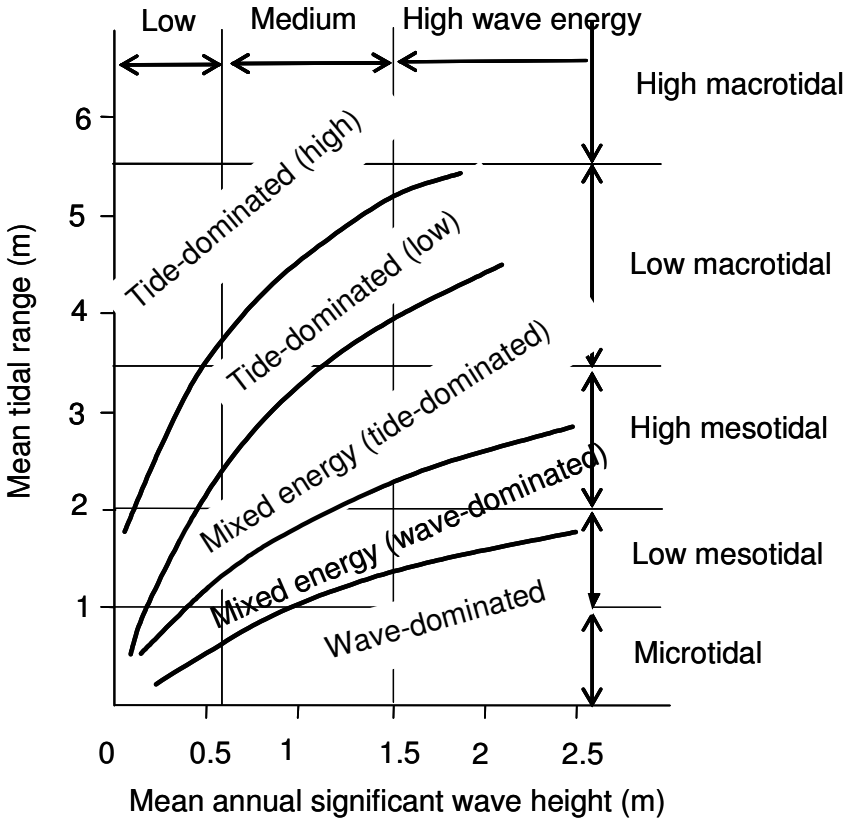

Figure 1.4: Hydrodynamics based classification of tidal inlets (after Hayes, 1979).

This is an obvious choice perhaps and fairly qualitative, but not an entirely satisfactory one with respect to the nature of the tides as a morphology driver. That is, for a given tidal range, semi-diurnal tides drive twice as large $\hat{Q}_{tide}$, $\overline{Q}_{tide}$ and generate twice as large velocities through the inlet compared with diurnal tides. In other words, the tidal period or angular frequency $\omega_{\text{tide}}=2\pi/T_{\text{tide}}$ is important. The Heap et al. (2001) classification takes into account both tidal period and wave period via wave and tidal energy, which do not consider the influence of the bay surface area A_{b}. In the following equation, the strength of the tides as morphology drivers is presented in terms of the peak tidal discharge:

$$\hat{Q}_{\text{tide}} = \omega_{\text{tide}} a A_b \tag{0.1}$$

where the tidal amplitude a may be the actual amplitude in the bay a_{b} or the amplitude in the ocean a_{o}. Using a_{b} corresponds to using the actual tidal prism in O'Brien's formula, which includes more detailed geo-features of the individual bay and the entrance, and we refer to the corresponding peak discharge as the *actual* peak discharge,

$$\hat{Q}_{\text{tide, actual}} = \omega_{\text{tide}} a_b A_b \tag{0.2}$$

as opposed to the *potential* peak tidal discharge, which is an external parameter with respect to inlet morphology

$$\hat{Q}_{\text{tide, pot}} = \omega_{\text{tide}} a_o A_b \tag{0.3}$$

The question then is: How to compare peak tidal discharge with waves as inlet morphology drivers? There are two fairly obvious, dimensionally correct choices and the simplest one is $\sqrt{gH^5}/\hat{Q}_{\text{tide}}$, which compares $\hat{Q}_{\text{tide}}$ to the sediment transporting capacity of the waves as per the CERC formula for littoral drift, see e.g. Nielsen (2009) p 271. A slightly more complicated measure is $gTH^2/\hat{Q}_{\text{tide}}$, which brings in the wave period T, which is known to be important in relation to runup height (Nielsen, 2009, p 126) and the waves' ability to build berms (Takeda and Sunamura, 1982), which may eventually close inlets. Alternatively, T can be brought in by replacing the wave height in $\sqrt{gH^5}/\hat{Q}_{\text{tide}}$ by the runup scale $\sqrt{HL_0} = \sqrt{H\frac{gT^2}{4\pi}}$ which leads to $\frac{\sqrt{g(HL_0)^{2.5}}}{\hat{Q}_{\text{tide}}} \sim \frac{\sqrt{g^{3.5}H^{2.5}T^5}}{\hat{Q}_{\text{tide}}} = \frac{g^{1.75}H^{1.25}T^{2.5}}{\hat{Q}_{\text{tide}}}$. Unfortunately, the presently available data does not enable a definitive choice of the best among these relative wave strengths. However, using the simplest, the sketch of de Vriend et al. (1999) in Figure 1.3 is then quantified in dimensionless

terms as in Figure 1.5 in which the horizontal axis indicates river flow dominance, the vertical axis indicates wave dominance and closeness to the origin indicates tidal dominance.

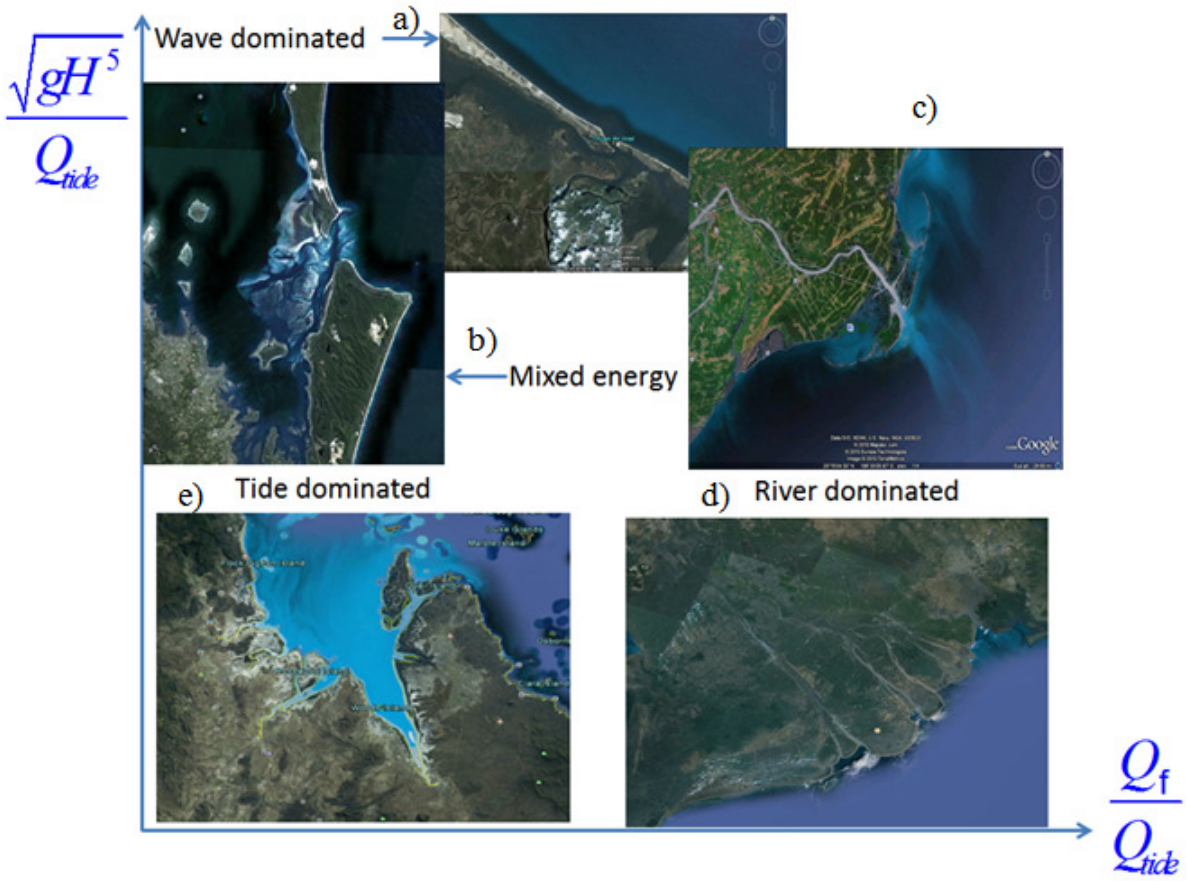

Figure 1.5: Inlet classification in terms of relative wave strength to tide $\frac{\sqrt{gH^5}}{Q_{\text{tide}}}$ and relative freshwater to tide $\frac{Q_{\text{f}}}{Q_{\text{tide}}}$ (Google Earth images).

Q_{tide} can be taken as mean tidal discharge $\overline{Q}_{tide}$ or peak tidal discharge $\hat{Q}_{tide}$. It can be interpreted that:

a) Large $\frac{\sqrt{gH^5}}{Q_{tide}}$ indicates wave dominated environment, together with a low tidal range. Barrier coasts with inlets are the typical feature of this kind, e g, Thuan An inlet in Vietnam (Figure 1.5a) (Lam, 2009), the Manning River, NSW, Australia (Figure 1.6) (Roper et al., 2011); Anclote Pass, San Francisco in USA, The Senegal River in Africa (Wright, 1977).

Figure 1.6: The Manning River mouth at Harrington, NSW, Australia. An example of high wave energy environment (Google Earth image).

b) Moderate $\frac{\sqrt{gH^5}}{Q_{tide}}$ and small $\frac{Q_f}{Q_{tide}}$: In such cases, mixed energy coasts have typical features of both an ebb tidal delta and a flood tidal delta, such as the inlet between Moreton and Nth Stradbroke islands near Brisbane, Australia (Figure 1.5b) or The Wadden Sea (Figure 1.7). When $\frac{Q_f}{Q_{tide}}$ increases with moderate wave energy, the river delta form as occurs at Balat estuary in Vietnam (Figure 1.5c) is usually observed.

c) Small $\frac{\sqrt{gH^5}}{Q_{tide}}$ and large $\frac{Q_f}{Q_{tide}}$ result in a river dominated delta. With abundant sediment supply from the catchment, the delta extends further seaward. The Mekong River delta in Vietnam is one example of this type (Figure 1.5d) with an average annual flow ca 15850 m^3/s (Le, 2004). The Mississippi River, USA, is another illustration with an average discharge of 17000 m^3/s at the mouth in Louisiana (Elliott, 1932).

Figure 1.7: The Wadden Sea, NL. An example of mixed energy environment

Figure 1.8: Yangtze-Kiang, China: An example for highly tide-dominated coast with low wave energy and a large $\overline{Q_{tide}}$, tidal amplitude = 3.8 m (from World delta data base, 2004).

d) Small $\frac{\sqrt{gH^5}}{Q_{tide}}$ and small $\frac{Q_f}{Q_{tide}}$ characterizes an environment of low wave energy, low river influence but a strong tidal current. This environment is tidal dominated by funnel estuary shape such as Thames and Bristol river mouths in UK, Bay of Fundy (de Vriend, 1999) or Broad Sound channel in Australia (Figure 1.5e). With moderate $\frac{Q_f}{Q_{tide}}$, sand islands parallel to the tidal currents result in formation of flood/ebb tidal deltas. Examples are the Fly River in Papua New Guinea, the Ord River, Australia; Klang (Malaya); Shattal- Arab (Iraq); Yangtze-Kiang (China) in Figure 1.8 (Wright et al. 1973).

Measuring the inlet shaping 'strength' of the tides in terms of $\hat{Q}_{tide,pot}$ instead of the tidal prism (O'Brien 1931, 1969, Bruun 1978 and others) or the tidal range (Hayes 1979 and Heap et al 2001) is an improvement, as illustrated below in relation to the inlets in Figure 1.9.

Figure 1.9: Three neighbouring inlets at 20°49'S 116°26'E in Western, Australia. In this area the spring tidal amplitude is around 2.2 m and the tides are predominantly semi-diurnal. The mean significant wave height is of the order 0.7 m, Baldock et al (2006).

The two smaller inlets show some wave influence while the larger one on the right shows the canonical funnel shape of a tide dominated system. These systems clearly have the same H/R_{to}-ratio and should thus have similar morphology according to the Hayes or the Heap et al classifications. The influence of estuary area might be captured by Bruun's (1978) classification in terms of the ratio between tidal prism P and annual littoral drift $\overline{Q_{sy}}$ in that the larger system will have larger P. However, the small river like system on the left does not indicate significant littoral drift, so the wave influence is better described simply in terms of the wave height as in $\frac{\hat{Q}_{\text{tide,pot}}}{\sqrt{g\overline{H_s}^5}}$ rather than in terms of $\overline{Q_{sy}}$ as in $P/\overline{Q_{sy}}$.

With surface areas 0.04 km^2, 0.06 km^2 and 0.60 km^2 respectively, the three inlets (from left to right in Figure 1.9) have $\frac{\hat{Q}_{\text{tide,pot}}}{\sqrt{g\overline{H_s}^5}}$-values of respectively 10, 15 and 147. This sample thus indicates that total tide-dominance on inlet morphology occurs upwards from $\frac{\hat{Q}_{\text{tide,pot}}}{\sqrt{g\overline{H_s}^5}}=140$ while wave dominance occurs for $\frac{\hat{Q}_{\text{tide,pot}}}{\sqrt{g\overline{H_s}^5}}$ below 15.

This new, quantitative classification method is applied in the following section to 184 estuaries along the NSW coast, Australia.

1.3 APPLICATION OF NEW DIMENSIONLESS PARAMETERS FOR CLASSIFICATION OF NSW ESTUARIES, AUSTRALIA

1.3.1 Data available and instructions for calculation

To classify the coastal systems considering the three dominant 'forces': tides, waves, river flow, as well as the tidal basin details, the two dimensionless parameters $\frac{\sqrt{gH^5}}{Q_{\text{tide}}}$ and $\frac{Q_f}{Q_{\text{tide}}}$ introduced in Section 1.2.2 will be used flexibly. This method is applied to 178 estuaries in NSW, Australia based on the available data taken from Roper et al. (2011) in comparison with the classification scheme of Roy et al. (2001) and Heap et al. (2001). In this case, $\hat{Q}_{\text{tide,actual}}$ is calculated for 80 estuaries with

tidal prism P provided. For the remaining 98 ICOLL systems with dominant closed condition without P, we use the potential peak tidal discharge $\hat{Q}_{\text{tide,pot}}$.

We use $\frac{\hat{Q}_{\text{tide}}}{\sqrt{gH^5}}$ and $\frac{Q_{\text{f}}}{\sqrt{gH^5}}$ to represent the relative tidal strength and river flow to wave influence. These parameters have been calculated for each of the estuaries and results are presented in different groups according to Heap et al (2001): wave dominated estuaries (WDE), wave dominated deltas (WDD), river dominated (RD), tidal dominated estuaries (TDE), bays and ICOLLs.

$\overline{H_s}$ used to calculate $\sqrt{gH^5}$ is taken from seven wave recording stations along the NSW coast at depths varying from 62 to 100m, which have been recording for more than 20 years (Coghlan et al., 2011; Shand et al., 2011). $\overline{H_s}$ of the station closest to the estuary is chosen for the calculation and noted in the tables.

$\hat{Q}_{tide}$ is computed as

$$\hat{Q}_{tide} = \frac{P\pi}{T} \tag{0.4}$$

where, T is the tidal period, T=12 hours 25 minutes =44712 s for semi-diurnal tides, which is the dominant tidal component along NSW coast. Tidal prisms P are taken from the data set of Roper et al., (2011) cf. Appendix 9. The tidal prism was adjusted from tidal gauge measured almost at spring tide through the three-stage process cf. pp 45-46 of Roper et al. (2011).

For ICOLL systems, $\hat{Q}_{\text{tide,pot}}$ is estimated from the bay surface area A_{b} and the ocean tidal range R_{to}.

$$\hat{Q}_{\text{tide,pot}} = \frac{R_{\text{tO}} A_{\text{b}} \pi}{T} \tag{0.5}$$

while Q_{f} is calculated as

$$Q_{\text{f}} = \text{Total annual flow/time in seconds per year (31536000s)} \tag{0.6}$$

where the total annual flow is taken from Roper et al, (2011) cf. Appendix 8 for the current land-use condition, which is calculated using the 2CSalt model with input rainfall data from 1975 to 2007.

Other information for each estuary is also presented in Appendix 1 such as location (latitude, longitude), estuary surface area (including or excluding salt marsh), tidal range adjusted for spring tide, name of estuary class according to Roy et al. (2001) and Heap et al. (2001), entrance condition such as generally open (O), intermittent (I), Trained (T), usually closed (C), response

classification and subclass. Labeling for each estuary is kept the same as in Roper et al, (2011) for easy reference.

1.3.2 Summary of data and results of calculation for different coastal system groups

Based on $\frac{\hat{Q}_{\text{tide}}}{\sqrt{gH^5}}$ and $\frac{Q_{\text{f}}}{\sqrt{gH^5}}$ considering the classification of Roy et al. (2001) and Heap et al. (2001), together with morphology features described as in Figure 1.3 and Figure 1.5 three main groups have been distinguished, as shown in Table 1.2. These three groups are: wave dominated coasts including 3 subclasses: wave dominated estuaries (WDE), wave dominated deltas (WDD) and ICOLLs; tide dominated coasts including: estuaries (TDE) and bay (or embayment); and river dominated coasts (RD). All estuaries are plotted in terms of $\frac{\hat{Q}_{\text{tide}}}{\sqrt{gH^5}}$ and $\frac{Q_{\text{f}}}{\sqrt{gH^5}}$ in Figure 1.10. Detailed information for each group is presented in Appendices 1.1 to 1.4.

Table 1.2: Three groups of NSW estuaries based on $\frac{\hat{Q}_{\text{tide}}}{\sqrt{gH^5}}$ and $\frac{Q_{\text{f}}}{\sqrt{gH^5}}$

Group name	subclass & number of estuaries	$\frac{Q_{\text{f}}}{\sqrt{gH^5}}$	$\frac{\hat{Q}_{\text{tide}}}{\sqrt{gH^5}}$	Note
Wave dominated $\frac{\hat{Q}_{\text{tide}}}{\sqrt{gH^5}} < 75$	WDE (35)	0.005÷2	1÷75	
	WDD (16)	0.05÷7	3÷100	This group has 6 inlets belonging to RD, 3 inlets belonging to TDE.
	ICOLLs (100)	<0.1	0.08÷75	
Tidal dominated $\frac{\hat{Q}_{\text{tide}}}{\sqrt{gH^5}} > 75$	Bay (5)	0.003÷0.12	200÷875	
	TDE (13)	≥0.005	75÷715	This group has label 13, 67, 132 belong to RD
River Dominated $\frac{Q_{\text{f}}}{\sqrt{gH^5}} \geq 2$	RD (9)	≥ 2	27÷715	This group has some cases belonging to WDD and TDE

As can be seen from Figure 1.10 and Table 1.2, clear ranges have been identified for three main groups:

1) wave dominated coast with $\frac{\hat{Q}_{\text{tide}}}{\sqrt{gH^5}} < 75$,

2) tidal dominated coast with $\frac{\hat{Q}_{tide}}{\sqrt{gH^5}} > 75$

3) river dominated coast with $\frac{Q_f}{\sqrt{gH^5}} \geq 2$.

However, the subclasses of the wave dominated group is not clear.

In the river dominated groups, there are 6 wave dominated-rivers and 3 are tide dominated-rivers. The Clarence River (13) has the strongest river dominance with $\frac{Q_f}{\sqrt{gH^5}} = 10.8$.

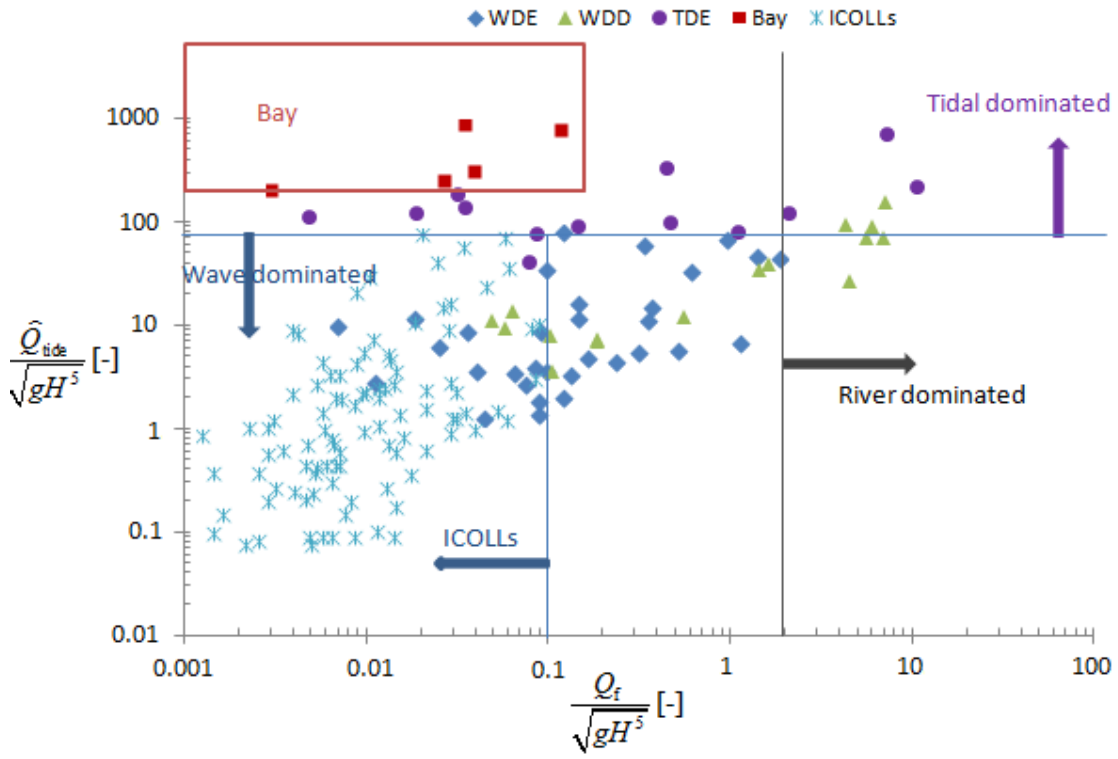

Figure 1.10. Classification in terms of $\frac{\hat{Q}_{tide}}{\sqrt{gH^5}}$ and $\frac{Q_f}{\sqrt{gH^5}}$ for 178 estuaries in NSW, Australia.

The 'bay' group shows strong tide dominance at different levels and very small influence of waves and river flow. Jervis Bay has the largest value of $\frac{\hat{Q}_{tide}}{\sqrt{gH^5}} = 875$ corresponding to the largest tidal prism and very small $\frac{Q_f}{\sqrt{gH^5}} = 0.04$ and Batemans Bay (133) with funnel shape has

$\frac{\hat{Q}_{\text{tide}}}{\sqrt{gH^5}} = 319$. The Hawkesbury River (67) has the strongest influence of tide with $\frac{\hat{Q}_{\text{tide}}}{\sqrt{gH^5}} = 711$ as well as strong river dominance with $\frac{Q_{\text{f}}}{\sqrt{gH^5}} = 7.23$ in the TDE group.

Wave dominated coastal systems are the majority along the NSW coast, with 150 out of 178 estuaries. There are some special points, which should be noted about this group.

Three WDD such as the Richmond River (9), the Hastings River (43) and Hunter River (56) have $\frac{\hat{Q}_{\text{tide}}}{\sqrt{gH^5}} > 75$ but have the morphological features of wave dominated coast with barrier. This can be explained by the river training jetties at the entrances making the tide penetration stronger, but the wave dominated features may have been present earlier before jetties were built. Therefore, they should be re-classified as TDE rather than WDD as per new classification.

Among the ICOLLs such as Werri (99), Terrigal (63), Cockrone Lake (65), which are known to be closed by the waves between floods, we find $\frac{\hat{Q}_{\text{tide}}}{\sqrt{gH^5}} \leq 2$ and $\frac{Q_f}{\sqrt{gH^5}} < 0.04$.

To refine the three subclasses of wave dominated inlets, it may be necessary to consider other influencing factors such as wave period and the location, as in exposed to waves, sheltered by a headland or 'with or without training works'.

This new classification for NSW estuaries almost agrees with Roy et al. (2001) for most groups; while it only agrees with Heap et al. (2001) for the wave dominated group Appendices 1.1 to 1.4.

In conclusion, the quantitative classification of inlets in terms of $\frac{\hat{Q}_{\text{tide}}}{\sqrt{gH^5}}, \frac{Q_f}{\sqrt{gH^5}}$ or alternatively $\frac{\hat{Q}_{\text{tide}}}{\sqrt{gH^5}}, \frac{Q_f}{\hat{Q}_{\text{tide}}}$ as in Figure 1.5, makes good sense in that it accounts properly for the influence of the tidal period and the bay area in the strength of the tide as a morphological driver. It also seems efficient in that the borderline between tide dominated (funnel shaped) and wave influenced inlets has been found to lie around $\frac{\hat{Q}_{\text{tide}}}{\sqrt{gH^5}} = 75$ for the microtidal NSW Coast (Figure 1.10) as well as for the macrotidal north west coast of Australia (Figure 1.9).

Chapter 2

INLET HYDRAULICS

2.1 INTRODUCTION

Tides, waves and river flow are the main forcing agents which shape coastal inlets. The cross-sectional area of the inlet depends on the ability of the ebb-tidal flow in the inlet including river flow to flush out the sediment brought into the inlet by waves through long-shore and/or cross-shore processes. When these flushing forces are not strong enough due to low river discharge in the dry season to balance the effects of larger waves in the monsoon season, the tidal inlet may close.

Figure 2.1 presents a sketch of a single inlet–bay system with hydrodynamic forcing from tides, river flow Q_f and overwash flow Q_{over} from large waves across the sand spit.

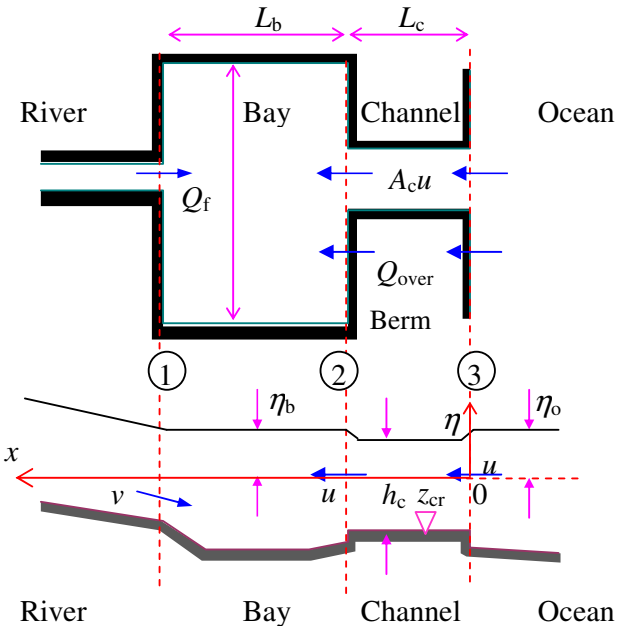

Figure 2.1: A single inlet, single lake (node) - bay system.

To understand the morphodynamics of tidal inlets, hydrodynamic processes are the key forcing giving bed shear stress and sediment transport patterns and bed level changes. Thus, understanding the hydraulics may eventually allow us to evaluate the morphological state of systems and to predict its morphological development. The details of the flow- and associated bed-

shear-stress pattern are however beyond the capability of present day models (see Chapter 7, Chapter 9), so the following is concerned simply with the mean velocity Q/A_c.

Further discussion related to the influence of flow patterns on the stability of inlet cross sections will be presented in Chapter 5.

2.1.1 Tidal forcing

Ocean tides contain lunar and solar components. These result, according to the equilibrium theory of tides (Darwin, 1899), from local imbalances between the gravitational pull from the Moon (Sun) and the centrifugal force associated with the Earth's motion around the centre of mass of the Earth-Moon (Earth-Sun) system. If the Earth's axis was perpendicular to the Ecliptic Plane we would only have semi diurnal tides, but due to the inclination of this axis (ca 22.5^o) we get mixed diurnal/semi-diurnal tides, cf. Nielsen (2009) Figure 4.2.2.

Darwin's simple theory is for an Earth uniformly covered by water, but the presence of the continents complicates the picture as the tidal waves are forced around the continents under the influence of the Coriolis force. A complicated picture (e.g. Nielsen 2009, Figure 4.1.1) results with astronomical tides, which vary greatly from place to place. The tidal range at a given point also varies in a fortnightly cycle with maxima when the forcings from the Moon and the Sun are additive. This is known as the neap-spring cycle.

Purely lunar tides would be periodic with period equal to the lunar day, ca 24 hours 50 minutes, while purely solar tides would have a period of 24 hours. With both forcings contributing, true periodicity only occurs at much longer time scales related to the periodicity of the Earth's and Moon's orbits.

For the purposes of hydraulic analysis we generally consider the tide as a simple harmonic in the first approximation, or at the next level, as mixed diurnal/semi-diurnal with the diurnal period being ca 24 hours 50 minutes or 24.5 hours (for practical reasons dealing with half-hourly readings).

Tides are important for inlet hydraulics in two ways:

1: Their direct forcing of bay tides and the associated inlet currents; and

2: Modulation of wave overwash

Figure 2.2 shows mixed diurnal/semi-diurnal tides of the form (2.1), where i is imaginary unit, $i = \sqrt{-1}$. The effect of the phase φ_{o2} on the pattern of high tides and hence on the berm overwash potential, which is shown in Figure 2.2, seems not to have been widely appreciated.

$$\eta_o = a_{o1}\cos(\omega t) + a_{o2}\cos(2\omega t - \varphi_{o2}) \qquad (2.1)$$

$$= \mathrm{Re}\{a_{o1}e^{i\omega t} + a_{o2}e^{i(2\omega t-\varphi_{o2})}\}$$

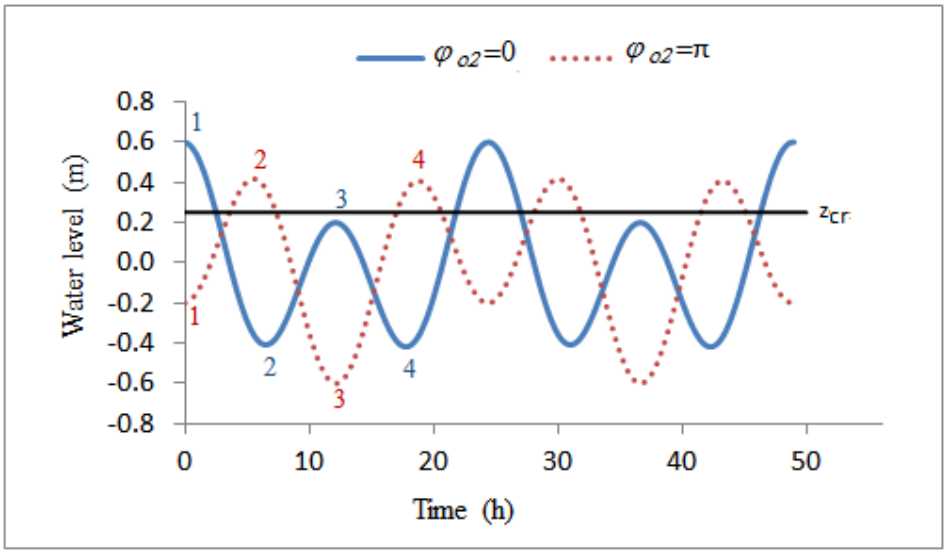

Figure 2.2: Due to their different patterns of high tides, very different overwash potential results from tides of the fixed amplitudes (a_{o1}, a_{o2}) but different phase lag φ_{o2}.

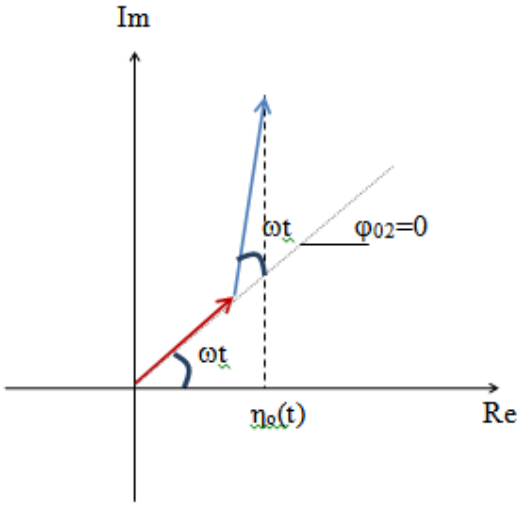

Figure 2.3: Mixed tides resultant of two rotating vectors (diurnal, semi-diurnal) in the complex plane for the particular case of $\varphi_{o2} = 0$. The physical tide is the real value (= x-coordinate of the resultant vector).

The water level variation is quite different for the two cases: when $\varphi_{o2} = 0$ (blue line) and $\varphi_{o2} = \pi$ (red dotted line), even though the amplitudes of the two components are kept the same. That

is, φ_{o2}= 0 gives alternating high highs and low highs in the ocean resulting in a strong diurnal component to the bay tide, while the very even ocean highs for $\varphi_{o2}=\pi$ lead to almost purely semi-diurnal bay tide. This issue, and its implications for overwash, will be discussed in detail in Section 3.6.

It is sometimes useful to think of the surface elevations of tides and other waves as the real-part of complex numbers corresponding to vectors rotating in the complex plane as shown in Figure 2.3 and Figure 2.4.

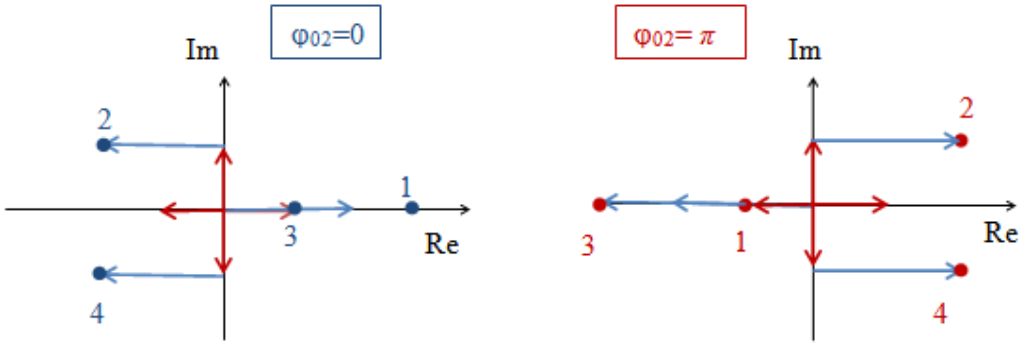

Figure 2.4: Complex vector illustration of the very different bichromatic tides with fixed (a_{o1}, a_{o2}) but different phase lag φ_{o2} = (0, π). The Points 1, 2, 3, 4 are corresponding to ωt = 0, $\pi/2$, π and $3\pi/2$ respectively, also plotted in Figure 2.2.

2.1.2 Bay response to tidal forcing

The response of the bay or estuary to the ocean tide for each harmonic component can be expressed in terms of a response frequency function $F(\omega)$ defined by

$$\begin{aligned}\eta_b &= a_b \cos(\omega t - \varphi) = \mathrm{Re}\left\{F(\omega) a_o e^{i\omega t}\right\} \\ &= \left|F(\omega)\right| a_o \cos\left[(\omega t) + Arg\left\{F(\omega)\right\}\right]\end{aligned} \tag{2.2}$$

The frequency response function $F(\omega)$ shows the relation between bay tides and ocean tides with gain $G = |F(\omega)|$ and phase lag φ =-Arg{$F(\omega)$} as illustrated in Figure 2.5.

The propagation and shape distortion of ocean tides into a lagoon, river, or estuary depend on many factors such as bay surface area A_b (Figure 2.1) entrance cross sectional area A_c, length of channel L_c. If the channel is very long, the tidal wave may vanish before reaching the channel end. If the channel is short, the tidal wave acts like a partly standing wave with frictional damping. If a system with a long inlet channel is close to the Helmholtz frequency (or pumping mode) then the inertia of the water in the channel becomes important.

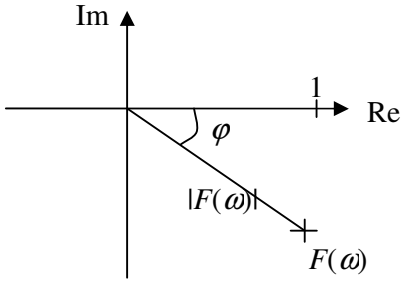

Figure 2.5: The frequency response function $F(\omega)$ in the complex plane.
Perfect response corresponds to $F = 1$.

In systems without the influence of friction, 'ideal' systems or systems with a strong convergence of the estuary banks, as the Bristol Channel (Figure 2.6) the tide propagates without significant dissipation $D_E \approx 0$. In this case, we have (approximate) conservation of energy flux:

$$E_{f1} W_1 = E_{f2} W_2 = \text{constant} \quad \Leftrightarrow \quad R_1^2 W_1 = R_2^2 W_2 \tag{2.3}$$

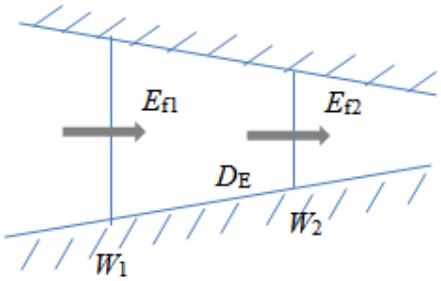

Figure 2.6: Tidal wave propagation in a tapering (converging) estuary.

Thus, the energy flux E_f [W/m] and the tidal amplitude will increase upstream, possibly resulting in the upstream tide becoming larger than the ocean tide. In fact, even if $D_E \neq 0$, the increase in the tidal range due to convergence of the banks may balance or overcompensate the damping due to friction, giving constant or even landward increasing tidal range.

Conversely, for friction dominated systems such as Lake Conjola (Figure 2.9), where the lake is separated from the inlet by a long shallow channel, $\boldsymbol{E_f}$ is gradually reduced by friction. The tidal wave is then dampened significantly as it travels upstream (Figure 2.7).

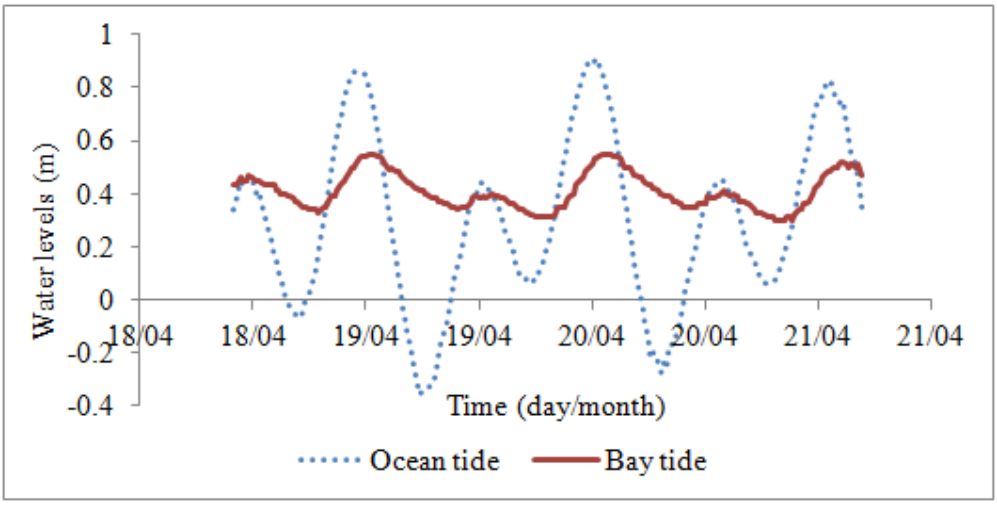

Figure 2.7: Tidal range dampened significantly from 1.3 m in the ocean to 0.2 m inside Lake Conjola. Data from Manly Hydraulics Laboratory.

2.1.3 Phase relations between horizontal velocity u and surface elevation η

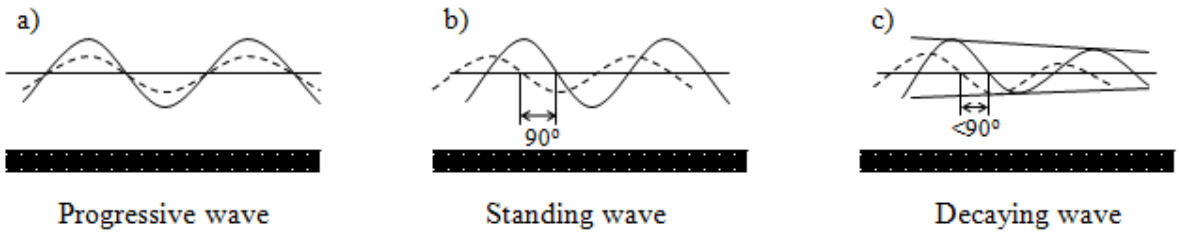

Figure 2.8: Phase difference between u and η for different wave. u: ----; η: —
See section 2.4.1 for phase relations near a weir.

Phase relations between the horizontal velocity u and the surface elevation η depend on what kind of wave is considered. For a frictionless progressive wave u is in phase with η as shown in Figure 2.8a. For a standing wave u leads η by 90^o cf. Figure 2.8b. For a wave decaying due to friction u leads η by angle between 0 and 90^o as in Figure 2.8c, cf. Nielsen 2009, page 164.

2.1.4 Fresh water flow

Varying river (fresh water) flow Q_f changes the inlet morphology in competition with tidal and wave forcing, as mentioned in Section 1.1.2 with the illustration in Figure 1.4. The inlet can change from a 'negative estuary' where evaporation exceeds freshwater input, or barrier coast with lagoon when $Q_f \approx 0$ to a funnel shaped bay or river mouth when Q_f is large. In terms of hydraulics, Q_f influences significantly the bay tides in the wet season or during flood events.

Q_f may influence the tidal range and phase lag in the bay through two different mechanisms:

1: It reduces bay-tide amplitude a_b and increases the phase lag due to non-linearly increased friction $\sim L_c|u|u$; and

2: The general water-level rise due to Q_f gives a greater bay surface area A_b leading to a smaller a_b for a given ocean tide and entrance opening.

Additional tidal harmonics may also be generated through the non-linear friction term. However, if the river flow is strong enough to scour out an untrained entrance, resulting in improved hydraulic efficiency, the tidal amplitude in the bay may increase and the phase lag may be reduced during and after flooding.

2.1.5 Overwash flow

Another inflow contribution comes from the wave overwash flow rate Q_{over} across the berm or the sand spit in front of the lagoon during a storm wave event. Figure 2.1, Figure 2.9 and Figure 2.10 show examples of wave overwash observed at Lake Conjola, NSW, Australia during the event around 9th April 2006.

Q_{over} can be calculated based on runup theory and the wave pump efficiency. The wave pump efficiency is the ratio between the useful pump work $\rho g \Delta q_{\text{over}}$ [W/m] and the incoming wave energy flux E_f :

$$\varepsilon = \frac{\rho g \Delta q_{\text{over}}}{E_f} \tag{2.4}$$

where Δ is the pumped height, ρ is the water density. The efficiency varies from around 3.5% in rip and atoll systems through to 40% – 50% on steep artificial ramps, cf. Figure 3 in Nielsen et al. (2008). In cases with significant freeboard, Δ may be approximated by (2.52), which is the case for the overwash events studied in this thesis.

Another group of overtopping expressions is based on swash truncation and the runup models by Peregrine & Williams (2001) and Baldock et al. (2005).

Various empirical formulae from breakwater related works can also be applied for Q_{over} such as Van der Meer & Janssen (1995), Hedges & Reis (1998) and Pullen et al. (2007).

Q_{over} is, according to (2.4), proportional to the energy flux of the incoming waves and hence to the wave height squared but will be modulated by the tide. Figure 2.2 shows how Q_{over} and hence the bay tide may have diurnal or semi diurnal behavior depending on φ_{o2} i.e., the relative phasing between the diurnal and semi-diurnal components of the ocean tide. The overwash term is applied to compute tidal anomalies of Lake Conjola in Section 2.5.

Figure 2.9: Lake Conjola, NSW, Australia (Google Earth image) where a significant flood event driven by wave overwash occurred in April 2006. The vegetation pattern gives an indication as to which part of the spit is regularly overtopped by waves.

Figure 2.10: Wave overwashed at the entrance of Lake Conjola (left), flooding in Caravan Park (yellow point in Figure 2.9 - right). Photos are provided by Dave Hanslow.

2.2 HYDRAULIC MODELS OF INLET-BAY SYSTEMS

The basic models of inlet-bay systems fall in two families:

1) **Weir models** which ignore inertia of the water in the inlet channels and friction along the channel; and
2) **Finite-channel-length models** which acknowledge inertia and friction along the channels.

The friction is usually assumed to be quadratic corresponding to fully rough turbulent flow.

2.2.1 Weir models

For an inlet with insignificant channel length we use weir flow as a simple model corresponding to:

$$A_b \frac{d\eta_b}{dt} = W_c\sqrt{g}\left[\frac{2}{3}\left(Max\{\eta_o,\eta_b\}-z_{cr}\right)\right]^{3/2} sign\left(\eta_o-\eta_b\right)$$
$$\Updownarrow \qquad (2.5)$$
$$\frac{d\eta_b}{dt} = \frac{W_c\sqrt{g}}{A_b}\left[\frac{2}{3}\left(Max\{\eta_o,\eta_b\}-z_{cr}\right)\right]^{3/2} sign\left(\eta_o-\eta_b\right)$$

See Figure 2.1 for notation. The well proven theory for (broad-crested) weir flow assumes critical flow over the crest with a depth equal to 3/2 of the available total head and zero friction loss.

Coming from unidirectional (non-reversing) river flow, this model has the problem that the flow rate does not vanish when the two water levels become equal. This issue is addressed by the following two optional conditions:

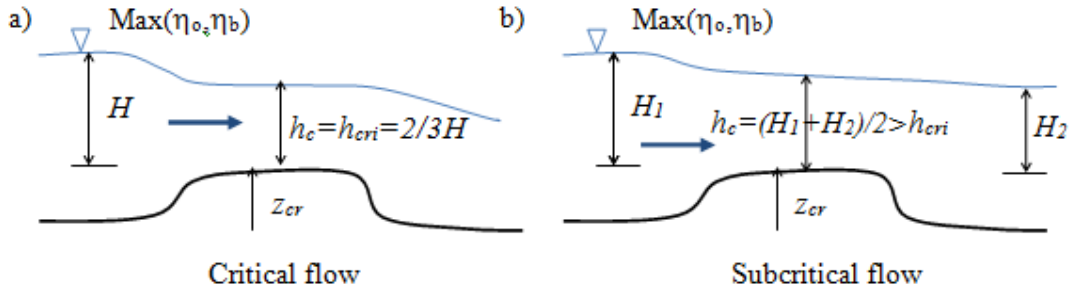

Figure 2.11. Two flow regime of Weir model applied for inlet a) critical flow; b) subcritical flow.

1: Critical flow over the crest

(Figure 2.11a) with "critical depth"

$$h_c = h_{cri} = \frac{2}{3}\left(\mathrm{Max}\{\eta_\mathrm{O},\eta_\mathrm{b}\}-z_\mathrm{cr}\right) \qquad (2.6)$$

where z_{cr} is the invert inlet (~weir crest) level, the velocity over the crest is taken as $\sqrt{gh_{cri}}$;

2: Subcritical flow

(Figure 2.11b) with water depth

$$h_c = \text{Average } (\eta_b, \eta_o)\text{-}z_{cr} \text{ and velocity is } \sqrt{2g\,|\eta_\mathrm{O}-\eta_\mathrm{b}|}\,. \qquad (2.7)$$

The weir model then works by checking $\mathrm{Min}\left\{\sqrt{gh_{cri}}\,,\sqrt{2g\,|\eta_\mathrm{O}-\eta_\mathrm{b}|}\right\}$ to identify flow regime leading to

$$\frac{d\eta_b}{dt} = \frac{W_c}{A_b} h_c \,\mathrm{Min}\left\{\sqrt{g h_{cri}}\,,\ \sqrt{2g\,|\eta_O - \eta_b|}\right\} \mathrm{sign}(\eta_O - \eta_b) \qquad (2.8)$$

For z_{cr} approaching high tide level, *HT*, the lagoon water-level becomes constant near the high tide level, $\overline{\eta_b} \to HT$ and the lagoon tide range vanishes, $\sigma_b \to 0$ while the phase lag approaches $\pi/2$. Near $z_{cr} = HT$ the lagoon tide may be diurnal or semi diurnal depending on φ_{o2}, as explained in Figure 2.2.

A time constant *T* for this system may be defined by

$$T = \frac{A_b}{W_C \sqrt{g(HT - z_{cr})}} \qquad (2.9)$$

2.2.2 Finite-channel-length models of inlet-bay systems

Inlet-bay systems with finite channel lengths are significantly more complicated than weir systems, with the main difficulty arising from the non-linear nature of the flow resistance in the channel. This then leads to three levels of model complexity;

1. Models which take full account of the nature of turbulent friction. Such models need to be numerical;
2. Models which account for the non-linearity by analytical perturbation approaches, making use of Fourier expansions in dealing with essentially simple harmonic tidal forcing; and
3. Analytical models to linearized equations.

The Saint-Venant equations

The basic equations for one dimensional flow in an inlet channel are known as the Saint-Venant system of equations for long waves (hydrostatic pressure and uniform velocity throughout the depth) in one dimension.

$$B\frac{\partial \eta}{\partial t} + \frac{\partial Q}{\partial x} = 0 \qquad (2.10)$$

$$\frac{\partial u}{\partial t} + u\frac{\partial u}{\partial x} + g\frac{\partial \eta}{\partial x} + gS_f = 0 \qquad (2.11)$$

(1) (2) (3) (4)

The quadratic friction term (4) assumes fully rough turbulent flow. Eq (2.10) expresses the conservation of volume, and (2.11) is Newton's second law.

Using the log-law formula for the mean velocity,

$$\overline{V} = \frac{\sqrt{S_f g A_c / P_c}}{\kappa} \ln \frac{12 A_c / P_c}{k_s} \tag{2.12}$$

(4) becomes

$$S_f g = \frac{\kappa^2 \left|\overline{u}\right| \overline{u}}{R \ln^2 \frac{12 A_c / P_c}{k_s}} \tag{2.13}$$

in which t is time (s); x is longitudinal coordinate along channel axis (m); η is water level (m); Q is flow discharge (m³/s); B is surface width (m); P_c is channel wetted perimeter (m); g is gravity acceleration (m/s²); u is velocity (m/s); $\overline{u}$ is mean velocity (m/s); κ is von Karman's constant, κ ≈ 0.4; S_f is the friction slope; and k_s is the bed roughness (m).

The first term (1) of the momentum equation (2.11) is the inertia term representing local acceleration. The others are convective acceleration (2), pressure gradient (3) and friction (4) terms.

The following is a brief account of the literature on applications of the St Venant equations in estuarine modeling:

Analytical solutions for the system of equations can be obtained using simplifying assumptions as done by Keulegan (1967). He gave an analytical solution neglecting local acceleration (1) i.e., a steady solution and river inflow influence. Other authors, e.g. King (1974), Özsoy (1977), Escoffier & Walton (1980), Walton & Escoffier (1981) included the effect of local inertia but only the work of Escoffier & Walton (1980) provided an analytic solution taking into account tributary inflow. Most of these models seem unrealistic to consider only the elementary types of ocean forcing functions rather than typical astronomical tides.

Similar to DiLorenzo (1988) model, Walton (2004) extended the analytical solutions to ocean tides consisting of a number of harmonics and presented the results in dimensionless form. However, the latter requires solving simultaneously a system of two non-linear equations using trial and error to produce results. Walton (2004) suggested that numerical inlet models such as that of Van de Kreeke (1967) and Seelig et al. (1977) should be used to provide realistic tidal response for the linear system with the ocean tides consisting of a number of astronomical constituents.

Research works specifically interested in providing solution for tidal propagation along funnel shape estuaries are available in the literature, Jay (1991), Friedrichs & Aubrey (1994), Lanzoni & Seminara (1998), Savenije et al. (2008). Recently, Toffolon & Savenije (2011) modified the linear solution considering the influence of inlet width and depth convergence, which is expressed in dimensionless and complex numbers.

2.3 SIMPLIFIED FINITE-CHANNEL-LENGTH SYSTEMS

2.3.1 Simplifying assumptions

To obtain analytical solutions for the system of equations (2.10) and (2.11), the following simplifying assumptions are applied (similar to Keulegan, 1967).

- The bay and ocean current velocities are negligible compared to those in the inlet channel.
- The bay is relatively small and deep so spatial gradients in the water surface at any instant can be neglected, $\omega\frac{\sqrt{A_b}}{\sqrt{gh}} << 1$.
- The ocean tide is sinusoidal so that the ocean tidal water level η_o can be presented as

$$\eta_o = a_o \cos(\omega t) = \mathrm{Re}\{a_o e^{i\omega t}\} \tag{2.14}$$

This assumption can also be expanded with additional overtide components.

- The flow velocity in the channel is sinusoidal with an offset, $v = (Q_f + Q_{over})/A_c$, representing the river discharge and/or the overwash inflow.

$$u = \hat{u}\cos(\omega t + \phi) + v \tag{2.15}$$

- The flow area in the channel A_c and the wetted perimeter P_c are assumed constant. Otherwise tidal pumping will occur as discussion later in Section 2.4. In the notation of Figure 2.2 tidal pumping becomes important when z_{cr} is near or above the low tide level.

2.3.2 Integrated equation of motion

For an inlet-bay system like the one in Figure 2.1, the long wave equations (2.10) and (2.11) can be integrated from the bay entrance ($x = 0$) to the ocean exit ($x = L_c$) of the inlet yielding:

$$A_b \frac{\partial \eta_b}{\partial t} = A_c u + Q_f + Q_{over} \tag{2.16}$$

where the depth averaged current $u = Q/A$ is positive landwards

$$u = \frac{A_b}{A_c}\frac{\partial \eta_b}{\partial t} - \frac{Q_f}{A_c} - \frac{Q_{over}}{A_c} \tag{2.17}$$

and

$$\eta_o = \eta_b + \frac{L_c}{g}\frac{\partial u}{\partial t} + F\frac{|u|u}{2g}. \tag{2.18}$$

Equation (2.18) can be spelled out in terms of the channel geometry and bed roughness as in (2.19) by using the log-law expression (2.13) for the friction term,

$$\eta_o = \eta_b + \frac{L_c}{g}\frac{\partial u}{\partial t} + \frac{L_c}{g}\frac{\kappa^2 \left|\bar{u}\right|\bar{u}}{\frac{A_c}{P_c}\ln^2\frac{12A_c/P_c}{k_s}} \tag{2.19}$$

so that the differential equation for bay tides become

$$\begin{aligned}\eta_o = \eta_b + \frac{L_c}{gA_c}\left[A_b\frac{\partial^2\eta_b}{\partial t^2} - \frac{\partial Q_f}{\partial t} - \frac{\partial Q_{over}}{\partial t}\right] + \\ + \frac{F}{2g}\left(\frac{A_b}{A_c}\right)^2\left|\frac{\partial\eta_b}{\partial t} - \frac{Q_f + Q_{over}}{A_b}\right|\left(\frac{\partial\eta_b}{\partial t} - \frac{Q_f + Q_{over}}{A_b}\right)\end{aligned} \tag{2.20}$$

in which F is referred to as the dimensionless overall impedance of the inlet by O'Brien & Clark (1974) and Jarrett (USACE, 2002) and accounts for total the head loss:

$$F = k_{en} + k_{ex} + f\frac{L_c}{4R} = m + f\frac{L_c}{4R} \tag{2.21}$$

where friction coefficient f can be rewritten in terms of the channel parameters via the log-law, giving

$$f = 8\left(\frac{u_f}{\bar{V}}\right)^2 = \frac{8\kappa^2}{\ln^2\frac{12A_c/P_c}{k_s}}. \tag{2.22}$$

Then (2.21) can be written as

$$F = m + f\frac{L_c}{4A_c/P_c} = m + \frac{2\kappa^2 L_c P_c/A_c}{\ln^2\frac{12A_c/P_c}{k_s}} \tag{2.23}$$

k_{en}, the entrance loss coefficient, takes values from 0.05 up to 0.25 for dual jetties. A value of k_{ex} = 1 implies a relatively deep bay and complete loss of velocity head. Many investigators have chosen the sum $m = k_{en} + k_{ex} = 1$ for case studies like in Shemdin & Forney (1970), Escoffier & Walton (1980), Van de Kreeke (1985), DiLorenzo (1988).

2.3.3 Linearization of the friction term

The quadratic friction term in (2.18) and (2.20) is one reason that the tide in the bay is not sinusoidal even if the ocean tide is sinusoidal as recognised by Keulegan (1967). Another reason is varying channel cross section. However, for the present we assume A_c to be constant in computation, while the tidal pumping, which results from time-variable A_c, is left to Section 2.4.

To derive analytical solutions for the system of equations (2.17) and (2.18), the non-linear friction term in (2.18) needs to be linearized or expressed as a Fourier series. Using a simple harmonic velocity in the form

$$u = \hat{u}\cos(\omega t) \tag{2.24}$$

i.e., Q_f, Q_{over}= 0, Lorentz (1926) adopted the following linearization for the quadratic term

$$|u|u \approx \frac{8\hat{u}}{3\pi}u \tag{2.25}$$

corresponding to using only the leading term of the Fourier expansion of

$$|\cos(\omega t)|\cos(\omega t) = \frac{8}{3\pi}\cos(\omega t) + \frac{8}{15\pi}\cos(3\omega t) + \text{HFT}\,. \tag{2.26}$$

As noted by Lorentz (1926) and Walton & Escoffier (1981), the equivalence of tidal work is obtained by (2.25) since the frictional dissipation, assuming a simple harmonic velocity, gets a non-zero contribution only from the first harmonic of the shear stress:

$$\overline{u\tau} = \overline{\cos\omega t\left(\frac{8}{3\pi}\cos\omega t - \frac{8}{15\pi}\cos 3\omega t + ...\right)} = \overline{\cos\omega t\frac{8}{3\pi}\cos\omega t} = \frac{4}{3\pi} \tag{2.27}$$

Analytical solution for linearized friction

Without contributions from Q_{f} and Q_{over} and after linearization, Equation (2.20) becomes

$$\eta_o = \eta_b + \frac{L_c}{g}\frac{A_b}{A_c}\frac{\partial^2\eta_b}{\partial t^2} + \frac{4F}{3\pi g}\left(\frac{A_b}{A_c}\right)^2\left(\frac{\partial\eta_b}{\partial t}\right)_{\max}\left(\frac{\partial\eta_b}{\partial t}\right) \tag{2.28}$$

which, with the constant coefficients T_1 and T_2, can be written

$$\eta_{\text{O}} = \eta_{\text{b}} + T_1\frac{\text{d}\eta_b}{\text{d}t} + T_2^2\frac{\text{d}^2\eta_b}{\text{d}t^2} \tag{2.29}$$

where the time constants are

$$T_2 = \sqrt{\frac{L}{g}\frac{A_{\text{b}}}{A_c}} = \frac{1}{\Omega_H} \tag{2.30}$$

and

$$T_1 = \frac{4F}{3\pi g}\left(\frac{A_b}{A_c}\right)^2\left(\frac{d\eta_b}{dt}\right)_{\max} = D_1\left(\frac{d\eta_b}{dt}\right)_{\max} \tag{2.31}$$

The physical meaning of T_2 is the period corresponding to Helmholtz frequency Ω_H while T_1 describes the geometrical and frictional features of the system.

Methods for determining solution for steady tidal forcing are given in the following. These solutions will, for natural systems, be superimposed by transients, the details of which are show in Section 6.5.1.

For convenience, when dealing with linear(ized) processes, the complex notation is preferred. The tides in the ocean and the bay, for the case of monochromatic tide, can be rewritten in the complex form as

$$\begin{aligned}\eta_o &= a_o \cos(\omega t) = \mathrm{Re}\{a_o e^{i\omega t}\} \\ \eta_b &= a_b \cos(\omega t - \varphi) = \mathrm{Re}\left\{F(\omega) a_o e^{i\omega t}\right\} = \left|F(\omega)\right| a_o \cos\left[(\omega t) + Arg\left\{F(\omega)\right\}\right].\end{aligned} \tag{2.32}$$

A solution of (2.28) using (2.32) is derived as follows:

Replace $\frac{\mathrm{d}\eta_b}{\mathrm{d}t} = a_b i\omega e^{i\omega t}$; $\frac{\mathrm{d}^2\eta_b}{\mathrm{d}t^2} = -a_b\omega^2 e^{i\omega t}$; and $\left(\frac{d\eta_b}{dt}\right) = a_b\omega$ into (2.28) and cancel the common factor $e^{i\omega t}$ to get

$$\begin{aligned} & a_o = a_b + i\omega^2 D_1 \left|a_b\right| a_b - \omega^2 T_2^2 a_b \\ & \Downarrow \\ & \left|a_o\right| = \left|a_b\right| \left|1 + i\omega^2 D_1 \left|a_b\right| - \omega^2 T_2^2\right| \\ & \Downarrow \\ & \left|a_o\right|^2 = \left|a_b\right|^2 \left(\left(1 - \omega^2 T_2^2\right)^2 + \omega^4 D_1^2 \left|a_b\right|^2\right). \end{aligned} \tag{2.33}$$

Put $X = |a_b|^2$ then obtain quadratic equation

$$\omega^4 D_1^2 X^2 + \left(1 - \omega^2 T_2^2\right)^2 X - \left|a_o\right|^2 = 0. \tag{2.34}$$

Solving (2.34) yields the bay tide amplitude $|a_b|$ as

$$\left|a_b\right| = \sqrt{X} = \left(\frac{\left(\left(1 - \omega^2 T_2^2\right)^4 + 4\omega^4 D_1^2 \left|a_o\right|^2\right)^{1/2} - \left(1 - \omega^2 T_2^2\right)^2}{2\omega^4 D_1^2} \right)^{1/2}. \tag{2.35}$$

Alternatively, an iterative solution to (2.28) can be solve for $F(\omega)=a_b/a_o$:

$$F(\omega) = \frac{a_b}{a_o} = \frac{1}{1 + i\omega^2 D_1 \left|a_b\right| - \omega^2 T_2^{\,2}}, \tag{2.36}$$

which requires iterative solution, but will then give $\varphi = -Arg\{F(\omega)\}$ as well as $G = |F|$.

Figure 2.12 shows an example of $F(\omega) = f(a_o)$. With other parameters kept constant, a_o increases from 0 m to 2.2 m. A_b=2 km^2, A_c = 30 m^2, semi-diurnal, T_2 = 3 s.

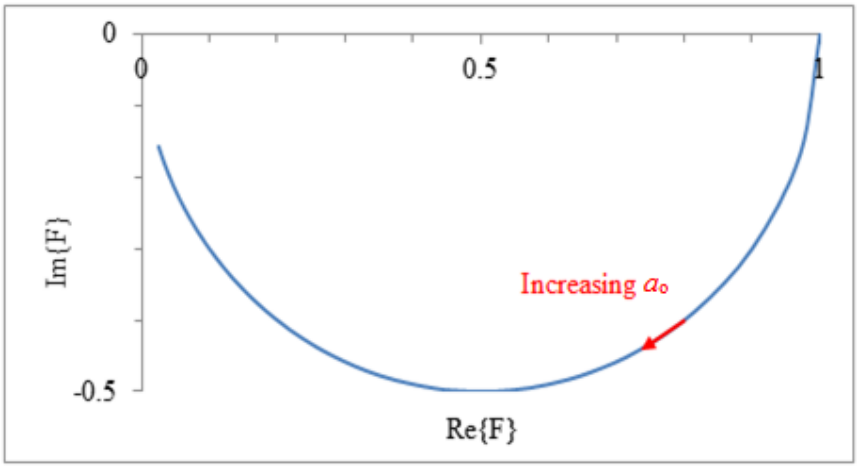

Figure 2.12: $F(\omega)=f(a_o)$ based on Eq (2.36) with $0 < a_o < 2.2$ m.

2.3.4 Influence of Q_f on $\eta_b(t)$ through $|u|u$: Fourier expansion of $|\cos \omega t+v|(\cos \omega t+v)$

The influence of Q_f through the quadratic friction term is investigated through a perturbation expansion with $v/\hat{u} = Q_f/(A_c \hat{u})$. We seek a Fourier expansion in the form:

$$y(t) = \left|\cos\omega t + \frac{v}{\hat{u}}\right|\left(\cos\omega t + \frac{v}{\hat{u}}\right) = A_o + A_1\cos\omega t + B_1\sin\omega t + A_2\cos 2\omega t + B_2\sin 2\omega t + \text{HFT}. \quad (2.37)$$

The behavior of the first three non-zero coefficients are shown in Figure 2.13. As can be seen, when $v/\hat{u} \le 0.5$, a third harmonic is generated in the order of less than 20% of the initial first harmonic, however it vanishes when $v/\hat{u} > 0.5$ and is replaced by a second harmonic with the order of half of the original first harmonic. For example, with $v/\hat{u} = -1$, corresponding to $Q_f = -\omega a_b A_c$, Eq (2.37) becomes

$$|\cos\omega t - 1|(\cos\omega t - 1) = -1.5 + 2\cos\omega t - 0.5\cos 2\omega t + \ldots \quad (2.38)$$

corresponding to the "o" in Figure 2.13.

With $A_0 = -1.5 < -1$, this means that the steady current is slowed more by friction due to the presence of the tidal flow. $A_1 = 2$ means that tides is affected more than twice as much by friction in presence of Q_f and $A_2 = -0.5$ means that a second harmonic is generated in the bay.

Making use of the coefficients from Figure 2.13, (2.18) becomes

$$\eta_o = \eta_b + \frac{L_c}{g}\frac{\partial u}{\partial t} + \frac{F\hat{u}^2}{2g}\left(A_0 + A_1\cos\omega t + A_2\cos 2\omega t + \ldots\right). \qquad (2.39)$$

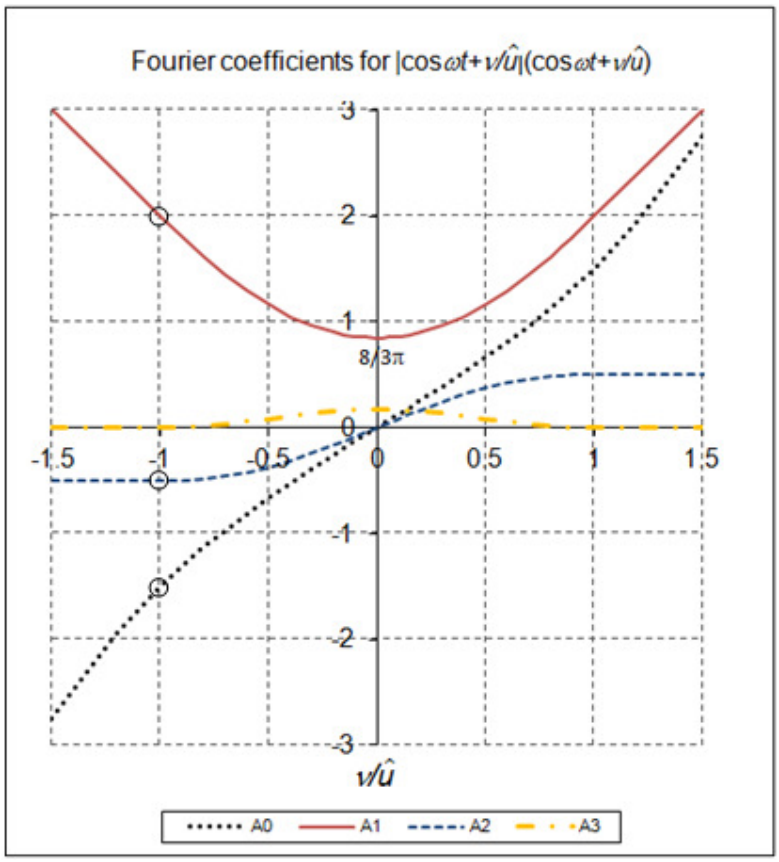

Figure 2.13: The influence of river flow velocity in non-linear friction term (2.37).

To study the effect of the tide on the steady over-height in the lake, steady terms of (2.39) is considered:

$$\eta_b = \eta_o - \frac{F\hat{u}^2}{2g}A_0 \qquad (2.40)$$

compared to the case with η_b=constant and river flow only, $\hat{u}=0$ which gives

$$\eta_b = \eta_o + \frac{F}{2g}\left(\frac{Q_f}{A_c}\right)^2. \qquad (2.41)$$

So the effect of the tide on the mean over-height of the bay through the quadratic drag is enhancement by the factor

$$-\hat{u}^2 A_0 \left(\frac{A_c}{Q_f}\right)^2 = -\frac{\hat{u}^2}{v^2} A_0 = -\frac{A_0}{a^2} = -(-1.5)/1 = 1.5\,.$$

That is, 50% increase in the steady bay level due to a superimposed tidal flow of equal magnitude to Q_f ($Q_f = -\omega a_b A_c$).

By comparison to the purely tidal case, $Q_f = 0$, corresponding to (2.25), the friction effects on the primary tidal component is enhanced by factor $A_1/\frac{8}{3\pi}$. In this case $2/\frac{8}{3\pi} = 2.35$.

For the purpose of deriving an analytical solution, Dronkers (1968) and Van de Kreeke (1969) expanded the linearization term for river flow. However, the river flow velocity should be small compared to tidal velocity. A more practical approach for the linearization of the quadratic friction term with the presence of river flow was taken by Lorentz's (1926):

$$|u|u \approx \frac{8\left(\hat{u} + |v|\right)}{3\pi} u\,. \tag{2.42}$$

By using the linearization (2.42), then (2.18) simplifies to

$$\eta_o = \eta_b + \frac{L_c}{g}\frac{du}{dt} + \frac{4F}{3\pi g}\left(\hat{u} + |v|\right)u \tag{2.43}$$

which implies that the oscillating tidal flow in the inlet can be superimposed on the constant river run-off discharge. However, this expression having a linearly increasing A_1 in the notation of (2.37) and Figure 2.13 is in conflict with the actual behaviour of the Fourier coefficients which is displayed in Figure 2.13. That is A_1 grows as v^2 (not v) from the current-free value of 8/3π.

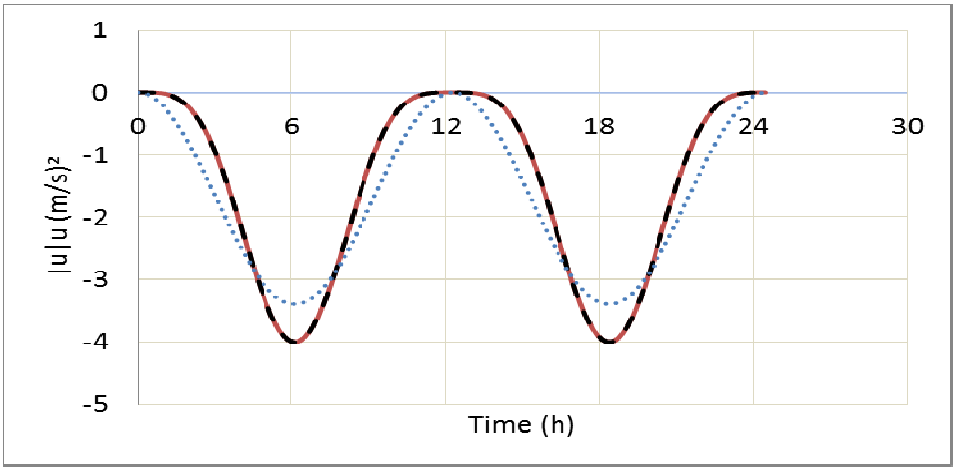

Figure 2.14: Comparison between the non-linear friction term |u|u (—) and the Fourier expansion (----) in Eq (2.38) and linearized (. . .) in Eq (2.42) with $v/\hat{u}$ =-1.

A comparison between results of the linearization by Lorentz's (1926) in Eq (2.42) and the complete non-linear friction term in equation (2.38) with $\hat{u}$ =1 m/s and v=-1 m/s is shown in Figure 2.14. The Fourier expansion truncated at 2nd order coincides with non-linear friction term, while the linearization obviously has low agreement. The maximum error occurred at the trough, showing a 0.55 $(m/s)^2$ overestimate compared to the non-linear result.

Other approaches to simplify analytical solutions include: Leblond (1978) re-examined the balance of momentum in shallow rivers such as the Saint Lawrence and the Fraser. He found that the friction forces exceeded acceleration over most of the tidal cycle and the long time lags associated with low waters can be explained as a simple diffusion phenomenon rather than by a simple wave propagation model. Escoffier & Walton (1980) provided an analytic solution taking into account Q_f without the $\partial u / \partial t$ term. Godin (1985) found and expressed a relationship between the tide and the freshwater discharge by analysing the tidal records, but did not show a clear analytical solution. Vongvisessomjai & Rojanakamthorn (1989) utilised a perturbation method to solve analytically nonlinear the differential equation (2.10), but the application was still incomplete for natural rivers.

Solutions given by Jay (1991) and Friedrichs & Aubrey (1994) were derived for strongly converging channels with a linearlised friction term. While Savenije (1998, 2001) provided a relatively simple analytical equation for describing tidal damping and amplification of "ideal" estuaries in a Lagrangian reference frame. Horrevoets et al. (2004) validate the assumption of Savenije (2001) and derived analytical solution for an equation expanded with Q_f. Vongvisessomjai & Chatanantavet (2006) developed an analytical model to simulate water surface fluctuation and tidal flow based on the Vongvisessomjai & Rojanakamthorn (1989) method and harmonic analysis. The analytical solutions consist of one part for steady flow, which represents the influence of river flows, and another one for the unsteady flow, which represents the influence of tides. Recently Lam (2009) provided quartic equation to determine $\hat{u}$ with the inertial term and linearization of friction term. However, no solution has been provided in an explicit form. River flow influence will be investigated further for simple cases in Section 2.4.

2.4 FREQUENCY RESPONSE FUNCTION OF THE LINEARISED SYSTEM

The traces of the frequency response function in the complex plane during morphological changes will be studied in detail in Sections 2.4.1 and 2.4.2. Hence we shall briefly discuss the traces of F corresponding to varying the friction and inertia coefficients in the linearized differential Equation (2.27).

The expression (2.36) for the frequency response function $F(\omega)$ can be rewritten in a shorter form with $T_1 = D_1\omega/|a_b|$:

$$F(\omega) = \frac{1}{1 + i\omega T_1 - \omega^2 T_2^{\,2}} \tag{2.44}$$

with the gain $$G = |F(\omega)| = \frac{1}{\left(\left(1-(\omega T_2)^2\right)^2 + (\omega T_1)^2\right)^{1/2}} \tag{2.45}$$

and phase lag $$\varphi = -Arg\{F(\omega)\} = \arctan\frac{\omega T_1}{1-(\omega T_2)^2} \tag{2.46}$$

which is in similar form to Walton's (2004) solution [cf. Eqs (12) and (13) in Walton (2004)].

Figure 2.15 and Figure 2.16 show the response function $F(\omega)$ for different ratios of (T_1 /T_2).

1: In the friction free case of T_1=0 or T_1/T_2=0, the frequency response function becomes

$$F(\omega) = \frac{1}{1-\omega^2 T_2^{\,2}} \tag{2.47}$$

which is real-value with

$$|F(\omega)| = \begin{cases} 1 \to +\infty & for \quad \omega T_2 < 1 \\ -\infty \to 0 & for \quad \omega T_2 > 1 \end{cases} \quad \text{and} \quad \varphi = \begin{cases} 0 & for \quad \omega T_2 < 1 \\ 180^o & for \quad \omega T_2 > 1 \end{cases}$$

which is represented the red arrows in Figure 2.15.

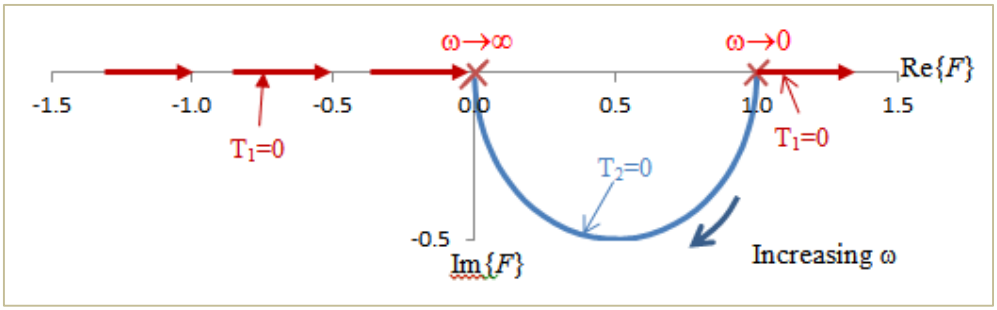

Figure 2.15: $F(\omega)$ corresponding to the friction free equation (2.47) and friction dominated (2.48).

2: In case of T_2=0 or T_1/T_2=∞, the friction dominated condition without inertial term e.g., vanishing L_c, the frequency response function is given by

$$F(\omega) = \frac{1}{1 + i\omega T_1} \tag{2.48}$$

which traces the blue half circle in Figure 2.15 from (1, 0) for perfect response ($\omega T_1 \to 0$), (0,-0.5) to the origin ($\omega T_1 \to \infty$). The Gain reduces monotonically and the phase lag increases from 0 to 90° for increasing ω.

3: Two intermediate cases with $T_1/T_2 = 1$, and $T_1/T_2 = 0.33$ are also presented in Figure 2.16, the larger the ratio of T_1/T_2, corresponds to increasing frictional dissipation, the smaller the curve size. For moderate T_1/T_2 we see an initial increase in gain and then the gain reduces, while the phase lag increases from 0 to 180°. The red point, $F(\omega) = 1$ at very small ωT_2 for any T_1/T_2, shows that at low frequency (long period) we get perfect response without phase lag.

These solutions to Equation (2.44) presented in Figure 2.16 for different ratios of T_1/T_2 are quite similar to those of Walton & Escoffier (1981) for different damping coefficient $D = \frac{F}{2L_c}\frac{A_b}{A_c}a_o$. The ratio T_1/T_2 has the same effect as D in damping bay tide as shown in Figure 2.17 since $T_1 \sim D$ (proportional, cf. Eq (2.31)).

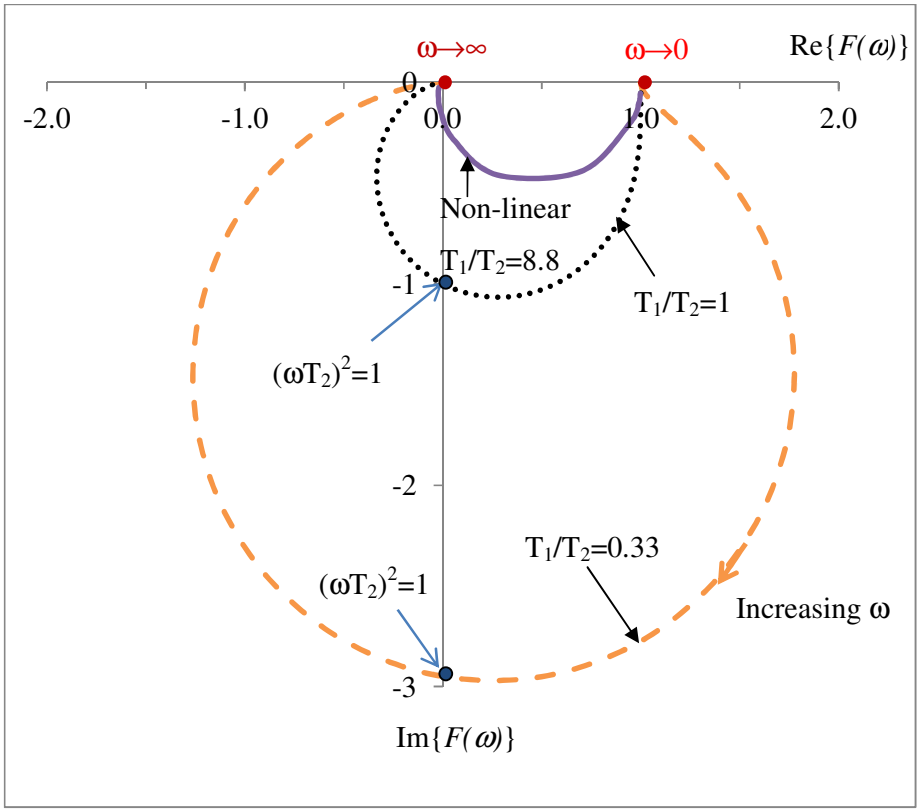

Figure 2.16: $F(\omega)$ corresponding to T_1/T_2=0.33 (---), T_1/T_2=1 (····) calculated from Eq (2.44) and results from numerical solution of the non-linear Eq (2.18) with T_1/T_2= 8.8 (—).

For Avoca Lake, Australia, which has been studied in some detail in the present work, friction dominates, corresponding to T_1/T_2 =8.8 (or D_1 = 105) which is common in nature.

The numerical solution of (2.18) is very close to the linear solution (2.48), confirming the statement by Walton (2004) that linear(ized) systems can provide results very close to complicated non-linear solutions.

At points where the curves in Figure 2.16 intersect the Im{}-axis, corresponding to 90° phase- lag we have $\omega T_2 = 1$ or $\omega = \sqrt{\frac{gA_c}{L_c A_b}} = \Omega_H$ which is sometimes referred to as the Helmholtz frequency.

It is noted that both the phase lag and amplitude of the flow velocity in the inlet are depending on the rate of inflow (Q_f+Q_{over}). For a small and deep bay, the difference in phase of water level in the bay and flow velocity in the inlet is π/2 (u ~ dη_b/dt) implying a "standing or pumping mode".

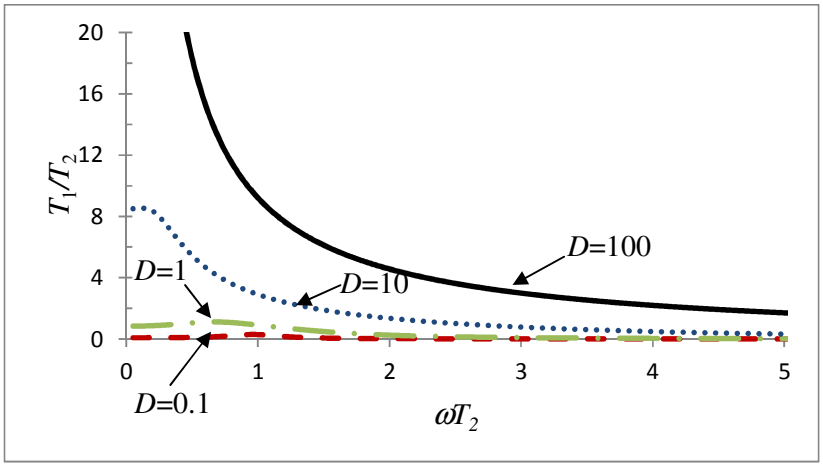

Figure 2.17: Relation between T_1/T_2 and ωT_2 corresponding to different damping coefficient D of Walton and Escoffier (1981).

$F(\omega)$ as an indicator of morphodynamic change

For an inlet system in morphological equilibrium, the frequency response function for each harmonic component (F_1 for the diurnal and F_2 for the semi-diurnal) usually appears as one point or a tight orbit surrounding a stable point in the complex plane as shown by the Brunswick Heads data in Section 4.2 Figure (4.19). When the system is forced out of equilibrium due to extreme waves or a flood, F will go far away from the stable point. In particular, large waves during periods with low rainfall may lead to inlet closure or $F \rightarrow 0$.

Subsequently, it takes time to turn back to normal condition. Events of this nature will be investigated and discussed in Chapter 4 case studies, and the time scales of F reverting to "normal" after extreme events will be used as indicators of morphodynamic time scales.

2.4.1 Estuary response to monochromatic tides

This section investigates the influence of inlet morphological change on tidal response as expressed by F, i.e., we look at traces of F in the complex plane during morphological change. These behaviours of F according to the Weir model and a numerical finite-channel-length (L_c) model are referenced against the simple expression (2.48) for the frequency response of a 1st order linear system. This section is restricted to monochromatic tides, while mixed diurnal/semi-diurnal tides are considered in the next section.

For an inlet with significant channel length, we use Mathematica® to solve the fully non-linear differential equation (2.20) with Q_f, Q_{over} = 0. The channel cross sectional area can be changed depending on the flow regime and water level in the ocean and the bay $A_c = W_c h_c$. The water depth through the entrance h_c is calculated from (2.6) or (2.7). We can change W_c, z_{cr} corresponding to morphological change.

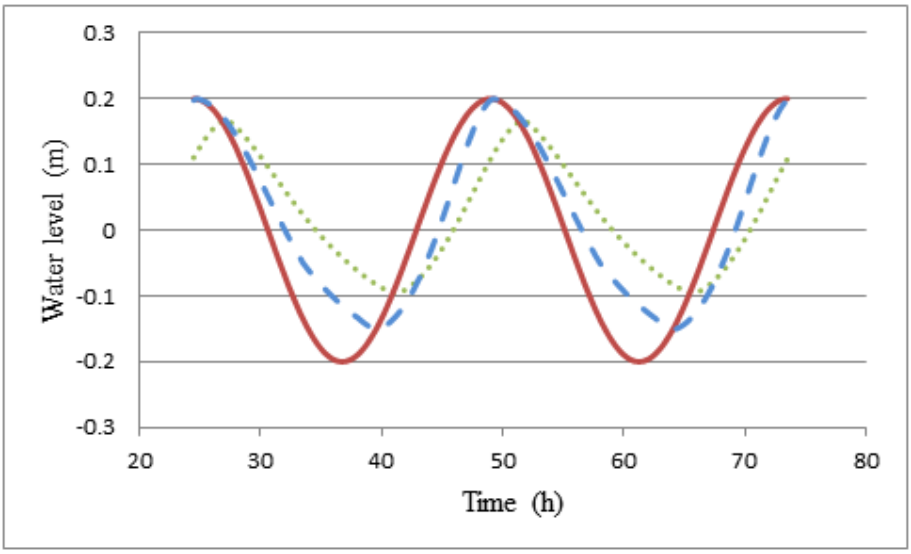

Figure 2.18: η_b calculated from two models: weir (----) and finite-channel-length with L_c = 600m (....) and z_{cr} = -0.3m from η_o (—). Other geometrical parameters: $A_b = 6.3\times10^5 m^2$, W_c = 20m.

As an example, we apply the weir model and the finite-channel-length model to Avoca Lake, New South Wales, Australia with the following parameters: Monochromatic ocean tide $\eta = a_o\cos(\omega t)$, a_o= 0.2 m, ω = 0.256 rad/hour for the diurnal constituent. Bay surface area A_b =

6.3×10^5 m^2, channel width W_c = 20 m. The aim is to illustrate lagoon response, quantified by F, to inlet morphology change expressed as changing crest level. Thus, z_{cr} increased from -1 m to +0.1 m in steps of 0.2 m until z_{cr} = -0.4 m, and in steps of 0.1 m for the rest. For the finite-channel-length model, the addition parameters are length of channel Lc = 600 m and a constant friction factor F= 4.5, corresponding to $T_2 \approx 1390$ s and the damping coefficient $D \approx 23$ or $D_1=2.15\times10^9$. Figure 2.18 shows η_b from these two models.

The model outputs are subjected to harmonic analysis to extract the primary harmonic component $a_b\cos(\omega t-\varphi)$ and hence the amplitude a_b and the phase-lag φ. Comparison with the ocean tide $\eta_o = a_o \cos\omega t$ then gives the gain $G = a_b/a_o$ and the frequency response function $F(\omega) = Ge^{-i\varphi}$, which is plotted in the complex plane in Figure 2.19. The two points with red circles show the difference in $F(\omega)$ from the two models for z_{cr} = -0.3 m.

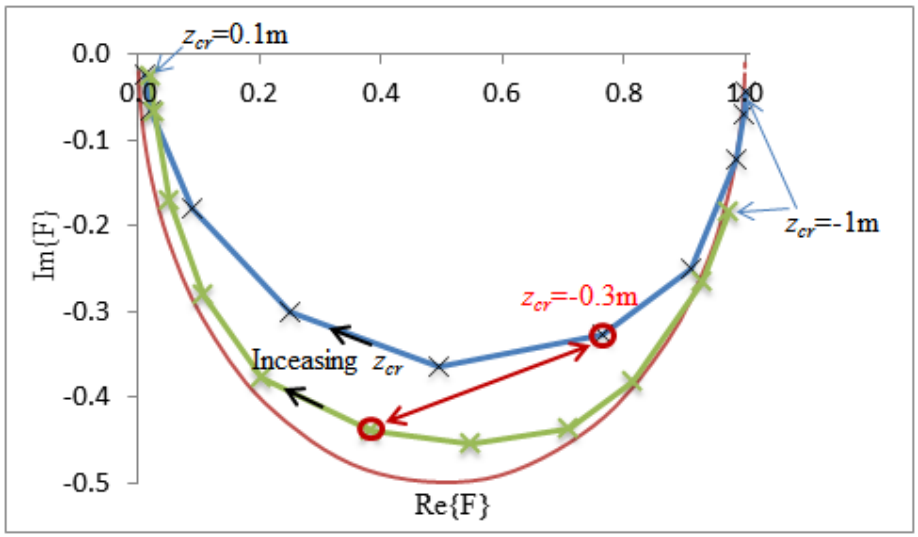

Figure 2.19. Results of $F(\omega)$ in comparison with the inertial free (2.48) (—) with the numerical solution for the weir model (—x—) and the finite-channel-length model solution (—x—). z_{cr} increase from -1 m to 0.15 m.

This figure shows that the weir model gives a larger gain and a smaller phase lag compared to the finite-channel-length model. This reflects the extra inertia and friction associated with the finite-length channel compared to the 'zero-length' weir. The finite-channel-length model is thus closer to the friction dominated solution (2.48) shown as the red semi-circle.

As z_{cr} increases all three curves are traced clockwise from F=1 (perfect response) for $z_{cr}\rightarrow-\infty$ towards the origin (zero response) for z_{cr} approaching the high tide level.

- **Signature of Q_f and A_b in tidal attenuation**

The examples above did not take into account the river discharge effects. This section, without the ambition to provide the analytical solution including river flow, uses Mathematica® to numerically solve the nonlinear Eq (2.20) with Q_{over}= 0 to investigate and compare two ways in which the addition of a significant flood (large Q_f) change the bay tide compared with a purely tidal (Q_f=0) situation. The two mechanisms are:

1: During a flood, a large Q_f raises the mean water level inside the bay. This would generate no change or insignificant change in the bay surface area A_b if the banks of the bay were steep (Figure 2.20 left). However, this is not often seen in a natural bay topography. Many estuaries and coastal lagoons are bordered by flat salt marshes giving large $dA_b/d\eta_b$ as, for example, the lower reaches of the Brunswick River, see Figure 2.20 right. Such a large increase in A_b affects the tidal oscillations of the bay, damping tidal amplitude and increasing the phase lag. Mathematically, when A_b increases, the damping coefficients D_1 and T_1 increase causing tidal attenuation, as illustrated by Eq (2.31) and Figure 2.21.

2: A large Q_f also increases the velocity u through the channel resulting in a larger friction term ~ $|u|uL_c$ which will also reduce the bay tides.

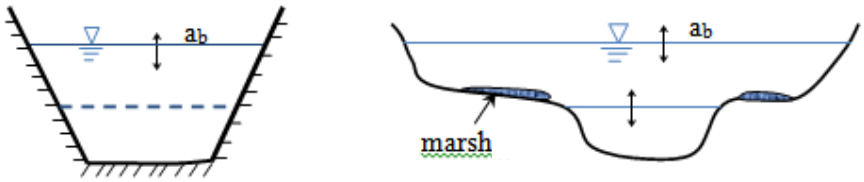

Figure 2.20. Different bay type results in change of A_b as the mean water level increases.

Table 2.1. Results of $F(\omega)$ for different case of Q_f and A_b.

Q_f (m^3/s)	$\lvert F(\omega)\rvert$	φ	A_b (m^2)	$\lvert F(\omega)\rvert$	φ
0	1	0.146	1×10^6	1	0.146
50	0.76	0.31	5×10^6	0.557	0.946
100	0.453	0.38	10×10^6	0.314	1.246
150	0.303	0.36	20×10^6	0.179	1.39
200	0.215	0.3	40×10^6	0.101	1.435

It is fairly clear that the influences of Q_f on $\eta_b(t)$ via the two different mechanisms are somewhat similar, but we seek insights in the finer details of the changes by varying A_b and Q_f independently, see Table 2.1. The differences are illustrated via different paths of $F(\omega)$ in the complex plane as shown in Table 2.1 and Figure 2.21 (left).

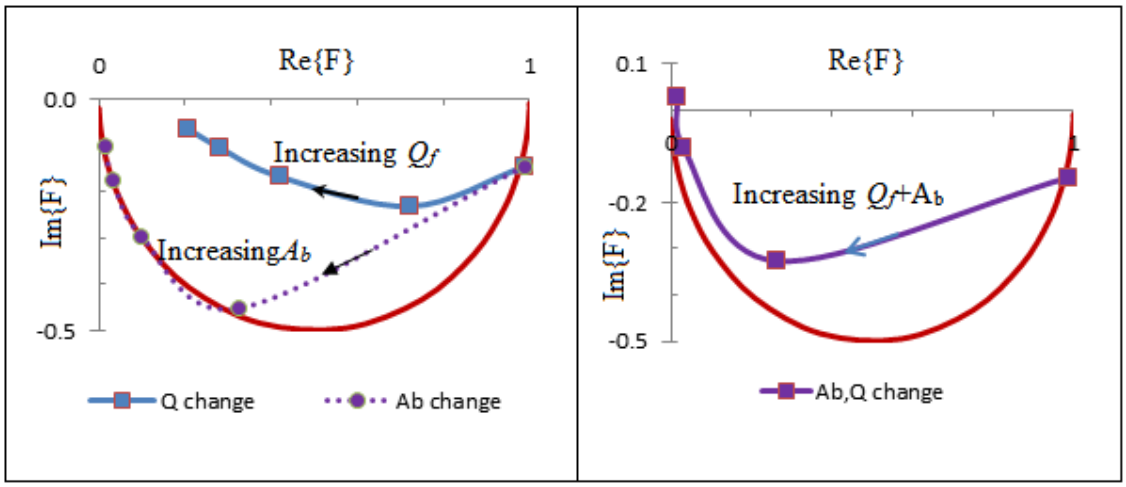

Figure 2.21: Different trend of $F(\omega)$ by changing Q_f and A_b (left), Q_f+A_b (right), eq (2.48) (—).

As can be seen from the results, $|F(\omega)|$ is in both cases reduced and the phase lag increases when Q_f and A_b are increased. However, the trend of $F(\omega)$ change from initial condition toward the origin is quite different. The $F(\omega)$ trend due to increasing the Q_f is quite far away from the expression (2.48) with the phase lag quite stable after first change from $Q_f = 0$ to 50 m^3/s and much smaller compared to that from increasing A_b. The path of $F(\omega)$ due to increasing A_b sticks close to $F(\omega)$ given by (2.48) and tends towards the origin with almost 90^o phase lag. One may argue that an A_b-increase because of a flood; it cannot happen in isolation, but should coincide with increase in Q_f. The results of some tests with combined Q_f- and A_b-increases together are shown in Figure 2.21 (right). It is seen the signature of damping in tide by increasing A_b dominated over Q_f with the $F(\omega)$ trend being quite similar to the trend due to A_b-increase by itself. The results from this test not only show which factor (Q_f vs A_b) is dominant. It also gives a tool for inferring changes to the topography of the bay system, which may themselves be difficult to measure, from changes in tidal response, i.e., changes of $F(\omega)$.

2.4.2 Mixed diurnal and semi-diurnal ocean tides.

Most of the field sites considered in the present study are exposed to mixed diurnal/semi-diurnal tides. Hence, the following section extends the tidal response discussion from the monochromatic scenarios discussed above to bichromatic, usually predominantly semi-diurnal tides.

As an example, consider the ocean tide of

$$\eta_o = a_{o1}\cos(\omega t) + a_{o2}\cos(2\omega t - \varphi_{o2})$$

with a_{o1}= 0.1 m, a_{o2}= 0.4 m, φ_{o2}= π/2. These amplitudes are typical for the South East Coast of Australia from where most of the field data for this study comes from. The Phase angle φ_{o2} varies through the neap-spring tidal cycle.

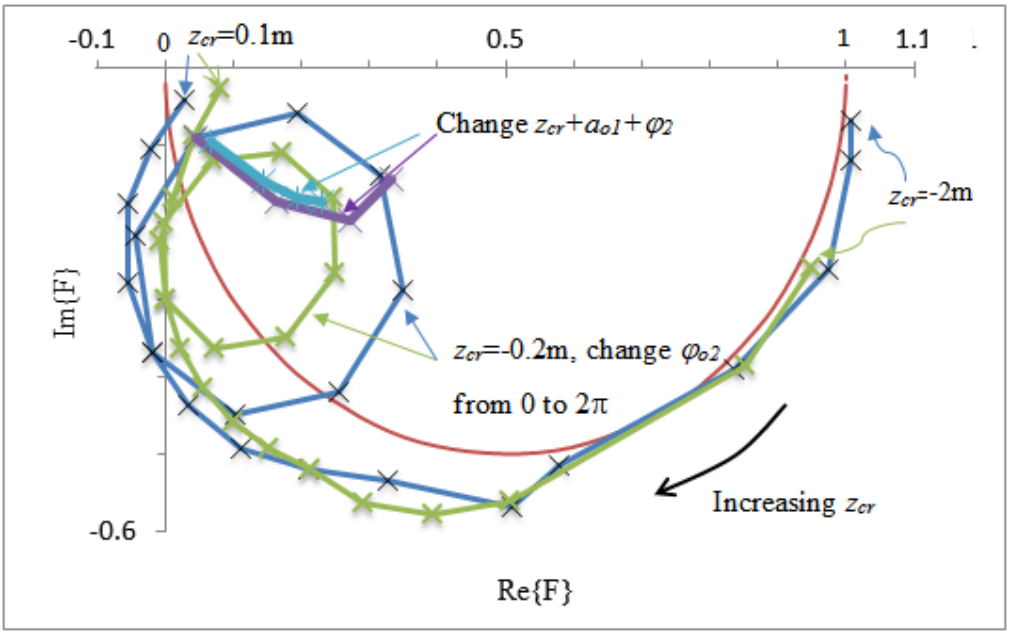

Figure 2.22: Diurnal $F_1(\omega)$ for different cases of increasing z_{cr} from -2 m to 0.1 m, change amplitude and loops generated by change φ_{o2} from 0 to 2π; equation (2.48) (—), weir model (—x—) and the finite-channel-length model (—x—).

The bay geometry was the same as that in the monochromatic tide cases above. The results for $F_1(\omega)$ corresponding to z_{cr} increasing from -2 m to 0.1 m is shown in Figure 2.22 for the diurnal component and $F_2(\omega)$ and for the semi-diurnal in Figure 2.23.

As can be seen, the results for $F_1(\omega)$-paths for increasing z_{cr}, from the weir model and from the finite-channel-length model, are quite close to each other (Figure 2.22). This means that the influence on F_1 of the friction term through the channel length can be negligible. Conversely, the $F_2(\omega)$-paths for the two models are very different with the finite-channel-length model resulting in

much less gain and a greater delay (Figure 2.23). This means that the friction term is very important and needs to be taken into account for estimating the primary component response, F_2.

The semi-diurnal is the primary constituent with its behaviour being quite stable to any changes in either z_{cr}, the ocean tide amplitude or the change in φ_{o2}, Figure 2.23. Conversely the diurnal component response (the change of F_1) is really strong for an increase in the z_{cr} (perhaps heading towards inlet closure) or any spring/neap variation of the ocean tide, Figure 2.22. A prominent loop in the F_1 trace is evident when the phase difference between the two ocean components changes from 0 to 2π. The paths of F_2 show no loops.

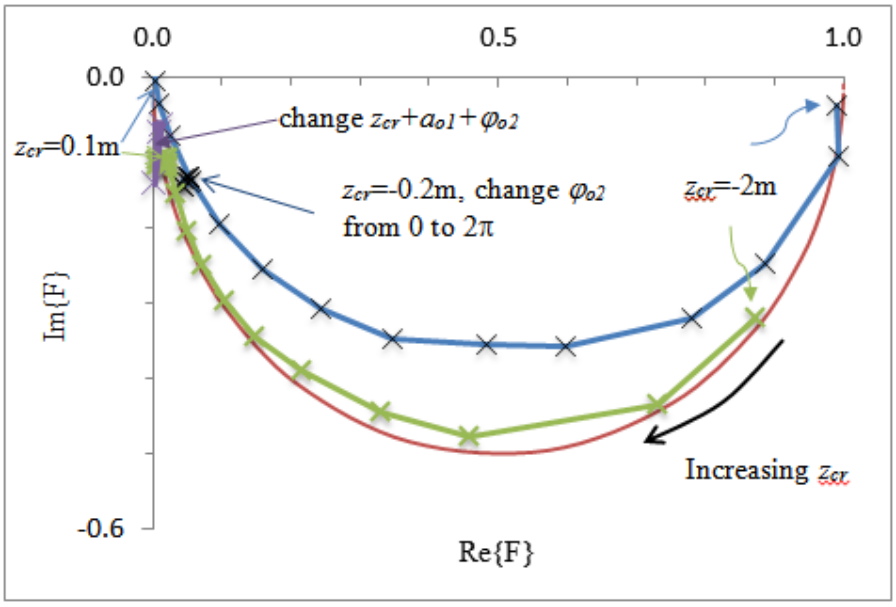

Figure 2.23: Semi-diurnal $F_2(\omega)$ for z_{cr} increasing from -2m to 0.1m and change amplitude in comparison with the analytical solution of equation (2.48); equation (2.48) (—), weir model (—x—) and the finite-channel-length model (—x—).

Similar paths of $F_1(\omega)$ and $F_2(\omega)$ were seen when the z_{cr} increases (simulating inlet closure) toward origin when inlet approaches a complete closure.

Regarding the influence of the river flow on the inlet closing process, this case simulates the situation closer to the nature. When Q_f increases, it can scour out the channel, z_{cr} reducing. When Q_f reduces, z_{cr} increases back to its normal level. $F_1(\omega)$ and $F_2(\omega)$ corresponding to this case is presented in Figure 2.24 based on the finite-channel-length model.

The stronger response of the diurnal was observed as in the previous case. The semi-diurnal component seems insensitive to this event, which could be due to the flow rate being too small. For the diurnal component, a loop in the path of F_1 is created when Q_f changes together with z_{cr} and also for the case where z_{cr} changes with a_{o1}.

We found that, when Q_f increases and z_{cr} reduces, G_1 increases and φ_1 reduces. This could be explained as follows: when the channel scours out, the channel cross-section increases, and therefore becomes more efficient. When Q_f reduces, z_{cr} increases back to normal, an opposite trend was seen with G_1 reducing and φ_1 increasing.

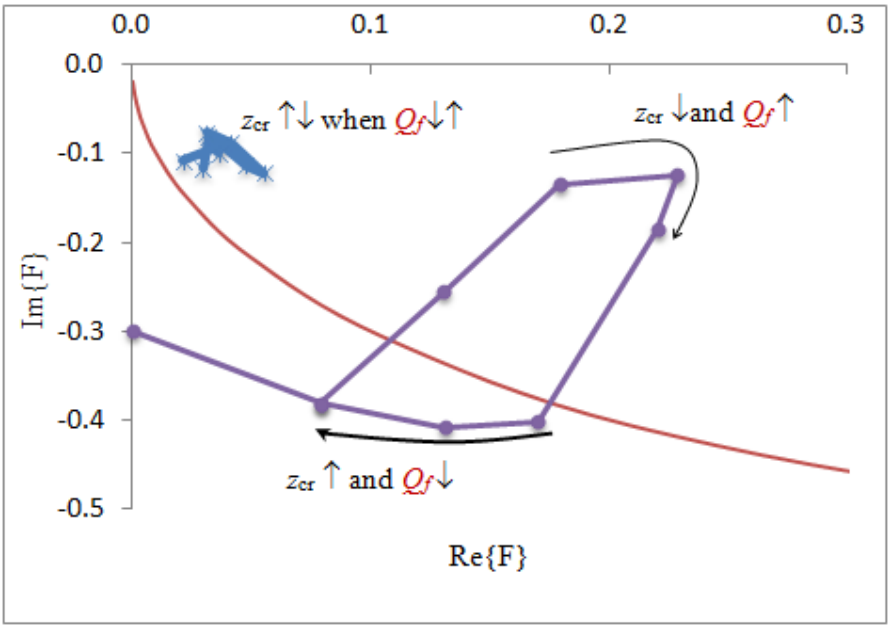

Figure 2.24. Results of $F_1(\omega)$ and $F_2(\omega)$ corresponding to Q_f increasing from 0 to 15 m^3/s and z_{cr} reducing from 0 to -0.2 m, Q_f reducing from 15 m^3/s to 0 z_{cr} increasing from -0.2 m back to 0. $F(\omega)$ in Equation (2.48) (—); diurnal $F_1(\omega)$ (—•—) and semi-diurnal $F_2(\omega)$ (—x—).

The results for the dominant semi-diurnal component are similar to the monochromatic results but the behaviour of the subordinate, diurnal component, is more complex than the results in the monochromatic tides case. A clearer understanding of the behaviour of F_1 is hoped to develop as more real tide records are analysed from events of morphological inlet changes.

2.5 LAKE CONJOLA TIDAL ANOMALIES SIMULATION

2.5.1 Introduction

Lake Conjola in Southern, New South Wales, Australia experienced a significant flooding event around 9th April 2006 (Figure 2.25). At that time, very large waves with unusually long periods arriving from the south, seemed to be the main driving force for flooding through strong overwash flows. During this flooding, fresh water inflow and ocean surge were insignificant. This case is used

to illustrate the importance of wave overwash as a driving force and to evaluate different existing formulae to determine Q_{over} for a natural Lake-sand barrier system.

2.5.2 Lake Conjola morphology and available data

Lake Conjola is located at 35°16'00"S and 150°30'11"E, about 200 km South of Sydney (Figure 2.25). The lagoon surface area is ca 5.9 km^2 (Allsop, 2009) and the catchment area is ca 145 km^2. This system is classified as a predominantly open lake, being open 62% of time (GHD, 2012). The system consists of 2 lakes and a long channel. The main Lake Conjola with surface area ca 4.3 km^2 is connected to the ocean by a shallow sandy channel around 3 km long and about 1 m deep. Berringer Lake, a smaller lake with surface area of ca 1.5 km^2, is located around 1.5 km from the entrance. It is connected to the main channel via a relatively short and narrow passage (Haines & Vienot, 2007). The entrance to the lake located close by Cunjurong northern rock shelf, is rather shallow (1m depth) and narrow (30 m wide). The entrance channel separates the large sand lobes and long sand spit (Figure 2.26).

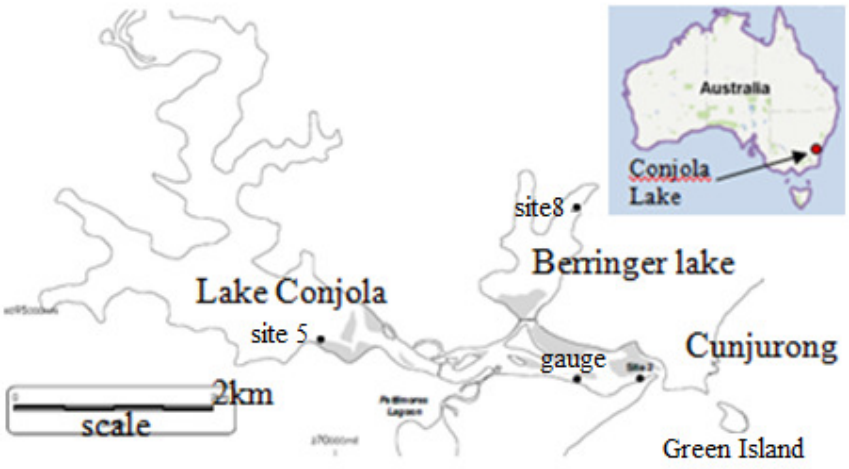

Figure 2.25: Location of Lake Conjola, NSW, Australia (sketch modified from source Allsop, 2009). For a close-up of the lower part of the system see Figures 2.9 and 2.10.

Britton & Partners (1999) found that inlet closure events occurred eight times since 1937, and all closure events were related to washover during severe wave storms. The length of the over-washed berm is ca 300 m (Figure 2.26), and the berm crest is 1.2-1.5 m above mean sea level. The maximum velocity at the entrance in flooding season is ca 1 to 1.4 m/s. The damping coefficient is estimated as $D \approx 350$ for normal conditions, this means that the friction term dominates the system.

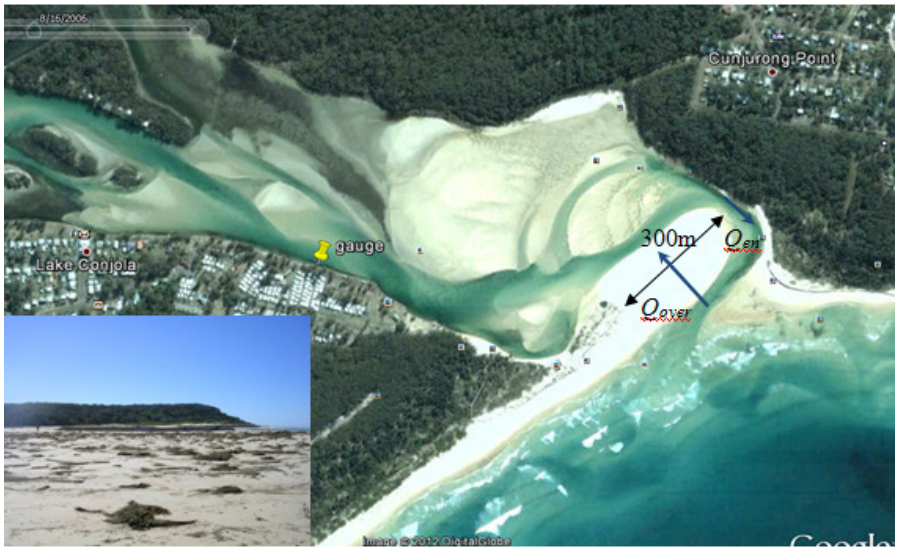

Figure 2.26: Closer view of Lake Conjola's entrance (16/8/2006) from Google Earth and location of tidal gauge. The Berm was overwashed in an extreme wave event on 9 April 2006 with debris left after event (bottom left), photo provided by Dave Hanslow.

During the large wave event in April 2006, the lake water level increased significantly overflowing its banks and flooding the roads and a caravan park (Figure 2.10). Photographs show that the berm was overtopped at some stage during 6th to 11th April 2006 and debris was left after event (Figure 2.26). The lagoon water levels were measured by a water level gauge located 1.3 km upstream from the entrance. Ocean tides were mixed, predominantly semi-diurnal with a range of ca 1m during the event. The peak tide measured in the lake at 5:30 AM on 9 April 2006 was 1.31 m, more than a meter above expected level, 0.5 m higher than peak ocean tides (Figure 2.27). The corresponding anomaly was the highest ever recorded at Lake Conjola (Allsop, 2009; Kulmar & Hesse, 2008). A maximum offshore significant wave height, H_s, of *ca* 5 m occurred with the peak wave period (T_p) greater than 15 s. Wave direction during the event was from south to south east so that, the fronting berm was directly exposed to the waves, potentially resulting in significant wave setup and surf beat (Allsop, 2009; Kulmar & Hesse, 2008). A simultaneous oceanic surge measured at the ocean tide station (Eden) ranged between 0.3 m and 0.4 m.

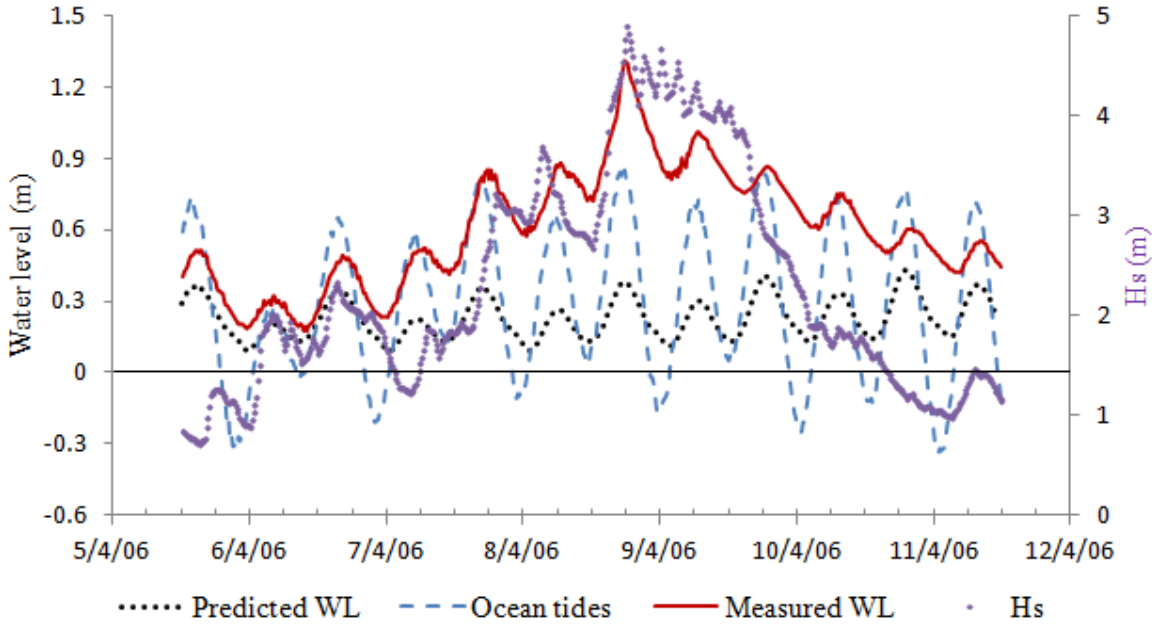

Figure 2.27. Available data for the event from 6th to 11th April 2006.

2.5.3 Two node hydrodynamic model

Traditionally, a one-node system was first investigated with the nominal surface area A_b being the whole bay surface area including Berringer Lake and Lake Conjola farther inside (Figure 2.25).

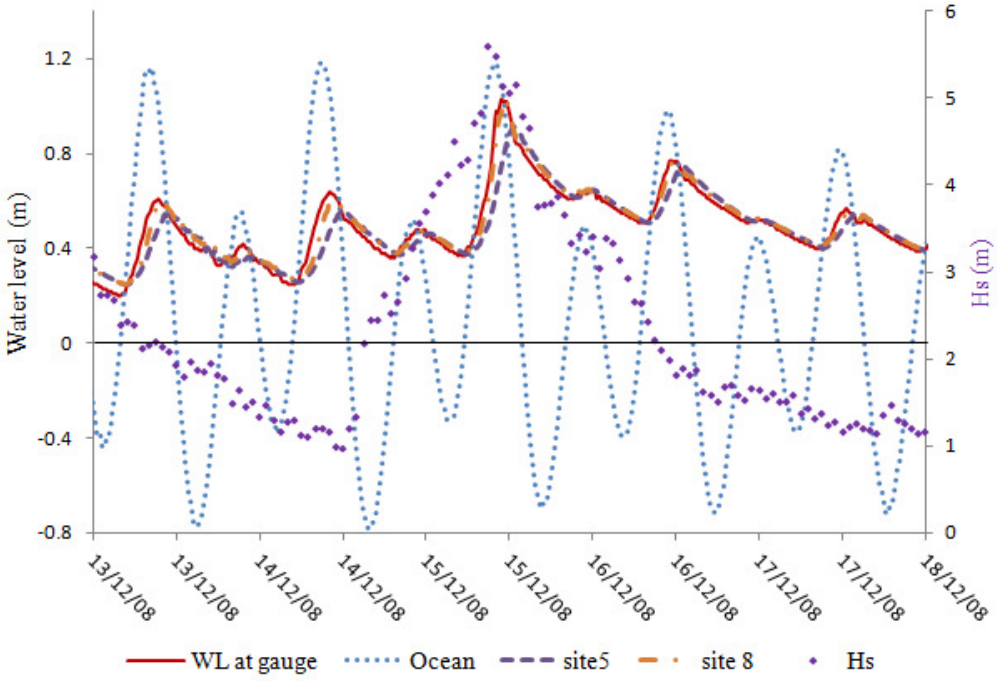

Figure 2.28. Water levels at different locations at Lake Conjola in the event Dec 2008.

However, results from one-node model by Thuy et al. (2011) show that the wave pump efficiency, ε, required to lift up whole lake level of ca 1 m, is 9 times the suggested value by Nielsen et al. (2001) and Callaghan et al. (2006a) for natural systems. This resulted in unrealistic velocity through the entrance and over the berm. Later they used a two nodes model to obtain a better agreement with measurements reflecting the real behaviour of the Lake Conjola system with $\varepsilon = 0.035$. In the two-node model, Lake 1 is the combination of the channel surface area and Lake Berringer while Lake 2 is the larger Lake Conjola farther inside (Figure 2.25). In addition, data from the December 2008 event (Figure 2.28) supports the two node approach. As can be seen, water levels measured at gauge were similar at site 8 in Berringer Lake while water levels at site 5 in Lake Conjola were well below and delayed. Therefore, the two-node model was chosen adopted.

In this case, $Q_f = 0$, due to insignificant rainfall. Hence the continuity equation for Lake 1 is

$$A_{b,1}\frac{\partial \eta_{b1}}{\partial t} = Q_{overwash} - Q_{en} + Q_{2-1} \tag{2.49}$$

$$Q_{2-1} = f\left(\eta_{b,2} - \eta_{b,1}\right) \tag{2.50}$$

and for Lake 2

$$A_{b,2}\frac{\partial \eta_{b,2}}{\partial t} = -Q_{2-1} \tag{2.51}$$

where $\eta_{b,1}$ and $\eta_{b,2}$ are the lake water surface elevations near the entrance and well within the lagoon and $Q_{2\text{-}1}$ is the discharge between the two nodes, positive from the inner node, see Figure 2.29. The overwash inflow Q_{over} across the berm is presented in 2.5.3.1 and the entrance outflow Q_{en} is obtained by the log-law friction model in 2.5.3.2. The solution method is a 4th order Runge-Kutta scheme.

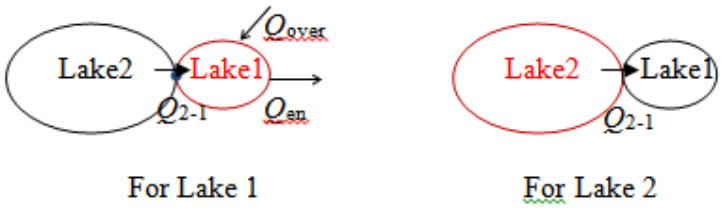

Figure 2.29. Sketch of calculation scheme for two node model.

2.5.3.1 *The overwash flow over the Lake Conjola spit*

Q_{over} is calculated and compared among 3 groups of models:

1) wave pump model;

2) overtopping related to swash truncation process (referred as swash model); and

3) empirical overtopping models.

The suitable model will be chosen based on the best agreement with measurements.

1): The wave pump concept was introduced by Bruun & Viggosson (1977) for non-breaking waves and extended by Nielsen et al. (2001, 2008) for rip currents. This concept was applied successfully for studying atoll flushing by Callaghan et al. (2006a). Thuy at al. (2011) applied the concept to simulate tidal anomalies for Lake Conjola for this event. However, the berm level of 2 m used in calculation seemed too high (after observing another overwash event in July 2011). The overwash unit flow rate q_{over} [m^2/s] is estimated using the wave pump efficiency concept in Eq (2.4)

In a scenario where water is pumped over a berm crest, which is well above the offshore still water level, SWL, the lifting height Δ is simply taken as the berm crest height above the SWL as in Figure 2.30.

$$q_{over} = \varepsilon \frac{E_f}{\rho g \Delta} = \varepsilon \frac{E_f}{\rho g (z_{berm} - SWL)} \tag{2.52}$$

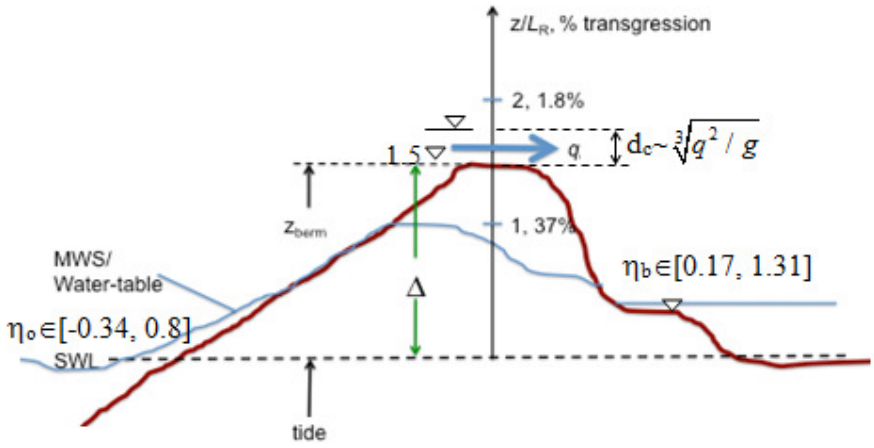

Figure 2.30: Notation and run-up scaling (L_R) for berm overwash. The % of waves transgressing corresponding to the ratio z/L_R in a Rayleigh distribution.

An extension to this is to include the critical flow depth, assuming that the flow across the berm is critical. z_{berm} is taken as 1.5 m AHD from field measurement 2011 and 2012. The lifting height then becomes

$$\Delta = (z_{berm} - SWL) + \sqrt[3]{q_{over}^2 / g} \tag{2.53}$$

The wave energy flux is calculated using sine wave theory:

$$E_f = \frac{\rho g H_{0,rms}^2}{16} \frac{g T_p}{2\pi} \tag{2.54}$$

in which $H_{0,rms}$ is the off-shore root mean square wave height and T_p is the spectral peak wave period.

These data gathered by Nielsen et al. (2008) indicate a weak dependence of q_{over} on the relative freeboard, $\Delta/(\sqrt{H_0 L_0}\tan\beta_F)$ (cf. Hanslow & Nielsen (1993) Figure 10).

2): Regarding breaking waves on a truncated beach, Baldock et al. (2005) found that the overtopping discharge derived by Shen & Meyer (1963), developed further by Peregrine & Williams (2001), underestimates Q_{over} by an order of magnitude compared to data and their numerical model based on Baldock & Holmes (1999). Later, Guard & Baldock (2007) developed a new swash model based on the non-linear shallow water equations and got realistic Q_{over} values by accounting for the shoreward momentum in surf-zone bores. Later, Baldock & Peiris (2010) expressed the relationship between dimensionless overtopping volume and dimensionless truncation point based on the Guard & Baldock (2007) solution with their k varying from 0 to 1.5. The parameter k represents different incoming mass and momentum fluxes at the seaward boundary (i.e., the point of bore collapse on a beach).

The overwash flow rate per unit length of berm q_{over} from Baldock & Peiris (2010) is:

$$q_{over} = \frac{R^2 V(E)}{2\sin(2\beta)T_p} \tag{2.55}$$

where β is the berm slope, R is run up limit height by Hunt (1956) given by

$$R = \begin{cases} \tan\beta\sqrt{H_o L_o} & \xi_o < 2 \\ H_o\sqrt{\dfrac{\pi}{\tan\beta}}\left(\dfrac{2\pi h_o}{L_o}\right)^{1/4} & \xi_o > 2 \end{cases} \tag{2.56}$$

with the surf similarity parameter given by $\xi_o = \dfrac{\tan\beta}{\sqrt{H_o / L_o}}$ and $V(E)$ is the total volume overtopping (including part of critical and supercritical flow) with $E = 2\Delta/R = 2(Z_{berm}\text{-SWL})$. $V(E)$ is calculated from the table derived by Hogg et al. (2011) with different k. k=0 corresponds to the analytical solution of Shen & Meyer (1963). k=1 corresponding to fully developed nearly uniform bores, i.e., a near horizontal water surface elevation behind the bore front, with both flow depth and flow velocity behind the front decreasing linearly with time. k>1 may represent the case, where continual incoming flow overruns the initial shoreline motion originating from bore collapse.

3): Laudier et al. (2011) applied several empirical overtopping models such as Van der Meer & Janssen (1995), Hedges & Reis (1998) and Pullen et al., (2007) for a barrier beach fronting a lagoon. They found that three of them worked similarly well with a reduction factor γ_r = 0.72-0.87

for two narrow- banded wave case; however, the European model (Pullen et al. 2007) had the best overall agreement with data and especially for broad-banded and double peak wave spectra. These empirical formulae are strongly dependent on slope geometry and used for breakwater with free overtopping. These overwash formulae are listed below:

Van der Meer & Janssen (1995), further referred as VJ model has an exponential form

$$\begin{aligned} \frac{q_{\text{over}}}{\sqrt{gH_{ST}^3}} &= \frac{A}{\sqrt{\tan\beta}}\xi_o \exp\left[-B\frac{R_c}{\gamma_r \xi_o H_{ST}}\right] \qquad \xi_o \le 2 \\ \frac{q_{\text{over}}}{\sqrt{gH_{ST}^3}} &= C\xi_o \exp\left[-D\frac{R_c}{\gamma_r H_{ST}}\right] \qquad \xi_o > 2 \end{aligned} \tag{2.57}$$

where H_{ST} is the significant wave height at the toe of the structure, which is hard to determine/define for natural sand barriers. Thus, as an alternative $R_{2\%}$ is utilized. T_{p} is the peak wave period; γ_r is the reduction factor for tuning, which depends on beach permeability, berm character, non-normal wave incidence and surface roughness. γ_r =0.72 - 0.87 is suggested by Laudier et al. (2011). The empirical coefficients A=0.06, B=5.2, C=0.2, D=2.6 are determined from laboratory data.

Pullen et al. (2007), referred further as the EU model, used the same type of formula but with different empirical coefficients; A=0.067, B=4.75, C=0.2, D=2.6. They used $T_{\text{m-1.0}}$ instead of T_{p}, between which the relationship is $T_{\text{p}} = 1.1\ T_{\text{m-1.0}}$.

Hedges & Reis (1998), referred to as the HR model is based on the physical equation of discharge over the weir,

$$\frac{q_{\text{over}}}{\sqrt{gR_{\max}^3}} = \begin{cases} A\left(1-\dfrac{R_c}{\gamma_r R_{\max}}\right)^B & \text{for } 0 \le \dfrac{R_c}{\gamma_r R_{\max}} < 1 \\ 0 & \text{for } \dfrac{R_c}{\gamma_r R_{\max}} \ge 1 \end{cases} \tag{2.58}$$

where, they used $R_{\max 37\%}$ and gave the relationship between H_s and $R_{\max 37\%}$ depending on different ranges of ξ_o. The coefficients A and B are function of slope, cf. Laudier et al. (2011).

2.5.3.2 *The flow rate through the Lake Conjola entrance channel*

The entrance flow rate was modelled as a finite channel length model because the channel length L_c at Lake Conjola is significant of order 1300 m. The model with friction given by the log-law in terms of the mean hydraulic depth, $R = A_c/P$ and the Nikuradse roughness k_s is used:

$$Q_{en} = \frac{A_c}{\kappa}\sqrt{g\frac{|\eta_o - \eta_b|}{L_c}R}\ln\frac{12R}{k_s}\,\mathrm{sign}(\eta_o - \eta_b) \qquad (2.59)$$

2.5.4 Application, results and discussion

2.5.4.1 *Overwash flow rate at Lake Conjola*

The overwash flow rate per unit width q_{over} by different methods is compared in Figure 2.31 based on ocean tides, z_{berm} and wave information. The wave pump efficiency ε=0.035 is chosen for Lake Conjola as suggested by Nielsen et al. (2001, 2008), Callaghan et al. (2006) and Thuy et al. (2011). For the swash model, k=1 is chosen as it provided a good description for usual conditions and corresponding to fully developed nearly uniform bores as suggested by Guard & Baldock (2007). An average reduction factor γ_r = 0.78 is applied for three empirical overtopping models as suggested by Laudier et al. (2011).

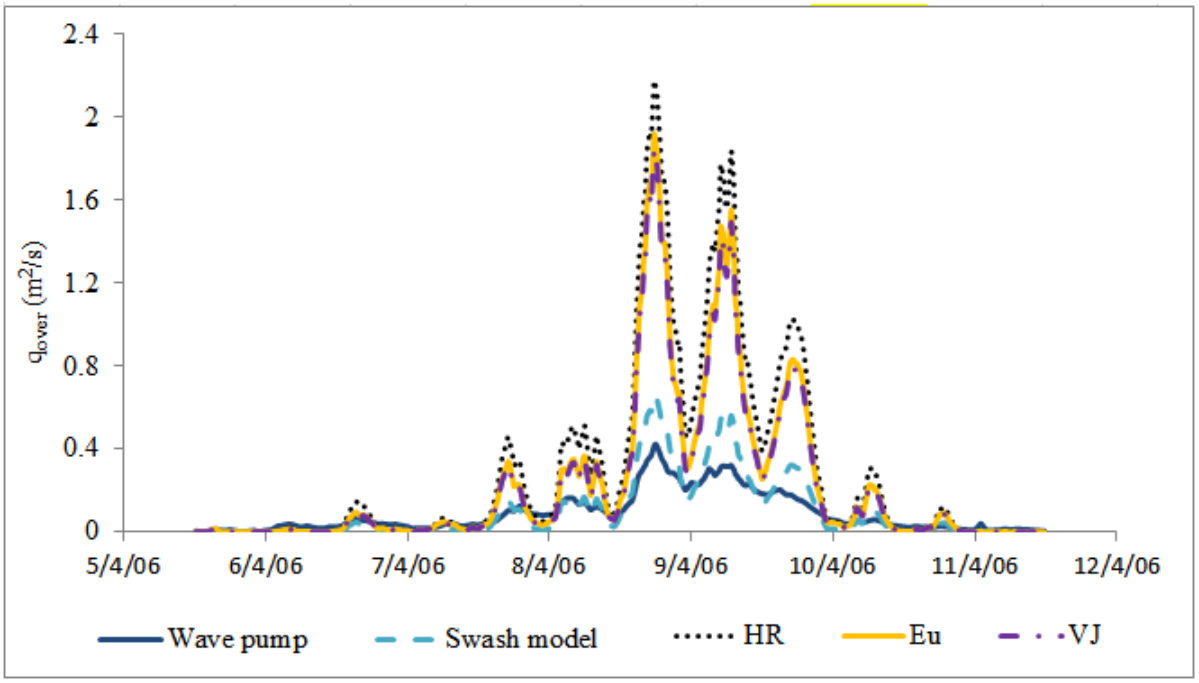

Figure 2.31: Results of overwash flow rate q_{over} (m^2/s) by different models: wave pump model with ε = 0.035, swash model with k = 1, empirical HR, Eu and VJ model with reduction factor γ_f = 0.78.

As can be seen, the three empirical models similarly give higher overtopping flow rates, by a factor of 5 compared to the lowest q_{over} from wave pump model, and a factor of 3 compared to the swash model. All models are active when H_s>2.5m and q_{over} is almost zero for H_s<2.5m. The q_{over} predicting was utilized to force the two node model to calculated bay water levels. The constant entrance cross section is chosen for simulation period with a rectangular shape of: 30 m width and

1m depth. These dimensions are based on measurements from Google Earth images, field surveys in 1993, 2008, 2011 and 2012 as well as other related reports.

2.5.4.2 *Comparison of water levels from different Q_{over} models*

Simulated water levels using different Q_{over} models are presented in Figure 2.32. In general a group of empirical models overestimate the water level especially during the period of intensive wave activity. Wave pump model and swash model are close to measurements, but similarly underestimate water levels. Wave pump model has better agreement with measurements compared to other models.

In particular, the three empirical models similarly predict 1 to 1.5 m above measured water levels from late 8/4 to 10/4/2006 corresponding to the largest values of Q_{over} (Figure 2.31). The HR model persistently gives higher high water levels than the other two models in this group. To match the peak levels these models require a much larger cross section area of the order 80 m width with the same 1m depth. Such large throat cross section area has not been observed before. In addition, the tidal range is still very large, a factor 2 to 3 of the measured tidal range even if the peak is matched. Therefore these empirical models are not suitable for this case. To improve the results, the reduction factor γ_r needs to be decreased together with adjustments of the channel cross section.

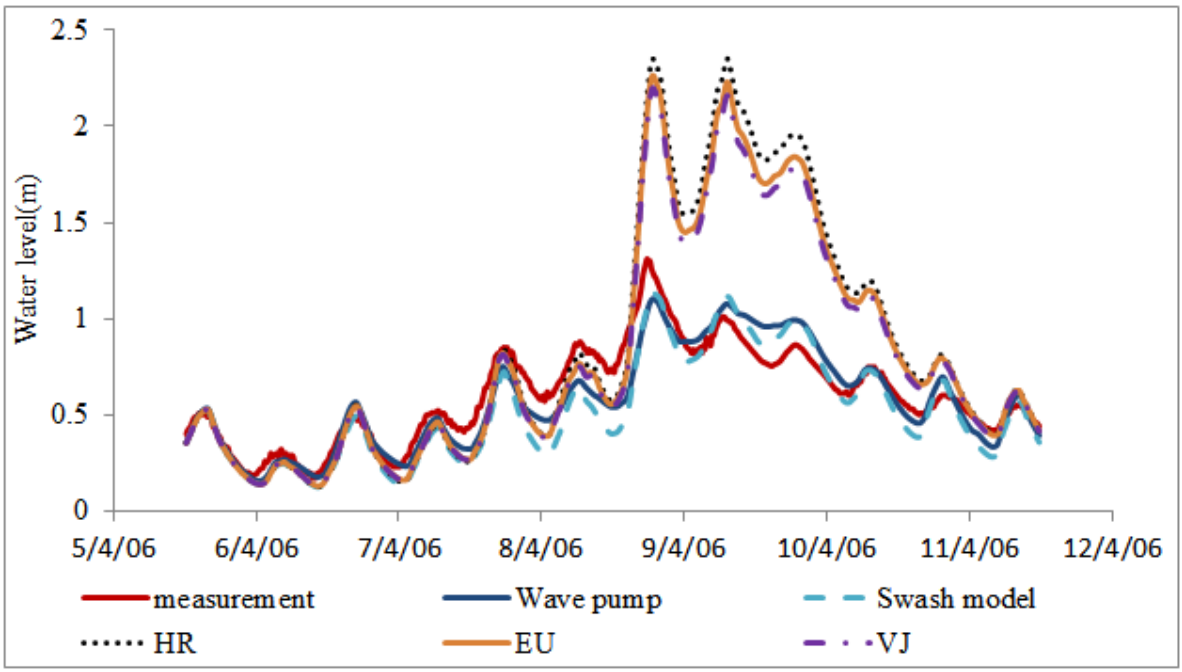

Figure 2.32: Results of water levels from different overtopping models: wave pump model with $\varepsilon = 0.035$, swash model with $k = 1$, empirical HR, Eu and VJ model with reduction factor $\gamma_r = 0.78$.

The wave pump model and swash model are similar in predicting same high water levels and same peak level even though wave pump model provide less overwash discharge than swash model (Figure 2.31). Both model underestimate ca 0.2 m of water levels during 8/4/2006 compared to measurements. However, the wave pump model matches measured tidal range and has a better agreement with measurements at low tides. Therefore, overall the wave pump model (ε=0.035) has better fit with measurements compared to other models with RMSE of 0.1 m and swash model (k=1) is the second one with RMSE of 0.15 m. To get further better agreement with measurement both models need to have slightly higher values of ε and k coefficient, as well as varying cross section in time.

2.6 CONCLUSIONS

The inlet hydraulic analysis was reviewed and presented for fixed inlet geometry under tidal forcing, river flow and wave overwash. Different hydraulic models for inlet–bay system were presented such as weir model and finite-channel length model. The solution of bay water level was presented in a complex frame.

The hydraulic analysis of inlets in terms of the frequency response function for the linearised system is investigated and illustrated for cases of monochromatic tide, mixed diurnal and semi diurnal tides. This analysis shows the influence of the increase of entrance invert level z_{cr}, river flow and bay surface area.

The results for the dominant semi-diurnal component of a mixed tide system are similar to the monochromatic results but the behaviour of the subordinate, diurnal component, is more complex than the results in the monochromatic tide cases.

The influence of the friction term on subordinate frequency response function, F_1, through the channel length can be negligible. However, it significantly influences the primary component response F_2.

The semi-diurnal F_2 behavior is quite stable to any changes in either z_{cr} or the ocean tide amplitude or the change in phase between two ocean components. Conversely the diurnal component response, F_1 is really strong for an increase in the z_{cr} (perhaps heading towards inlet closure) or any spring/neap variation of the ocean tide (Figure 2.22). A prominent loop in the F_1 trace is evident when the phase difference between the two ocean components change from 0 to 2π while the paths of F_2 show no loops. Similar paths of $F_1(\omega)$ and $F_2(\omega)$ were seen when the z_{cr} increases (simulating inlet closure) toward origin when inlet approaches a complete closure.

The influence of the river flow on the response of a monochromatic tide shows different signatures via increasing A_b or via increased friction ~ $|u|uL_c$. For mixed tide cases, the effect of Q_f increasing the hydraulic efficiency is clearly seen in F_1 rather in F_2.

- *The April 2006 Lake Conjola flooding event*

A case of inland flooding at Lake Conjola illustrates the importance of wave overwash as a driving force. The two nodes model provides a good agreement with measurements, and reflects the real behaviour for the Lake Conjola system.

Three types of overwash models were investigated with calibration parameters based on previous studies. ε=0.035 is chosen for wave pump model, k=1 for swash model and γ_r = 0.78 is applied for three empirical overtopping models. The wave pump model provides the lowest overwash flow rate q_{over}. The group of three empirical models similarly gives highest q_{over}.

The simulated water levels using different Q_{over} models show that the group of empirical models overestimates the water level. The wave pump model and the swash model are comparable and give good agreement with measured water levels. The wave pump model best performs with matching measured tidal range and lowest RMSE.

Chapter 3

LAGOON AND ESTUARINE TIDE ANALYSIS

3.1 INTRODUCTION

This chapter introduces a new method of 24.5 hour moving window analysis of tidal records. A review of the traditional methods in tidal harmonic analysis and band pass filtering is also presented. The new method is based on the derivation of water-level statistics and hydraulic response functions from a 24.5 hour moving window. Time series of moving averages of water surface level $\overline{\eta_{24.5}}(t)$ and standard deviations $Stdv_{24.5}(t)$ are generated. Least-squares harmonic analysis (Boon & Kiley, 1978) is utilized to extract the diurnal (24.5 hours) and semi-diurnal (12.25 hours) amplitudes and phase at every hour based on the surrounding (centered) 24.5 hour period. By comparing the corresponding bay tidal amplitude and phase to the nearest ocean tide gauge, the gain $G(t)$ and the phase lag $\varphi(t)$ are calculated and are together presented in the response function $F(t)$ in the complex plane.

The application of this new method in inferring the morphological time scale T_{morph} and the hydraulic time scales T_1, T_2 (see Eq (2.29)) under different situations is presented. For example, $\overline{\eta_{24.5}}(t)$ and $Stdv_{24.5}(t)$ are used to find T_{morph} for inlet closure events (Figure 3.2), while the gain $G(t)$ of the primary component are utilized for extreme events such as flood or storm (Figure 3.3).

An investigation was carried out to find the best method of de-trending unsteady tidal records under extreme conditions or inlet closure events. The method of removing the average from the tidal record before harmonic analysis is chosen because of providing the best results with high accuracy for any trend.

The performance of different window lengths 24 hours, 25 hours and 49 hours is presented to confirm the reliability of the chosen window length of 24.5 hours. Besides, artifacts induced by the new method on T_{morph} are also investigated. T_{morph} calculated from $\overline{\eta_{24.5}}(t)$ provides consistent results for every case. The non-linear interaction between the two tidal components gives rise to somewhat erratic behavior of subordinate tidal component, which are not clearly interpretable at the present stage.

3.2 WINDOW LENGTH

Ocean tides at a particular point on the Earth are represented as the combination of finite number (N) harmonic components. Each of these has its own period, amplitude and phase angle as in

$$\eta_o = \overline{\eta_o} + \sum_{i=1}^{N} a_{oi} \cos\left(\frac{2\pi}{T_i} t - \varphi_{oi}\right) \tag{3.1}$$

The periods T_i reflect the periodicities of the Sun-Earth-Moon system, while the amplitudes a_i and phase angles φ_i are determined by fitting to measured data. $\overline{\eta}$ is the mean water level. Notation "o" stands for ocean.

Window length is the minimum period of tidal record required to determine tidal constituent characteristics with sufficient accuracy and stationarity. It depends on the number of constituents as well as their periods.

The record length T required to separate two components of spacing Δ_ω is as given by (Roos, 1997)

$$T = \frac{2\pi}{\Delta_\omega} \tag{3.2}$$

For example, the minimum record length required to separate the diurnal (T=24.5 hours) and the semi-diurnal (T=12.25 hours) constituent in the simplified form as shown in Chapter 2 from observation is

$$T = \frac{2\pi}{\Delta_\omega} = \frac{2\pi}{\frac{2\pi}{12.25\text{h}} - \frac{2\pi}{24.5\text{h}}} = 24.5\text{h} \tag{3.3}$$

However, to separate the principal lunar component, M_2 (T=12.42 hours) and the solar component S_2 (T=12 hours), the minimum window length is

$$T = \frac{2\pi}{\Delta_\omega} = \frac{2\pi}{\frac{2\pi}{12\text{h}} - \frac{2\pi}{12.42\text{h}}} = 352.94\text{h} \approx 14.7\text{days} \tag{3.4}$$

Similarly, 13.7 days of observation is required to separate diurnal tides O_1 and K_1.

3.2.1 Traditional window length (1 year)

The period of 369 days (about 1 year) is popularly applied as the standard length for tidal harmonic analysis (Ippen, 1966; Roos, 1997). This period contains almost all the values of the synodic periods with high accuracy and stationarity. For example, according to the Australian tides manual, 2011, the National Tidal Centre (NTC) officially uses at least one year observations to analyse 56

tidal constituents including the four major constants: semi-diurnal M_2, S_2 and diurnal O_1, K_1. The Manly Hydraulics Lab used the Foreman (1977) method to separate 69 harmonic tidal components from 366-days of continuous tidal records. One complete lunar cycle of 29 days is considered to be the minimum period for analysis of the four above major constituents.

Tidal records can be analysed and presented using other alternative methods in both time and frequency domains. One method is spectral analysis with a moving window in time, which requires a window length that is short enough to see the variations and long enough for reasonable accuracy for the spectra. Abe & Ishii (1981) applied this method for studying tsunami to find travel time of edge waves with 2 hour window. Later, Hinwood & McLean (2001) used moving windows with lengths of 3 days and 14 days to determine amplitudes and phases of 5 standard tidal constituents. Their work will be reviewed in more detail in the next section as it is closest to the new method introduced and applied in this thesis.

Another widely used method is wavelet analysis (Jay & Flinchem, 1999), which is often applied in geophysics. However, the relation between physical forcing functions and wavelet parameters is difficult both conceptually and analytically.

Hinwood & Aoki (2013) used frequency–band analysis to examine eleven years of tidal record. They Fourier transformed the data, divided the transform into bands centered on selected frequencies such as 6 hours, 12 hours, 24 hours....2 years, then inverse transformed them. They identified the dominant frequency bands and the corresponding physical processes. The limitation of this method is that errors may be introduced into the harmonic analysis, when the time series contains a dominant component or large, rapid fluctuations caused by typhoon storm surge.

3.2.2 The Hinwood and McLean window (3-14 days)

Hinwood & McLean (2001) analysed tidal records using a moving window analysis for Lake Conjola in order to examine the response of the five main tidal constituents to inlet morphodynamics, including rapid scour, rapid accretion toward inlet closure and slow accretion.

Initially, they used a 14 day window moving in steps of one day. Later, they used a 3 day window moving in steps of one day.

They also simulated the behavior of a simple basin (Figure 2.1) using the 1D equation of motion in dimensionless form with resistance parameters and river flow corresponding to Lake Conjola.

They concluded that the model and the moving window tidal analysis are useful tools for management of tidal systems without full data of river flow and bathymetry.

The moving window analysis introduced by Hinwood & McLean (2001) is a simple and straightforward way to investigate tidal records in comparison to the traditional method of using one year harmonic analysis. Based on a ten-month tidal observation, from March 1999 to December 1999, of Lake Conjola and Jervis Bay ocean tides, time series of mean water level and five principal components including M_2, S_2, O_1, K_1 and N_2 were found by a moving window analysis. Comparison of amplitudes and phase lag between the bay and ocean was carried out. These five constituents were required to limit periodic fluctuations of the calculated components and provide stable results under storm conditions.

A 14-day window was the minimum required for obtaining stable values of the 5 coefficients mentioned above. However weather events (storm surges and/or large waves) vary on a shorter time scale [see e.g., Figure 1.6.7 of Nielsen, (2009)]. On the other hand, the diurnal and semi-diurnal tides are the main objects of interest and they require at least 24.5 hour window length as per Eq (3.3).

3.2.3 24.5 hour moving window

Aiming at resolving the diurnal and the semi-diurnal tides without distinguishing between solar and lunar components, we adopt a moving window method with window length of 24.5 hours and moving forward every hour instead of every day. The length of the window is sufficient for analysis of two basic diurnal and semi diurnal constituents as shown in Eq (3.3).

The simplest output of the moving 24.5 hour window method are time series of moving averages of water surface level, i.e.,

$$\overline{\eta_{24.5}}(t) = \frac{1}{24.5h}\int_{t-12.25h}^{t+12.25h} \eta(t')\,\mathrm{d}t' \tag{3.5}$$

and the corresponding standard deviations $Stdv_{24.5}(t)$.

Under equilibrium conditions, harmonic analysis can be applied directly to tidal records. However, under transient conditions with water levels rising due to rainfall and/or large waves and subsequently reducing after the event, de-trending before harmonic analysis is necessary to make sure the results are meaningful. After removing $\overline{\eta_{24.5}}(t)$ from measurement (Figure 3.1), least-square harmonic analysis (Boon & Kiley, 1978) is utilised to extract diurnal (24.5 hours) and semi-diurnal (12.25 hours) amplitudes [$a_1(t)$, $a_2(t)$] and their phases [$\varphi_1(t)$, $\varphi_2(t)$] every hour based on the surrounding (centred) 24.5 hour period.

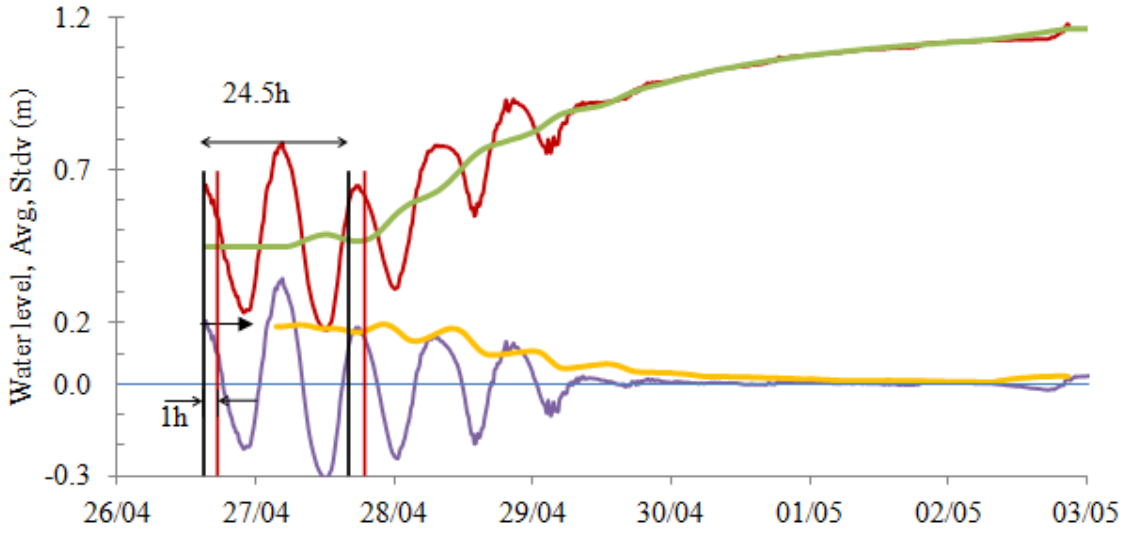

Figure 3.1: Example of moving 24.5 hour window for Avoca lake water levels (—), moving average $\overline{\eta_{24.5}}(t)$ (—), de-trended water levels (—) by removal $\overline{\eta_{24.5}}(t)$ from tidal record and $Stdv_{24.5}(t)$ (—).

By comparing the bay tidal amplitudes [$a_{b1}(t)$, $a_{b2}(t)$] to the nearest ocean tide gauge [$a_{o1}(t)$, $a_{o2}(t)$], the gain is given as:

$$G_j = \frac{a_{bj}}{a_{oj}} \tag{3.6}$$

where j=1, 2 with 1 for diurnal and 2 for semi-diurnal. Phase lags are determines as per Eq (3.7),

$$\varphi_j = \varphi_{bj} - \varphi_{oj} \tag{3.7}$$

Correspondingly, the complex frequency response functions F_j, cf. Section 2.1.2 and Figure 2.5, are

$$F_j = G_j e^{-i\varphi_j}. \tag{3.8}$$

3.2.4 Morphological time scale T_{morph} determined from 24.5 hour moving window analysis

The morphology of tidal inlets is primarily controlled by tides, waves, freshwater inflow and sediment supply. A significant change in any factor or a combination of them causes the inlet to move towards a new equilibrium. The time scale at which an inlet responds to these changes is called the morphological timescale T_{morph}. The difference between the actual state and an equilibrium state is usually expressed as an exponentially decaying function $e^{-t/Tmorph}$. The time constant T_{morph} in the exponential function varies from days to weeks as seen in small lake systems (e.g., Avoca lake, Wamberal, Terrigal, Cockrone lagoons NSW, Australia in Table 6.1) to months with seasonally closing inlets (Thuan An, Tu Hien, My A lagoons in Central coast of Vietnam). The

recovery time for the coast and river mouths along Miyagi prefecture, Japan, after the March 2011 Tsunami with a wave height of 20 m, ranges from 25 days for Arahama coast to 75 days for Akaiko coast, or 180 days for Nanakita River depending on sediment supply (Tanaka, 2012). T_{morph} can also be extremely long as O'Connor et al. (1990) estimated for the Welsh River Usk responding to barrage construction, which will reduce the tidal range from 12 m to 4 m. They suggested T_{morph} = 180 years. T_{morph} may be even longer, e.g. 350 years for Dollard's tidal flat in The Netherlands, responding to sea level rise (Eysink, 1990).

To determine T_{morph}, one might analyse measured throat areas and/or the volumes of the flood/ebb tidal deltas. They are however costly to measure. A future alternative approach may be to use process-based models. These are however likely unreliable.

In this study, we infer T_{morph} from hydraulic data. The logical starting point is to use time series of $\overline{\eta_{24.5}}(t)$ and $Stdv_{24.5}(t)$ as in Figure 3.1. Later we extend the analysis to the complex response function F_j corresponding to (3.8).

T_{morph} can be determined by fitting these parameters with exponential functions. The selection of a parameter to be fitted depends on the particular cases. For example, for the inlet closure event in Figure 3.2, $\overline{\eta_{24.5}}(t)$ and $Stdv_{24.5}(t)$ clearly show exponential form and it is convenient to fit function of the forms:

$$\overline{\eta_{24.5}}(t) = \eta_{\text{finish}} + \left[\eta_{\text{start}} - \eta_{\text{finish}}\right] e^{-(t-t_{\text{start}})/T_{\text{morph}}} \tag{3.9}$$

and

$$Stdv_{24.5}(t) = Stdv_{\text{start}}\, e^{(t-t_{\text{start}})/T_{\text{morph}}} \tag{3.10}$$

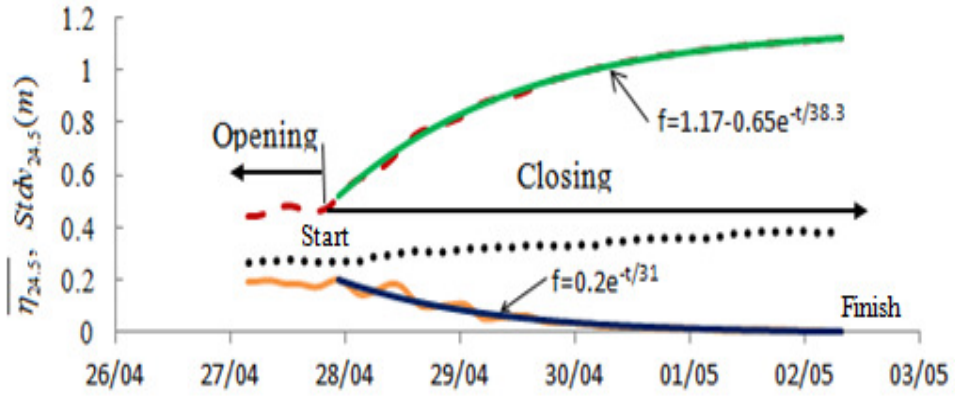

Figure 3.2: Example of exponential curves fitted to $\overline{\eta_{24.5}}(t)$ and $Stdv_{24.5}(t)$ for a closure event (Event 3) in Avoca Lake 2011.

We considered the starting time for the closing process to be when the $\overline{\eta_{24.5}}(t)$-line starts rising and the standard deviation starts reducing. The ending time for closing process is when $Stdv_{24.5}$ vanishes. For such closure events of Avoca Lake, NSW, AU are discussed in Section 4.1.

Under other extreme events such as a flood or storm waves, fitting $\overline{\eta_{24.5}}(t)$ or $G_i(t)$ of a primary constituent are more suitable depending on the trend of these parameters and which parameter represents change in the morphology of the whole bay-inlet system. For example, T_{moph} was extracted by fitting G_2 for Brunswick Heads, AU, flooded in May 2009 in Figure 3.3 (cf. Section 4.2), and fitting G_1 for Pensacola Pass, US in Hurricane Katrina 2005 (cf. Section 4.4)

$$G_j(t) = G_{j,\text{finish}} + \left[G_{j,\text{start}} - G_{j,\text{finish}}\right] \mathrm{e}^{-(t-t_{\text{start}})/T_{\text{morph}}} . \qquad (3.11)$$

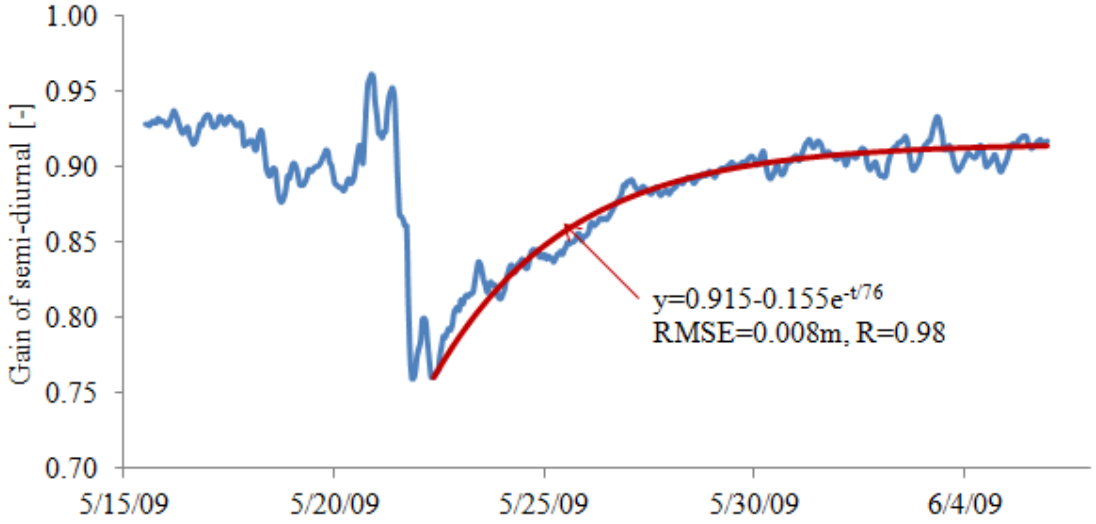

Figure 3.3: Example of exponential fitting curves for $G_2(t)$ for Brunswick Heads, Au, flooded in May 2009.

This method has also been applied to compute time constants T_{morph} for a number of inlets in the US and Australia with different waves and tides as well as different basin scales. Finally, the expectation of relationship between T_{morph}, H_s and the nominal tidal discharge $\hat{Q}_{tide} = A_b R_{to}/T$ (A_b is the bay surface area, R_{to} is the ocean tidal range and T is tidal period) will be provided in Section 6.5.2. This method and resulting relationships can be used for managing tidal system without extensive river flow and bathymetry data.

3.2.5 Hydraulic time constants $T_1(t)$ and $T_2(t)$ from $G(t)$ and $\varphi(t)$

Looking for T_{morph} via hydraulic data, one must keep in mind that the hydraulic system filters input data in accordance with its hydraulic time constants T_1 and T_2 in Equation (2.44) or (3.12).

Correspondingly, these can be obtained from tide data via G_j and φ_j for each component. This is based on the frequency response function $F(\omega)$ for linear equations with constant coefficients:

$$\begin{aligned} F_j(\omega) &= G_j\, e^{-i\varphi_j} = \frac{1}{1+i\omega_j T_1 - \omega_j^2 T_2^2} \\ \Leftrightarrow \quad \frac{1}{G_j} e^{i\varphi_j} &= 1+i\omega_j T_1 - \omega^2 T_2^2 \end{aligned} \tag{3.12}$$

This equation enables determination of the hydraulic time constants from $1/F_j(\omega)$ as in Figure 3.4 with measured gain G_j and phase lag φ_j under the assumption of a linear equation with constant coefficients.

$$\begin{aligned} \mathrm{Re}\left\{\frac{1}{F(\omega)}\right\} &= \frac{1}{G_j}\cos\varphi_j = 1-\omega_j^2 T_{2,j}^2 \quad \Leftrightarrow \quad T_{2,j} = \frac{\sqrt{1-\dfrac{\cos\varphi_j}{G_j}}}{\omega_j} \\ \mathrm{Im}\left\{\frac{1}{F(\omega)}\right\} &= \frac{1}{G_j}\sin\varphi_j = \omega_j T_{1,j} \quad \Leftrightarrow \quad T_{1,j} = \frac{\sin\varphi_j}{\omega_j G_j} \end{aligned} \tag{3.13}$$

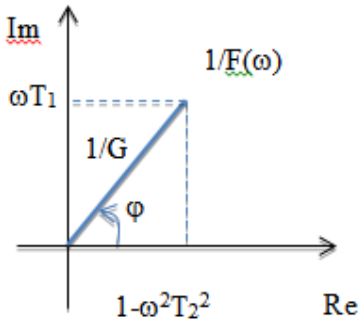

Figure 3.4: $1/F_j(\omega)$ in the complex plane.

Comparing with (2.30) and (2.31) these "measured" time constants can be related to the inlet geometry as in

$$\begin{aligned} \sqrt{\frac{L}{g}\frac{A_b}{A_C}} &= T_2 = \frac{\sqrt{1-\dfrac{\cos\varphi_j}{G_j}}}{\omega_j} \\ \frac{4F}{3\pi g}\left(\frac{A_b}{A_C}\right)^2\left(\frac{d\eta_b}{dt}\right)_{\max} &= T_1 = \frac{\sin\varphi_j}{\omega_j G_j} \end{aligned} \tag{3.14}$$

Thus, time series of T_1, T_2 will give an idea about change of system geometry between a normal condition and an extreme or closure event. Details will be presented in Chapter 4. Note that

$T_1(t)$ estimates depend on the instantaneous amplitude as indicated by Eq (3.14) because of the linearization of the quadratic friction.

3.3 INFLUENCE OF RECORD TREND AND METHOD OF DETRENDING

To investigate the influence of record trend on the results of 24.5 hour moving window analysis, various tests were carried out on records without trend and records with trend. The results of these exercises show that the 24.5 hour moving window gives reliable amplitudes and phase lags for regular tides under normal condition without any trend. For records having significant trend due to flood, storm wave or inlet closure, it is necessary to de-trend before analysing. Linear de-trending in each window is only appropriate for the case of linear trend with any slope but not suitable for other non-linear trend such as exponential or unsteady. Removing the moving average from the tidal record, $\eta(t) \to \left(\eta(t) - \overline{\eta_{24.5}}(t)\right)$, provides the best results with high accuracy for any trend. Consequently, this method of de-trending is chosen.

3.3.1 Using 24.5h moving window for regular tides

Under normal condition, bay tides and ocean tides can be represented as a regular wave. Without de-trending, harmonic analysis is carried out for two regular data series η_1 and η_2

$$\begin{aligned} \eta_1 &= 0.2\cos\left(\frac{2\pi}{24.5\text{h}}t - \frac{\pi}{4}\right) + 0.3\cos\left(\frac{2\pi}{12.25\text{h}}t - \frac{\pi}{2}\right) \\ \eta_2 &= 0.1\cos\left(\frac{2\pi}{24.5\text{h}}t - \frac{\pi}{2}\right) + 0.2\cos\left(\frac{2\pi}{12.25\text{h}}t - \frac{3\pi}{2}\right). \end{aligned} \tag{3.15}$$

The results of harmonic analysis using 24.5 hour moving window show exactly the same as it should be with $G_1(t)$=0.1/0.2=0.5; $G_2(t)$=0.2/0.3=0.67; $\varphi_1(t)$=π/2-π/4=π/4; $\varphi_2(t)$=3π/2-π/2=π. This test confirms the method can work well in normal conditions.

Figure 3.5 shows gain and phase lag without de-trending before analysis for Brunswick Heads in May 2009 (cf. Figure 4.14 in Section 4.2 for water level data). Under normal conditions, before 19/5 and after 24/5, G_2 and φ_2 (P2) are quite stable; G_1 and φ_1 (P1) fluctuate around a constant value. Hence, without de-trending, the results of 24.5 hour moving window are acceptable for normal conditions.

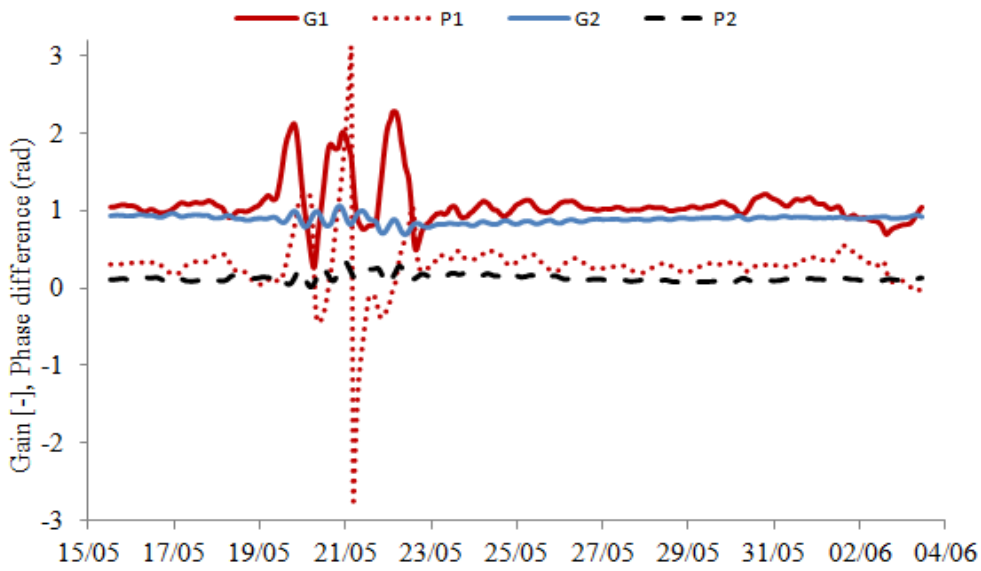

Figure 3.5: Gain and phase difference without de-trending before harmonic analysis for Brunswick Head during flood event May 2009.

3.3.2 Using 24.5h moving window for tides with trend

During the closing process of an inlet, bay water levels increase approaching a constant level (cf. Figure 3.1). Under extreme conditions such as flood or storm waves, bay and ocean tides increase significantly towards the peak, then reduce and come back to the normal state when the storm is over (cf. Figure 2.27). Harmonic analysis without de-trending causes an error in the amplitude and phase of each component for bay and ocean tides as the initial point and the ending point of period are not in the same level. This results in meaningless values of the frequency response function (gain and phase lag). In many cases, it leads to wrong interpretation of behavior of inlet system, without physical link to changing external forcing. For example, Figure 3.5 shows gains and phase lags for Brunswick Heads during a flood event without de-trending. It is not possible to explain the oscillation of results (from 20/5 to 23/5) corresponding to any change of inlet in terms of morphology or flooding (increasing Q_f).

In this section, tests were implemented to determine the appropriate method for de-trending tidal records during and after extreme events.

3.3.2.1 Linear de-trending method

- **Data series with linear trend**

A simple case was investigated with regular data series generated from η_1 in (3.15) with superimposed linear trend $y=a\times t$ with different slopes: $a\in[0.005: 0.02]$ hour^{-1}.

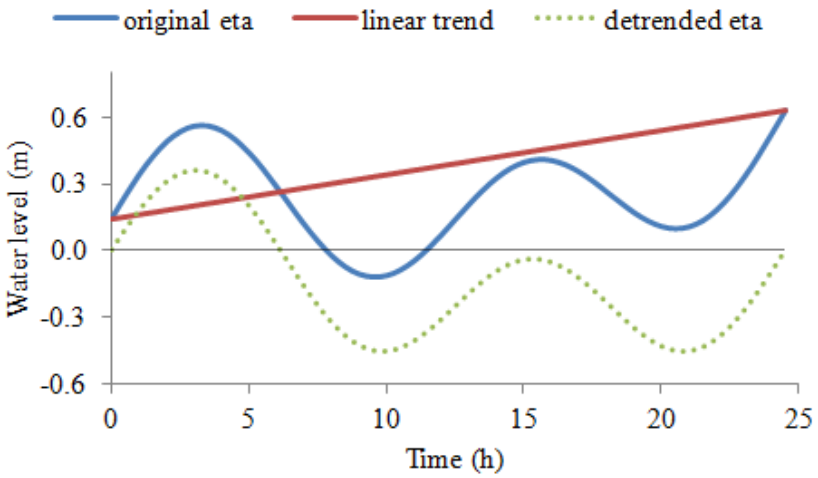

Figure 3.6: Linear de-trending in each window.

Linear de-trending is executed in each window as described in Figure 3.6. A linear function $y_1=b+a\times t$ was constructed based on ending points of each window, with

$$\eta_{\text{de-trended}} = \eta - y_1 . \tag{3.16}$$

Figure 3.7 shows Gains and phase differences using the linear de-trending method for Brunswick Heads during flood event May 2009. During the flood period from 20/5 to 23/5, G_2 of the primary component shows a clear understandable trend. The results of the harmonic analysis for $\eta_{\text{de-trended}}$ show perfect return of G=1 and phase lag φ=0 compared to the original η_1. This perfect result is independent of the slope of the trend line.

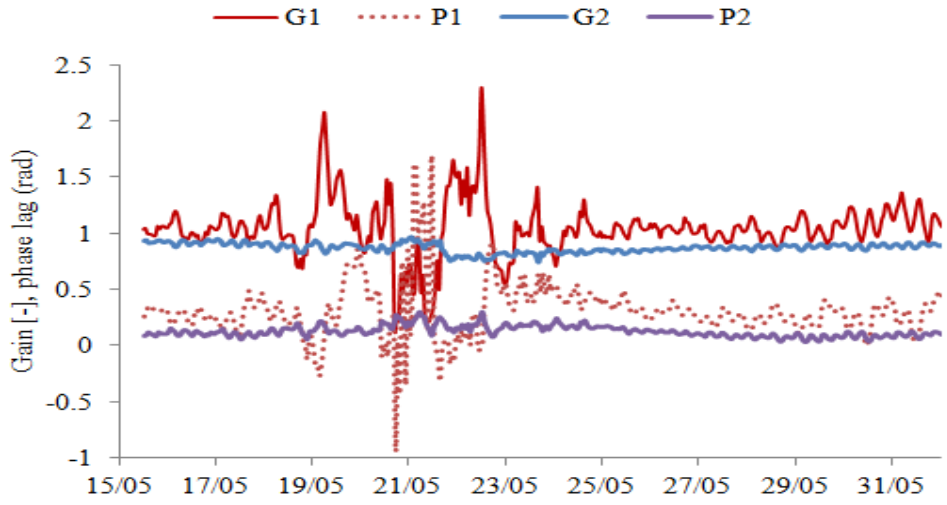

Figure 3.7: Results of Gain and phase difference with linear de-trending before harmonic analysis for Brunswick Head during flood event May 2009.

However, G_1 and φ_1 fluctuate even though they reduce one peak (from 3 to 2 peaks) as compared to that without de-trending in Figure 3.5. The reason for this may be the non-linear trend in the Brunswick data. In particular, many windows containing peaks have two trends: upward trend toward the peak and downward trend after the peak, whereas the linear de-trending method just considers one trend corresponding to the two end points of each 24.5 hour period. Thus we can conclude that linear de-trend is adequate only for tidal records having one pure linear trend.

- **Data series with unsteady trend**

Further tests have been carried out for data series with non-linear trends. One typical example is the exponential trend of the closing process as shown in Figure 3.1. To simplify, various data series were generated from η_1 by adding the exponential trend $y=1-e^{-t/T}$. Figure 3.8 shows data series with different time constant T=20 hours, 30 hours, 40 hours.

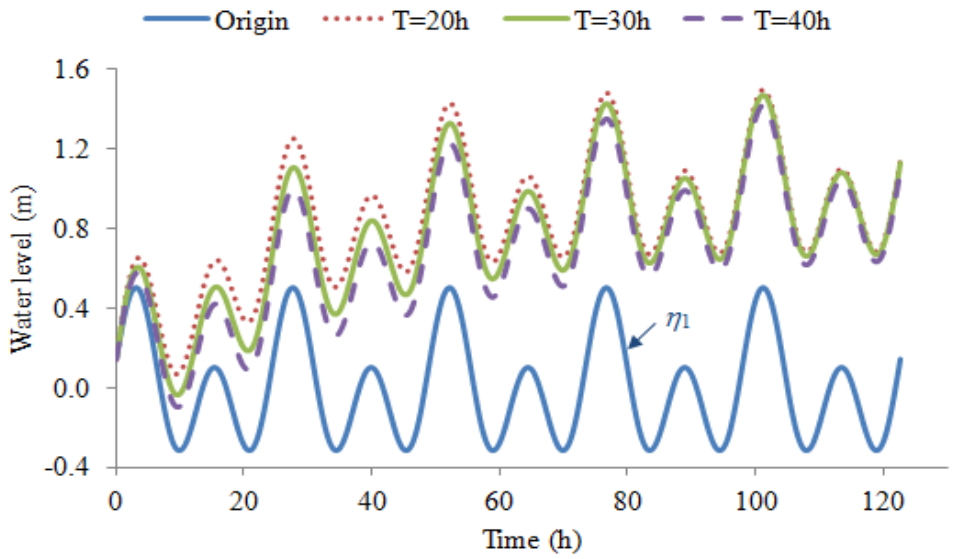

Figure 3.8: Harmonic analysis using 24.5 hour moving window for data series having exponential trend $y=1-e^{-t/T}$ with different values of the time constant T.

The results in Figure 3.9 were obtained by using the linear de-trending method and 24.5 hour moving window. Perfect accuracy for comparison is the point (1,0) in the complex plane. As can be seen, the error of the diurnal component is larger than the error of the semi-diurnal. Large error occurs in the beginning when the water levels are trending upwards rapidly. The error is larger for data series with shorter time constant (Figure 3.9).

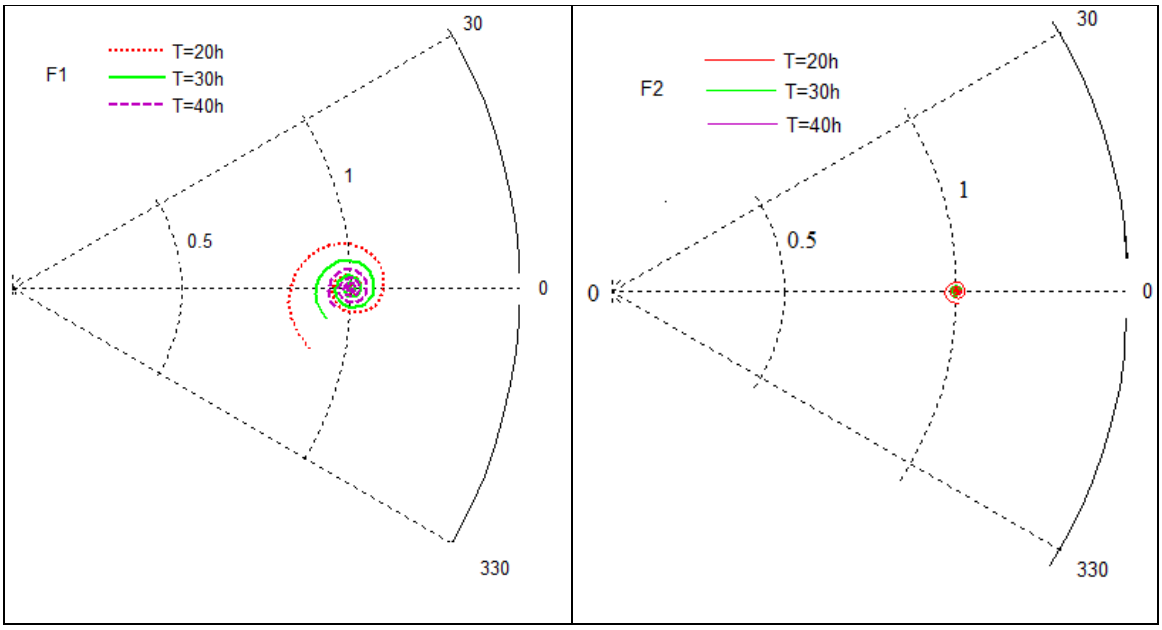

Figure 3.9: Comparison between results of amplitude and phase for diurnal (left) and semi-diurnal (right) by using 24.5 hour moving window with linear de-trending for data series having exponential trend with original data. The perfect results are at the point (1, 0) in complex plane.

It can be concluded from the above tests that the linear de-trending method in each window is not appropriate for data series with unsteady trend. Since almost all tidal records under extreme conditions or closure events have unsteady trends, it is necessary to seek another method, which removes the trend before harmonic analysis.

3.3.2.2 De-trending by removing $\overline{\eta_{24.5}}(t)$ from the data

The moving average $\overline{\eta_{24.5}}(t)$ shows the general trend of tidal record with either exponential function or any function. Hence why not remove it first from the original data before harmonic analysis. This method can remove any trend either linear or exponential form, with

$$\eta_{\text{de-trended}} = \eta - \overline{\eta_{24.5}} \,. \tag{3.17}$$

For better accuracy the data series should be extended at least 12.5 hour prior the period of interest to ensure that $\overline{\eta_{24.5}}(t)$ presents correct trend. The new de-trending method is applied to the data series in Figure 3.8 and the results is shown in Figure 3.10. The maximum error is 3%, corresponding to the tight orbit around (1, 0) of perfect response.

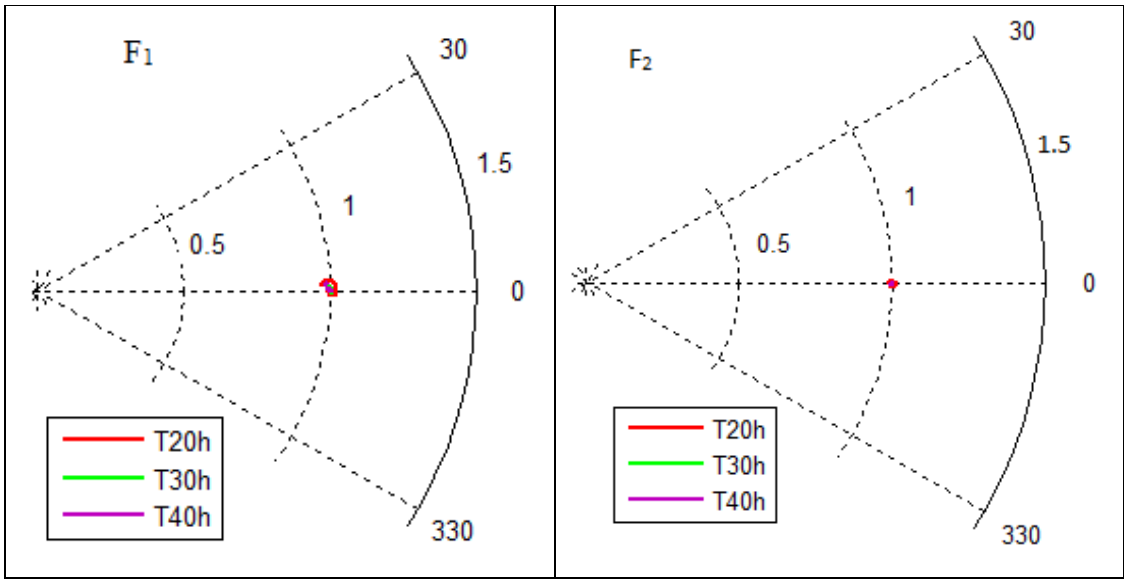

Figure 3.10: Results from using 24.5 hour moving window with removing average de-trending method for data series having exponential trend. The results of amplitude and phase: diurnal (left), semi-diurnal (right) are close to the perfect (1, 0).

The de-trending method shows really good performance with high accuracy in previous test. Then it is applied for Brunswick Head during flood event May 2009.

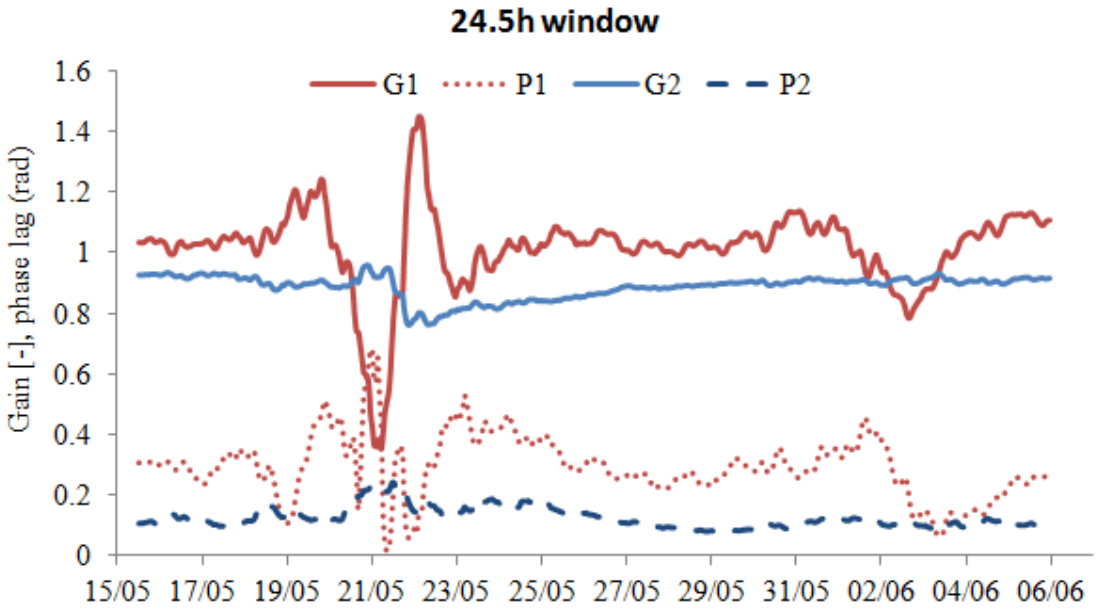

Figure 3.11: Gains and phase differences obtained with de-trending by removing average before harmonic analysis for Brunswick Heads during the May 2009 flood event.

The results for Gain and phase difference for both components (Figure 3.11) are improved compared to that of linear de-trend method in Figure 3.7, with understandable behaviour and less erratic oscillation.

In conclusion, the de-trending method (3.17) is an appropriate method for any unusual tidal records under storm waves, flood or a closure event. The method of de-trending by removing $\overline{\eta_{24.5}}(t)$ from tidal records is therefore applied for further analysis of this document.

3.4 DIFFERENT MOVING WINDOW LENGTH PERFORMANCE

In Section 3.1, the work of Hinwood and McLean, 2001 was reviewed. Their method calculated five tidal constituents. This leads to the requirement of a longer window for stable and reliable amplitude and phase of each component. However, the longer window attenuates the shorter events (3-5days). Hence, we chose the shorter 24.5 hour window. One may argue for a 24 hour window corresponding to solar day, or a 25 hour for the lunar day. The following results of slightly different window lengths for same event in Brunswick Heads may answer.

Figure 3.12 shows the results of harmonic analysis using 24 hour moving window. Figure 3.13 used 25 hour moving window and Figure 3.14 used 49 hour moving window. In all cases the average de-trending method, Eq (3.17), was used.

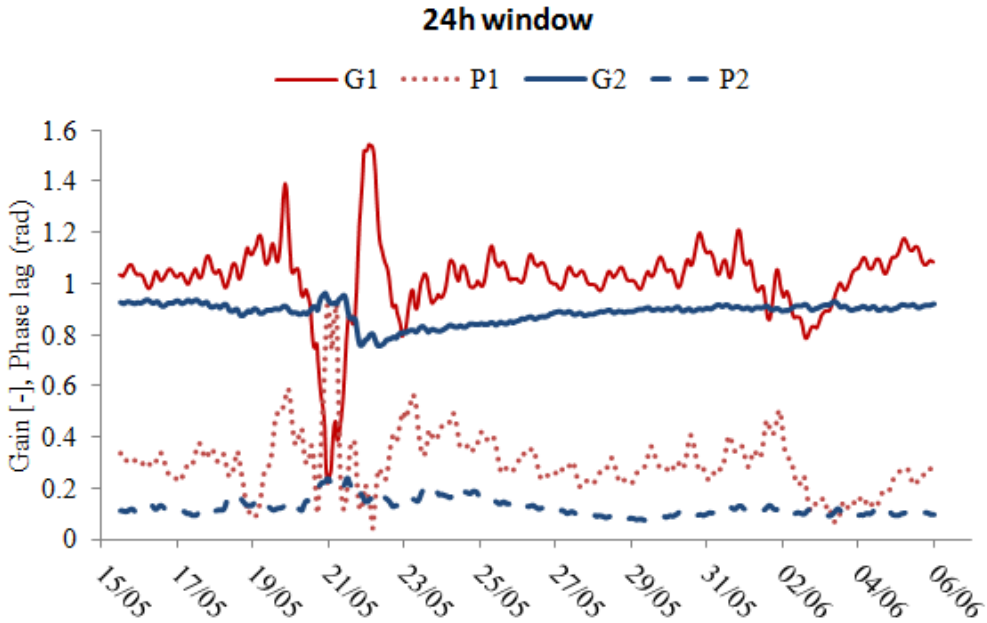

Figure 3.12: Gain and phase lag with de-trending by removing $\overline{\eta_{24}}(t)$ using 24 hour moving window for Brunswick Heads during flood event May 2009.

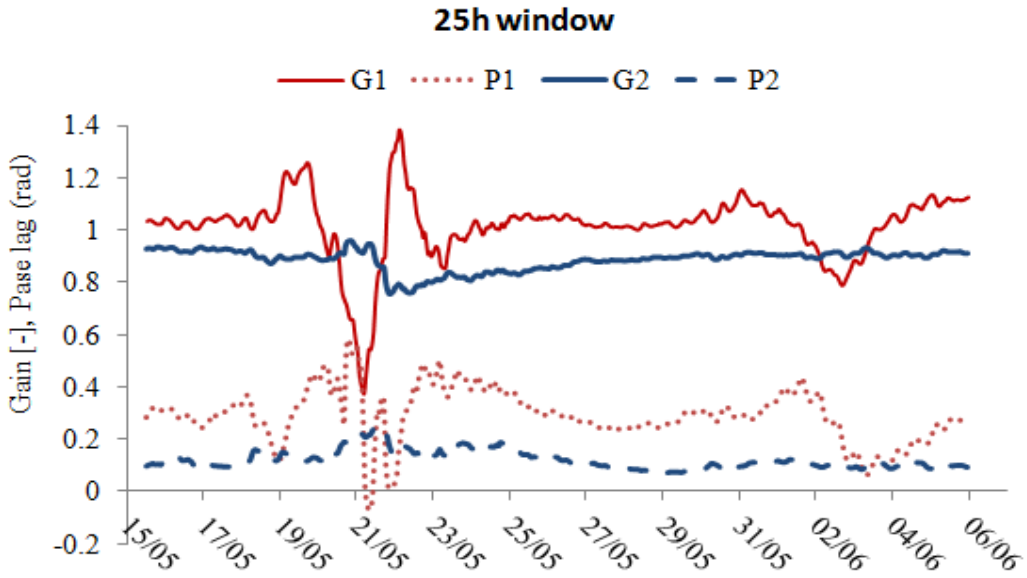

Figure 3.13: Gain and phase difference with de-trending by removing average using 25 hour moving window for Brunswick Heads during flood event May 2009.

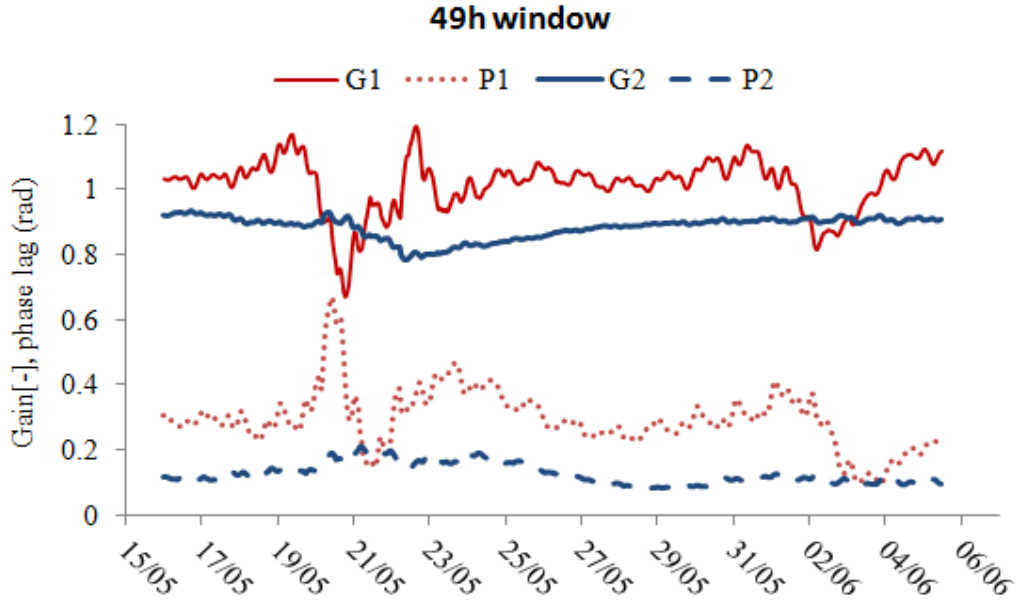

Figure 3.14: Gain and phase difference with de-trending by remove average using 49 hour moving window for Brunswick Heads during flood event May 2009.

Compared with the 24.5 hour results in Figure 3.11, they all show a similar pattern. The longer window is the smoother and least oscillating. However, the 25 hour window can smoothen not only results of semi-diurnal but also diurnal. The differences in magnitude of G_1, G_2 at peak and trough reduces with a longer window. This change is observed for the diurnal with lesser impacts for the semi-diurnal. As expected, the 49 hour window gives more smoothing and may thereby in

other cases (though not in this one) miss useful information. The 24.5 and 25 hour windows, show no extra instability issues and are therefore preferred because of potentially better resolution.

3.5 ARTEFACT OF METHOD ON T_{MORPH} BY FITTING DIFFERENT PARAMETERS

T_{morph} from closure events in Avoca Lake (Figure 3.2) showed that there were slight differences in T_{morph} as determined by $\overline{\eta_{24.5}}(t)$ and by $Stdv_{24.5}(t)$, ranging from 4 hours to 7 hours. The reason for these difference is that while the water level stops varying ($Stdv_{24.5} = 0$) indicating inlet closure, $\overline{\eta_{24.5}}(t)$ may continue rising due to water still coming from the catchment. It is suggested that T_{morph} calculated by fitting $Stdv_{24.5}$ is preferred for showing a physically realistic time scale when waves are involved in the closing process by building up the berm at the entrance.

To investigate the influence of a 24.5 hour moving window on determining T_{morph}, an exercise has been carried out with water level $\eta(t)$ presented as

$$\begin{aligned}\eta(t) &= 1 - e^{-t/T_a} + 0.2e^{-t/T_d}\cos\omega t \\ &= f_{a1}(t) + f_{d1}(t).\end{aligned} \tag{3.18}$$

f_{a1} has exponential form with known timescale T_a which represents the original trend of the record (e.g., closing process), while f_{d1} represents the original standard deviation of record with known timescale T_d.

Table 3.1. Comparison of initial and estimated timescales for three scenarios.

Case		Initial timescale	Estimated timescale
1	T_a	50	50
	T_d	50	48.7
2	T_a	70	70
	T_d	50	57
3	T_a	50	50
	T_d	70	60

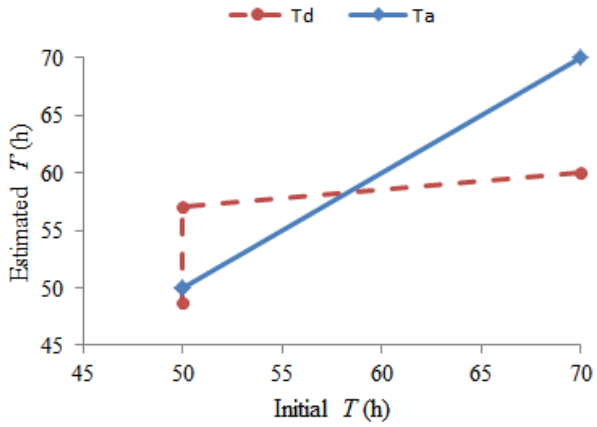

After generating $\overline{\eta_{24.5}}(t)$ and $Stdv_{24.5}(t)$, T_{morph} is determined by fitting with exponential functions and comparing with the original timescales of T_a and T_d. Three cases have been tested

with relative difference between two original timescale T_a=T_d, T_a>T_d and T_a<T_d. Details of different cases and results of fitting are shown in Table 3.1 and in Figures 3.15 through Figure 3.17.

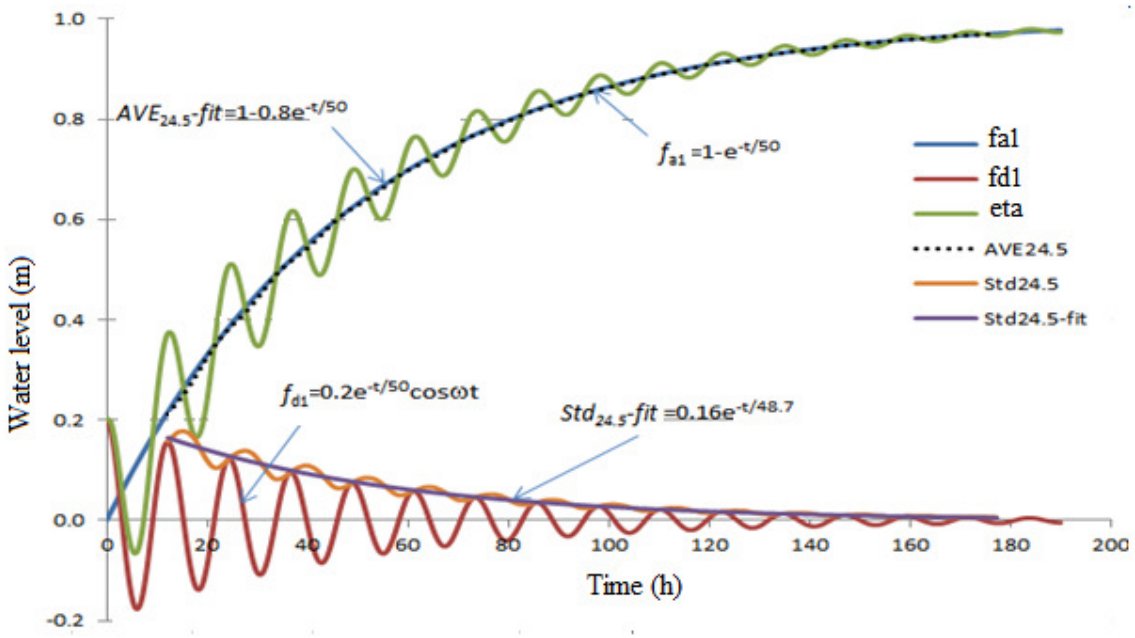

Figure 3.15: Case 1, input T_a=T_d=50 hours, output T_a=50 hours, T_d=48.7 hours.

The results from the three cases show that $\overline{\eta_{24.5}}(t)$ generated by 24.5 hour moving window method almost coincides with f_{a1} with the same timescale T_a, this means the method captures T_{morph} without bias. However, a different story can be seen from the standard deviation. $Stdv_{24.5}(t)$ generated by 24.5 hour moving window method is different from f_{d1}. $Stdv_{24.5}(t)$ usually uplifts with the fitting trend like upper envelope of initial one and smaller amplitude of variation as in Figures 3.15, 3.16, 3.17. The estimated timescale is different from the initial T_d. This means that the method influences timescale determined using $Stdv_{24.5}(t)$. The level of influence varies and may relate to T_a/T_d. The difference is insignificant (less than 3%) for T_a = T_d, while it is much larger when $T_a \neq T_d$.

For Case 2 with input T_a=70 hours > T_d=50 hours, the output T_d=57 hours is longer than initial one. This case can represent the situation when rain fall or a wave event increases mean water levels significantly while less variation due to tides. These events disturb and lengthen T_a leading to T_a>T_d. Closure Event 1 (Figure 4.6) is an example for this case when the closure starts at neap tide. However, if we consider Event 1 starting at spring tide, when wave event passed through, the time scale is similar to case 1.

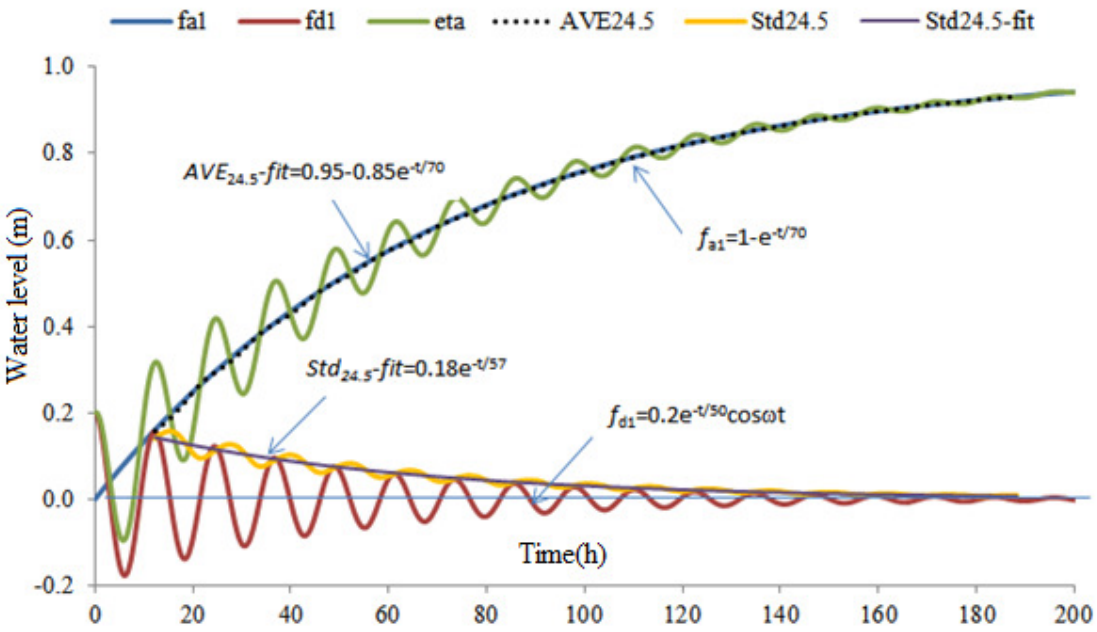

Figure 3.16: Case 2, input T_a=70 hour s> T_d=50 hours, output T_a=70 hours, T_d=57 hours.

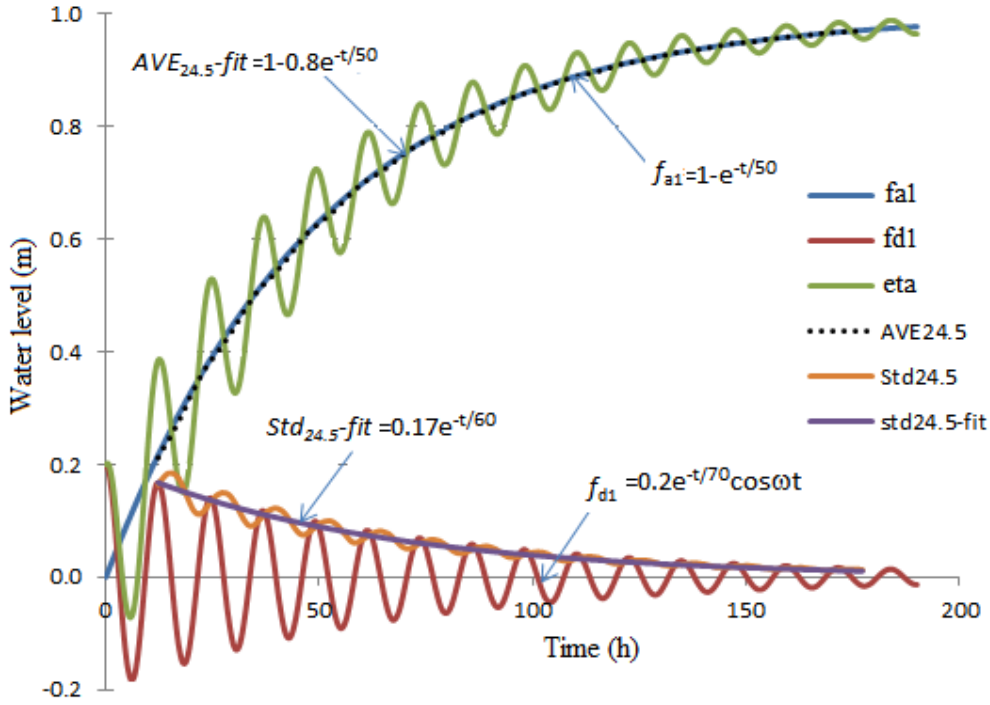

Figure 3.17: Case 3, input T_a=50 hour s < T_d=70 hours, output T_a=50 hours, T_d=60 hours.

On the other hand, for Case 3 with initial T_a=50 hours < T_d=70 hours, the method shortens the time scale of standard deviation with output T_d=60 hours. This case may represent the scenario when rain fall is very intensive and during short time coincident with a wave event.

It can be concluded that the method gives reliable values of T_{morph} for situations with (T_a=T_d). However, it can give biased results if $T_a \neq T_d$.

3.6 NONLINEAR INTERACTIONS OF DIURNAL AND SEMIDIURNAL TIDES

From the analysis of four closure events of the Avoca Lake (Figure 3.18), we observed abrupt changes of G_1. So, what are the possible sources for this erratic response? The answer can be the coincidence between the morphodynamics of the inlet during closing process and the phase difference between the two main ocean components changing as seen in Figure 2.2 and Figure 3.20. The following section will illustrate this by using the weir model from Section 2.2.1.

The analysis results for the Avoca Lake closure event during 26 Apr to 2 May 2011 by 24.5 hour moving window are presented in Figure 3.18, through Figure 3.20.

Figure 3.18 shows G_2 decreasing monotonically due to the morphological change while the path of G_1 towards zero is erratic.

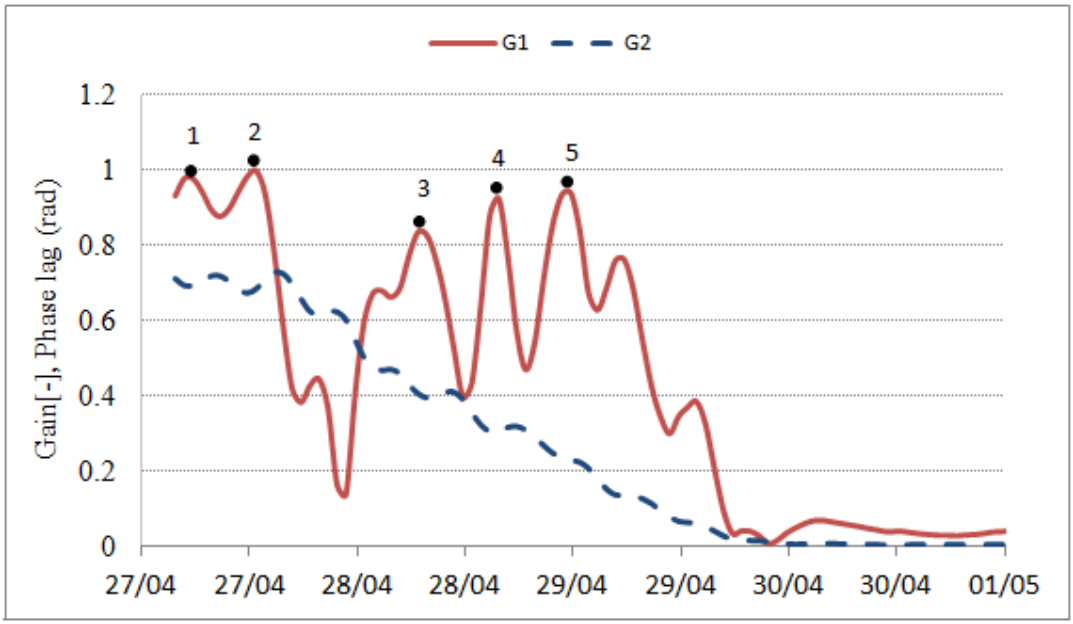

Figure 3.18: G_1 and G_2 generated by the 24.5 hour window method for Avoca Closure Event 3 during Apr 2011 after de-trending η_b.

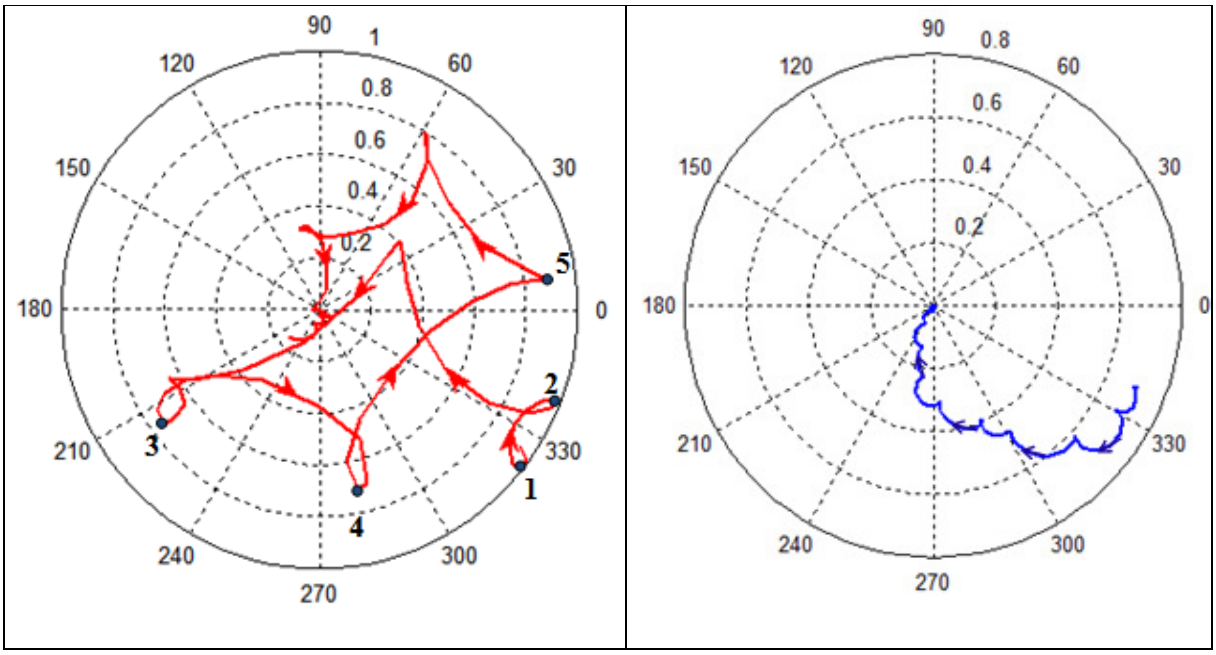

Figure 3.19: Response functions F_1 (left) and F_2 (right) after de-trending η_b for Avoca Closure Event 3.

It is seen that G_1 varies rapidly and takes values greater than unity while G_2 performs quite stably with small variation, G_{2max} being less than 0.7. G_1 is found to be abrupt with a large variation and multiple peaks larger than unity. The question posed here is what are the possible reasons for the erratic behavior of F_1?

It can be attributed to the morphology changes during closing process, represented by increasing weir height z_{cr} in the simple weir model. Increasing z_{cr} results in distortion of the tidal shape and generates higher harmonics. Another candidate reason for changing G_1 is a changing phase-shift, φ_{O2}-φ_{O1}, between the two ocean tide components. Figure 3.20 shows that φ_{O2}-φ_{O1} changes by nearly π during the considered closure event.

To investigate how this change in phase generates a large variation in G_1, a simple experiment is carried out utilising the simple weir model, from Section 2.2.1.

The input ocean tidal elevation is

$$\eta_o = a_{o1}\cos(\omega t - \varphi_{o1}) + a_{o2}\cos(2\omega t - \varphi_{o2}) \qquad (3.19)$$

with a_{O1}=0.1 m, a_{O2}=0.4 m which are typical near Avoca. The weir crest level is fixed at z_{cr}=0, and φ_{O1} is also fixed, φ_{O1}=0, while φ_{O2} changes from 0 to π. The resulting water levels in the bay for the two extremes viz., φ_{O2}=0 and φ_{O2}=π are shown in Figure 3.21 and Figure 3.22. These cases correspond to the phase extremes of the two components observed in the ocean tides in Figure 3.20.

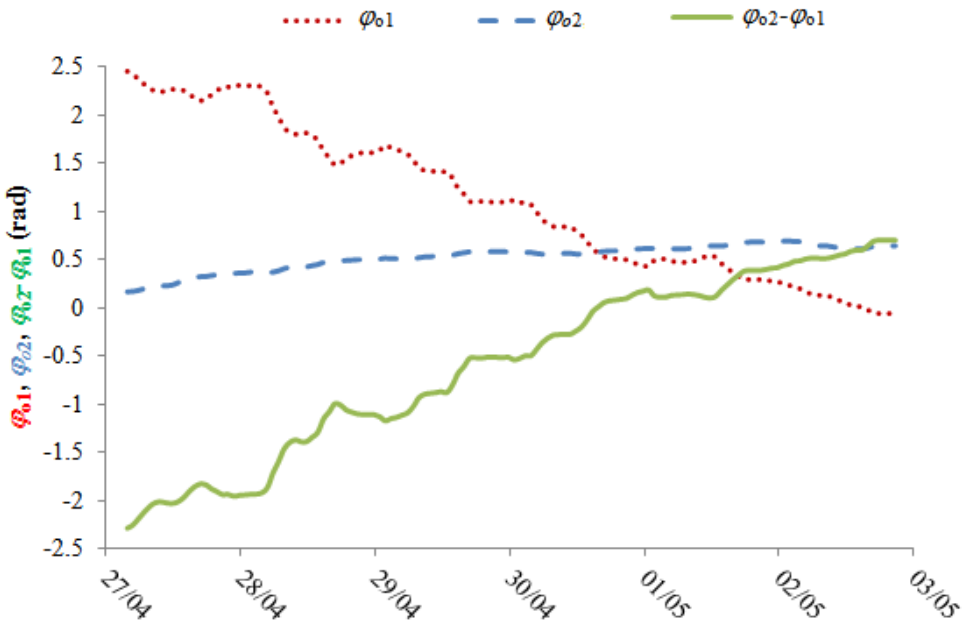

Figure 3.20: Phase difference between ocean semi-diurnal and diurnal for Avoca closure Event 3.

We see that although a_{O1} and a_{O2} are the same φ_{O2}=0 gives alternating high highs and low highs in the ocean resulting in a strong diurnal component in the lake (Figure 3.21), while φ_{O2}= π gives very even highs in the ocean leading to a purely semi-diurnal lake response (Figure 3.22).

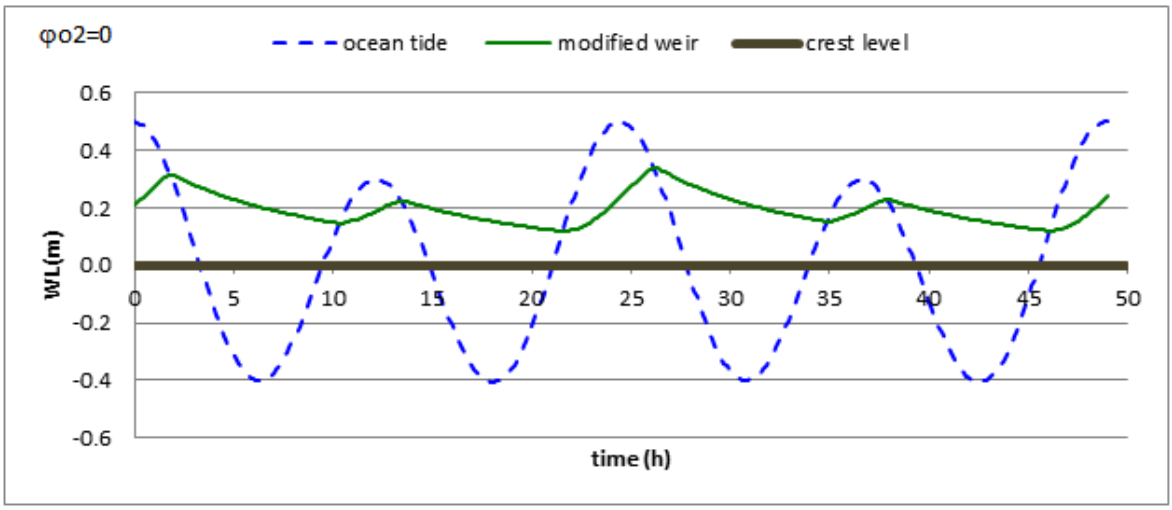

Figure 3.21: Ocean tides and bay tides generated by modified weir model with φ_{o2}=0.

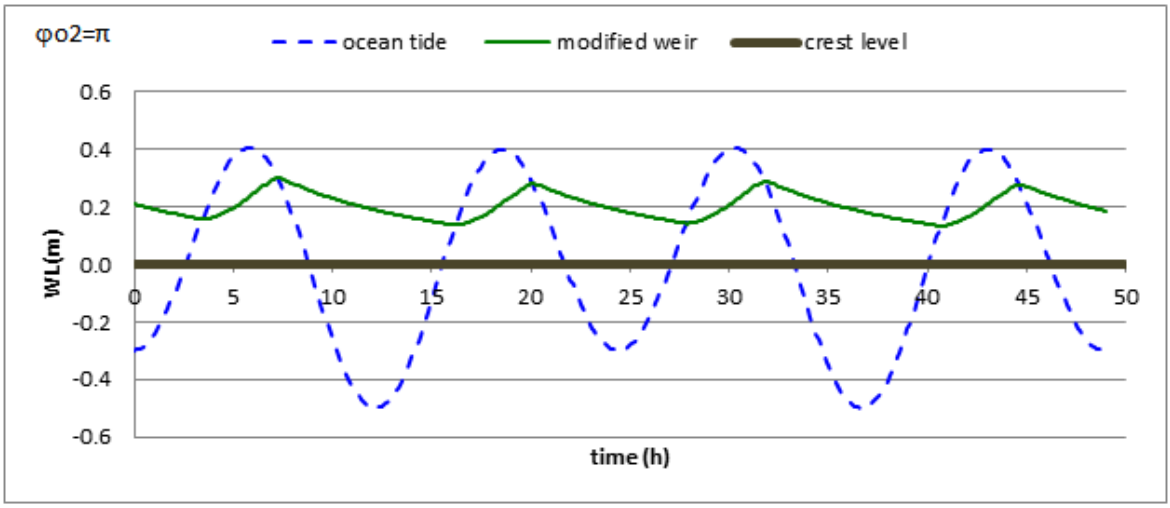

Figure 3.22: Ocean tides and bay tides generated by modified weir model with $\varphi_{o2}=\pi$.

Detailed results are shown in Table 3.2 and also plotted in the complex plane (Figure 3.23).

Table 3.2. G_1, G_2 and phase lag φ_1, φ_2 for case $\varphi_{o2}=0$ and $\varphi_{o2}=\pi$

φ_{o2}	G_1	φ_{b1}-0	G_2	$\varphi_{b2}-\varphi_{o2}$
0	**0.49**	**1.021**	**0.149**	**-5.08**
π/2	0.369	1.623	0.144	1.189
π	**0.1**	**1.102**	**0.143**	**-5.03**
3π/2	0.346	0.416	0.152	-5.02

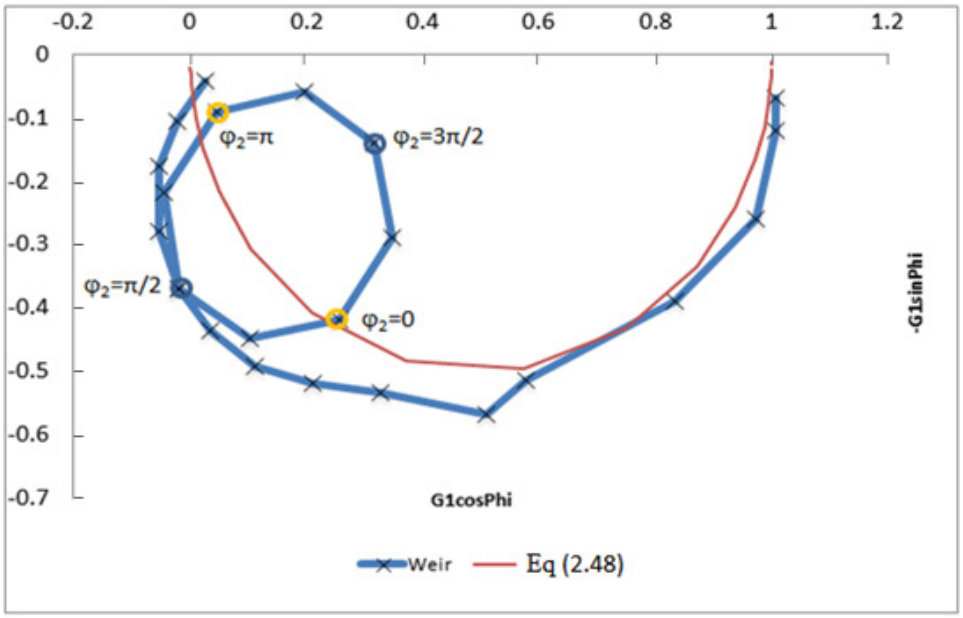

Figure 3.23: Response function F_1 with loop in the complex plane generated by changing φ_{O2}-φ_{O1} from 0 to 2π, while keeping z_{cr}=0.

As can be seen from Figure 3.23, a G_1 loop is generated by changing φ_{O2}-φ_{O1} from 0 to 2π. G_1 drops from 0.49 for φ_{O2}-φ_{O1} =0 to 0.1 for φ_{O2}-φ_{O1} =π corresponding to the yellow point sitting nearly on Eq (2.48), while another yellow point sits close to the origin.

A clear diurnal tide in the bay is observed (Figure 3.21) due to the significant difference between low-highs and high-highs in the ocean. This corresponds to G_1 being large for φ_{O2}-φ_{O1} =0.

For φ_{O2}-φ_{O1} =π (Figure 3.22) all ocean high tides are equal and G_1 is negligible. That is why G_1 drops to 0.1 for φ_{O2}-φ_{O1} =π (one fifth of G_1 for φ_{O2}-φ_{O1} =0). The size of such G_1 loops depend on $z_{cr,}$ see Figure 3.24.

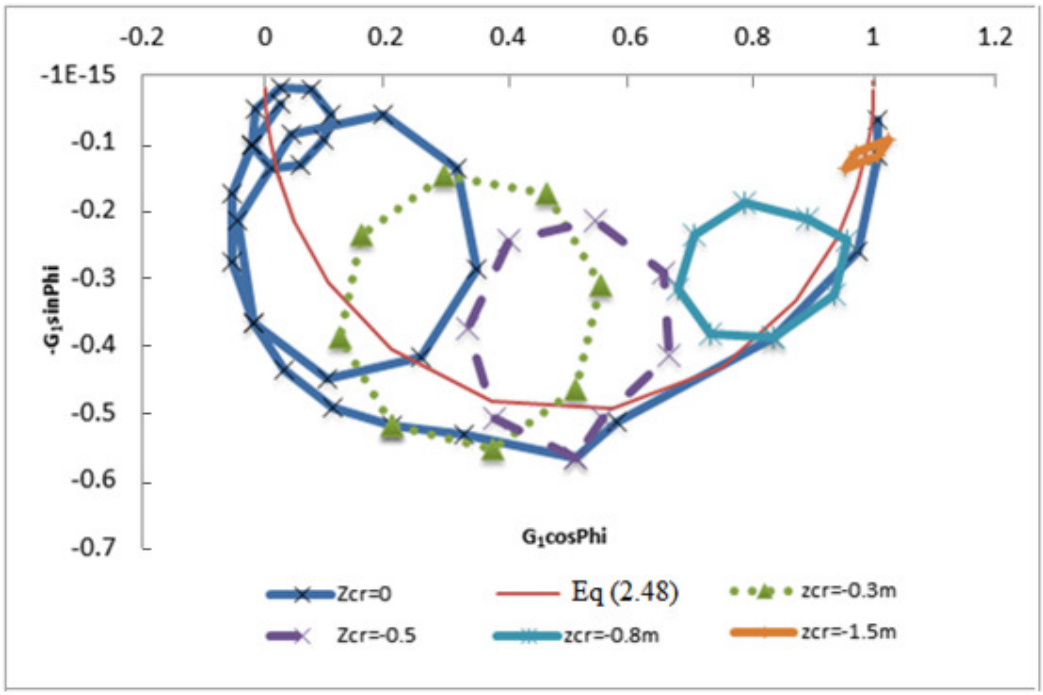

Figure 3.24: Response function F_1 with loop size in the complex plane depending on z_{cr}.

In conclusion, the change in morphology (in this example simply changing z_{cr}) together with the change in phase-difference between the two ocean tide components (φ_{O2}-φ_{O1}) causes large variation in F_1, including loops.

It is acknowledged that the actual morphology leading to the observations in Figures 3.18 and 3.19 was of course not a simple weir. Nevertheless, the behavior of the weir model provides interesting insights into the roles of morphology and ocean tide component phasing in generating the complex behavior of G_1.

Chapter 4

MORPHODYNAMICS INFERRED FROM MEASURED TIDES

In this chapter, the 24.5 hour moving window method is applied to analyse the tidal records for different case studies to infer the inlet morphodynamics under extreme conditions such as coastal storm or catchment flooding. This chapter presents analysis of two closure events of Lake Avoca; a major storm event at Brunswick Heads**,** an overwash event at Lake Conjola which was simulated in Chapter 2 and, Hurricane Katrina at Pensacola Pass in the US.

4.1 TWO CLOSURE EVENTS OF LAKE AVOCA

4.1.1 Description of Lake Avoca

Avoca Lake is located in Brisbane County Water region, NSW (Figure 4.1). Its surface area is 0.63 km^2 which is 5% of its catchment area, (Gosford City Council, 1995).

Figure 4.1: Avoca Lake, NSW, Australia. Image from Google Earth.

The response of Avoca Lake to the ocean tidal range of 1 m is usually around 0.2 m with the mean lagoon water surface elevation of 0.4 m above MSL. The inlet is located in the middle of the 1.5 km long Avoca Beach with headlands on both ends which limit the long shore sediment transport (Webb and Associates, 1995). The berm elevation typically builds to 2.8 m to 3 m. The entrance berm is 90% mechanically opened when lagoon level reaches 2.1 m (Gosford City Council, 1995).

Berm building and Closure

Weir et al. (2006) pointed out two different modes of berm development fronting Avoca entrance from 2 closures in 2003 and 2004. However, they only described processes occurring after the berm height disconnected the lagoon from the ocean. Our emphasis is on the process of disconnection exemplified by the 4 tide records in Figure 4.2.

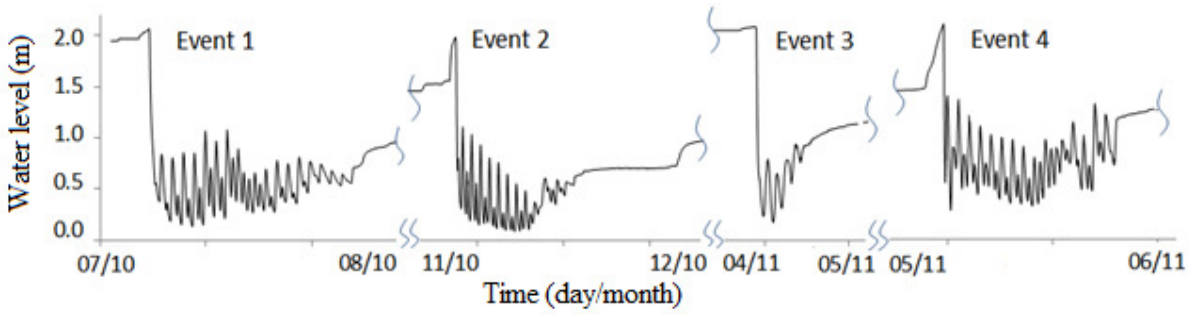

Figure 4.2: Lagoon tides showing four closure events in Avoca Lake during July 2010 to July 2011. Data from Manly Hydraulics Laboratory (MHL).

The average duration of artificial openings is 23 days, which is similar to the figure for natural openings reported by Webb and Associates, (1995).

Between July 2010 and July 2011, there were four opening/closure events (Figure 4.2) triggered by flooding concerns. The available data taken from Manly Hydraulic Lab (MHL) including ocean tides at Patonga, lake tides at the station located about 600 m from the entrance, significant wave height H_s at Sydney, daily rain fall at Kincumber and calculated run up by Hunt's (1956) formula for each event are presented in Figure 4.3, Figure 4.5.

Out of these four events, Event 3 shows the expected simple behavior of the tidal envelope monotonically narrowing and the average level increasing towards the time of closure. The other events are more complex. An analysis of the four Avoca closure events was summarised in Thuy et al. (2012). However, Thuy et al. (2012) focused on Event 3 and the frequency response functions presented in this paper were obtained without de-trending. The results were corrected in Thuy et al. (2013a). The following section will show more detailed results and discussion of events 1 and 3.

4.1.2 Analysis of closure events

A 24.5 hour moving window is utilized to analyse bay and ocean tides to determine morphodynamic time scale as well as the response of the inlet during the closing process.

4.1.2.1 Morphological time scales T_{morph}

Time series of $\overline{\eta_{24.5}}(t)$, and $Stdv_{24.5}(t)$ are generated and used to determine morphodynamic time scales. The results show that an exponential function is an adequate model for representing the closing processes (Figure 4.4, Figure 4.6). Different functional forms as in Eq (3.9), (3.10) and (3.11) have been tested. These four closing events fall into two categories:

A) closing starts during neap tide (Events 2 and 3). Event 3 is chosen to present in detail for this group as shown in Figure 4.4.
B) closing starts at neap tide, being disturbed by storm waves (Event 1) or rain fall (Event 4) then followed by secondary closing starting at spring tide. Event 1 is chosen to present in detail for this group as shown in Figure 4.6.

Figure 4.3 shows the available data for Avoca Lake during closure Event 3. The $Stdv_{24.5}(t)$ of the ocean indicates that it was opened during neap tide leading to inlet closure just a few tidal cycles after the opening. This event is typical for cases that start closing at neap tide. During the opening processes, sand from the berm is eroded and deposited in the near shore (surf zone). When tidal flow becomes weaker during neap tide, the wave action can transport sediment from the surf zone into the entrance and eventually build the berm above the tidal level.

This event illustrates that the best time for opening the entrance is during spring tides to avoid rapid closure as in this case. Opening during or just before spring tide lengthens the opening duration (as seen in the other events) and improves water quality due to improved water exchange.

Water levels inside the bay were well above the ocean tide from the opening time till the end of the closing process. The time scale determined by $\overline{\eta_{24.5}}(t)$ is 38 hours (Figure 4.4), which is 7 hours longer than T_{morph} determined by $Stdv_{24.5}(t)$.

The first day after opening, $\overline{\eta_{24.5}}(t)$ and $Stdv_{24.5}(t)$ were quite stable with regular tidal cycle, but when closure started, the low tide levels, points as I, J, K in Figure 4.3, increased corresponding to inlet bed level increase.

- **Event 3**

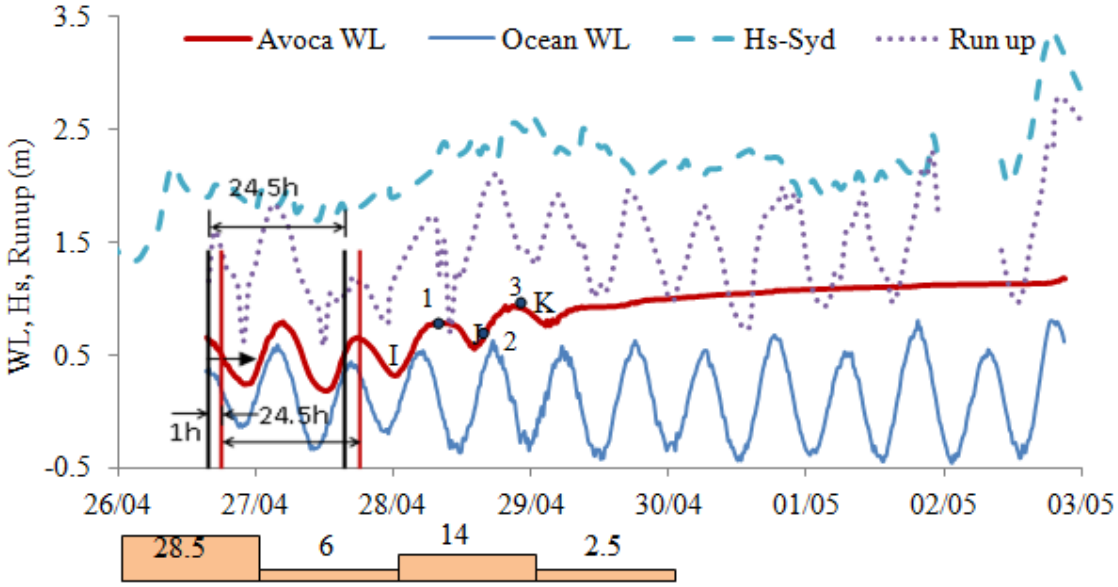

Figure 4.3: Data of closure Event 3 from 26 Apr 2011 to 3 May 2011: ocean tides, lake tides, significant wave height H_s, daily rain fall and run up calculated by Eq (2.56).

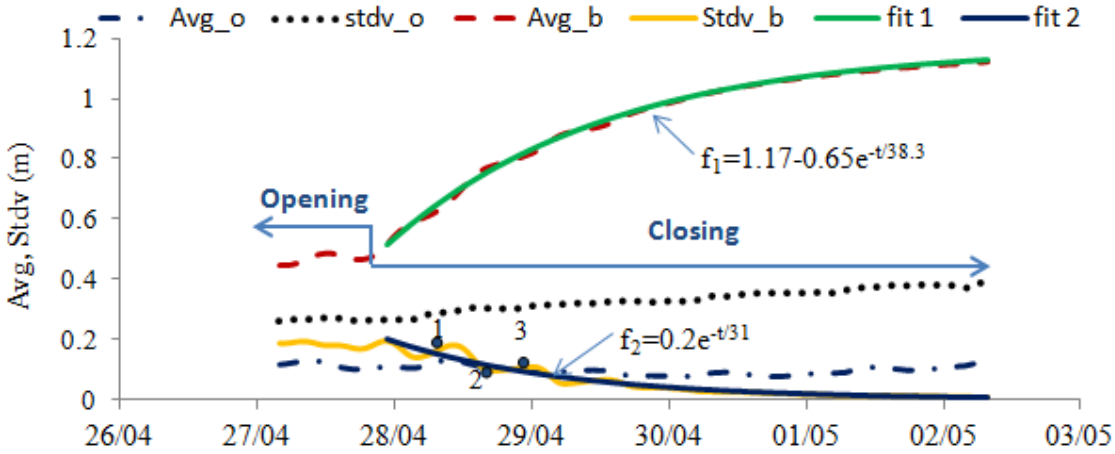

Figure 4.4: $\overline{\eta_{24.5}}(t)$ and $Stdv_{24.5}(t)$ of ocean tide, lake tide for Event 3 together with two exponential fitting curves of $\overline{\eta_{24.5}}(t)$ & $Stdv_{24.5}(t)$ for the lake.

Figure 4.5 shows the water level and wave height data and Figure 4.6 presents results of moving window analysis for Event 1 from 9 July 2010 to 3 Aug 2010. This event is typical for inlet closure starting at neap tide then being disturbed by a wave event (19 to 24 July in Figure 4.5), resulting in a longer closing process, followed by secondary closing starting at spring tide as seen from $Stdv_{24.5}(t)$ of the ocean Figure 4.6.

- **Event 1**

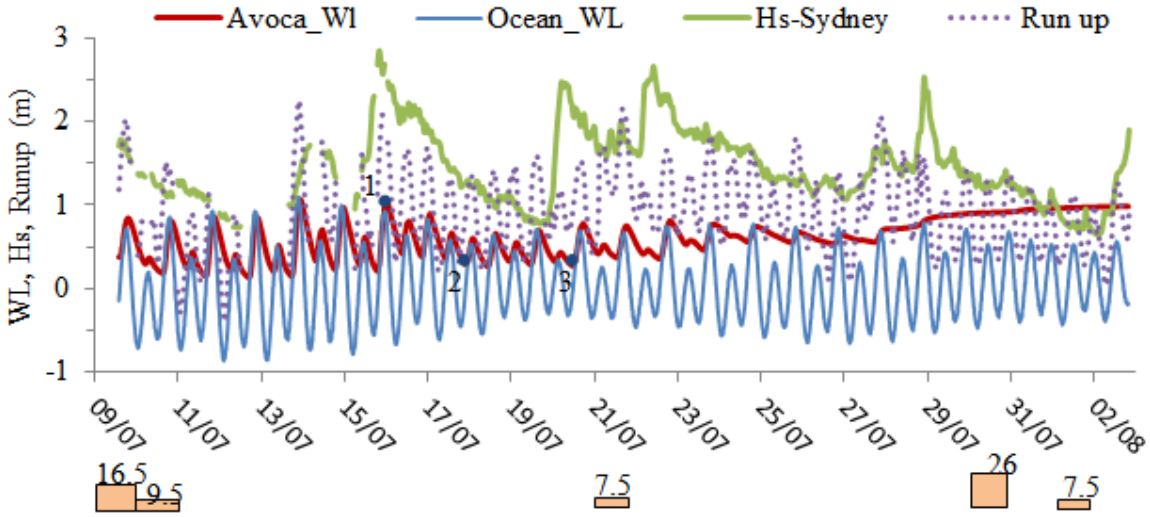

Figure 4.5: Water levels, wave height, daily rain fall and wave run up for closure Event 1 (Jul 2010).

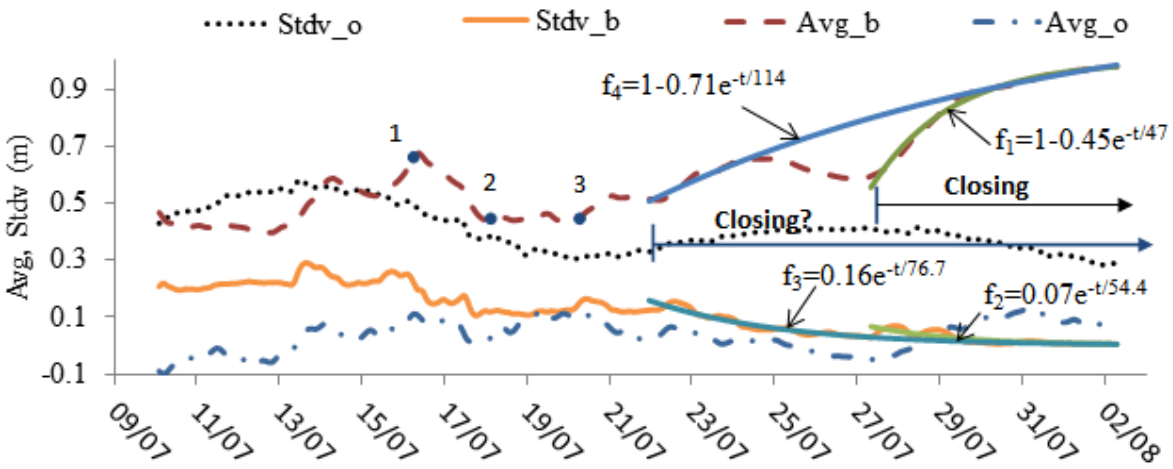

Figure 4.6: $\overline{\eta_{24.5}}(t)$ and $\mathrm{Stdv}_{24.5}(t)$ with fitting curves for Event 1 (Jul 2010).

From the time when the inlet was opened to around 15 July, the system was dominated by tides with ocean tide higher than the bay tide. Then, at the first spring tide, a wave event with H_s = 2.8 m occurred. During the wave event 16, 17 July, waves bring more sediment into the entrance, making it shallower. After the wave event, the channel invert level lowered due to draining and the inlet bed level remained constant from point 2 to point 3. The inlet would have closed at neap tide if higher waves with longer period causing higher run up during 21 - 22 July 2010 had not occurred. Wave over-wash again makes inlet bed level increase as seen from increasing trend of low waters. From 24 July, when H_s abated, the lagoon water level was still higher than the ocean tide. This

draining of the lagoon by gravity occurred until 27 July where the channel invert level appeared to remain constant (Figure 4.5, Figure 4.6). Hence, the draining of the lagoon disturbs and lengthens the closing process. Subsequently, the inlet experiences normal forcing and completes the closing process at spring tide.

There was a significant difference in time scale (2 or 3 times) calculated by $\overline{\eta_{24.5}}(t)$ and $Stdv_{24.5}(t)$ if the closing process is considered to begin at neap tides. However, if the closing process is considered to start at spring tide, the difference in T_{morph} becomes insignificant: 47 hours versus 54 hours. In this case, only f_3 from fitting $Stdv_{24.5}(t)$ with T_{morph} =76.7 hours shows the real physical change of inlet closing corresponding to bed level increase as seen from increasing trend of low waters from 22 July. This is supported by similar value of T_{morph}=80 hours obtained from the stable trend of G_2 in Figure 4.9.

There were slight differences (some hours) in T_{morph} as determined by $\overline{\eta_{\text{b},24.5}}(t)$ versus $Stdv_{\text{b},24.5}(t)$ or G_2 for the two events. The reason is that, while water level oscillations ceasing indicates inlet closure, $\overline{\eta_{\text{b},24.5}}(t)$ may continue rising due to water still arriving from the catchment. Therefore, T_{morph} calculated by fitting $Stdv_{\text{b},24.5}$ or the primary gain G_2 is preferred for getting a physically realistic time scale, rather than $\overline{\eta_{\text{b},24.5}}(t)$.

Closure events 1 and 4 are examples where the closure is starting at neap tide. Rainfall or wave events disturb and lengthen resulting $T_{morph,\bar{\eta}} > T_{morph,stdv}$. However, if we consider Events 1 and 4 to start closing at spring tide, when rain and/or big waves have passed, the $T_{morph,\bar{\eta}}$ and $T_{morph,stdv}$ are only slightly different.

4.1.2.2 Frequency response functions F for the two Avoca events

After removing $\overline{\eta_{24.5}}(t)$ from η_{b}, harmonic analysis based on the 24.5 hour periods has been carried out, and the gains $G_1(t)$, $G_2(t)$ and phase lags $\varphi_1(t)$, $\varphi_2(t)$, Figure 4.7, as well as the complex frequency response functions $F_1(t)$ and $F_2(t)$ were determined.

From the geometry of Avoca Lake, A_{b}=6.3×10^5 m^2, a_{o}=0.5 m, L_{c}=600 m, A_{c} estimated for inlet after manually opening is ca 20 m^2, we find damping coefficient $D = \dfrac{FA_b a_o}{2L_c A_c}$ = 52.5 with inlet dimensionless overall impedance F=4. This shows that the inlet is a friction dominated system cf. Section 2.4. Therefore, the response function should be similar to Eq (2.48) for a 1$^{\text{st}}$ order linear

system and the investigation was done by the finite-channel-length model in Section 2.4.2 when z_{cr} is increasing.

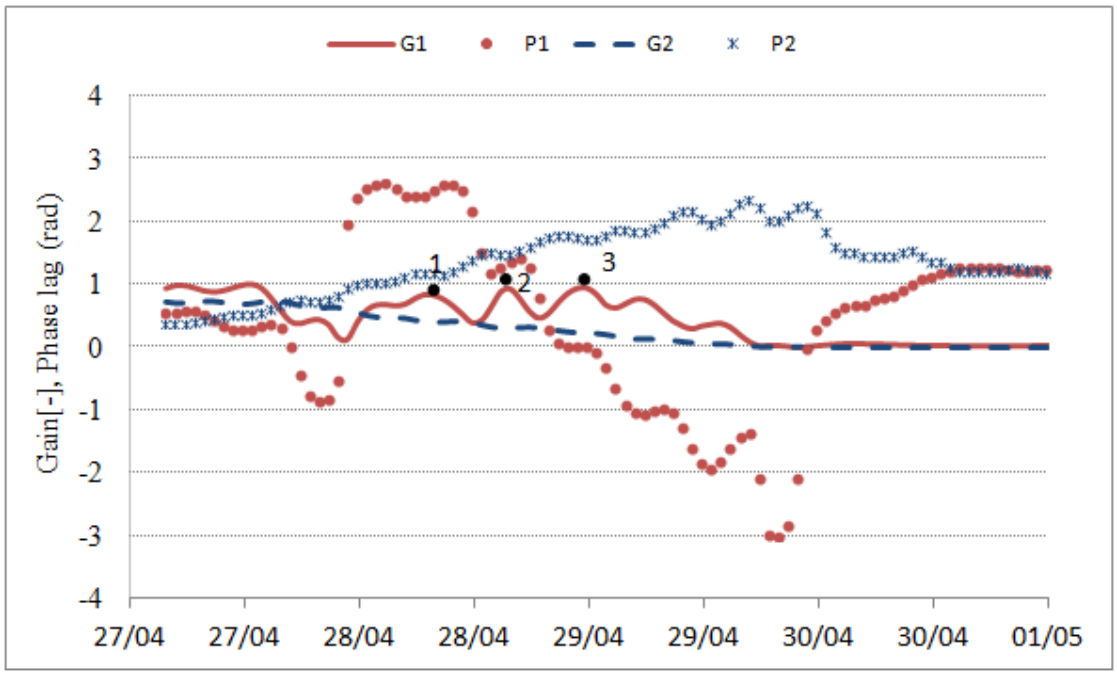

Figure 4.7: Gains and phase lags of the two 24.5-hour tide components for Closure Event 3.

The F_1- and F_2-traces in the complex plane for the two Avoca events (Figure 4.8, Figure 4.10) show that F_2 representing the dominant, semi-diurnal component, is fairly stable, while F_1 representing the subordinate, diurnal tide component, is much more volatile.

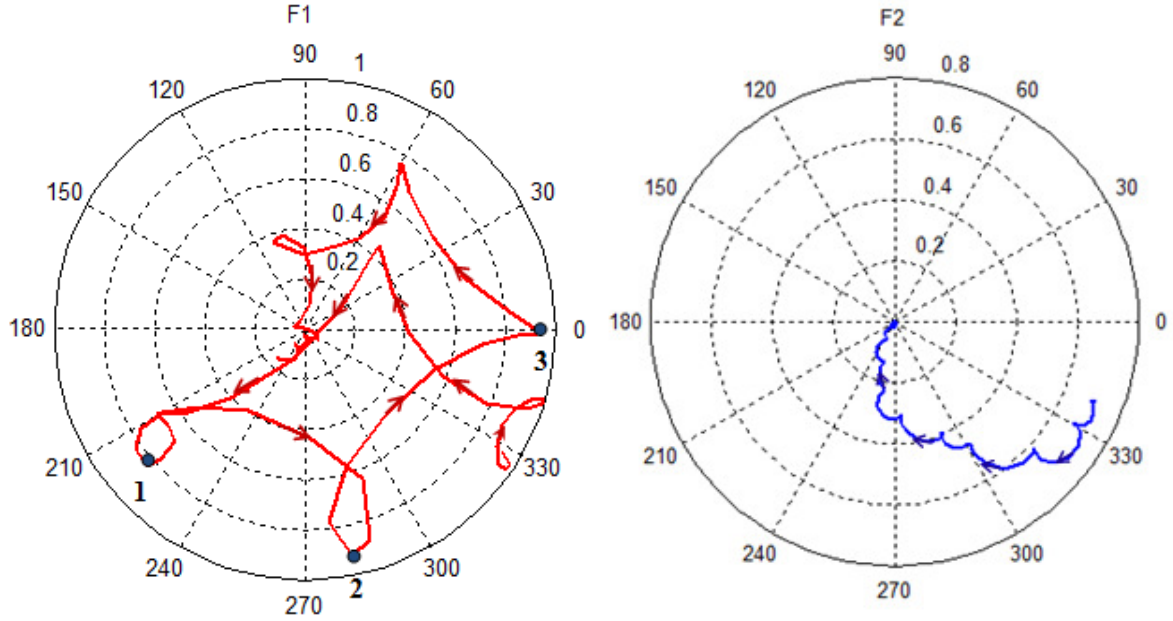

Figure 4.8: Tracks of F_1 (diurnal) and F_2 (semi-diurnal) in the complex plane for Closure Event 3.

Correspondingly, $G_2 = |F_2|$ is quite stable, $G_{2,max} < 0.7$, otherwise around 0.3 to 0.4 under normal conditions, while $50^o < \varphi_2 < 60^o$ (Figure 4.9, Figure 4.10 right).

Through the same events, G_1 shows abrupt changes in response to rain fall or large waves with large variation and multiple-peaks (Figure 4.7, Figure 4.9). Maximum values range from 0.9 to 1.1 for different events otherwise without event it can be stable at $0.7 < G_1 < 0.8$ and φ_1 similar to φ_2 (Figure 4.9).

G_1-values greater than unity occurred in Event 1 related to overtopping from large waves. Such high G_1-values are found when only the highest of the two high tides lead to inflow to the lagoon system, cf. Figure 2.2. Thus, the $G_2>1$-values are peculiar to mixed diurnal/semidiurnal systems. They do not occur with monochromatic diurnal tides.

G_2 starts responding to the closing process earlier than G_1 and G_2 follows a more or less "exponential decay" (Figure 4.7). At that time φ_2 in general shows an increasing trend compared to normal conditions while φ_1 changes rapidly without any particular trend. Hence, in the complex plane F_2 makes a general track close to the linear friction-dominated solution Eq (2.48), while F_1 is quite chaotic with various loops. Towards the end of the closing process, F_1 and F_2 approach the origin in different ways.

The (F_1, F_2)-behavior near complete closure also differs between events. Thus φ_2 is almost constant at around 90^o in Event 1 (Figure 4.10right) and 120^o for Event 3 (Figure 4.8). φ_1 is switching between lags and leads in Event 3 (Figure 4.8left).

Immediately before closure, for all events, F_1 and F_2 are both rotating vectors with rapidly changing phase, as they approach the origin. This rapidly varying phase can be explained in that the ocean phase is still growing, while the lagoon shows no further phase- (time-) change causing the phase-lag to vary with the ocean phase. However, it is difficult to understand the diurnal phase-switching that occurred much earlier in Event 3 (Figure 4.7).

Figure 4.9 and Figure 4.10 show the results for Avoca Event 1. Typically for Avoca, the closing process is lengthened by a wave event. There were large waves H_s = 2.5-2.8 m around 16 July, 20 July and 22 July, which is reflected in 3 peaks of G_1. However, no clear influence is seen in G_2, which remains stable around 0.3 with $50^o < \varphi_2 < 60^o$ (Figure 4.9). This corresponds to the tight orbit of F_2 (Figure 4.10 right) before neap tides. After that G_2 keeps reducing and φ_2 increases to almost 90^o. That is, F_2 is approaching the origin corresponding to complete closure. Before the arrival of the large waves on 16 July, G_1 remains stable around 0.8 and φ_1 around 60^o (Figure 4.9) corresponding to tight orbit of F_1 (Figure 4.10 left). Then G_1 goes up to reach a peak value of 1.1.

Point 1 in Figure 4.9, corresponds to overwash by large waves Figure 4.6:. Further detail of amplitudes for both components with point G_1=1.1 are presented in Figure 4.11.

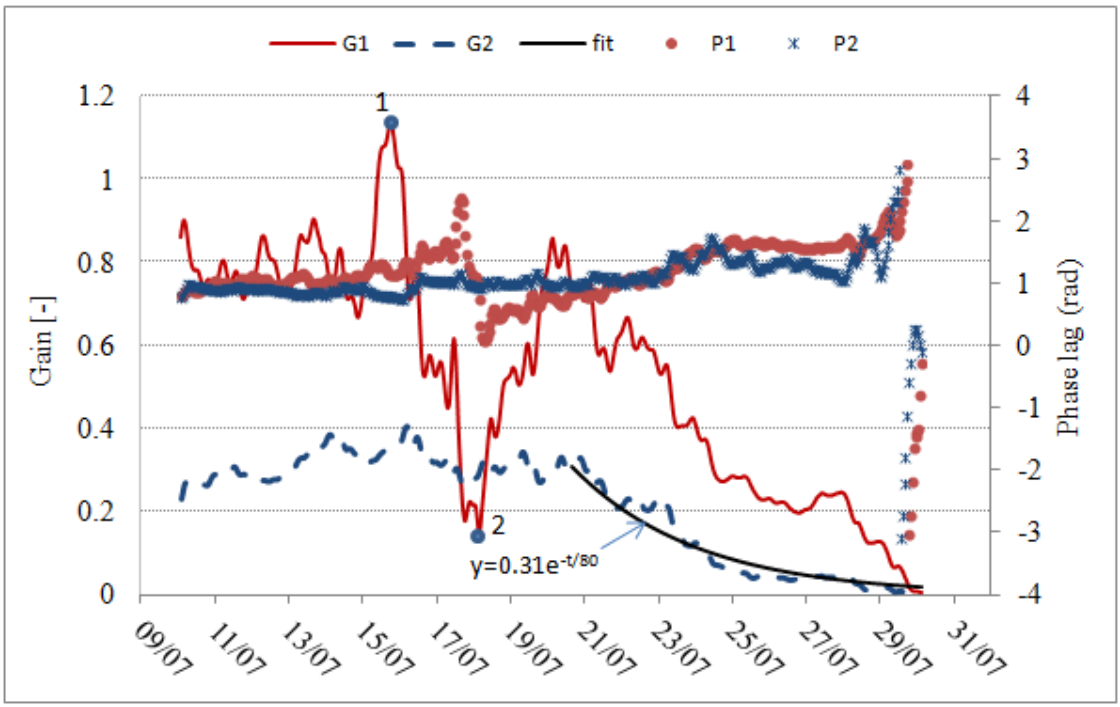

Figure 4.9: Gains and phase lags of the two 24.5-hour harmonic components for Avoca Closure Event 1.

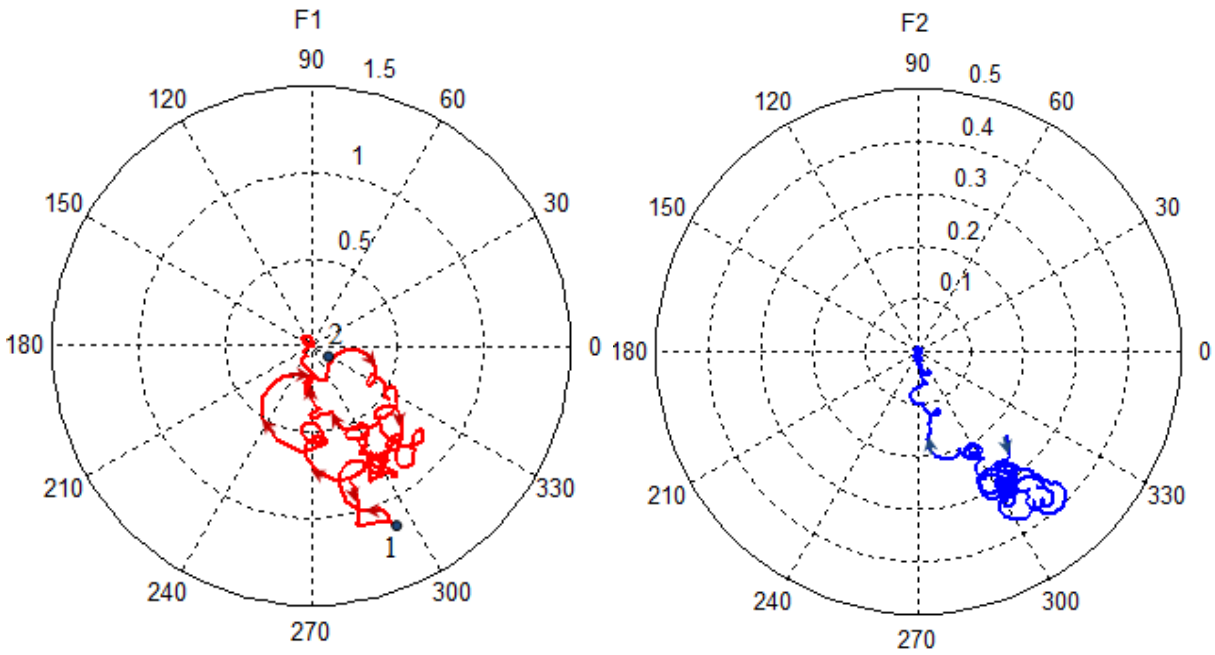

Figure 4.10: The tracks of F_1 (diurnal) and F_2 (semi-diurnal) in the complex plane for Avoca closure Event 1.

When the large waves cease, G_1 reduces to 0.1 at Point 2 (Figure 4.9) then climbs before the high waves on 20 July. The tracks of F_1 are quite messy but φ_1 consistently tends towards 120° as F_1 approaches the origin.

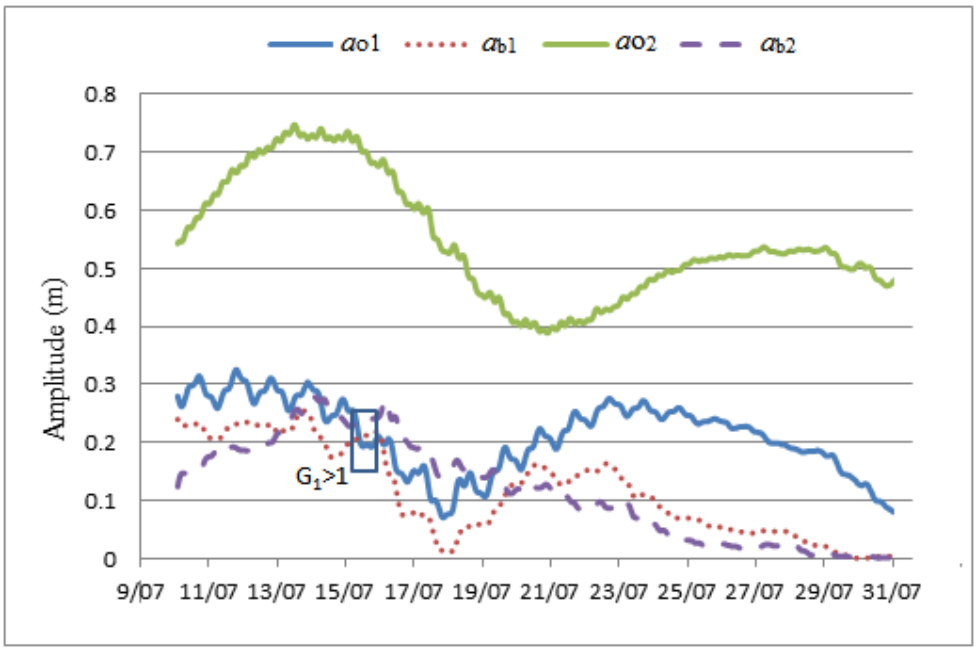

Figure 4.11: Amplitude of two tidal components for Avoca Closure Event 1 with the G_1>1-point indicated by the box.

Figure 4.12 shows the hydraulic time constant T_1 for the semi-diurnal for the two closure events when gain and phase lag are known (Eq 3.13).

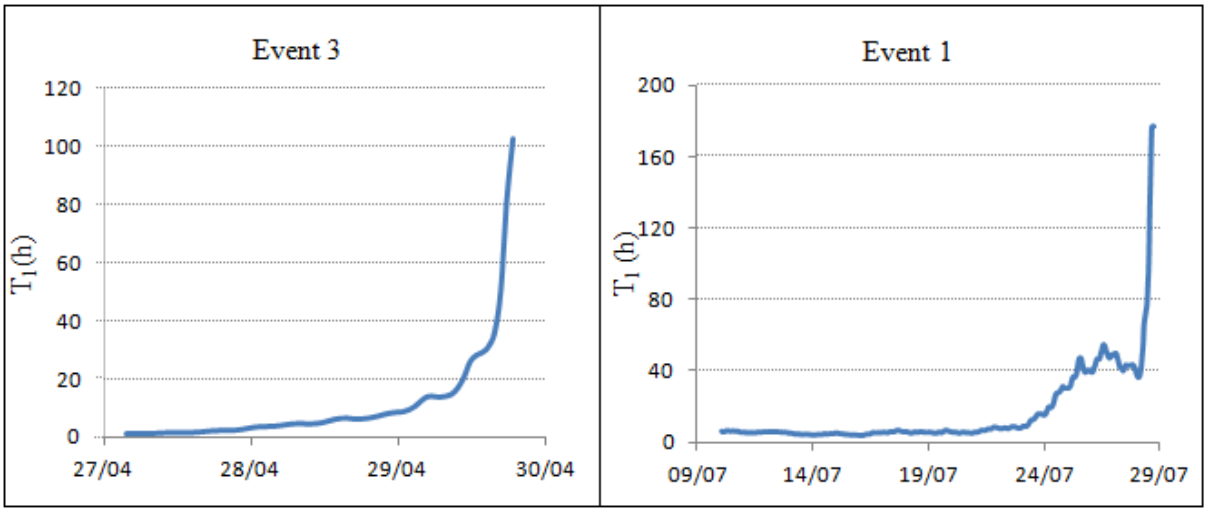

Figure 4.12: The hydraulic time constant T_1, defined in Eq (3.14) for semi-diurnal for two closure events.

T_1 is the time constant describing the geometrical and frictional features of the system as shown in Eq (2.44) and in Section 2.3.3. As can be seen T_1 is quite small: 2 to 5 hours under normal conditions after manual opening. Then T_1 starts increasing as the inlet starts closing. Towards the end of the process it approaches very large values in order of 1500 to 2000 hours. T_1 increase nicely along an exponential curve without disturbance during Event 3. Otherwise, it fluctuates due to disturbances such as storm waves as in Event 1. T_1 is not well defined from $F_1(t)$ for the diurnal component due to F_1 behaving much more erratically than F_2. T_2, the inertial time constant, is not well defined for any of two components.

4.2 STORM EVENT OF MAY 2009 AT BRUNSWICK HEADS

4.2.1 Description of Brunswick Heads and the storm event

In order to understand further the morphological changes of inlets under extreme conditions, that would push them out of equilibrium; as well as how the inlet system recovers; the severe storm in May 2009 is chosen.

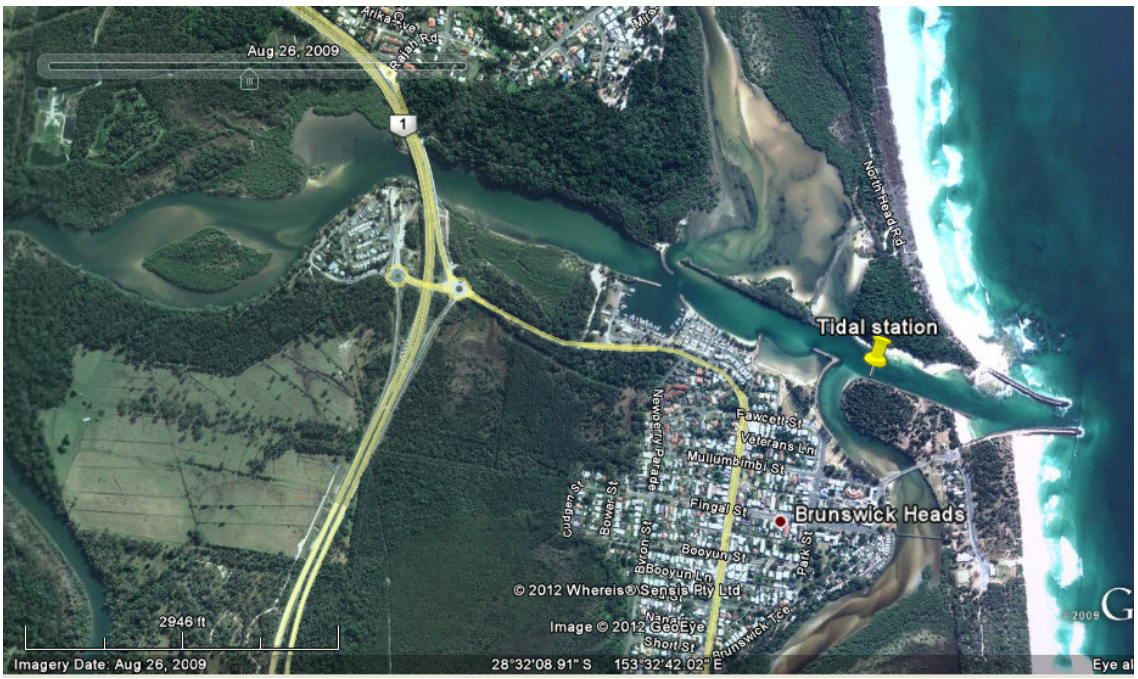

Figure 4.13: The Brunswick River entrance with the BHTG tide gauge about 630 m from the ends of the breakwaters. While the entrance banks (rock walls) are steep, much of the estuary has very flat slopes near MSL. (Image from Google Earth).

Brunswick Heads is located at 28°32'17.22"S and 153°33'29.65"E (Figure 4.13). The Brunswick River tidal system is a medium sized system with catchment area of ca 200 km^2 with surface area of 3.3 km^2 (Roper et al. 2011) and 4.8x10^6 m^3 spring tidal prism (Hanslow et al. 1996). The physical features of the catchment vary from steep, heavily vegetated slopes to grassy flood plain and flat swamp land behind the coastal dunes (Webb and Associates, 1986). The entrance is trained by two parallel breakwaters approximately 300 m long (Hanslow et al., 1996). A shallow bar fronts the breakwaters that is expected to wash out during major floods.

The storm considered here occurred between 20 May 2009 and 24 May 2009, however the data analysis period was extended further before and after the event from 15 May 2009 to 5 June 2009 to gain a general view of the morphodynamic processes as indicated by the tides. The variation of H_s, the ocean tide at Coffs Harbour, the water level at the Brunswick River entrance tide gauge (BHTG) during the selected period are presented in Figure 4.14 and the daily rain fall at Myocum in the Brunswick River catchment is presented Figure 4.15.

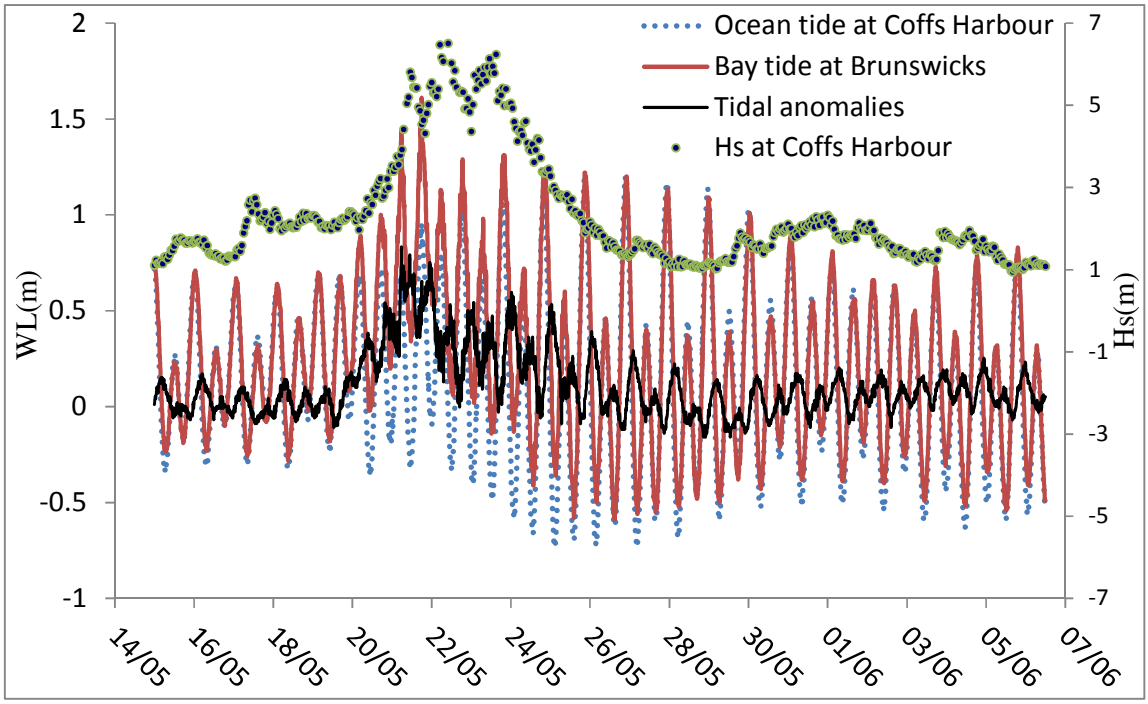

Figure 4.14: Available H_{sig}, ocean water levels $\eta_O(t)$ at Coffs Harbour, tide levels at the BHTG $\eta_R(t)$ and tidal anomalies at the BHTG from 15/5 to 6/6/2009.

At Brunswick Heads (BHTG) the highest tidal anomaly of 0.84m was observed on 21 May at 05:45, 12 hours before a peak water level of 1.62 m at the BHTG (Figure 4.14). The highest significant wave height observed during this event, H_s = 6.5 m occurred on 22 May, H_s > 5 m continued from May 21 to May 23 2009 with the wave period being consistently ca 12 s-13 s

compared to normal conditions: H_s = 1.5-2 m and T = 8-10 s. High waves coinciding with intensive rainfall of nearly 200 mm occurred on 21 May, with peak tidal anomalies and peak BHTG water levels observed on that day.

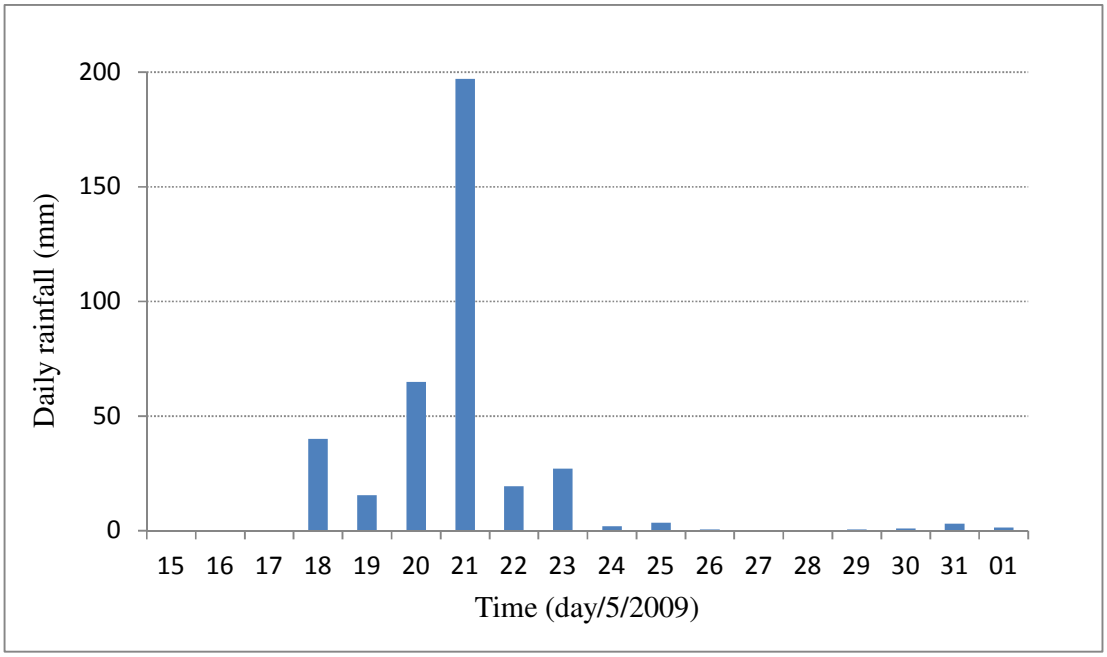

Figure 4.15: Daily rainfall [mm] at Myocum, May 2009.

4.2.2 Results of 24.5 hour moving window analysis

- **Means and standard deviations**

The hourly mean water level $\overline{\eta_O}(t)$ and standard deviation $Stdv_O(t)$ from a central, 24.5 hour moving window analysis are shown in Figure 4.16: $Stdv_O(t)$ shows that this event happened after the neap tide. Similar trends and magnitudes are observed for $Stdv_O(t)$ and $Stdv_R(t)$ with maximum $Stdv_O(t)$ being 0.6 m. The mean (24.5 hours) river water level $\overline{\eta_R}(t)$ increases and reaches a peak of 0.85 m on 21 May, same day as the maximum rainfall. $\overline{\eta_R}(t)$ then declines as the rain fall abates even though the highest waves persisted. This agrees with earlier observations (Dunn et al. 2000) that the BHTG is not measurably influenced by wave setup.

$\overline{\eta_O}(t)$ shows an ocean storm surge of the order of 0.35 m on 22 May. However, the reason for the smaller peak seen on 19 May in the $\overline{\eta_O}(t)$ was not found. The difference between $\overline{\eta_R}(t)$ and $\overline{\eta_O}(t)$ has the same trend as $\overline{\eta_R}(t)$ and has a peak of 0.55 m (Figure 4.16:). $\overline{\eta_R}(t)$ returns to normal on 28 May, i.e., 6 days after the peak of the storm/rainfall event.

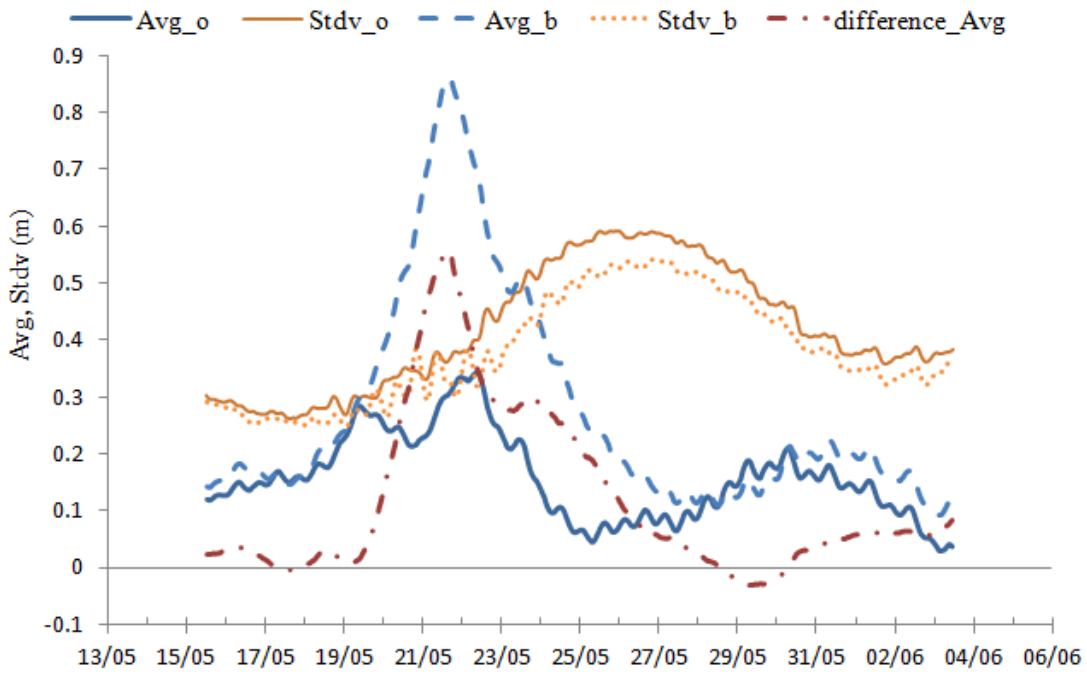

Figure 4.16: $\overline{\eta_O}(t)$, $\overline{\eta_R}(t)$, $Stdv_O(t)$, $Stdv_R(t)$ from 24.5 hour moving window analysis and mean super-elevation of the BHTG above the ocean: $\overline{\eta_R}(t) - \overline{\eta_O}(t)$ for the May 2009 event at Brunswick Heads.

- **Diurnal and semi-diurnal harmonics from 24.5 hour moving window analysis**

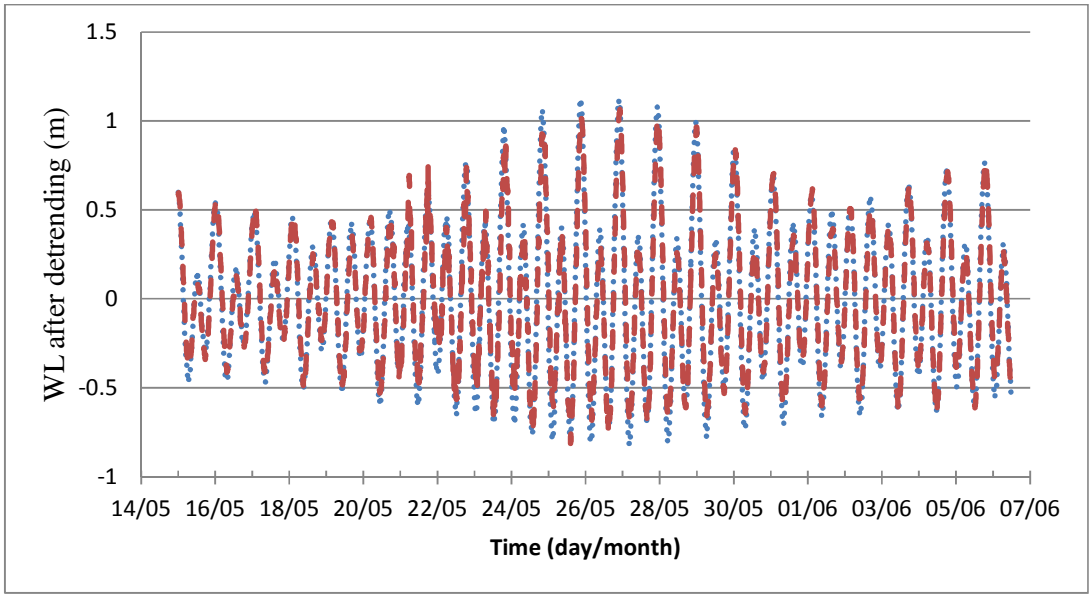

Figure 4.17: Ocean water levels at Coffs Harbour, blue dots; and at the BHTG, red dash after removal of the 24.5 hour means.

The de-trended water levels for both ocean and river appear as in Figure 4.17. Around the spring tides of 26 May, the mixed diurnal/semi-diurnal tides have very uneven highs while the lows are very even. This generates large diurnal amplitudes in rivers and coastal lakes and correspondingly large, sometimes >1, G_1-values.

While frequency response functions for a monochromatic system (purely diurnal or purely semidiurnal) will always be less than unity, bichromatic systems like the one considered here, cf. Figure 4.18, often gives $|F| > 1$ for the subordinate (minor amplitude) component due to non-linear effects.

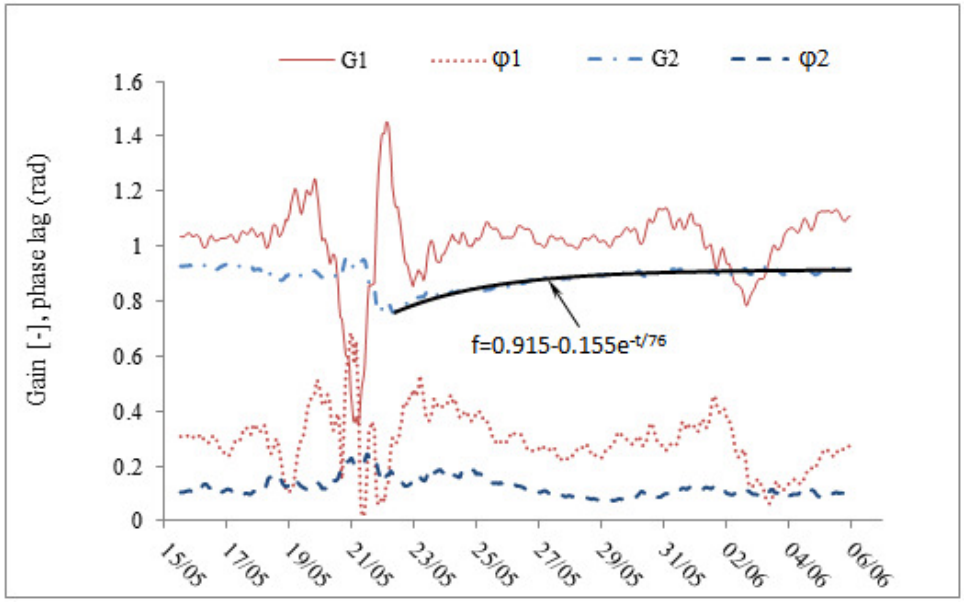

Figure 4.18: Gains and phase lags of the two tidal components obtained with a 24.5 hour moving window together with fitting exponential function for G_2 to obtain T_{morph}=76 hours.

Figure 4.19 shows the tracks of F_1 and F_2 in the complex plane through the event considered here. The gain $G_2 = |F_2|$ and the phase lag φ_2 of the semi-diurnal component increased on 21 May during the same time when the mean water level reached its peak (rain fall was the heaviest), and both of them reduced on 22 May when the mean water level reduced and then the G_2 increased towards its equilibrium value.

The increasing trend around 21 May of G_2 is similar to the tidal analysis of Hinwood & McLean (2001) for Lake Conjola. However, they found that the phase lag at that time decreased. They explained that the tidal response as a result of scour out of the inlet, leading to larger entrance cross section area, which is hydraulically more efficient. The Brunswick River entrance shows no clear increase in hydraulic efficiency during the May 2009 event considered here.

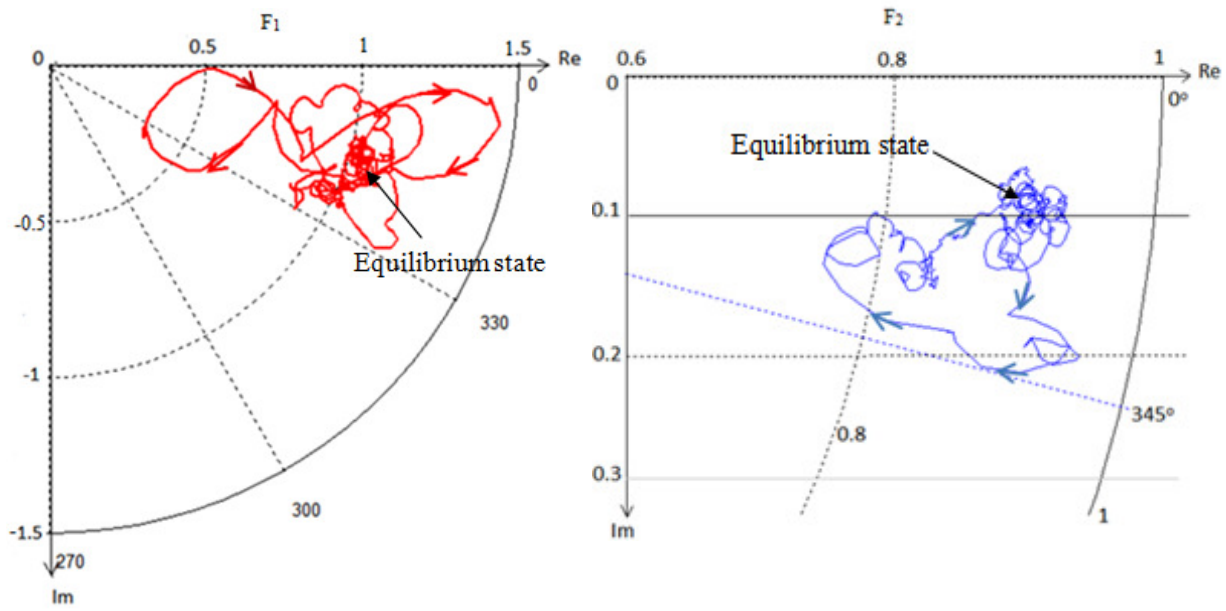

Figure 4.19: The tracks of F_1 and F_2 in the complex plane for the considered May 2009 event. The dominant semi-diurnal component shows modest variability and as expected remains smaller than unity. The subordinate, diurnal component shows very large F_1-values, up to ca 1.4. This is due to non-linear effects combined with the very uneven highs tides at the time of the event, cf. Figure 4.17.

On the contrary perhaps, $|F_2|$ decreased at the time of peak fresh water flow Q_f. Such a behavior can be related to the non-linear nature of the bottom friction with a large Q_f, which reduces tidal response as explained in Section 2.4.1. This trend was confirmed by the tidal hydrodynamic modeling by Hinwood & McLean (2001).

The response of BHTG for the semi-diurnal component is close to perfect under normal conditions, namely $G_2 = |F_2| = 0.91$ and $\varphi_2 = 0.1$radians (=6°). The response function F_2 makes a small loop (Figure 4.19 right) during the storm when the system floods with a large Q_f and then comes back to the initial point when it recovers. The modest size of the loop shows that the Brunswick Entrance does not really change much, even under such a severe event.

The amplitudes of the two components for BHTG and the ocean at Coffs Harbor are compared in Figure 4.20.

The important deviations from normal tidal response happen around midnight 20-21 May are:

1): The semi-diurnal river amplitude a_{R2} drops somewhat in magnitude and stays low until after June 1 before getting back to its equilibrium fraction of the ocean amplitude.

2): The diurnal response is erratic from around midday 20 May to around midday 23 May with $G_1 = |F_1| > 1$ occurring around midnight 21-22 May.

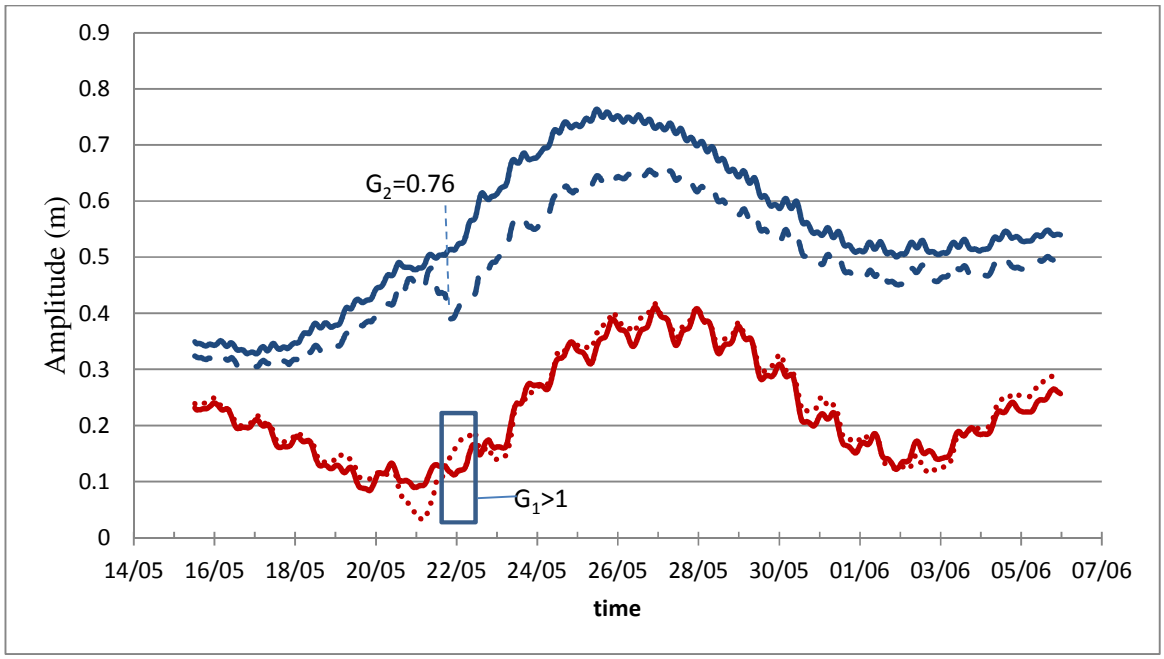

Figure 4.20: Amplitudes of the diurnal (red, lower) and semi diurnal (blue, upper) tidal components at BHTG (dash or dot), and the ocean at Coffs Harbor (full line).

Time scale for changing G_2 in the Brunswick River entrance (T_{hyd}).

The hydraulic response data above show that the dominant semidiurnal component gets reduced during the storm event and recovers more or less exponentially as indicated by Figure 4.19.

Whether this is reflecting significant morphological change or "just hydraulics" as in the influence of Q_f on F_1, F_2 via the non-linear friction term, is not clear at present. Whatever the nature of the change, - the time scale as indicated by the trend line equations in Figure 4.19 is around 76 hours.

It should be noticed that the morphological time scale T_{morph} and the similar time scale of changing hydraulic efficiency T_{hyd} were obtained using the same method of fitting $G(t)$ for the primary component. These are both longer than the primary hydraulic time scales T_1 and T_2 used in the frequency response function Eq (3.12).

4.3 OVERWASH FLOOD EVENT IN LAKE CONJOLA

4.3.1 Recall Lake Conjola information

The simulation of anomalies for the overwash event around 9th April 2006 at Lake Conjola has been carried out in Section 2.5. In this chapter, we recall the available data and information of the Lake to study the morphological time scale as well as the response functions of this natural and dynamic sandy inlet-bay system corresponding to the event.

Figure 4.21: Oblique aerial photo of Lake Conjola – pre 1998 (MHL).

A detailed description of Lake Conjola is given in Section 2.5, Figures 2.25, 2.26. Brief information about the Lake and the event is summarized here. The lagoon surface area is ca 5.9 km^2, which consists of 2 lakes. The main water body Lake Conjola (4.3 km^2) is about 3 km away from the entrance, and Berringer Lake (1.5 km^2) is located around 1.5 km from the entrance. The main Lake is connected to the entrance through a long, shallow channel of 1 m depth and of 30 m width. There are large sand lobes of flood tidal delta and long sand spits surround the entrance area. This system is a predominantly open lake, remaining open more than half of the time.

During the storm event in April 2006, the lake water level increased significantly to 1.31 m, which is more than 0.5 m higher than peak ocean tides (Figure 4.22). Overflowing of the banks and road flooding due to waves overtopping the berm, were observed at some stage between 6th to 11th April 2006. The ocean tides were mixed, predominantly semi-diurnal with a range of ca 1 m during the event. No significant rainfall was recorded during that time. A maximum offshore significant wave height, H_s, of *ca* 5 m or H_{rms} =3.5 m occurred with peak wave period (T_p) greater than 15 s. Wave direction during the event was from south to southeast so that, the fronting berm was directly exposed to the waves. The available data is shown in Figure 4.22 for this event from 6 April 2006 to 8:30 14 April 2006.

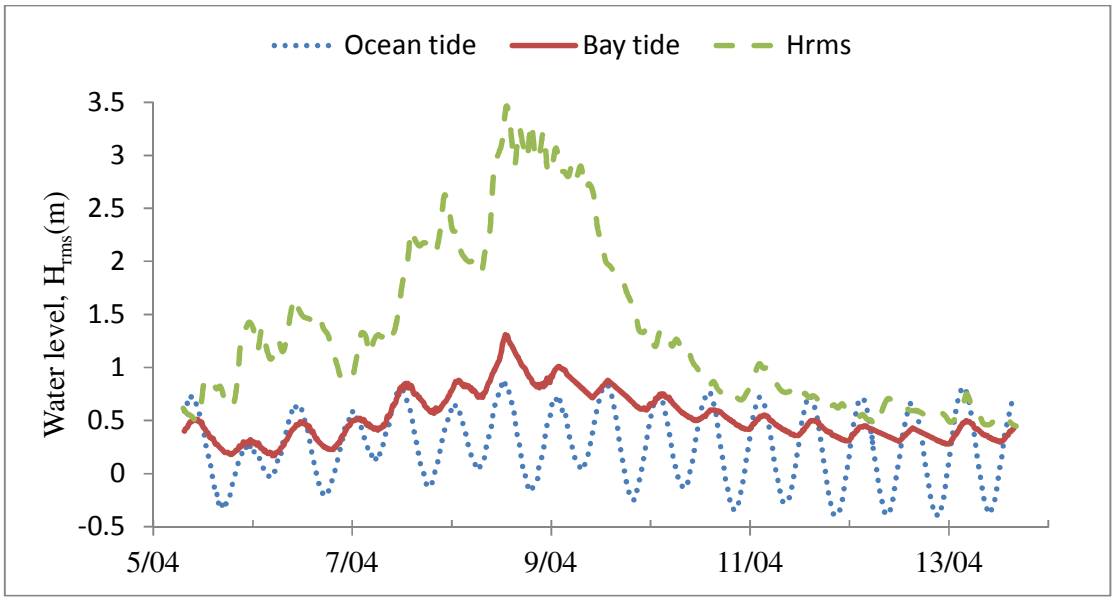

Figure 4.22: Available data for the event from 6th to 14 April 2006 at Lake Conjola: measured bay tides at gauge 1.3 km from the entrance, η_b at Jervis Bay and H_{rms} at Sydney.

Britton & Partners (1999) reviewed previous studies and investigated further Lake Conjola's entrance processes. They identified four basic entrance states: regime state, flood scoured state, intermediate state and storm washover state. The regime state is the steady period when the entrance naturally and gradually forms without any sudden changes such as floods or storms. Flood scoured state describes the condition whereby a major flood washes out significant amount of sand resulting in widening of the entrance. After floods, the entrance infills rapidly before approaching the regime condition. The intermediate state usually takes from 1 to 2 years. Storm washover is characterized by a sudden change caused by a severe storm waves washing over the entrance spit leading to blocking of the entrance channel. The entrance is likely to close, in fact from 1937 to 1999, all closure events (eight times) were due to washover during severe storms.

This section is on application of the 24.5 hour window method to analyse the tidal records. The time scale for inlet recovery after the event and the inlet response to the event in terms of hydrodynamics is shown here.

4.3.2 Results of 24.5 hour moving window analysis

- **Moving means and standard deviations**

Figure 4.23 shows $\overline{\eta_{24.5}}(t)$ and $Stdv_{24.5}(t)$ with subscript "o" for ocean and "b" for bay tide. $\overline{\eta_o}(t)$ increases from 0.15 m to 0.36 m and remain at surge level for two days (mid of 7 April 2006 to mid

of 9 April 2006). $\overline{\eta_o}(t)$ started responding when H_{rms}=2.2 m was exceeded and remained elevated till $H_{\rm rms}$ fell below 3 m. $\overline{\eta_b}(t)$ increases to a peak of 0.96 m and lasts for about one day corresponding to the largest waves. The difference between $\overline{\eta_b}(t)$ and $\overline{\eta_o}(t)$ at the peak was 0.6 m compared to 0.5 m difference between peak of η_b and η_o. Before and during the storm, η_b and η_o both clearly show higher high and lower low tide with different tidal range. After the storm, the bay tidal range became even and much smaller (about 1/4 of ocean tidal range) than before storm (1/2 of ocean tidal range) as seen in Figure 4.24. This implies that wave overwash drives sedimentation of the channel.

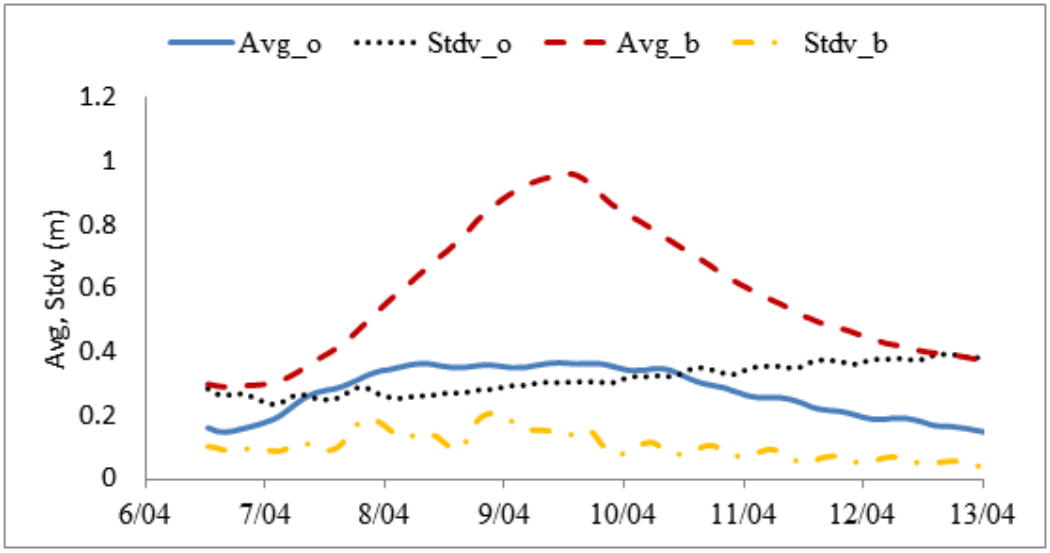

Figure 4.23: $\overline{\eta_{24.5}}(t)$ and $Stdv_{24.5}(t)$ for April 2006 event at Lake Conjola, "o " denotes for ocean, b for bay.

$Stdv_{\rm O}(t)$ shows that this event happened just after the neap tide (Figure 4.23). Opposite trends and magnitudes are observed for standard deviation. $Stdv_{\rm O}(t)$ increases toward spring tide while $Stdv_{\rm b}(t)$ decreases after the storm. $Stdv_{\rm b}(t)$ fluctuates corresponding to wave height increasing in two steps. However, the change in $Stdv_{\rm b}(t)$ is quite small of the order of 0.1 m.

- **Harmonic analysis results**

The results of harmonic analysis after de-trending are presented in Figure 4.25. In general, G_1 is more sensitive to the event than G_2. However, the phase lag φ_1 is quite stable during peak storm period, then it switches from lag to lead after the storm.

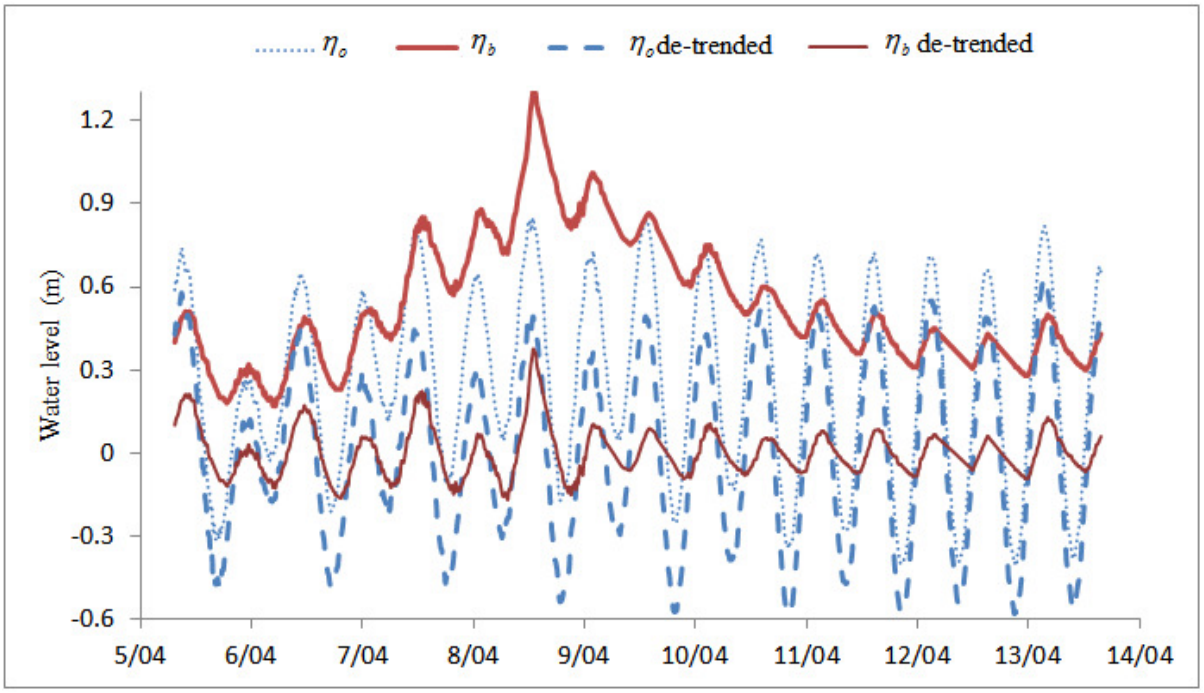

Figure 4.24: Ocean and bay water levels before and after removal of the 24.5 hour means at Conjola.

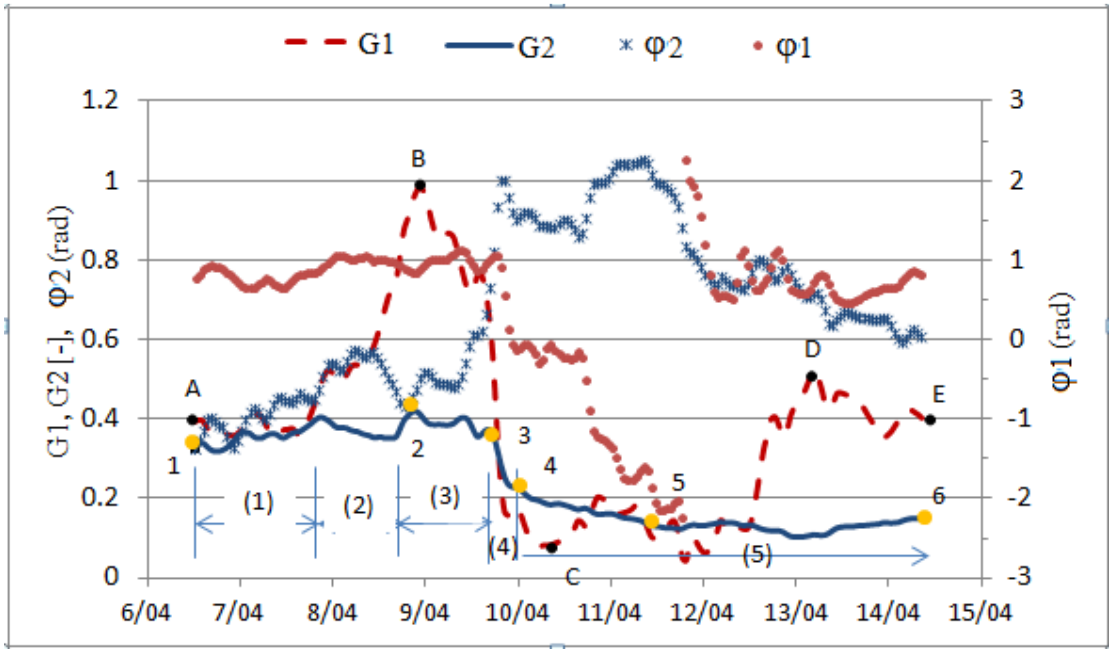

Figure 4.25: Gain and phase lag for diurnal and semi-diurnal lake tides obtained with 24.5h moving window.

G_2 changes in 2 steps, the higher level is around 0.37. There was a slight increase during the peak period around 9 April. It suddenly falls off when H_{rms} starts decreasing from 3 m to 1.5 m.

Then G_2 reduces gradually to an equilibrium value of 0.13. The phase lag φ_2 is also divided into two periods before and after the storm and opposite trend compared with φ_1.

The gains and phase lags in Figure 4.25 may be divided into 5 periods corresponding to the change in channel cross-section related to invert inlet level z_{cr} change.

Period (1), before 17:30 7/4, represents normal conditions when H_{rms} was quite low, around 1.5 m, both gains and phase lags of the two components are stable at $F_1 \approx$ (0.4, 45°) and $F_2 \approx$ (0.35, 25°) in Figure 4.25 and tight orbits in Figure 4.26.

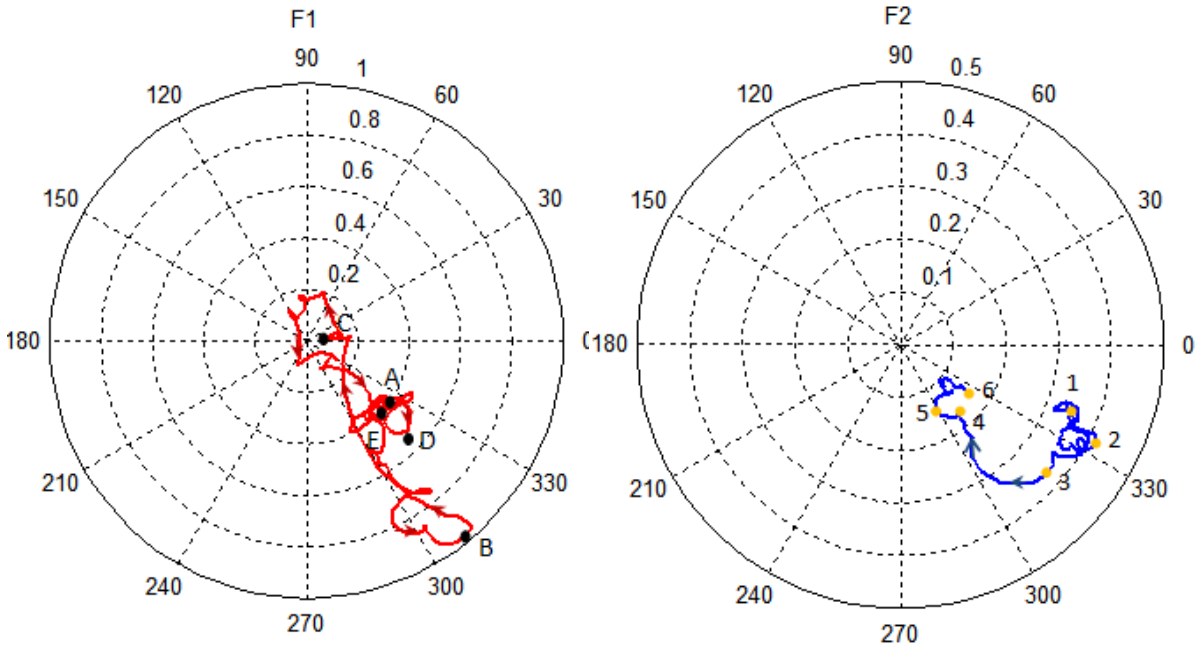

Figure 4.26: The tracks of F_1 and F_2 in the complex plane for the April 2006 event at Lake Conjola. The dominant F_2 shows modest variability and maximum G_2 of 0.41 (point 2) and maximum φ_2=60° point 5. G_1 shows very large range from 0.1 to 1 and phase switch between lag and lead. The traces of F_1 and F_2 follow some typical points as in Figure 4.25.

Period (2), around 8 April, when 2 m < H_{rms} < 3 m, $\overline{\eta_b}(t)$ increases, G_2 goes down slightly with φ_2 increasing in Figure 4.25 corresponding to z_{cr} increase. This shows the same trend as F due to z_{cr} increasing in the simulations in Section 2.4.1 and 2.4.2 for mono- and bi-chromatic ocean tides. This case is characterised by gradual accretion when medium size waves transport sand from near shore to fill up the entrance causing a reduction of a_b and delay in phase. This is the same as described in Hinwood & McLean (2001).

Period (3), around 9 April, $\overline{\eta_b}(t)$ increases corresponding to highest wave height from 3 to 3.5 m. G_2 goes up slightly with φ_2 reducing in Figure 4.25. However, G_1 jumps up to nearly 1 while φ_1 marginally declines. This state shows the same response to flood event analysed by Hinwood & McLean (2001) for Lake Conjola. The significant rise in water level due to wave overtopping has the same effect as flooding by rain fall since it scoured and enlarged the entrance when flow drained back to the ocean, making the entrance more hydraulically efficient.

Period (4), very short period end of 9 April after storm, H_{rms} dropped from 3m to 1m leading to sudden fall of $\overline{\eta_{\text{b, 24.5}}}(t)$, G_1 and G_2 sharply reduced, especially G_1. φ_2 increases much more than φ_1 (Figure 4.25). This state is intermediate after flood, the entrance infills rapidly before approaching regime condition as described by Britton & Partners (1999). The medium waves transport suspended sand eroded from the flood tide delta and entrance due to storm waves, and deposit it in the entrance. This state is quite similar to period 2 but different in mean water lever trend and speed of accretion due to enriched sediment supply after the storm.

Period (5), steady or recovery state from 10 April, H_{rms} reduced to lower than 1m, leading to less energy for onshore sediment transport. Then G_2 reduces gradually to the equilibrium value of 0.13 which is 2 times less than G_2 before the storm (Figure 4.25) due to the entrance being filled up to narrower area. φ_2 also reduces from 60^o to 30^o, whereas G_1 reduces to the very low magnitude of 0.08, then has erratic movement around 0.13 before climbing back to the stable state as before storm with F_1= (0.4, 45^o).

Figure 4.26 shows the tracks of F_1 and F_2 in the complex plane. During periods (1), (2), (3) F_2 is quite close to a stable state F_2= (0.35, 30^o) then runs closer to the origin for period (4) and (5). The starting point 1 and ending point 6 are quite far apart. This shows different morphology of entrance before and after storm. F_1 shows very large range of G_1= 0.1 to 1 and φ_1 from 45^o to 60^o except the switch between lag and lead period. The starting point A and ending point E are quite close to each other due to a_{o1} reducing toward spring tide (Figure 4.27).

Morphodynamics of the inlet during different periods can be explained more persuasively with the estimation of z_{cr} from inverse modeling as attempted in Thuy et al. (2011). However, the Lake Conjola system behaves as a system of two lakes connected as showed in Section 2.5.3. Therefore the inverse modelling cannot be implemented without the availability of measured water levels at Site 5 (Figure 2.25). It is suggested that the local authorities may set up a permanent gauge at Site 5 for further and better research and prediction of morphodynamics of the entrance of Lake Conjola.

Further amplitude details of both components for ocean and bay tide are shown in Figure 4.27. The semi-diurnal amplitude a_{o2} is obviously large and increases towards spring tide from 0.3 to 0.54. However, a_{b2} and diurnal amplitude of bay and ocean tides have decreasing trends after the storm and towards end of the event. a_{b1} and a_{b2} show the same pattern with different magnitude. a_{b1} nearly vanishes after the storm, due to the ocean highs becoming very even, cf. Figure 4.24.

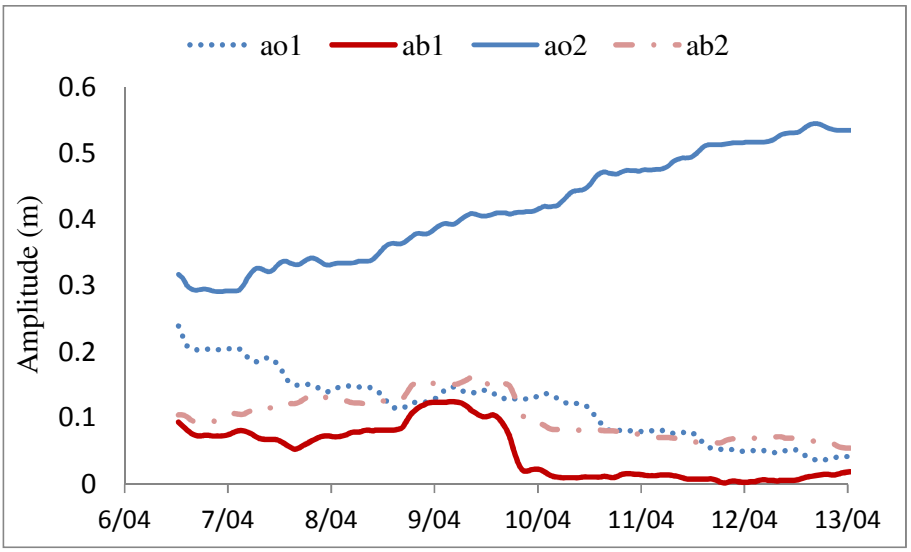

Figure 4.27: Amplitude of two components for ocean and bay tides for April 2006 event at Conjola.

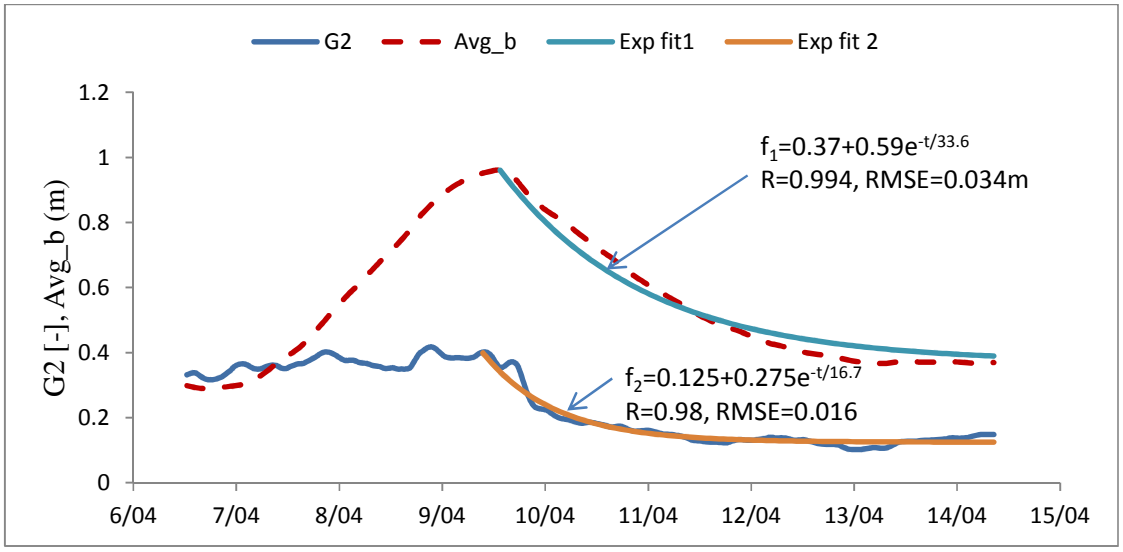

Figure 4.28: G_2 aid $\overline{\eta_b}(t)$ and $Stdv_b$ with exponential curves fitted, yielding T_{morph}= 33.6 hours by fitting $\overline{\eta_b}(t)$ and T_{morph}=16.7 hours by fitting G_2.

- **The morphodynamic time scale for the Lake Conjola entrance**.

The hydraulic response data above show that $\overline{\eta_b}(t)$ and G_2 get increased slightly during the storm event and recovers to lower G_2 and more or less exponentially as indicated in Figure 4.28. The results of T_{morph} by fitting $\overline{\eta_b}(t)$ is 33.6 hours, twice that of fitting G_2 (T_{morph}=16.7 hours). The T_{morph}-value obtained by fitting G_2 is more associated with the morphodynamics of channel, while the timescale from fitting $\overline{\eta_b}(t)$ is associated with the whole system draining slowly after the storm.

4.4 HURRICANE KATRINA IN PENSACOLA PASS, USA

4.4.1 Description of Pensacola pass, USA and Hurricane Katrina in 2005

- **Description of study area**

Pensacola pass is located in the westernmost part of the State of Florida in Escambia county (Figure 4.29). This pass connects the Gulf of Mexico to Pensacola bay. Pensacola Pass is bordered by Santa Rosa Island with a sand barrier 80 km long to the East and a 24km sand spit off Perdido key to the West. The Pass is located at 30°19.5'N and 87°18.5'W. The inlet is quite natural without structures along the shore line of Santa Rosa Island, however, two small jetties (100 m long) on Perdido key inside the Pass allow a significant amount of sand flow through and over them (Browder and Dean, 1999).

Figure 4.29: Pensacola pass, Florida, US image from Google Earth relative to the track of Hurricane Katrina (2005), the yellow point is Pensacola tidal station.

The Pass is an unjettied Federal navigation inlet with an authorized channel depth of 11 m (MLLW) and width of 150 m which was maintained by dredging. Since 1991, no dredging has been conducted in the channel. The pass entrance width is around 1050 m. The tide in this region is micro-tidal, with mainly diurnal tide with an average tidal range around 0.43 m (Armbruster, 1997). Tidal prism (P) at spring tide is around 2.7×10^8 m^3 and the throat area is around 10000 m^2 (Powell, 2006). The annual $\overline{H_s}$ is 1m with wave period of 5 s.

Hurricane Katrina's impact to Santa Rosa Island was predominantly in the form of swash, larger overwash penetration into the bay and breaching of the sand spit especially the narrow and lower section in Fort Pickens unit in Figure 4.29 (Claudino-Sales et al., 2008). Average shoreline retreated of 30 m in Fort Pickens unit was evaluated by Houser & Hamilton (2009) and no significant shoreface recovery was observed after a year. There is scarce data related to morphology change at the entrance or ebb tidal deltas.

The morphodynamics of Pensacola inlet under extreme storm conditions such as Hurricane Katrina and its recovery after the storm is attempted in this section using 24.5 hour window method. The results of this method are then compared with that of a process based model in Chapter 7.

- **Available data from Hurricane Katrina**

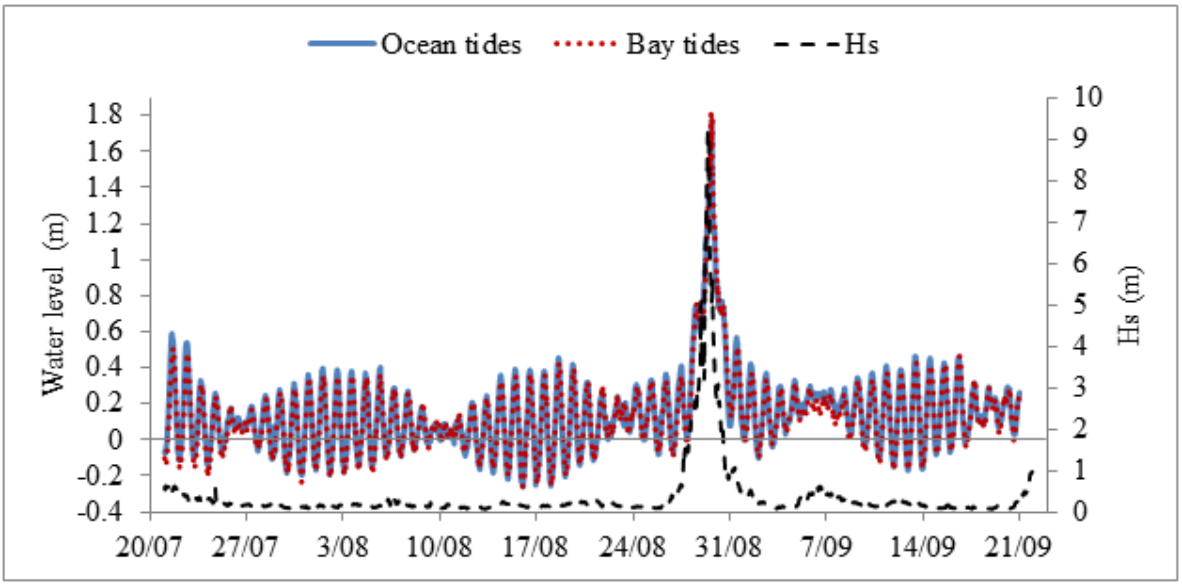

Figure 4.30: Ocean Water level at Dauphin station, Bay water level at Pensacola, and H_s at 21 m depth, from 21 July to 11:15 20 September 2005 including Hurricane Katrina from 28 August to 31 August 2005.

Hurricane Katrina occurred and impacted on the Pensacola inlet from 28 August to 31 August 2005. In order to find the morphological time scale T_{morph}, the data for analysis is extended 3 spring/neap tidal cycles pre storm and 1 spring/neap tidal cycle post storm, from 21 July to 20 September 2005 (Figure 4.30). The expected T_{morph} is long compared to other case studies, unfortunately we cannot extend further after Hurricane Katrina due to the occurrence of Hurricane Rita afterwards. In order to see clearer the change in water level as well as tidal gain and phase lag, the shorter period from 8:00 27 August to15:15 4 September 2005 is presented in Figure 4.31.

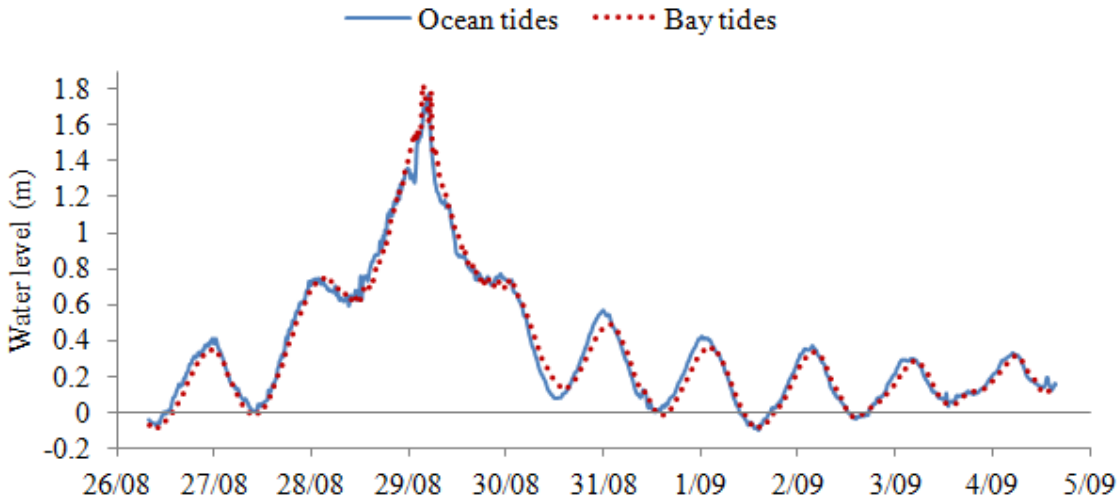

Figure 4.31: Ocean Water level at Dauphin station, Bay water level at Pensacola, Short period: 8:00 27 August to15:15 4 September 2005.

Water levels are taken from the website http://tidesandcurrents.noaa.gov/gmap3/. River flow is insignificant and was not considered in this model. Ocean tides are taken from station 8735180 located on Dauphin island - 75 km west of Pensacola (Figure 7.7). Bay tides are taken from Pensacola station 8729840 inside the Pensacola bay, ~18 km from the entrance (the yellow point in Figure 4.29). The wave and wind information was taken from station 42040 south of Dauphin island at a depth of 164 m (Figure 7.7) from http://www.nodc.noaa.gov/BUOY/. The wave transformation model ndbc.exe taken from Coastal Inlet Research program (CIRP) was utilized to transfer waves from 164 m to ca 21 m depth.

The ocean and bay water levels as well as the significant wave height H_s at 21 m depth are presented in Figure 4.30. The peak water level in the ocean of 1.77 m occurred at 17:00 29 August 2005, which was 6 cm less than the peak in the bay and with a delay of 1.5 hours compared to peak time in the bay. This was opposite in trend compared with normal conditions, wherein the ocean tide is higher and leads the bay tide. The peak occurred at spring tide, which was

expected to be about 0.45 m. This means that Katrina generated ~1.4 m surge in the bay corresponding to maximum offshore H_s= 9 m at 12:00 29 August 2005 with peak period T_p=14 s and wind speed of 31 m/s. Wind direction before the peak was mostly from southeast while after peak it was from southwest. Wind directions were slightly different from the wave directions from peak time to the end period, before peak time the difference of direction varied between 50° and 90°. Before and after the 4 days of hurricane, the H_s was less than 0.5 m.

4.4.2 Results of 24.5 hour moving window analysis

- **Means and standard deviations**

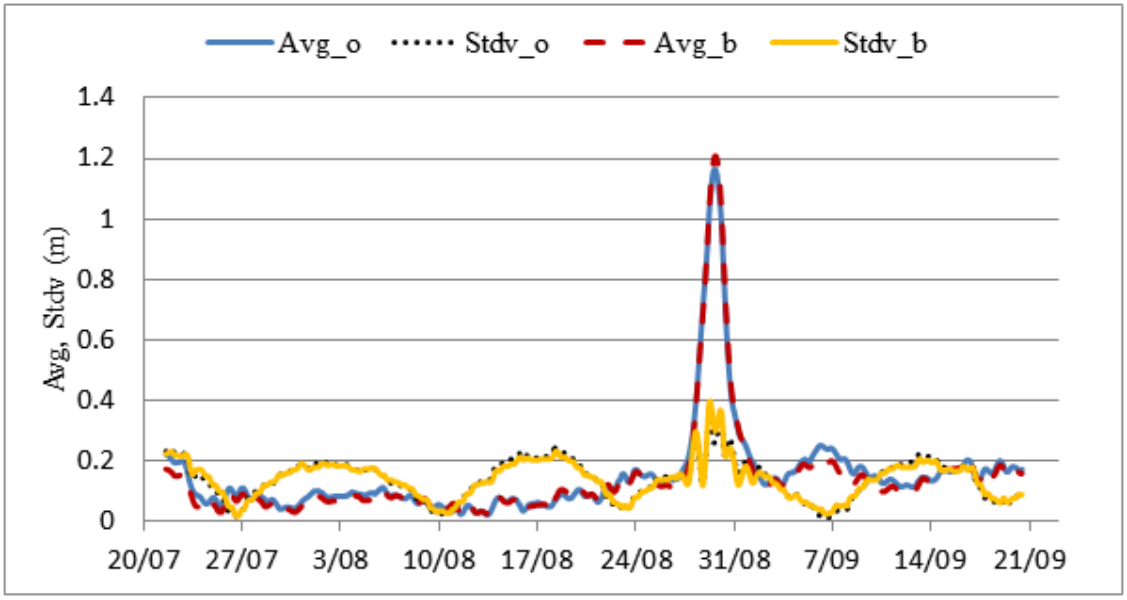

Figure 4.32: $\overline{\eta_{24.5}}(t)$ and $Stdv_{24.5}(t)$ of ocean and bay tides by 24.5 hour moving window.

Figure 4.32 shows $\overline{\eta_{24.5}}(t)$ and $Stdv_{24.5}(t)$ for the ocean and the bay tides by using 24.5 hour moving window. The hourly ocean mean water level $\overline{\eta_o}(t)$ almost coincides with $\overline{\eta_b}(t)$ of the bay, except at peak storm $\overline{\eta_b}(t)$ is slightly higher than $\overline{\eta_o}(t)$ and at the next spring tide after hurricane $\overline{\eta_b}(t) < \overline{\eta_o}(t)$. This case is rather different from other storms analysed before since $\overline{\eta_o}(t)$, $\overline{\eta_b}(t)$ increased and reduced simultaneously, while in other storms, during the draining period, the η_b always higher than η_o. A similar pattern of $Stdv(t)$ is observed for bay and ocean. There is a slightly larger value of $Stdv_b(t)$ compared to $Stdv_o(t)$ at the storm peak. The reason for $\overline{\eta_{24.5}}(t)$ and $Stdv_{24.5}(t)$ of ocean and bay tides being almost the same may be the long sand spit along Fort Pickens unit being breached by Hurricane Ivan (2004) and Denis (2005) and not yet recovered resulting in the bay being quite

open to the ocean.

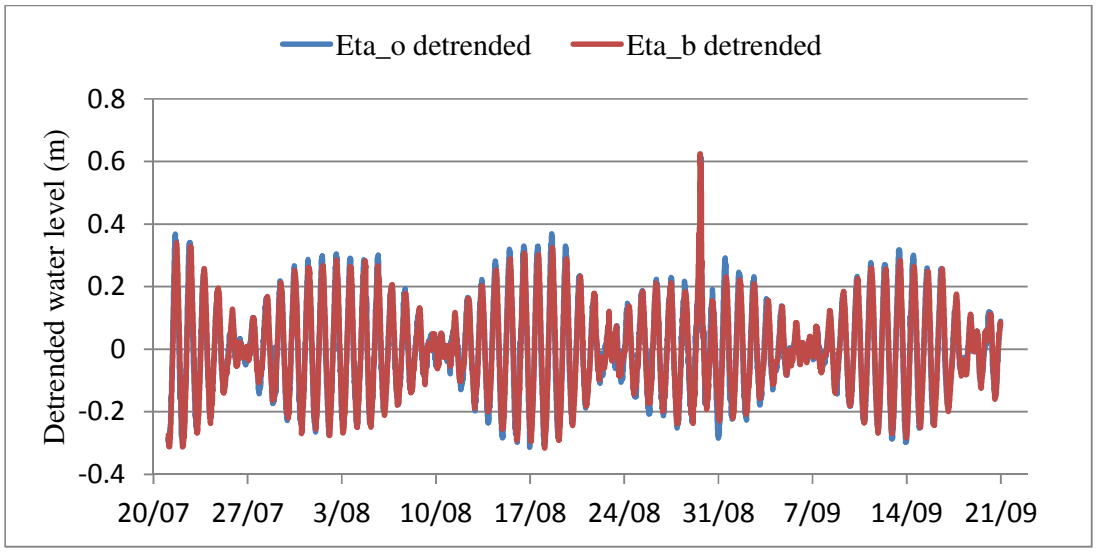

Figure 4.33: De-trended ocean and bay water level after removing $\overline{\eta_{24.5}}(t)$.

The ocean and the bay water levels were de-trended by removing $\overline{\eta_{24.5}}(t)$ as shown in Figure 4.33. However, using this de-trending method is not effective for this case because η_b after de-trended is still very high compared to other tides. To deal with this issue, a shorter window length is required, however the primary component is diurnal, hence window length cannot be less than 24.5 hours. At this time we may accept this to continue for further investigation bearing in mind the accuracy of harmonic analysis around half window before and after peak time.

- **Harmonic analysis results**

G_1 and φ_1 from harmonic analysis after de-trending are presented in Figure 4.34 and a_{o1}, a_{b1} in Figure 4.35. Spring tide is denoted by S and N denotes neap tide. In general, G_1 is more or less stable at 1.0 and phase lag $\varphi_1 \approx 7^o$. This is also illustrated in Figure 4.35 where a_{o1} and a_{b1} nearly coincide with each other except at spring tide and especially at the storm peak. This means that the sudden changes in G_1 and φ_1 are possibly due to wave overwash during Hurricane Katrina. Details of the changes in G_1 and φ_1 during the hurricane are provided in Figure 4.37 and Figure 4.38 corresponding to the shorter period of water levels.

Amplitudes at spring tides perform unevenly as shown in Figure 4.35, one higher at around 0.3 m then followed by the lower one about 0.25 m. At neap tide, amplitude nearly vanishes, but still inside bay the amplitude is higher than in the ocean, it may due to the oscillation caused by wind in the large bay, but not related to any morphological change or resonance. For example the

first neap tide (at N_1 in Figure 4.34), a_{o1}=0.005 m, a_{b1}=0.023 m results in G_1=4.5. Other neap tides show the same pattern but less profound.

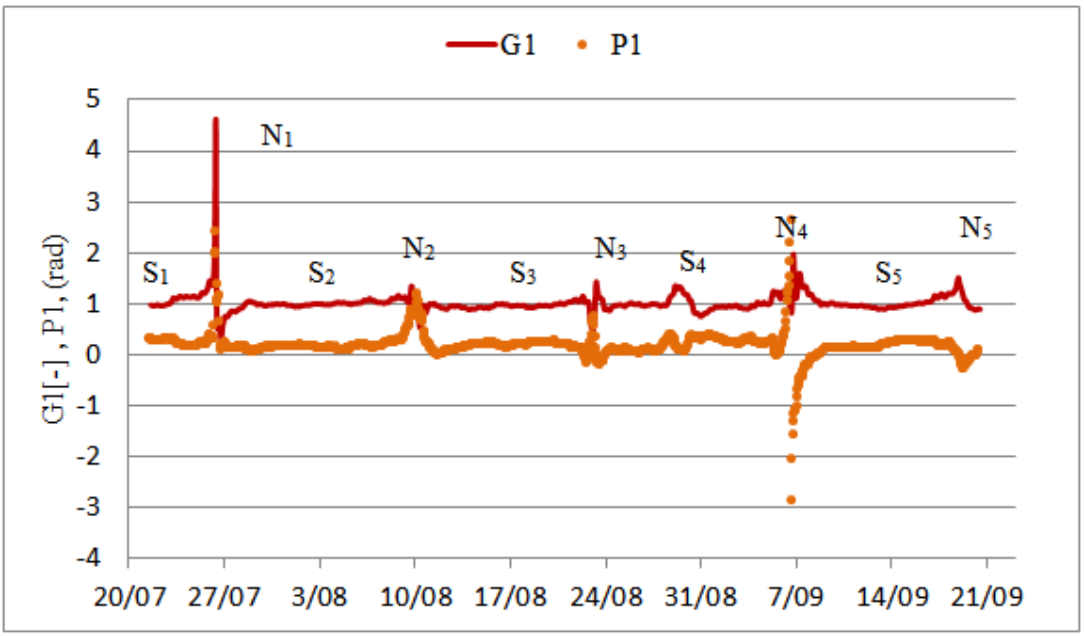

Figure 4.34: Gain and phase lag of the diurnal tide obtained by 24.5 hour moving window.

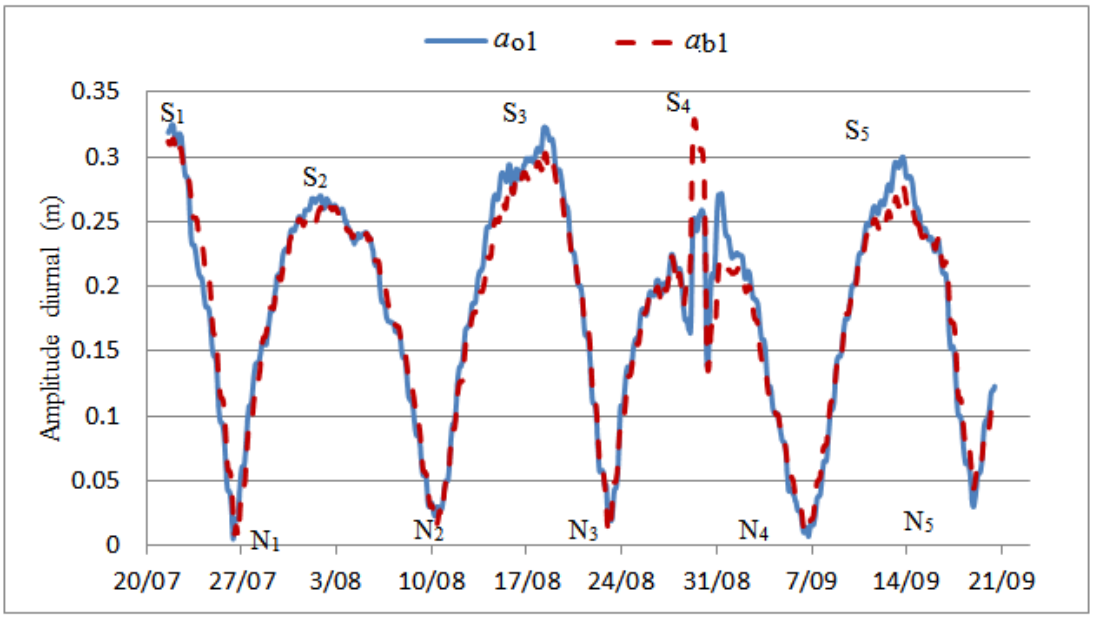

Figure 4.35: Amplitude of diurnal: a_{o1} for ocean tides, a_{b1} for bay tides.

G_2 and φ_2 are presented in Figure 4.36. In general, G_2 is more or less stable at 0.5 and φ_2=30° - 40° for most of the time including the storm period from 29 August to 3 September. However, around neap tides, G_2 and φ_2 are erratic, G_2 jumps to very large values in the order of 10

to 20. The amplitude is quite small of the order of 0.03 m, except at the peak storm where a_{o2} and a_{b2} both increase to more or less 0.1 m.

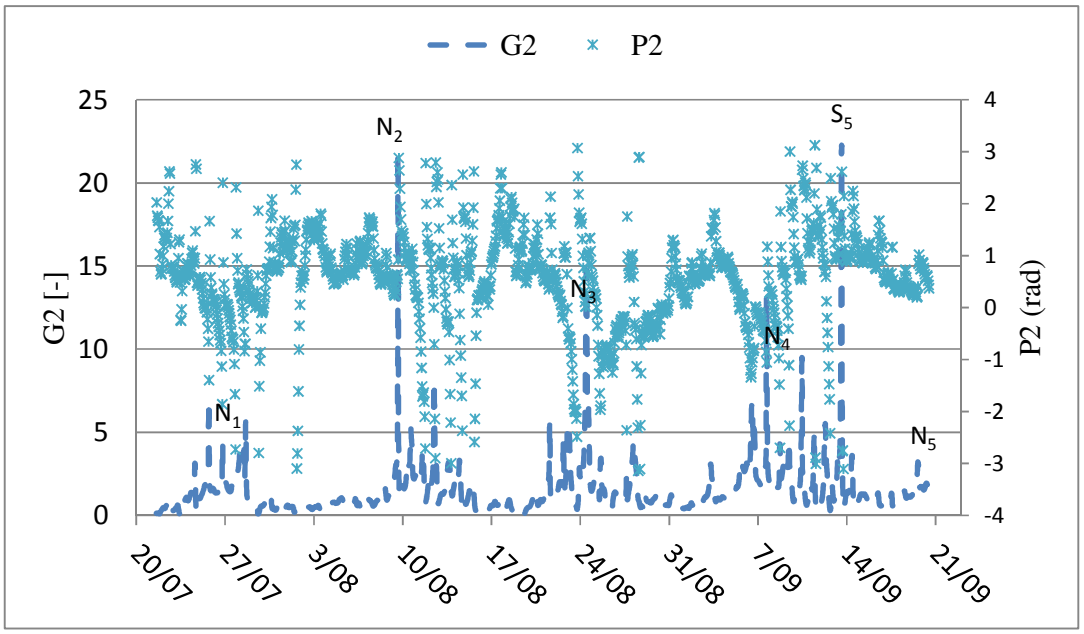

Figure 4.36: G_2 and φ_2 obtained by 24.5 hour moving window.

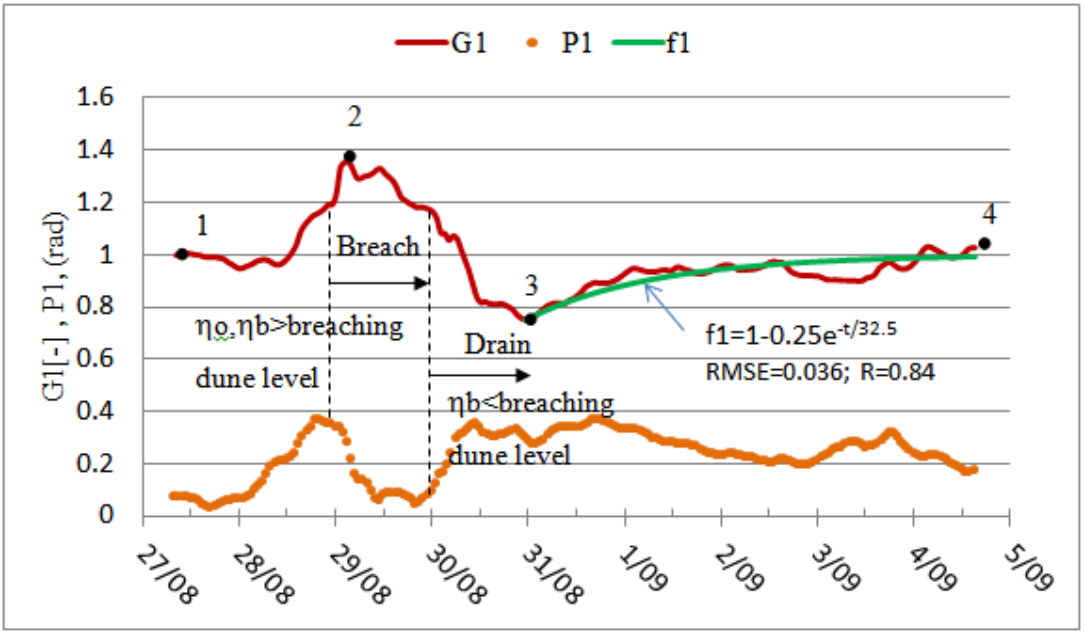

Figure 4.37: G_1 and φ_1 for the short period: 8:00 27 August to15:15 4 September 2005.

Figure 4.37 presents G_1 and φ_1 for short period from 27 August to 4 September 2005 with a fitted exponential curve. The increasing trend around 28 August 2005 of G_1 and φ_1 corresponds to increasing mean water levels which imply the inertial term increases its influence. During this

period the surge increases with possible overtopping through some low and narrow sections of the sand barriers (Figure 4.37). However, later on when G_1 is still increasing toward the peak of 1.35, φ_1 reduces may be due to the breaching in some parts of sand barriers leading to the bay becoming quite open to the ocean, or breaching the barrier makes the system more or less like funnel shape at high water level, G_1>1. It may be also due to overwash. After that, around 29 August G_1 and φ_1 both reduce corresponding to mean water level decrease after the storm passed through. During 30 August G_1 continues to decrease and φ_1 increases again. This may relate to η_b being lower than barrier breach levels and entrance cross section is narrower due to sediment deposited by littoral drift. From this time the normal draining process starts with $\eta_b > \eta_o$. G_1 is lowest at 0.78 when the draining process finishes, with $\varphi_1 \approx 20^o$. The system starts its recovery when G_1 rises up back to its normal value ≈ 1, while φ_1 decreases. Figure 4.38 illustrates F_1, F_2 in the complex plane with typical points in Figure 4.37.

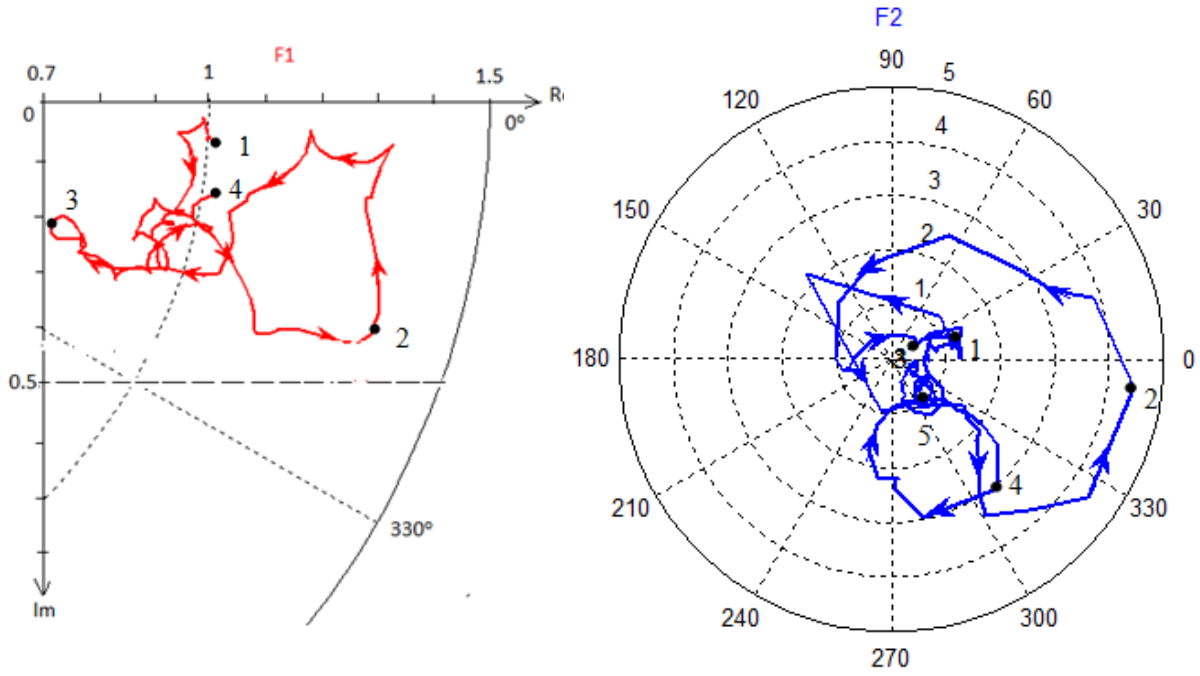

Figure 4.38: The tracks of F_1 correspond to the dominant mode and is therefore less erratic than F_2 for short period: 8:00 27 August to15:15 4 September 2005.

- **Morphological time scale**

The hydraulic response data above show that the dominant diurnal component gets reduced during the storm event and recovers more or less exponentially as indicated in Figure 4.37. The morphodynamic time scale obtained by fitting an exponential function is 32.5 hours. This seems

quite short for such a huge event. As for the Brunswick River storm event in Section 4.2.2, the response change in Figure 4.37 and Figure 4.38 seem to be simply hydraulic rather than morphological change.

4.5 SUMMARY OF EVENT ANALYSIS OUTCOMES

The application of 24.5 hour moving window analysis is tested for four case studies with different external forces and different inlet scales. A summary of each of the four test cases is given below:

- **Closure events of Lake Avoca, Australia**

Two closure events that occurred in July 2010 and another in April 2011 in Lake Avoca were analysed. By analyzing mean water level $\overline{\eta_{b,24.5}}(t)$, standard deviation $Stdv_{24.5}(t)$ and gain $G_2(t)$, the starting and ending periods of inlet closure is determined. The closing process begins during the neap tides and takes about 1.5 days for Event 3 (Figure 4.4) while being lengthened to 4 days by storm wave events for Event 1 (Figure 4.6, Figure 4.9). An exponential function performed well for event 3 without any wave or rain-fall event.

Slight differences, of the order of a few hours, in T_{morph} as determined by $\overline{\eta_{b,24.5}}(t)$ and by $Stdv_{b,24.5}(t)$ for the two events, could be attributed to:

(i) artifact of the method cf. Section 3.3.

(ii) variations in the physical features of the particular system, for example, while $Stdv_{24.5} \rightarrow 0$ indicating the inlet closing, $\overline{\eta_{b,24.5}}(t)$ may continue rising due to water still arriving from the catchment.

Harmonic analysis on the de-trended water levels for the dominant, semi-diurnal component is fairly stable, while the subordinate, diurnal component is more volatile. Across the four events, under the normal conditions before closing start, G_2 is around 0.3 to 0.4 and $G_1 \approx 0.7$-0.8, while $\varphi_1 \approx \varphi_2$ around 50^o to 60^o. The highest value of G_2 in the order of 0.6 - 0.7 occurred just after manually opening the inlet, whereas G_1 shows abrupt changes in response to rain fall or large waves with large variation and multiple-peaks in order of 0.9 -1.1.

G_2 responds earlier to the closing processes than G_1. Toward inlet closure, G_1, $G_2 \rightarrow 0$ with exponential trends except for disturbances due to wave or freshwater events. φ_2 increases during closure events, while φ_1 does not show clear trends and sometimes switches from lag to lead. This causes clear tracks of F_2 towards the origin, while the tracks of F_1 are quite messy with a lots of loops. Near complete closure, F_1, F_2 approach the origin with almost consistent phase lag at around

90^o to 120^o (Figure 4.8 right and Figure 4.10) except F_1 in Event 3 turning around the origin (Figure 4.8 left).

The friction related hydraulic, time constant T_1 in Eq. (3.13) for the semi-diurnal component for two events (Figure 4.12) is quite small (2 to 5 hours under normal conditions) after manual opening. However, T_1 starts increasing as the inlet starts to close; towards the end of the process it approaches very large values of the order of 1500 to 2000 hours. T_1 increases following an exponential curve when there is no disturbance during Event 3. However, it fluctuates reflecting disturbances such as rain fall or storm waves in other events. T_1 is erratic for the subordinate, diurnal component.

- **Brunswick Heads storm event.**

The Brunswick River entrance shows no clear increase in hydraulic efficiency during or after the event. G_2 and φ_2 increased on 21 May when the mean water level reached its peak (rainfall was the heaviest), and both reduced on 22 May when the mean water level reduced and then G_2 increased towards its equilibrium value (Figure 4.18).

G_2 decreased at the time of peak fresh water flow Q_f. Such a behavior can be related to non-linear bottom friction, which with a large Q_f gives increased bottom friction, hindering tidal response or increase A_b during elevated water levels. F_2 is close to perfect under normal conditions, namely $G_2 = 0.91$ and $\varphi_2 = 0.1$ radians (=6°). F_2 makes a small loop during the storm when the system floods and then comes back to the initial point when it recovers. The modest size of the loop shows that the Brunswick Entrance does not really change much, even under such a severe event.

The time scale by fitting G_2 during the recovery process is around 76 hours. It most likely a hydraulic time scale rather than reflecting significant morphological change.

- **Lake Conjola in overwash event**

The response of Lake Conjola is quite dynamic during the event and can be divided into 5 stages corresponding to the change in inlet invert level z_{cr}. Stage-1: normal conditions before the storm; Stage-2 is characterized by gradual accretion and Stage-3: entrance scoured out when flow drained back to the ocean. However, the change during three periods is not significant, F_2 close to (0.35, 30^o). Stage-4 is filling up period after the storm leading to sudden fall of the $\overline{\eta_{b,24.5}}$, gain of both components especially G_1. The smaller waves after the storm transports the suspended sand eroded from the flood tide delta and entrance, and deposit back to entrance. Stage -5: recovery stage, wave height reduced to lower than 1m, leading to less sediment transport. The channel recovers but approaches new stable state which is different from the beginning one.

It is suggested that the local authorities may set up a permanent gauge at Site 5 in Lake Conjola (Figure 2.25), so that the estimation z_{cr} from inverse modelling can be implemented. Z_{cr} together with F_1, F_2 can be used to better explain the inlet morphodynamics during different period.

The morphodynamic time scale T_{morph} by fitting exponential function with G_2 is 17 hours (Figure 4.28).

- **Pensacola Pass during and after Hurricane Katrina**

Quite different from the previous cases, the large Pensacola bay system showed no clear impact of Hurricane Katrina on the hydraulic efficiency. Similarly to the Brunswick Heads case, the tidal response changes reflect hydraulic, not morphological change.

Harmonic analysis shows that G_1 under normal conditions is more or less stable at 1 and phase lag $\varphi_1 \approx 7^o$ (Figure 4.34). During the hurricane G_1 increases to a peak of 1.35 then reduces to 0.8 before recovering back to ca 1 (Figure 4.37).

The changes in F_1 during the Hurricane can be explained by wave overwash and sand barrier breaching. For example, when G_1 still increases toward the storm peak while φ_1 reduces around 29 August (Figure 4.37), it may be due to the breaching leading to improved tide access to the bay. The performance of the subordinate, semi-diurnal constituent is quite erratic.

The result of fitting exponential function to G_1 is 32.5 hours which is simply a time scale for hydraulic readjustment while the system needs much more time for morphological recovery of sand barrier as shown in Houser & Hamilton (2009).

In conclusion, T_{morph} can be determined by fitting exponential curve to $\overline{\eta_b}(t)$, $Stdv_b(t)$ or to the gain of the primary component G_2 for closure events as Avoca or overwash event in Lake Conjola. The fitting with gain of dominant component for other extreme conditions as Brunswick Heads or Pensacola may provide hydraulic time scales only. The reason is that the event related morphology change for the larger, regulated systems, is usually not significant enough compared to the cross section to be measurable via the tidal record.

Overall, these examples show that storm and flood events of the typical duration of 2-5 days can be analysed successfully with the new 24.5 hour window technique. At least as far as $\overline{\eta_{24.5}}$ and the dominant tidal constituent is concerned. At the present state it is not clear how the more erratic behaviour of the subordinate tidal component can be interpreted.

Chapter 5

INLET STABILITY

5.1 INTRODUCTION

Although inlets are always changing in response to variations of the forcing from tides, waves and freshwater flow the hypothetical concept of inlet equilibrium is useful and has received much research attention. This chapter is a review and an update of this research.

There are several definitions for inlet stability in terms of longshore position, cross sectional area A and balances of driving forces. The inlet is considered stable when it is not migrating and when its cross-sectional area is fixed at an equilibrium value A_{eq} or performs steady oscillations about A_{eq}.

Inlet stability can be considered at different time scales from a day to spring-neap tidal cycles to seasons or years. Lake Wonboyn, NSW, Australia displays day-to-day stability although periodic morphological changes occur each tidal cycle as illustrated by Figure 5.1 and 5.2. A scarp occurs at each tidal cycle at low water slack (Figure 5.2), but the spit is rebuilt by waves and flood currents before the next high water slack.

Figure 5.1: Top view of Wonboyn inlet from the rocks on the southern side, NSW, Au in December 2010, the inlet looks the same at every high water slack, reference to the star pickets.

Figure 5.2: Wonboyn inlet at low tide in December 2010.

Figure 5.3: Canh Duong inlet, Hue, Vietnam, shorelines measured in 27 February 2010 (—) with two velocity transects (S_1, S_2) and shorelines measured in 13 February 2011 (—) plotted on Google Earth image 22 February 2009.

An example for seasonal, dynamic stability is *Canh Duong* inlet in Hue province, Vietnam. The shorelines are eroded back significantly each wet season but are quite similar each February for the years 2009, 2010, 2011, see Figure 5.3.

Pambula Lake, NSW, Australia, Figure 5.4, has been stable without periodic oscillations for years. The reason is that, unlike Wonboyn, it is protected from the dominant SE waves by the southern headland so that wave-reworking around each high tide is insignificant and, unlike Canh Duong, fresh water flows are insignificant compared to the tidal flows.

The stable state of an inlet as well as morphological time scales can be inferred easily via tidal record analysis using a 24.5 hour moving window method as described in Chapter 3. The stable state is then reflected by the response functions of the primary tidal constituents being fixed or tracing tight orbits in the complex plane. See the case studies in Chapter 4 (e.g., Figure 4.19).

Figure 5.4: Image of Pambula Lake from Google Earth 2006.

With a broader point of view, Bruun (1962) stated that overall stability must include a system of inlet and ocean bars. He evaluated the inlet stability level by the balancing of opening forces by tidal prism P and the closing forcing presented by total annual littoral drift $\overline{Q_{sy}}$. His idea was that: the larger the ratio $P/\overline{Q_{sy}}$ the more likely the inlet is to stay open in a stable state. These definitions will be discussed in detail in the following sections.

With a fairly large littoral drift $\overline{Q_{sy}} \approx 0.5\times10^6$ m^3/year along the NSW coast, all but the largest inlets would be unstable when located on a straight coast. Hence, most of them are found next to headlands, which mitigate the influence from $\overline{Q_{sy}}$.

In terms of conservation of sediment, inlet stability is the condition of an inlet when there is no gradient of sediment transport between bay-ward and sea-ward cross sections or $\Delta Q_s = 0$ in Figure 5.5.

Sediment transport in the bay is mainly driven by quasi-steady currents $\bar{u}$ due to Q_{tide} and Q_f (sometimes by Q_{over}), while in the ocean, it is driven by waves, $\tilde{u}$, as well as by the tidal currents $\bar{u}$.

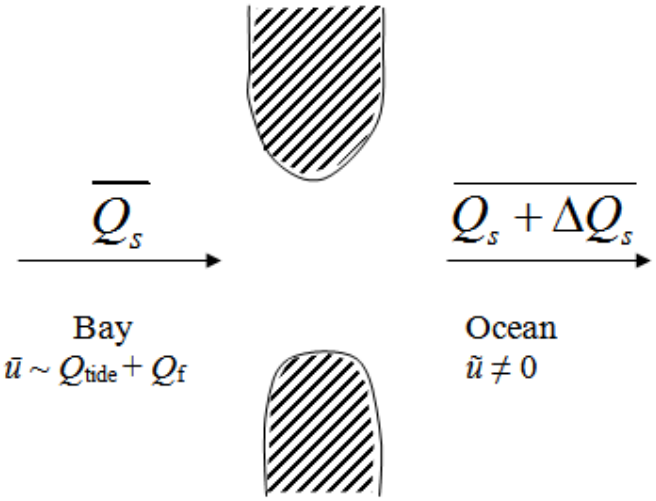

Figure 5.5: Concept of inlet stability. Sediment transport processes in the bay are due to tide and precipitation and can be considered quasi-steady, while the sediment transport in the ocean and surf-zone are wave dominated and thus oscillating on the time-scale of the wave period.

Estimation of the sediment transport rates in Figure 5.5 are still beyond the state-of-the-art, Section 7.4. Hence, stability analysis based on sediment transport rates has not progressed significantly beyond the well-known Escoffier curve (1940), in Figure 5.8 below.

5.1.1 Historical equilibrium relationships

Although tidal inlets are very complex in terms of hydrodynamic and morphodynamic aspects, many empirical relations are available to estimate bulk features, typically pertaining to long-term inlet equilibrium and useful for predicting inlet morphodynamics as done in Section 6.2.

5.1.1.1 Inlet channel cross section at equilibrium ($A_{eq} \sim P_{eq}$)

Initially, the relationship between equilibrium inlet cross-sectional area A_{eq} (m^2) and the equilibrium tidal prism P_{eq} (m^3) was sought by empirical approaches and field measurements. The general form of the relationship is presented as

$$A_{eq} = a_1 P_{eq}^n \tag{5.1}$$

where, n is an empirical exponent and a_1 is a constant with units depending on n. Later, many researchers tried to after-rationalise the empirical findings through considerations of hydraulic and sediment transport processes.

According to the overview by Van der Wegen et al. (2010) and Stive et al. (2009, 2012), n and a_1 depend on the inlet's geological setting, sediment supply and the adjacent ocean environment. Van der Wegen et al. (2010) synthetized $0.72<n<1.2$, but the majority of researchers find $0.85<n<1.1$. For many coasts the exponent n is found to be of the order 1, e.g., (LeConte, 1905); Jarrett (1976) and Van de Kreeke (1990b). The constant a_1 is in the range between 5.6×10^{-5} and 9.3×10^{-4} with SI-units depending on n.

Empirical approach to $A_{eq} \sim P_{eq}$

LeConte (1905) first sought $A_{eq} \sim P_{eq}$ relationships from a small number of measurements on inlet entrances and harbours along the Pacific coast in the USA. He found n=1 and different a_1 for two groups: Natural inlets and trained inlets. The constant a_1 for protected inlets was found to be larger by 30% compared to unprotected inlets.

O'Brien (1931) followed up on the pioneering work of LeConte (1905) by extending it to the Gulf, Pacific and Atlantic coasts of the USA. He defined the cross-sectional area A relative to MSL at the throat (narrowest part of the inlet). O'Brien (1969) showed that $a_1=4.69\times10^{-4}$ and n=0.85 are best–fit for 28 inlets (with and without jetties); but for 8 non-jettied entrances $a_1=1.08\times10^{-4}$ and n=1. Qualitatively, a positive correlation between A_c and P for natural inlets makes sense since channels are likely to be larger if they convey large discharge. An obvious disadvantage of the relation is that the constant of proportionality is dimensional. In addition, O'Brien (1969) commented that it would be better to use $\hat{Q}$ instead of P, which relates to the capacity of tidal current to maintain an open inlet. That reasonable argument is considered in this thesis further leading to the investigation described in Section 5.3.

Stive et al. (2009) argued that the inlets studied by O'Brien (1969) do not have the same littoral drift and tidal conditions; therefore the relationship should not be expected to be valid. However some researchers proved that it is valid under certain conditions. For example, Hinwood

et al. (2012) used a process based model to identify attractors for entrance channel morphology. They found that A~P of tidal dominated entrances correspond to the tidal attractor has a good fit with the O'Brien relation with n=1, whereas very constricted entrances have river flow dominance with A~P falling below the O'Brien lines. Stive et al. (2009) pointed out that only Dieckmann et.al (1988) and Van de Kreeke (1998) provided reliable A-P relationship for the Dutch and German Wadden Sea with n ranging between 0.81 and 1 because their data set fulfills the requirement of phenomenological similar conditions.

108 inlets along the Pacific, the Atlantic and Gulf coasts of the USA have been analysed by Jarrett (1976). Jarrett (1976) used different values of a_1 and n for different tidal conditions and classified inlets into groups of unjettied inlets, inlets with a single or two jetties. Jarrett (1976) realized that the similarity within inlet groups was necessary to provide more reliable results. In which, a_1=1.58 $\times 10^{-4}$ and n=0.95 for all inlets, n is slightly larger than 1 for unjettied inlets and a single jetty inlets, while $n \approx 0.85$ for dual jettied inlets. So far, the empirical A_{eq}~P_{eq} relationship presented by Jarrett (1976) provides the most comprehensive data set and a reasonable fit for most inlets around the US coastline (Stive et al. 2012). Lanzoni & Seminara (2002) and Van de Wegen et al. (2010) used process based models to study the evolution of tidal inlets. Their final equilibrium cross sectional area A_c fit quite well with $A_{eq} \sim P_{eq}$ by Jarrett.

Around the world, the A_{eq}~P_{eq} relationship was derived for specific areas with different values of a_1 and n. For example, Shigemura (1980) investigated a large number of inlets (totaling 231) belonging to four major coasts of Japan. He found that $0.45<n<0.69$, which is low (the lowest n=0.45 for west coast of Kyushu) depending on different coastal areas. Surprisingly, when they classify groups based on the ratio between throat area and its mean surface area by using regression method, the A-P relationship resulted in $0.8<n<1$, which is quite close to Jarrett (1976). Using similar method, the A-P relationship was derived for 32 inlets in South China Sea by Zhang (1987), in which $n \approx 1$ but a_1 is double that of the values estimated for American inlet data and 1/10 of Japanese data. These results reflect the inlet geomorphology being intermediate between sandy coast of The US and rocky coast of Japan. Hume & Herdendorf (1993) derived the relationship for 82 New Zealand inlets of different plan forms with the coefficients having a larger range compared to other parts of the world [$0.72<n<1.17$ and = $9.5\times10^{-5}< a_1<1.48\times10^{-2}$, SI units] including funnel shaped, river mouth estuaries and coastal embayment, which have low magnitude of n. Townend (2005) worked on 66 UK inlets, which showed similar scatter as that of NZ inlets. All of these studies show that A-P relationship is a complex problem, in which P is an important factor but is not unique, it is necessary to consider the shape of inlet or geo-morphological features of inlet to

derive reliable relationship so that it can be used to evaluate the cross-sectional stability of tidal inlets, which is mentioned in the next Section.

Stive et al. (2012) and Hinwood et al. (2012) found that the equilibrium cross sectional area of much smaller inlets is larger than A estimated from the typical A_{eq}~P_{eq}. A_{eq} does, no doubt, not depend on P_{eq} exclusively. Most researchers agree that the tidal period is essential. The range of wave height to ocean tide range may also change things.

Theoretical approaches to A_{eq} ~ P_{eq}.

Various researchers have tried to obtain the parameters of the A_{eq}~P_{eq} relationship using theoretical approaches. Escoffier (1940) argued for a relationship between cross sectional area, mean flow velocity and area change as discussed further around Figure 5.8 below. The concept of *stability shear stress* was later introduced by Bruun & Gerritsen (1960). Similarly, the early work by Krishnamurthy (1977) expressed minimum cross sectional area required for stability based on a critical bed shear stress τ_{cr} for movement of sediment. Later, Friedrichs (1995) and Hughes (2002) extended this by computing an A_{eq} based on the hypothesis that at equilibrium, the bottom shear stress τ_e at maximum tidal discharge equals some constant times τ_{cr}. (This means τ_e is the shear stress needed to maintain a zero net transport gradient along the channel, if $\tau > \tau_e$ there will be net erosion and $\tau < \tau_e$ there will be net deposition). Kraus (1998) argued that τ_e is not necessarily equal to τ_{cr} because, a certain transport capacity is needed to remove the sediment deposited by littoral drift. And indeed, Bruun and others have pointed out that equilibrium conditions usually correspond to peak tidal velocities close to 1m/s, which is much greater than the critical velocity (~0.3m/s) for onset of sediment motion.

Hughes (2002) formula

$$A_{eq} = 0.87 \frac{W_{eq}^{1/9}}{[(s-1)g]^{4/9} d_{50}^{1/3}} \left(\frac{P_{eq}}{T_{tide}} \right)^{8/9}, \qquad (5.2)$$

which is likewise based on a Shields criterion, contains a dimensional coefficient, which takes into account the effect of non-sinusoidal tides. W_{eq}[m] is equilibrium channel width, s is sediment specific density (ρ_s/ρ), d_{50} [m] is the median grain size and T_{tide} is the tidal period. The derived relationship matches data from 102 inlets in the USA and results from 18 small-scale, movable-bed models, which are not matched by the previous empirical relationships. The formula has best agreement with the data set of Townend (2005) in UK.

Friedrichs (1995) recommended that for embayments protected from waves, the τ_{cr} criterion would lead to an upper boundary for A along the bay. Gao & Collins (1994) pointed out the possible influence of Q_f on final A_{eq}. Tambroni & Seminara (2010) also used this concept to explain the A_{eq}~P_{eq} relationship, but they considered that a dynamic equilibrium of the inlet related to Q_{sy} may exist while static equilibrium is assumed for the adjacent tidal channel.

In another approach Van de Kreeke (1992, 2004), Kraus (1998), Suprijo & Mano (2004), Stive & Rakhorst (2008) and Stive et al. (2009) derived analytical A_{eq}~P_{eq} relationships based on the dynamic balance between ebb tidal sand transport and wave induced sediment transport entering the inlet.

Stive et al. (2009) indicated that a particular A_{eq}~P_{eq} relationship is only valid for inlets that have phenomenological similarity (fairly similar hydrodynamic and morphological conditions). Their theoretical investigation concluded that the exponent n should be larger than 1. Tran et al. (2011) using a process based model and Larson et al. (2011), found $n > 1$, in agreement with Stive et al (2009). However, this is not supported by observed data. The reason may be the violation of phenomenological similarity or the violation in estimating P_{eq} as defined by O'Brien (1931). In addition, Hughes (2002), Jarrett (1976) and O'Brien (1969) show that n should be slightly less than 1 due to the dependence of velocity profile and/or the resistance coefficient on the Reynolds number. This is also proved by physical model experiments by Seabergh 1979, Byrne et al. 1980.

Kraus (1998) derived a relationship with $n = 0.9$ and a_1 given by

$$a_1 = \left(\frac{\alpha \pi^3 N^2 W_e^{4/3}}{Q_{sy} T^3} \right)^{0.3} \tag{5.3}$$

in which α is a transport related coefficient of the order 0.1-1, N is the Manning coefficient [$L^{-1/3}T$], Q_{sy} [L^3T^{-1}] is the gross longshore transport rate arriving at the inlet.

Larson et al. (2011) developed an analytical model for A_{eq} based on Kraus' (1998) approach for three particular cases of inlet geometry:

1) constant width,

2) constant depth,

3) constant ratio of width/depth.

Their analytical solution gives n = 1, 1.5 respectively 1.2 for the three inlet-shape-cases above. However, n-values greater than 1.0 are in conflict with the data in Figure 5.19.

Using dimensional analysis in Section 5.3 we found $n<1$ and n=0.94 for 27 natural inlets on the Florida coast and 11 natural inlets around the USA coast (Figure 5.19). The relation between

A_{eq} and external forces is presented in (5.23) as a function of peak tidal discharge $\hat{Q}_{tide}$ and wave height H.

A latest derivation of the A_{eq}~P_{eq} relationship uses the concept of equilibrium concentration, which was proposed by Di Silvio (1989). This concept was successfully applied to analysing equilibrium conditions of Texel Inlet and Haringvliet Estuary on the Dutch coast by Gerritsen et al. (2003). They used the Engelund & Hansen formula for total sediment transport with the assumption of an equilibrium sediment concentration in the inlet.

5.1.1.2 Inlet channel volume, area and volume of ebb and flood delta

Instead of the cross sectional area, Eysink (1991) suggested that the channel volume $V_{c,eq}$ below MLW relates to the tidal prism at equilibrium as

$$V_{c,eq} = \alpha_c P_{eq}^{1.5} \tag{5.4}$$

where α_c [$L^{-1.5}$] is an empirical coefficient. This relation is usually used with adjusted α_c in the ASMITA model (Stive et al., 1998) to investigate long-term evolution of tidal inlet systems. Alternatively, Shigemura (1980) presented a relation between throat width and tidal prism at equilibrium.

Ebb tidal delta volume V_{Ebb}

The equilibrium volume of an ebb shoal will be reached when sediment transport to the ebb shoal is bypassed to the down drift beach or to the channel and then to flood shoal. Walton & Adam (1976) applied volume estimation of the ebb tidal delta V_{Ebb} [m^3] using the method of Dean & Walton (1973), analysing 44 inlets, which were considered to be at equilibrium in the USA. They provided the relationship between V_{Ebb} and tidal prism as

$$V_{Ebb} = C_e P^{1.23} \tag{5.5}$$

where $C_e = 2.1\times10^{-2}$ $m^{-3\times0.23}$.

This relation is usually utilized with adjusted C_e in ASMITA model (Stive et al., (1998) to investigate long-term evolution of tidal inlet and adjacent coast.

Later, Marino & Mehta (1987) and Hicks & Hume (1996) confirmed the overall relation of Walton & Adam (1976) for a different group of inlets in USA and New Zealand respectively. They found that P_{eq} is the most important parameter governing the equilibrium V_{Ebb} but the coefficients vary with the wave climate.

Dean & Walton (1973) revealed that V_{Ebb} on mildly exposed coasts is larger than that on highly exposed coast for the same P. This corresponds to the trend of the data in Figure 5.6, which support the relationship

$$V_{Ebb} = 24139\left(\frac{\hat{Q}_{tide}}{\sqrt{gH^5}}\right)^{0.78} \quad [m^3] \tag{5.6}$$

Even though the correlation, R^2= 0.56, is modest, these data indicates, that V_{Ebb} increases with increasing tidal dominance over the waves. For details of the data set see Appendix 2. Eq (5.6) indicates a weaker dependency of V_{ebb} on P compared to $P^{1.23}$ in Eq (5.5) but closer to the dependency obtained from de Vriend et al., (1994) with $P^{0.6}$. Eq (5.6) is used to illustrate the dynamic response of V_{ebb} of Pensacola inlet under a hurricane condition in Section 6.5.1.

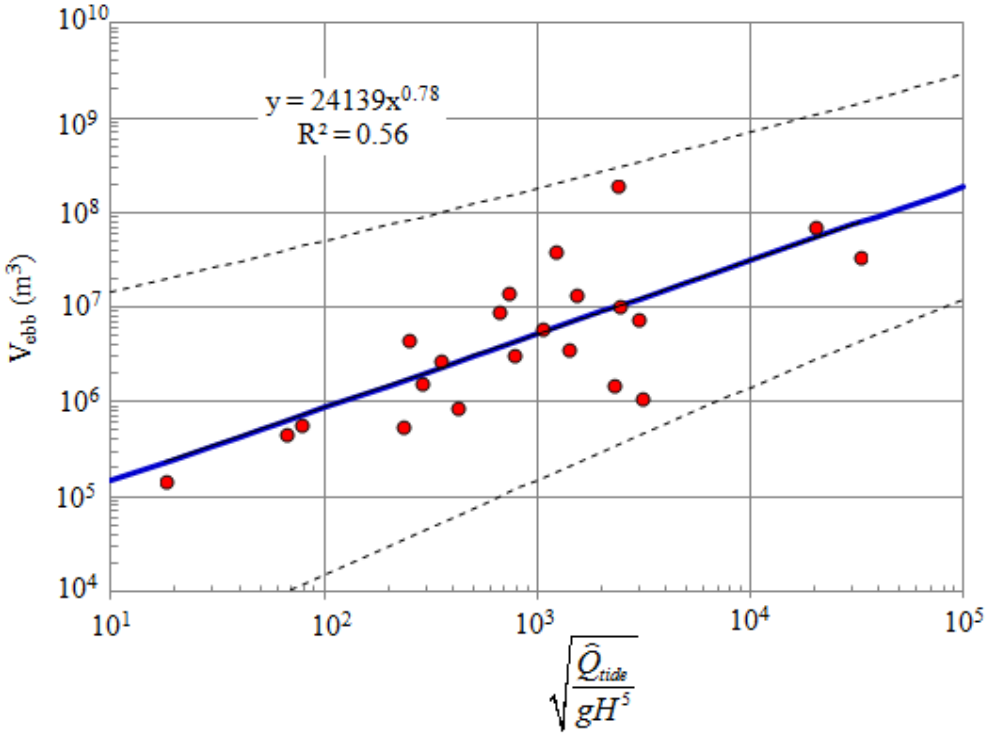

Figure 5.6: V_{Ebb} versus the *relative tidal strength* $\frac{\hat{Q}_{tide}}{\sqrt{gH^5}}$ with 95% confidence limits for 22 natural inlets on the coast of Florida, USA. Data from Powell (2003).

Flood tidal delta volume V_{Flood}.

Flood tidal deltas can form when the flood tide together with the waves are able to transport marine sand into a relatively wide and deep bay. However, determination of the volume and area or volume of a flood shoal is difficult because it is hard to distinguish the flood tidal delta from the

bay bottom (Kraus, 2010). Battling these challenges, Carr de Betts (1999) and Carr de Betts & Mehta (2001) investigated 67 inlets in Florida, characterized by mild waves and small tidal prisms. They defined the flood shoal volume as the total of the near field deposit (the visible part of the flood shoal assumed in equilibrium with typical flood currents), and the far field deposit (a movable thin layer spread out around the near field deposit). They obtained relationships for each part of the flood shoal with spring tidal prism as shown in Table 5.1.

Table 5.1: Flood shoal volume and area versus spring tidal prism.

Type of flood deposit	Flood shoal volume	Flood shoal area
Near field deposit	$4.06\times10^{3}P^{0.314}$	$1.4532\times10^{4}P^{0.254}$
Far field deposit	$1.53\times10^{4}P^{0.314}$	$3.4122\times10^{4}P^{0.244}$
Total V_{flood}	$2.04\times10^{4}P^{0.298}$	$4.7585\times10^{4}P^{0.249}$

All of the previous empirical relationships show that tidal prism is a determining factor controlling inlet morphology although $0.21<R^2<0.39$ is modest.

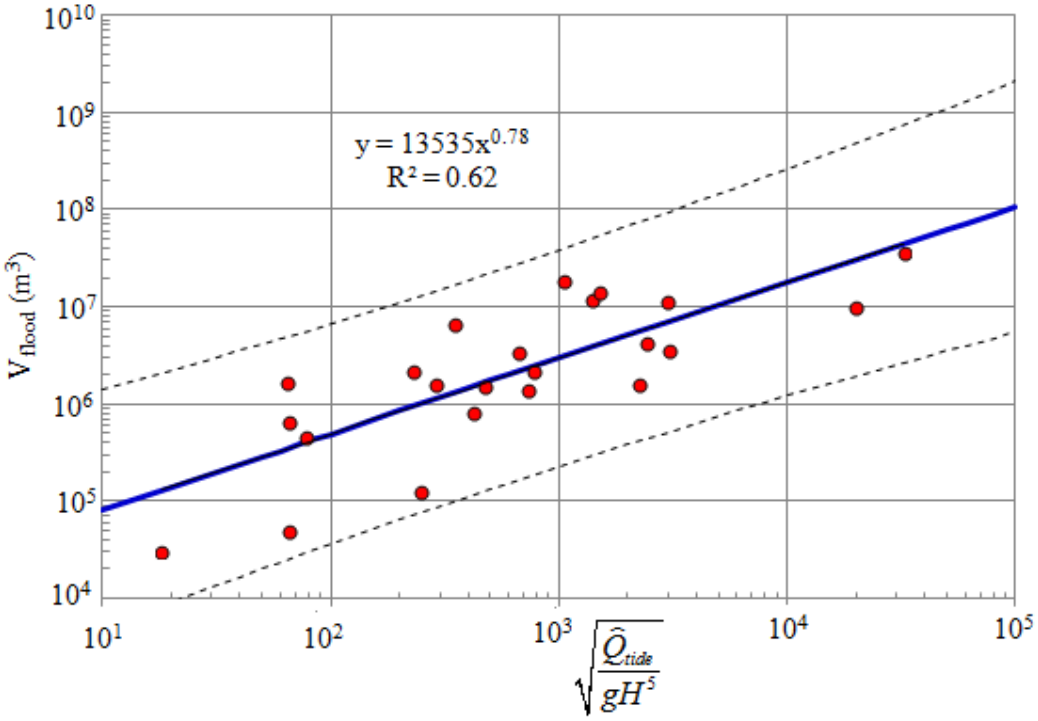

Figure 5.7: V_{Flood} versus tidal dominance measured by $\hat{Q}_{tide}/\sqrt{gH^5}$ with 95% confidence limits for 23 natural inlets on the coast of Florida, USA. Data from Powell (2003).

The data in Figure 5.7 support (with higher correlation coefficient than previous studies)

$$V_{Flood} = 13535\left(\frac{\widehat{Q}_{tide}}{\sqrt{gH^5}}\right)^{0.78} \quad [m^3] \tag{5.7}$$

The similar power for V_{Ebb} (0.78) in Figure 5.6 and V_{flood} in Figure 5.7 indicates the same tidal influence, through $\widehat{Q}_{tide}/\sqrt{gH^5}$. However, the larger constant in (5.6) compared to (5.7) shows that V_{ebb} is always larger than V_{flood} in this coastal region, therefore these inlets belong to tide dominated estuaries. (Detail of the data set cf. Appendix 2). These relations can be used in the Hoan et al. (2011) model to study the spit growth or dynamic response of V_{flood} of an inlet under extreme conditions as presented in Section 6.5.1.

5.1.2 Cross-sectional stability

A hydraulic stability curve (Figure 5.8) introduced by Escoffier (1940) suggests a relation between maximum flow velocity and cross sectional area. The Escoffier diagram describes that a change in flow area induces a change in flow velocity that will maintain or counteract the induced change.

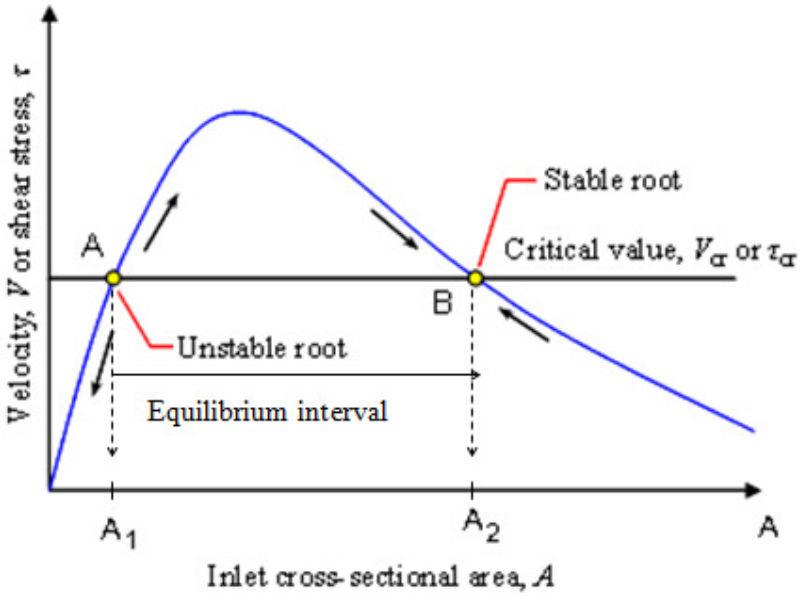

Figure 5.8: Escoffier's diagram or "the inlet closure curve".

The cross-sectional areas A_1 and A_2 in the diagram are equilibrium flow areas, corresponding to maximum velocity equal to a critical value of the order 1m/s. At these points, the peak velocity is large enough to move sediment carried into the inlet by littoral drift. For $A_1<A<A_2$, the tidal sediment transport capacity is larger than required to remove wave-advected sand and A will increase until it reaches A_2. When $A<A_1$ the inlet will close, so that A_1 represents a limit of instability while A_2 represents the stable (equilibrium) flow area A_{eq}. Any change in the inlet that

brings its cross-sectional area out of equilibrium size will result in a change in inlet velocity that forces to return the inlet to its equilibrium value by associated deposition or scour.

Based on Escoffier's (1940) approach, van de Kreeke (1985) developed a similar inlet closure curve by replacing peak flow velocity with a peak bottom shear stress in a stability analysis. Later this approach was extended to multiple inlet systems (van de Kreeke, 1990a, b).

Kraus (2010) concludes from a literature review that mean-peak velocity $\overline{\hat{V}}$ through a stable inlet is around 1m/s. This velocity value is related to the peak discharge $\hat{Q}_{\text{tide}}$ based on tidal prism P presented by Keulegan & Hall (1950),

$$P = \int_0^{T/2} \hat{Q}_{\text{tide}} \left(\frac{2\pi}{T} t \right) dt \tag{5.8}$$

by

$$\overline{\hat{V}} = \frac{\hat{Q}_{\text{tide}}}{A} \tag{5.9}$$

where A is the stable inlet channel cross-sectional area below mean sea level (MSL).

Applying the linear (n=1) empirical relation between A and P (O'Brien, 1931), then

$$\overline{\hat{V}} = \frac{\pi}{aT} \tag{5.10}$$

for semi-diurnal inlets, T=12 hours 25 minutes = 44712 s, $5.65\ 10^{-5} < a < 1.08\ 10^{-4}$, $0.65 < \overline{\hat{V}} <$ 1.24 m/s, while for diurnal tides, T= 89424 s, $0.325 < \overline{\hat{V}} < 0.62$ m/s. These implications seem strange.

Lam (2009), used analytical solutions of inlet hydraulics to estimate the effects of including Q_f, (but still no waves). The result is Figure 5.9, where Escoffier's tide-only-curve ($Q_f = 0$) has become the family of blue curves for different Q_f. Correspondingly, the stable equilibrium (A_2 in Figure 5.8) has become a range between B to C.

The closure point A_1 does not exist, ie, the inlet remains open when Q_f is significant (no waves to compete with Q_f).

Taking into account all "forces", Stive et al, (2009) improved this approach by explaining that the stable status of an inlet depends on several rival factors, namely the power of the tidal prism, perhaps quantified as $Q_{\text{tide,pot}} = P/T_{\text{tide}}$, the strength of the waves and the strength of the river discharge Q_f.

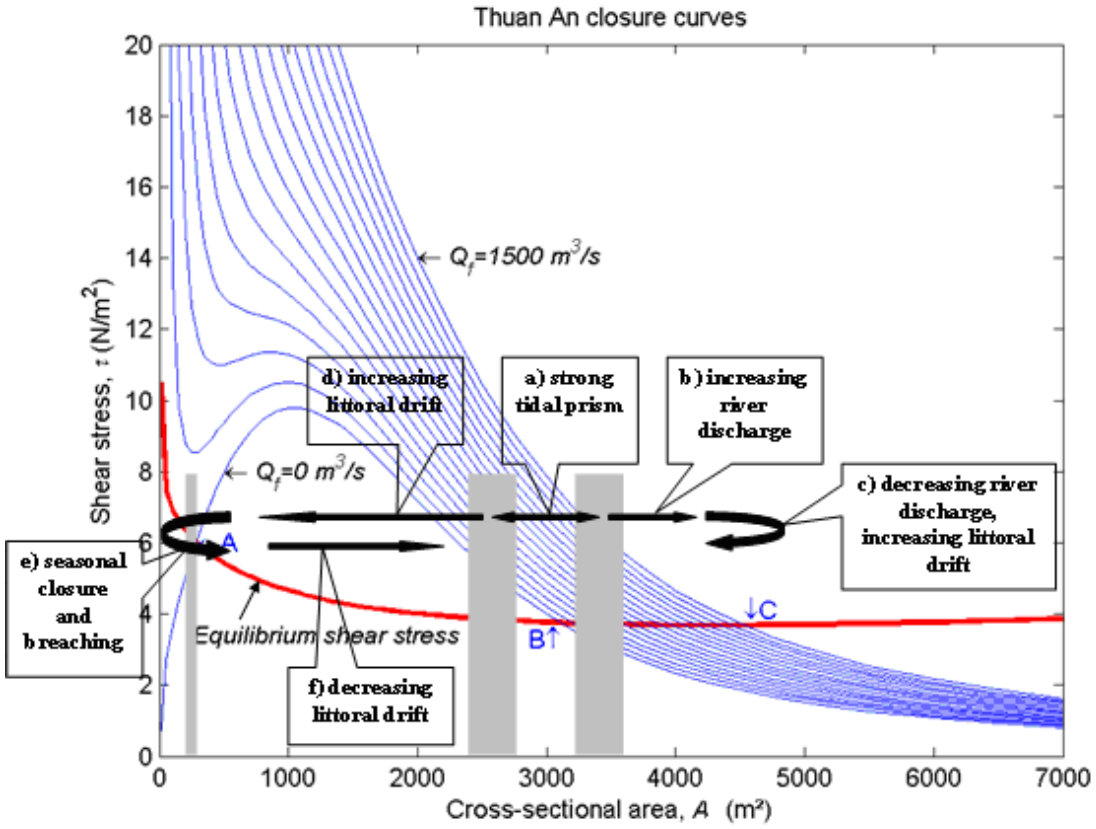

Figure 5.9: The dependence of equilibrium on forcing processes based on model results of Thuan An inlet, Hue, Vietnam (Stive et al., 2009).

a) With a strong tidal prism, a suitable littoral drift which is balance with sediment transport by ebb inlet current and no river discharge, a tidal inlet could get an equilibrium state around point B;

b) If Q_f increases, the inlet will move toward point C with a larger cross-sectional area.

c) If the river discharge decreases and/or the littoral drift increases then the inlet channel will get more sedimentation to have a smaller cross-sectional area.

d) If the river discharge is insignificant and the littoral drift increases strongly, the inlet will move to the unstable point at A and perhaps close.

e) With strong littoral drift and weak flushing ability, the inlet will experience seasonal closure and breaching under the fluctuation of wave climate and river flow.

f) When the littoral drift decreases, the inlet will have a tendency to move to the stable equilibrium point again.

An obvious improvement of this model is to include the waves explicitly (e g, via H_s) and work with two dimensionless variables, e.g., $\left(\frac{Q_{\text{tide}}}{\sqrt{gH^5}}, \frac{Q_{\text{tide}}}{Q_f}\right)$ or perhaps rather the external parameters $\left(\frac{Q_{\text{tide,pot}}}{\sqrt{gH^5}}, \frac{Q_{\text{tide,pot}}}{Q_f}\right)$ as shown in Section 1.1.3.

5.1.3 Sediment bypassing criteria

The stability of a tidal inlet can also be considered in the light of its capacity for sediment bypassing, which is the transport of sediment from the updrift to the downdrift margin of the inlet.

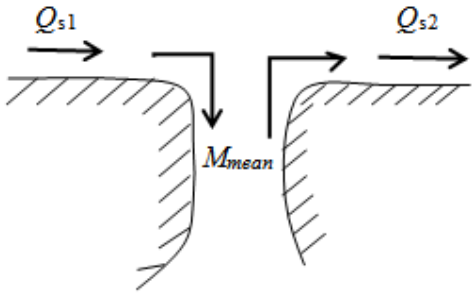

Figure 5.10: Inlet by passing

Bruun & Gerritsen (1959) first described the natural mechanisms of inlet sediment bypassing and proposed a parameter *r'* to indicate the type of this process

$$r' = \overline{Q_{sy}} / \hat{Q}_{tide} \tag{5.11}$$

where $\overline{Q_{sy}}$ is the mean long-shore sediment transport rate [m^3/year] and $\hat{Q}_{\text{tide}}$ is the peak discharge through the inlet during spring tidal conditions [m^3/s].

A value of $r' < 10–20$ indicates predominant tidal flow by-passing (with little or no bar formation), the system bypasses sand through transport of sand by tidal currents in channels and by the migration and accretion of sandbars and tidal channels.

A value of $r'>200–300$ indicates predominant bar by-passing with typical bar or shoal formation, the system bypasses sand by wave-induced sand transport along the outer margin of the ebb-delta (terminal lobe). Later, Bruun & Gerritsen, (1960), Bruun (1966, 1978, 1990) converted this ratio to

$$r = P / \overline{Q_{sy}} \tag{5.12}$$

to describe the overall inlet stability, where $\overline{Q_{sy}}$ is the annual littoral drift [m³/year], P [m^3/tidal cycle].

Based on the value of r, the stability of an inlet is rated as good, fair, or poor and the mechanism of bypassing is determined as detailed in Table 5.2.

Table 5.2: The overall criteria for inlet stability in terms of by-passing capacity

$r = \frac{P}{\overline{Q_{sy}}}$ [-]	**Inlet stability situation**
<20	Poor- inlet becomes unstable, over flow channels, may be closed, impossible for navigation
20 – 50	Poor –all inlets are typical bar-bypassers, highly variable channel in location and area with possible multiple channels and may several shallow ocean bars, navigation difficult
50 – 100	Poor to fair– the inlet is typical bar-by-passing and unstable; entrance with wider and higher ocean bars, increasing navigation problems
100 – 150	Fair – mixed of bar-by-passing and tidal by-passing the entrance has low ocean bars, minor navigation problems
> 150	Good – episodic by-passing, the inlet is tidal by-passing; entrance with little or no ocean bar outside gorge and good flushing

For example, Castelle et al. (2007) investigated Currumbin Inlet, Queensland, Australia and found $r = 3.2$ corresponding to $P = 1.6\times10^6$ m^3 and $\overline{Q_{sy}} = 5\times10^5$ m^3/year by this criterion. This indicates that by-passing plays a more important role than tidal effects, and the inlet is not stable but prone to closing. Another example is Jumpinpin Inlet, Queensland, Australia with $r = 49$ ($P = 50\times10^6$ m^3 and $\overline{Q_{sy}} = 1.02\times10^6$ m^3/year) investigated by Mirfenderesk & Tomlinson (2008). They found that bar – bypassing is typical for this inlet and it is unstable, ie, it has been closed in historical times.

The bypassing mechanism introduced by Bruun & Gerritsen (1959, 1960) did not consider the influence of river flow. This was partly amended by Kana et al. (1985), FitzGerald (1988) and Gaudiano & Kana (2001) who considered "episodic bypassing". In these models, the episodic occurrence of storm or river flow was taken into account. During such an episodic event, a portion of the ebb tidal shoal or downdrift bypassing bar detaches and migrates downdrift. Hands & Shepsis (1999), and Kraus & Lin (2002) investigated some particular bypassing cases that related to such extreme flood events or El Niño.

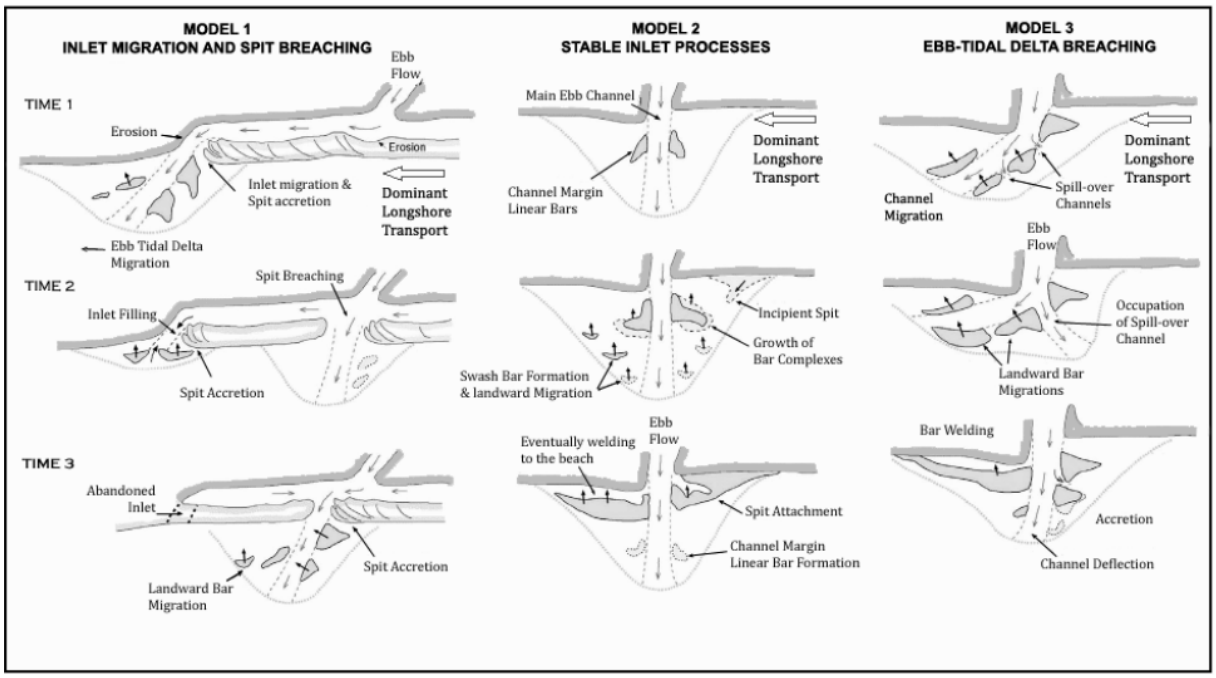

Figure 5.11: Model of inlet bypassing for mixed energy coasts (from FitzGerald et al., 1978; FitzGerald, 1982).

FitzGerald (2005) described three mechanisms of sand bypassing for natural inlets:

1) Stable inlet processes;

2) Ebb tidal delta breaching and

3) Inlet migration and spit breaching.

Figure 5.11 shows these mechanisms for mixed energy coasts.

1) Stable inlet processes (model 2 in Figure 5.11)

This mechanism occurs at inlets which do not migrate, i.e., the main channels are fixed as Price Inlet, South Carolina, USA (Figure 5.12). Most of the sand that enters the inlet is transported offshore by the dominant ebb tidal current and deposited on the terminal lobe. Sand bypassing takes place through the formation, landward migration, and welding of bar complexes to the downdrift shoreline. The development of the bar complex for Price inlet from 1973 to 1977 was presented in Figure 20, p.209 of FitzGerald (1988). This process results from the stacking and coalescing of swash bars on the ebb shoal. The swash bar moves onshore due to strong landward flow across the swash platform. Breaking and shoaling waves over the delta create bores, which increase flood tidal current and reduce ebb current, resulting in net landward transport of sediment on both sides of the main ebb channel. The growth of bar complexes from swash bars is the result of their decreased onshore migration rate as they move up to the nearshore ramp. When the bar

complex welds to the upper beach and another one attaches to downdrift shore, then new sediment gradually deposits on the downdrift beach, completing the bypassing process.

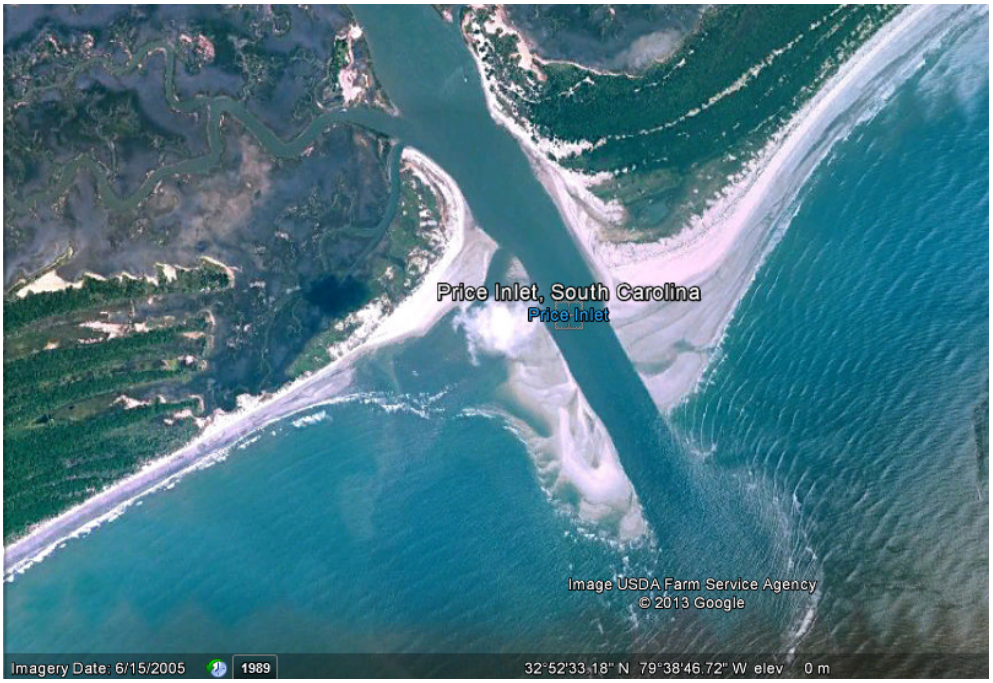

Figure 5.12: Price Inlet, South Carolina, USA – an example of FitzGerald's stable inlet processes mechanism.

2) Ebb tidal delta breaching (model 3 in Figure 5.11)

Sediment inlet bypassing occurs at inlets with stable throat position but the main ebb channels migrate via ebb tidal delta like the wag of dog's tail, (FitzGerald, 2005). Figure 5.13 shows Breaches Inlet, SC, USA as an example of this mechanism. Different from the first mechanism, the sand entering the inlet is delivered by longshore transport causing sand accumulation on the updrift side of the ebb tidal delta that deflects the main ebb channel. The deflection continues until the channel is nearly parallel the downdrift shoreline. This condition is hydraulically inefficient for tidal flow through the inlet, leading to new, shorter, direct seaward pathway through ebb tidal delta. The breaching tends to occur during spring tide or storm surge when tidal prism is very large. More tidal prism is gradually diverted to the new main ebb channel causing less and less discharge through the former one, which ultimately is filled with sand. A larger part of the ebb tidal delta is now on the downdrift side of the new main channel and moves onshore. A bar complex is formed, which migrates landward and attaches to the downdrift shoreline. This mechanism results in large packets of sand bypassing the inlet.

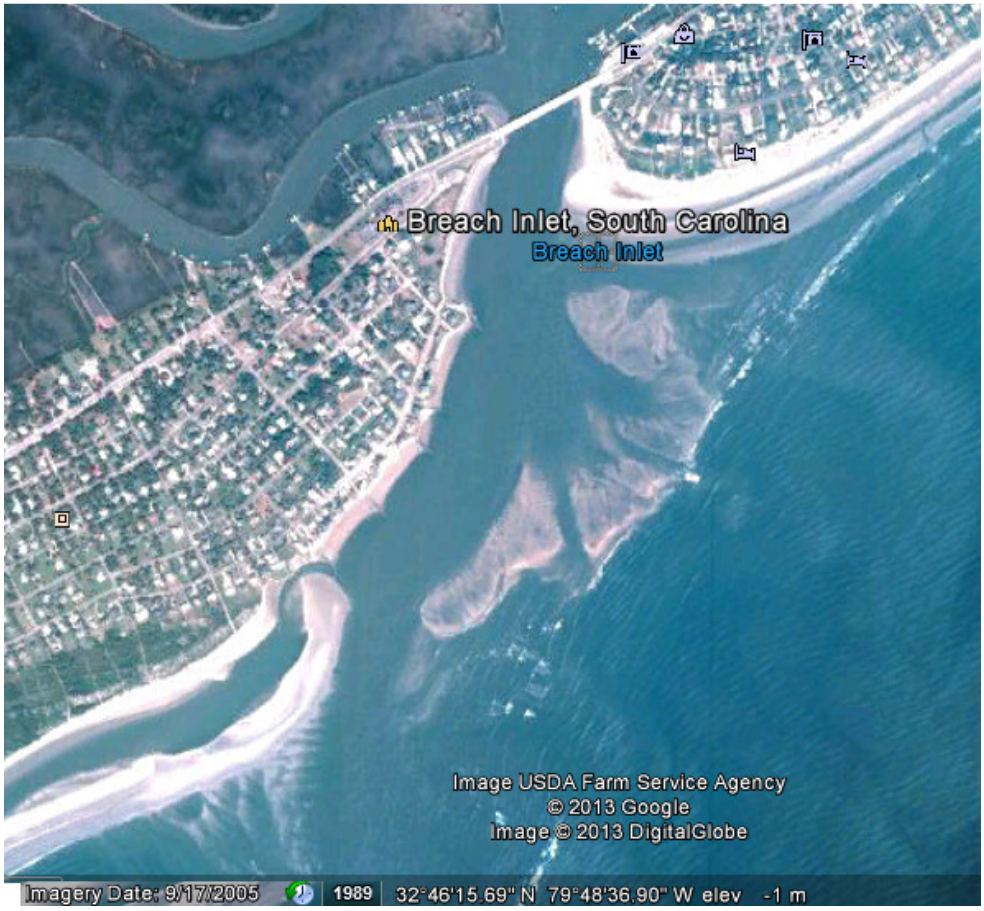

Figure 5.13: Breaches Inlet, South Carolina, USA – an example of FitzGerald's ebb tidal delta breaching mechanism.

3) Inlet migration and spit breaching (model 1 in Figure 5.11)

Inlet sediment bypassing occurs at migrating inlets where rich sediment supply and a dominant longshore transport direction exist. Therefore, the spit growth lengthens the barrier and the inlet migrates by eroding the downdrift shore. As inlet migration lengthens the tidal channel water exchange between ocean and bay is reduced. This type of inlet is similar to Lake Conjola (Figure 2.9), except that the downdrift rocky region limits inlet migration and further growth of the sand spit. Ultimately, the spit is breached to form a new inlet. The tidal prism is diverted to the new inlet and the old one is closed. The breaching usually happens during storm or river flood, while the closure may occur during wave overwash events as in Lake Conjola. Towards the end of this process, large amounts of sand from the barrier are transferred from updrift to downdrift.

5.2 WHY DO SANDY INLETS NOT JUST GROW WIDER AND WIDER?

According to Escoffier (1940), an inlet is hydraulically stable if its cross-sectional area becomes bigger than the stable value, A_2 in Figure 5.9. Then the flow velocity in the inlet will reduce and be unable to erode sediment out from the inlet causing sediment to deposit in the inlet to reduce the inlet cross-sectional area.

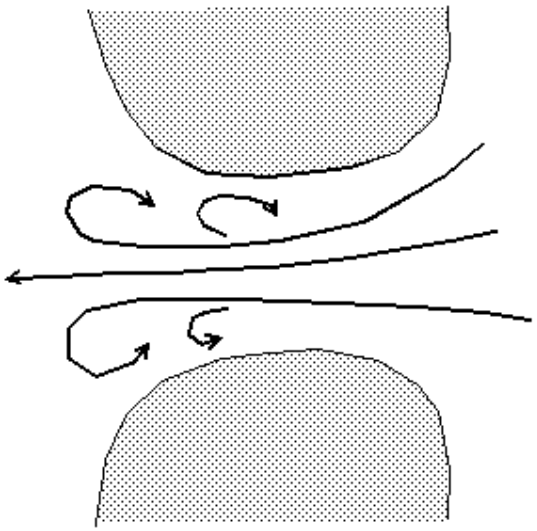

Figure 5.14: Flow pattern due to inlet geometry. A single velocity Q/A or a uniform shear stress along the wetted perimeter are rarely justified and therefore not a good basis for inlet stability models.

In fact, Escoffier's description calls for more detail. That is, $\overline{V} = Q/A$, the cross-section-averaged flow velocity is not enough for predicting opening versus closing of the inlet, because, the distribution of flow velocity is essential and depends strongly on the inlet shape. The strongest currents are concentrated in the central portion of the inlet, which has larger water depth while, near the banks, only weak currents occur or there are even currents in the opposite direction due to eddies. This situation is schematized in Figure 5.14, while the actual occurrence in Canh Duong Inlet, Thua Thien-Hue Province, Vietnam is shown in Figure 5.16.

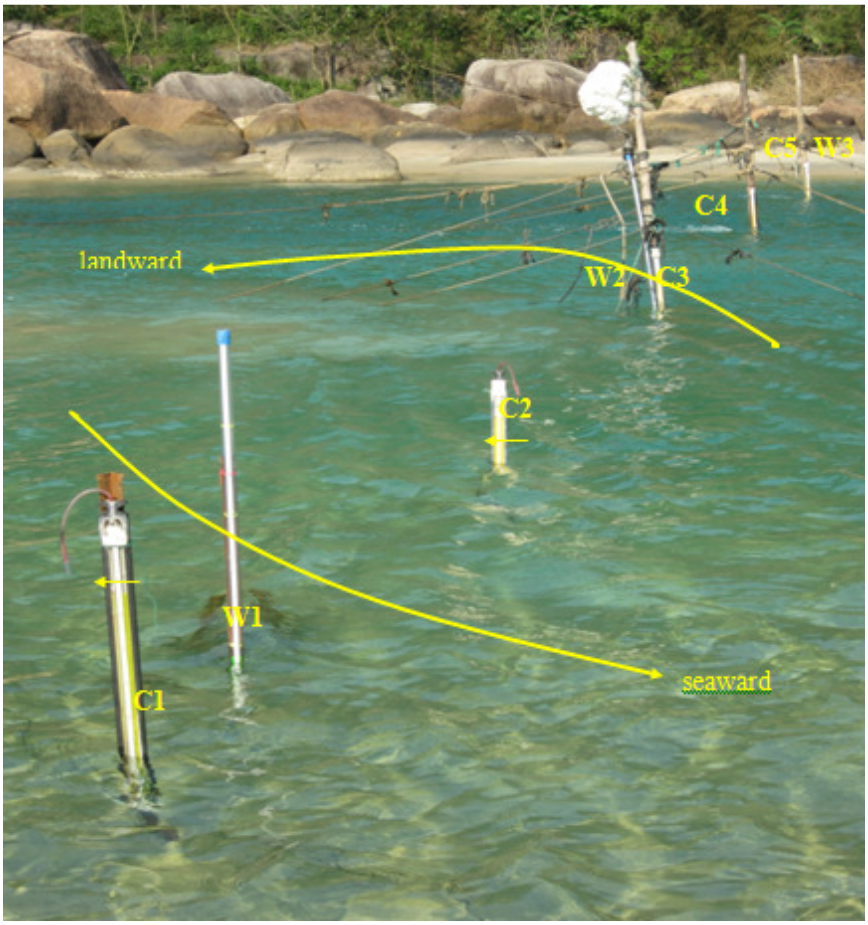

Figure 5.15: Locations for observations of water levels and currents at Canh Duong inlet in Hue, Vietnam. Note the strong surface turbulence at C4 indicating velocities >1m/s while velocities are zero or towards the right at C1 near the bank.

From our observations at the Canh Duong inlet (Figure 5.3), we found that during flood tides, the strong landward flow is concentrated near the western bank, while near the eastern bank, currents run seaward due to the occurrence of an eddy. In Figure 5.15, the locations of the current meters are indicated from C1 to C5 and the locations of the stilling wells are indicated from W1 to W3. The strongest landward current (> ~ 1 m/s) appears at C3 and C4 as indicated by the white water. The corresponding time series are shown in Figure 5.16. At C5, near the west bank, the current is also strong but it is not as strong as at C4. At C2, the current is quite weak, seaward at the beginning then turning to landward due to changing eddy positions. At C1 near the east bank, the weak "flood-current" is in the seaward direction.

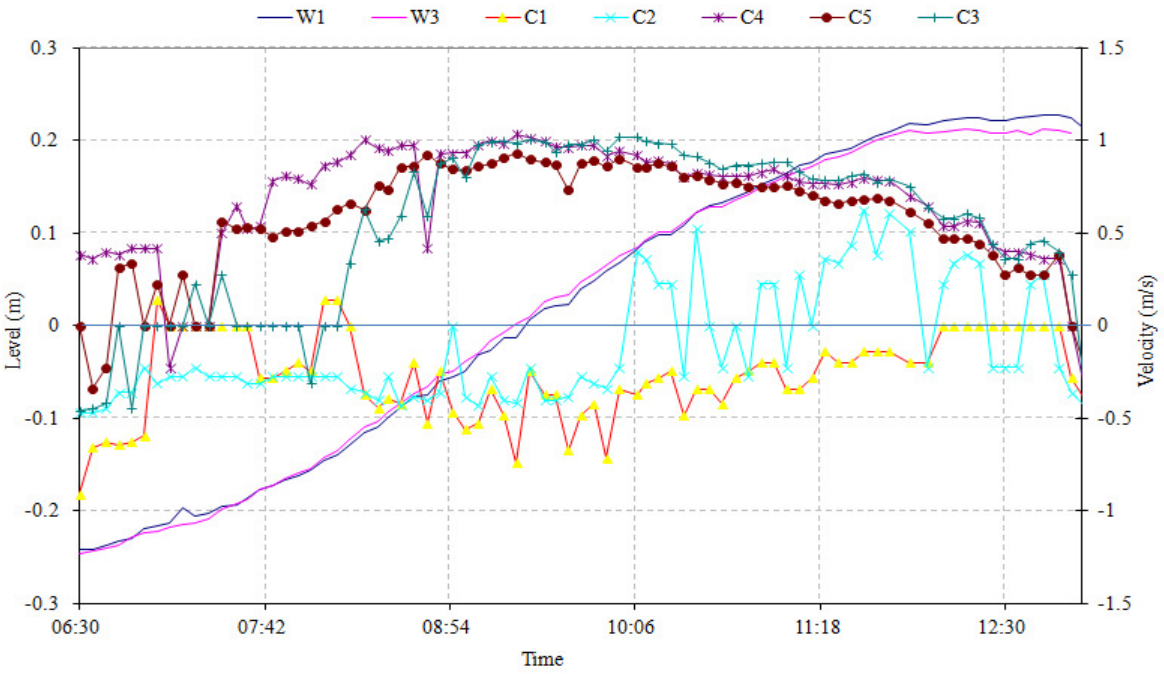

Figure 5.16: Observed water levels and currents obtained from the instruments in Figure 5.15.

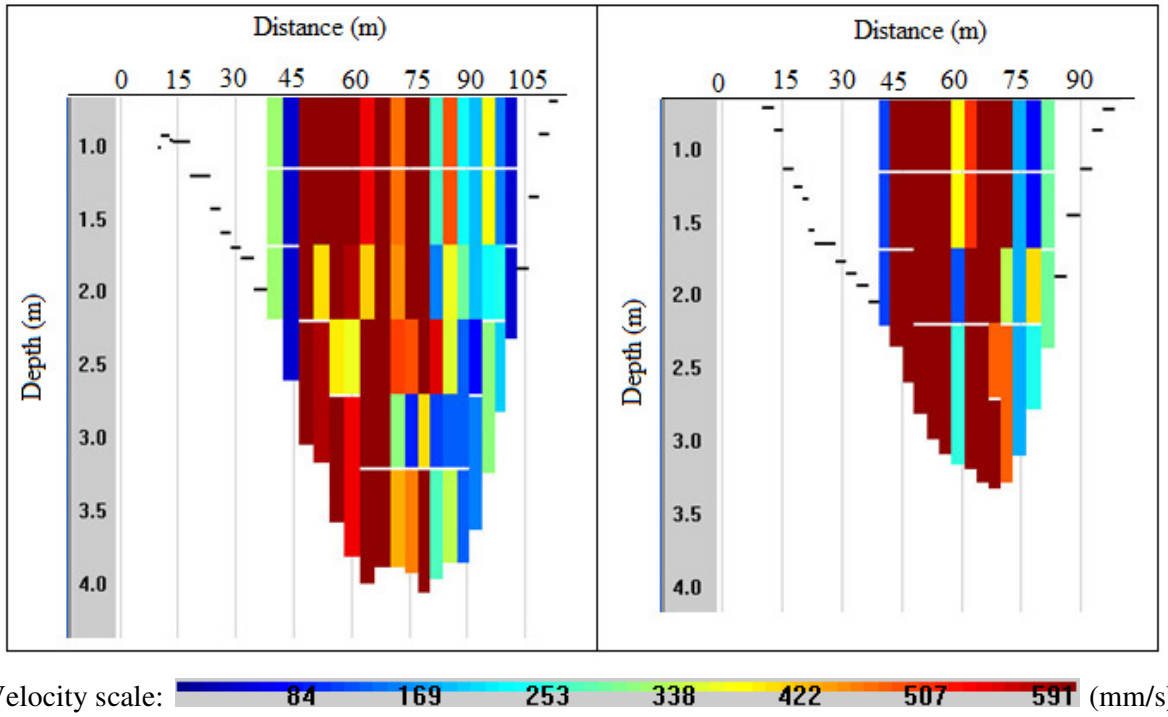

Figure 5.17: Distribution of flow velocities at upstream transect S_1 (left) and downstream transect S_2 (right) measured at around 12:00 using FlowQuest 600. Positions of S_1, S_2 were presented in Figure 5.3.

Data from an acoustic current profiler also show the strong currents concentrated in the central part of the cross-section as in Figure 5.17, but it fails to pick up the seaward flows near the

banks. In this situation, application of the averaged flow velocity Q/A as a single indicator of erosion versus accretion would lead to a prediction of inlet opening. However, in reality, the currents near the banks were very weak, and could not scour the banks to open up the inlet.

That is, in order to understand the stability of sand spits and inlet morphology in general, some rather fine details of the flow need to be considered.

5.3 DIMENSIONAL ANALYSIS OF INLETS AT EQUILIBRIUM

Scientific discoveries are usually not made with dimensional analysis. However, dimensional analysis can provide very succinct after-rationalisations, which clarify the necessary assumptions with a minimal number of words. A great example is the log-law. It was developed over a number of years by Prandtl, von Karman and others in the 1920s. However, its validity or otherwise was brilliantly summarized by Landau & Lifshitz (1987) p.174, using dimensional analysis. Without claiming to rival Landau & Lifschitz, we shall try and make similar use of dimensional analysis to gain understanding of the equilibrium conditions for tidal inlets. Another use for dimensional analysis is to reduce the number of variables by defining minimal, yet complete sets of dimensionless variables. The discussion above, of historical inlet stability models, calls for this application. That is, at least three competing "forces": Tides, fresh water and waves must be considered and three is too many dimensions for simple maps. We need to boil it down to two, and dimensional analysis can do this. For example (Q_{tide}, Q_{f}, H, g) can be represented by the complete and minimal set $\left(\frac{Q_{\text{tide}}}{\sqrt{gH^5}}, \frac{Q_{\text{tide}}}{Q_{\text{f}}} \right)$.

We start with the simplest possible case and step up the complexity as discrepancies between the results of the simple analysis and data crystalizes. We use N for the number of physical variables and R for the rank of the corresponding exponent matrix, which is usually the number of the basic dimensions (mass [M], length [L] and time [T]) involved.

$\mathbf{F(A_{eq}, P_{eq}) = 0}$

Our first application relates to the $A_{\text{eq}} \sim P_{\text{eq}}$ relationship discussed above. If indeed A_{eq} was a function of P_{eq} only, this could be expressed as

$$\text{F}(A_{\text{eq}}, P_{\text{eq}}) = 0 \qquad (5.13)$$

In this case we have N=2 and R=1 so dimensional analysis says that the story told by (5.13) can be told more simply with a single dimensionless variable. This has to be $\frac{A_{\text{eq}}}{P_{\text{eq}}^{2/3}}$ or a power thereof and the story must be

$$\frac{A_{\text{eq}}}{P_{\text{eq}}^{2/3}} = \text{constant} \tag{5.14}$$

or $A_{\text{eq}} \propto P_{\text{eq}}^{2/3}$. That is, the much talked about exponent n must be 2/3 if indeed A_{eq} was a function of P_{eq} only whereas the numerous investigations, reviewed in Section 5.1.1.1, have led to n=0.85-1.1, or perhaps just $n \approx 1$.

The conclusion is that the story must be more complicated than (5.13), so we proceed by stepwise increased complexity.

$\mathbf{F(A_{eq}, P_{eq}, T_{tide}, g) = 0}$

The logical first additional player to involve would be the tidal period T_{tide}. However, a story of the form $F(A_{\text{eq}}, P_{\text{eq}}, T_{\text{tide}},) = 0$ has no equivalent in terms of a complete set of dimensionless variables. We need to include another parameter which includes time in its dimension. Perhaps it makes sense to bring in gravity g, leading to $F(A_{\text{eq}}, P_{\text{eq}}, T_{\text{tide}}, g) = 0$. In this case we have N=4 and R=2, so we need two independent dimensionless variables, e.g.,

$$\frac{A_{\text{eq}}}{P_{\text{eq}}} = \Phi\left(\frac{P_{\text{eq}}}{g^3 T_{\text{tide}}^6}\right) \tag{5.15}$$

Plotting these two dimensionless variables against each other would bring out the fact that a relation like $A \sim \text{const} \times P^n$ can indeed not be universal. The tidal period must be included.

$\mathbf{F(A, \hat{Q}_{tide}, g) = 0}$

Several authors have suggested that the peak tidal flow rate $\hat{Q}_{tide}$ might be a better predictor of A_{eq} than P as in Section 1.1.3. However, the key variables A and $\hat{Q}_{tide}$ cannot by themselves form a dimensionless group. We need another variable with [T] in it. Based on Froude hydraulic thinking one might chose g for this purpose, leading to

$$F(A, \hat{Q}_{\text{tide}}, g) = 0. \tag{5.16}$$

For these variables, Buckingham's π-theorem says that just one dimensionless variable is needed to describe the system, e g,

$$\frac{\widehat{Q}_{tide}^2}{gA^{5/2}} = \text{constant} \tag{5.17}$$

implying

$$A \sim \widehat{Q}_{tide}^{0.8} \tag{5.18}$$

This case is close to the data set provided by Jarrett (1976) for group of natural inlet in Gulf coast with n=0.84.

F(A, $\widehat{Q}_{\text{tide}}$, w_s)=0

Let's try to bring in [T] via the sediment settling settling velocity instead, i.e., consider

$$F(A, \widehat{Q}_{\text{tide}}, w_s) = 0\,. \tag{5.19}$$

Dimensional analysis then gives

$$\frac{\widehat{Q}_{tide}}{Aw_s} = \text{constant}\,. \tag{5.20}$$

I.e., $A \sim \widehat{Q}_{tide}^{1.0}$ for constant w_s. This is promising if the settling velocity in fact varies little among the inlet data which support $A \sim \widehat{Q}_{tide}^{1.0}$.

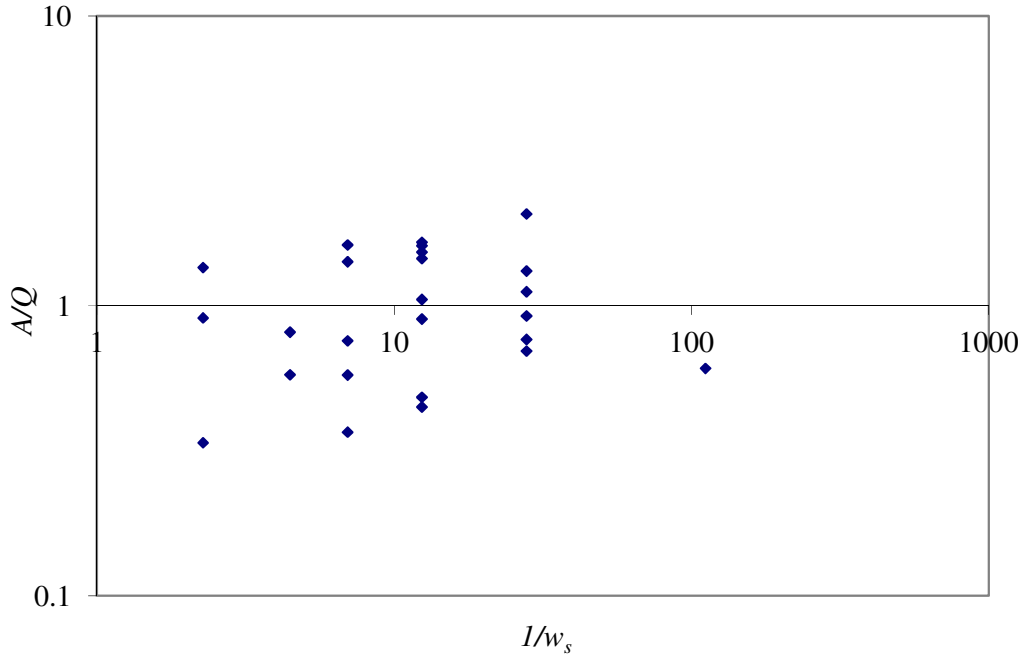

Figure 5.18: The relationship between $\frac{A}{\widehat{Q}_{tide}}$ and $\frac{1}{w_s}$ for the data set taken from Powell (2003) for 27 natural inlets without jetties on the coast of Florida, USA.

As can be seen in Figure 5.18, the data show no clear correlation between $\frac{A}{\bar{Q}_{tide}}$ and $\frac{1}{w_s}$, so the simple case with *N*=3 variables does not work. More practically, *N*=4 may be required for analysis.

_N_=4 with [T] from _g_.

Consider next the case of

$$F(A, \bar{Q}_{\text{tide}}, g, H) = 0 \tag{5.21}$$

i.e., compared with (5.16) we have added the wave height. We are then led to a relation between two variables, e.g.,

$$\frac{A}{H^2} = \Phi_2\left(\frac{\bar{Q}_{tide}}{\sqrt{gH^5}}\right) \tag{5.22}$$

This has the potential to bring some insight about the relation between throat cross section and wave height. I.e., perhaps a plot of $\frac{A}{H^2}$ versus $\frac{\bar{Q}_{tide}}{\sqrt{gH^5}}$ can quantify a trend between the totally $\hat{Q}_{tide}$ -dominated or $\frac{\bar{Q}_{tide}}{\sqrt{gH^5}} \to \infty$ scenarios, which tend to be funnel shaped bays or river mouths Figure 1.5e, where the inlet has widened as far as possible between geological or man-made restraints. The other extreme being simply inlet closing $A \to 0$ for $\frac{\bar{Q}_{tide}}{\sqrt{gH^5}} \to 0$.

The data set is taken from Powell (2003) for 25 natural inlets without jetties on the coast of Florida, USA and 11 natural inlets from CIRP data around the coast of USA, viz from NJ, SC, NC, AL, GA, WA, OR and CA. Figure 5.19 supports the formula

$$A = 4.1H^2\left(\frac{\hat{Q}}{\sqrt{gH^5}}\right)^{0.94} = 4.1\hat{Q}^{0.94}g^{-0.47}H^{-0.35} \approx 1.86\left(\frac{\hat{Q}}{\sqrt{gH}}\right) \tag{5.23}$$

in agreement with previous relationship which include waves directly or indirectly via long shore sediment transport e g Kraus (1998). We also note that if T_{tide} is fixed, so that $P \propto \hat{Q}_{tide}$, this implies $A \propto \frac{P}{\sqrt{gH}}$ corresponding to the exponent *n*=1 in the relation $A_{\text{eq}} = cP_{\text{eq}}{}^n$ in agreement with many of the studies reviewed in Section 5.1.1.1. (Detail of the data set cf. Appendix 2).

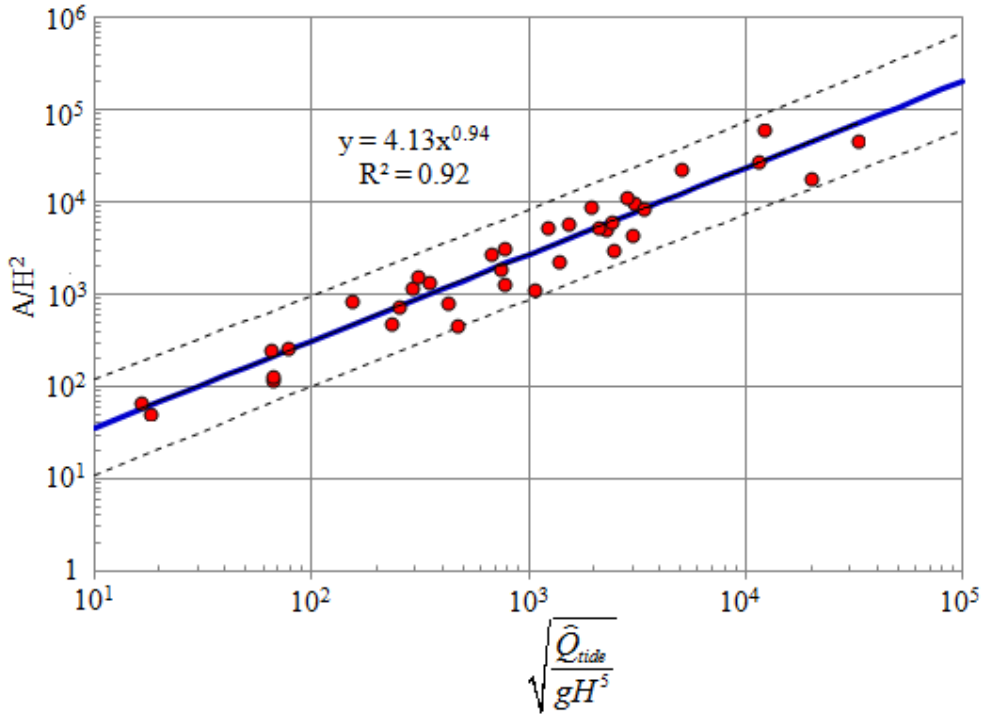

Figure 5.19: Relation between A versus $\frac{\hat{Q}_{tide}}{\sqrt{gH}}$ with 95% confidence limits for inlets at equilibrium.

This solution has weak negative wave height dependence $A_{eq}(H^{-0.48})$ compared to the Larson et al (2011) results which fall in the range from A_{eq}~$H^{-0.83}$ to A_{eq}~$H^{-1.25}$ depending on geometry restriction. Unfortunately, the presently available database does not deliver a definitive message on the power of H. The problem is that the range of Q_{tide} is too large compared to the range of H leading to any trial for the role of H becoming futile. Resolution of the question awaits an improved database with better and further ranging wave data.

5.4 SUMMARY

This chapter presented different definitions for inlet stability in terms of longshore position, cross sectional area, A and balances of driving forces at different time scales from days, months and seasons to years. A new concept of inlet in stable state via tidal record analysis is introduced and applied in Chapter 4 (e.g., Figure 4.19). Fixed response functions F of the primary tidal constituents or F tracing tight orbits in the complex plane reflects the equilibrium state of an inlet.

This chapter reviewed historical equilibrium relationships such as inlet channel cross section at equilibrium, inlet channel volume, area and volume of ebb and flood tidal delta. Almost all

relationships are based on an important parameter - inlet tidal prism, presenting 'tidal force', while many researchers pointed out that tidal period, river flow, wave energy, sediment supply, etc need to be taken into account in these relations. Besides, the explanation of cross sectional stability or inlet closure is also reviewed based on Escoffier's (1940) curve and a number of its extended or modified versions.

The contribution to inlet stability aspects is in terms of finding new relationships between morphological parameters and external forces such as spring tidal prism P, tidal period T, and mean annual significant wave height $\overline{H_s}$. Based on a data set of 23 natural inlets in Florida, USA, two new relationships between V_{Ebb} and V_{Flood} and the relative tidal strength $\hat{Q}_{tide}/\sqrt{gH^5}$ have been constructed as (5.6) and (5.7). In addition, a new relationship between cross section area A and $\hat{Q}_{tide}/\sqrt{gH}$ is determined in (5.23) based on dimensional analysis and a data set of 36 natural inlets in and around the US with high correlation (R^2=0.94). This formula is in agreement with previous relationships, which include waves directly or indirectly via long shore sediment transport eg, Kraus (1998) or an 'ocean sediment concentration' Hinwood et al (2012) and imply that stronger waves means smaller A. It also supports for the relationship, $A_{\text{eq}} = a_1 P_{\text{eq}}^{\ n}$ with exponent n<1 in previous studies. However, A has weak negative wave height dependence compared to previous studies.

Chapter 6

INLET MORPHODYNAMICS

6.1 INTRODUCTION TO INLET MORPHODYNAMICS

In Chapter 5 we found that peak tidal discharge $\hat{Q}_{tide}$, ocean significant wave height H_s and inlet cross section A_C are related by Equation (5.23), see Figure 5.19 on reasonable goodness of fit and most of the scatter may well be due to non-steady wave conditions and spring/neap tide cycles so that measured A_C-values are really never equilibrium values. This is true even in the absence of freshwater flow effects, which are random in many areas while perhaps quasi-periodically seasonal in others. Other observed inlet parameters would similarly always be transient rather than equilibrium values. This chapter describes the attempts made in the present study to understand these transients, i.e., to understand inlet morphodynamics.

In some parts of the world, seasonal weather changes drive major morphological changes in inlets, while variations due to individual storms are less significant. Seasonal changes are considered in Section 6.3.

In other parts of the world inlet morphodynamics are driven by tides, fresh water flow and waves without clear seasonal periodicity. That is the case for the coast of New South Wales, Australia from where a large amount of data for the present study has been sourced (cf Section 6.4). The mean length of time $\overline{T_{open}}$, a given inlet stays open is analysed by simple statistics. $\overline{T_{open}}$ is a simple indication of the morphodynamic time scale T_{morph}. T_{morph} from 24.5 hour moving window analysis of tides has been determined for many closure events which showed a clear exponential trend to obtain the relationship between T_{close} and external forces.

It is found that the response to extreme changes in forcing depends strongly on inlet size, from small inlets, which open and close several times every year, to larger systems where the effect of even the most severe weather events are not- or barely measurable via changes to the inlets hydraulic performance.

6.2 EVOLUTION OF TIDAL INLETS REVIEW

For each hydrodynamic condition $\left(\frac{\hat{Q}_{\text{tide}}}{\sqrt{gH^5}}, \frac{Q_{\text{f}}}{\hat{Q}_{\text{tide}}} \right)$ the inlet system and its elements have a corresponding morphological equilibrium state as reviewed in Section 5.1.1 through the relationships with cross section area, volume of ebb tidal delta, and volume of flood tidal delta. During unusual weather, significant change of Q_{f} or H results in changes away from equilibrium. The morphology of tidal inlets runs out of equilibrium. Subsequently, it may return to the previous equilibrium, move towards a new equilibrium or close. The time scale at which an inlet responds to these changes is called the morphological timescale T_{morph}. Different elements in a system may respond with different timescales from days to months or years.

The difference between the actual state and the equilibrium state is an exponentially decaying function, $e^{-t/T_{\text{morph}}}$, if the rate of change is proportional to the distance from equilibrium as in

$$T_{\text{morph}} \frac{dy}{dt} + y = x \quad \text{or} \quad \frac{dy}{dt} = \frac{x - y}{T_{\text{morph}}} \tag{6.1}$$

where $y(t)$ is a morphological parameter of the inlet, e.g., V_{ebb} (V_{flood}) the volume of the ebb (flood) tidal delta or throat area A_{c} and $x(t)$ is the equilibrium value of this parameter which would be reached if the present drivers stayed constant.

For example

$$\frac{dA_c}{dt} = \frac{A_{c,eq}(t) - A_c(t)}{T_{morph}} \tag{6.2}$$

where $A_{\text{c,eq}}(t)$ would be given by Equation (5.23) in terms of the instantaneous wave and tide parameters:

$$A_{\text{c,eq}}(t) = 4.1 \times \hat{Q}_{\text{tide}}(t)^{0.94} g^{-0.47} H_{\text{s}}(t)^{-0.35}. \tag{6.3}$$

The general solution of (6.1) and solution for specific generic cases (e.g. linear increase or simple harmonic oscillation) are presented in Section 6.5.

Such exponential trends were earlier presented by O'Cornnor et al. (1990), Eysink (1990), Cleveringa et al. (2007). Their works dealt with macro-scale phenomena and assumed that each system parameter works independently from the others. This may be true for certain elements, but not for all. A deviation from the morphological equilibrium of any element will lead to morphological changes in other elements of the system.

Local morphological change occurs in accordance with

$$n\frac{dZ_b}{dt} = -\frac{\partial q_{s,x}}{\partial x} - \frac{\partial q_{s,y}}{\partial y} \tag{6.4}$$

where n is the solid fraction of the bed sediment, $q_{s,x,}$ $q_{s,y,}$ are sediment transport rate per unit width in the x and y directions and Z_b is the bed elevation.

Correspondingly, in general terms, an inlet will widen or narrow when the gradient of sediment transport between bay-ward and seaward cross sections or ΔQ_s is non zero as illustrated by Figure 6.1.

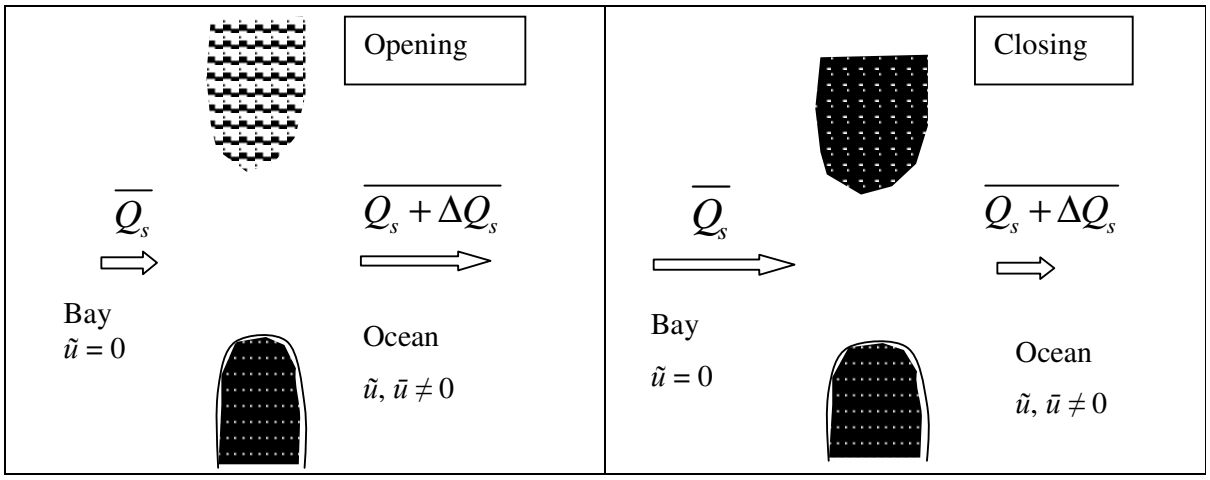

Figure 6.1: Inlet opening and closing process.

De Vriend et al. (1993) classified two methods often used to study the evolution of tidal inlets:

1) behaviour oriented (or aggregated) modelling

2) process-based modelling.

The latest simple method is inferring morphodynamics from tidal records analysis (Hinwood & McLean, 2001; Thuy et al. 2012, 2013a, 2013b).

The behaviour oriented modelling approach, also known as semi-empirical long-term modelling, combines empirical equilibrium relations of inlet systems and basic physical principles (such as conservation of sediment and water mass in a larger scale) without describing the underlying physical processes. The geometry is simplified in this modelling approach by aggregation into a number of morphological elements such as ebb tidal delta, tidal channel and inter-tidal flats. The equilibrium state of each element depends on hydrodynamic forcing, e.g. tidal prism P or R_t and morphometric condition, e.g. basin area A_b. Of the two approaches, to investigate the same phenomenon, behaviour-oriented models are usually much simpler than process-based models. Hence, these models are faster and more suitable for model fitting rather than computing straightforwardly the behaviour from a mathematical system with preset parameters as in the

process based approach (de Vriend et al., 1993). However, the limitation of the behaviour oriented approach is that detailed morphological information is lost and results strongly depend on the equilibrium assumptions.

The early work on behaviour oriented modelling approach is Escoffier's (1977) stability analysis for tidal inlets that used an empirical A~P relation. Van de Kreeke (1990b) used a similar technique to investigate the stability of systems with multiple inlets. He found that two or multiple inlets systems cannot be stable. However, de Swart & Zimmerman (2009) concluded a reverse statement by reviewing other researchers' work. Di Silvio (1989) proposed a simple box model for the basin with channels and tidal flat. Van Dongeren & de Vriend (1994) divided an inlet system into a chain of consecutive boxes, this model works well in small basin but not for large basin due to the concept limitation. Stive et al., (1998) and Stive & Wang (2003) introduced the concept of macro scale process-aggregated modelling, embedded in the ASMITA (Aggregated Scale Morphological Interaction between a Tidal basin and Adjacent coast) model. The assumption in this approach is that no change occurs if all elements are in equilibrium. Any distortion of any element will result in morphodynamic interaction between these elements and adaptation of the whole system toward equilibrium or closure depends on element's morphodynamic adaptation with different timescales. In this model, the exponential decay only applies to small disturbances whereas it can be applied to an arbitrary disturbance as in e.g. Eysink (1990). The timescale in this model depends on a number of physical characteristics of system (e.g. vertical exchange rate, diffusion exchange rate between two elements, dimension of sediment concentration) while timescale in Eysink (1990) model is an empirical input parameter. Van Goor et al. (2003) pointed out that the capability to predict morphodynamic evolution of this model can be decades or centuries, including the impact of slow processes such as sea level rise. However, Van de Wegen et al. (2010) commented that despite of obtaining good results the method applies empirical relationship without physical explanation and the relationships are assumed constant over time, which may not be always true. They found from the process-based model results that the empirical A-P relation is valid for a decadal time scale but not applicable for centurial time scale.

Another approach to study the evolution of tidal inlets is through process-based models which are based on detailed descriptions of the underlying physical processes such as hydrodynamics, sediment transport and bed level updates. In contrast to the behaviour oriented approach in which the formulations are derived for the basin as a whole, the process-based models derive micro or mesoscale level description of the bathymetry and physical conditions on a local grid or per cross–section. This kind of modelling is only suggested for morphodynamic prediction at short timescales (from days to years) due to problems with reaching morphodynamic equilibrium.

Some studies in fact did not achieve equilibrium in the sense of zero net sediment transport (e.g., Hibma et al., 2003a). Similarly issue is found when $\underline{A}$ increases for similar P by Van de Wegen et al. (2010). In contrast, Hanson et al. (2003) and de Swart & Zimmerman (2009) reviewed a large number of process-based modelling works, which proved the presence of equilibrium states for meso-scale morphological features, especially 1D model for long-time simulation. The complexity of these process based models is another drawback because of difficulty in gaining more physical insight into which process is responsible for the observed phenomenon. A major limitation of this approach is that detailed (small scale) description of physical processes is needed to come to large scale results leading to inevitably long computation time. Therefore idealized models have been developed for complex process-based model (Elias et al., 2006, Hibma et al., 2004). The idealized models using simplified geometries, forcing and physical formulations contrast with complex models which require detailed data as input and include much more relevant processes to describe closely the behaviour of interested system. Many researchers (e.g., Schuttelaars and De Swart (1996, 2000); Lanzoni & Seminara (2002)) proved that the earlier models with these simplifications can reveal realistic spatial macro features and ability to make long-term morphodynamic computations. The results from idealized models can be analysed using standard mathematic tools to obtain physical insight. Using this insight, complex process-based models are now able to reproduce results of idealized models and tackle more complex geometrical and more variable forcing conditions with longer time scale using advanced techniques (Lesser et al., 2004; Elias et al., 2006). For example DELFT3D-FLOW "online" version, which performs the hydrodynamic calculation simultaneously with computation of the transport of heat and salinity can bring a lot of advantages: 1) 3D hydrodynamic processes and adaptation of non-equilibrium sediment concentration are accounted automatically in calculation of suspended sediment; 2) the density effects of sediment in suspension are included automatically in hydrodynamic computations; 3) bathymetry change can be immediately fed back to hydrodynamic calculation; and 4) sediment transport and morphological simulations are simple to present with less data file requirement to communicate between different modules.

Hibma et al. (2004) reviewed a large number of works using process-based models to investigate channel-shoal patterns. Hibma et al., (2003a) used intermediate models to compare between 1D idealized model of Schuttelaars and De Swart (1996, 2000) and complex process-based model DELFT3D (Roelvink & van Banning, 1994; Wang et al., 1991, 1995). They found no qualitative influence of simplification on the morphodynamic equilibrium but different boundary condition of the bed at the entrance of estuary has essential effect on the model results. Therefore they recommended that the model region should be extended to include the ebb tidal delta to study

the evolution of tidal basins. However, Duijts (2002) proved that a single branch 1D model is insufficient to predict Stoke's drift and horizontal residual circulation, which contribute to morphology. Hibma et al. (2003b) used 2D depth-averaged complex process based model in a rectangular schematized basin to compare with idealized models. They found that the overall patterns agree qualitatively with observations and recommend it as a tool to study channel-shoal in estuaries. Coeveld et al. (2003) used a 3D process-based model to study strong nonlinear-domain, they found that the secondary residual flow has minor role compared to primary residual flow. Therefore, 2D depth-averaged flow formulation is sufficient to simulate the development of channel-shoal. The recent works of Marciano et al. (2005) for fractal channels, Van de Wegen et al. (2010) and Dissanayake et al. (2009, 2012) which studied impact of sea level rise on tidal inlet/basin used the same approach of Hibma et al. (2003b). However, none of these models included wind waves as external forces assuming waves to be of minor importance compared to the tidal motion.

To study the morphodynamics of a coastal system under extreme conditions such as flood, storm or closure event, complex process-based model are often preferred. Ranasinghe et al. (1999) developed a 3D process-based model to simulate inlet closure, which tries to include the contributions of undertow, wave asymmetry and bottom boundary drift to sediment transport. Lam (2009) used a 2DH version of DELFT3D to investigate inlet morphodynamics under the historical flood with reasonable results related to reoriented channel, barrier breaching and scour of inlet. William & Pan (2011) studied the evolution and sand bypassing at a dynamic inlet under two storm conditions, in which one storm caused inlet closure. Even though they used 2DH process-based models, their results agreed with the stability concept of Escoffier (1940) and Bruun & Gerritsen (1959, 1960). The total volume change of different units in the inlet system compared to initial bathymetry as well as cross section area reached equilibrium quite fast (~ 100hours), which is similar to the closure events for small basin inlet discussed in Section 4.1. This modelling approach is utilized to investigate the evolution of Pensacola Pass in US under Hurricane Katrina 2005 in the next chapter.

In a different manner, Hinwood et al. (2012) used a simple one dimensional process-based model to find the stable cross section parameters corresponding to given tidal forcing and/or river flow. For each case the profile parameters converged to a tidal- or a river flow attractor depending on the initial cross section parameters. The remarkable achievement is that this simple model finds a tidal attractor, which agrees with O'Brien's empirical *A-P* relationship. The river flow attractor has a much smaller *A*, which falls in Escoffier's 'closing range' for purely tidal flows. However, it stays open due to an enforced freshwater flow. The influence of waves is mimicked by an 'ocean

sediment concentration' which is carried into the inlet during flood tide. It subsequently has to be flushed out during the ebb tide and for this to happen, the systems moves towards a smaller *A* when waves get stronger. Unfortunately, Figures 6a and 6b in their paper are reversed, which cause confusion. Unfortunately, this paper was overlooked until fairly late in the present study. If the paper had clarified the relation between 'the ocean sediment concentration', $C_{O,}$ and actual wave parameters it might have served as a convenient starting point for the present study of the competing influences of waves versus tides (and fresh water) in inlet morphodynamics.

The latest simple method is inferring morphodynamics from tidal record analysis using a moving window. Any change of inlet morphology under different weather condition is reflected in variation of tidal response. Hinwood & McLean (2001) first applied the method to analyse the response of 5 tidal components to inlet morpho-dynamic changes forced by storms, floods and wave event with window lengths of 3 to 14 days. They concluded that the moving window tidal analysis method is a useful tool for management of tidal systems without full data of river flow and bathymetry. Thuy et al. (2012), modified the method adopted in Hinwood & McLean (2001) but with a shorter window-length of 24.5 hours and examined the two main harmonic components to capture closure events with shorter time scales and reduce the distraction from too many constituents. Thuy et al. (2013a,b) improved the accuracy of results by de-trending water levels before doing the 24.5 hour analysis. They enhance the visualization of the results by displaying the response function in the complex plane.

Apart from behaviour oriented models or process based models of the morphodynamics of ebb tidal deltas, the "Inlet reservoir model" introduced by Kraus (2000) is another tool to predict ebb or flood shoal growth, the recovery of ebb or flood shoals or verify bypassing action. The concept sketch of the "Inlet reservoir model" is shown in Figure 6.2. This model is based on the conservation of sand volume, the identification of morphologic features and sediment pathways and the existence of an equilibrium volume of each unit.

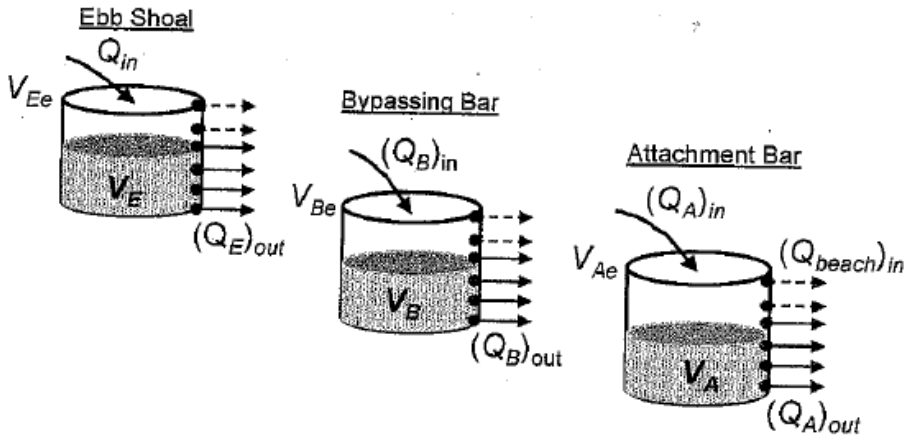

Figure 6.2: The sketch of the Inlet reservoir model concept, source from Kraus (2010).

As can be seen from Figure 6.2, the model consists of three main morphologic units: ebb shoal, bypassing bar and attachment bar, and the sediment transport assumed to be predominant from left to right. The model works as a series of leaking reservoirs with the priority order from left to right. The evolution of each component is described as an exponential function forced by Q_{in} and Q_{out}. Q_{in} is assumed known and Q_{out} is proportional to Q_{in} corresponding to the ratio between the existing volume and the equilibrium volume. The Inlet reservoir model was successfully applied in works done by Kraus et al. (2003), Erickson et al. (2003), Militello & Kraus (2001), Zarillo et al. (2003) for particular inlets in the US. Hoan et al. (2011) added one more morphological unit: the flood shoal into the "Inlet reservoir model" of Kraus (2000) to develop the spit growth model based on previous version of Kraus (1999). They achieved reasonable agreement with unrestricted spit growth observations, but less satisfactory comparisons with restricted growth, i.e. opposing spits moving towards inlet closure.

An analytical model for the evolution of inlet cross-sectional area was attempted by Larson et al. (2011). It is applied for a simple case of barrier breaching due to river run off without considering tidal flow and also ignores the first stages of breaching. They presented the evolution of relative inlet area as a function of the ratio between longshore sediment transport rate and inlet transport rate in equilibrium. The cross section is assumed to be constant in depth. They had good agreement with two sets of laboratory data for the evolution of inlet width during breaching process. This steady flow solution is at most relevant to a breakout scenario. The later tidal stage clearly has oscillatory flow. The Authors' Figure 1 indicates that relatively greater Q_{sy} means faster inlet growth towards equilibrium; this seems strange.

6.3 SEASONAL OPENING/CLOSURE CYCLES QUALITATIVELY

The phenomenon of seasonal closure of inlets or estuaries can be observed at many coasts such as the south-eastern coast of Brazil, the southern coast of South Africa, the south-western coasts of India and Sri Lanka, Japan and the central coast of Vietnam. Their typical characteristics are small tidal range R_{to} (less than 1.5 m), wind-wave dominated coastal environment with strong seasonal variations in rainfall, as shown in Figure 6.3, and wave climate. These inlets are usually closed for a number of months every year due to either the formation of sand spit across their entrances (Ranasinghe et al., 1999) or flood or ebb tidal deltas. Then, they are opened again by strong river flood currents.

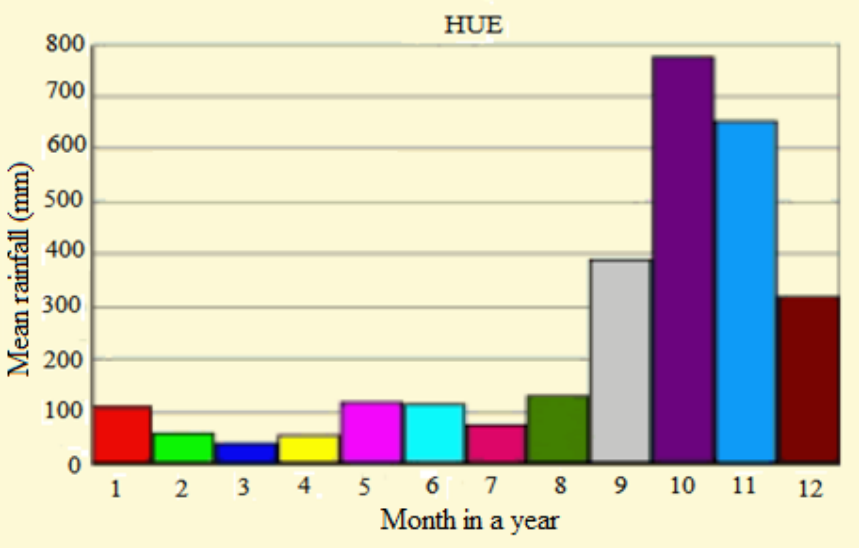

Figure 6.3: Seasonal variation of mean monthly rainfall (mm) in Hue province, VN (source: Vietnam Water Resources Atlas (MONRE, 2003)).

6.3.1 Seasonal opening/closure cycle of an inlet

The seasonal opening/closure cycle of an inlet can be divided into three main stages as stated by Tung et al. (2007). The example of Tu Hien inlet in Vietnam is shown in Figure 6.4 presenting the three main stages of the opening/closure cycle.

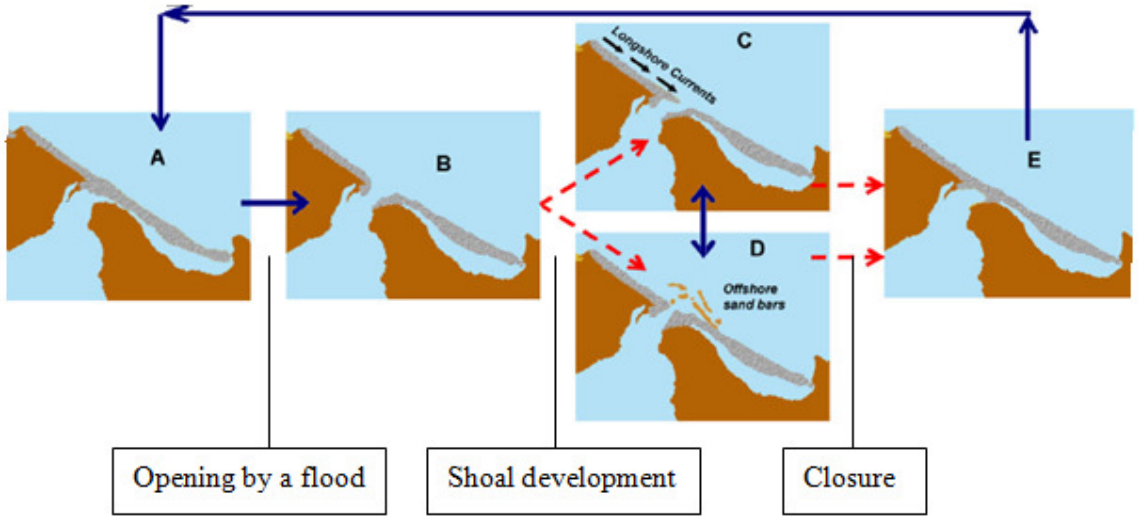

Figure 6.4: Concepts of the seasonal opening/ closure cycle of an inlet, after Tung (2007)

The three main processes are:
1: The scouring out by a flood A→B
2: Development of shoals after flood B →C or D
3: Closure C or D → E=A

The first stage occurs in the wet season when the sand barrier across the inlet entrance is breached due to an extreme river flood event. During this stage, the inlet entrance area is initially inundated, and then scour of the flood plain occurs, while major parts of the sand spit are eroded. The breaching removes sediment from the barrier and the river and deposits it in an offshore sand bar (Figure 6.4B).

The shoal development stage can fall in two different categories depending on wave driven sediment transport. One evolution is the accumulation and expansion of sand spits at the entrance in the dominant littoral drift direction. It causes the inlet channel to be lengthened and change direction (Figure 6.4C). Another development is the landward migration and emergence of offshore sand bars due to shore normal wave action (Figure 6.4D). In this case, the littoral transport is less dominant and the ebb shoals are formed more symmetric compared to the previous case.

The last stage is usually in the dry season when river flows drop off significantly. The inlet then becomes much narrower and shallower and with enough wave action, it may fully close (Figure 6.4E, A).

- ***Closure dominated by longshore processes***

This mechanism illustrated in Figure 6.4C, inlet currents interacting with longshore currents control the inlet closure. The longshore current is interrupted by the inlet current inducing formation of a shoal up drift of the inlet. The longshore sediment transport ($Q_{s,y}$) controls the size and the growth

rate of the shoal. In most cases, the inlet migrates down drift because of ebb tidal current decrease as it is diverted by longshore current and also develops a smaller shoal down drift of the inlet. The updrift shoal continues growing due to persistent supply of sediment till it becomes an emergent spit across the inlet entrance. If the inlet current is strong enough to remove sediment which has settled in the channel mouth, instead of the spit prograding downdrift, marginal bars will form on either side of the main channel. If the inlet current is not strong enough to erode settled sediment, the spit continues to accrete and prograde until the inlet becomes completely blocked. This mechanism of inlet closure dominates on straight beaches with large Q_{sy}.

- ***Closure dominated by shore normal processes***

This mechanism illustrated in Figure 6.4D can only dominate when the inlet currents and $Q_{s,y}$ are small (u<1m/s) corresponding to a micro or mesotidal environment where tidal prisms would be small. The weak inlet current interacts with onshore sediment transport $Q_{s,x}$ due to swells. Under stormy conditions, sand is transported offshore from the beach and surf zone resulting in the formation of a longshore bar at the breaker line. When the storm subsides and swell waves dominate, sand is again transported onshore. There are also two cases, if ebb flows are strong due to large river flow (wet season) or large tidal range, onshore sediment transport will be obstructed (Fitzgerald, 1988). When Q_f reduces in the dry season and the ebb flow weakens, continuing onshore transport leads to closure of the inlet. This $Q_{s,x}$ mechanism is interesting because many seasonal tidal inlets have the same features as described above where $Q_{s,y}$ is small due to near-normal wave incidence.

In short, to simulate seasonal inlet closure, a morphodynamic model should include tidal current, wave height and direction in both $Q_{s,y}$ and $Q_{s,x}$ and river flow.

However, Bertin et al. (2009) argue that the above conclusion may not be general as it was shown at other sites that fair weather condition promote inlet development while inlet shoaling and closure occur rather during storms and larger waves according to Oliveira et al. (2006). Bertin et al. (2009) also give one more mechanism for inlet infilling in storm season by the increase in mean water level inside lagoon (during storm surge) which reduces tidal asymmetry, which is ebb dominance in shallow inlet in fair weather, causing increased sand fluxes to enter the inlet. Such different states may originate from site specific characteristics at 'Obidos' with the combination of meso-tidal range and extremely energetic wave climate, while most of wave dominated inlets occur in micro-tidal environments.

6.3.2 A conceptual model for seasonal evolution an inlet

Stive et al. (2012) summarized work done by Lam (2009), Tran & Stive (2009), Tran (2011) for a number of seasonally opening/closing inlets along the central coast of Vietnam. They developed a conceptual model based on the Escoffier diagram (Figure 6.5, Figure 6.6). The inlet changes from a narrow, shoaling or closed state in the dry season to widening, or breaching state in the flood season depending on the dominant force of the littoral drift to infill the channel over the inlet current, which include Q_{tide} and Q_f flushing sediment out of the inlet. They explain inlet morphodynamics by an extended Escoffier diagram in two major processes

1) variation of the closure curve due to significant difference of Q_f in dry and flood season (Figure 6.5); and

2) variation of the equilibrium curve V_e corresponding to different littoral drift in monsoon or storm season and non monsoon or calm period (Figure 6.6).

The difference between their extended Escoffier diagram and most empirical relations is that two unstable equilibrium points and two stable equilibrium points were presented corresponding to variation of the closure curve or equilibrium curve in different seasons instead of assuming only one "ideal" equilibrium point (Stive et al. 2012).

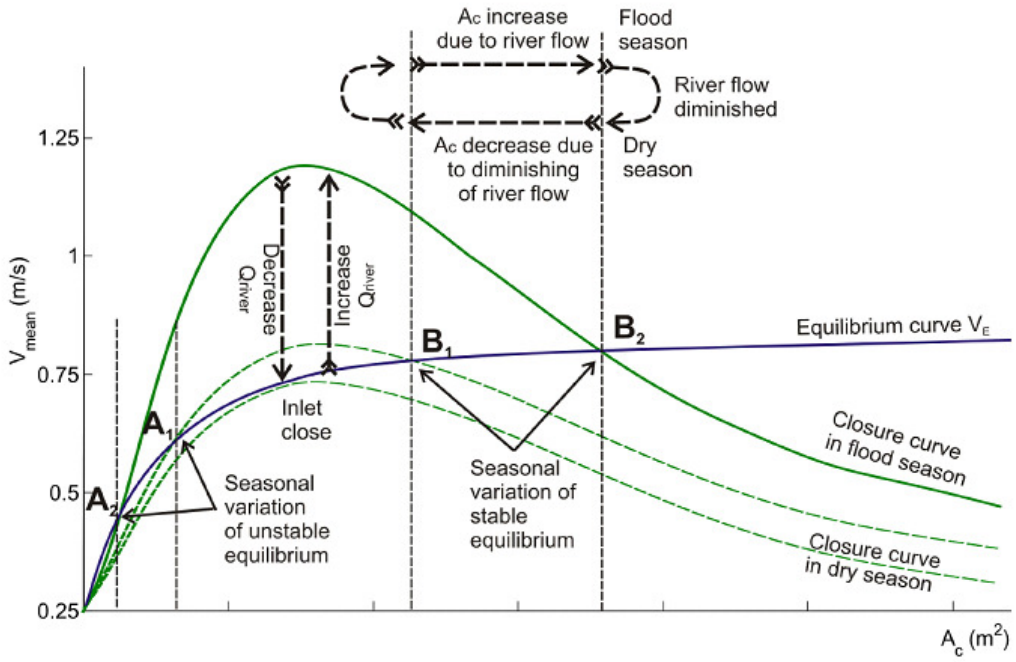

Figure 6.5: Escoffier diagram extended for seasonal variation of the closure curve (Points A_1, A_2 are the unstable equilibrium points, points B_1 and B_2 are the stable equilibrium points corresponding to seasonal variation of the closure curve in the flood season and the dry season (Stive et al. 2012).

In process 1, Figure 6.5 (Stive et al. 2012) shows the extended Escoffier diagram for seasonal variation of the closure curve between significant Q_f and small Q_f. The short term equilibrium point, B_2, on the equilibrium curve V_e corresponds to the maximum river discharge in the flood season and the long term equilibrium B_1 corresponds to the minimum river flow in dry season. The cross-sectional area (A_c) at B_2 may grow significantly compared to that of point B_1 due to the contribution of river discharge to the total $\hat{Q}$ during a major flood event. The new B_2 equilibrium lasts only for a short period during flooding. When the flood diminishes, A_c reduces gradually to point B_1 in the dry season.

It may take several years to return from B_2 after an event to the old equilibrium B_1 as Lam (2009) indicated based on long-term behaviour investigation using ASMITA model for the Thuan An inlet. The recovery period is either long or short depending on the exposure to wave action of different morphological elements of the inlet system. For Thuan An inlet after the extreme flood event of November 1999, it took 7 years for the less exposed inlet channel, 5 years for the more exposed ebb tidal delta and 3 years for the most exposed adjacent coasts to return to their previous equilibrium. Numerical and physical model investigations show that littoral drift and wave reworking is the main process for the system elements to restore to the equilibrium condition. During the recovery period, other extreme river floods may occur that lead to longer times for the system restoration.

If the dry closure curve is below the equilibrium curve (the closure curve fails to reach the equilibrium curve) then the inlet channel will not be able approach B1 equilibrium and the inlet closes (Figure 6.5). The inlet channel may reopen due to a major flood event generating currents which breaches through a sand spit or flushes away shoals at the entrance. After breaching, riverine currents in combination with the ebb tidal currents are strong enough to flush out the sediment accumulated in the inlet channel and maintain the cross-sectional area of the inlet channel. At the end of this cycle, the inlet channel has rolled back to the equilibrium state in the flood season (point B2 in Figure 6.5).

In process 2, Figure 6.6 Stive et al. (2012) show the extended Escoffier diagram for seasonal variation of the equilibrium curve between monsoon or storm season induced strong littoral drift and non-monsoon or calm season with low littoral drift. The central coast of Vietnam, as an example for this category, experiences large seasonal fluctuations of littoral drift caused by seasonal changes of the wave climate during the monsoon period and in storm season resulting in different equilibrium states of the inlet channel (Stive et al., 2012; Tran & Stive, 2009).

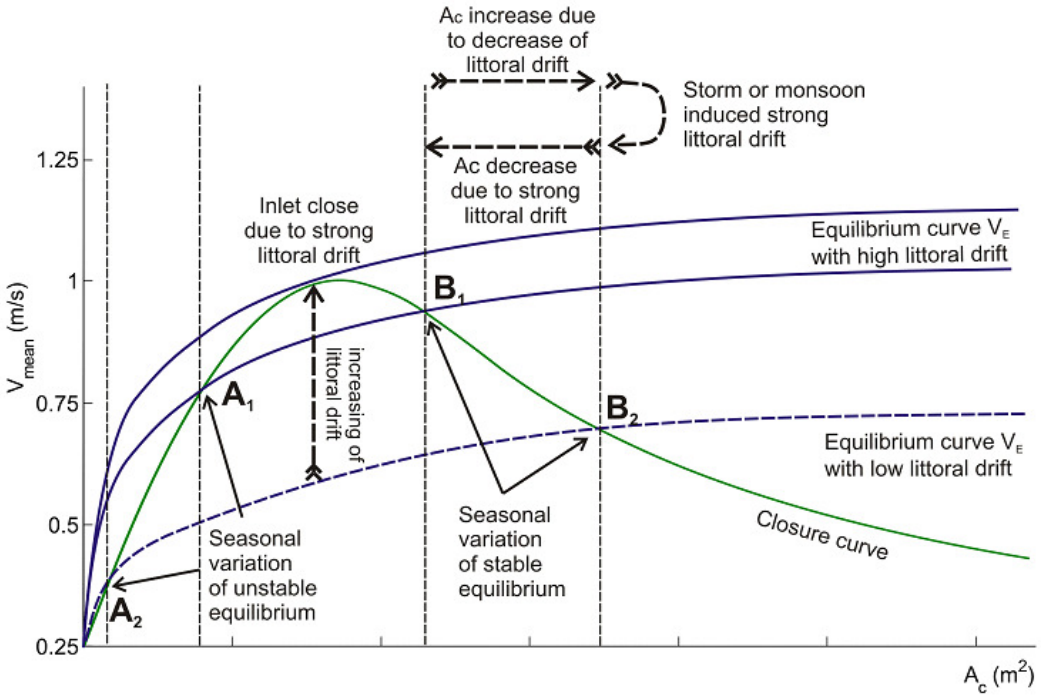

Figure 6.6: Escoffier diagram extended for seasonal variation of the equilibrium curve, modified and extended after Tran & Stive (2009) *(Points A_1, A_2 are the unstable equilibrium points, points B_1 and B_2 are the stable equilibrium points corresponding to seasonal variation of equilibrium curves)*. (Source: Stive et al., 2012).

In the monsoon or storm season, the equilibrium curve shifts up due to high littoral drift whereas the inlet cannot develop to an equilibrium state and is going to close if the equilibrium curve rises up above closure curve (Figure 6.6). In contrast, during the non-monsoon season or calm period, the equilibrium curve drops down due to lower littoral drift. The seasonal variation of the equilibrium curve causes seasonal fluctuations of the stable B_1, B_2 and the unstable equilibrium point A_1, A_2 of an inlet as shown in Figure 6.6. It is similar to the variation of the closure curve as in Figure 6.5, but from a different source. The lager cross section area A_c at equilibrium B_2 during the calm period reduces to smaller A_c at equilibrium B_1 in monsoon season. In some cases, an inlet channel which is in a stable equilibrium during a low littoral drift period may become unstable during a very strong littoral drift period when the equilibrium curve shift above the closure curve causing the inlet fail to reaching B_1. Tu Hien inlet, Hue, Vietnam experiences instability due to seasonal variation, which results in a 9 year cycle of stable and unstable conditions (Lam, 2009).

Many tidal inlets discharge large amounts of fresh water mainly during the monsoon or storm season, the seasonal variation would be a combination of the above two processes. The consideration of all factors viz., P, Q_{sy} and Q_f was mentioned in section 5.1.2 through the work of Lam (2009). Tran & Stive (2009) summarized the characteristics of more than 12 seasonal coastal

inlets along the central coast of Vietnam. Inlets shoal and/or mostly close during the dry season when small river discharge in combination with weak tidal currents enable high littoral drift induced by summer South West monsoon to close the entrance. During the wet season storms (from October to February) and North East monsoon seasons, even though the littoral drift induced by wave action is stronger in summer monsoon, the large river discharge is dominant. Inlet currents can breach a sand spit or flush out shoals at the entrance, to enlarge *A*c. After flood and breaching Q_f decreases, however it may still be sufficient to keep the inlet open against the sediment transported into inlet channel during the NE monsoon.

6.4 NON-SEASONAL OPENING AND CLOSURE OF SANDY INLETS

Sandy inlets on open coasts will typically go through cycles of opening up due to fresh water flooding and subsequent closure due to wave's action.

While the neap-spring variation of the tidal forcing and its distribution on at least two frequencies, Figure 6.7a, is already a significant challenge, the analysis is made extremely challenging by the erratic behaviour of the other two natural drivers: rainfall and ocean wave heights (see Figure 6.7a, b, c).

a)

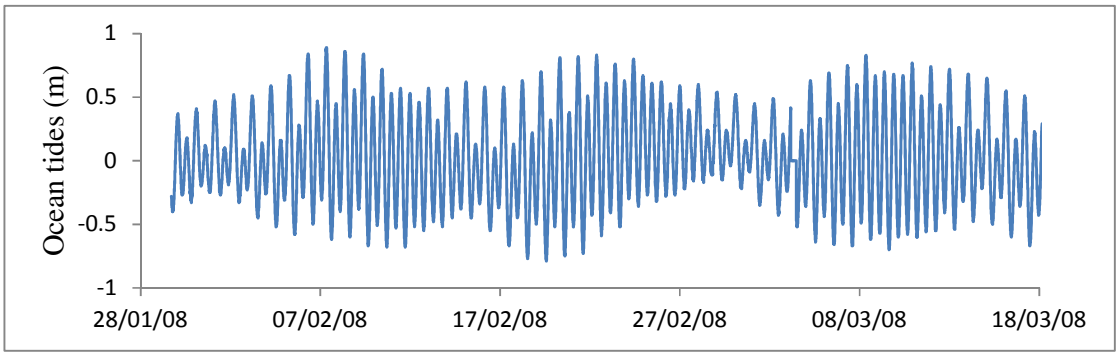

b)

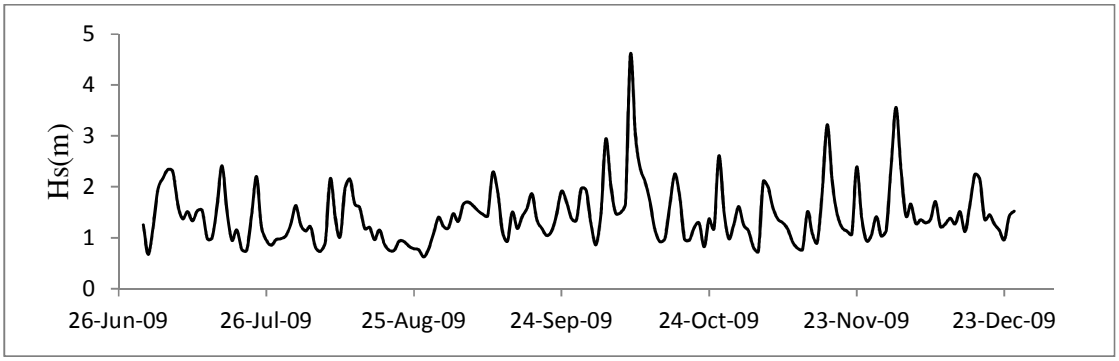

c)

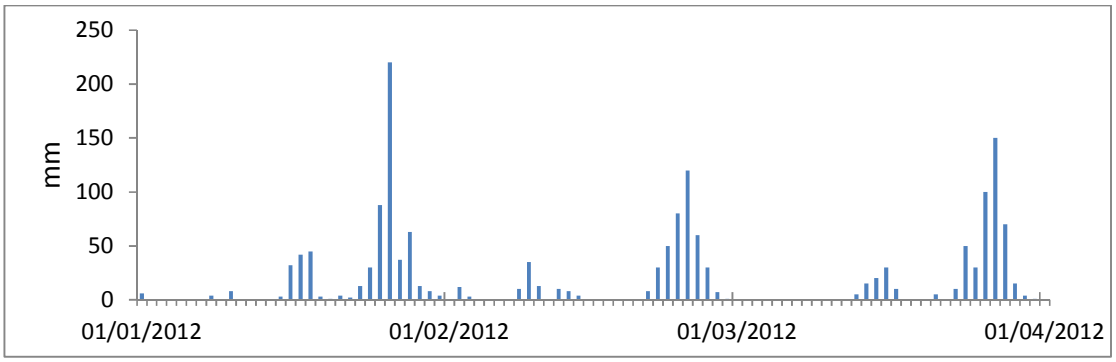

Figure 6.7: Example of the basically non-seasonal variations of Ocean tides (a), offshore wave heights (b), and rainfall (c) along the coast of NSW Australia.

Therefore, the analysis progresses in a stepwise fashion, starting with simple statistics like the fraction of time a given inlet stays open Fr_{open} or the mean length of time it stays open, $\overline{T_{open}}$,. The latter, $\overline{T_{open}}$, is a simple indication of the morphodynamic time scale T_{morph}, which is more precisely defined in terms of an exponentially asymptotic process as in $y(t) = y(0)\exp(-t/T_{morph})$.

Werri Lagoon on the South Coast of NSW, Australia, Figure 6.8, is a small estuary, exposed to the dominant SE waves with $\overline{H_s} \approx 1.6\text{m}$ which are quite efficient at moving sand on the scale of this inlet. Consequently the waves usually close the inlet after only a few days.

Werri's inlet, like most similar inlets, is partly protected from waves by the northern headland. However, severe wave events from the SE will overwash the berm. Thus, the brief rise of the lagoon water levels on 3 August 2010, see Figure 6.9, coincided with the biggest waves of the year. On this day H_s exceeded 6m for a few hours at the Sydney wave rider buoy. A similar, but more extreme overwash flooding event in Lake Conjola was discussed in Section 4.3.

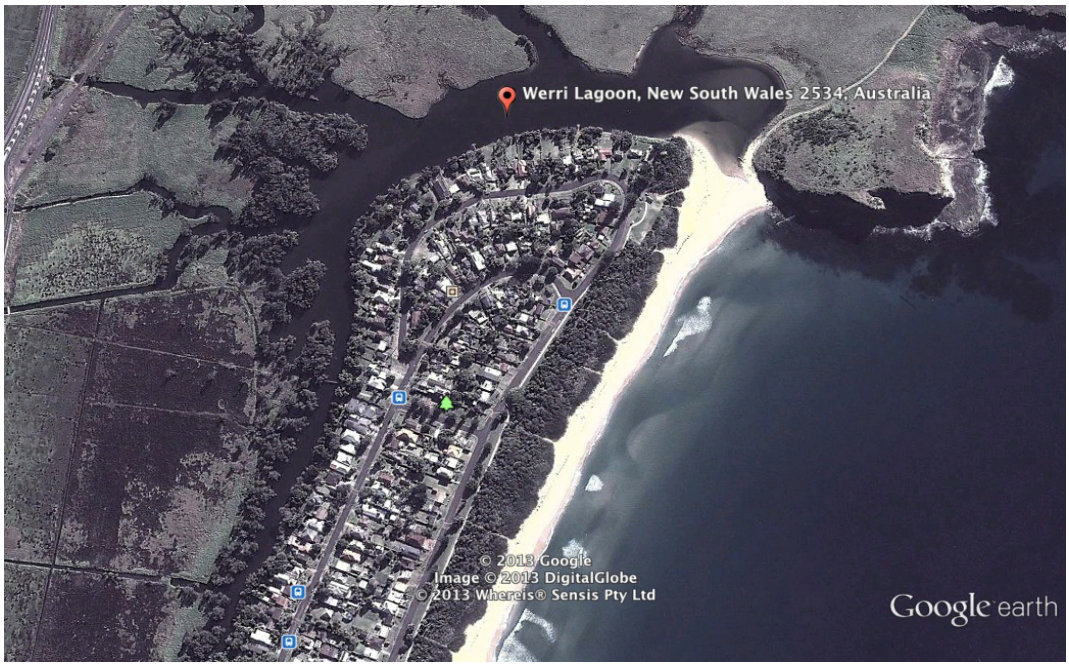

Figure 6.8: Werri lagoon Estuary, surface area A_b= 0.142 km^2, catchment area 16.5 km^2 $\overline{H_s}$ =1.6 m, mean tidal range R_{to}= 1.0 m.

The breakout processes, described recently by Wainwright (2012) are usually too fast to be analysed via tide gauge records. The closing processes are however well resolved and, as shown by the examples in Figure 6.9, they are highly varied. For example, the last one in June 2011 is quite straightforward, with monotonically decreasing lagoon tide range and an apparently constant mix of diurnal and semi-diurnal tidal constituents. Others, e.g., the one in early August 2010 is far from monotonous, displaying three local tide- range-maxima on the way to closure. The one in late October to early November 2010 is at first predominantly diurnal, then almost purely semi diurnal and finally strongly diurnal before closing.

The dimensional analysis exercise, leading to Figure 5.19 indicates that the balance between forcing from waves and ocean tides is perhaps best quantified through the relative tide dominance parameter, $\frac{\hat{Q}_{\text{tide}}}{\sqrt{gH^5}}$, where the peak tidal flow can be taken as the actual value in an equilibrium situation, or as a potential value defined by the driving ocean tide and the lake area. For our present purpose of analysing transients, the latter is more appropriate, and the corresponding wave height is the mean significant wave height. For Werri Lagoon we get

$$\frac{\hat{Q}_{\text{tide, pot}}}{\sqrt{gH^5}} = \frac{\pi R_{\text{to}} A_{\text{b}} / T_{\text{tide}}}{\sqrt{g\overline{H_{\text{s}}}^5}} = \frac{\pi \times 1 \times 0.142 \times 10^6 / (12.25 \times 3600)}{\sqrt{9.8 \times 1.6^5}} = 1.0 \qquad (6.5)$$

which is at the lower extreme of the data in Figure 6.10.

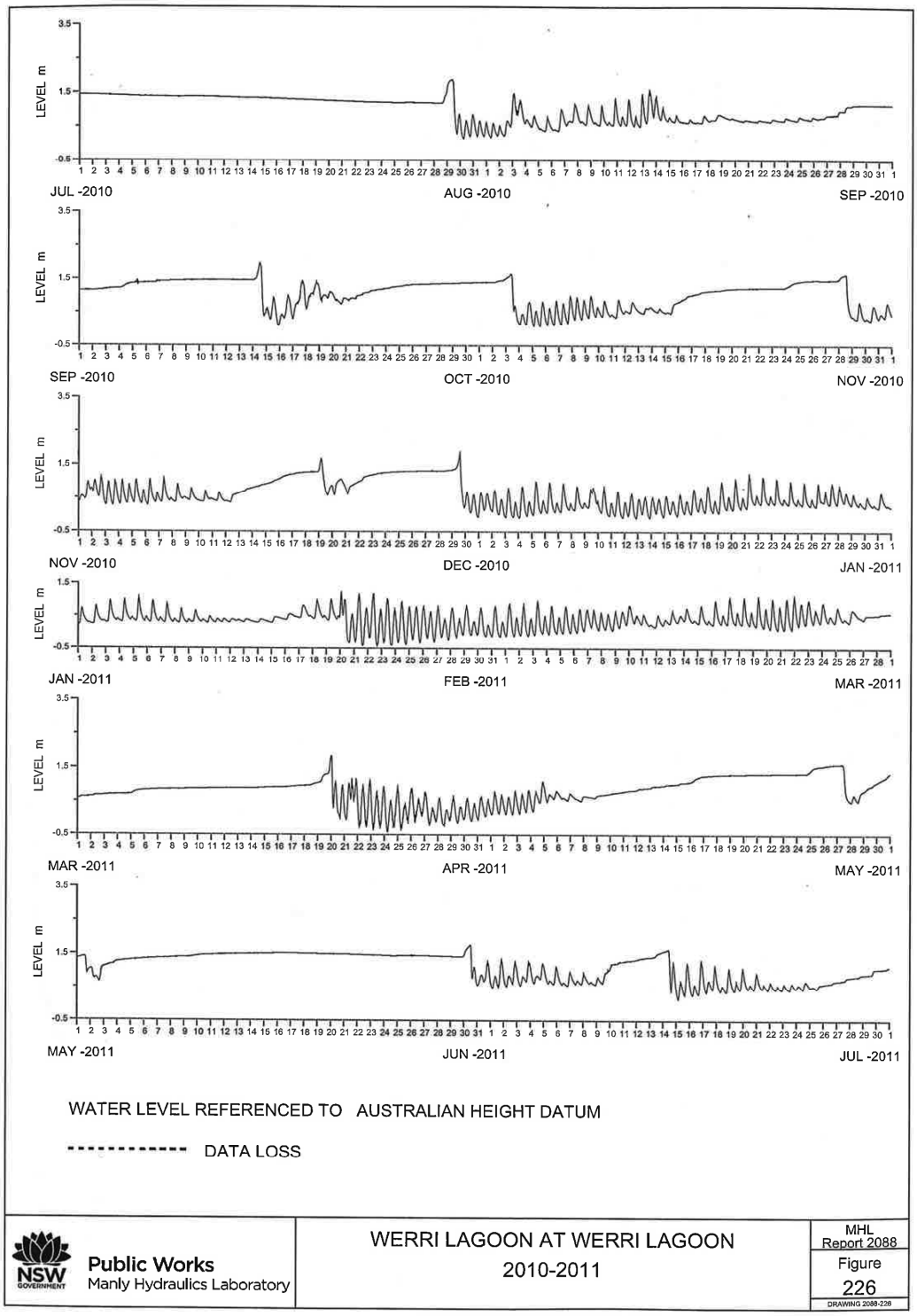

Figure 6.9: A year worth of tides recorded in Werri Lagoon. All of these breakouts except 2 (19 November 2010 and 14 June 2011) were 'man–made'. Hence the breakout levels are not a measure of the typical berm height for this location. Data courtesy of Manly Hydraulics Laboratory.

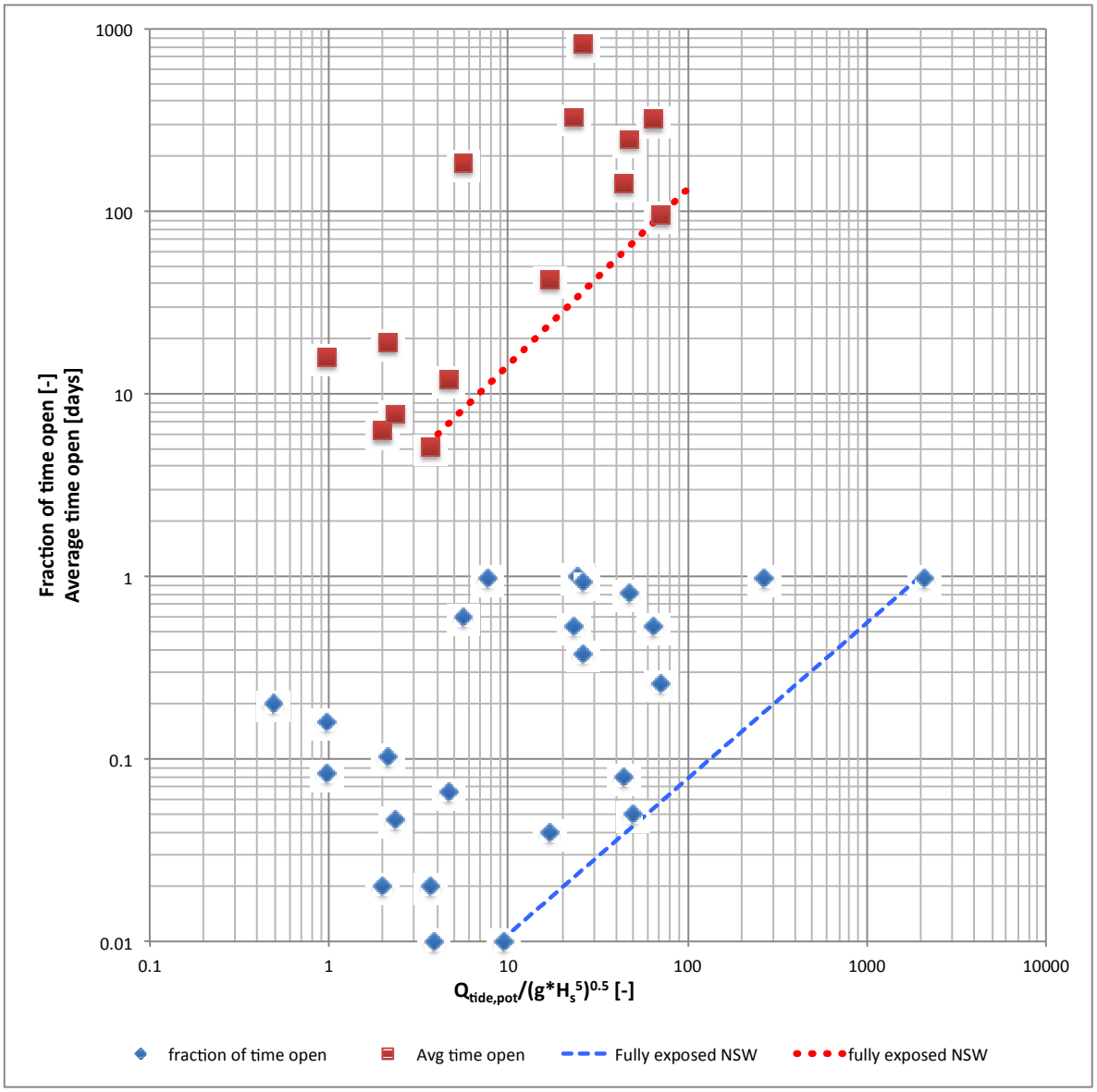

Figure 6.10: Fraction of time open and average time staying open plotted against the relative tidal dominance, based on tide potential as in Equation (6.5). The data included here are all from the NSW coast of Australia and the same mean ocean tidal range of 1.0m and the same $\overline{H_s} \approx 1.6\text{m}$ is used for all. The actual wave forcing will depend on offshore topography and the degree of sheltering of the inlet from a headland. Many inlets are opened artificially when the lagoon water level reaches a "council trigger level". Data from Manly Hydraulics Laboratory.

The fraction of time open varies quite erratically for $\frac{\hat{Q}_{\text{tide,pot}}}{\sqrt{gH^5}}$ <100, but beyond this value no inlets have been reported closed for extensive periods of time. The large and rather iconical

Shoalhaven inlet, which is currently closed, is difficult to fit into this classification because it shares its estuary with the permanently open Crookhaven inlet.

The average time open, is somewhat better behaved with an identifiable trend close to (6.6) but with a range corresponding to a factor 5 either way.

$$\overline{T_{\text{open}}} = 5\frac{\hat{Q}_{\text{tide, pot}}}{\sqrt{gH^5}} \tag{6.6}$$

It is difficult to determine where exactly the relationship for fully exposed, natural (never artificially opened) systems sits, with the present available data. The dotted lines in Figure 6.10 indicate the relationships for totally exposed inlets with ample sand supply and no artificial openings for the NSW coast of Australia.

6.5 DETERMINATION OF T_{morph} FROM TRANSIENT INLET BEHAVIOUR

Not all inlets close, but all display a degree of transient behaviour in response to changing forcing from rain, tides ocean surges and waves. These transients can be observed, either directly via topographical surveys or indirectly via the inlets influence on the estuary tides. The latter is by far the most economical and due to lack of survey data, often the only option. However, it requires a good understanding of the ways in which tidal response depends on inlet geometry as investigated in Chapter 2. Beyond $\overline{T_{\text{open}}}$, the morphodynamic indications from estuary tides are initially sought through the basic statistics: moving 24.5 hour average $\overline{\eta_{24.5}}$ and the corresponding standard deviation $stdev_{24.5}$ which were introduced in Section 3.1.4. Subsequently a more detailed analysis is attempted via the complex frequency response functions F_1, F_2, of the diurnal and semi diurnal tidal components, again based on 24.5 hour moving window analysis.

6.5.1 Dynamic analysis based on $T_{\text{morph}}\frac{dy}{dt} + y(t) = x(t)$

We now consider inlet morphodynamics that obeys the generic linear differential equation

$$T\frac{dy}{dt} + y(t) = x(t) \tag{6.1a}$$

where $x(t)$ is the input, $y(t)$ is the output and T is the time constant. The equation may alternatively be written as

$$\frac{dy}{dt} = \frac{x(t) - y(t)}{T} \tag{6.1b}$$

i.e., it models a system where the rate of change is proportional to the deviation from the forcing. If the input x is constant we see that $y=x$ is the steady or equilibrium solution.

Hence, the forcing function $x(t)$ should correspond to the equilibrium value of the inlet parameter y under study. For example, if we study inlet cross sectional area A_C, we use the equilibrium formula

$$A_c = 4.1 \times \hat{Q}_{tide}^{0.94} g^{-0.47} H_s^{-0.35} \tag{5.23}$$

to generate the input function

$$x_A(t) = A_{c,eq}(t) = 4.1 \times \hat{Q}_{tide}(t)^{0.94} g^{-0.47} H_s(t)^{-0.35} \tag{6.7}$$

The solution for Eq (6.1) in the special case of equilibrium state x= constant= y_{eq} is

$$y(t) = y_{eq} + \left[y_0 - y_{eq} \right] e^{-t/T} = x + \left[y_0 - x \right] e^{-t/T} \tag{6.8}$$

which is shown in Figure 6.11a.

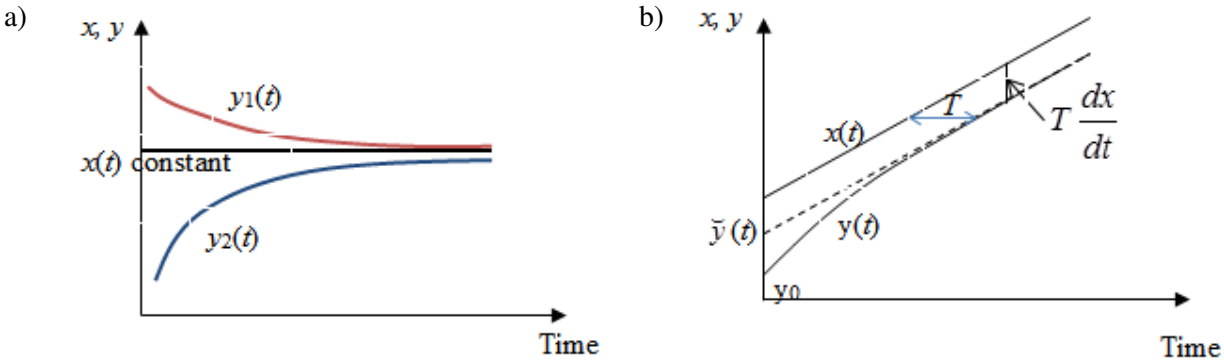

Figure 6.11: According to (6.1) a morphological element adjusts in an exponential fashion towards its asymptotic form. (a) constant forcing; (b) linearly increasing forcing.

Closure events at Avoca Lake Figure 4.4, 4.6, the storm event at the Brunswick River Figure 4.18 or the overwash event at Lake Conjola Figure 4.28 are real examples to demonstrate this.

For a steadily increasing $x(t)$ = At + B, Eq (6.1) has the linear asymptotic

$$\breve{y}(t) = \mathrm{A}(t\text{-}T) + \mathrm{B} \tag{6.9}$$

and the instantaneous solution

$$y(t) = \breve{y} + \left[y_0 - \breve{y} \right] e^{-t/T} \tag{6.10}$$

as shown in Figure 6.11b.

Based on a given time series of $x(t)$, $y(t)$, can be expressed as a convolution over all previous x-values:

$$y(t)=\int_{-\infty}^{t} x(t')\xi(t-t')\,dt'=\frac{1}{T}\int_{-\infty}^{t} x(t')e^{-\frac{t-t'}{T}}\,dt' \qquad (6.11)$$

where $\xi(t-t')=\frac{1}{T}e^{-\frac{t-t'}{T}}$ is called the impulse response function for the system.

For this exponential impulse response function the convolution for a discrete time series with time step δ_t is particular simple by using the recursive formula

$$y(t)=y(t-\delta_t)e^{-\frac{\delta_t}{T}}+\left[1-e^{-\frac{\delta_t}{T}}\right]x(t)\approx y(t-\delta_t)e^{-\frac{\delta_t}{T}}+\frac{\delta_t}{T}x(t) \qquad (6.12)$$

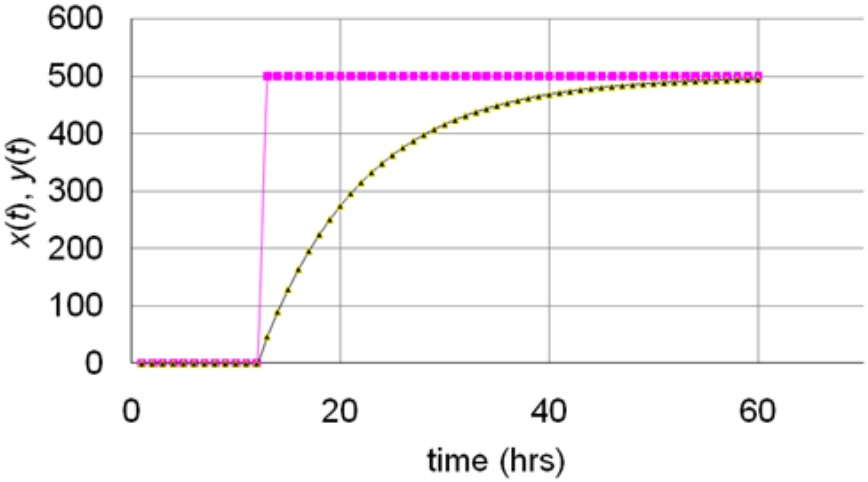

Figure 6.12: Convolution of $x(t)=\begin{cases}0 & for\,t<0\\ 500 & for\,t>0\end{cases}$ with T=10 hours ; □ ~ $x(t)$, ▲ $y(t)$.

The qualitative behaviour of this convolution is illustrated in Figure 6.12 with $x(t)=\begin{cases}0 & for\,t<0\\ 500 & for\,t>0\end{cases}$ as an example.

The qualitative behaviour of the convolution (6.12) is illustrated in Figure 6.13 for $x(t)=\sin\omega t$ with $\omega T=1$. Gain $|F(\omega)|=\frac{1}{\sqrt{1+(\omega T)^2}}=0.707$ and phase lag = $-Arg\{F(\omega)\}=-Arg\left\{\frac{1}{1+i}\right\}=\ =-\left(-\frac{\pi}{4}\right)=\frac{\pi}{4}$. This example corresponds to lagoon tidal response to a simple harmonic ocean tide as discussed in detail in Section 2.4 with T being the hydraulic time scale T_{hyd}.

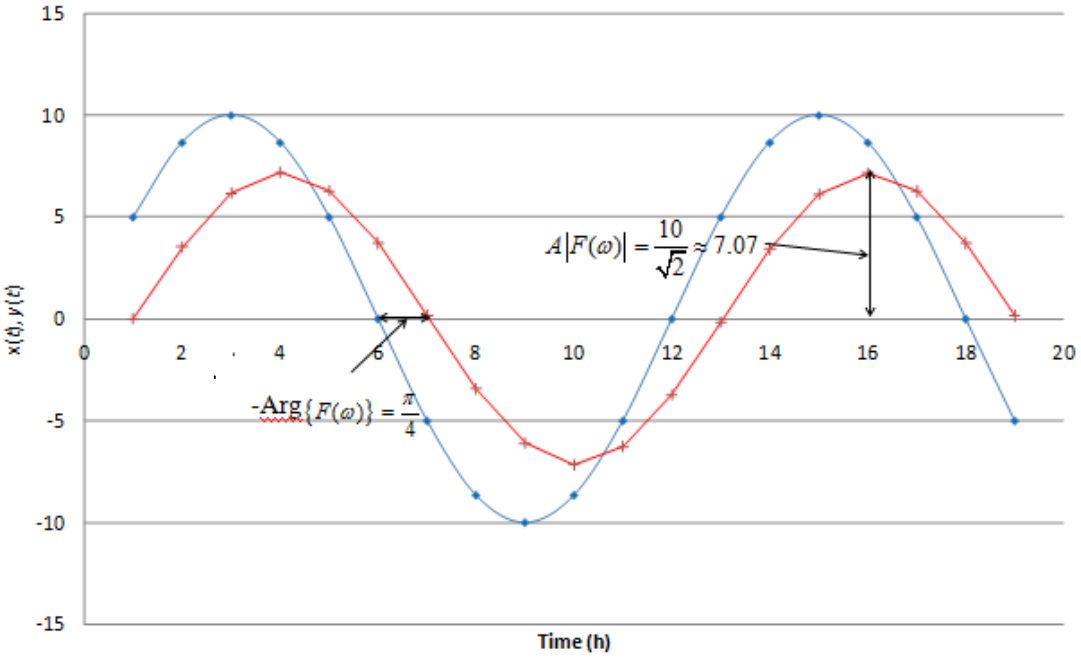

Figure 6.13: Convolution of $x(t)=\sin\omega t$ with $\omega T=1$. T= 1.9h. ω = 0.523rad/h. ◆ ~ $x(t)$, + ~ $y(t)$.

Now consider the $T\dfrac{dy}{dt}+y=x$-model applied to variations of the inlet cross sectional area A_C of Pensacola pass, Florida, US in accordance with Equation (6.7). The peak tidal discharge $\hat{Q}_{tide}(t)$ is assumed to oscillate between 9488 m^3/s at spring tide and 4313 m^3/s at neap tide with $\overline{Q}$ =6900 m^3/s as indicated in Figure 6.14.

The significant wave height is assumed to vary as in Figure 6.14 with average value around 1m and displaying a major storm with $H_{s,\max}$ = 9 m occurred at spring tide, similar to Hurricane Katrina 2005. We apply (5.23) via

$$x_A(t)=A_{c,eq}(t)=4.1\times\hat{Q}_{tide}(t)^{0.94}\,g^{-0.47}H_s(t)^{-0.35} \tag{6.7}$$

and then the convolution (6.11), (6.12) with δ=1 hour, T=360 hours; $A_c(t_{\min})$ = $y(t_{\min})$ = 7681 m^2 corresponding to $\hat{Q}_{tide}$ =9488 m^3/s and $\overline{H_s}$ =1 m.

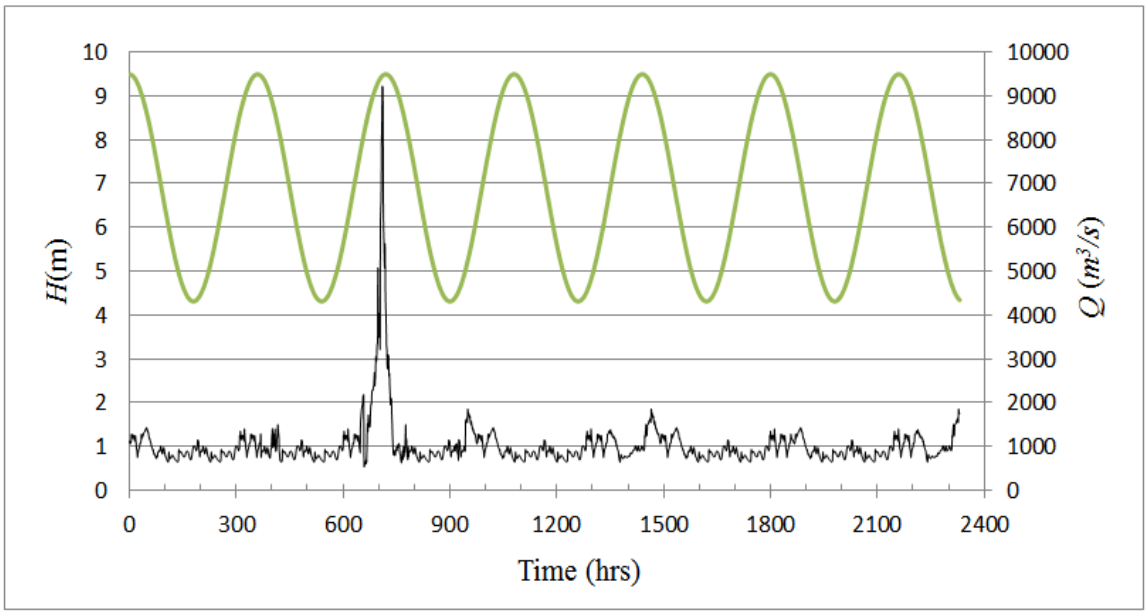

Figure 6.14: $\hat{Q}_{tide}(t)$- thick line and $H(t)$-thin line with one large hurricane event.

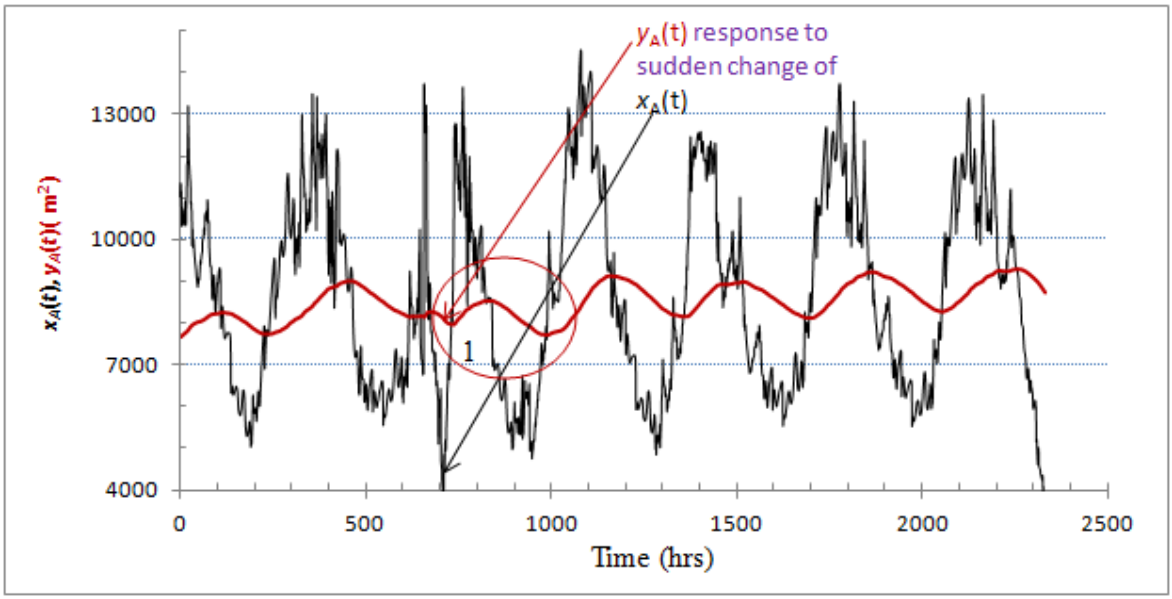

Figure 6.15: Time series of $x_A(t)$ as in (6.7) based on $H(t)$, $\hat{Q}_{tide}(t)$ and the corresponding $y_A(t)$ as in (6.12) with T_{morph}=30 days =360 hours.

It is seen from Figure 6.15 that the neap/spring variation of $\hat{Q}_{tide}(t)$ changes $x_A(t)$ and $y_A(t)$. Erosion (inlet opening) takes place during spring tide; accretion follows during the next neap tide. $y_A(t)$ lags about 55-100 hours behind $x_A(t)$.

$y_A(t)$ regularly increases from 7681 m^2 to approach equilibrium at y_A=9000 m^2 corresponding to (6.7) with $\overline{Q}$=6900 m^3/s and $\overline{H_s}$=1 m. The large hurricane waves make $x_A(t)$ smaller and $y_A(t)$ responds quickly during storm period, droping insignificantly (300 m^2) from 8280 m^2 to 7980 m^2 corresponding to accretion of entrance. When $x_A(t) = y_A(t)$ (point 1 on Figure 6.15), $x_A(t)$ and $y_A(t)$ return to the regular trend which is neap/spring dominant. However the magnitude of $y_A(t)$ are still low until the system reaches equilibrium at around 1030 hours. The reason for the insignificant accretion response is that the event occurred during spring tide in erosion process; hence the effect from large wave is limited or much reduced. The effect of large waves on A_c is small compared to the effect of neap/spring tide variation.

Similar to the inlet area example above we now consider ebb tidal delta volume dynamics based on the equilibrium formula (5.6). Under normal condition

$V_{Ebb} = 24139\left(\frac{\hat{Q}_{tide}}{\sqrt{gH^5}}\right)^{0.78} = 24139\left(\frac{9488}{\sqrt{9.8\times1^5}}\right)^{0.78} = 12.5\times10^6\ m^3$. $x_{Vebb}(t)$ is then the equilibrium value of V_{Ebb} corresponding to the instantaneous $\hat{Q}_{tide}(t)$, $H(t)$ so we can generate

$$x_{V_{ebb}}(t) = 24139\left(\frac{\hat{Q}_{tide}(t)}{\sqrt{gH(t)^5}}\right)^{0.78} . \qquad (6.13)$$

Then $$y_{Vebb}(t) \approx y_{Vebb,}(t-\delta_t)e^{-\frac{\delta_t}{T}} + x_{Vebb}(t)(1-e^{-\frac{\delta_t}{T}}) \qquad (6.14)$$

As can be seen from Figure 6.16, under normal conditions, even though $x_{Vebb}(t)$ shows more influence by wave variation than $x_A(t)$, $y_{Vebb}(t)$ still experienced predominance by spring/neap tidal cycle. $y_{Vebb}(t)$ has nearly opposite trend with $x_{Vebb}(t)$, $x_{Vebb}(t)$ reach max value corresponding to $\hat{Q}_{\max}$ at spring time, while $y_{Vebb}(t)$ has min value.

When a large hurricane comes, large waves make $x_{Vebb}(t)$ decrease significantly leading to a remarkable decrease of $y_{Vebb}(t)$ from 11.9×10^6 m^3 to 10.1×10^6 m^3 (Figure 6.16). The erosion rate due to large waves is enhanced because the event occurred during erosion process at spring tide.

In each of example above the choice of a shorter T_{morph} would lead to shorter response and vice versa.

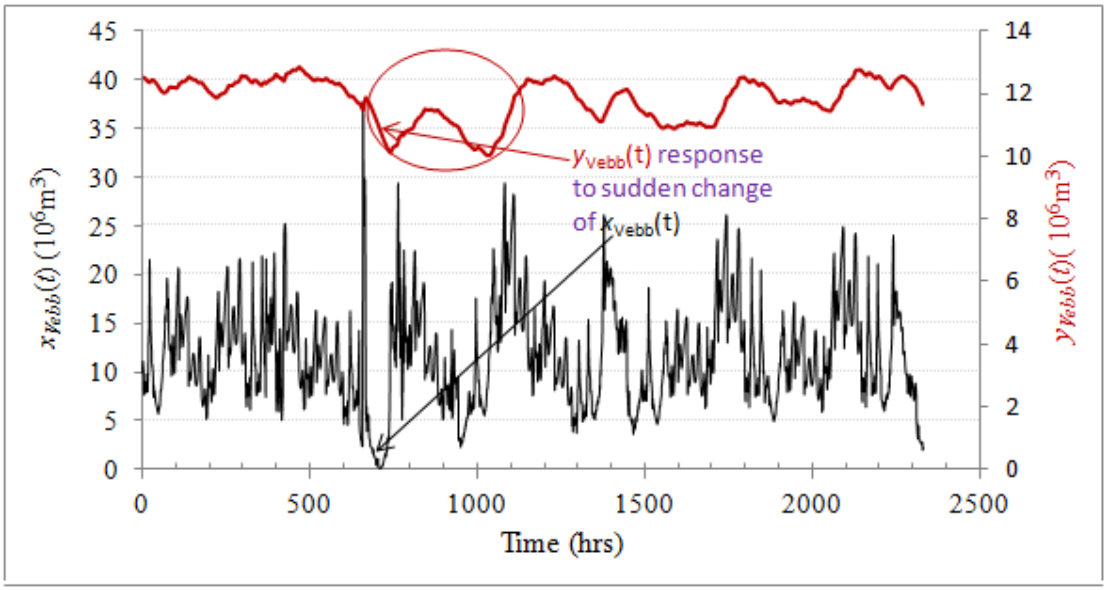

Figure 6.16: Time series of $x_{Vebb}(t)$ as in (6.13) based on $H(t)$, $\hat{Q}_{tide}(t)$ and the corresponding $y_{Vebb}(t)$ as in (6.14) with T_{morph}=30 days =360 hours.

6.5.2 T_{morph} from 24.5 hour moving window analysis of tides

To determine the morphological short-term time scale, one usually analyses data from a field survey or a physical model, of for example, the inlet throat area or the volume of flood/ebb tidal delta. Such data are however scarce because of the significant cost involved. An alternative approach is to use numerical models which are often unreliable due to uncertainties in translating physical phenomena into mathematical terms. In this section we apply a new approach to find T_{morph} by using the 24.5 hour moving window described in Chapter 3 applied to a number of inlets in AU with different waves and tides for different events as well as for different basin scales as demonstrated in Chapter 4. The expectation from this method is to provide a relationship between T_{morph} and the relative wave dominance $\frac{\sqrt{gH^5}}{\hat{Q}_{tide}}$. For the present purpose, $\hat{Q}_{tide}$ is estimated as the potential peak tidal discharge $\hat{Q}_{\text{tide,pot}} = \pi A_b R_{to} / T$.

Analysis of different morphological features, e.g. A_c or V_{ebb} or the hydraulic gain G often leads to different values of T_{morph}. T_{morph} is then chosen as the average value of T_{morph} from $\overline{\eta_{24.5}}$, *Stdv* or G. H is chosen as the maximum H_s of storm event or $\overline{H_s}$ during closure period for closure event. The tidal range in the ocean R_{to} is the average ocean tidal range during the storm or closure period.

6.5.2.1 Analysis of tidal records for closure events

Table 6.1 shows the summary of parameters such as A_b, $\overline{H_s}$, $\overline{R_{to}}$, relative wave strength $\frac{\sqrt{gH^5}}{\hat{Q}_{tide,pot}}$ and T_{morph} for 13 closure events of 7 inlets. The available data during these events and their fitting curve for T_{morph} are presented in Appendix 3. In among plenty of ICOLLs in NSW Australia, the inlets with bay area A_b<0.7 km^2 show clear cut closing process with exponential decay. It seems logical because the smaller lagoons have short closing period compared to the duration of wave events cf. Figure 6.7b,

Table 6.1. Summary external forces and T_{morph} for 13 closure events for details see Appendix 3

No	Inlet Name & event	Time event	A_b	$\overline{H_s}$	$\overline{R_{to}}$	$\sqrt{gH^5}$	$\hat{Q}_{tide,pot}$	$\frac{\sqrt{gH^5}}{\hat{Q}_{tide,pot}}$	T_{morph} from $\overline{\eta_{24.5}}$	T_{morph} from *Stdv*	T_{morph} From G_2	T_{morph} Chosen
			km^2	m	m	m^3/s	m^3/s	[-]	h	h	h	h
1	Avoca 1	9/7 - 3/8/10	0.63	1.6	0.98	10.1	43.4	0.23		77	80	78.5
2	Avoca 2	5/11 - 28/11/10	0.63	1.4	0.77	7.3	34.1	0.21	86	92		89.0
3	Avoca 3	26/4 - 3/5/11	0.63	2.23	0.76	23.2	33.6	0.69	38.3	31		34.7
4	Avoca 5	24/4-30/4/08	0.63	1.9	0.51	15.6	22.6	0.69		50.3	41.1	45.7
5	Wamberal	29/4 - 3/5/11	0.6	2.2	0.78	22.5	32.9	0.68			39	39
6	Werri 1	7/11 - 19/11/09	0.14	1.25	0.77	5.5	7.6	0.72			25	25
7	Werri 2	1/04 - 13/05/10	0.14	1.4	1	7.3	9.8	0.74			54	54
8	Dee Why 1	17/3 - 16/4/12	0.24	1.3	0.6	6.0	10.1	0.60		31	22	26.5
9	Dee Why 2	18/4 - 28/5/12	0.24	2	1	17.7	16.9	1.05		30	42	36
10	Terrigal 1	18/1 - 5/2/11	0.52	1.6	0.6	10.1	21.9	0.46		47.2	43.6	45.4
11	Terrigal 2	13/3-24/3/12	0.52	1.6	0.92	10.1	33.6	0.30		120		120
12	Cockrone	21/6-25/6/08	0.33	1.8	0.85	13.6	19.7	0.69		65	59	62
13	Back lagoon	14/12-18/12/10	0.36	0.94	0.61	2.7	15.4	0.17		99.2		99.2

As can be seen from Table 6.1, 0.94 m < $\overline{H_s}$ < 2.3 m and 0.5 m< $\overline{R_{to}}$ <1 m. This results in $\frac{\sqrt{gH^5}}{\hat{Q}_{tide,pot}}$ ranging from 0.17 (Back lagoon) to 1.05 (Dee Why event 2). Consequently T_{morph} ranges from 25 hours to 120 hours. T_{morph} is normally average of T_{morph} from *Stdv* and G_2. These are more closely associated with the inlet closing process than T_{morph} derived by fitting $\overline{\eta_{24.5}}$ which may continue varying after closure due to rain water input. Some cases have only one option of T_{morph}

due to only one parameter being suitable for exponential curve fitting. The relationship between $\frac{\sqrt{gH^5}}{\bar{Q}_{\text{tide,pot}}} \sim T_{\text{morph}}$ is presented in Figure 6.17 and

$$T_{morph} = 31.6\left(\frac{\sqrt{gH^5}}{\bar{Q}_{\text{tide,pot}}}\right)^{-0.69} \text{ (h)} \qquad (6.15)$$

Even though the correlation, R^2=0.62, is modest, the results show a clear trend of T_{morph} decreasing with increasing $\frac{\sqrt{gH^5}}{\bar{Q}_{\text{tide,pot}}}$.

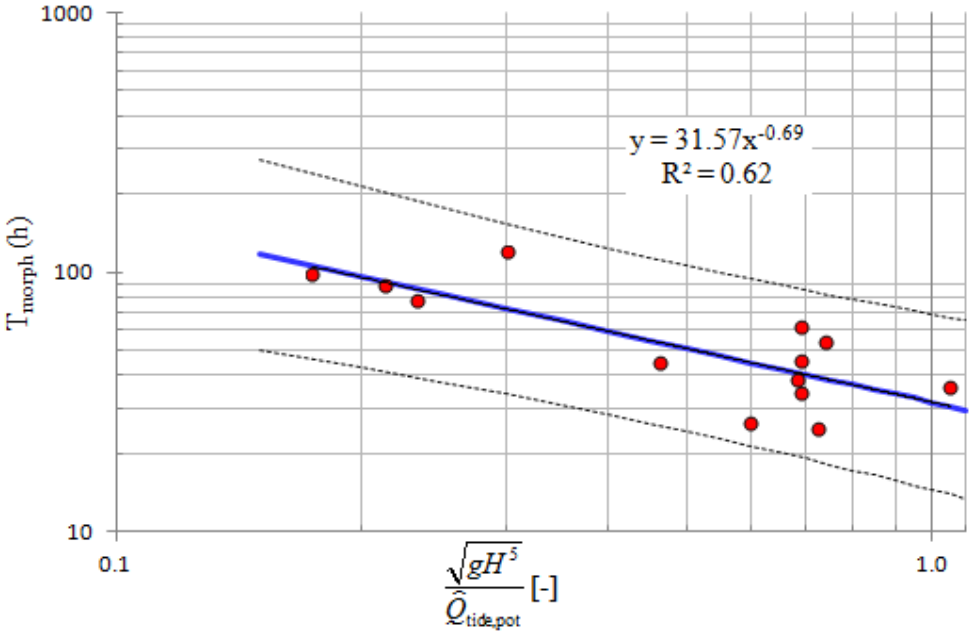

Figure 6.17: T_{morph} vs $\frac{\sqrt{gH^5}}{\bar{Q}_{\text{tide,pot}}}$ with 95% confidence limits of 13 closure events corresponding to 7 NSW inlets with A_b<0.7 km^2.

6.5.2.2 Analysis of tidal recovery after a major flood in the Brunswick River

Apart from closure events, the 24.5 hour moving window was also used to analyse tidal records during a major flood event at Brunswick River (Section 4.2). The hydraulic response shows that the gain of the dominant component G_2 gets reduced during the peak discharge then recovers more or less exponentially back to the equilibrium state from before the storm (Figure 4.18). The reasons being

(a) rise of mean water level cause surface water area increase, and/or

(b) river flow increase results in increased velocity, increasing the non-linear friction term in the momentum equation.

The increasing of G_2 trend at peak water level (Figure 4.18) is similar to the tidal analysis of Hinwood & McLean (2001) for Lake Conjola. However, they found that the phase lag at that time decreased, while the phase lag at the Brunswick River entrance increased. This means there is no clear evidence of enlarged entrance due to scour out by large Q_f leading to more hydraulic efficiency during the Brunswick event.

The modest size of the G_2 loop (Figure 4.19) shows that the Brunswick River entrance does not really change much, even under such a severe event, perhaps due to the stabilizing effect of the two breakwaters. The time scale obtained by fitting G_2 during recovery process is around 76 hours. This may be a hydraulic time scale T_{hyd} rather than morphological time scale T_{morph}.

A quite similar pattern was observed at Pensacola Pass in the US (Section 4.4, Figure 4.37) relation to Hurricane Katrina.

It can be concluded that the 24.5 hour moving window method can infer T_{morph} relation to inlets with small bay areas especially for closure events but not for larger inlets or inlets protected by breakwaters. For the larger partly regulated system, the morphology change is usually not significant enough compared to the cross section to be measurable via the tidal record. Hence the T determined by the method for these larger systems is just hydraulic timescale T_{hyd} not T_{morph}.

6.5.2.3 Analysis of tidal efficiency changes due to storm surges at Thyborøn Inlet

In the previous section it was found that changes to the tidal response in the Brunswick River inlet during a major flood event were due to temporarily different hydraulic parameters (Q_f and A_b) rather than due to morphological change e.g. scour of the entrance bar.

Thyborøn inlet in Denmark, which has been steadily opening and becoming more hydraulically efficient (Knudsen et al, 2012) over a number of years experiences a different kind of major flushing events, which might be the cause of the long term opening. That is, while the Limfjord system, Figure 6.18, has a small catchment compared to its surface area and therefore does not flood due to rain fall, it experiences large high water events (1.5 m to 2 m above MSL, see Figure 6.19) driven by storm surges in the North Sea. In the following we look for evidence of lasting hydraulic efficiency gain due to the strong outflow which follows these high water level events.

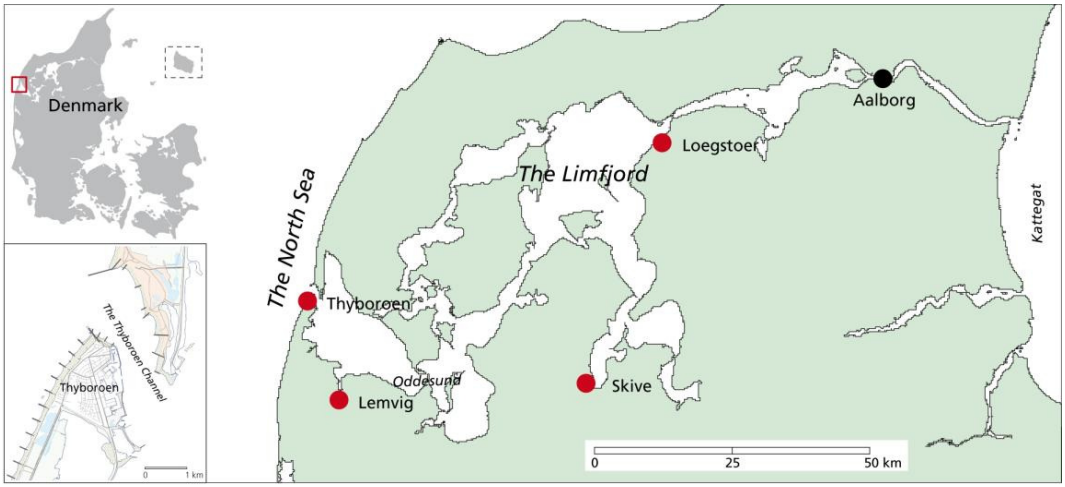

Figure 6.18: The Limfjord estuary, Denmark is connected to the North Sea through the Thyborøn inlet. Source: Knudsen et al (2012).

The data in Figure 6.19 show that these surges, with periods of 3 to 5 days, penetrate with full peak height (surge 2, 3, 4).

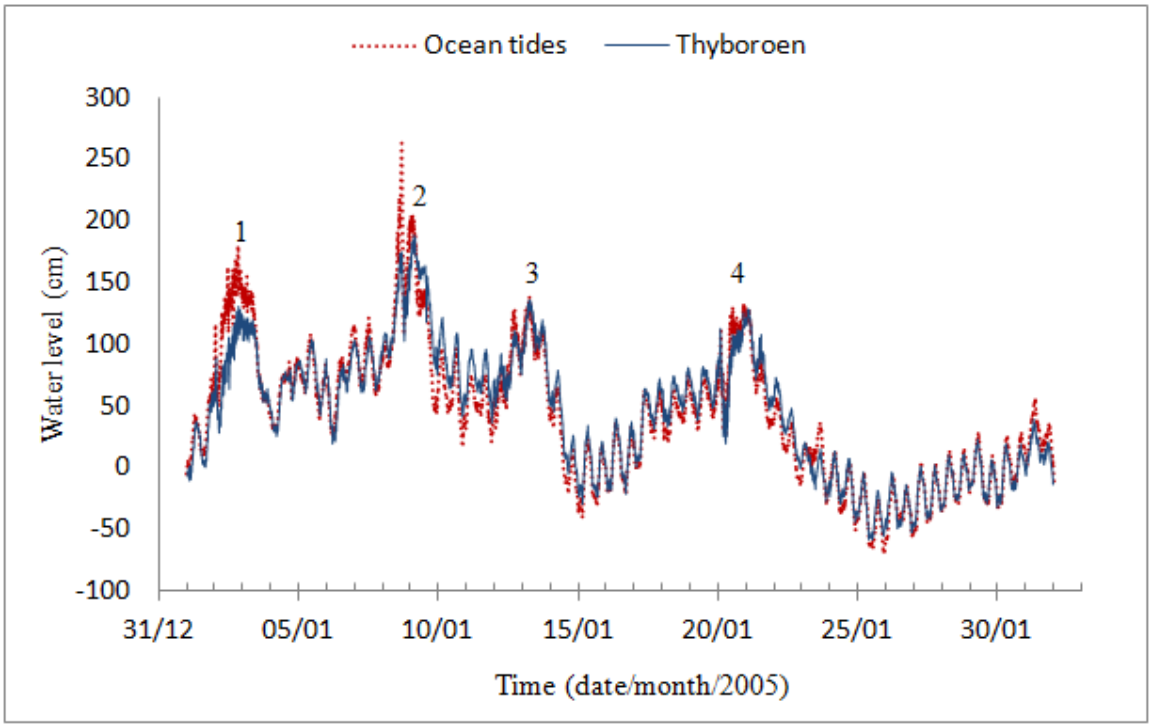

Figure 6.19: Water levels in the North Sea (Ocean tides) and Thyborøen station, station shown in Figure 6.18. Data courtesy of the Danish Coastal Authorities. During January 2005, 4 storm surge events penetrated with nearly full peak height through Thyboroen.

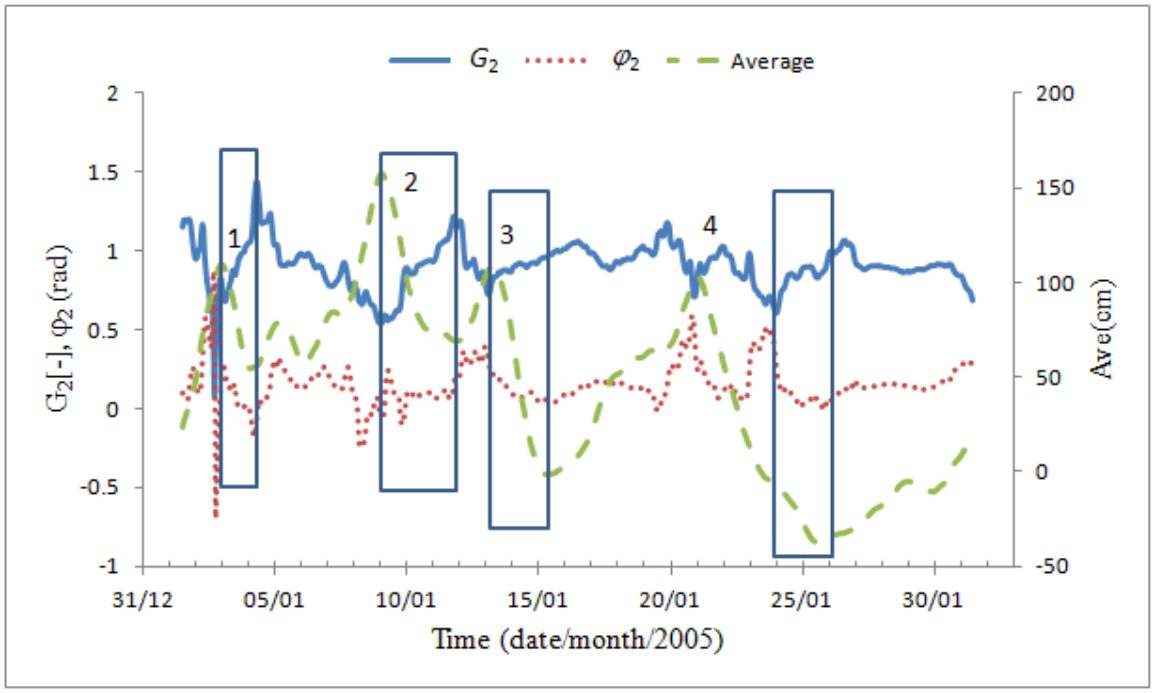

Figure 6.20: Gain G_2 and phase lag φ_2 of the primary component, and $\overline{\eta_{24.5}}$ by 24.5 hour moving window at Thyborøen station.

Figure 6.20 shows the gain G_2 and phase lag φ_2 of the primary component and $\overline{\eta_{24.5}}$ by 24.5 hour moving window. During surge events 1, 2, 3 in Figure 6.20, following the flushing event $\overline{\eta_{24.5}}$ drops, G_2 increases and φ_2 reduced. This indicates that the inlet scours out due to the significant outflow resulting in increased hydraulic efficiency. However there is no evidence of a long-term increase of the hydraulic efficiency.

During 22-24 January of surge event-4 drainage process, the non-linear friction term reduces G_2 and increases φ_2. After that, from 24-26 January the increase of hydraulic efficiency takes place. This was supported by measured entrance cross section as presented in Knudsen et al (2012).

6.6 CONCLUSIONS ON MORPHODYNAMICS

The description of inlet morphodynamics of different time scales is presented in this chapter. The different methods used to study the inlet morphodynamic were reviewed in which seasonal opening/closure of inlets is an important aspect.

Regarding the non-seasonal opening/closing of inlets, the fraction of time the inlet is open varies quite erratically for $\frac{\hat{Q}_{\text{tide, pot}}}{\sqrt{gH^5}}$<100 but beyond this value no inlets have been reported closed

for extensive periods. The average time of staying open $\overline{T_{\text{open}}}$ is somewhat better behaved with an identifiable trend with $\frac{\hat{Q}_{\text{tide, pot}}}{\sqrt{gH^5}}$ as in Eq (6.6) but with a range corresponding to a factor 5 either way. However, it was difficult to determine the exact relationship for fully exposed, natural (never artificially opened) systems with the presently available data.

The determination of T_{morph} from transient inlet behaviour with assumption of the linear system as in (6.1) and general solution as well as specific solutions were presented. The illustration is based on (5.6 and 5.23) for Pensacola Pass inlet. The illustration shows that the effect of large waves $A(t)$ is insignificant compared to the influence of spring/neap tide variation, whereas it is profound on $V_{ebb}(t)$.

T_{morph} from 24.5 hour moving window analysis of tides has been carried out for many closure events with A_b<0.7 km^2 in NSW, Australia, which showed distinctive exponential trend. The results show a clear trend of T_{morph} decreasing with increasing $\frac{\sqrt{gH^5}}{\bar{Q}_{\text{tide,pot}}}$. See Figure 6.17 and Eq (6.15).

It can be concluded that the method of 24.5h moving window can be used to determine the time scale of change of tidal response through typical storm events with 2-5 days duration. For smaller, untrained inlets this response is usually due to morphological change. For larger trained inlets, e.g. the Brunswick River entrance, the response changes are mainly hydraulic i.e. larger T_{hyd} by e.g. (Figure 4.18) due to greater A_b during flood or increase frictional resistance to tides due to superimposed flood flow as per Eq (2.28).

The 24.5 hour moving window method is also effective in analysing surge events for large systems such as Thyborøn, Denmark, which was found to have higher hydraulic efficiency following the flushing of the inlet by the outflow which follow major surge.

Chapter 7

ASSESSMENT OF THE STATE OF THE ART OF NUMERICAL MORPHOLOGICAL MODELS OF INLETS

7.1 INTRODUCTION

While inlet morphodynamics was addressed broadly in Chapter 6, the large literature on detailed process based models was not covered. These models are extremely popular with consultants and researchers who expect to learn physics from these models. However, it is not correct for all cases. Hence, in order to assess the ability of state of the art numerical models for inlet morphodynamics, it was decided to test a well calibrated, new numerical model on its 'home turf' considering a major event, where a clear morphological signal was expected. The choice was to test the CMS model of the US Army Corps of Engineers at modeling the morphological changes caused by Hurricane Katrina on Pensacola Pass. The best morphodynamic results obtained from the model show that CMS model has poor predictive capability with respect to simulating morphological seabed changes associated with that major event and the reasons for that are pointed out in Section 7.4.

We are grateful for the generous support we received from Dr Nick Kraus, and after his untimely illness and passing away, from his younger colleagues Dr Julie Dean Rosati, Dr Lihwa Lin, Tanya Beck and others.

7.1.1 Pensacola Pass

Pensacola Pass, the subject location for the present test, is located at $30^{o}19.5'$N and $87^{o}18.5'$W, in the westernmost part of the State of Florida in Escambia County (Figure 4.29). This pass connects the Gulf of Mexico to Pensacola Bay. Pensacola Pass is bordered by Santa Rosa Island with a sand barrier 80 km long to the East and a 24 km sand spit off Perdido key to the West (Figure 7.1). The inlet is quite natural without structures along the shore line of Santa Rosa Island, however, two small jetties (100 m long) on Perdido key inside the Pass allow a significant amount of sand flow through and over them (Browder and Dean, 1999).

The Pass is an un-jettied Federal navigation inlet with an authorized channel depth of 11 m (MLLW) and width of 150 m, which used to be maintained by dredging. Since 1991, no dredging has been conducted for the channel. The pass entrance width is around 1050 m. The tide in this region is micro-tidal, with mainly diurnal tide with an average tidal range around 0.43 m

(Armbruster, 1997). The tidal prism (P) at spring tide is ca 2.7×10^8 m^3 and the throat area is ca 10^4 m^2 (Powell, 2006).

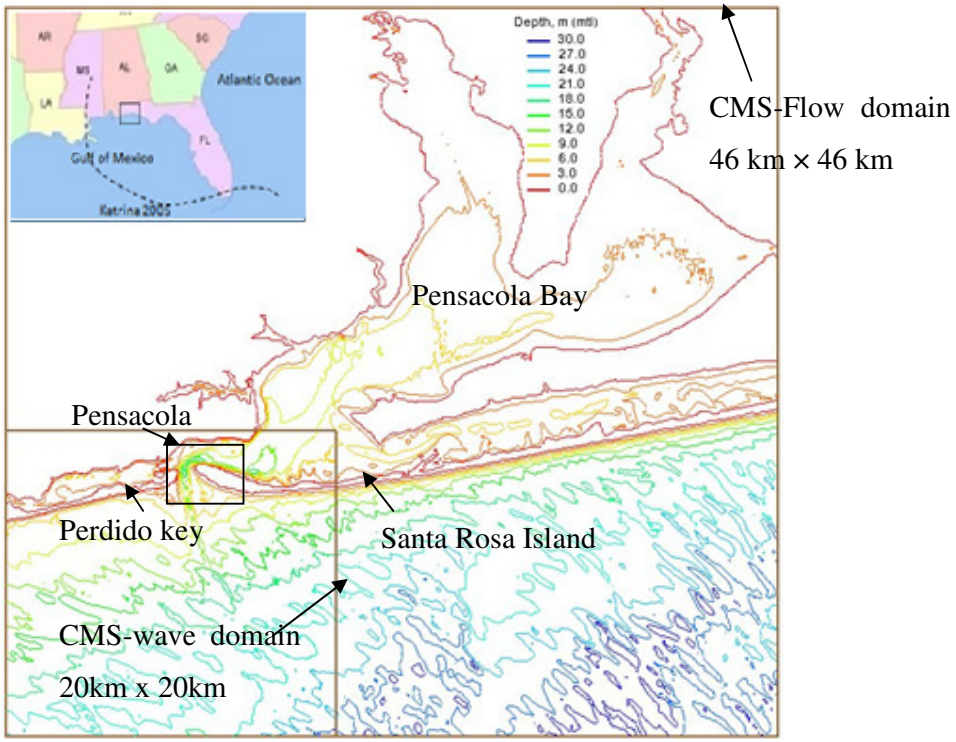

Figure 7.1: Location of the study area and the Domain area for CMS-Flow and CMS-Wave for Pensacola Pass.

The annually average significant wave height is ca 0.6 m with typical wave period of 5 s. Hindcast data from 1976 to 1995 by USACE (Tracy and Cialone, 1996) indicate 60% incident waves from the east, while representative wave height from CIRP source is 1m. The average maximum flood and ebb currents in the channel are 0.82 m/s to 0.92 m/s respectively (Degnon, 1996). Sediment size varies depending on the region, inside Pensacola bay and offshore grain size is fine 0.21 mm, with sand on the barrier of Santa Rosa Island and Perdido Key, 0.36 to 0.4 mm (Work et al., 1991) and average grain size in the various swash zones and channels is 0.32 mm (Lin et al., 2009).

Dredging to maintain channel navigation was carried out frequently with a dredge quantity of 1.76×10^5 m^3/year from 1883 to 1958, increasing to 4.24×10^5 m^3/year from 1958 to 1991, and rapidly jumping up to 7×10^5 m^3/year in 1990 and 1998 (Browder & Dean, 1999). Since then, no more information of dredging is available.

The storm history in this area from 1880 to 2009 showed that there were 48 storms, mostly hurricanes. From statistics, the 100-year storm event peak surface elevation, including tide, wind and surge, barometric pressure effects is approximately 3.54 m above MSL. The most erosive

storms in recent years were Hurricane Elena and tropical storm Juan (1985), Hurricanes Erin and Opal (1995), Hurricane Georges (1998), tropical storm Isidore (2002), Hurricane Ivan (2004) and Hurricane Dennis and Katrina (2005). The available hydraulic data and coastal areas were presented in section 4.4.1.

- **Impact of recent hurricanes on the Pensacola Pass coastal area**

According to Browder (2004), approximate erosion loss of 2.3×10^6 m^3 above the 4.6m contour was observed during Hurricane Ivan (2004). After Denis, Hurricane Katrina occurred August 2005, a Category 1 hurricane at landfall, was more intensive than Hurricane Ivan with a central pressure of 902mb and its peak wind intensity of 280 km/h (Fritz et al., 2007). Fortunately, it had its landfall along the boundary of Louisiana and Mississippi, around 235 km to the west of Pensacola. Hence the erosion caused by Katrina was limited and much less compared to the loss by Hurricanes Ivan and Denis as cited by Claudino-Sales et al (2008) and Clark and LaGrone (2006).

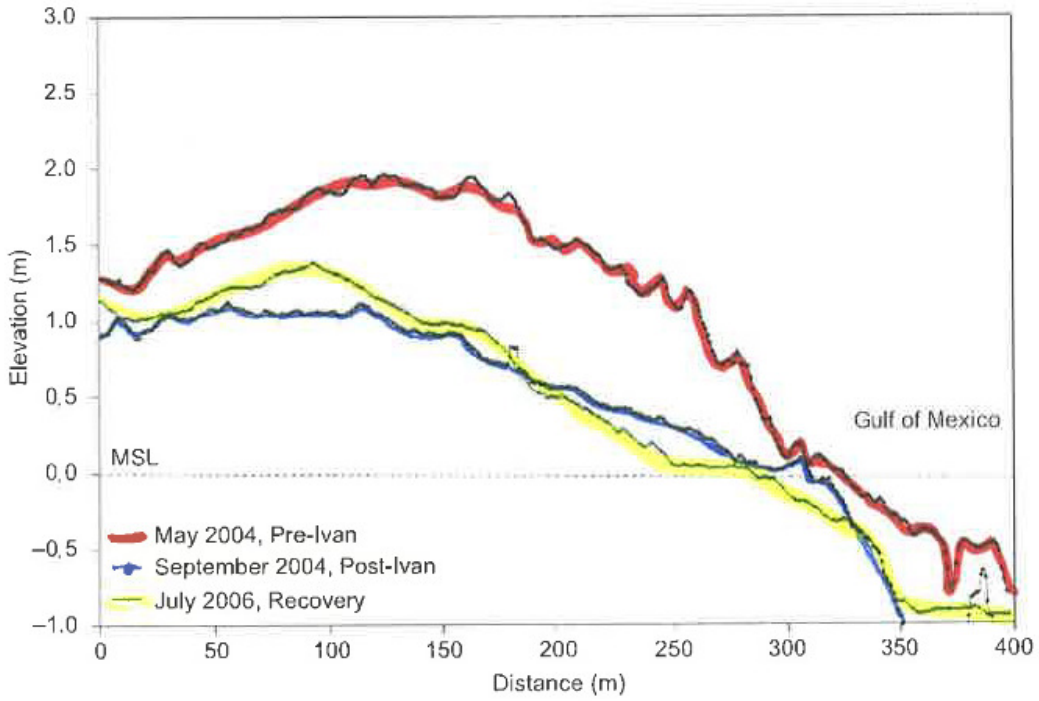

Figure 7.2: Average profiles of Fort Pickens units for May 2004 (Pre-Ivan), September 2004 (Post-Ivan) and July 2006 (recovery). Figure from Houser & Hamilton (2009).

Hurricane Katrina's impact to Santa Rosa Island was predominantly by swash (Claudino-Sales et al., 2008). However, dune recovery on this island before Hurricane Dennis and Katrina was insignificant and allow overwash penetration into the bay and breaching of the sand spit (especially the narrow and lower section in Fort Pickens unit in Figure 4.29, around 5 km from right tip of the

entrance). Houser & Hamilton (2009) quantified the beach and dune recovery by comparing bathymetry data between pre-Katrina and a year after using LiDAR. Their results show that to the west of Pensacola beach (Fort Pickens unit- closer to the entrance), the shoreline retreated by an average of 30m, and no significant shoreface recovery was observed (Figure 7.2).

a)

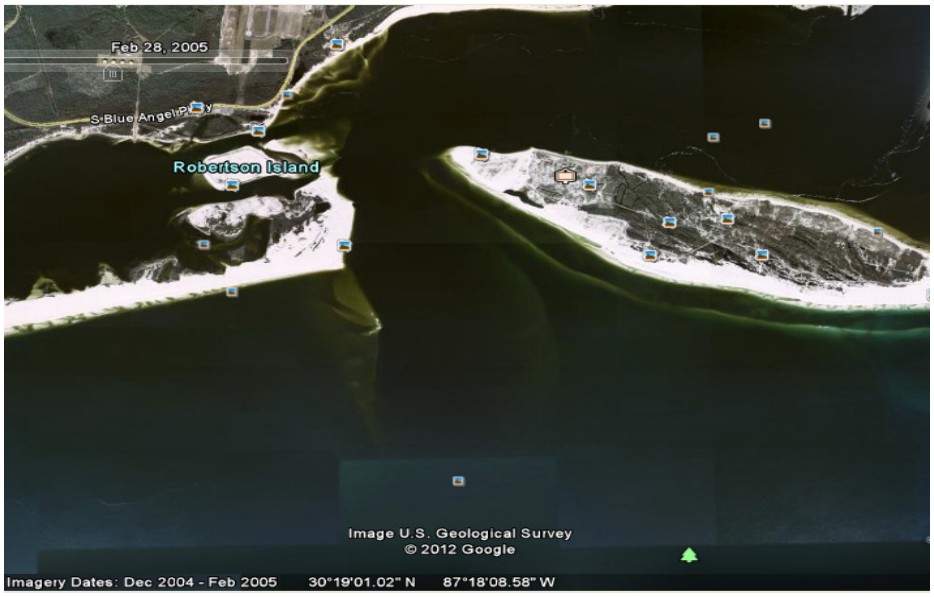

b)

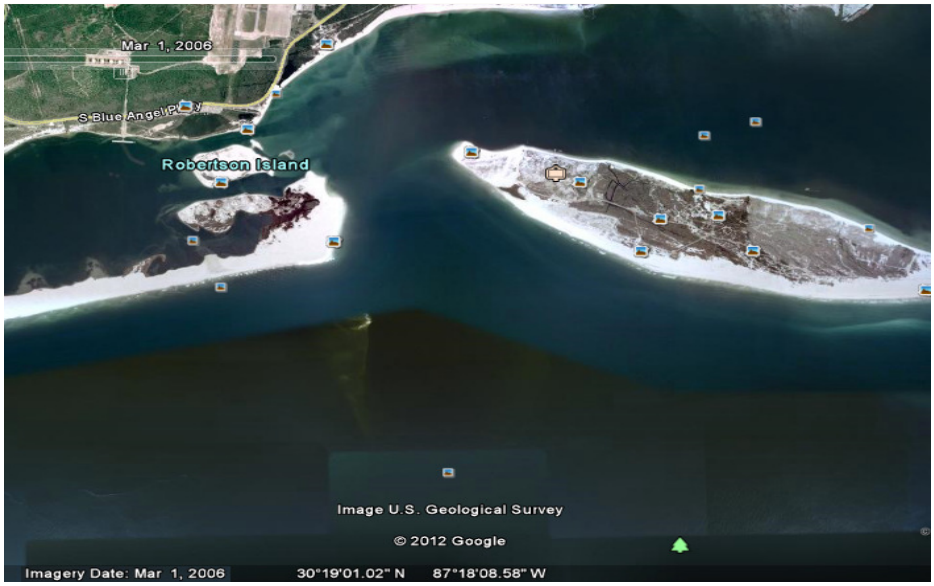

Figure 7.3: Pensacola inlet images (a) before Katrina (2/2005) and (b) after Katrina 1/3/2006 from Google Earth.

Hapke & Christiano (2007) suggested that the shoreline recovery within Fort Pickens unit may be less than 10m between September 2005 (just after Katrina) and July 2006. This was due to a lack of available sediment, which commonly occurs in breaches and washover where sediment is

transported into the lagoon. The surviving dune probability was unstable and continued to erode due to insufficient sediment supply (Houser et al., 2007).

The before and after photos in Figure 7.3 show that the shoreline changes caused by Hurricane Katrina were moderate while the inlet shoals probably changed significantly, albeit without supporting measurements.

7.2 THE CMS MODEL

The CMS model is one of the state of the art numerical models with a non-equilibrium sediment transport (NET) simulation (Wu et al., 2010), which is expected to be superior to equilibrium models such as MIKE21 (DHI, 2011) and Delft 3D (WL| Delft Hydraulics, 2011).

7.2.1 Governing equations for the water motion

The CMS hydrodynamic model (called CMS-flow) computes unsteady water levels and depth averaged current velocities $\vec{u} = (u, v)$ by solving the usual 2D horizontal shallow water equations for continuity and momentum cf. Wu et al. (2010).

The presence of waves, is acknowledged in the bed shear stress formulation:

$$\begin{aligned} \tau_{bx} &= c_f \rho (u^2 + v^2 + 0.5 u_{wm}^2)^{1/2} u \\ \tau_{by} &= c_f \rho (u^2 + v^2 + 0.5 u_{wm}^2)^{1/2} v \end{aligned} \tag{7.1}$$

where u_{wm} is the maximum orbital wave velocity. Here, it is important to note that, this bed shear stress will always be in the direction of the current, which is not always realistic. Correspondingly, the calculated equilibrium sediment transport rates $\overrightarrow{q_{s,eq}}$ will always be in the direction of the current. This assumption is one of reasons leading to unrealistic morphodynamic predictions in Section 7.4.

7.2.2 The wave model

The CMS-Flow is coupled with a 2-D spectral (phase-averaged) wave transformation model called CMS-Wave (formerly known as WABED, an acronym for "Wave-Action Balance Equation Diffraction"). Wave action density is chosen in this model since it is conserved when waves travel across a variable current field. The term "phase-averaged" means that the wave shape is not resolved, so velocity skewness or acceleration skewness, which are important for wave sediment transport modeling (Nielsen 2009, p 270), are not predicted. This underestimates the wave role in transporting sediment. The lack of such surf-zone details in the CMS model is another reason for its underestimation of the wave-erosion during Hurricane Katrina as shown in Section 7.4.

There are four optional wave breaking formulae falling in two groups:

(1) wave breaking energy dissipation with various breaker criteria and by truncating the tail of the Rayleigh distruction extended by Miche (1944) and extended Goda (1970);

(2) integral wave energy dissipation over the spectrum with a bore-type model (Battjes & Janssen 1978 or Chawla & Kirby 2002). Based on comparisons between simulated results and laboratory data, 'extended Goda' and 'Battjes & Janssen' are suggested to produce accurate wave heights for coastal inlets (Zheng et al., 2008).

7.2.3 The sub-model coupling

In the CMS model, the flow, wave and morphology changes are dynamically coupled as flow chart in Figure 7.4.

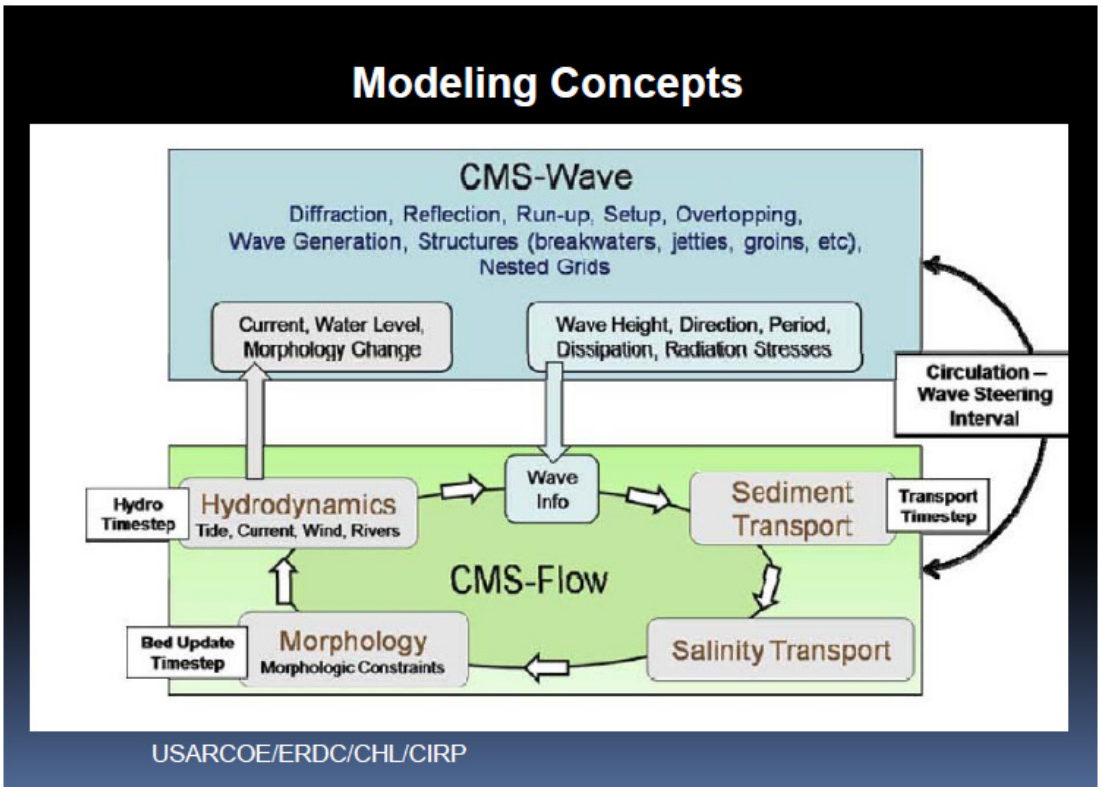

Figure 7.4: Flow chart of the CMS morphodynamics modeling process (CIRP, 2011).

The wave model is executed first for one wave steering interval. Wave information such as wave height, period, direction and radiation stress gradients are then passed to the flow and sediment transport models. Wave variations are interpolated on the flow grid. The grid used in the wave model can be different from the flow model grid, however the same grid configuration must be used for flow and sediment transport models. Time steps for flow and sediment transport can be different depending on the stability of individual models.

7.2.4 Governing equations for sediment transport

The CMS model provides three sediment transport formulations viz.,

(i) equilibrium model: total-load formulation that solves the Exner equation for the bed level variation as in (7.2);

(ii) semi-equilibrium model: formulation that solves suspended-load transport using the advection-diffusion equation and the bed-load mass balance equation (Buttolph et al., 2006);

(iii) non-equilibrium model: formulation that solves non – equilibrium total load formula as in (7.5). Brief details of the three models are now given:

7.2.4.1 Equilibrium total-load transport model

The equilibrium model is based on

$$\left(1-p'_{\mathrm{m}}\right)\frac{\partial h}{\partial t}=\frac{\partial q_{\mathrm{s,eq,j}}}{\partial x_{\mathrm{j}}}+\frac{\partial}{\partial x_{\mathrm{j}}}\left[D_{\mathrm{s}}\left|q_{s,eq}\right|\frac{\partial h}{\partial x_{\mathrm{j}}}\right] \tag{7.2}$$

where, p'_m is sediment porosity, D_s is an ad-hoc bed slope coefficient to improve model stability, $q_{\mathrm{s,eq}}$ equilibrium total load sediment transport and h is still water depth. This model based on the assumption that the sediment transport vector $\vec{q_s}$ is in balance instantaneously with the forcing processes at each computational node. In relation to Figure 7.4, this means that an equilibrium model assumes the full equilibrium q_{s} from the very start of the sand bed.

The $q_{\mathrm{s,eq}}$-formulae that are available in the CMS are: Watanabe (1987) which computes $\overrightarrow{q_{\mathrm{s,eq}}}$ and the Lund-CIRP model which computes $q_{\mathrm{s,eq}}$ in the direction of the current. For more detailed formulae one can refer to the CMS model documentation (Buttolph et al., 2006).

7.2.4.2 Semi-Equilibrium total-load transport model

A semi equilibrium version is available where the modified Exner-Equation (7.2) is combined with expressions for sediment pickup P and deposition rates:

$$\left(1-p'_{\mathrm{m}}\right)\frac{\partial h}{\partial t}=\frac{\partial q_{\mathrm{s,eq,j}}}{\partial x_{\mathrm{j}}}+\frac{\partial}{\partial x_{\mathrm{j}}}\left[D_{\mathrm{s}}\left|q_{s,eq}\right|\frac{\partial h}{\partial x_{\mathrm{j}}}\right]+P-w_{\mathrm{f}}c_0 \tag{7.3}$$

with

$$P=-\varepsilon\left.\frac{\partial c}{\partial z}\right|_{z=a}=c_a w_f\,. \tag{7.4}$$

For more details, see the CMS model documentation (Buttolph et al., 2006).

7.2.4.3 *The Non-equilibrium model (NET)*

It is generally accepted that q_s changes gradually towards the equilibrium value $q_{s,eq}$. The CMS model uses the adaptation length approach suggested by Wu (2004), which is discussed below, to mimic this process.

The adaptation length L_t for bed level change is defined via the bed updating equation

$$(1-p'_m)\frac{\partial h}{\partial t}=\frac{1}{L_t}\left(q_{s,eq}-q_s\right) \tag{7.5}$$

which is used instead of the (physically based) Exner equation. The operator is free to choose a convenient value of L_t but a default value of 10m is suggested. This novel, but basically ad-hoc approach to bed updating, avoids the difficult numerical issues associated with the Exner equation see e. g. Callaghan et al. (2006b).

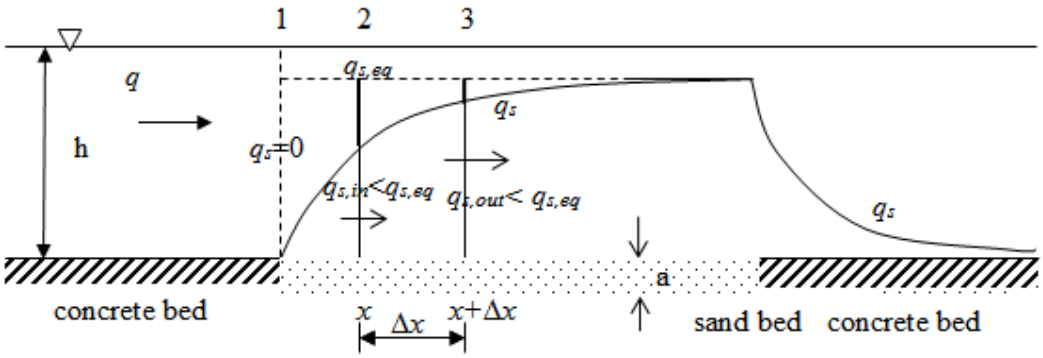

Figure 7.5: Sketch of the adaptation of q_s from non-equilibrium to equilibrium.

The physical meaning of (7.5) in relation to the conservation of mass e.g. the Exner equation can be illustrated as follows. Take the simple example of a flume with a sand bed following a concrete bed, so that q_s=0 at the start of the sand bed - cross section 1- in Figure 7.5.

The flow discharge per unit width q is maintained constant corresponding to the equilibrium sediment transport $q_{s,eq}$ which will occur some distance along the sand bed. The sediment transport rate $q_s(x)$ gradually increases towards the equilibrium value $q_{s,eq}$ and L_t is the length scale of this adjustment process as in (7.8). On the concrete bed after the sand section, $q_s(x)$ will again gradually reduce to 0. If we then assume that the sediment transport rate adjusts in accordance with

$$\frac{\partial q_s}{\partial x}=\frac{1}{L_t}\left(q_{s,eq}-q_s\right) \tag{7.6}$$

then the rate of change is proportional to the deviation from the equilibrium value. Then (7.5) follows from insertion Eq (7.6) in the Exner equation:

$$(1-p'_m)\frac{\partial h}{\partial t} = -\left(1-p'_m\right)\frac{\partial Z_b}{\partial t} = \frac{\partial q_s}{\partial x} = \frac{1}{L_t}\left(q_{s,eq} - q_s\right) \tag{7.7}$$

In other words, equation (7.5) is correct if q_s behaves as an exponential,

$$q_s = q_{s,eq}\left(1-e^{-x/L_t}\right), \tag{7.8}$$

which is a solution to (7.6).

The transport adjustment time scale T_t for the scenario in Figure 7.5 would be $T_t=L_t/\langle u\rangle$, corresponding to fluid particles on the average taking $L_t/\langle u\rangle$ to travel the distance L_t. When suspended load is dominating, an alternative time scale is defined by vertical scale of the suspension distribution L_s and the sediment settling velocity w_f, $T_t=L_s/w_f$. For some suspension-dominated scenarios, this may be several seconds, corresponding to the recommended default value L_t=10 m and <u> ~ 1 m/s. If q_s is dominated by bed load, q_s reaches $q_{ts,eq}$ very quickly, T_t<<1 s. So, for a bed-load dominated case, the physically based L_t should be very small (<<10 m). This would however most likely lead to computational instability.

The options for choosing L_t in CMS, are (a) a sum of suspended load and bed load adaptation length L_s, L_b as q_t is a combination of suspended load and bed load, or (b) the maximum of the two values, i.e., L_s or L_b, or (c) given by user, i.e..

a) $L_t=r_sL_s+(1-r_s)L_b$ or
b) $L_t=\max(L_s, L_b)$; or
c) L_t = user defined

The adaptation length L_t as per (b) i.e., maximum of either L_s or L_b is recommended by CIRP experts to provide the most stable execution of CMS.

Wu (2007) and Sanchez & Wu (2011) recommended that the adaptation length should be investigated from field measurements on morphology changes. That is, L_t is a calibration parameter or, in Magnus Larson's words: "a convenient ad-hoc approach to introduce some spatial delay effects" (personal communication 2011).

The sediment adjustment length L_t is used in the CMS model because of the well established numerical issues faced when solving the Exner equation in terms of stability and accuracy, even in significant simpler scenarios than inlets where breaking waves are important as well as tidal currents. A brief summary of these difficulties follows.

The 1D sediment conservation law for bathymetry change (Exner Equation) is

$$\frac{\partial Z}{\partial t} = -\frac{\partial q_x}{\partial x}, \tag{7.9}$$

where Z is bed elevation and q_x is the (bulk volume) sediment transport rate in the x-direction for a given porosity. Although this appears simple to solve, and can be solved analytically for reasonably simple q_x-Z relationships, it turns out that it is difficult to solve numerically, with simple and memory efficient schemes being unconditionally unstable (Press et al., 1992). Various schemes introduce ad-hoc diffusion (as in Equation (7.2) and (7.3)) that artificially reduces sand wave amplitude and dispersion, that generates spurious bed level oscillations (Callaghan et al., 2006b; Roache, 1972). In addition, second order, finite difference schemes result in high wave number (or frequency) oscillations that result in morphological change being reduced to noise (Johnson and Zyserman, 2002).

From our stability analysis with 1D and 2D cases, it was found that in order to obtain close agreements with analytical solutions as well as stability, the bed update scheme should:

- be upwind,
- the number of grid cells per bed-form wave length should be larger than 10 and
- the time step should be chosen so that Courant-Friedrich-Levy condition CFL ≤0.7 for 2D and CFL≤1 for 1D.

For example, a Sand dune in inlet channels has been found to have wave lengths between 5 to 10 times the flow depth (Wu, 2007). For example, in this inlet where the water depth is about 10 m, these sand waves would range from 50 m to 100 m and hence grid size should be no greater than 5 m or less. Assuming these bed forms migrates with speeds of approximately 1 m per hour; Δt for bed updating should be less than 3.5 minutes, which is easily achieved albeit with significant introduction of smoothing (e.g., Callaghan et al. 2006b, figure 4). Whereas in coastal seas, the dominant bed forms are long and short wave ripples with length scale of 10^3-$10^4 d_{50}$ (Van Rijn, 2007a) corresponding to 0.2 to 3 m and resulting in grid size of 0.02 to 0.3 m. It is difficult to meet model spatial requirements in the entrance with such small grid sizes. Assuming these bed forms in the surf zone have a speed of 0.3 m/h (Gallagher et al., 1996), then bed updating Δt should be less than 2.8 hours, again achieve, however, introducing significant diffusion in the inlet solution. That is, it is impossible to meet stability requirements while limiting diffusion for various bed forms over whole domain (Callaghan et al. 2006b).

The CMS model with L_t = 10 m and with a much larger grid (smallest grid size 10×15 m) used in the Pensacola model, was stable. However, as will be shown below, the results were unrealistic and do certainly not amount to real predictive capability.

7.3 MODEL SET UP, SUB MODELS, CALIBRATION AND SENSITIVITY TESTING

7.3.1 Sub model domains

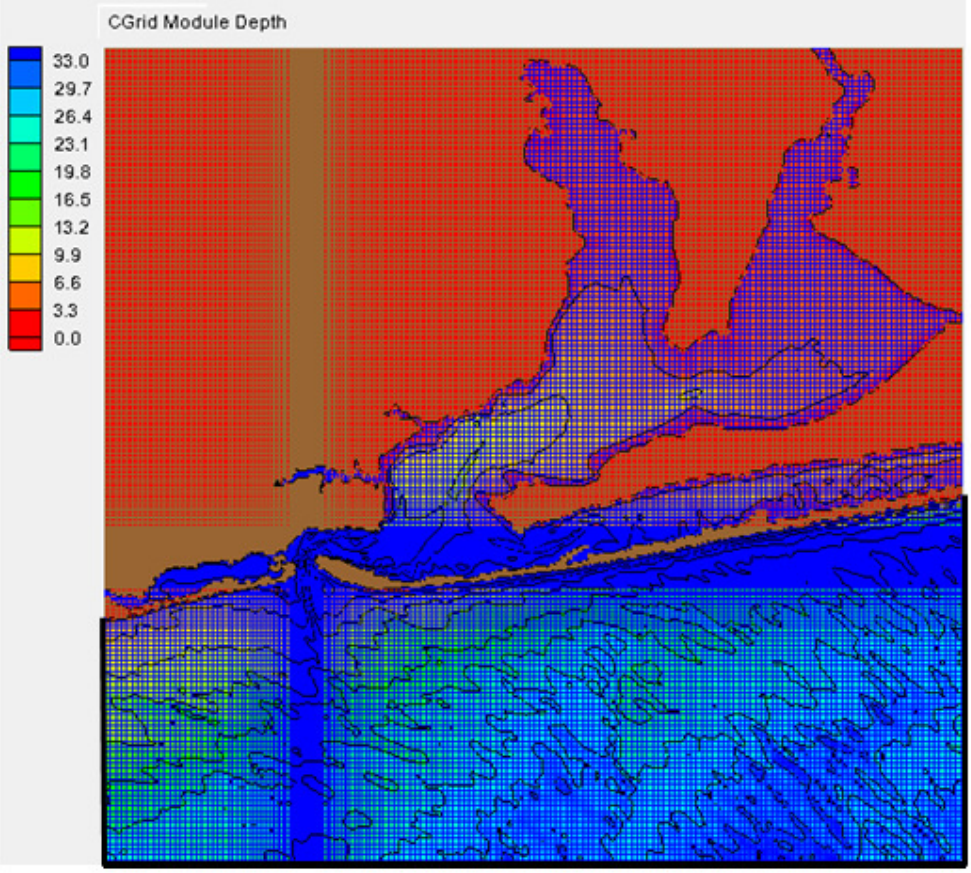

Figure 7.6: Flow domain, boundary (black line) and grid (196×190), size 10×15 m - 150×150 m, also shown in Figure 7.1.

The Pensacola pass inlet model is adopted from the Coastal Inlet Research Program (CIRP), USACE. The Pensacola pass model was set up by Lihwa Lin in 2009 using the CMS model to simulate morphological change and channel infill for the period from 1998 to 2008. The model was calibrated by Lihwa Lin (CIRP) and was found efficient to simulate long term channel infilling. In this model the flow domain covers nearly the whole basin of Pensacola bay with the size of the model being 46 km by 46 km, the distance from the shoreline to the open south boundary is around 14 km. The central study area around Pensacola inlet was set up for wave domain (located in lower left corner of flow domain) with size of 20 km by 20 km as in (Figure 7.1). Even though the sediment transport domain as well as the bed updating area is covered by the whole flow domain, the wave domain is the area of interest for morphodynamic investigation under storm condition where wave and tidal current superimpose.

The Cartesian grid includes 196×190 cells with grid size ranging from fine (10 m×15 m) close to the entrance to larger size (150 m×150 m) off shore or inland, Figure 7.6. The wave domain includes 100×105 cells with the same size generated from flow grid (Figure 7.1). Bathymetry was projected from horizontal global Florida North state plane coordinate system and NAD83, for vertical in m NAVD88. The deepest part along the right hand boundary is around 33 m, while in front of the channel it varied from 18 to 21 m (Figure 7.1).

7.3.2 Data sources for boundary and forcing conditions

The boundary conditions of the model are driven by measured ocean tides and waves forced as wave energy spectra from offshore observations. River flow is insignificant and was not considered in this model. The open boundary of the model includes 3 sections viz., West, South and East boundaries (Figure 7.6).

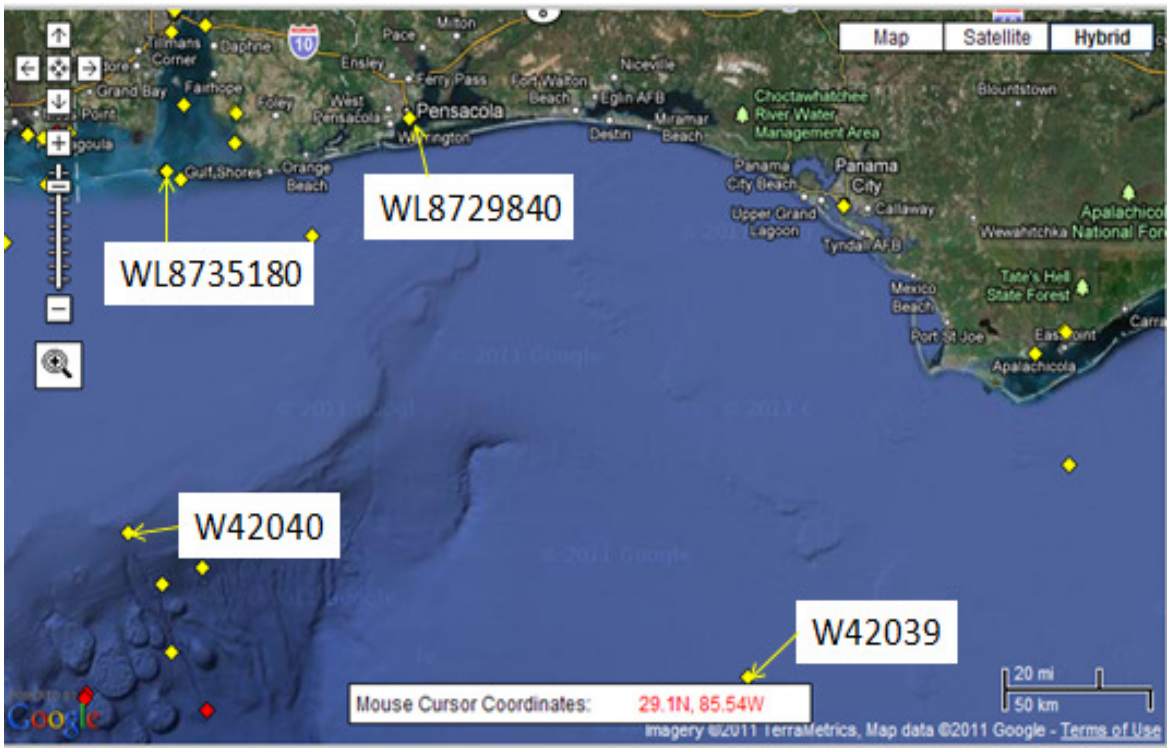

Figure 7.7: Location of tidal gauses (WL) and wave buoys (W).

Water level was taken from station 8735180 (30°15'N, 88°4.5'W), located at Dauphin island, 75 km southwest of Pensacola. Water levels for calibration were taken from Pensacola station 8729840 (30°24.2'N, 87°12.6'W) inside the Pensacola bay. Wave and wind information was taken from station 42040 (29.212°N, 88.207°W) south of Dauphin Island at depth of 164 m.

Another wave station 42039 (28.791°N, 86.008°W) is located well at East Southeast Pensacola in 307 m water depth. The locations of these stations are shown in Figure 7.7.

Water levels at hourly intervals (GMT) at tidal gauges respect to MSL were collected from http://tidesandcurrents.noaa.gov/gmap3/. Wind speed and directional information was used under storm conditions. The wind direction convention is the oceanographic convention (moving to). Directional wave spectra were collected by National Data Buoy Center (NDBC) from http://www.nodc.noaa.gov/BUOY/ begm.html. Wave input spectra were prepared with 30 frequencies, 35 directions as CMS-wave format.

Four different forcing conditions are presented for the hydrodynamic model: 1) normal measured tides for one month duration; 2) measured water levels during Hurricane Katrina (Section 7.3.3.1); 3) idealized normal tide and wave (cf., Section 7.3.4), and 4) combined measured Hurricane Katrina water levels with idealized normal condition (cf., Section 7.3.5). Forcing 1 and 2 are for hydrodynamic model calibration while forcing 3 and 4 are for morphodynamic prediction.

7.3.3 Flow model calibration, wave and sediment sensitivity testing

7.3.3.1 Flow model calibration

During the model calibration process, several cases have been implemented to test the sensitivity of parameters to make sure the flow model works stably and give reasonable results. A time step of 0.8 s is found reasonable and used for CMS flow and the ramp duration is 4hours. The good agreement between observed and calculated water levels in terms of magnitude and phase was defined at Pensacola for one month tidal forcing in normal conditions (March 2004 is shown in Figure 7.8) with root mean square error (RMSE) of 0.048 m.

Model performs better during spring tides. There was no velocity measurement for calibration for this area; however the calculated velocity (Figure 7.8) was reasonable in terms of magnitude and phase.

Under storm conditions, the hydraulic modeling period covered 14 days including 3 days during Hurricane Karina (17 August 2005 to 30 August 2005) Figure 7.9.

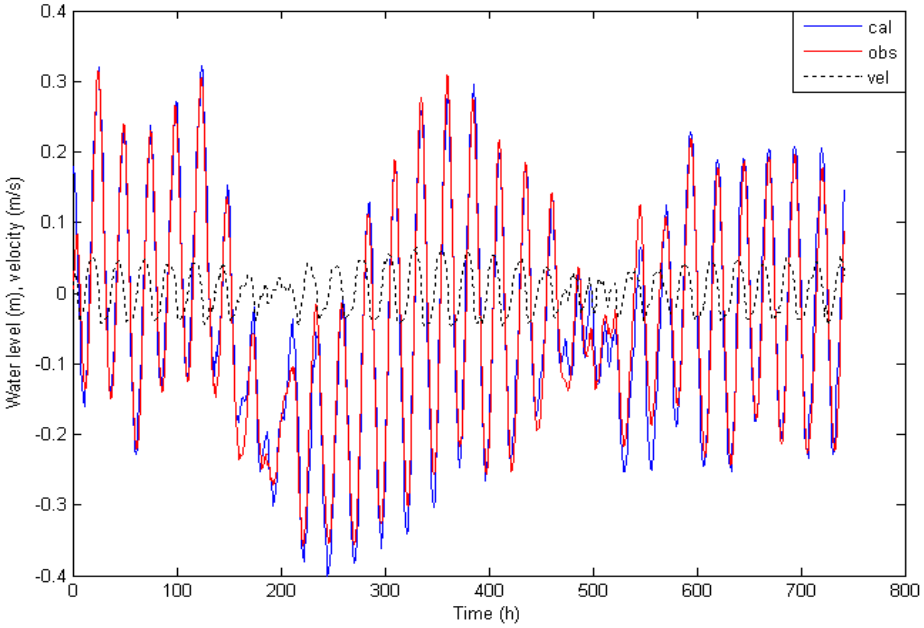

Figure 7.8: Observed and calculated water levels at Pensacola in March 2004.

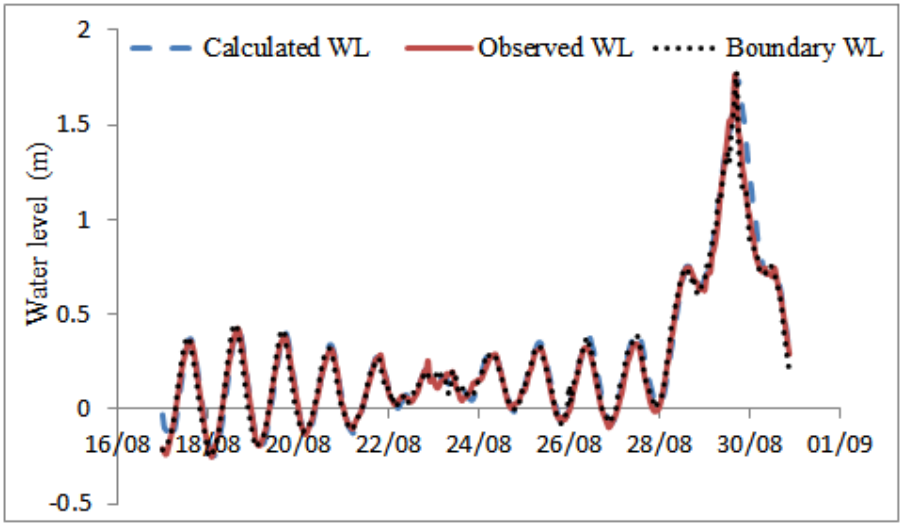

Figure 7.9: Comparison among calculated and observed water levels at Pensacola station, observed boundary water levels at Dauphin island from 0:0 17 August 2005 to 21:00 30 August 2005.

Figure 7.9 shows good agreement between computed and measured water levels (RMSE =0.1 m). Computed water levels have best fit in phase during the rising phase then getting delay about 1 to 2 hours after the peak. The difference between calculated and measured water levels at the peak is insignificant (1.73 m compared to 1.77 m). Water levels and velocity field at the hurricane peak time of 17:00 29 August 2005 are shown in Figure 7.10.

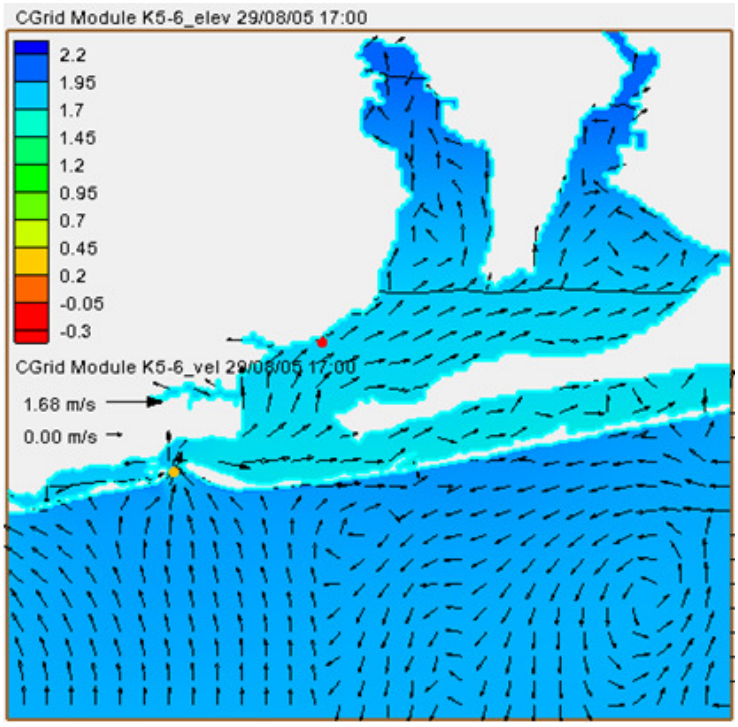

Figure 7.10: Water levels and velocity field in the domain by wave and flow steering at peak storm time, Red point is Pensacola tidal station. Yellow point for extracting velocity.

The water levels are reasonable at high tide and wind direction from south to north. The velocity field in the place where water flows through the wave boundary are in the reverse direction (Figure 7.10), however it is far away from the area of interest and therefore has limited influence to the coast and inlet.

7.3.3.2 Sensitivity test for the CMS-Wave model

The strong forcing period of Hurricane Katrina was adopted for these sensitivity tests, as the overall aim of these tests is to study the morphological change under storm conditions. Significant wave height (H_s), peak period T_p and wind speed are illustrated in Figure 7.11. The peak significant wave height was 9m and corresponding T_p=14.3 s with a wind speed of 31 m/s. Wind directions before and after the peak wave were mostly from the southeast and south west, respectively. Wind directions were slightly different from wave directions from just before peak waves arrived until this storm passed. In the leadup to the peak wave condition, wind and wave propagate with direction difference between 50^o to 90^o.

To make sure wave model performs stably and gives reasonable results, some sensitivity tests are carried out.

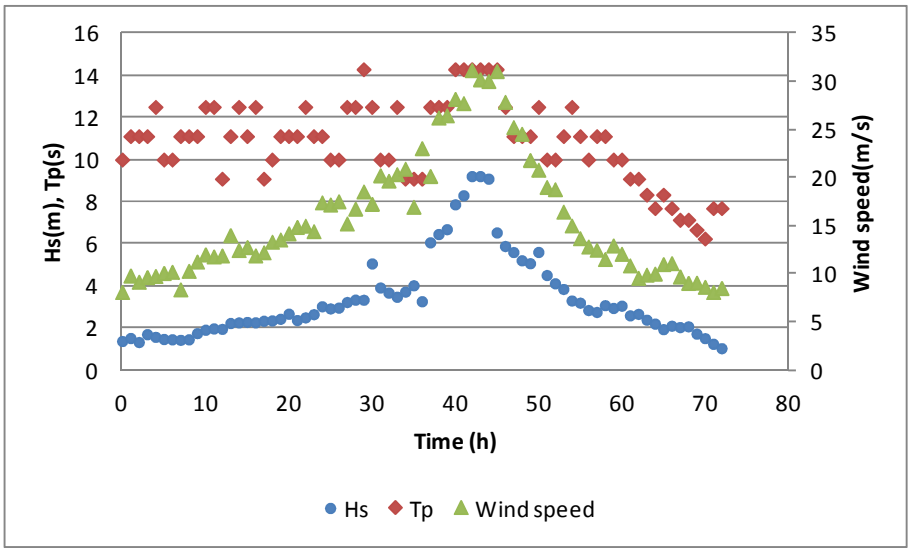

Figure 7.11: Significant wave height H_s, peak period T_p and wind speed during the storm.

Different Manning numbers, (n=0.01, 0.025, 0.04, 0.07, 0.1 s/m$^{1/3}$), spatially constant, were investigated with minor change in nearshore wave condition as in Figure 7.12. Therefore n=0.025 was chosen for all further runs.

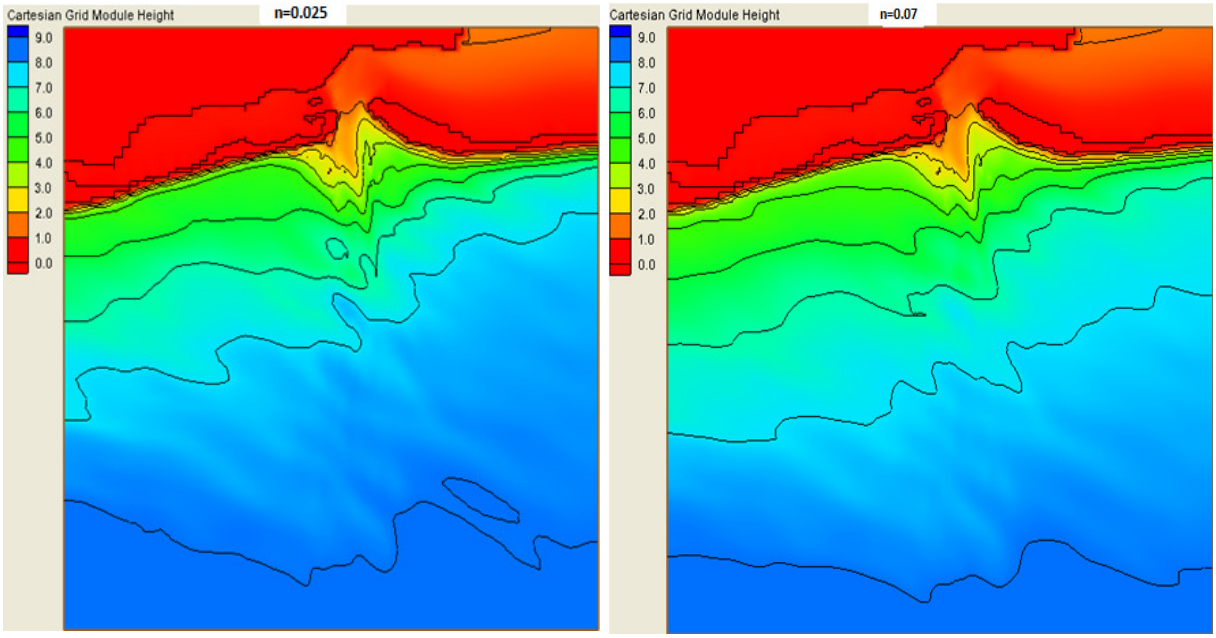

Figure 7.12: Wave field by using Manning friction coefficient n=0.025 (left) and n=0.07 (right) corresponding to peak wave at boundary.

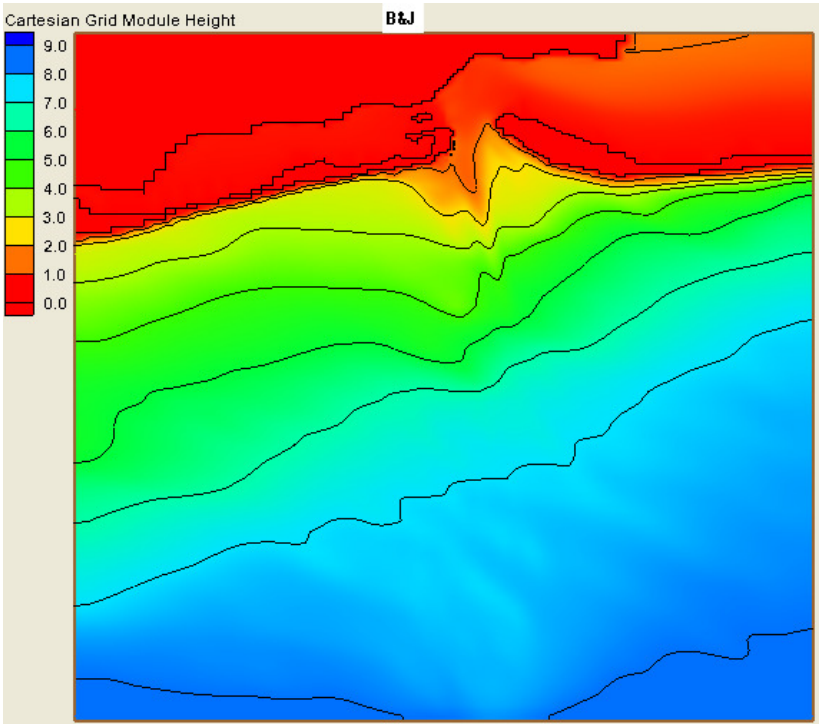

Figure 7.13: Results of wave field by Battjes & Janssen, (1978) wave breaking formulae corresponding to peak waves at the boundary.

One of the important factors in modeling nearshore waves is selecting the wave breaking formulation. When waves start to break in the nearshore area, the energy dissipation becomes a dominant process that controls the wave heights. Judging from the nearshore wave fields, the Battjes & Janssen formula looked the most acceptable (Figure 7.13). Hence it was chosen for the further tests.

The comparison of wave field between two cases of with and without nonlinear wave-wave interaction shows that they are similar; therefore it was not necessary to add the nonlinear wave effect.

7.3.3.3 Sensitivity test for sediment transport model

The most important influence on coastal morphodynamics prediction is sediment transport formulation. All available formulations were investigated. The model parameters were set (Table 7.1) after carrying out tests to be sure that all tests were stable.

Table 7.1 Summary of chosen model parameters.

Chosen parameters		Recommended parameters	Chosen parameters		Recommended parameters
Δt for Hydrodynamic models	0.08s	CFL restriction	bed load and suspended load scale factor	1	default
Δt for sediment transport models	4s	≥Δt of Hydrodynamic	bed slope coefficient	1	default
Δt for morphology update	20s	≥Δt of Hydrodynamic	porosity grain size	0.4 0.21mm	default default

A summary of all tests is shown below with positive (negative) values for accretion (erosion) rates.

Results of morphology change for different models

- Equilibrium, total load
  - + Watanabe: -0.16 m to 0.2 m
  - + Lund-CIRP: -0.40 m to 0.8 m
- A/D, concentration profile
  - + van Rijn: -0.6 m to 1 m
  - + Exponential: -0.6 m to 1 m
  - + Lund-CIRP: -0.7 m to 1 m
- NET, transport capacity
  - + Watanabe: -0.4 m to 0.5 m
  - + van Rijn: -0.8 m to 1.6 m
  - + Lund-CIRP: -0.8 m to 2 m

Watanabe provides smallest q_s & least morphodynamics

Lund-CIRP provides strongest morphodynamics

van Rijn provides medium response

Figure 7.14 and Figure 7.15 express the morphology change at the end of simulation period of 78h.

The predicted morphology changes using Watanabe's formula in the total load equilibrium and NET models are much smaller compared to other formulae, in agreement with Sanchez & Wu (2011).

Simulations using Watanabe's formula requires longer adaptation length of L_t = 15 m for stability, while the other formulae were stable with the default value of L_t =10 m. The advection-diffusion model gives similar morphology for the three concentration profile options. However, the van Rijn- and the exponential concentration profile provide similar ranges of morphology change, with the magnitude being slightly less than that from the Lund-CIRP profile. The Lund-CIRP and

the van Rijn formulae in NET model similarly give the strongest response. Therefore, the Lund-CIRP formula in the NET model, with the Van Rijn concentration profile in advection-diffusion model, is used for further tests.

Total load equilibrium: Watanabe
With transport rate coefficient Co= 0.5 (max)

Total load equilibrium: Lund-CIRP

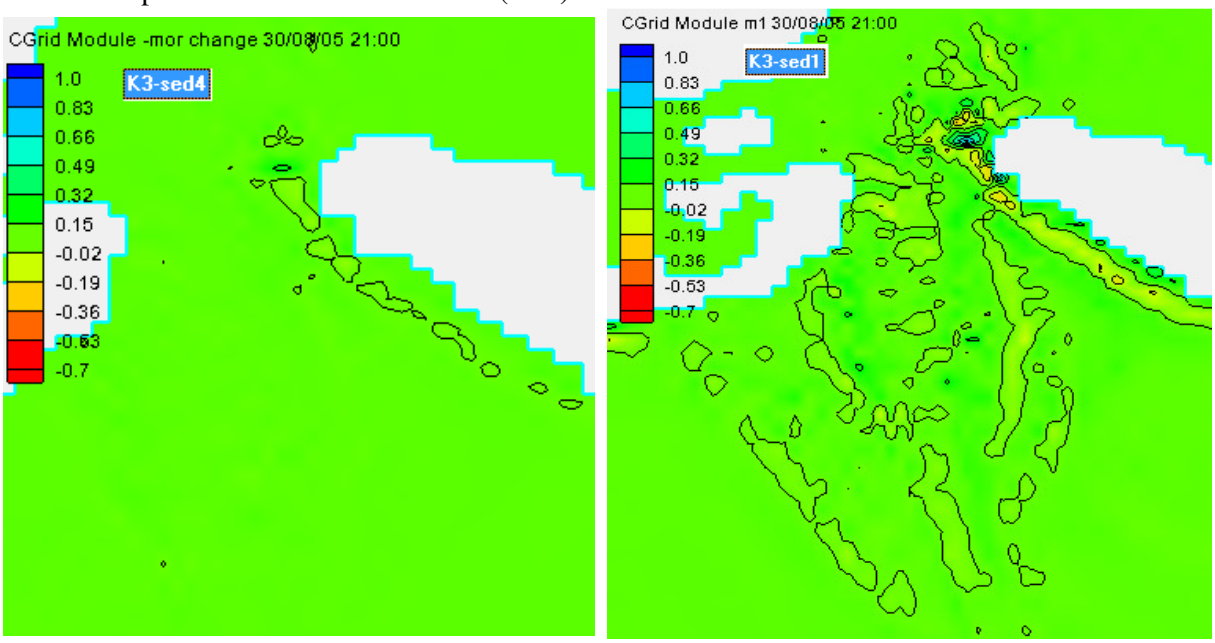

Figure 7.14: Morphology change by total load equilibrium model with sediment transport Watanabe's formula (left) and Lund-CIRP (right).

Regarding the time needed to spin up the model, a number of cases with different durations were carried out under normal conditions using the NET-Lund-CIRP formula. The normal condition is tidal range = 0.5 m and wave height H_s=0.48 m, T_p=6.1 s, Dir=170.95^o (section 7.3.5). The purpose of these tests is to determine the spin up period required to obtain ± 0.1 m accuracy. Simulations with different run periods of 4 days, 11 days, 20 days and 30 days were carried out. Finally, the spin up period of 11days was chosen for the morphology model accepting ±0.1 m accuracy.

Changing the bed load and suspended load scale factors results in unstable simulation. Hence, the default values were kept. For the NET-Lund-CIRP model, different adaptation lengths (L_t) were tried, i.e., L_t=15 m, 20 m, 30 m, leading to unstable predicting compared to L_t=10 m. The results of morphology change with constant L_t=10 m are similar in pattern and magnitude L_t =max (L_b, L_s) and using bed load adaptation factor of 10 and suspended load adaptation length method of Armanini & Silvio (1986). Therefore the constant adaptation length L_t=10 m was chosen for NET-Lund-CIRP model for further tests. As discussed in connection with Figure 7.5, such a large L_t

would have little physicals basis except for areas with very large bedforms and/or wave breaking generating large vertical concentration profile scales.

Advection-diffusion model with van Rijn concentration profile

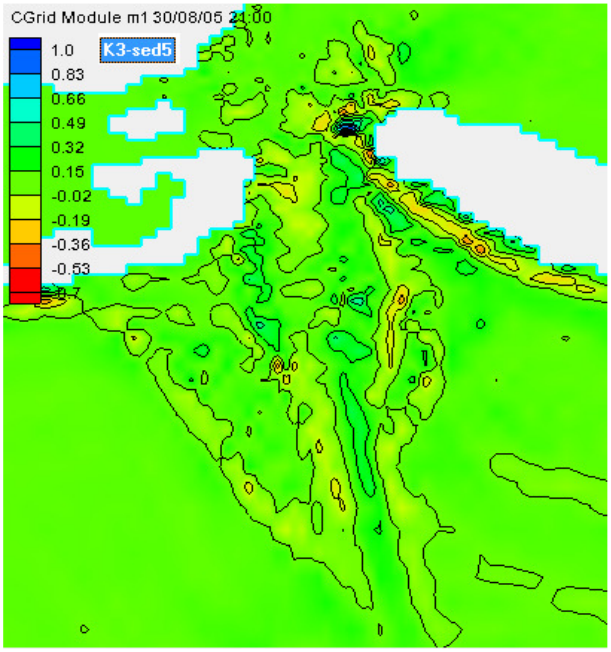

Advection-diffusion model with Lund-CIRP concentration profile

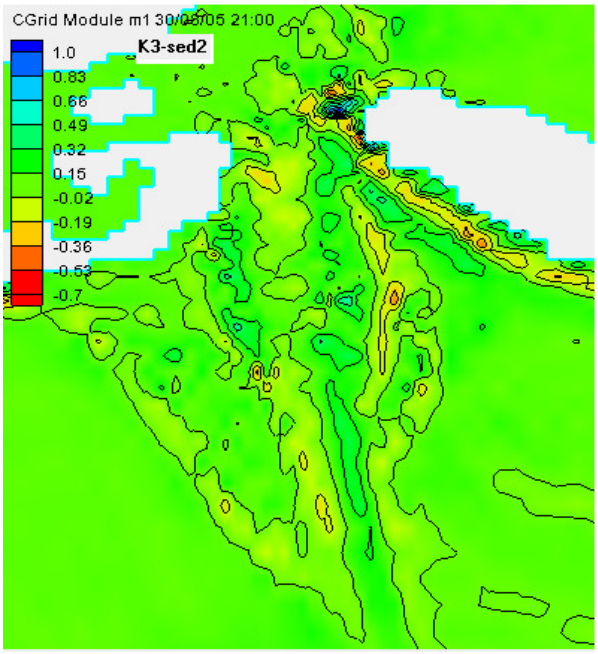

Advection-diffusion model with exponential concentration profile

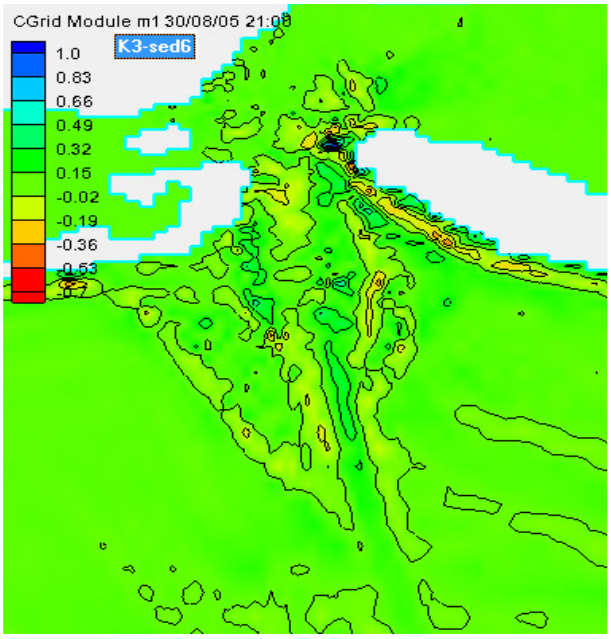

NET model with LUND- CIRP transport capacity total adaptation length L_t=10 m

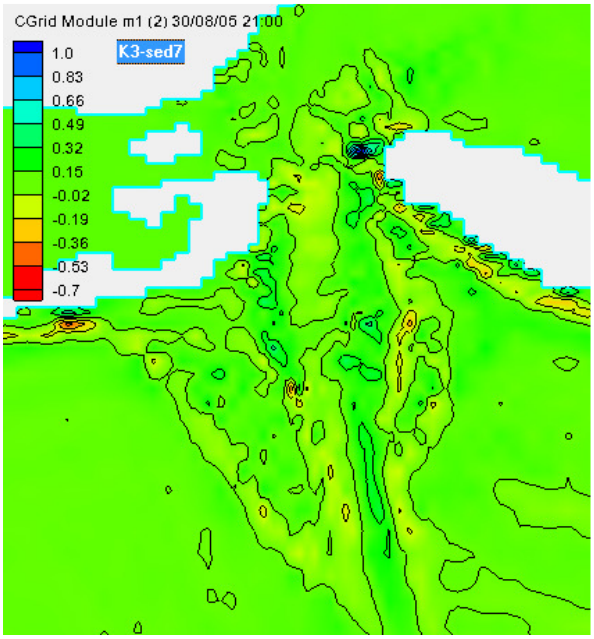

NET model with van Rijn transport capacity, Lt=10 m

NET model with Watanabe transport capacity, Ct=0.5, Lt=15 m.

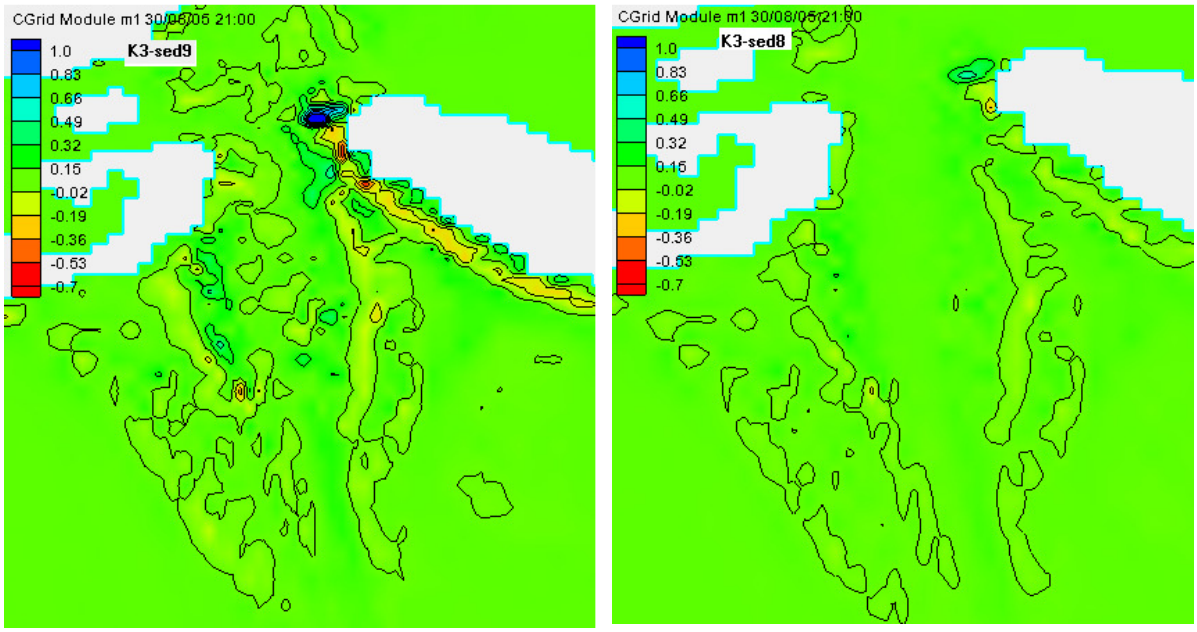

Figure 7.15: Morphology change by A/D model with different concentration profile and NET model with different sediment transport capacity formulae.

7.3.4 Idealised normal condition for morphology model

To determine the *normal condition* for the morphology model to be used during spin up and recovery after the storm (to avoid complex condition caused by spring/neap cycle), the representative tide and wave condition were determined from 10 years of records.

7.3.4.1 Representative tide

The representative tide is chosen based on the assumption that the long term effect of natural tidal forcing can be almost cumulative effect on morphology of single tide. Hourly water levels from 2000 to 2010 were available to establish the representative tide. The 2010 data was chosen as it was storm free. A period of 28 days was taken, including two spring tides and two neap tides (Figure 7.16). The mean tidal range of this period then was multiplied by 1.1, which according to Winter et al. (2006) reproduces the best morphodynamic effect. One tidal cycle with nearly the same tidal range of (0.5 m) in 28 days was picked up (red cycle in Figure 7.16). By slightly adjusting this tidal cycle so that its range is 0.5 m and the average value is zero, the so called representative tide is obtained.

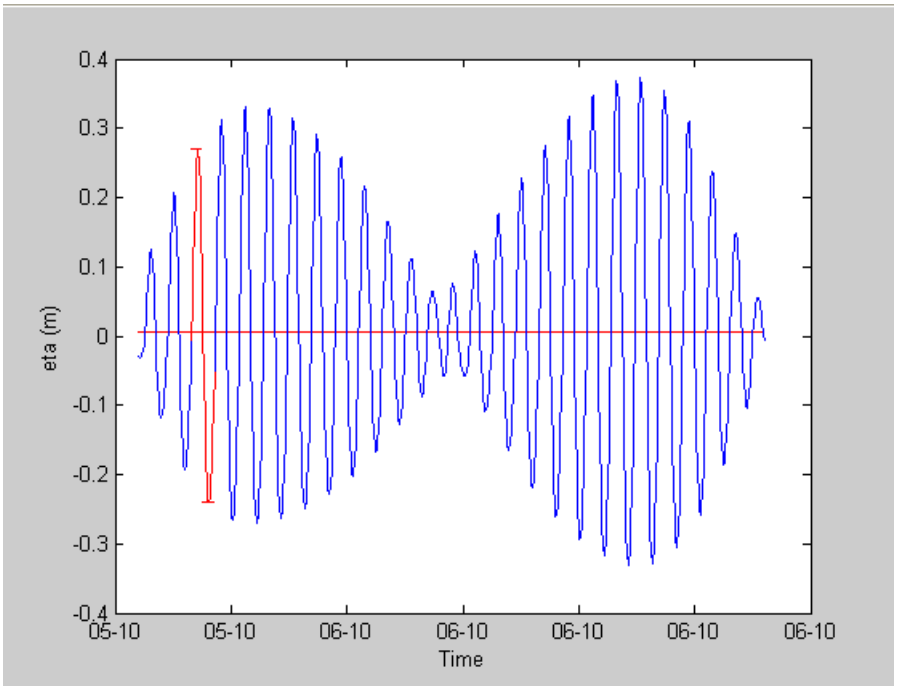

Figure 7.16: Representative tide (red color) in 28 days measured water levels

7.3.4.2 Normal wave condition

Wave data from station 42040 covering 2000 to 2010 shows no storms and has $\overline{H_s} \approx 0.48$ m, which was chosen as *the normal condition*. Wave direction and wave period determined by average records corresponding to $\overline{H_s} \pm 20\%$. The resulting mean wave period is 6.1 s, and wave direction is 170° from the north (mean wave direction from South-East). Figure 7.17 presents wave rose for all coming waves and waves range (0.8 -1.2) $\overline{H_s}$.

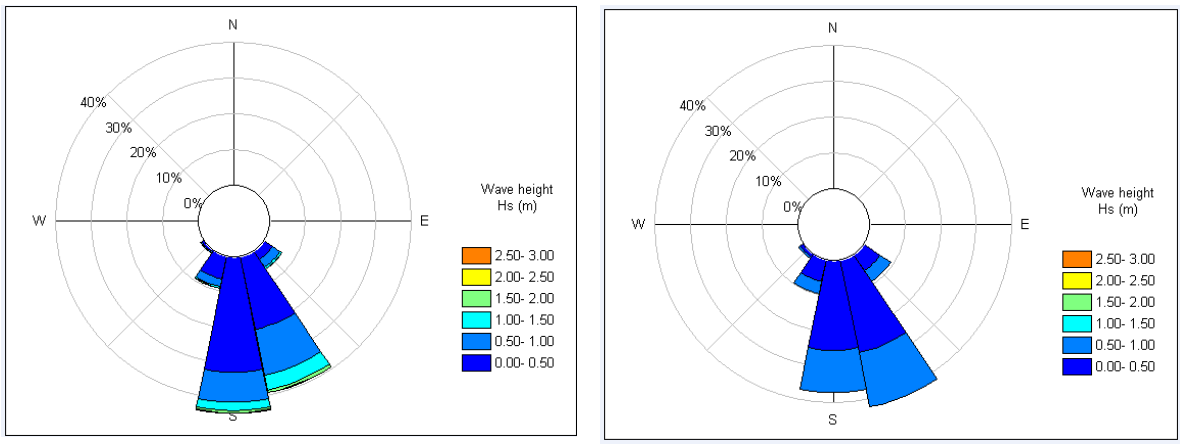

Figure 7.17: Wave roses for all incoming waves (left) and waves range from $0.8\,\overline{H_s} < \overline{H_s} < 1.2\,\overline{H_s}$ (right) from 2000 - 2010.

The results agree with previous report (Browder & Dean, 1999) about Pensacola. The average wind speed is ca 6.6 m/s with mean wind direction being 152.4°

7.3.5 Boundary conditions for morphology model and hydrodynamic model results

7.3.5.1 Boundary condition for morphodynamic model

From the start to the end of Hurricane Katrina, the measured water levels, winds, waves were provided as input. Then idealised normal conditions were applied using representative tide of 0.5 m range and mean wave conditions (H_s=0.48 m, wave direction=170°, T_p=6.1 s) (Figure 7.18).

7.3.5.2 Hydrodynamic model results

Figure 7.18 shows the computed water level is in phase with water levels at boundary, a bit larger than at the boundary at high tide except the peak. Water levels and velocity fields are similar in all domains at storm peak as presented in Figure 7.10. The pattern of flow is nearly the same and magnitude of velocity is slightly less compared to the case run for hydrodynamics only with the maximum Froude number remaining below 0.35. The velocities at the centre of the entrance are shown in Figure 7.19. Ebb dominance is observed at the inlet entrance. The wave field at peak wave conditions, which occurred 7 hours before the peak water level, has a similar pattern as in Figure 7.13.

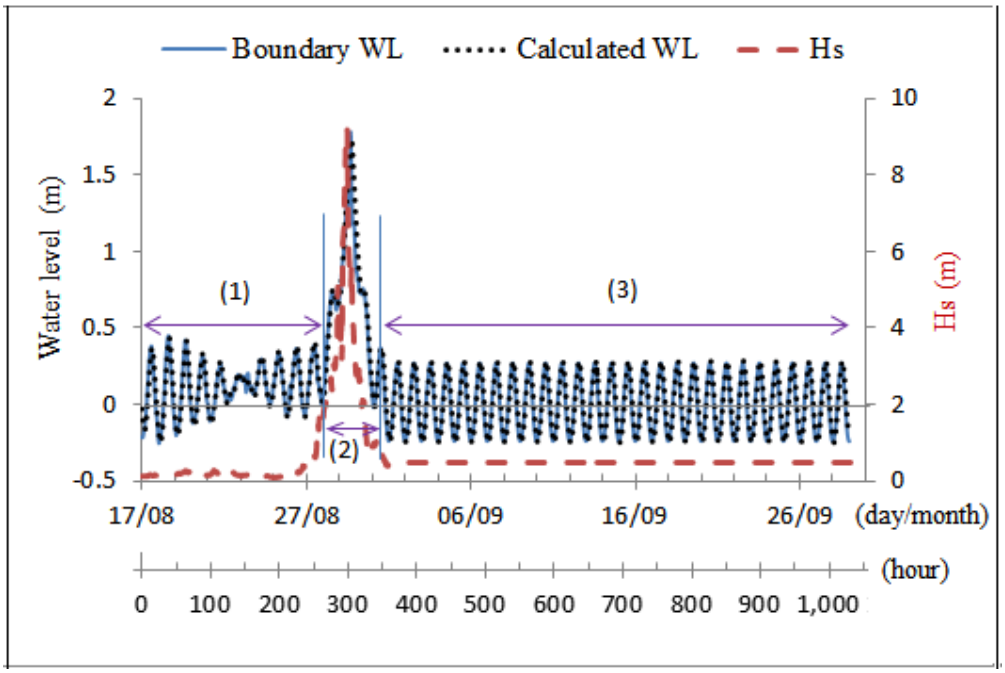

Figure 7.18: Boundary and calculated water levels; H_s for 1032 hours simulation including Hurricane Katrina. Three periods for calculating average sediment transport vector in Section.

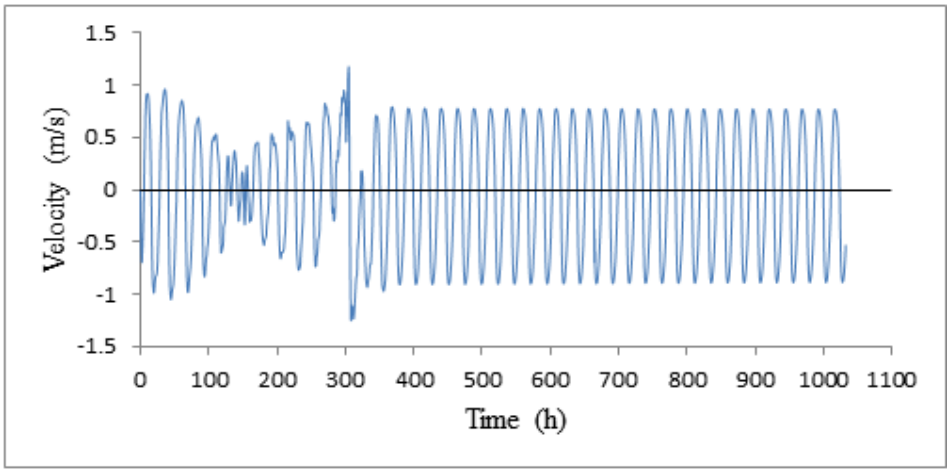

Figure 7.19: Calculated velocity at the middle point of the entrance (yellow point in Figure 7.10).

7.4 MORPHODYNAMIC MODEL RESULTS

7.4.1 Results of morphology change

Figure 7.20 shows the morphology changes after 1032 hours. The left panels are results based on the advection-diffusion model with Van Rijn concentration profile and the right panel results are based on NET model with Lund-CIRP transport capacity. Positive values represent accretion, and negative values represent erosion. The upper panels describe morphology change and show a qualitative difference between the two models. The lower panels present the same results highlighting the smaller scale morphology changes (-0.5 to 0.5 m).

The NET-Lund-CIRP model has stronger response with a larger range of morphology changes (-4 m to 3.2 m) compared to A/D-van Rijn model (-1.7 m to 2.3 m). The patterns of change are quite similar for the two models but are different in magnitude. In terms of maximum bed level change rates, the van Rijn model gives more accretion than erosion, while NET-Lund-CIRP provides more erosion than accretion. A large region just inside the bay as well as the left hand side of entrance seaward and the right coast eroded severely. A large area on the right hand side of the entrance, both sides of channel, off shore channel, and inside the bay showed accretion

A/D with van Rjin's concentration profile

NET: LUND-CIRP transport capacity

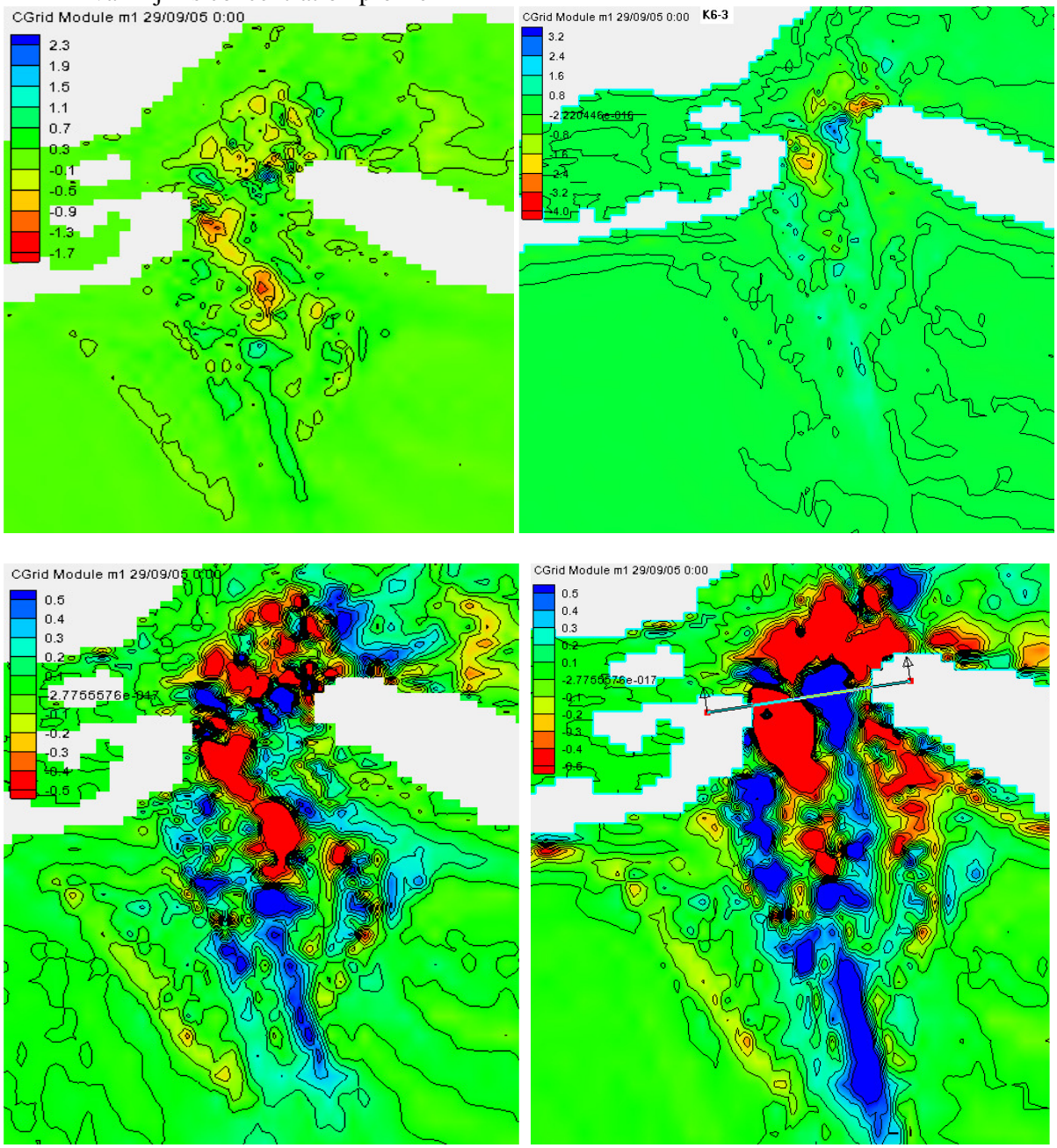

Figure 7.20: Morphology change after simulation period of 1032h, left for A/D model with van Rjin's concentration profile, right for NET model with Lund-CIRP transport capacity. +: accretion, -: erosion; Upper panels with free scale and lower panel with (-0.5 m to 0.5 m) scale.

To gain further insight into the morphology change at the entrance and the nearshore area, the three most dynamic areas in Figure 7.20 and Figure 7.21 are further investigated. The left (L) and right (R) areas where two ebb tidal deltas are present were perhaps expected to be washed out

during the storm. However, from the visual observations of the model results, only a small area near the edge of the left and right deltas showed erosion. The area inside the square box, denoted "A", extends further to the no-morphology change area, and the combination of L and R is denoted by "T" is further discussed.

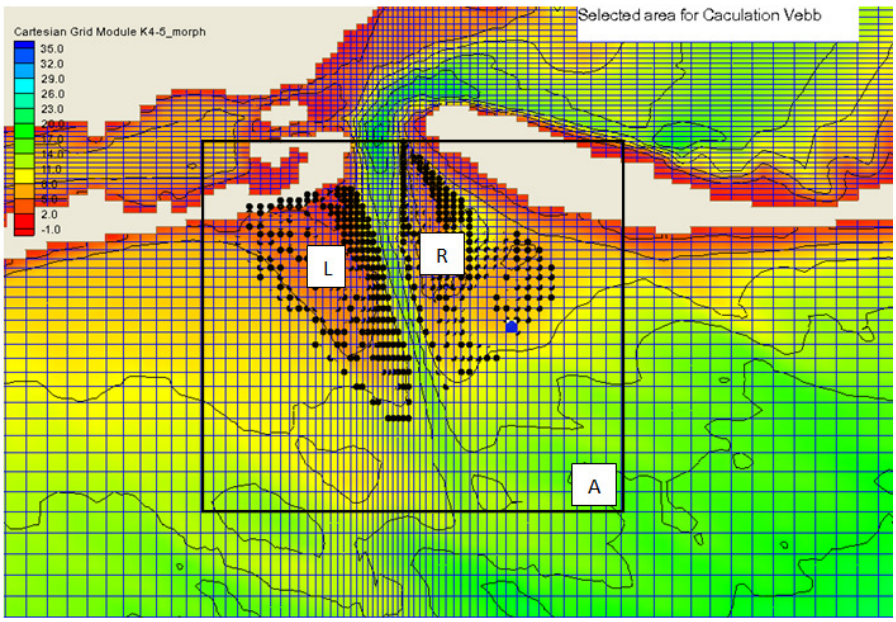

Figure 7.21: Three most dynamic regions considered for further investigation
L: left, R: right and A: inside square.

Time varying volume change of each area of interest is as follows:

$$V_{change}(t) = \text{Sum}\,[-(\text{morphology}(t) - \text{morphology}(t\text{-}1)) \times A_{cell}] \quad (7.10)$$

where $V_{change}(t)$ is normalized by dividing by the total area of the region of interest.

$$Z_{change}(t) = V_{change}/[\text{sum}(A_{cell})] \quad (7.11)$$

$$Z_{cum\ change}(t) = \text{cummulative } Z_{change}(t). \quad (7.12)$$

Overall, the results of Z_{change} (Figure 7.22) and $Z_{cumchange}$ (Figure 7.23) confirm the earlier comment that the NET-Lund CIRP model responds more strongly than the advection-diffusion-van Rjin model. Significant difference in performance between two models during the storm is seen, while similar accretion patterns after the storm are experienced, except the erosion trend of region A by NET-Lund CIRP (Figure 7.23).

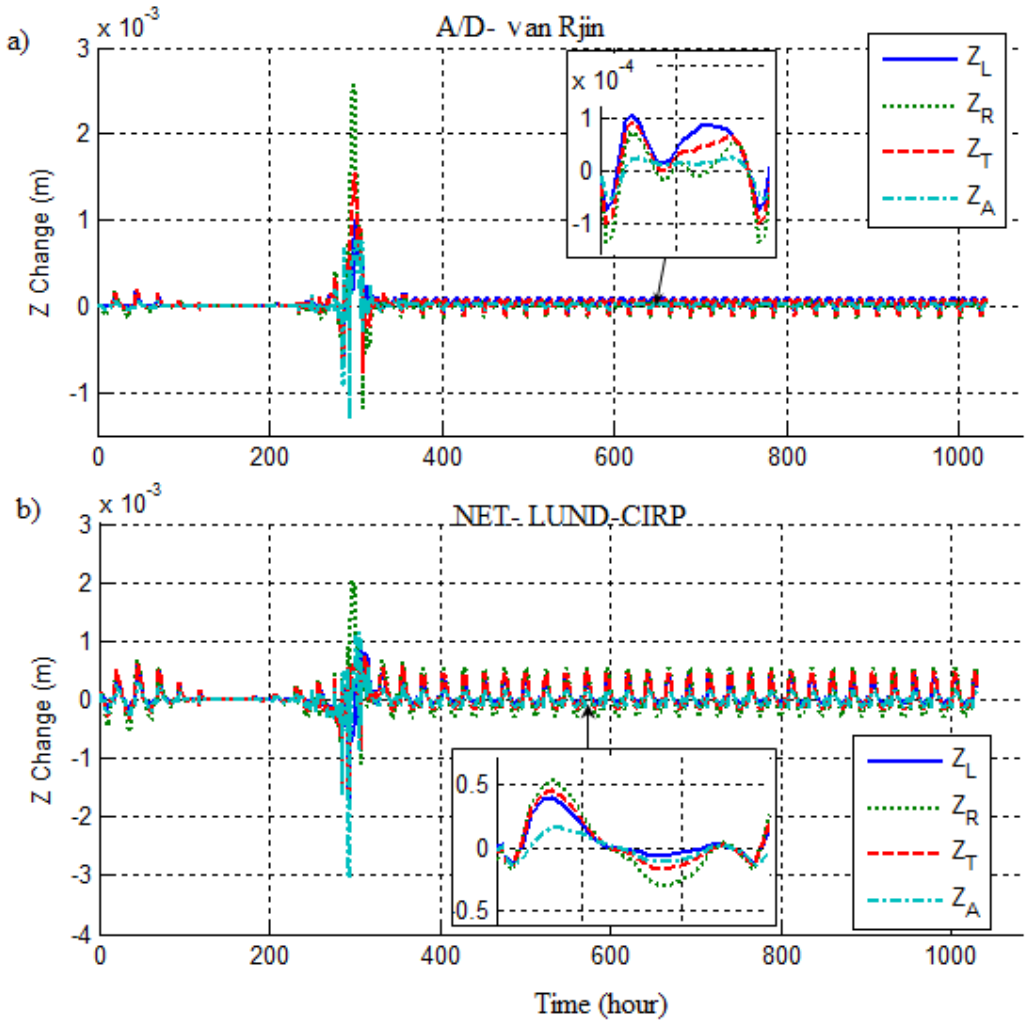

Figure 7.22: Comparison $Z_{change}(t)$ by 2 models for 4 areas of interest.

a) $Z_{change}(t)$ by A/D- van Rjin model; b) $Z_{change}(t)$ by NET: LUND- CIRP model.

2 small windows show zoom in of $Z_{change}(t)$ by 2 models in daily tidal cycle during recovery period.

As can be seen from Figure 7.22, Z_{change} during the storm by A/D-van Rjin is ca 10-25 times compared to that of the recovery period, which is higher than this ratio of 5-15 times by NET-Lund CIRP. The Z_{change} during storm by A/D- van Rjin shows the accretion dominance especially in region A, while erosion dominance is shown by NET-Lund CIRP. After the storm, predominant accretion is clearly seen on daily tidal cycle by both models, but in different manners (cf. zoomed inset figures of Z_{change} for a tidal cycle).

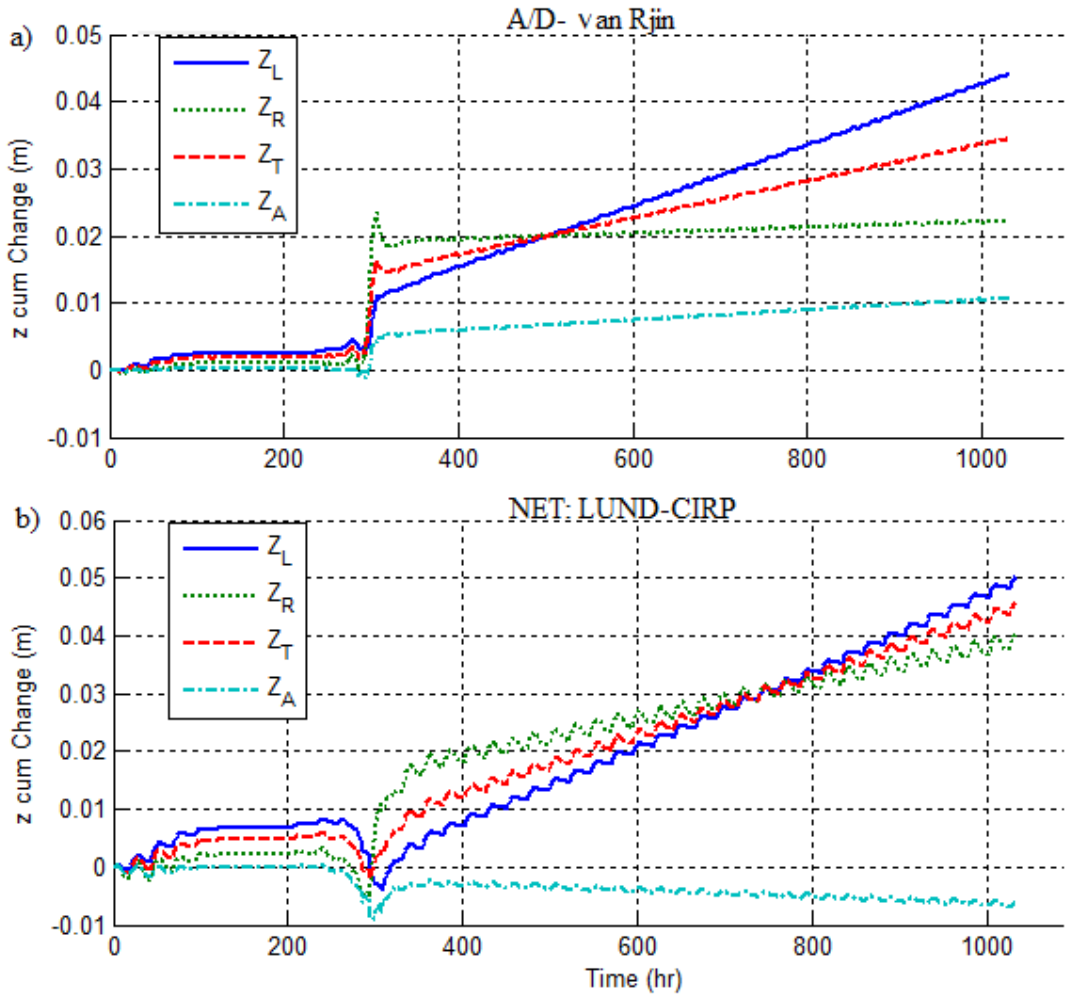

Figure 7.23: Comparison of $Z_{cumchange}(t)$ by 2 models for 3 areas of interest.
a) $Z_{change}(t)$ by A/D- van Rjin model; b) $Z_{change}(t)$ by NET: LUND- CIRP model.

Figure 7.23 shows $Z_{cumchange}(t)$ for the two models. Before the storm, both models show that the morphology was stable with constant $Z_{cumchange}$. During the hurricane, $Z_{cumchange}$ behave differently between A/D- van Rijn and NET-Lund CIRP. In all regions, L, R, T and A, $Z_{cumchange}$ by A/D- van Rijn slightly reduce (erosion) then jump up sharply, which means large accretion, whereas $Z_{cumchange}$ by NET-Lund CIRP show a drop, especially for region A corresponding to remarkable erosion compared to other regions during large wave influence. A NET-Lund CIRP result agrees with arguments provided above. Both models show a post-storm accretion trend for most regions except in region A by NET-Lund CIRP. However, it seems unrealistic that the eroded area is very little during the storm and has recovered very rapidly after the storm.

Both models show that the two areas i.e., the left (L), right (R) have obvious accretion trend continuing after Hurricane Katrina. Accretion speed in L was much higher than in R. Region T has

accretion speed equal to mean speed of L and R. It takes shorter time by the A/D-van Rijn model for L to catch up with the same accretion speed as R than by the NET-Lund CIRP for 200 hours and 450 hours respectively. The increasing trend in L, R, T is linear with no sign of approaching an equilibrium value.

In addition, a tidal cycle is seen for NET-Lund CIRP, while it is less pronounced with the A/D-van Rijn model. It may be due to Lund CIRP assuming sediment transport rate q_s is in the current direction, whereas waves do not contribute to the transport. Therefore, it reflects the tidal dominant current in $Z_{cumchange}$. A quite strange trend is shown by $Z_{cumchange}$ for R, T by A/D-van Rijn: They suddenly reduce a bit just after storm before further continuously rising.

The increasing or decreasing trend in each region during a short simulation (1032 hours) is likely to be just the beginning of a long-term evolution process, which needs continuation of model runs for longer period to see the change in trend toward equilibrium state. The T_{morph} could be years as seen in (Figure 7.2). However, the limitation of the model computational resources did not allow running further; therefore it is impossible using this model to estimate about T_{morph} for this case.

The same problem of inability to reach equilibrium state was found in DELFT3D model by Hibma et al. (2003a), Van de Wegen et al. (2010) and de Swart (2013). Larson commented in his review of this thesis that "the inability of the CMS model to reach equilibrium is common to all such detailed models". Even though, Hanson et al. (2003) and de Swart & Zimmerman (2009) reviewed a large number of process-based modelling works, which show the presence of equilibrium states for meso-scale morphological features, especially simplified 1D model for long-time simulation. To predict long-term recovery process under normal condition after storm, a hybrid combining process-based and behaviour-oriented models should be applied using the reduced concept by Roelvink et al., (1998). The concept assumes that small changes in bed do not cause significant change in the flow and wave pattern. Therefore local flow velocity and orbital motion can be parameterised as a function of local depth only from continuity correction. Since q_s is calculated from flow velocity and orbital velocity, local q_s also can be parameterised as a function of local depth, starting from an initial transport field. Hybrid modelling can take an initial transport field from smaller scale process-based model as input for large scale model. By this way model covers full spectrum from micro to macro scale and can investigate coastal inlet evolution with time scale up to centuries. However, the success of model mostly depends on quality of initial transport field, which cannot be ensured (with factor 2-10) as presented in Section 7.4.3 and Section 9.3.

In comparison to the results of the evolution of a dynamic inlet under storm conditions studied by William & Pan (2011), Pensacola inlet's cross section area is more than 20 times larger than their inlets and Pensacola's basin area is huge compared to their basin. That is the reason why

their inlet cross section area and the total volume change of different coastal elements could reach equilibrium fast within ca 100hours.

Even though the simulation period is short, it is obvious that the quantitative change in morphology during storm compared to normal condition is most likely unrealistic. The more sensible model of NET-LUND-CIRP, which agrees with observation of erosion ebb tidal delta, is chosen for further investigation.

7.4.2 Evolution of the throat area

Apart from morphology changes around the ebb tidal delta, another important part of the inlet system is the inlet gorge. To understand how it changed during and after the storm, a cross section was considered through the narrowest of the entrance as shown in Figure 7.20 (lower- right).

Figure 7.24 presents the change of the throat section by the NET-LUND-CIRP model through 4 time intervals as shown in Figure 7.25 from (1) the initial condition at 17 August 2005 to (2) the peak of the storm (29 August 2005), (3) reached peak area at 8 September 2005 and (4) final cross section at end of period. It was observed that the right side bed was continuously accreting while the left side bed was continuously eroding with a maximum z_{change} about 2 m. However, the rate of change is insignificant compared to the maximum depth of 18m and cross sectional area.

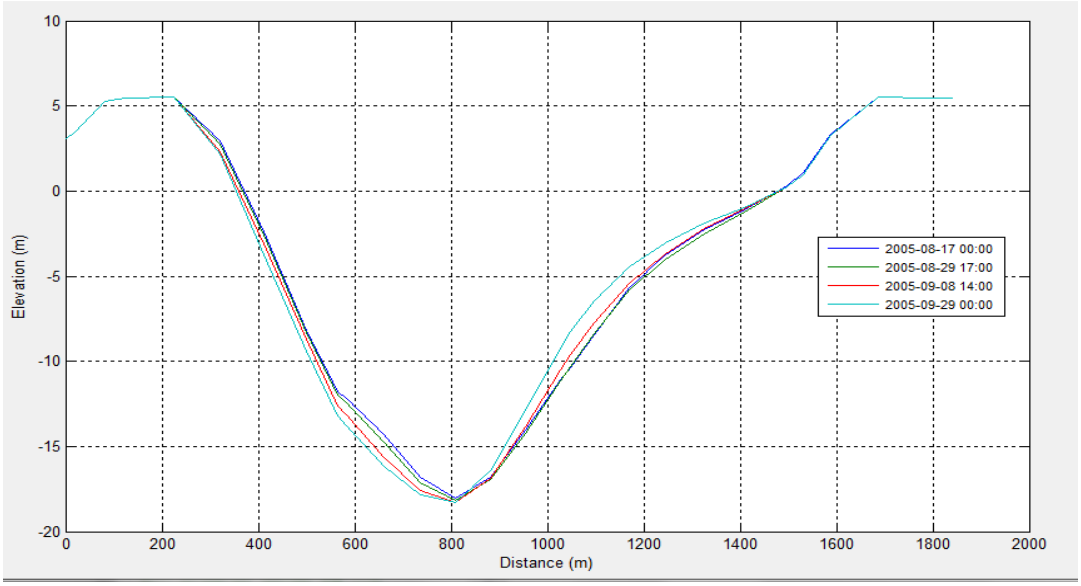

Figure 7.24: Throat section at different times: (1) beginning of the simulation; (2) peak storm time, (3) 8 days after storm with A_{max} and (4) end of simulation. The time pointed in Figure 7.25.

The cross sectional area $A(t)$ varying with time is shown in Figure 7.25. An unremarkable change in throat area with an increase of 170 m^2, only 1.7% of the area before the storm, is seen. It took 8 days to erode to the largest area, and then recovered (accreted) back to the initial condition

after 20 days. Under normal conditions, the model clearly shows a reducing trend. These results are similar to changes in the ebb tidal deltas. The divergent throat area (Figure 7.25) indicates this model is unable to quickly reach an equilibrium position.

$A(t)$ (Figure 7.25) trends during and after the storm are different to observations of Bertin et al. (2009), Williams & Pan (2011) as well as the illustration in Section 6.5.1 in Figure 6.15.

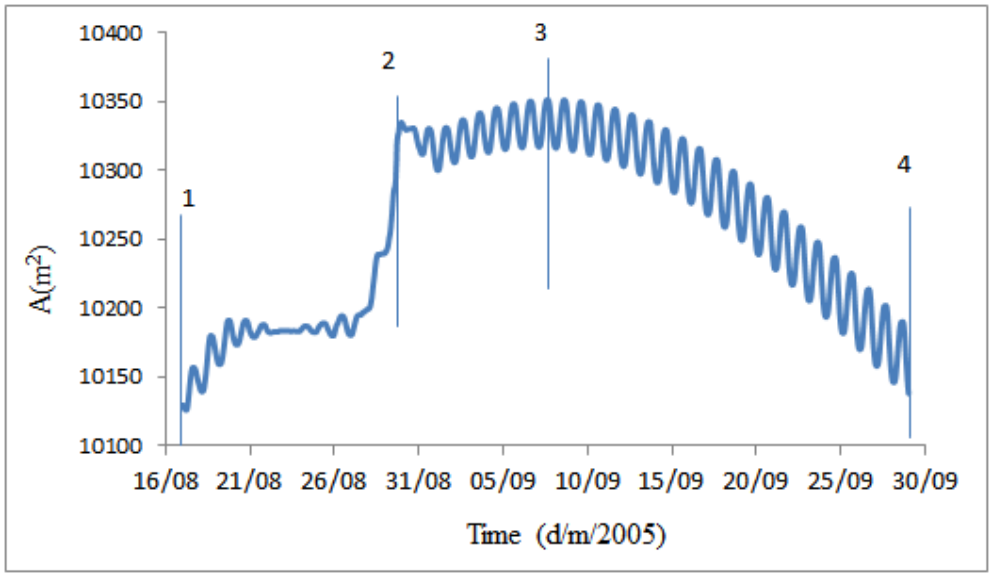

Figure 7.25: Throat area varying with time and 4 cross sections were shown in Figure 7.24.

They pointed out that the sediments eroded from the ebb tidal delta and the adjacent beach during storms, driven by onshore wave radiation stress gradients and the acceleration and convergence of longshore transport toward the inlet, deposit at the entrance and narrow the cross section. After the storm, the predominant ebb currents move sand from the inlet back to ebb shoal. However, the inlets in their case studies were quite shallow, (1.5-2.5 m), compared to Pensacola (18 m). This may causes different behavior of these inlets.

The insignificant morphology change predicted by the model during storm could mean that the hydraulic efficiency of the inlet is not much influenced by the hurricane. In other words, the morphology change is usually not significant enough (only 1.7%) compared to the cross section to be measurable via the tidal record. Hence the water level as well as response function of primary component gets back to normal condition very quickly after the event as shown in Figure 4.37. It may imply that the T_{morph} obtained in Section 4.4 by analysing tidal records for Pensacola Pass reflect local equilibrium or hydraulic time scale but may not be related to morphological change.

There are some simple robust models such as Hoan et al. (2011), Larson et al. (2011) and Hinwood et al. (2012) as reviewed in Section 6.2. However, they are not applicable for this case.

Hoan et al. (2011) developed a spit growth model, but found less satisfactory comparisons with restricted growth example, i.e. opposing spits moving towards inlet closure. The analytical model for the evolution of inlet cross-section area by Larson et al. (2011) was applied for a simple case of barrier breaching due to river run off without considering tidal flow. Hinwood et al's (2012), simple one dimensional process-based model, used 'ocean sediment concentration - C_O' corresponding to influence of waves but did not clarify the relation between C_O and actual wave parameters. The hybrid modelling to predict long-term evolution of A could be used with risky initial transport field (cf. next Section), which may lead to wrong morphological developments.

7.4.3 Investigation on sediment transport

In order to tackle the expectation of waves contributing significantly to sediment transport under combined wave-current flows, further investigation on sediment transport rates has been carried out during three periods as defined in Figure 7.18; (1) period between 2 hours and 262 hours, just before storm; (2) period between 263 hours to 339 hours, during the storm, and (3) period during normal condition after the storm between 340 hours and 1032 hours. The average sediment transport vector $\overline{\overline{q_s}}$ for each period for NET-Lund-CIRP model was computed and presented in table 7.2.

Table 7.2: The average sediment transport for 3 periods.

	(1)-pre storm	(2)- during storm	(3)-after storm
$q_{sx}(10^{-3}m^2/s)$	-2.16 to 1.69	-4.45 to 3.92	-1.6 to 0.928
$q_{sy}(10^{-3}m^2/s)$	-3.167 to 2.41	-7.68 to 5.24	-2.46 to 1.35
$\overline{q_{sx}}(10^{-3}m^2/s)$	-0.136 to 0.082	-0.4 to 0.46	-0.26 to 0.126
$\overline{q_{sy}}(10^{-3}m^2/s)$	-0.156 to 0.056	-0.66 to 0.61	-0.35 to 0.095
max $\vec{q}_{mean}(10^{-3}m^2/s)$	0.156	0.67	0.35

The results show that the maximum $\overline{\overline{q_s}}$ for the normal condition period was half of the maximum $\overline{\overline{q_s}}$ during the storm. That is the probable reason why the ebb tidal deltas in Section 7.4.1 recover very fast after the storm.

Figure 7.26 and Figure 7.27 show $\overline{\overline{q_s}}$ fields ($q\times10^3$ m^2/s) for periods 2 and 3 respectively as well as labels of erosion and accretion areas. The area L1, L2, L3 on the left; M1, M2, M3 in the

middle, R1, R2, R3, R4 on the right corresponding to morphology change in Figure 7.20 (lower-right).

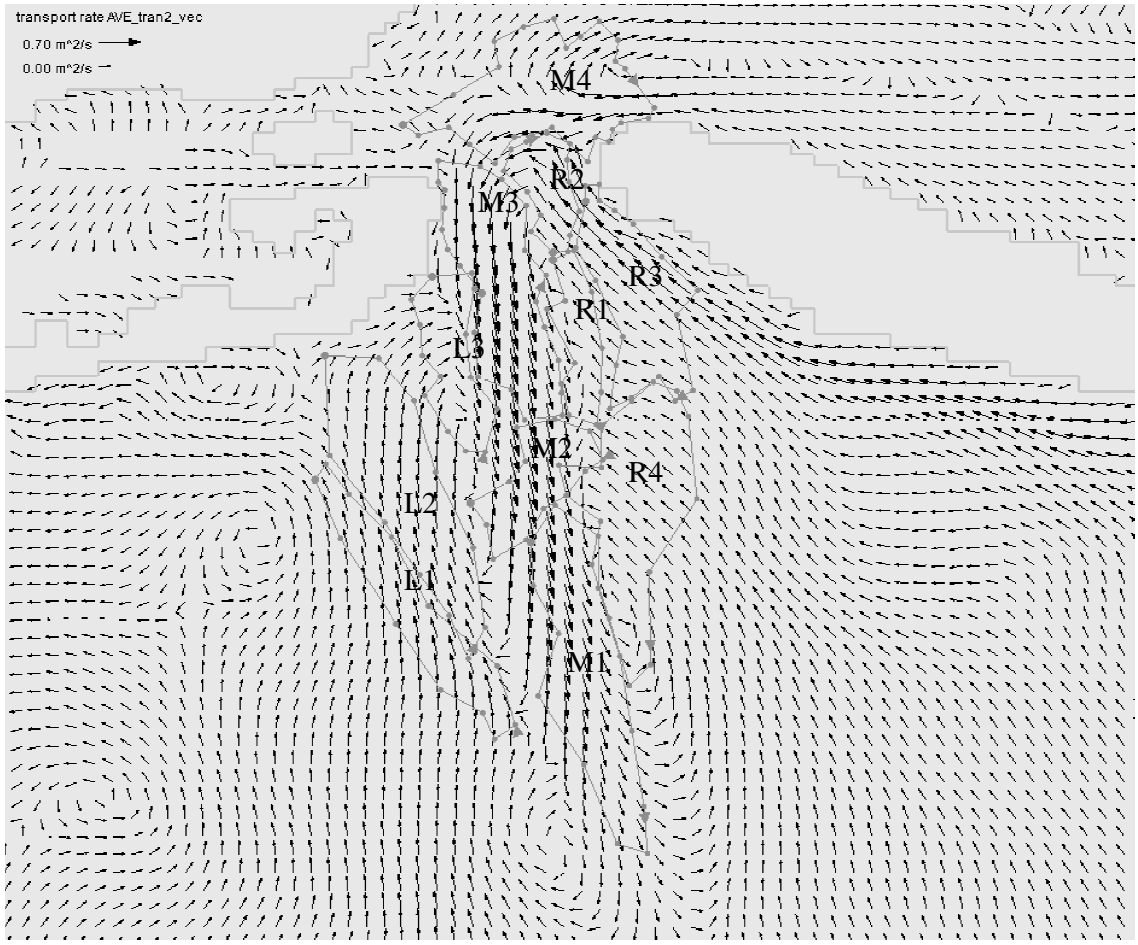

Figure 7.26: Average sediment transport vector field for period 2. Note that the CEMS model predicts no shore-normal $\overline{\overline{q_s}}$ from this major wave event.

Sediment transport pathways were investigated using the difference between $\overline{\overline{q_s}}$ into and out of each region. As can be seen in Figure 7.26, during the storm, longshore sediment transport along the right sand spit increased toward the entrance causing erosion in R3. The sand eroded from R3 then deposits in the deeper part on the right of the entrance R2. The sediment which is eroded from just inside the entrance, M4, one part deposits on the flood tidal delta, another part together with sediment eroded by strong ebb current from inlet M3 gets deposited in M1 and M2. This corresponds to strong velocities in the inlet that are gradually reducing offshore. Sand transports from outer edge of ebb tidal delta, L1, accrete on the inner part of ebb tidal delta L2 and L3.

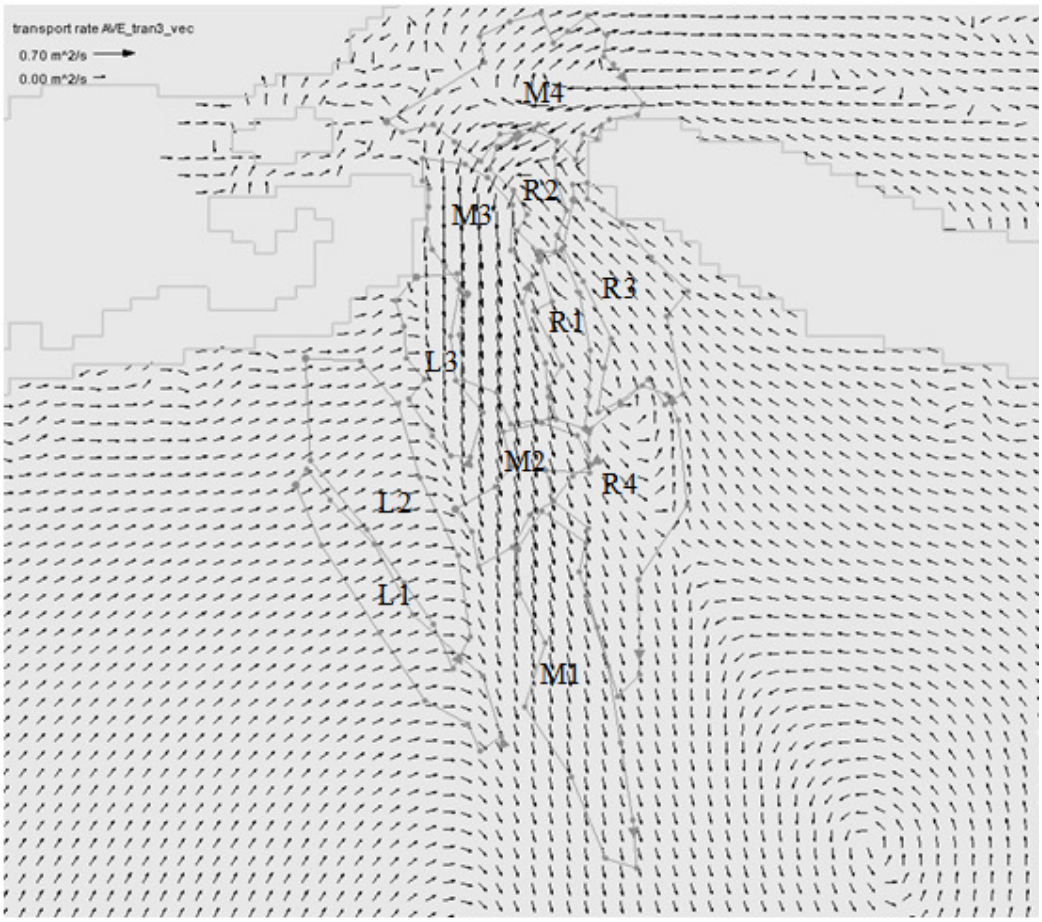

Figure 7.27: Average sediment transport vector field for period 3.

Figure 7.27 shows the $\overline{\overline{q_s}}$ pattern for the normal condition that was very calm and without significant vortex formation. Even though the gradient of sediment transport vectors in and out was confused, the sediment is seen to be transported from the inlet to the right ebb shoal R1 and R4. Compared to the pattern during the storm, $\overline{\overline{q_s}}$ in three regions: L1, L2 and R4 have different directions, whereas in other regions it remains the same. The magnitude of $\overline{\overline{q_s}}$ for the entire domain is quite large: half compared to the storm condition. That is a probable reason for the ebb tidal deltas to recover quickly as shown in Section 7.4.1. However, the influence of storm and normal waves on sediment transport predicted by model is insignificant, which is difficult to qualitatively understand and is in disagreement with the evidence from Houser & Hamiton, (2009).

To improve the clarity of these arguments, detail assessment of $\overline{\overline{q_s}}$ around the inlet is now presented, with particular focus on $\Delta\overline{q_s}$ between key inlet regions (Figure 7.28 and Figure 7.29).

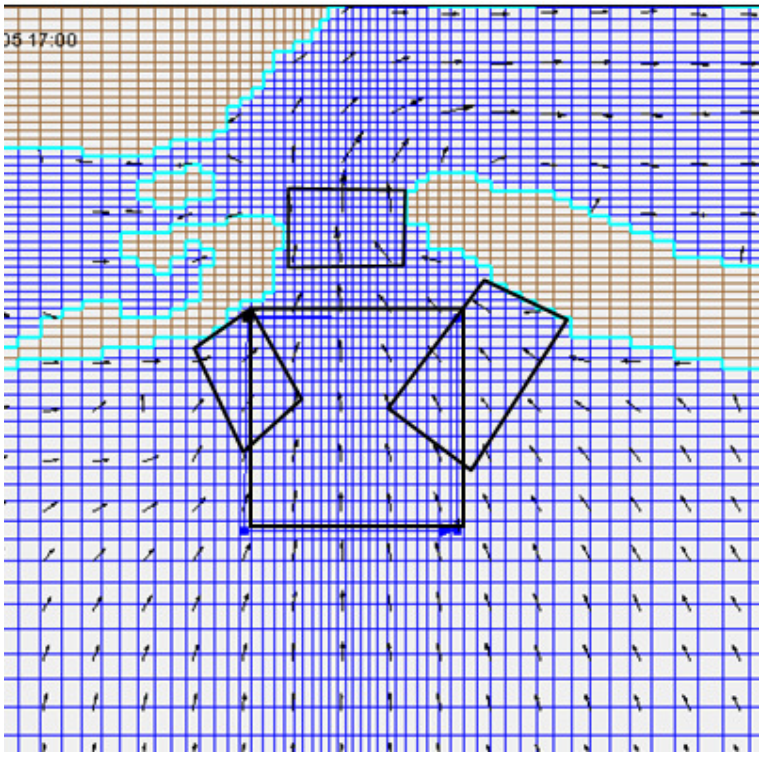

Figure 7.28: Interested regions for calculation $\overline{q_s}$ during 3 periods.

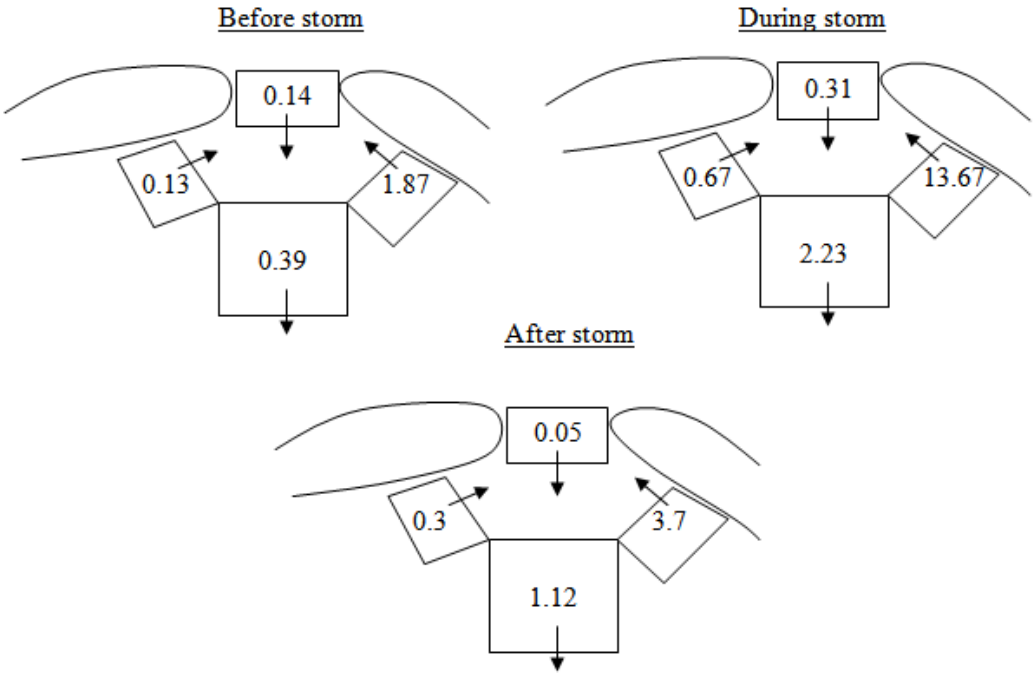

Figure 7.29: $\overline{q_s}$ (10^{-3} m^2/s) for different regions before, during and after storm.

Figure 7.29 shows that during the storm, $\Delta\overline{q_s}$ between right beach and the entrance is nearly 4 times compared to that of the recovery period. This results in erosion on the right beach and accretion at the entrance. The results agree qualitatively with observed from Houser & Hamiton, (2009) albeit underestimated. The 4 times difference between storm and calm conditions explains why these areas recover quickly while no significant shoreface recovery was observed after one year as indicated in Figure 7.2 (Houser & Hamiton, 2009). The $\overline{q_s}$ difference between during and post storm for left beach and middle offshore area is a factor of approximately two and is in general agreement with Figure 7.26 and Figure 7.27. The net $\overline{q_s}$, when considering surrounding beaches, inlet and ebb tidal shoal, has a storm magnitude 4 times larger than the recovery condition, somewhat smaller than expected. The $\Delta\overline{q_s}$ investigation for different key areas in Figure 7.29 shows that the cross section area is significantly accreted during storm, which agrees with observations from other case studies. After a storm, sand deposition into the channel is still continued but 1/4 less than that of during storm. Even though it is not sure if the accretion stops after sometime and turn to erosion for longer simulations, the interpretation of model results via $\Delta\overline{q_s}$ makes more sense than $A(t)$-analysis from single cross section (Section 7.4.2), which may lead to opposite statement with observations.

The underestimation of $\Delta\overline{q_s}$ by CMS during the storm comes from the sediment transport models being essentially a current model with a bit of extra stirring from the waves. That is, the bed shear stresses are always in the direction of the depth-averaged currents and consequently, so is $\overline{q_s}$. That is, the model does not cater for sediment transport in the direction (or opposite direction) of wave travel either within the surfzone or in deeper water. Such a 2HD model can never predict shoreline erosion or shore-normal sediment movements from a wave event, because, the eroding $\overline{\overline{q_s}}$ in a pure wave event is shore-normal, while there can be no depth averaged shore-normal currents.

In order to predict shoreline erosion from a pure wave event, the model must be able to deal with the undertow: the near-bed current which transports sediment offshore Nielsen (2009) p138-139, while the depth averaged current is zero. The huge shoreline erosion by the large waves, which did happen during Hurricane Katrina, was analysed via LiDAR data by Houser & Hamiton, (2009); Claudino-Sales et al., (2008). There results have a different pattern from Figure 7.26, which is dominated by long shore sediment transport. For such conditions, it is necessary to have a numerical model such as ShoreCIRC for realistic modeling or at least using 3D version to describe correctly the current profile resulting in a better sediment transport prediction.

Also, the waves are assumed to be sinusoidal in the CMS model; this means no net sediment transport is generated. All investigators, e g, O'Donoghue & Wright (2004), Ribberink & Al-Salam (1994); Nielsen, (2009) p 270, Ruessink et al (2012); van der A et al. (2010a), Shimamoto et al. (2013) now agree that velocity skewness and acceleration skewness must be included in realistic breaking and nonbreaking wave sediment transport models. The lack of such surf-zone details in the CMS model is one of many reasons leading to underestimation of the wave-erosion during Hurricane Katrina.

7.5 CONCLUSIONS FOR PENSACOLA PASS MODELLING

The capacity of the 2DH-CMS model to predict the morphological changes due to Hurricane Katrina at the Pensacola inlet was investigated by considering $Z_{change}(t)$, $Z_{cumchange}(t)$ of the ebb tidal delta areas L, R, T and of the total area A as well as the change in throat cross section area $A(t)$.

The model predicted that sediment eroded from the eastern beach is deposited in the entrance during stormy condition at a rate 4 times larger than normal condition (Figure 7.29). The results agree with physical processes described by Bertin et al. (2009), Williams & Pan (2011) during storm, but are an underestimate compared to observation from Houser & Hamiton, (2009). This explains why the ebb tidal deltas and fore beaches recover quickly while no significant shore face recovery was observed after one year (Houser & Hamiton, 2009).

The model was unable to reach a static or dynamic equilibrium. Perhaps, a portion of these disappointing results relate to bed updating and the chosen model is not good enough to investigate long-term morphology evolution. However, detail measurements of both sediment transport rates with simultaneous bed elevation changes under storm conditions would be required to separate numerical errors from bed updating from sediment transport prediction errors.

The model's treatment of wave influence on the sediment transport process is too simplistic: Bed shear stresses are always in the direction of the depth-averaged current (see Eq (7.1)) and hence, so is q_s. The model only predicts wave spectra, not wave asymmetry and, hence, velocity- and acceleration skewness of the wave motion is not available for the sediment transport modeling. A related issue is that the hydraulic model is depth-averaged meaning that it cannot model the shore-normal qs which occurs during storms but requires separation of the onshore directed wave driven flow near the surface and the undertow, which carries sediment off shore near the bottom. Hence, it is not really surprising that the simulation results are poor, which is agreed to by Larson in his review of this thesis. He commented that "the inability of the CMS model to reach equilibrium is common to all such detailed models. At our present state of knowledge we need to formulate governing equations that ensure that equilibrium is reached".

Chapter 8

LABORATORY EXPERIMENTS ON BARRIER SEDIMENT TRANSPORT

8.1 INTRODUCTION

Sediment transport and morphology changes related to inlet dynamics are not completely understood due to multiple interactions between different processes of waves, currents, and sediments (e.g., Pensacola Inlet, Chapter 7). State-of-the-art numerical models, such as the CMS model, which necessarily simplify natural processes, to solve the governing equations, are unable to predict the morphology change of complicated systems such as the tidal inlets under storm conditions. Therefore, in order to understand qualitatively the sediment transport processes and the challenges for present and future numerical models, laboratory experiments were conducted. The data from these experiments serve to test existing sediment transport models in Chapter 9.

Many experiments have been conducted in the past on non-breaking waves, transformed over impermeable rigid obstacles (Beji and Battjes, 1993; Beji.e.t al., 1992; Ma et al., 2010), and sediment transport studies of onshore bar migration under the influence of waves and currents (Hsu and Yu, 2008). However, there is scarce information on the sediment transport or morphology changes over rippled sand barriers. The morphology change of a sand barrier in front of a tidal inlet entrance due to sediment transport processes induced by waves with and without currents is the subject of this chapter.

The results illustrate the challenges related to complicated vertical velocity distributions in combined wave-current flows and the relations between near-bed fluid velocities and sediment transport rates, even in 2DV flows.

8.2 THE EXPERIMENTAL SETUP

Experiments were carried out on a 3 m long barrier made of fine sand with initial 1:5 front and lee slopes; 0.25 m high at the centre, in a water depth of 0.5 m. Wave heights and flow velocities were measured during each test of one hour duration. Sand bed levels were measured after one hour and were considered as initial profile for the next run. Sediment transport rates $q_s(x)$ for each run were calculated from the changes in sediment volume.

8.2.1 The flume, the wave maker and the recording instruments

- ***The wave flume and wave maker***

Experiments were carried out in a 19.1 m long, 1 m high and 1 m wide flume at the School of Civil Engineering, The University of Queensland. The flume was equipped with a piston wave generator at one end, located 2.9 m from the beginning of the channel (Figure 8.2). A 3 m long sand barrier was located in the middle of the flume. Figure 8.1 shows the wave flume with sand barrier (left) and the instruments set up including wave gauges and the acoustic Doppler velocity meter, ADV (right).

A computer controlled hydraulic wave maker was capable of generating regular waves, combined waves and random waves via the software program PACIFIC (Baldock et al., 2005). In this study, regular waves were generated with different wave heights and periods. The wave paddle is 6.45 m long, 0.9 m high and can generate maximum wave height of 14 cm at 0.5 m water depth. Wave frequencies range from 0.1 to 2 Hz, with maximum water depth up to 0.9 m. The water depth of 0.5 m was chosen in the present study. No breaking or overtopping of the channel wall occurred during the experiments. Passive wave absorbers were placed at the end of the flume to minimize wave reflection and to stabilize the water level. A reversible hydraulic pump was used to generate flow in either direction, with a V-notch weir to measure the flow rate Q (Figure 8.2).

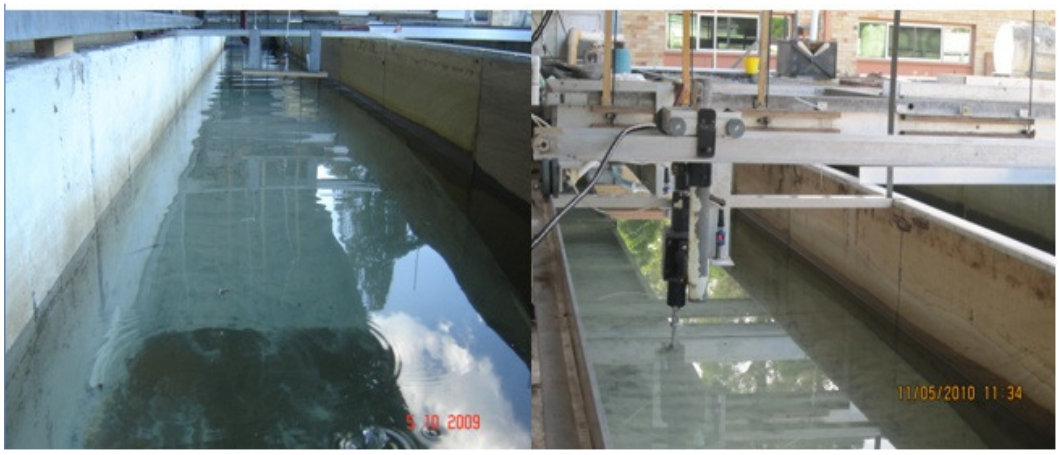

Figure 8.1 : View of the wave flume and the instruments (wave gauge and ADV).

- ***Recording equipment***

Measuring rods were set up on a trolley (Figure 8.2) to measure the sand profile. The trolley can be moved easily along the channel top on rails fixed on the flume side-walls. Its elevation was checked frequently to ensure that the measurement error was between 1mm.

Microsonic® Mic+25/IU/TC acoustic displacement sensors with an accuracy of 0.18 mm and response time of 50 ms (Microsonic 2005) are utilized to measure the water surface

displacements $\eta(t)$. The wave gauges were set up above the water surface with the vertical displacement range from wave gauges to water surface between 3 cm and 25 cm. Three wave sensors were placed (i) at the beginning of channel (x=0 m), (ii) at one fifth of the wave length to check the reflection coefficient (Baldock and Simmonds, 1999), and (iii) on top of the sand barrier (x=8.5 m), for all the cases (Figure 8.2). For certain cases, additional sensors were placed up slope and down slope of the sand bar.

a)

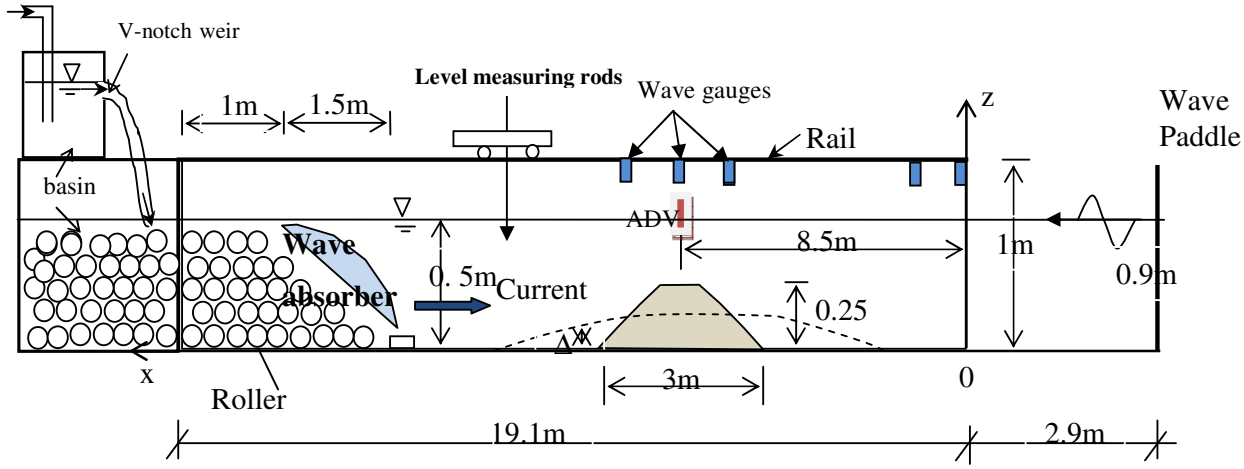

b)

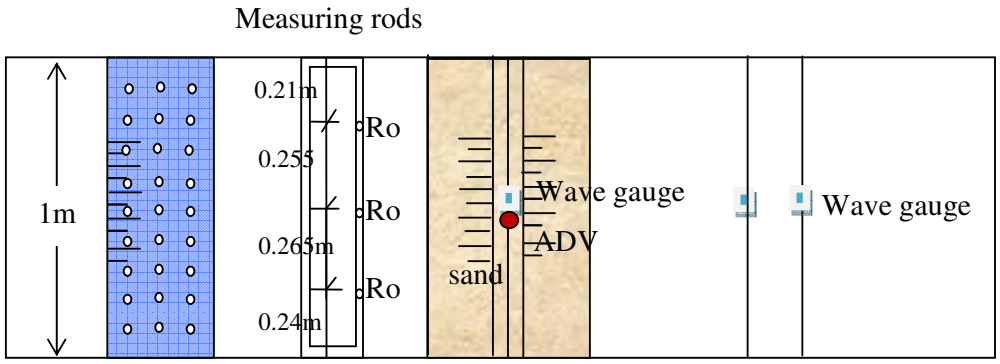

Figure 8.2: (a) Sketch of wave flume and locations of the wave gauges. b) Plan view of the flume.

A 2D side-looking Sontek® micro Acoustic Doppler Velocimeter (ADV) with 1% accuracy for velocities u < 1.7 m/s was used to measure horizontal velocities at one point at a time.

A sand hump was formed in the middle of the flume representing either a sand barrier at a tidal inlet entrance or an offshore bar. The sand hump geometry was chosen depending on the typical dimensions of offshore sand bars and the capacity of the wave flume to ensure no wave breaking and no channel wall overtopping occurred. The barrier was initially made in a trapezoidal shape with both the front and lee slopes of 1:5, 0.5 m crest width and 0.25 m crown height and 3 m length (Figure 8.2a).

8.2.2 The sediment

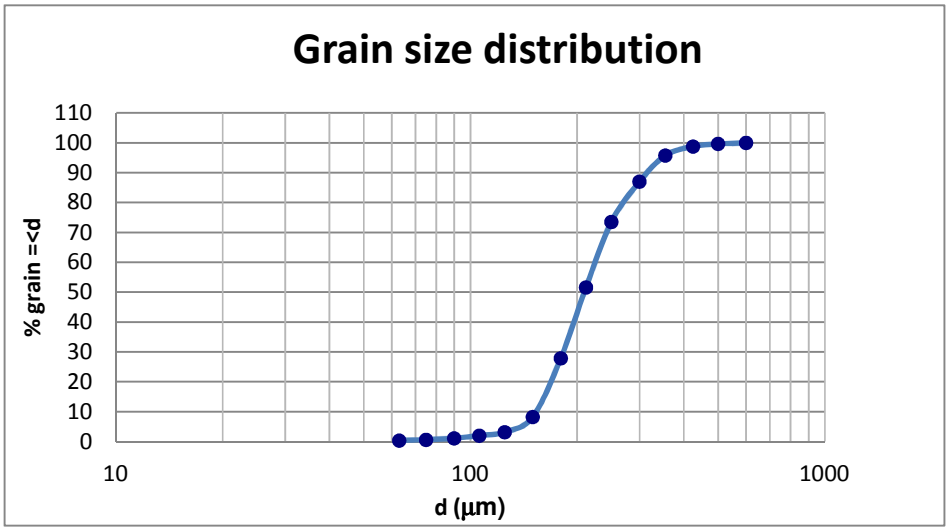

Figure 8.3. Grain size distribution of the sediment used in experiments.

The sand hump was formed uniformly across the channel following its design profile/cross-section drawn on the channel walls. To have the sand totally compacted after the sand hump is formed, the wave maker is operated for a whole day with a wave height of 10 cm with the sand hump covered with a filter cloth to arrest the sand movement. The sediment used for the experiments is fine sand and the grain size distribution of this sand is shown in Figure 8.3 with d_{50} = 0.21 mm and d_{90} = 0.32 mm.

8.3 HYDRODYNAMIC DATA ACQUISITION AND DATA ANALYSIS

Four regular waves (W1, W2,…) combined with 6 currents (C1, C2, …) totaling 24 combinations were generated in a water depth of 0.5 m. The currents were generated in two directions viz., same as wave propagation (Q>0) and against wave propagation (Q<0). In general, W+C stands for wave and current in the same direction, while W-C stands for waves and current in opposite directions.

The label used for each combination includes information of wave case and flow conditions (provided in terms of discharge). For example W1Q10 is the combination of wave case 1 and current in the direction of wave propagation with discharge Q = 10 L/s.

The wave parameters are shown in Table 8.1 where k is wave number, h is water depth, L is wave length.

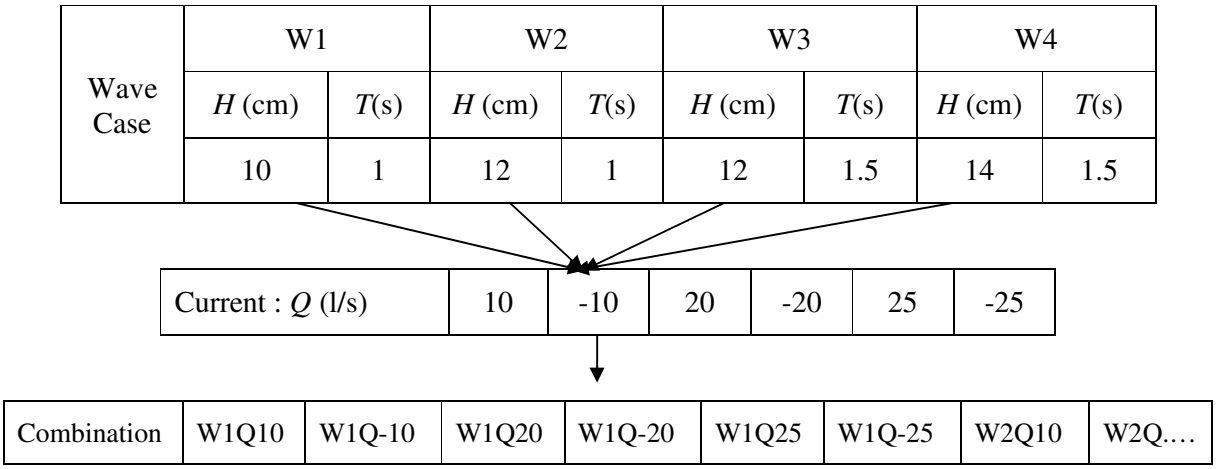

Table 8.1: wave parameter for two period and two zones

T(s)	*kh*		*L/h*	
	x=0 *h*=0.5 m	*x=8.5 m* *h*=0.25 m	*x=0* *h*=0.5 m	*x=8.5 m* *h*=0.25 m
1	2.1	1. 2	3	5.2
1.5	1.2	0.72	5.8	8.7

8.3.1 Water surface time series data and analysis

Each wave and/or current condition was run for one hour during which water surface elevations $\eta(x_i,t)$ were measured, processed and analysed. The water surface elevation $\eta(t)$ is obtained initially by transferring electrical voltage signals to surface displacement based on the calibration curve for the each displacement sensor. Then the spikes were cut out and smoothened by low-pass FFT filtering and inverted to a smmothed $\eta(t)$. An equivalent root mean square sine wave height can be calculated as $H_{rms}= \sqrt{8Var(\eta)}$.

The reflection is not only due to the wave absorber at the end of the wave flume but also due to the sand hump. The data set $\eta(t)$ at x=0m and at L/5 were used to check the reflection coefficient K_r by the program Ref-slope (Baldock and Simmonds, 1999). K_r for the shorter wave period (W1 and W2) with and without current are low ranging from 3% to 7%. For the longer wave period (W3 and W4) with and without current, K_r=0.14-0.22. In general a W+C combination causes greater K_r than W-C because a following current increases the wave speed and hence the wave length.

8.3.1.1 Wave transformation over the sand barrier for waves only

In this section the comparison of non-breaking wave transformation over the bar between different cases without current is presented. The results of wave transformation for W1 and W2 are similar, the same pattern is also observed between W3 and W4. Therefore W1 and W4 are chosen for discussion.

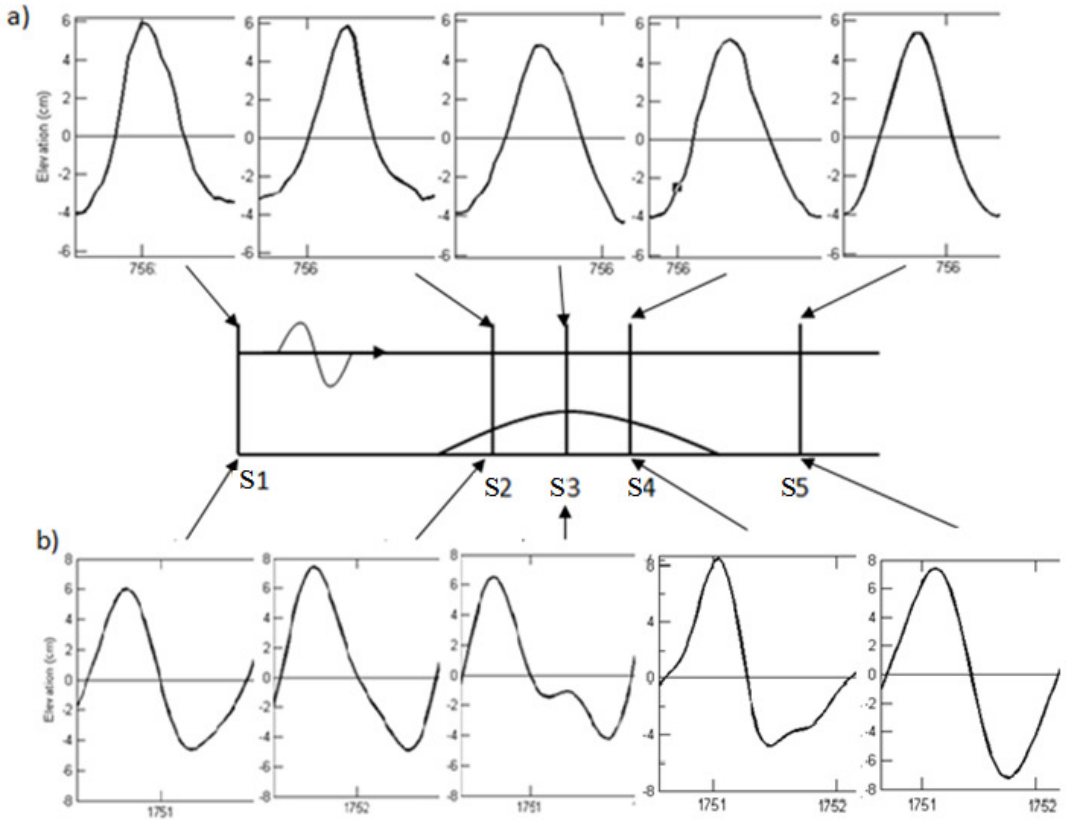

Figure 8.4: Transformation of waves over the sand bar (a) W1: H=10 cm, T=1 s; (b) W2: H=14 cm, T=1.5 s at different transects: S1(x=0 m); S2(x=8 m), S3(x=8.5 m), S4(x=9.5 m), S5(x=10.3 m);

The comparison of non-breaking wave transformation over the barrier between W1 and W4 is shown in Figure 8.4 a, b for different transects from the beginning of the flume S1(x=0 m) to middle upslope S2(x=8 m), over the top of the hump S3(x=8.5 m), down slope S4(x=9.5 m) and behind the hump S5(x=10.3 m).

For Case W1, as waves propagated over the bar, the waves were nearly vertically symmetric (Figure 8.4 a). A velocity skewed 'Stokes wave' is generated while the waves traverse shallow water (up slope) resulting in sharp crests and obtuse troughs at S2. Wave crests were less sharp at S3, then on the way down to deeper water it increased at S4 with regularly releasing insignificant amplitude of second order harmonics (Figure 8.5 left) and finally back to nearly the original shape

at S5. The influence of reflection in this case was insignificant with K_r= 0.03. The observations from Case-1 were in agreement with Beji & Battjes (1993) (c.f. Figure 2 in their paper) for short wave transmission over a bar. There seems to be less difference in terms of wave transformation over obstacles with fixed bed compared to permeable and movable bed, for the wave conditions and sand hump configuration considered.

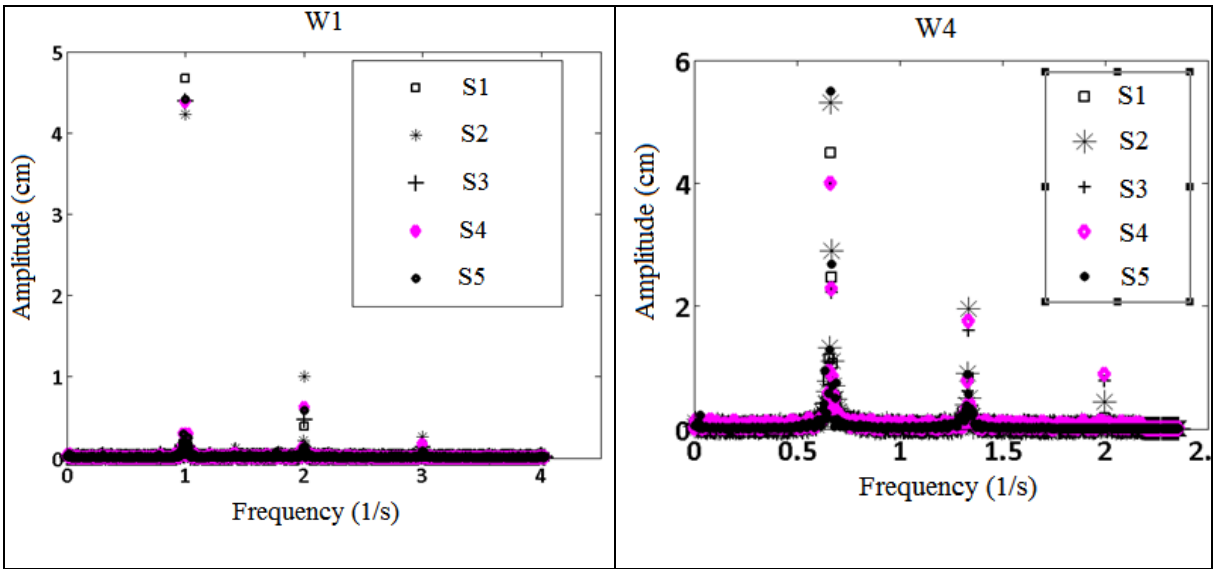

Figure 8.5: Amplitude spectra at 5 locations of W1 (left); W4 (right).

For relatively long waves, higher harmonics are generated when the waves propagate over submerged obstacles (Beji & Battjes, 1993; Beji et al., 1992). When regular waves travel upslope, they gradually become saw-tooth shaped. At this stage, the bound harmonic- primarily 2nd harmonics- are rather small. If waves continue to propagate in a shallow region, the higher harmonic components may become significant due to energy flow from the primary harmonic to higher harmonics. This phenomenon leads to dispersive tail waves traveling at nearly the same speed as the primary waves. Then long waves following dispersive tails pass into deeper water downslope where they decompose or release bound harmonics into several smaller amplitude waves with nearly the same frequency. Drastic and rapid changes in wave forms appear at the beginning stage as energy exchanges among different wave components, and then it re-adjusts with increasing depth for several wave lengths till equilibrium is reached. Similar observations were obtained in W4 (for comparison cf. Figure 2 in Beji & Battjes (1993)) wherein transmitted waves were shorter than the incoming waves and became multiple crested after passing over the sand bar (Figure 8.5right).

In contrast with that of W1, wherein the transmitted waves had saw-tooth shape and root mean square wave height (H_{rms}) increased at S2, the skewness reduced at the top of the bar S3 with dispersive tail, then again increased at S4 with higher harmonic decomposition and finally back to nearly original shape at S5. This wave height was influenced by wave reflection wherein the reflection coefficient for the wave absorber is 0.2. The generation of higher harmonics in W4 was more significant than W1 as seen in the spectra in Figure 8.4. However, there is no evidence of the frequency-downshift phenomenon (the peak frequency shift from the initial dominant frequency to a lower one) stated by Ma et al. (2010).

8.3.1.2 Wave transformation over the sand barrier for wave-current combinations

When waves interact with currents, Turpin et al. (1983) and Nielsen (2009) theoretically show that wave train over varying depth was stabilized by following current by reducing wave steepness as well as increased speed. In contrast, an opposing current steepens the waves and reduces the group velocity. The shortening effect may cause wave breaking or wave blocking if the opposing current is strong enough. Lai et al. (1989) and Ma et al. (2010) observed frequency downshift occurring with strong opposing currents even without wave breaking, but this was not observed in weak opposing currents.

In the present experiment, no wave blocking was expected due to the strongest opposing current 0.10 m/s being far less than half of group velocity ($C_{g,min}$ =0.75 m/s) corresponding to T=1 s. The results of H_{rms}/H_i (H_i = incident wave height), for all wave cases combined with different opposing currents were compared and presented at different locations along the barrier in Figure 8.6. The combinations with T=1.5 s (red lines) show that H_{rms}/H_i increase upslope and reduces on top of the barrier then increase again downslope before coming back to nearly original shape towards the end of flume. H_{rms}/H_i of wave only cases was higher than that of combined cases, which is absent from the literature. The opposite trends are observed for cases with shorter period T=1 s (blue dashed lines) with H_{rms}/H_i increasing with increasing opposing current. These cases agree with literature when the mean period T_{mean} of bound wave were found to be the same as originally generated.

T_{mean} of bound wave, at x=0 for any combination of wave and current was the same as that generated. However a slight change in T_{mean} was observed at x=8.5 m. In particular T_{mean}, which reduced from 1 s (1.5 s) to 0.94 s (1.497 s) for the strongest opposing current. T_{mean} did not change for weaker currents. Lengthening of waves was found with strongest following current from 1 s to 1.12 s. However, this was not observed for T=1.5 s.

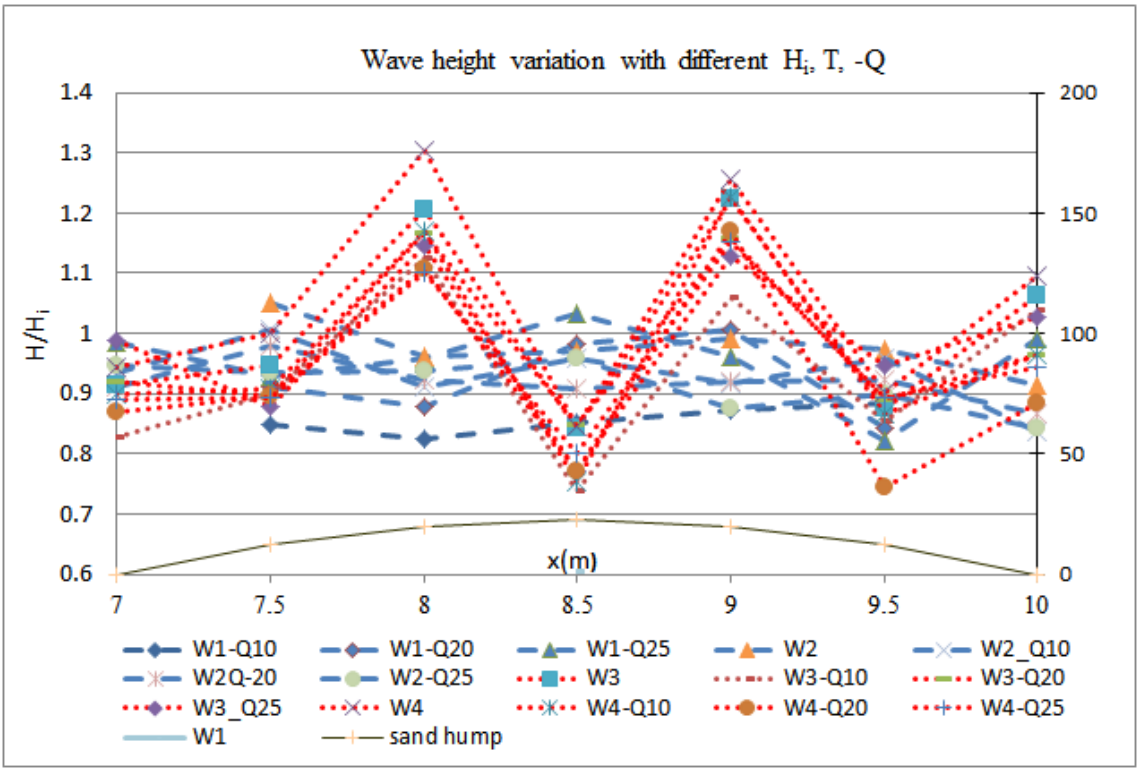

Figure 8.6: H_{rms}/H_i for all wave cases with opposite currents, the blue dashed lines for cases with T=1 s, the red dotted lines for cases with T=1.5 s.

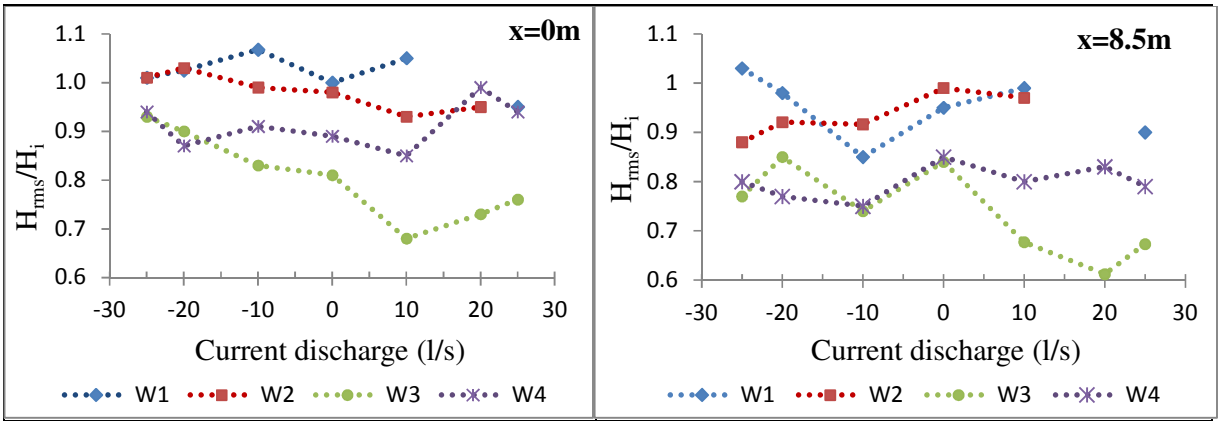

Figure 8.7: H_{rms}/H_i for all combinations of 4 different wave cases and 6 different currents at x=0 m (left) and x=8.5 m on top of the barrier (right).

Figure 8.7 shows H_{rms}/H_i for all combinations of 4 different wave cases and 6 different currents at x=0 m (left) and x=8.5 m on top of the barrier (right). At x=0 m (Figure 8.7 left), for the same wave period, the lower original wave height generated a higher H_{rms}/H_i. For the same wave condition, increased opposing current resulted in increased H_{rms}/H_i. However increase in the following current resulted in reduced H_{rms}/H_i for Q=10 L/s only.

At x=8.5m (Figure 8.7 right), H_{rms}/H_i behaved differently compared to the beginning of the channel because it is in shallower depth with half water depth and also due to deformation of wave while propagating upslope. H_{rms}/H_i reduces in all combinations with either following or opposite current $Q = \pm 10$ L/s and increases for combination with current Q = -20 L/s, however inconsistent trend is observed for $Q = \pm 25$ L/s, 20 L/s.

8.3.2 Horizontal velocity time series and analysis

The ADV is usually located above the top of the hump at x=8.5 m, around 5 cm from the bed. The horizontal velocity component U_x is aligned longitudinally to the flow direction and the transverse component (U_y) oriented normal to the flume side wall (Figure 8.2a-right). The longitudinal velocity is around 10 times larger than transverse velocity; hence the analysis is focused on U_x. Low-pass filtering was used to reduce noise before calculating U_{ave}, U_{max}, U_{min}, U_{rms}, velocity skewness R_u. The shape of $U_x(t)$ was also "sharp crested" with obtuse troughs corresponding to the shape of $\eta(t)$.

In few particular cases, in order to obtain the vertical structure of the wave induced currents, the ADV is moved at different elevations in the water column. Sometimes, the ADV is placed at the front face or at the back face of the sand hump to investigate the difference between the current structures at these points.

The vertical U_{ave}-profile in the absence of waves was logarithmic as expected. For wave only conditions, the Eulerian mean velocity in a zero net flow situation is positive near the surface negative in the centre and positive near the bed due to boundary layer streaming, (Nielsen, 2009, p 43). Over ripple beds, the wave boundary layer thickness increases considerably, so the negative part of the Eulerian U_{ave}-profile started well above the ripple crests. The oscillatory velocity amplitude close to the bed was influenced by vortex formation. Other studies, Dimas & Kolokythas (2011); Hurther & Thorne (2011) and Ojha & Mazumder (2010) have noticed this up to six ripple heights above the ripple crest. When waves and current are combined the velocity profile of following current get a maximum value then regularly decreases toward the surface (Klopman, 1994; van Doorn, 1981). This decreasing trend is found for all current strength if time average bed shear stress is in the direction of wave train. In contrast, the opposing current profile increases quickly toward the surface as in the experiments of Klopman (1994). The observations of wave superimposed current, in both directions, were different from existing simple wave-current boundary layer model which has a logarithmic profile and increases monotonically above the wave boundary layer as explained by Nielsen & You (1996) in terms of the wave Reynolds stresses.

The comparison of U_{ave} profile for current only (Q=-25 L/s), wave only W4 and wave combined opposing current W4Q-25 are presented in Figure 8.8 at different locations along the wave flume.

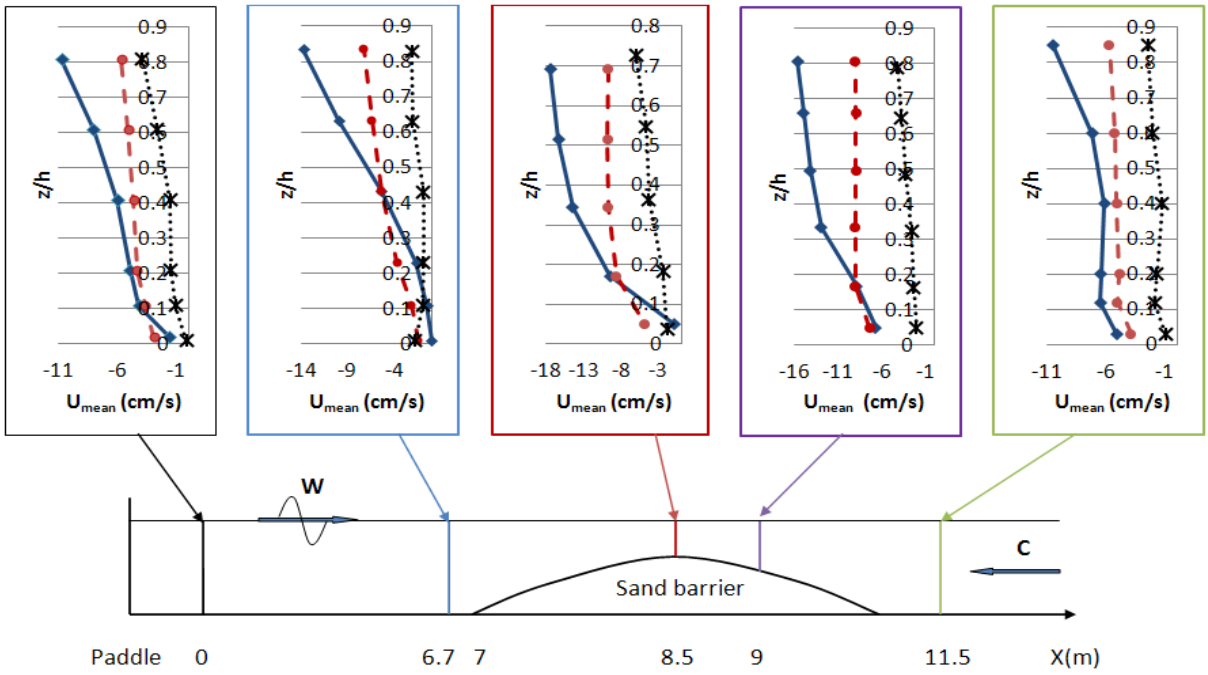

Figure 8.8: U_{ave} -profiles at different locations along the sand bar for waves only W4; --●--; current only, Q = -25 L/s …∗… ; W4 with opposing current (-25 L/s) -◆- .

For the wave only cases, velocity profiles illustrated negative value for all water depths due to inability to measure velocity above wave trough. And the limitation of ADV is that the ADV should be at least 1.5cm above the bed, thus boundary layer streaming cannot be measured. The magnitude of the wave-induced velocity is larger on the sand barrier than elsewhere where water depths are comparatively larger. The velocity profile of combined wave and strongest opposing current agreed with the flat-bed observations of van Doorn (1981) and Klopman (1994) (cf. Figure 1, 2 in Nielsen & You (1996)). The velocity increased very quickly toward the surface for the locations x=0 m, x=6.7 m and x=11.5 m, whereas it increased gradually on the sand bar. Opposing current dominated above 0.3h from the bed, while insignificant magnitude is observed close to the bed at 3 first sections. The profile shape is almost concave while only the profile in front of sand bar is convex. Profiles of following currents have the same shape as van Doorn (1981), the magnitude being less than opposing current due to subtraction of wave induced current above the trough-level (not presented here).

In summary, the velocity observations above and near the hump showed similarities with previous flat-bed experiments and simple analytical models but detailed modeling would require a high resolution 2DV model, perhaps an extended model of that presented by Klopman (1994), if at all possible at present.

To prepare for sediment transport calculation, with simple models based on the free stream velocity, phase averaged velocities for all cases were evaluated and summarized in Table 8.2. Measurements were made on top of the barrier at 5cm above the bed. The phase averaged velocity shapes are similar between combinations W1/W2 and W3/W4. Therefore results of W1 and W4 are chosen for presentation with the maximum current in both directions in Figure 8.9.

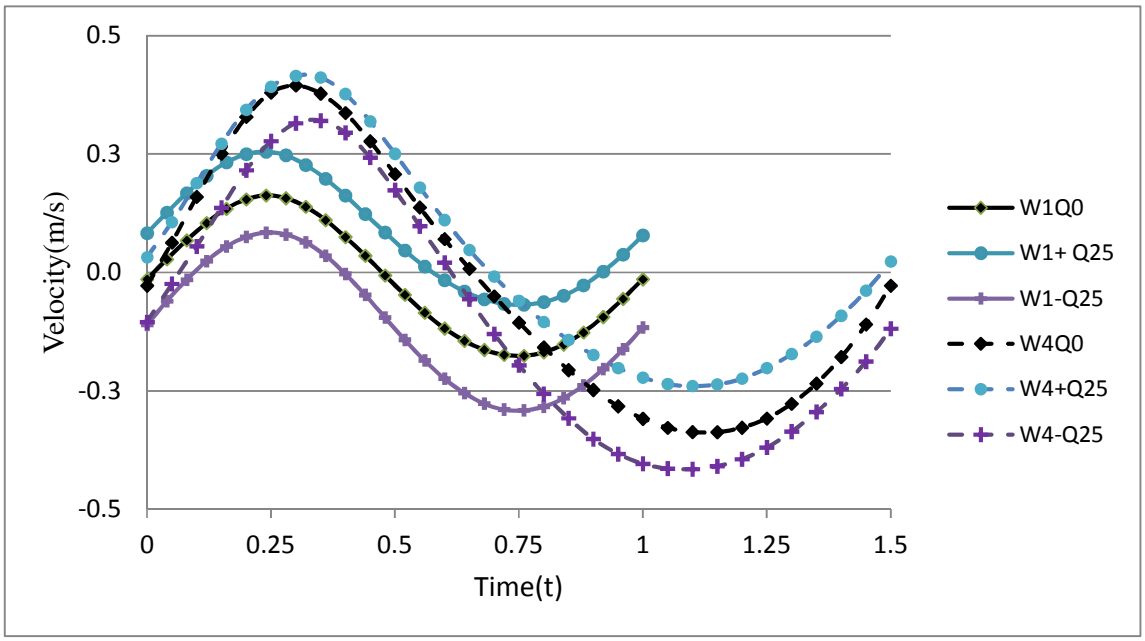

Figure 8.9: Phase average velocity at the point on center top of the barriers of W1 and W4 combined with strongest following and opposing current.

As can be seen in Figure 8.9, W1 (solid lines), the velocity of almost all combinations has nearly simple harmonic and symmetric shape except for the cases with Q = -25 L/s, which displays quite a long and deep trough. The velocity skewness, defined as $R_u = u_{max}/(u_{max}-u_{min})$ by Ribberink & Al-Sallem (1994), is ranging from 0.51-0.54 for almost all combinations except R_u=0.59 for W1Q+25, which increase in the shoaling zone. For waves only, the wave induced current $\tilde{u}$ =17 cm/s and the mean velocity $\bar{u}$ = -1.4 cm/s (table 8.2). The net onshore direction for strongest following current with $\bar{u}$ = 8.3 cm/s and net offshore direction for strongest opposing current with $\bar{u}$ = -11 cm/s. For W4 (dashed lines), a skewed shape was observed even with wave only, wherein

the crest was sharp and the trough obtuse. The stronger the current the more asymmetric it becomes, especially for opposing current. The combinations with T=1.5 s usually have $0.56<R_u<0.59$ (table 8.2), which is higher than all combination of W1 and W2. Wave induced velocities (W4) ranged between a maximum of 40 cm/s and a minimum of -34 cm/s with $\bar{u}$=-2.8 cm/s. For the strongest following current $\bar{u}$ reached +3.7 cm/s, respectively -10.6 cm/s for the strongest opposing current (Table 8.2). The degree of asymmetry can be presented via acceleration skewness, $R_a = a_{max}/(a_{max}-a_{min})$ as in Watanabe & Sato, (2004). The results of R_a for different combinations are shown in table 8.2, which range from 0.5 to 0.53 for the combinations of wave period T=1 s and larger for combinations of T=1.5 s, the highest value R_a=0.58 belongs to W4.

Table 8.2: Summary current statistic parameters

Test	Uavg	Urms	Umin	Umax	StdvU	Ru	Ra
	(cm/s)	(cm/s)	(cm/s)	(cm/s)	(cm/s)	[-]	[-]
W1Q0	-1.43	17.01	-17.97	16.55	12.03	0.52	0.50
W1Q-10	-6.25	15.68	-21.36	10.40	11.09	0.52	0.51
W1Q-20	-9.26	19.14	-28.23	10.62	13.53	0.51	0.50
W1Q-25	-11.01	19.10	-29.81	8.85	13.51	0.51	0.51
W1Q+10	1.56	17.40	-14.97	20.45	12.30	0.53	0.50
W1Q+25	8.33	16.45	-7.30	26.38	11.63	0.58	0.53
W2Q0	-1.49	18.69	-19.74	18.38	13.24	0.52	0.50
W2Q-10	-5.05	16.77	-21.69	12.50	11.86	0.51	0.50
W2Q-20	-9.97	19.73	-29.43	10.55	13.95	0.51	0.51
W2Q-25	-10.32	19.50	-29.13	10.06	13.79	0.52	0.51
W2Q+10	1.35	17.64	-15.14	19.96	12.47	0.53	0.53
W2Q+20	4.69	17.28	-11.93	23.90	12.22	0.54	0.53
W2Q+25	6.32	18.57	-11.53	26.18	13.13	0.53	0.51
W3Q0	-2.72	31.39	-28.60	37.39	22.19	0.59	0.54
W3Q-10	-6.13	32.50	-35.26	32.67	22.98	0.57	0.55
W3Q-20	-7.15	32.88	-36.14	34.38	23.25	0.59	0.50
W3Q-25	-9.60	33.12	-39.56	30.77	23.42	0.57	0.52
W3Q+10	0.57	29.92	-26.80	35.73	21.16	0.56	0.55
W3Q+20	3.56	31.07	-24.64	39.11	21.97	0.56	0.54
W3Q+25	5.36	31.58	-22.98	42.38	22.33	0.57	0.55
W4Q0	-2.81	35.79	-34.47	40.08	25.31	0.58	0.58
W4Q-10	-6.53	36.09	-37.68	38.26	25.52	0.59	0.54
W4Q-20	-8.87	36.54	-40.24	36.42	25.84	0.59	0.51
W4Q-25	-10.60	36.45	-43.25	33.49	25.77	0.57	0.51
W4Q+10	-0.13	33.2	-29.32	39.14	23.48	0.57	0.56
W4Q+20	3.77	34.6	-26.91	44.21	24.47	0.57	0.55
W4Q+25	3.23	35.1	-25.56	43.25	22.89	0.58	0.54

8.3.3 Ripple dimension and prediction

Rippled bed was observed after each test as shown in Figure 8.10 for cases W1 and W4 at the top of the sand barrier. Ripple dimensions influence the sediment transport mechanism as well as boundary layer structure. Hence, ripple height and length were measured after each test for each case to calculate sediment transport rate in Chapter 9.

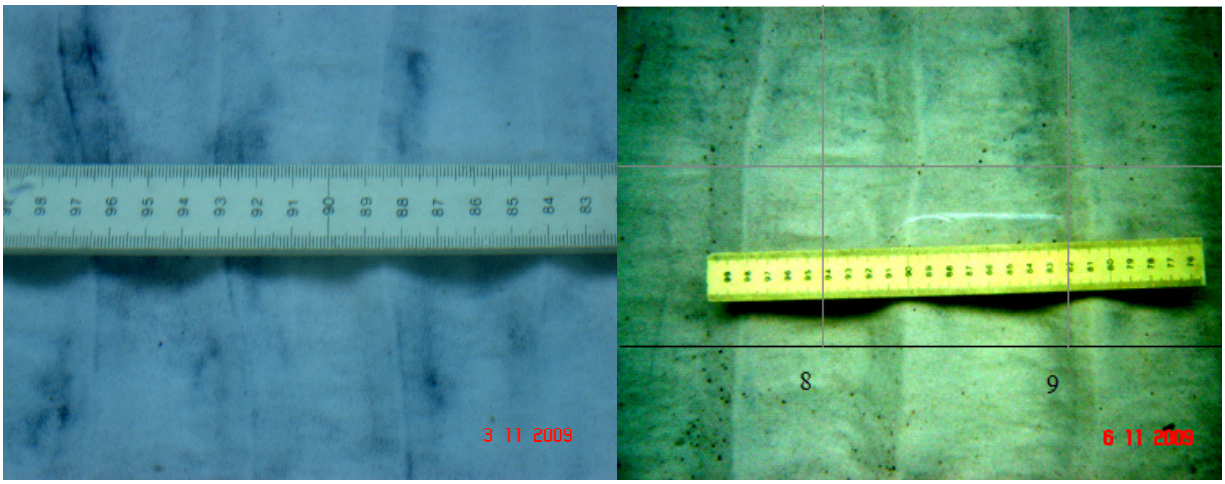

Figure 8.10: Ripple bed at top of the sand barrier for case W1 (left) and W4 (right).

From the visual observations during the experiments, the ripple properties changed during the initial 10 min of the test, but later on there is insignificant change. In general, larger and more regular ripples were located from top toward lee side of the sand bar. On the sides of the hump, ripple sizes changed regularly from medium to small size at the toes. From case W1 to case W4, due to the incremental increase of wave heights and wave periods, the ripple size became larger. However, the increment in wave period makes it more remarkable than the influence of growing wave height.

Table 8.3 shows the summary of ripple dimensions measured on top of the sand bar for different cases. The ripple length λ_r and ripple height η_r clearly fall in two groups. For T=1 s, W1 and W2, 0.0045 m<η_r<0.007 m and 0.045 m<λ_r<0.075 m with ripple steepness being around 0.11-0.12 except for two cases W1Q+25 and W2Q+20, where steepness was 0.093 and 0.085 respectively. The longer period waves (T=1.5 s) induced larger ripples with 0.01 m<η_r<0.0145 m and 0.07 m<λ_r<0.1 m, and larger steepness from 0.12 to 0.16 except two cases with lower steepness and smaller ripple size belong to W4Q-25 and W4Q+10.

The comparison between measured and estimated ripple dimensions using popular existing formulae, which best fit with large number of data set, by such as Nielsen (1981), Van Rijn (1993) and O' Donoghue et al. (2006) are presented in Table 8.3 and Figure 8.11, Figure 8.12. Basically,

vortex ripple size depends on the particle size d_{50}, wave period T and peak near bed orbital velocity, taken as U_1, i.e., the amplitude of the first harmonic of the phase averaged velocity. Several researchers have found ripple size to be dominated by the mobility number

$$\psi = \frac{U_1^2}{(s-1)gd_{50}} \tag{8.1}$$

where, s is sediment specific density and/or θ', skin friction Shields parameter (Nielsen, 1981), or Reynolds wave number (Catano-Lopera & Garcia, 2006a,b). In this study ψ ranges from 6.9 to 35, which indicates that ripple movement is slow and $0.081<\theta'<0.25$.

Table 8.3: Summary measured and calculated ripple dimension on top of the sand bar.

Test	Measured			Calculated by					
	η_r(m)	λ_r (m)	η_r/λ_r (–)	Nielsen (1981)		O'Donoghue et al.(2006)		Van Rijn (1993)	
				η_r (m)	λ_r (m)	η_r (m)	λ_r (m)	η_r (m)	λ_r (m)
W1Q0	0.0050	0.045	0.111	0.006	0.033	0.003	0.025	0.006	0.034
W1Q-10	0.0050	0.045	0.111	0.005	0.031	0.003	0.024	0.005	0.031
W1Q-20	0.0055	0.055	0.100	0.006	0.036	0.003	0.028	0.007	0.038
W1Q-25	0.0050	0.050	0.100	0.006	0.036	0.003	0.028	0.007	0.038
W1Q+10	0.0045	0.045	0.100	0.006	0.034	0.003	0.026	0.006	0.035
W1Q+25	0.007	0.075	0.093	0.006	0.032	0.003	0.025	0.006	0.033
W2Q0	0.0050	0.040	0.125	0.006	0.035	0.003	0.027	0.007	0.037
W2Q-10	0.0045	0.045	0.100	0.006	0.032	0.003	0.025	0.006	0.033
W2Q-20	0.0070	0.060	0.117	0.006	0.037	0.003	0.029	0.007	0.039
W2Q-25	0.0060	0.047	0.128	0.006	0.036	0.003	0.028	0.007	0.039
W2Q+10	0.005	0.05	0.100	0.006	0.034	0.003	0.026	0.006	0.035
W2Q+20	0.0055	0.065	0.085	0.006	0.033	0.003	0.026	0.006	0.034
W2Q+25	0.0065	0.05	0.130	0.006	0.035	0.003	0.027	0.007	0.037
W3Q0	0.0115	0.090	0.128	0.012	0.074	0.005	0.060	0.011	0.078
W3Q-10	0.0115	0.100	0.115	0.012	0.075	0.005	0.061	0.011	0.078
W3Q-20	0.0145	0.090	0.161	0.012	0.076	0.005	0.062	0.011	0.079
W3Q-25	0.0125	0.085	0.147	0.012	0.076	0.005	0.062	0.011	0.079
W3Q+10	0.013	0.09	0.144	0.012	0.072	0.005	0.058	0.011	0.076
W3Q+20	0.013	0.082	0.159	0.012	0.074	0.005	0.059	0.011	0.077
W3Q+25	0.0125	0.09	0.139	0.012	0.074	0.005	0.060	0.011	0.078
W4Q0	0.0140	0.100	0.140	0.012	0.079	0.005	0.065	0.011	0.080
W4Q-10	0.0130	0.092	0.141	0.012	0.080	0.005	0.065	0.011	0.080
W4Q-20	0.0110	0.070	0.157	0.012	0.080	0.005	0.066	0.011	0.080
W4Q-25	0.0070	0.070	0.100	0.012	0.080	0.005	0.066	0.011	0.080
W4Q+10	0.0085	0.102	0.083	0.012	0.076	0.005	0.062	0.011	0.078
W4Q+20	0.0115	0.09	0.128	0.012	0.078	0.005	0.064	0.011	0.079
W4Q+25	0.0125	0.092	0.136	0.013	0.082	0.005	0.066	0.012	0.085

Figure 8.11 and Table 8.3 show that Nielsen (1981) and Van Rijn (1993) similarly predict well ripple height especially for group of shorter period cases with RMSE of the order of 1.5 mm. Whereas, O' Donoghue et al. (2006) underestimates for all cases corresponding to all points fall far away below the perfect line.

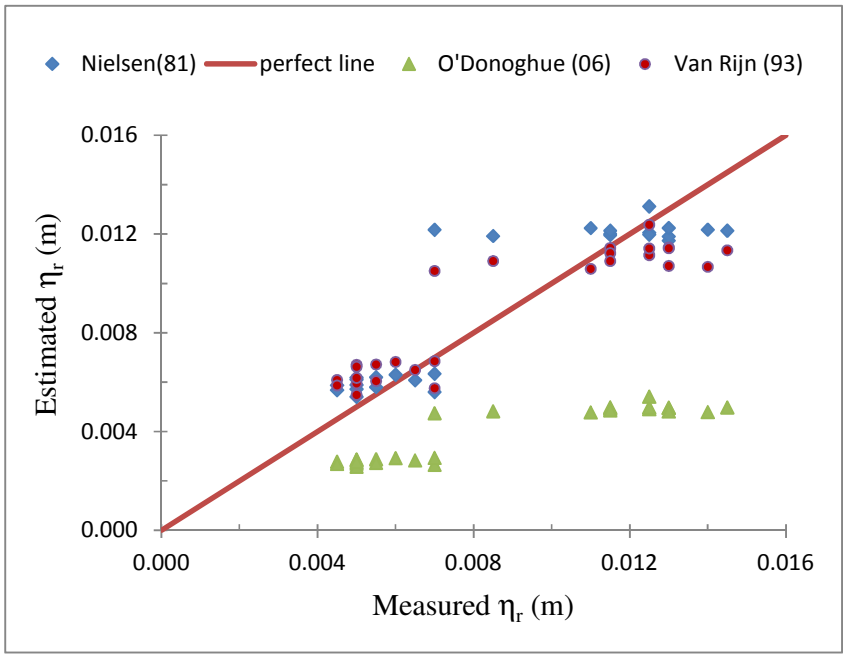

Figure 8.11: Calculated ripple height (η_r) by different formulae versus measurement.

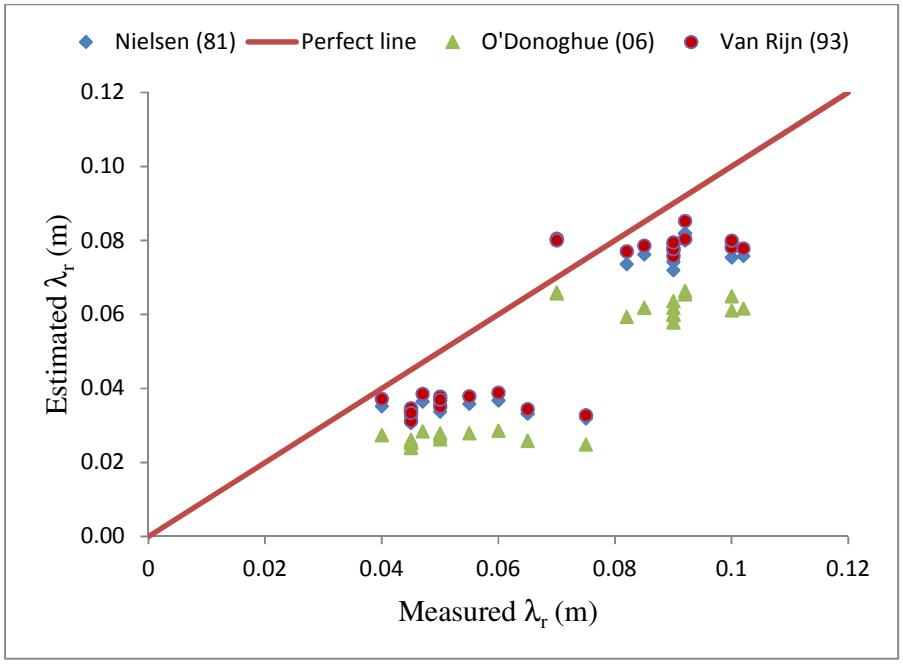

Figure 8.12: Calculated ripple length (λ_r) by different formulae versus measurement.

Figure 8.12 and Table 8.3 show that three methods underestimate ripple length, however Van Rijn (1993) predict slightly closer to the measurement compared to Nielsen (1981) with RMSE of 0.0165 m and 0.018 m respectively. On the other hand, O' Donoghue et al. (2006) least agrees with the measurement with RMSE of 0.028 m.

8.4 SEDIMENT TRANSPORT DATA AND ANALYSIS

Changes in the sand barrier profile was measured after one hour for each run and the corresponding sediment transport rates $q_s(x)$ were derived using the Exner Equation with boundary conditions of $q_s = 0$ on the concrete beds landward and seaward of the sand hump.

8.4.1 Method of measurement and calculation

Sand levels were measured along 3 longitudinal sections over the barrier: left (L), centre (C), and right (R). In order to obtain a representative, average bed level, the measurements were taken at x-positions which correspond alternately to ripple crests (subscript C) and ripple troughs along (subscript T) as shown in Figure 8.13. The mean profile $\overline{X_i}$, $\overline{Z_i}$ was calculated according to (8.2) by averaging the values of 6 points on the mean profile.

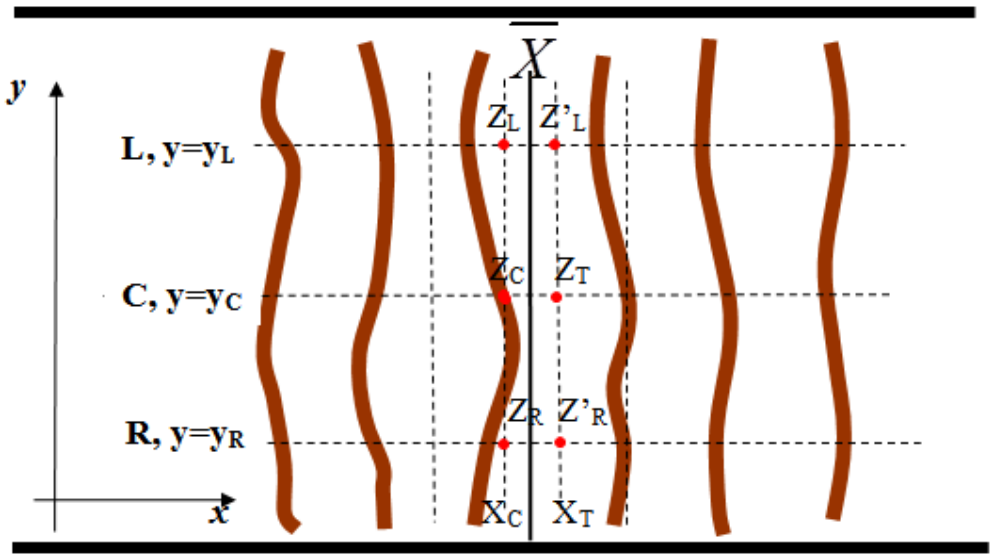

Figure 8.13: Sampling lines for $Z_s(x,y)$. The transects (x_i) are chosen so that the sampling points along 'C' are alternately on ripple crests and troughs.

$$\overline{X_i} = \frac{X_{Ci} + X_{Ti}}{2}$$
$$\overline{Z_i} = \frac{Z_{Ci} + Z_{Ti} + Z_{Li} + Z_{Ri} + Z'_{Li} + Z'_{Ri}}{6} \quad (8.2)$$

where X_{Ci}, X_{Ti} are the x-coordinates of the crest and the trough of the ripple i in centre line while Z_{Li}, Z'_{Li} are the elevations of the two points on the left transect corresponding to X_{Ci}, X_{Ti} and Z_{Ri}, Z'_{Ri} are the elevations of the two points on the right transect corresponding to X_{Ci}, X_{Ti} .

Time averaged sediment transport rates are calculated based on the conservation of sediment volume for a control volume as

$$\Delta\overline{q_s} = -n\frac{\Delta Z_b}{\Delta T}\Delta x \qquad \text{or} \qquad \overline{q_s}(x) = \overline{q_s}(x_o) - \int_{x_o}^{x} \frac{n\Delta Z_b}{\Delta T}\mathrm{d}x \,. \tag{8.3}$$

q_s at the starting point x_1 on the bare concrete floor in front of the sand barrier and at the end point x_2 on the bare concrete behind the barrier are zero. q_s was corrected corresponding to (8.4) due to progressive compression of the sand and imperfect Z_b measurements leading to minor, apparent bulk volume changes Δ_V

$$Z'_i = Z_i - \frac{\Delta_V}{BL} \tag{8.4}$$

and

$$\Delta_V = nB\int_{X_1}^{X_2} \Delta_{z_b}\,\mathrm{d}x \tag{8.5}$$

where B is the width of the channel.

The profile of the sand bar before and after test for case W1+Q25 and W4+Q25 is presented in Figure 8.14.

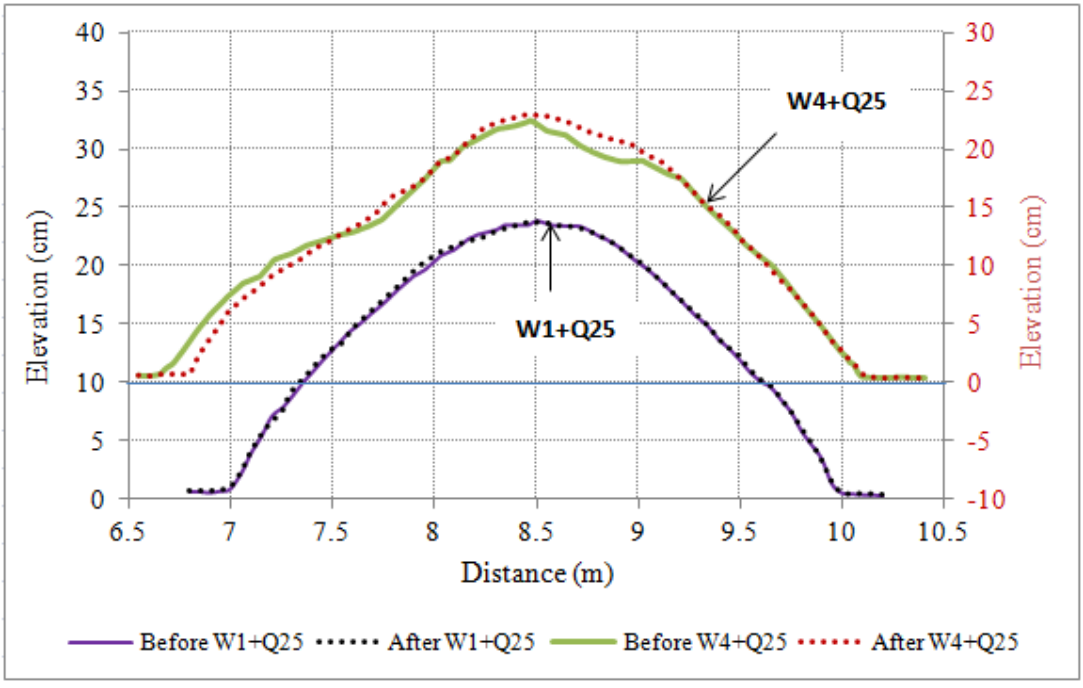

Figure 8.14: Sand bar profile before and after test for case W1+Q25 (lower) and W4+Q25 (upper).

The changes that occurred on the sand bar were clearly seen for the cases with longer period (1.5s) while is insignificant for the cases with shorter period (1s).

8.4.2 Sediment transport Results

A number of researchers have observed that the sediment transport due to waves only over rippled beds is predominantly against wave direction, Nielsen (1992), Section 6.3. However, recently Hurther & Thorne (2011) provided details of a case where onshore ripple migration corresponded shoreward q_s at twice the rate of the seaward net suspended transport.

The complexity of the interaction between waves and co-directional currents (on horizontal beds) was shown earlier by Inman & Bowen (1963) who found that superposition of a weak current increased the landward q_s but that further increase of the current lead to smaller q_s. Similarly, wave–current experiments of van Rijn (1993) showed seaward q_s in case of following currents.

In the present experiments, the q_s-direction for combined flows is most clear-cut in test case of W1 and W2. Hence, they are presented first. The comparison plots between waves only and waves combined with different currents for W1 are presented in Figure 8.15 and Figure 8.16 respectively.

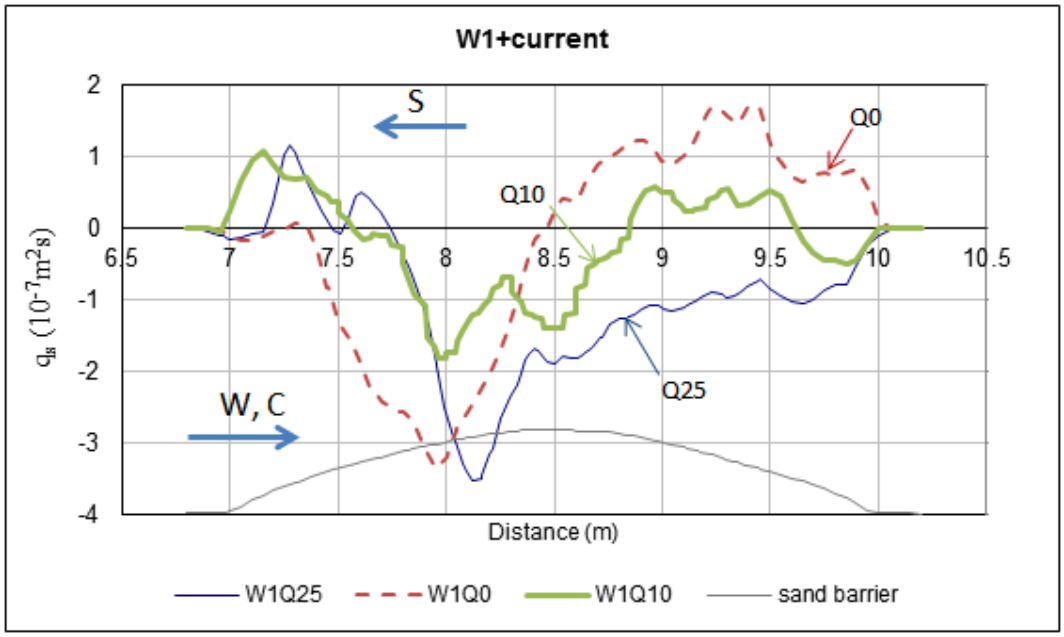

Figure 8.15: Measured sediment transport rate along the sand barrier for W1 with two following currents Q = 10 L/s and Q=25 L/s; arrows show direction of wave (W), current (C) and sediment transport (S).

As can be seen, the q_s-direction, is generally against the current irrespective of the current strength. However, this trend in the q_s-direction is clearest with the stronger currents. For example, in Figure 8.16 (Q = -20, -25 L/s), along the front side of the hump from x=7 m to x=8.7 m, q_s increases corresponding to erosion, while q_s reduces on the lee side of the hump corresponding to deposition.

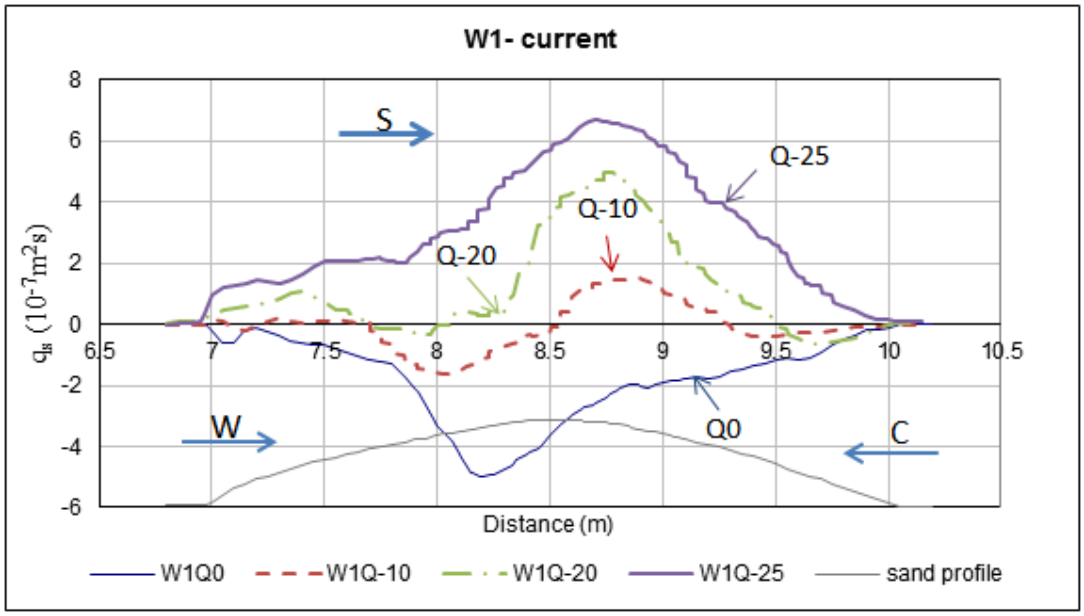

Figure 8.16: Measured sediment transport rate along the sand barrier for W1 with three opposing currents Q =-10, -20, -25 L/s.

The evidence also can be seen in Table 8.2, even though the net current is negative (offshore direction), sediment transport is onshore. With Q = 10 L/s either following or opposing current, it is not clear or possibly unstable, which may be due to the small net current. Similar trend of q_s against the current was seen in case W2, see Figure 8.17 and Figure 8.18. These cases are strong evidence for q_s not generally going in the same direction as the net flow as assumed in the CMS model.

In contrast, W3 and W4 do not show clear direction of q_s even though net currents are large and u_{rms} is much larger than that of W1 and W2. The measured q_s along the sand barrier for W4 with following and opposing currents are presented in Figure 8.19 and Figure 8.20 respectively.

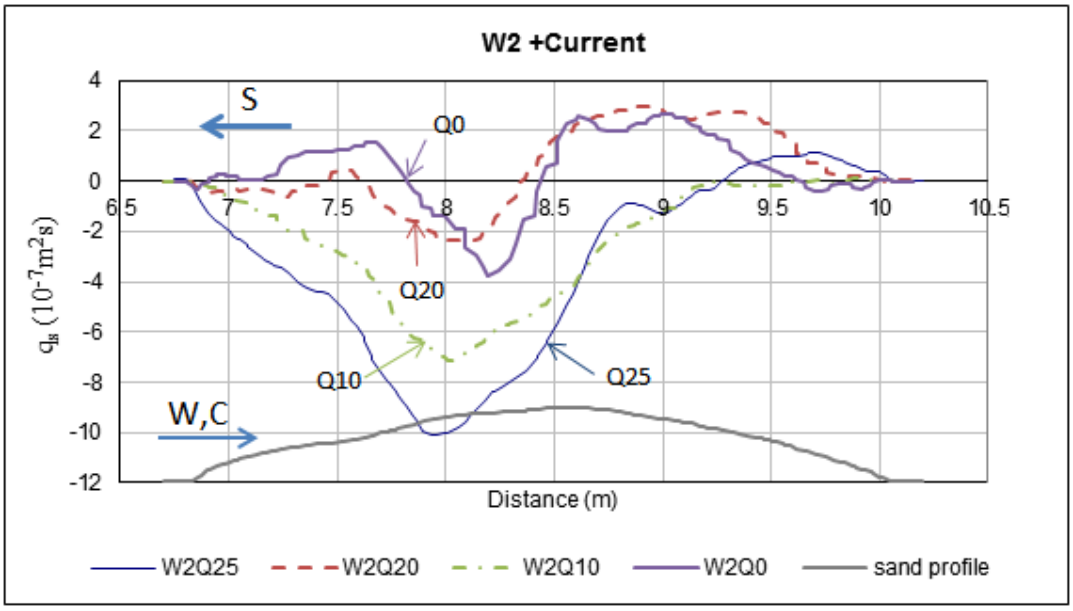

Figure 8.17: Measured sediment transport rate along the sand barrier for W2 with three following currents Q=10, 20, 25 L/s.

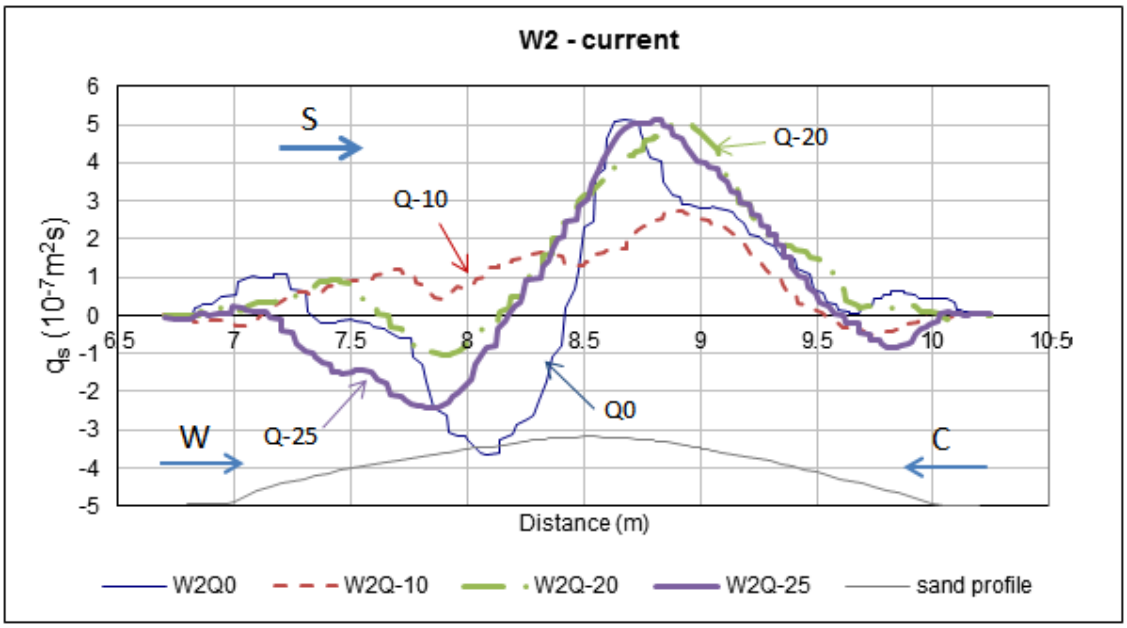

Figure 8.18: Measured sediment transport rate along the sand barrier for W2 with three opposing currents Q =-10, -20, -25 L/s.

Except for the combination of W4 and the strongest following current, Q = 25 L/s in Figure 8.19, q_s is in the direction of wave and current. In the case of wave only, there is no global q_s direction because the sand barrier is spread out with its top eroded and deposited on both sides.

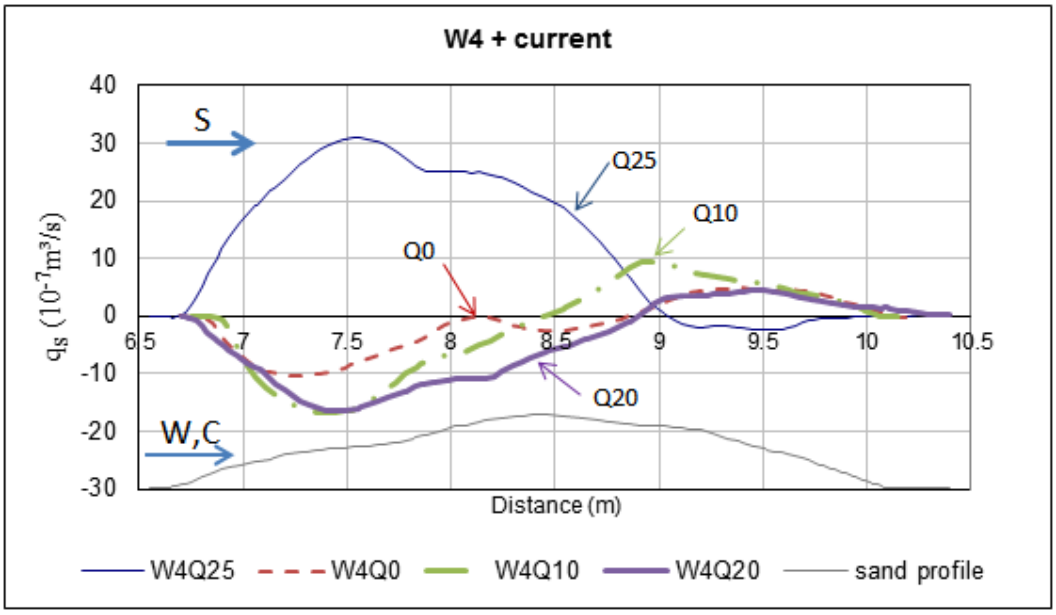

Figure 8.19: Measured sediment transport rate along the sand barrier for W4 with three following currents Q=10, 20, 25 L/s.

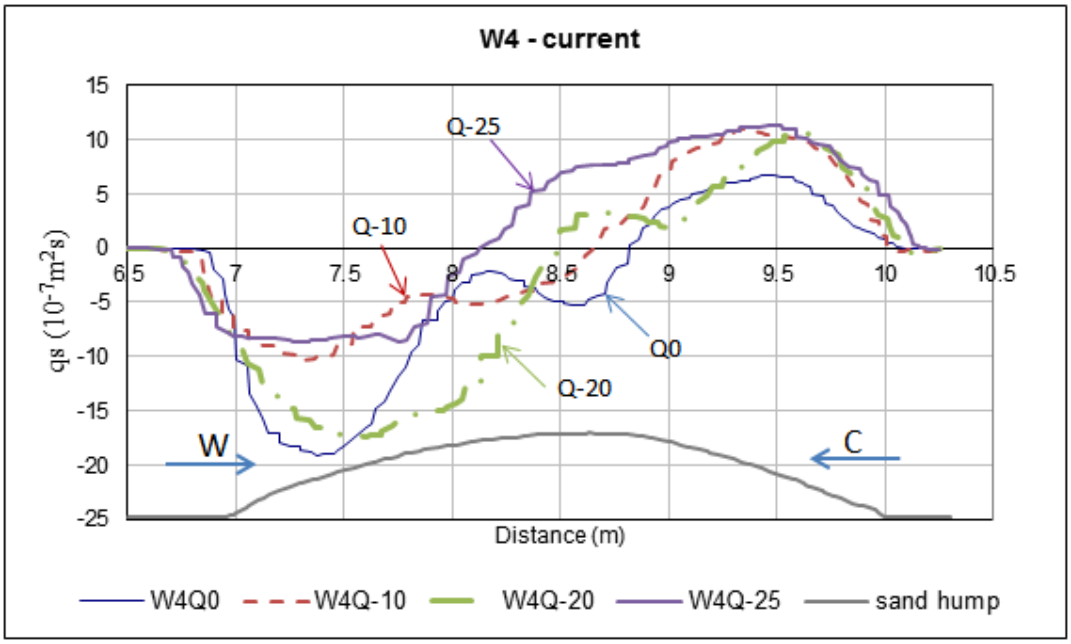

Figure 8.20: Measured sediment transport rate along the sand barrier for W4 with three opposing currents Q = -10, -20, -25 L/s. Arrows show the direction of wave (W), current (C).

For Q = -20, -25 L/s in Figure 8.20 net currents are rather strong -8.9, -10.6 cm/s respectively, resulting in remarkable erosion from x= 7.7 m till 9.5 m, however it is not very clear whether the eroded sediment deposited on the front or lee side.

8.5 CONCLUSIONS

The wave transformation over the barrier without current was similar and perhaps predictable based on previous results in the literature. However, when waves interact with currents the wave height change patterns were very complicated and many details were unforeseen. H_{rms}/H_i for the waves only case is higher than that of wave combined with opposing current for T=1.5 s in Figure 8.6, which is in disagreement with previous studies, while agreement was found for T=1 s. The mean period T_{mean} of bound waves were found to be the same as generated originally.

Velocity profiles at different locations along the flume were rather similar to that in the literature. Regarding the sediment transport rates calculated from the measured bed level change, the direction of sediment transport was clarified for each case with influence of current. Wave only cases induce negative current for all wave cases of the order of ca -1.5 cm/s, whereas wave combined with following current with discharge Q = 10 L/s results in net current $u_{ave} \approx$ 0.5-1.5 cm/s. This small net current did not result in clear direction of sediment transport except for the combination of waves W2.

In comparison with measured ripple dimension of all tests, Nielsen (1981) and Van Rijn (1993) formulae similarly predict well ripple height while underestimate ripple length. O' Donoghue et al. (2006) formula underestimate ripple height and ripple length.

Observations from analysis of the combinations of W1 and W2 show that sediment transport direction is opposite to the current direction. In other words, q_s is against wave propagation when waves and current are in the same direction; while q_s is in the wave propagation direction when the waves propagate against the current. The q_s-direction of sediment transport is not consistent in the combinations of W3 and W4. For W4 and the strongest following current (Q = 25 L/s) q_s is in the direction of waves and current. These cases show clearly that q_s cannot be generally assumed to be in the direction of the net flow as assumed in the CMS model.

Some cases had large net current but did not result in a clearly defined q_s-direction, while other cases had modest net currents but showed a very consistent q_s-direction. This means that q_s in terms of magnitude or direction depends not only on direction but also on the magnitude of net current. That is probably one of the main reasons why the CMS model predictions for morphology change of Pensacola Pass in Chapter 7 was unsuccessful.

The present data set is used to assess the applicability of existing q_s-formulae on ripple bed in non-breaking zone such as Ribberink & Al-Salem (1994), Nielsen (1992, 2006) in the next chapter.

Chapter 9

ASSESSEMENT OF EXISTING SEDIMENT TRANSPORT MODELS FOR SAND BARRIER DYNAMICS UNDER WAVES & CURRENTS

9.1 INTRODUCTION

Assessment of sediment transport formulae in a wave-current induced ripple bed morphology is the focus of this Chapter. Using available data of wave, velocity, bed change and ripple dimensions after each test case from the previous chapter, several sediment transport models were applied to find the most suitable model for the laboratory experiments and to understand qualitatively sediment transport under combined waves and collinear currents. Some candidate models work well and are widely used in non-breaking waves over ripple beds such as the diffusion model, the heuristic model, the grab and dump model of Nielsen (1988), however they were applicable for horizontal bed and not sloping bed. Another simple empirical model of Ribberink & Al-Salem (1994) was also tested due to its simplicity and similarity in the grain size as that used in our experiments. Nielsen's (2006) model, which accounts for acceleration skewness and boundary layer streaming is also investigated. The first three models are for predominantly suspended load and the last two for predominantly bed load. These models are tested against experimental data for almost all combinations of waves and current at the top of the sand barrier where velocity measurements are available. The SWASH (an acronym for Simulating WAves till SHore) model developed at the Delft University of Technology, The Netherlands is adopted to obtain the velocity along the sand barrier for case W1 and W4 without current, and the sediment transport rate is calculated and compared among the models.

9.2 EXISTING SEDIMENT TRANSPORT MODELS FOR NON BREAKING WAVES

Wave generated ripples occur in shallow coastal areas (h<25 m), where wave motion often dominates the near bed flow (Nielsen 2009). The sediment transport mechanism depends on the grain size. Ripple migration results in onshore sediment transport (Traykovski et al., 1999) while suspension above vortex ripples causes offshore transport under velocity skewed waves, like Stokes waves (Craghan, 1995; Hurther and Thorne, 2011; Sato, 1986). The coarser sand, with larger w_s, moves over the crest at low levels, while the finer sand is trapped in the lee side vortex (see Figure

9.1). At velocity reversal, this vortex is ejected upwards about one ripple height (Bijker et al., 1976) and transported offshore in the next half of wave cycle. By the next free stream reversal, the vortex decays and settles out. It is possible to combine both sediment transport mechanisms in case of mixed grain sizes or choose the dominant mechanism corresponding to dominant grain size.

The question about which model is more suitable for sloping beds, as in the barrier experiments described in Chapter 8 needs to be figured, which is attempted in this chapter.

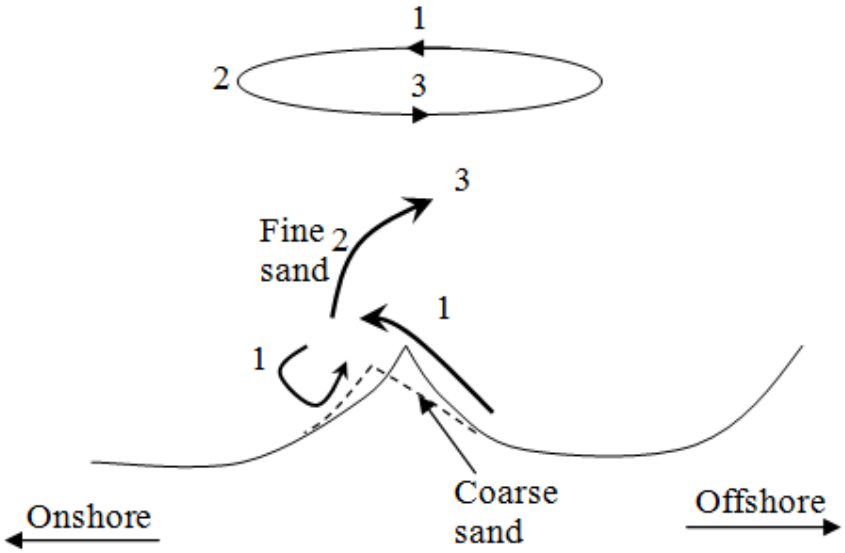

Figure 9.1: Illustration of ripple migration of coarse sand and vortex ripple of fine sand.

9.2.1 Bed load transport models

Bed load is the part of the total load which is supported by inter-granular forces as defined by Bagnold (1956). Bed load formulae are mainly based on the Shields parameter θ of the form $\Phi=\Phi(\theta)$. The Shields parameter shows the balance between mobilizing force (shear stress) and stabilising force (gravity).

The bed load transport rate q_b [L^2/T] is often expressed in the dimensionless form:

$$\Phi_b = \frac{q_b}{\sqrt{(s-1)gd^3}} \tag{9.1}$$

$$\theta = \frac{\tau}{\rho g(s-1)d} = \frac{u_*^2}{g(s-1)d} \tag{9.2}$$

where τ is bed shear stress [$ML^{-1}T^{-2}$], ρ is fluid density [ML^{-3}], g is the acceleration of gravity [LT^{-2}], d is median grain size [L], $u_* = \sqrt{\tau/\rho}$ is friction velocity [LT^{-1}].

An early empirical formula, which is used frequently, was given by Meyer-Peter & Müller (1948) (hereinafter referred as MPM48) based on fitting of a large amount of experimental data. The formula with the form $\Phi_b = k(\theta - \theta_c)^{1.5}$ predicts bed load in steady flow over flat beds. θ_c is the critical Shields parameter at which sediment motion starts. It is a weak function of the grain-Reynolds number $u_* d/\nu$ and found to be order of 0.05 for sand on flat bed in water. Shields type models ignore inertial force, which may become significant for coarse grains in accelerated flows (Baldock and Holmes, 1997; Hardisty, 1990; Nielsen, 1979).

Traykovski et al. (1999) used MPM48 with the instantaneous Shield parameter $\theta(t)$ of Nelsen (1992) and successfully predicted ripple migration from field measurements. Nielsen & Callaghan (2003) and Nielsen, (2006) modified the MPM48 with time varying Shields parameter $\theta(t)$, which accounts for acceleration skewness and boundary layer streaming. This update led to good agreement with data of Ribberink et al. (2000), Watanabe & Sato (2004) under saw-tooth asymmetry waves. Van der A et al. (2010a) in comparison among several recent transport models for sheet flow under acceleration–skewed oscillatory flow suggested that Nielsen (2006) works well for fine sand. Very good agreement with measured transport rates can be obtained by calibrating φ_τ, the weighting angle for drag force and pressure gradient force. Therefore, Nielsen (2006) (hereinafter referred as N06) is chosen for testing the current laboratory experiments. The model of Gonzalez-Rodriguez-Madsen (2007) was quite similar as Nielsen (2006) with added phase difference between free stream velocity and the bed shear stress. This formula is applied only for bed load- dominated conditions.

Beside the widely used Shields type models, empirical sediment transport rate formulae in the form of velocity moments

$$\overline{q_s} = K\overline{|u_\infty|^{p-1} u_\infty} \tag{9.3}$$

are often applied due to their simplicity. Ribberink & Al-Salem (1994) showed that the constants p=1 and K=0.00018 provided good prediction for 0.21mm sand but not for finer sands (Ribberink & Chen, 1993). The grain size of the present experiment is similar to their grain size with respect to d_{50} and to d_{10}, d_{90}. This model is chosen for testing.

9.2.2 Suspended load transport models

Different from bed load, suspended load is supported by upward fluid drag. According to Bagnold (1966) suspension occurs when $u_* \geq w_s$ (settling velocity) while van Rijn (1984) states that it will start at rather smaller bed shear velocity. The amount of suspended load is determined by a balance

between settling and entrainment from the bed, and it depends strongly upon the bed geometry: flat bed or ripple bed (Nielsen, 2009). The suspended sediment transport rate is usually presented in the form

$$q_s(t) = \int_0^D c(z,t)u_s(z,t)\,\mathrm{d}z \tag{9.4}$$

where c is the instantaneous sediment concentration, u_s is the instantaneous horizontal sediment velocity assumed equal to the horizontal velocity of the immediately surrounding fluid.

The concentration distribution over ripples under waves is sometimes taken to be in exponential form as in

$$c(z) = C_o e^{-z/L_s} \tag{9.5}$$

where, C_o is the reference concentration at the bed and L_s is the vertical scale [L].

Gradient diffusion is a simple approach to find concentration distributions by writing the turbulent upward flux as gradient diffusion with sediment diffusivity and balancing with the settling rate $\overline{w_s}\,\overline{c}$, $q_{s,z} = -K_s \dfrac{\partial \overline{c}}{\partial z}$. The solution is

$$\overline{c}(z) = c(z_o) e^{\int_{zo}^{z} \frac{w_s}{K_s} dz} \tag{9.6}$$

where: K_s is diffusivity, w_s is the sediment settling velocity.

Nielsen et al. (1978) and Nielsen (1979, 1988) applied the diffusion model to estimate suspended transport over ripples for constant diffusivity.

Another model describing the transport process occurring above the ripples, which uses a different philosophy, used in the simple Heuristic entrainment model suggested by Dean (1973) was applied by Nielsen (1988). The 'Grab & dump model' given by Nielsen (1988), the simplest model, was successfully applied for sediment transport over ripple beds without considering the distribution of concentrations. These three models account for velocity skewness which is adequate for Stoke waves but not suitable for saw-tooth asymmetric wave (Nielsen, 1992). These models all agreed well with lab measurements done by Schepers (1978) for finer sand (d_{50}=0.125 mm). However, only the 'Grab and dump model' had consistent magnitude agreement for coarse sand (d_{50}=0.485 mm). Nielsen (1988) explained that the settling velocity dependence of the diffusion- and heuristic entrainment models reduces the sediment flux too much for the larger grain size. Even though the 'Grab and dump model' estimates q_s better than other models in terms of magnitude and range of q_s variation, it has a miss-match in direction (cf. Figure 6.3.3, Nielsen 1992). These models are applied to the present experimental data due to their relevance with ripple bed and grain size.

9.2.3 Total load transport

Total load transport can be obtained by the summation of bed load and suspended load transport:

$$q_{tot} = q_b + q_s . \tag{9.7}$$

Based on the "half-cycle" concept proposed by Dibajnia & Watanabe (1992), there have been several upgraded models developed for ripple bed. This concept described the wave-average transport rate as the difference between the amount of sand transported during the positive 'crest' half cycle and that of transported during negative 'trough' half cycle. Dibajnia & Watanabe (1996) extended their 1992 work to accommodate bed load and suspension over ripples. It works well for velocity skewed conditions but not for acceleration skewed flows.

Watanabe & Sato (2004) used the same concept and added the effect of acceleration skewness. It also accounts for the phase lag contribution due to sand from the previous half cycle, which may still be in suspension. This results in best predictions for fine sand in amongst all recent models for the wide ranging data set of Van der A et al. (2010a).

Silva et al. (2006) also used the initial formula from Dibajnia & Watanabe (1992) and added an acceleration skewness effect on the Shields parameter.

The latest comprehensive model for rippled beds under non-breaking waves and currents was developed by Van der A et al. (2010b) based on the 'half-cycle' concept with τ as the main forcing parameter. This model takes into account the unsteady phase lag effect between velocities and concentrations, which is really important for ripple bed. In addition, the model also includes the effect of wave shape either as velocity or acceleration skewness. Moreover, the effect of progressive surface wave is considered through wave-Reynolds stress. The model can be applied for the case of wave and current at an angle. It was calibrated and showed good agreement with large scale data covering a wide range of flow conditions, grain sizes, periods, etc.

9.2.4 Selected transport models

Based on the above analysis five models are chosen for comparison viv., Ribberink & AlSalem (1994), Nielsen (2006), the diffusion model, the Heuristic entrainment model and the 'Grab and dump model' of Nielsen (1988). The first two models are bed load models and the last three models are suspended load models. Model details are as follows:

- **Ribberink & AlSalem (1994)**

Ribberink & AlSalem (1994), hereinafter referred as RA, did many experiments in sediment transport under asymmetric regular and irregular wave condition at full scale in a large oscillating water tunnel. The relation between net sediment transport rate and the third moment of the free stream velocity was found to be

$$\bar{q} = 0.00018\overline{u_{(t)}^3} \tag{9.8}$$

for $d_{50} = 0.21$mm.

They compared their measurements with other similar models, such as Bailard (1981) with p=3 for bed load, p=4 for suspended load, Madsen & Grant (1976) with p=6 or Sawamoto & Yamashita (1986) with n=3. The results showed good agreement (within factor 2) with the energetics total load sediment transport model of Bailard (1981) and the empirical model of Sawamoto & Yamashita (1986) but no agreement with Madsen & Grant (1976). Onshore sediment transport direction in thin layer close to bed (less than 2 cm) was observed during all experiment ($u_{\text{rms}} > 0.3$ m/s).

For rippled bed, experiments took place at lower velocity u_{rms}= 0.2 - 0.3 m/s, which is in a similar range with the present experiments (Table 8.2). Generally, q_s is in the onshore direction for small ripples but considerably lower with large ripples and still has a consistent linear relation with $\overline{u^3}$. Wave period is more important under rippled conditions, higher wave periods, give larger q_s. It can be seen in the present experiments (Table 9.1) but is not profound for wave period T=1 s and T=1.5 s.

With the same sediment (d_{10}, d_{50} and d_{90}) and ripples the RA model is compared with the measured q_s from Table 9.1. The settling velocity in their model corresponding to d_{50} was w_s=0.026 m/s, which is close to the estimation using Ferguson & Church (2004): w_s=0.025 m/s, which was chosen for the sediment transport calculations.

- **Nielsen (2006)**

Nielsen (2006), hereinafter referred as N06, and Nielsen & Callaghan (2003) modified the MPM48 model with time varying Shields parameter, which accounts for acceleration asymmetry and boundary layer streaming. This update led to good agreement with the data of Ribberink et al. (2000), Watanabe & Sato (2004) and Van der A (2010a) gained under saw-tooth asymmetric waves. The asymmetric wave shape and phase average velocities were shown in Figure 8.4 and 8.9 of the present sand barrier experiment. The instantaneous sediment transport rate is

$$q_s(t) = \phi(t)\sqrt{(s-1)\times 9.81\times d_{50}^3} \tag{9.9}$$

and the mobilize dimensionless number shows no sediment transport if the Shields parameter is less than the critical value.

$$\phi(t) = \begin{cases} 0 & if \quad \theta < 0.05 \\ 12\left(\theta(t) - 0.05\right)\sqrt{\theta(t)}\times SignU_* & if \quad \theta > 0.05 \end{cases} \tag{9.10}$$

Instantaneous Shields parameter include the acceleration skewness in $\theta_{2.5}$ and boundary layer streaming in $\Delta\theta$, the index 2.5 is used for bed roughness r=2.5d_{50}

$$\theta(t) = \theta_{2.5}(t) + \Delta\theta \tag{9.11}$$

$$\theta_{2.5}(t) = \frac{U_*(t)^2}{(s-1)gd_{50}} \tag{9.12}$$

where $U^*(t)$ is the instantaneous "sediment mobilizing velocity"

$$U_*(t) = \sqrt{0.5 f_{2.5}}\left(\cos\varphi_\tau \times u_\infty(t) + \sin\varphi_\tau \frac{u_\infty(t+\delta t) - u_\infty(t-\delta t)}{2\omega\delta_t}\right) \tag{9.13}$$

is a linear combination of the free stream velocity $u_\infty(t)$ and acceleration $\dot{u}_\infty(t)$ with weighting φ_τ between drag force driven by $u_\infty(t)$ and the pressure gradient governed by $\dot{u}_\infty(t)$. The 'weighting angle' is in the range $\varphi_\tau \in [0^o; 90^o]$ with φ_τ = 0 meaning drag dominated q_s while φ_τ=90^o corresponds to pressure gradient dominated q_s like the plug flows of Sleath (1999). The optimal value φ_τ=51^o was found for data set of Watanabe & Sato (2004). It was suggested that φ_τ be smaller for coarse sand, for stronger undertow and longer wave period.

The friction factor f can be calculated as (9.14) with different nominal grain roughness r=2.5d_{50} or other options as (9.18) and (9.19), which account for ripple dimension. $\hat{\theta}_{2.5}$ is the peak Shields parameter corresponding to (9.14).

$$f = \exp\left(5.5\left(\frac{r}{A}\right)^{0.2} - 6.3\right) \tag{9.14}$$

The boundary layer streaming induces a positive velocity onshore direction (Longuet-Higgins, 1958) and influences q_s via a Shields parameter increase $\Delta\theta$ in *N06*. It is incorporated via Reynolds stress $-\rho(\overline{\tilde{u}\tilde{w}})$ relying on dissipation data for flat beds of Carstens et al. (1969) as (9.16).

$$\Delta\theta = \frac{-\tilde{u}\tilde{w}}{(s-1)\times 9.81\times d_{50}} \tag{9.15}$$

$$-\tilde{u}\tilde{w} = \frac{kA^3\omega^2 f}{4\sqrt{2}} \tag{9.16}$$

in which A is the near-bed semi-excursion and ω_p the peak angular frequency for irregular waves

$$A = \frac{\sqrt{2}}{\omega_p}\sqrt{Var\,u(t)} \tag{9.17}$$

Other options of bed roughness including contribution s from moving sediment and/or ripple height η_r and ripple length λ_r are

or
$$r_{f10} = 170\sqrt{\widehat{\theta}_{2.5} - 0.05} \times d_{50} \tag{9.18}$$

or
$$r_{rip} = \frac{8\eta_r^{\,2}}{\lambda_r} + 170\sqrt{\widehat{\theta}_{2.5} - 0.05} \times d_{50} \tag{9.19}$$

cf. Nielsen (1992) p 158.

- **The Diffusion model** (Nielsen, 1988)

The diffusion model was first applied to determine suspended transport rate over rippled beds for constant diffusivity by Nielsen (1978, 1979 and 1988). This model used the traditional sediment transport formula (9.4), adopted distribution concentration profile as in (9.5) for steady part in which C_o was found experimentally. The unsteady part reflects the effect of wave skewness in ripple vortex entrainment and sediment transport and that oscillatory components of $c(z,t)$ decay more rapidly with z than mean concentration $\overline{c}$. The sediment transport rate is calculated as:

$$\begin{aligned}\overline{q}_s = C_{os}(A_b + A_f)\overline{u}L_s + C_{os}L_s\{A_f\sum_{n=1}^{2}\frac{U_n}{|\alpha_n|^2}\cos(n\omega t_d + 2\arg\alpha_n - n\omega t_n) + \\ + A_b\sum_{n=1}^{2}\frac{U_n}{|\alpha_n|^2}\cos(n\omega t_u + 2\arg\alpha_n - n\omega t_n)\}\end{aligned} \tag{9.20}$$

with

$$\alpha_n = \frac{1}{2}\sqrt{\frac{1}{4} + \frac{in\omega L_s}{w_s}} \tag{9.21}$$

and with the velocity given by

$$u(z,t) = \overline{u}(z) + \tilde{u}(t) = \overline{u}(z) + \sum_{n=1}^{\infty} U_n \cos n\omega(t - t_n) \tag{9.22}$$

and

$$\overline{c}(z) = C_o e^{-\frac{z}{L_s}}; \qquad C_o = \frac{\overline{p(t)}}{w_s} = C_{os}; \qquad C_n(z,t) = \frac{P_n}{w_s\alpha_n} e^{-\frac{\alpha_n z}{L_s}} e^{in\omega t} \tag{9.23}$$

where C_{os} is the C_o value for a sine wave of velocity amplitude U_1, which is calculated from

$$C_{os} = 0.005\,\theta_r^3 \tag{9.24}$$

with the ripple based Shields parameter

$$\theta r = \frac{\theta'}{(1 - \pi\eta_r/\lambda_r)^2} \tag{9.25}$$

and the skin-friction Shield parameter

$$\theta' = \frac{0.5 f U_1^2}{(s-1)gd}. \tag{9.26}$$

The pick up function $p(t)$ (Figure 9.2) shows the two reversal times t_d and t_u where sand is picked up with the vortex. A_b, A_f are the backward and forward entrainment coefficients which relate to the relative magnitudes of the shoreward and seaward extreme velocities U_{max} and U_{min}.

$$A_f = 0.5\left(\frac{U_{max}}{U_1}\right)^6 \tag{9.27}$$

$$A_b = 0.5\left(\frac{U_{min}}{U_1}\right)^6 \tag{9.28}$$

The vertical length scale of the exponential concentration profile L_s is calculated as

$$L_s = \eta_r\left\{1.24\exp\left[-40\left(w_s/U_1\right)^2\right]+0.2\right\} \tag{9.29}$$

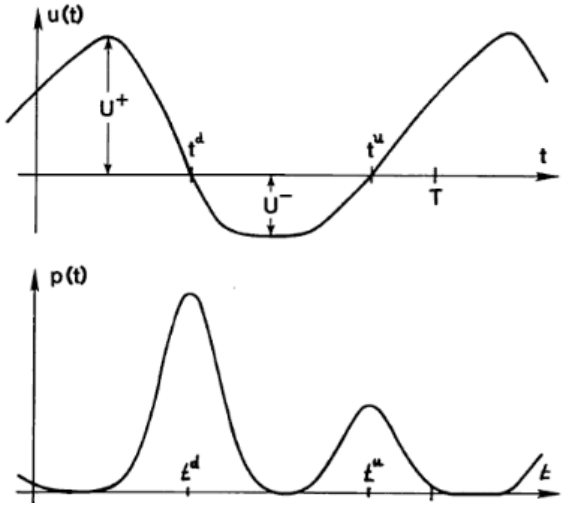

Figure 9.2: Illustration of large pick-up function corresponding to large vertical velocity during t_d and t_u, from Nielsen (1992).

- **The Heuristic model** (Nielsen, 1988)

The heuristic entrainment model presented by Nielsen (1988) is related to the convection (as opposed to diffusion) process, with the concentration profile simply determined from measurements. With this approach, q_s can be presented by time-averaged pick up rate and the average sand particles excursion. The convective transport model is more flexible and realistic than the diffusion model because the analytical solution can be obtained for all relevant distribution functions of average concentration whereas it is very limited for diffusion model. This model can be applied for irregular wave while the diffusion model cannot at least analytically. The current contribution Q_c is calculated as the first part of (9.30).

$$q_s = Q_c + C_{os}(A_b - A_f)L_s U_1 \frac{\omega L_s / w_s}{1 + (\omega L_s / w_s)^2} \tag{9.30}$$

- **The 'Grab and dump model' (Nielsen, 1988)**

The 'Grab and dump model' of Nielsen (1988), referred as GD hereinafter, is the simplest model for sediment transport over ripple beds without considering the distribution of sediment concentrations. This model is based on pick-up function with idea of the sand being entrained ('grabbed') in two parcels in each wave period at the time of free stream reversal. In each case, the grabbed sand is then transported over an average distance *A* in the opposite direction to velocities that entrained it, and dumped. *A* is the semi-excursion of water particle just above the boundary layer. Compared to diffusion and Heuristic models, GD is less dependent on grain size due to not including factor $\omega L_s/w_s$. This makes GD model presents true characteristic of shore normal sediment transport by non-breaking wave over ripple bed as stated by Nielsen (1992). Though this model is simple, the results are consistently in agreement with experiment data from Shepers (1978), Van de Graaff & Tilmans (1980), even with coarse sand, while other models are not. The GD model estimates q_s better than other models in terms of magnitude but still does not match the direction with measurements. However, Van der Werf et al. (2006) found from comparison with his measurements in large scale wave flume that this model often over estimates q_s but predicts correct direction for the majority of the data. This model always predicts offshore sediment transport. According to Van der Werf et al. (2006) the disagreement with measurement may come from different experimental scales in model calibration. The last three suspension models do not (so far) account for acceleration skewness and boundary layer streaming. Therefore, it does not have much influence on sediment transport rate.

$$q_s = Q_c + C_{os} w_s (A_b - A_f) A \tag{9.31}$$

9.3 COMPARISON BETWEEN MEASUREMENTS & THE CHOSEN MODELS AT ONE CROSS SECTION ON TOP OF SAND BARRIER

The horizontal velocity time series measurement for all cases of wave only as well as wave-current combinations were made mostly at the top of the sand barrier at *x*=8.5 m, see Figure 8.9 and Table 8.2. Therefore, q_s values from models and measurement will be compared first at this cross section.

The calculations of q_s were based on the two main components U_1, U_2 determined from phase averaged velocities and the measured η_r, λ_r were used. Results are summarised in Table 9.1 and Figure 9.3. The scatter of points shows that there is no evidence of any trend or correlation

between calculated and measured values. In addition, results of calculated sediment transport rate in many cases were in opposite direction with that of measurements.

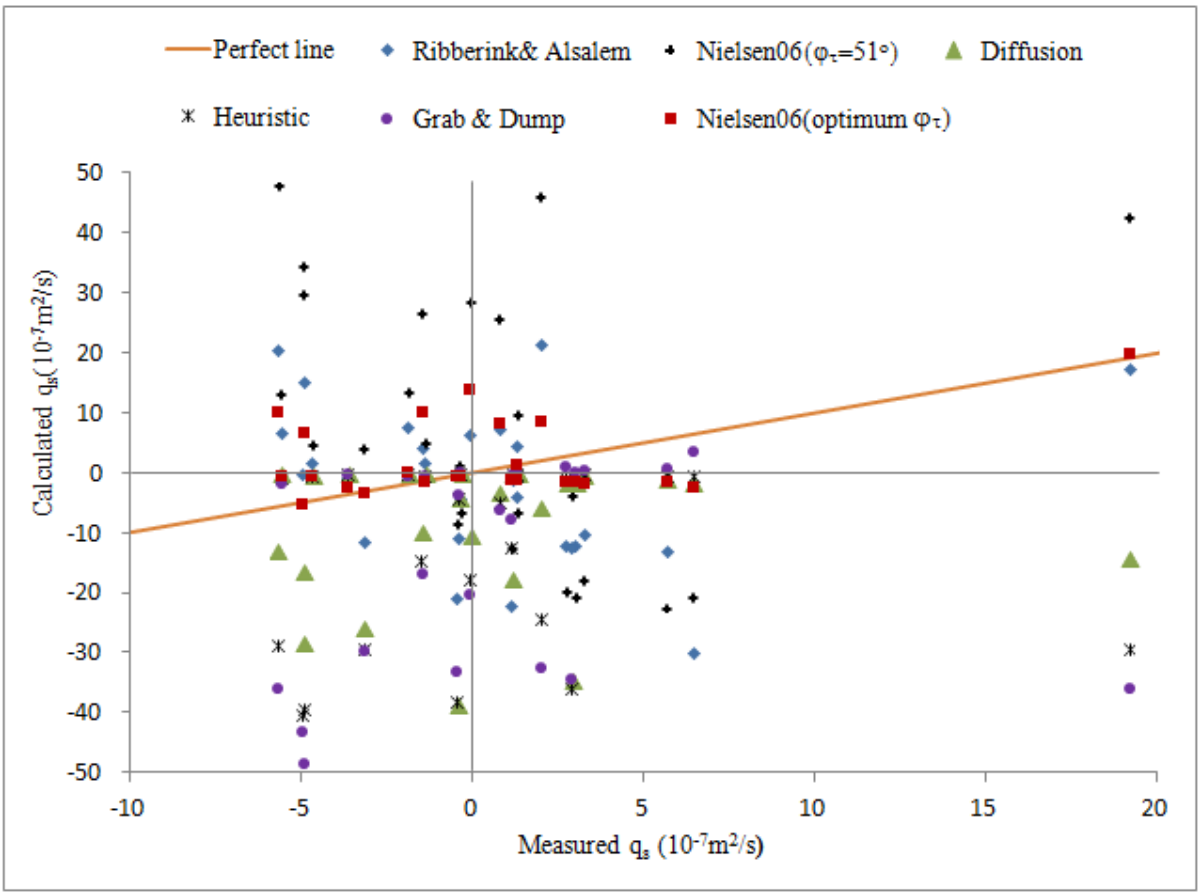

Figure 9.3: Calculated sediment transport rate at x=8.5m by different models versus with experiment.

The Ribberink & Al-Salem (1994) model provided least error compared to the measurement, from factor 3-7, with 70% prediction in wrong direction. Results of N06 with φ_τ=51^o has the second least error, but 70% predictions in opposite direction similar to RA model. N06 with optimum φ_τ for individual case provides much improvement in term or magnitude and direction. However it is still far from perfect agreement with measurements. The optimal φ_τ in 60% cases come to 90^o, which means total dominance by the pressure gradient even though the maximum acceleration skewness is only R_a=0.58 (Table 8.2). This seems unrealistic. The results are calculated based on skin friction factor $f_{2.5}$ corresponding to r=2.5d_{50}, q_s is 2 or 3 times larger if r_{rip} from (9.18) and (9.19) is used. The model is too sensitive with ripple dimension; too large magnitude of q_s does not make any reasonable sense.

Table 9.1: Summary q_s by different model in compare with measured q_s at x=8.5m (10^7 m^2/s).

Test	Masured	RA	N06 (φ_c=51°)	N06 (optimum φ)	Optimal φ	Diffusion	Heuristic	GD
W1Q0	-3.7	-0.8	-1	-2.2	55	0.01	0.01	0.05
W1Q-10	-0.4	-4.3	-6.4	-0.4	88	0.03	0.05	0.3
W1Q-20	3.3	-10.2	-17.8	-1.7	90	-0.3	-0.06	0.7
W1Q-25	5.7	-12.9	-22.4	-1.5	90	-0.8	-0.3	1.0
W1Q10	-1.4	1.9	5.1	-1.3	90	-0.07	-0.1	-0.2
W1Q25	-1.9	7.6	13.8	0.1	90	0.03	0.1	-0.3
W2Q0	1.2	-1.0	-0.8	-0.8	50	0.01	0.02	0.1
W2Q-10	1.3	-3.9	-6.3	-1.0	90	0.05	0.1	0.3
W2Q-20	3.0	-12.0	-20.6	-1.4	90	-1.5	-0.8	0.2
W2Q-25	2.7	-12.1	-19.7	-1.4	90	-1.4	-0.7	1.0
W2Q10	-4.7	1.7	5.0	-0.5	90	-0.08	-0.1	-0.2
W2Q20	1.3	4.5	10.0	1.3	86	-0.06	-0.13	-0.3
W2Q25	-5.6	6.8	13.3	-0.4	90	0.1	-0.5	-1.5
W3Q0	-1.5	4.4	26.9	10.1	0	-9.6	-14.4	-16.6
W3Q-10	-0.4	-10.8	1.4	-0.4	46.5	-3.9	-4.0	-3.5
W3Q-20	2.9	-12.3	-3.6	-1.5	65	-34.5	-35.6	-34.2
W3Q-25	1.1	-22.0	-12.3	-1.2	78	-17.6	-12.3	-7.7
W3Q10	-0.1	6.3	28.6	14.1	0	-10.3	-17.5	-20.1
W3Q20	-4.9	15.1	34.8	6.7	90	-16.3	-39.1	-48.4
W3Q25	2.0	21.5	46.4	8.8	90	-5.7	-24.1	-32.3
W4Q0	-5.0	0.0	30.0	-5.1	15	-28.2	-40.2	-43.1
W4Q-10	-3.2	-11.5	4.3	-3.1	37.4	-25.6	-29.3	-29.4
W4Q-20	-0.5	-21.0	-8.4	-0.5	70	-38.5	-37.9	-32.9
W4Q-25	6.5	-29.8	-20.5	-2.3	90	-1.4	-0.2	3.7
W4Q10	0.8	7.3	25.9	8.4	0	-2.9	-4.7	-5.9
W4Q20	-5.7	20.7	48.0	10.2	90	-12.8	-28.5	-35.9
W4Q25	19.2	17.5	42.9	20.0	79	-14.0	-29.1	-35.9

The group of 3 suspended transport models have positive correlation and have least agreement with measurement. The 3 models similarly predict much less value (factor 1/10) compared to measurements in combination of W1, W2 (T=1 s), while overestimating by a factor 10 for combinations with W3, W4 (T=1.5 s). The GD model gives the best prediction for direction of sediment transport (70% correct).

In general, none of the selected models simulated well the sediment transport rate obtained from the present experiment. The reason is possibly that all models are developed for flat bed but not for sloping bed. However, the point, which is calculated q_s, is located on top of the sand barrier which is the flattest part of the barrier.

The most important agreement with previous studies, e.g., Dibajnia & Watanabe (1992) and O'Donoghue & Wright (2004) for velocity skewed flow, is that 70% of the cases have net transport against the direction of the highest velocity (see yellow label in table 9.1). This may imply that those cases are dominated by velocity skewness.

It is common to compare q_s for many points along the flume to achieve the same trend as Figure 8.12, 8.13 rather than compare only one point for each case. It seems too early to conclude about applicability of those models for this experiment.

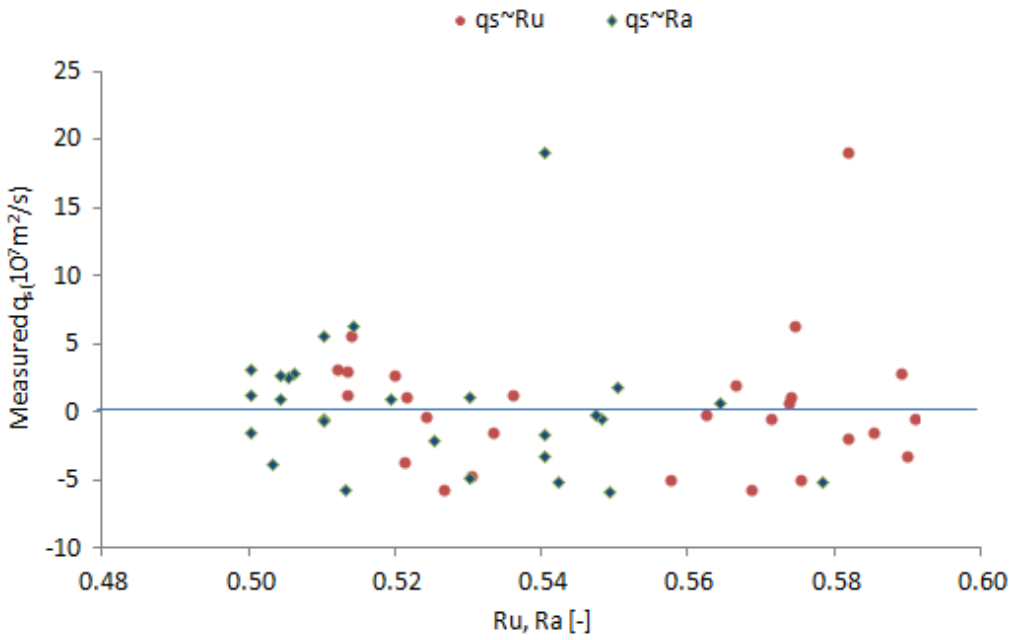

Figure 9.4: Measured q_s versus velocity skewness R_u and acceleration skewness R_a.

In order to check for a relation between q_s and velocity skewness R_u and acceleration skewness R_a, the measured q_s and R_u, R_a, calculated from measured velocity for all cases are plotted in Figure 9.4. As can be seen, there is no correlation between them, which as suggested by Van der A et al. (2010a, 2010b) that for fine sand negative correlation is found with R_u under velocity skewed flow and positive correlation with R_a under acceleration skewed flow. However, if we plot separate for each combination W1, W2, W3, W4, then the negative correlation with R_u is seen except each case has one point out of trend (Figure 9.5).

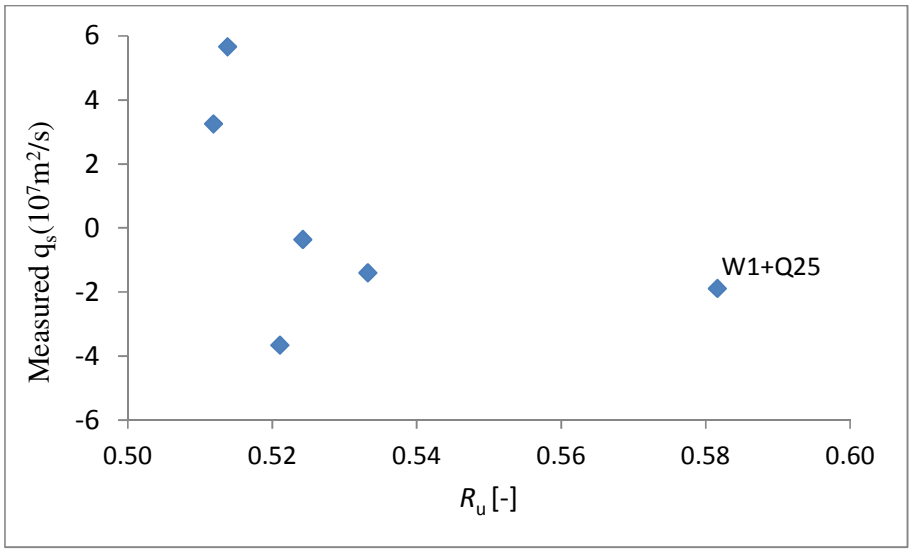

Figure 9.5: Negative correlation with velocity skewness R_u in combinations of W1 except case W1+Q25 has larger Ra, it may belong to acceleration skewed flow.

9.4 ADOPTED RESULTS FROM SWASH MODEL FOR SAND BARRIER

9.4.1 Introduction of the SWASH model and model set up

- The SWASH model

The numerical model used to simulate the hydrodynamics over sand bar in the laboratory is described in this section. The SWASH model developed at the Delft University of Technology is a general purpose numerical tool for simulating non-hydrostatic, free surface and rotational flows basically to describe complex, rapid flows and wave transformation in coastal waters, ports and harbours (Zijlema et al., 2011). SWASH is a state-of-the-art time-domain wave model solving governing Non Linear Shallow Water Equations (NLSWE) with a correction for non-hydrostatic pressure. SWASH can be run in both depth averaged mode and in multilayered mode. SWASH uses the explicit form of the continuity and momentum equation run in second order Leapfrog scheme (Smith et al., 2011). The major applications of SWASH model are in complex changes such as dike breaks, tsunami, and wave transformation in both surf and swash zones due to nonlinear interactions between wave and currents. The basic SWASH codes helps to run a wide range of time and space scales in both surface waves and shallow water flows. In this study, SWASH is used in non-hydrostatic 1D mode to simulate the flow and wave propagation in the wave flume over the sand bar.

- Model set up

The SWASH model is set up with the flume bathymetry, wave characteristics and flow rate as input. Bottom friction and turbulent eddy viscosity were used as tuning parameters to calibrate the model. The flume is discretized with a horizontal grid spacing of 5 cm and five layers were used in the vertical, i.e., the water depth is equally divided into 5 layers at each grid point. Even though more vertical layers could be used to obtain high resolution vertical velocity profile, 5 layers were found to be sufficient to obtain good correlation with the measurements. The initial data up to five minutes for each case was used to calibrate the model and on obtaining satisfactory comparison (correlation coefficient >0.9) between the model water levels and measured water levels, the model parameters were frozen and the model is run for a period of 1 hour. A computation time step of 0.01s is used and the data is stored at 25 Hz. Two cases W1 and W4 without additional current was simulated by the SWASH model and presented here. These simulations were carried out at the CSIR-National Institute of Oceanography, Goa, India, with the help of Dr. Jaya Kumar Seelam (alumni of UQ), and the velocities thus obtained were used further to assess the sediment transport models in the later sections.

9.4.2 Comparison model results and experiment data

The results obtained from the model are (i) surface water level variations and (ii) velocities at each of the vertical layer for each grid point. For validating the model results, the velocities obtained at the last layer from the model was compared with the measured velocities. Also, measured surface water levels were compared with model results. The water level and velocity comparisons are presented in Figure 9.6 for case W1. Both the water level and velocity compare well.

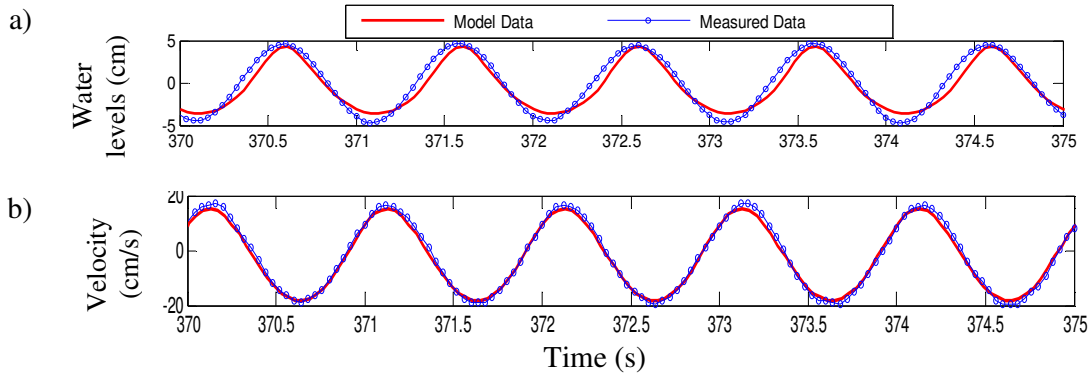

Figure 9.6: Comparison between model results and measurements (a) water levels and (b) velocity for W1.

For Case-W4, the comparison of water level and velocity using the initial profile show good agreement with water levels but the velocity is seen to deviate from the measurements, showing a large phase shift, towards the later stages of the model. The reason for this deviation could be due to significant change in the bathymetry over the time. Therefore Case-W4 was simulated with the final bottom profile obtained after the experiment and the model results were found to compare well with the measurements (Figure 9.7) both in water levels and velocity.

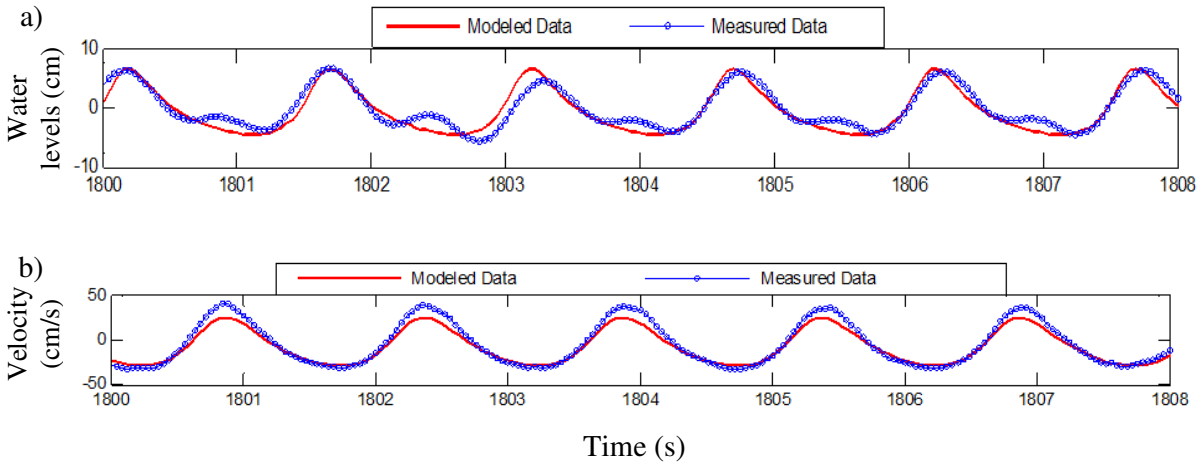

Figure 9.7: Comparison between model results and measurements (a) water levels and (b) velocity for W4 with final bathymetry profile.

The comparison between phase averaged velocity from measurement and from the model at x=8.5 m is shown in Figure 9.8.

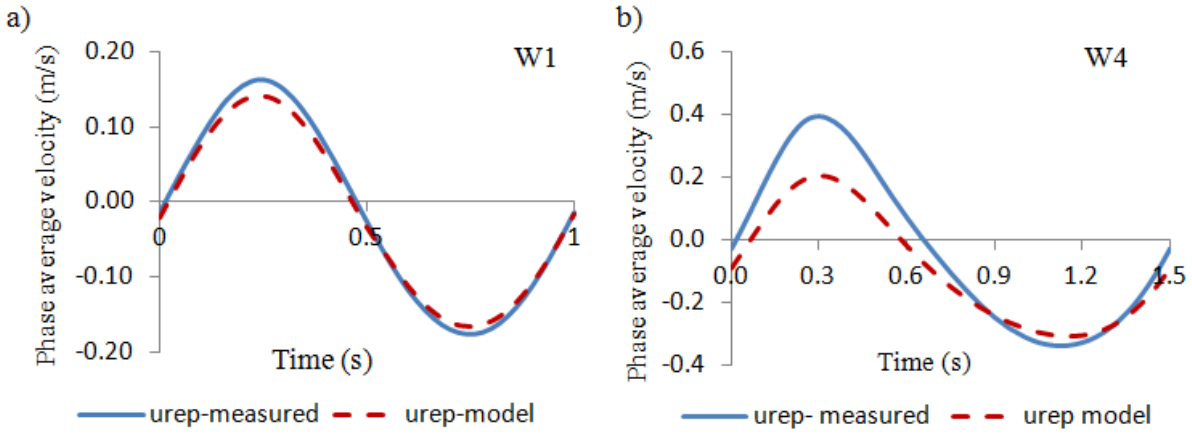

Figure 9.8: Comparision phase average velocity between measurement and model : a) W1; b)W4

There is very good agreement with data for case W1 in term of magnitude and phase, however less agreement for the case W4 especially with positive half cycle. It seems that the

SWASH model fails to predict the secondary waves when underestimates the peak velocity. Therefore the velocity results from different points along the sand bar for case W1 are deemed reliable, while in case W4 calculated q_s from the model may be less so.

9.4.3 Sediment transport rate along sand bar using model velocities in comparison with measured sediment transport rates

The q_s results by different models along the sand barrier for W1 are presented in Figure 9.9 and table 9.2. As can be seen q_s by N06 model with φ_τ=51^o is similar to that of RA model and closer to the measurements. RA has symmetric curve while N06 has asymmetric shape which is similar to shape of the measured q_s. Using φ_τ=0^o (~ drag dominated transport) in N06 improves the results but remains far from good agreement.

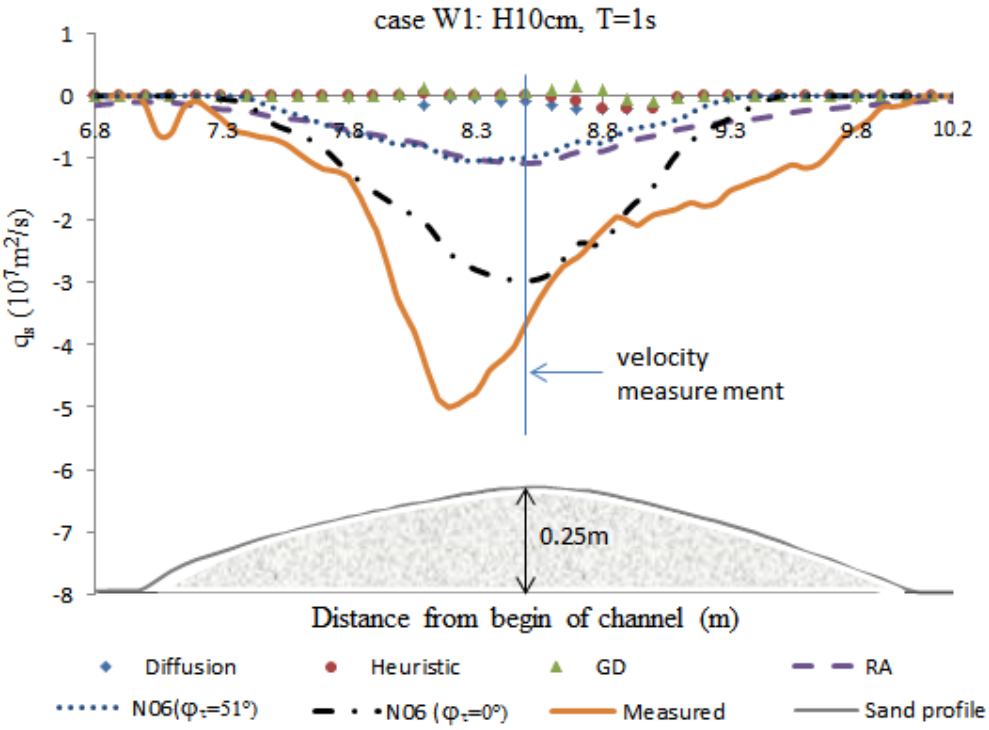

Figure 9.9: Calculated q_s by different models along the sand barrier for case W1. Nielsen06 model with φ_τ=51^o has better agreement with measurement, Nielsen06 with optimal φ_τ=0^o has best fit with measurement.

The three suspended transport models similarly predict very small sediment transport, q_s nearly zero. The results of this case at x=8.5 m by different models are quite similar in order of magnitude with the results calculated using measured velocity in table 9.1. The results are reliable but all models underestimate q_s, especially the suspended models.

Table 9.2: Results of q_s (10^7 m^2/s) by different models along the sand barrier for case W1

x(m)	Measure	Diffusion	Heuristic	GD	R&A	$N06_{2.5}$ φ_τ=51°	$N06_{2.5}$ φ_τ=0°	$N06_{f10}$	$N06_{rip}$
6.8	0	0	0	0.002	-0.15	0	0	0	0
6.9	0	0	0	0.002	-0.11	0	0	0	0
7	-0.15	0	0	0.002	-0.10	0	0	0	0
7.1	-0.6	0	0	0.002	-0.10	0	0	0	0
7.2	-0.09	0	0	0.003	-0.17	0	0	0	0
7.3	-0.37	0	0	0.003	-0.22	0	-0.05	0	0
7.4	-0.6	0	0	0.003	-0.24	-0.03	-0.13	-0.4	0.0
7.5	-0.69	0	0	0.003	-0.34	-0.19	-0.44	-4.1	0.0
7.6	-0.91	0	0	0.003	-0.38	-0.31	-0.61	-5.5	0.0
7.7	-1.17	0	0	0.003	-0.43	-0.45	-0.84	-7.2	0.0
7.8	-1.3	0	0	0.003	-0.55	-0.60	-1.22	-10.7	0.0
7.9	-2.08	0.001	0	0.012	-0.62	-0.67	-1.53	-12.5	-13.4
8	-3.31	-0.003	0.001	0.026	-0.70	-0.78	-1.80	-14.7	-19.7
8.1	-4.27	-0.153	0.02	0.118	-0.78	-0.80	-2.03	-15.4	-37.8
8.2	-5	-0.017	-0.001	0.029	-0.93	-1.01	-2.53	-19.1	-22.5
8.3	-4.77	-0.016	-0.001	0.025	-1.02	-1.04	-2.79	-20.5	-23.6
8.4	-4.25	-0.082	-0.008	0.04	-1.06	-1.01	-2.92	-20.1	-38.6
8.5	-3.65	-0.083	-0.007	0.066	-1.08	-1.00	-2.98	-20.2	-41.1
8.6	-2.97	-0.162	-0.037	0.082	-1.04	-0.91	-2.84	-18.3	-56.8
8.7	-2.6	-0.199	-0.092	0.141	-0.91	-0.74	-2.38	-14.8	-63.3
8.8	-2.16	-0.201	-0.196	0.108	-0.89	-0.76	-2.36	-15.0	-62.8
8.9	-2.01	-0.212	-0.222	-0.057	-0.73	-0.54	-1.83	-11.6	-56.7
9	-1.91	-0.192	-0.201	-0.076	-0.64	-0.48	-1.46	-9.7	-35.7
9.1	-1.8	-0.015	-0.013	-0.015	-0.54	-0.37	-0.90	-7.1	-13.3
9.2	-1.77	0	0	0	-0.47	-0.17	-0.58	-4.6	0.0
9.3	-1.53	0	0	-0.001	-0.41	-0.05	-0.37	-2.1	0.0
9.4	-1.36	0	0	-0.002	-0.37	0	-0.15	0	0
9.5	-1.19	0	0	-0.003	-0.30	0	-0.01	0	0
9.6	-1.16	0	0	-0.004	-0.23	0	0	0	0
9.7	-0.9	0	0	-0.005	-0.21	0	0	0	0
9.8	-0.52	0	0	-0.006	-0.16	0	0	0	0
9.9	-0.19	0	0	-0.006	-0.13	0	0	0	0
10	-0.13	0	0	-0.006	-0.10	0	0	0	0
10.1	-0.005	0	0	-0.006	-0.08	0	0	0	0
10.2	0	0	0	-0.006	-0.08	0	0	0	0

The q_s results from different models along the sand barrier for W4 are presented in Figure 9.10. As can be seen, N06 also gives a good agreement with the measurement compared to other models for φ_τ=50° for all points along the sand barrier. It has asymmetric curve closest to the measurement curve. By adjusting the φ_τ from 45° to 80°, a better agreement with measurement can be achieved. However the peak q_s on both sides cannot be achieved, not even adjusting φ_τ to the largest range.

RA is still consistent with negative value resulting in least agreement with measurement in terms of direction and magnitude. The heuristic model and the diffusion model have quite similar q_s and have good agreement with measurement from 7.8 m to 9 m. They also predict the direction quite well except for the area x<7.5 m and x>9 m, they still give q_s=0 even though ripple dimension is provided.

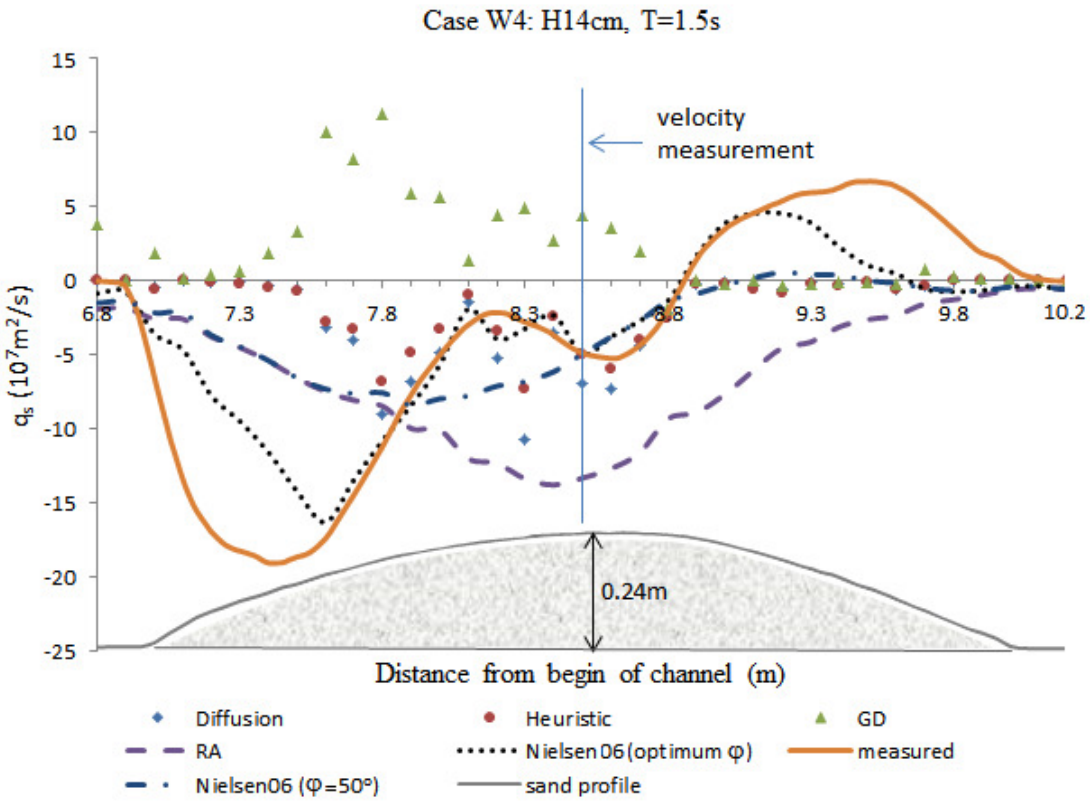

Figure 9.10: Calculated q_s by different models along the sand barrier for case W4.

GD in general gives opposite direction with the measurement, which is quite different from the good predictions of direction in section 9.3. It may be due to the results of SWASH model for this case being not good as in Figure 9.8 right panel.

9.5 CONCLUSION OF ASSESSMENT OF EXISTING SEDIMENT TRANSPORT MODELS

Different sediment transport models for non-breaking waves over ripple beds have been reviewed. Based on the good performance of models on ripples and fine sand, 5 models were chosen for comparison: Ribberink & AlSalem (1994), Nielsen (2006), the diffusion model, the heuristic model and the 'Grab and dump model' of Nielsen (1988). The first two models are essentially bed load models and the last three are essentially suspended load models. Results of comparison between

different transport models with measurement for all combinations at top of the sand barrier are presented.

The Ribberink & Al-Salem (1994) model provided least q_s-magnitude error compared to the measurements, but 70% prediction in wrong direction. Surprisingly, GD model gives the best prediction for direction of sediment transport (70% correct). Nielsen (2006) with optimum φ_τ for individual case provides much improvement in terms of magnitude and direction; however it is still far from agreement with measurement. The 3 suspended transport models have positive correlation and have least agreement with measurement. These 3 models similarly under-predict q_s-magnitude compared to measurements for W1, W2 (T=1 s), while they overestimate for combination of W3, W4 (T=1.5s).

The most important result agreeing with previous studies is that 70% of cases have net transport against the direction of highest velocity. The negative correlation between q_s and velocity skewness has been seen for each wave combinations separately Figure 9.5.

The results with velocities from the SWASH numerical model provided reliable predictions for case W1 (Figure 9.8) resulting in better estimates of sediment transport (Section 9.4.3).

The q_s-results from different models along the sand barrier for W1 show that all models under estimate q_s especially the suspended load model. N06 with φ_τ=51^o and the RA model predict much better than three suspended models in terms of magnitude and direction. N06 with φ_τ=0^o, (~drag force sediment transport) improves the results but is still far away from best fit with measurement.

The q_s-results by different models along the sand barrier for W4 show that Nielsen (2006) is still closest to the measurement compared to other models with φ_τ=50^o. Followed by the heuristic- and diffusion models, which have quite similar results of q_s and have good agreement with measurement from x=7.8 m to 9 m. They predict also quite well direction except for x<7.5 m and x>9 m, models provided q_s=0. RA and GD have least agreement with the measured q_s.

Even though Nielsen 2006 has better performance with waves W1 and W4, it is still hard to ensure its capability of its prediction. Surprisingly, the suspended models expected to work well for vortex ripple with fine sand performed poorly. This may be due to these models neglecting lateral diffusion, as well as the influence of bed slope. There should be more velocity measurements along sand barrier to evaluate the reliability of the SWASH model.

In summary, q_s-prediction under waves and currents on a rapidly varying bed, like the barrier considered here, Figure 9.9, do not provide good comparisons and therefore needs further work.

Chapter 10

CONCLUSIONS AND RECOMMENDATIONS

This thesis has presented a study on tidal inlets in their equilibrium and non-equilibrium states to gain a better understanding of their hydrodynamic and morphodynamic responses under the main 'forces' of tides, river flow and waves. Acknowledging the achievements and recognising the limitations of previous studies, this thesis introduced new methods and relationships that bring theories closer to the natural physics. This helps researchers and costal managers to have a clearer perspective of inlet dynamics while providing practical tools for predicting system response to extreme weather conditions or closure. The following section summarizes main achievements of this research and recommendations for further work.

10.1 NEW CLASSIFICATION OF COASTAL INLET SYSTEMS

Several methods exist to classify coastal systems; the most favoured and used classification is based on the hydro-morphological perspective related to ecological parameters. The literature review revealed that none of the previous methods consider quantitatively the three main driving agents that govern inlet morphodynamics. New methods of classification are introduced in this thesis based on dimensionless parameters which represent the relative strength of the three main forcing agents, viz., tide, river flow and waves. The non-dimensional parameters are $\frac{\sqrt{gH^5}}{\hat{Q}_{\text{tide}}}$ and $\frac{Q_f}{\hat{Q}_{\text{tide}}}$ in which tidal forcing is quantified in terms of the peak tidal discharge (actual or potential) and wave forcing represented in terms of sediment transport capacity. This new classification is applied to 178 inlets along the NSW coast of Australia, which revealed a clear distinction of three main groups Figure 1.10: **1)** wave dominated coast with $\frac{\hat{Q}_{\text{tide}}}{\sqrt{gH^5}} < 75$, **2)** tidal dominated coast with $\frac{\hat{Q}_{\text{tide}}}{\sqrt{gH^5}} > 75$ and **3)** river dominated coast with $\frac{Q_{\text{f}}}{\sqrt{gH^5}} \geq 2$. The new classification method compares well with other widely used classification schemes in the literature. The present method reduces discrepancies between hydrodynamic and morphodynamic classifications. This improved classification system allows better long-term prediction of inlet morphodynamics, enabling effective coastal zone management.

10.2 INLET HYDRODYNAMIC ANALYSIS

Hydrodynamic processes are key forcing giving bed shear stress, sediment transport patterns and bed level changes. Thus, understanding the hydraulics may eventually allow us to evaluate the morphological state of a system and to predict its morphological development. The inlet hydraulic analysis is presented with given inlet geometry and wave climate with the wave overwash flow rate Q_{over} added into the usual governing equations.

The hydraulic analysis of inlets in terms of the frequency response function for the linearised system is illustrated for cases of monochromatic and mixed diurnal/ semi diurnal tides. The dominant tidal component in a mixed tide system is similar to the monochromatic response, but the behaviour of the subordinate is more complex. The channel friction term influences the primary component more than the subordinate component. The response of the primary component is quite stable during changes to inlet morphology, ocean tide amplitude, the phase between two ocean components or Q_f, while the subordinate responds strongly. Both components respond similarly when an inlet approaches complete closure. The influence of Q_f on the response of a monochromatic tide shows different signatures via increasing A_b or through increase in friction ~ $|u|uL_c$.

A case of flooding at Lake Conjola is used to test different methods resulting in successful illustration of the importance of wave overwash as a driving force. Based on calibration parameters suggested from previous studies, empirical overtopping models greatly overestimate the water level corresponding to highest Q_{over}. The wave pump model and the swash model are comparable and give good agreement with measured water levels. The wave pump model performs best matching measured tidal range and lowest RMSE.

10.3 LAGOON AND ESTUARINE TIDE ANALYSIS

A new method of tidal analysis using 24.5 hour moving window is developed to resolve the highly transient hydro- and morpho-dynamics during storm and/or flood events, which usually last for 3 days or less. The method gives time series of the hydraulic response function for diurnal (F_1) and semi-diurnal component (F_2). Morphological time scales, T_{morph}, can then be obtained from $\overline{\eta_{24.5}}(t)$, $Stdv_{24.5}(t)$ or gain of primary component. However, erratic behavior of subordinate tidal component due to the non-linear interaction between the two tidal components is not clearly interpretable at the present stage. The result of inlet morphodynamics analysis from this new tide based method is more reliable than that from process based numerical models, and more economical than analysis from topographical surveys (which are usually not available).

Illustrations of using this method are presented in Chapter 4. Application of this new method for many closure events (with bay area A_b<0.7 km^2) in NSW show a clear trend of $T_{morph,\ close}$ decreasing with increasing dimensionless relative wave strength $\frac{\sqrt{gH^5}}{\hat{Q}_{tide,pot}}$, Eq (6.14). However, for large, partly regulated inlet systems trained by breakwaters, the morphology change is usually not significant enough, compared to the cross section, to be measurable via the tidal record. Hence the T determined by the method for these larger systems, e.g., Brunswick River or Pensacola Pass, is just hydraulic timescale T_{hyd} not T_{morph}. However, this method is an effective way to analyse surge or flood events for large systems to investigate the occurrence of changing hydraulic efficiency.

10.4 INLET STABILITY

For each hydrodynamic condition ($\hat{Q}_{tide}$, Q_f, H) the inlet system has a morphological equilibrium state. A new indicator of an inlet being in a stable state is the response functions of the primary tidal constituent tracing a tight orbit in the complex plane (cf. Figure 4.19). This is a better indicator than the lagoon tide on its own as it accounts for ocean tide variability.

Almost all previous relationships of inlets in equilibrium are based on the tidal prism representing tidal forcing. Many researchers have pointed out that tidal period also needs to be taken into account in these relations. Using $\hat{Q}_{tide}$ to quantify "tidal strength" and testing on a data set of 36 natural inlets in the USA, a new relationship between inlet cross sectional area A_c and $\hat{Q}_{tide}$ and H_s was obtained (Eq. 5.23). Other new relationships between volumes of ebb and flood tidal delta, V_{Ebb} and V_{Flood}, and $\frac{\hat{Q}_{tide}}{\sqrt{gH^5}}$ are also presented in Eq (5.6) and Eq (5.7). Subsequently these relations will be used in dynamic modelling based on convolutions with hydraulic or morphological impulse response functions.

10.5 INLET MORPHODYNAMICS

The scatter around these 'equilibrium relationships' may be due to non-steady wave conditions and spring/neap tides cycles so that measured A_C-values are never true equilibrium values. This is true even in the absence of freshwater flow effects, which are random in many areas while perhaps quasi-periodically seasonal in others. Other observed inlet parameters would similarly always be transient rather than equilibrium values. The evolution of inlet morphology parameters is

demonstrated by using the impulse response function and the 'equilibrium expressions' with variable forcing of $\widehat{Q}_{tide}(t)$ and $H_s(t)$.

In some parts of the world, seasonal weather changes drive major morphological change to inlets, while variations due to individual storms are less significant. In other parts such as the NSW coast, Australia, inlet morphodynamics are driven by tides, fresh water flow and waves without a clear seasonal periodicity. The fraction of time the inlet is open varies quite erratically for $\frac{\hat{Q}_{\text{tide, pot}}}{\sqrt{gH^5}}$ <100 but beyond this value no inlets have been reported closed for extensive periods. The average time of remaining open $\overline{T_{\text{open}}}$ from basic statistic is somewhat better behaved with an identifiable trend with dimensionless relative tidal strength as in Eq (6.6) and Figure 6.10. However, it was difficult to determine the exact relationship for fully exposed and natural systems (never artificially opened) with the present data.

10.6 ASSESSMENT OF THE STATE OF THE ART OF NUMERICAL MORPHOLOGICAL MODELLING

The CMS model of the U.S. Army Corps of Engineers has been used to study the Pensacola Inlet morphology changes during Hurricane Katrina. Though the hydrodynamics were captured by the model, it under predicted the morphology changes as observed in nature and expected. Insignificant erosion of the ebb tidal delta in the model results was unexpected. This is attributed to (i) improper model assumptions about bed shear stresses being in the direction as the depth averaged current, ignoring seaward sediment transport due to undertow during the storm; (ii) underestimation of the role of wave sediment transport by using wave spectra, which does not account for wave shapes in estimating sediment transport in the surf zone; and (iii) difficulties involved in numerical bed updating methods in terms of stability and accuracy. It is concluded that inlet evolution during storms is unlikely to be predicted by the CMS model.

10.7 EXPERIMENTS OF SAND BARRIER DYNAMICS UNDER WAVES & CURRENTS AND ASSESSMENT OF EXISTING SEDIMENT TRANSPORT FORMULAE

A series of laboratory experiments on a sand barrier, representing an offshore bar in front of an inlet without wave breaking, were carried out to understand the morphology change due to sediment transport processes induced by waves and currents. Analysis of the combinations of two wave cases with shorter period show that the sediment transport direction is opposite to the net flow direction. The direction of sediment transport (q_s) is variable in the combinations of other two wave cases

with relatively longer wave period. These cases show convincingly that, q_s cannot be generally assumed to be in the direction of the net flow as assumed in the CMS model.

Three formulae for estimation of ripple dimension were tested with ripple measurement on top of sand barrier for all experiments. Nielsen (1981) and Van Rijn (1993) formulae similarly predict well ripple height while underestimate ripple length. O' Donoghue et al. (2006) formula underestimate ripple height and ripple length.

Five state-of-the-art sediment transport (q_s) formulae, viz., Ribberink & AlSalem (1994), Nielsen (2006), the diffusion model, the heuristic model and the 'Grab and dump model' of Nielsen (1988) were tested for their applicability to the laboratory experiments. Comparison between these transport models with measured q_s at the top of the sand barrier for all test combinations showed that Ribberink & Al-Salem (1994) model provided the least q_s-magnitude error, but 70% of the prediction being in wrong direction (Figure 9.3); whereas the 'Grab and dump model' gives the best prediction for direction of q_s. Nielsen's (2006) model with optimum φ_τ for each case provides some improvement in terms of magnitude and direction; however, comparisons are far from general agreement with these measurements. The three suspended load models have positive correlation but least agreement with these measurements. These three models under-predict q_s-magnitude compared to measurements for shorter period waves, while they overestimate for combinations involving longer period waves. 70% of experiments had net sediment transport against the direction of highest velocity. This finding is in agreement with previous studies.

A 2D numerical model resolving the vertical structure of the flow was adopted to obtain near-bed velocities along the sand barrier for cases without current. For the case of low wave period, good agreement between model and measured velocities was obtained. The model velocities were utilized to compute q_s along the barrier for this case using different sediment transport models. All five models underestimate q_s especially the suspended load model. Nielsen (2006) with $\varphi_\tau=51^o$ and Ribberink & Al-Salem (1994) predict much better than the three suspension models in terms of magnitude and direction (Figure 9.9). Even though Nielsen (2006) with $\varphi_\tau=0^o$, (~drag dominated sediment transport) while shifting predictions toward measurements, minor differences remains. Predictability using Nielsen (2006) remains an open question. The suspended models expected to work well for vortex ripples and fine sand did not perform well, which could be due to these models neglecting lateral diffusion and bed slope influences. In summary, q_s-prediction under waves and currents on a rapidly varying bed, like the barrier considered here, is still beyond the state of the art models' capability.

10.8 RECOMMENDATIONS

10.8.1 Application of Research Findings

- The new classification method for coastal systems can be applied across the full range of forcings (tide, river and waves) for other areas where one of the forcings is relatively constant.
- The wave pump model and the swash model are comparable when computing Q_{over} for coastal lagoon system experiencing wave overwash. Therefore, flooding of these coastal lagoons can be now modelled.
- The 24.5 hour moving window is an effective tool to infer hydrodynamic and morphodynamic timescale for small lagoon with A_b <0.7 km^2 in closing events. Alternatively, for large systems this method can be used to investigate if the hydraulic efficiency changes during wave storms or flood events or to determine whether the inlet is stable or transient.
- The 3 equilibrium relations for A_c, V_{ebb} and V_{Flood} can be applied in dynamic modelling based on convolutions with hydraulic or morphological impulse response functions for natural inlet in similar coastal environment.
- The relation of $\overline{T_{open}}$ and $T_{morph,close}$ with external forces helps local authorities to forecast and react in time during extreme events, in navigation and flood control to mitigate the vulnerability of coastal area.

10.8.2 Matters for Further Research

The new classification and the new equilibrium relationships, were based on $\widehat{Q}_{tide}$, calculated from the actual tidal prism (except for ICOLLs). It would be worthwhile to consider $\widehat{Q}_{tide,pot}$, related to tide potential- 'tidal strength', and compare with present results to ascertain which method performs better.

Wave height dependence of A_{eq} need to be further studied based on improved database.

Erratic behavior of subordinate tidal component from 24.5hour moving window method need to be further investigated for interpretation.

Numerical modelling of morphodynamics should be improved by considering the wave induced effects on sediment transport. Further reliable velocity data from combined wave and current models should be used to test and confirm the capability of sediment transport models.

References

Abe, K. and Ishii, H., 1981. Study of shelf effect for tsunami using spectral analysis". In: K. Iida, T. Iwasaki and T.C. IUGG (Editors), Tsunamis: Their Science and Engineering, Sendai-Ofunato-Kamaishi, Japan, pp. 161-172.

Allsop, D., 2009. DECCW Lake Conjola data collection June 2008 to June 2009. MHL1929, NSW Department of Environment, Climate change and water. Manly Hydraulic Laboratory, 93 pp.

Armanini, A. and Di Silvio, G., 1986. A depth-integrated model for suspended sediment transport. Journal of Hydraulic Research, 24 (5): 437-442.

Armbruster, C.K., 1997. Morphologic responses of a low-energy, micro-tidal beach to winter cold front passages: North shore Santa Rosa Island, Florida. MS thesis Thesis, Louisiana State University, Baton Rouge, LA, 166 pp.

Bagnold, R., 1966. An approach of sediment transport model from general physics. Tech. Rep. 422–I, US Geological Survey Professional Paper, 37 pp.

Bagnold, R.A., 1956. The Flow of Cohesionless Grains in Fluids. Philosophical Transactions of the Royal Society of London. Series A, Mathematical and Physical Sciences, 249 (964): 235-297.

Bailard, J.A., 1981. An Energetics Total Load Sediment Transport Model For a Plane Sloping Beach. J. Geophys. Res., 86.

Baldock, T.E. and Holmes, P., 1997. Swash Hydrodynamics on a Steep Beach. Coastal Dynamics '97, Plymouth, U.K.: 784-793.

Baldock, T.E. and Holmes, P., 1999. Simulation and prediction of swash oscillations on a steep beach. Coast. Eng., 36: 219–242.

Baldock, T.E., Hughes, M.G., Day, K. and Louys, J., 2005. Swash overtopping and sediment overwash on truncated beach. Coastal Engineering, 52: 633-645.

Baldock, T.E. and Peiris, D., 2010. Overtopping and run-up hazards induced by solitary waves and bores. In: N.-A. Mörnerin (Editor), Tsunami Threat - Research and Technology. INTECH: 20.

Baldock, T.E. and Simmonds, D.J., 1999. Separation of incident and reflected waves over sloping bathymetry. Coastal Engineering, 38 (3): 167-176.

Baldock, T.E., Tomkins, M., Dalton, G., Skyllass-Kazacos, M. and Kazacos, N., 2006. Renewable energy sources for the Australian tourism industry, CRC for Sustainable Tourism, 80 pp.

Barton, J., Pope, A., Quinn, G. and Sherwood, J., 2007. Development of a methodology for assessing estuary pressures: relationships with catchment conditions. Stage 2 linking catchments to the sea - understanding how human activities impact on Victorian estuaries, Milestone 3 report to the National land and Water Resources Audit: review and expand the Victoria-wide classification, unpublished.

Battjes, J.A. and Janssen, J., 1978. Energy loss and set-up due to breaking of random waves. Proceedings 16th International Conference Coastal Engineering, ASCE: 569-587.

Beji, S. and Battjes, J.A., 1993. Experimental investigation of wave propagation over a bar. Coastal Engineering, 19 (1-2): 151-162.

Beji, S., Ohyama, T., Battjes, J.A. and Nadaoka, K., 1992. Transformation of Nonbreaking Waves Over a Bar. Proceedings of 23th International Conference Coastal Engineering, Venice, Italy: 51-61

Bertin, X., Fortunato, A.B. and Oliveira, A., 2009. A modeling-based analysis of processes driving wave-dominated inlets. Continental Shelf Research, 29 (5-6): 819-834.

Bijker, E.W., Hijum, E.v. and Vellinga, P., 1976. Sand transport by wave. 15th ICCE, Honolulu, 2: 1149-1167.

Boon III, J.D. and Kiley, K.P., 1978. Harmonic analysis and tidal prediction by the method of least squares - A User's Manual, Virginia Institute of Marine Science, Gloucester Point, Virginia, 49 pp.

Britton, P. and Partners, 1999. Lake Conjola entrance study. J3088/R2029, Patterson Britton & Partners, 224 pp.

Browder, A.E., 2004. Pensacola Beach, Florida, 2003 Beach Restoration Project - Hurricane Ivan 15-16 September 2004, Post-storm Monitoring Report, 80 pp.

Browder, A.F. and Dean, R.G., 1999. Pensacola Pass, Florida, Inlet management study. GFL/COEL-99/002, Coastal and Oceanographic Engineering Dept. University of Florida, 101 pp.

Bruun, P., 1962. Sea level rise as cause of shore erosion. American Society Civil Engineers Proceedings, Journal Waterways & Harbors Division, 88: 117-130.

Bruun, P., 1966. Tidal Inlets and Littoral Drift. P. Bruun,Washington DC, 193 pp.

Bruun, P., 1978. Stability of tidal inlets - Theory and Engineering. Developments in Geotechnical Engineering 23, 23. Elsevier Scientific, Amsterdam, 510 pp.

Bruun, P. (Editor), 1990. Harbor Transportation, Fishing Ports, Sedimentation Transport, Geomorphology, Inlets and Dredging. Port Engineering, 2. Gulf Publishing Co., Houston, London, Paris, Zurich, Tokyo, 928 pp.

Bruun, P. and Gerritsen, F., 1959. Natural By-Passing of Sand at Coastal Inlets. Journal of the Waterways and Harbors Division, 85: 75-107.

Bruun, P. and Gerritsen, F., 1960. Stability of Coastal Inlets. North-Holland Publishing Co., Amsterdam: 386-417.

Bruun, P. and Viggosson, G., 1977. The wave pump. Journal of the Waterway Port Coastal and Ocean Division, ASCE 103 (WW4): 449-469.

Burgess, R. et al., 2004. Classification framework for coastal systems 600/R-04/061, Office of Research and Development, US EPA, 66 pp.

Buttolph, A.M. et al., 2006. Two-dimensional depth-averaged circulation model cms-m2d: Version 3.0, report 2: Sediment transport and morphology change CHL-TR-06-9_CMS-M2D_V3_Rpt2, Coastal and Hydraulics Laboratory, ERDC, US Army Corps of Engineers, Vicksburg, MS, USA, 149 pp.

Byrne, R.J., Gammisch, R.A. and Thomas, G.R., 1980. Tidal prism-inlet area relations for small tidal inlets, Proc. 17th Int. Conf. Coastal Eng., 3. Amer. Soc. Civil Eng., New York, pp. 2517-2533.

Callaghan, D.P., Nielsen, P., Cartwright, N., Gourlay, M.R. and Baldock, T.E., 2006a. Atoll lagoon flushing forced by waves. Coastal Engineering, 53: 691-704.

Callaghan, D.P., Saint-Cast, F., Nielsen, P. and Baldock, T.E., 2006b. Numerical solutions of the sediment conservation law; a review and improved formulation for coastal morphological modelling. Coastal Engineering, 53 (7): 557-571.

Camenen, B. and Larson, M., 2005. A general formula for non-cohesive bed load sediment transport. Estuarine, Coastal and Shelf Science, 63: 249–260.

Camenen, B. and Larson, M., 2007. A unified sediment transport formulation for coastal inlet application. Technical Report ERDC-CHL CR-07-01, Coastal and Hydraulics Laboratory, ERDC, US Army Corps of Engineers, Vicksburg, MS, USA, 220 pp.

Carr de Betts, E.E., 1999. An examination of flood tidal deltas at Florida's tidal inlets, University of Florida, Gainesville, FL, 124 pp.

Carr de Betts, E.E. and Mehta, A.J., 2001. An assessment of inlet flood deltas in Florida. Proc. Coast. Dynamics' 01. ASCE: 252-262.

Carstens, M.R., Neilson, F.M. and Altinbilek, H.D., 1969. Bedforms generated in the laboratory under oscillatory flow. Coastal Eng Res Center, Fort Belvoir, VA. Tech Memo, Vol. 28.

Carter, R.W.G., 1989. Coastal Environments: an Introduction to the Physical Ecological and Cultural Systems of Coastlines. Academic Press, London, 617 pp.

Castelle, B. et al., 2007. Dynamics of a wave-dominated tidal inlet and influence on adjacent beaches, Currumbin Creek, Gold Coast, Australia. Coastal Engineering, 54 (1): 77-90.

Cataño-Lopera, Y. and García, M.H., 2006a. Geometry and migration characteristics of bedforms under waves and currents: Part 1, sandwave morphodynamics. Coastal Engineering, 53: 767–780.

Cataño-Lopera, Y.A. and García, M.H., 2006b. Geometry and migration characteristics of bedforms under waves and currents, Part 2: Ripples superimposed on sandwaves. Coastal Engineering, 53 (9): 871-792.

Chawla, A. and Kirby, J.T., 2002. Monochromatic and random wave breaking at blocking points. J. Geophys. Res., 107 (C7): 3067 (4-1 to 4-19).

Clark, R.R. and LaGrone, J., 2006. A Comparative Analysis of Hurricane Dennis and Other Recent Hurricanes on the Coastal Communities of Northwest Florida. 19th National Conference on Beach Preservation Technology: 19.

Claudino-Sales, V., Wang, P. and Horwitz, M.H., 2008 Factors controlling the survival of coastal dunes during multiple hurricane impacts in 2004 and 2005: Santa Rosa barrier island, Florida. Geomorphology 95: 295-315.

Cleveringa, J., Steijn, R.C. and Geurts van Kessel, J., 2007. Time-scales of morphological change of the former ebb-tidal deltas of the Haringvliet and Grevelingen (The Netherlands). River, Coastal and Estuarine Morphodynamics: RCEM 2007; Proceedings of the 5th IAHR The Netherlands, Chapter 6: 41-48.

Coeveld, E.M., Hibma, A., Stive, M.J.F., 2003. Feedback mechanisms in channel shoal formation. Coastal Sediments 2003. Florida, USA (proceedings on CD-ROM).

Coghlan, I. et al., 2011. High resolution wave modelling (HI-WAM) for Batemans Bay detailed wave study. Conference proceedings of Coasts and ports 2011, Canberra, Australia. Engineers Australia: 215-220.

Craghan, M., 1995. Topographic changes and sediment characteristics at a shoreface sand ridge-Beach Haven Ridge, New Jersey, Rutgers Univ., New Brunswick, N.J. , 123 pp.

Darwin, G.H., 1899. The tides and kindred phenomena in the solar system. Houghton, Mifflin and Co., New York, 390 pp.

Dastgheib, A., Wang, Z.B., de Ronde, J. and Roelvink, J.A., 2008. Modelling of mega-scale equilibrium condition of tidal basins in the Western Dutch Wadden Sea using a process-based model. Seventh International Conference on Coastal and Port Engineering in Developing Countries (PIANC-COPEDEC VII), Dubai, UAE: 17.

Davis, R.A. and Hayes, M.O., 1984. What is a wave-dominated coast? Marine Geology, 60 (1-4): 313-329.

de Vriend, H.J., Bakker, W.T. and Bilse, D.P., 1994. A morphological behaviour model for the outer delta of mixed-energy tidal inlets. Coastal Engineering, 23(3-4): 305-327.

de Vriend, H.J., Dronkers, J., Stive, M.J.F., van Dongeren, A. and Wang, Z.B., 1999. Coastal inlets and Tidal basins. Lecture Notes. TU Delft, Delft.

de Vriend, H.J. et al., 1993. Medium-term 2DH coastal area modelling. Coastal Engineering, 21 (1-3): 193-224.

Dean, R.G., Sc.D., 1973. Heuristic models of sand transport in the surf zone First Australian Conference on Coastal Engineering, 1973: Engineering Dynamics of the Coastal Zone, Sydney, N.S.W. Institution of Engineers: 208-214.

Dean, R.G. and Walton, T.L., 1973. Sediment transport processes in the vicinity of inlets with special reference to sand trapping. In: L.E. Cronin (Editor), Estuarine Research. Geology and Engineering. Academic Press, New York: 129-149.

Degnon, C. (Editor), 1996. Reed's Nautical Almanac: North American East Coast. Thomas Reed Publications, Inc., Boston, MA.

De Swart, H.E., 2013. Stability of tidal inlets and geometry of ebb-tidal deltas; their dependence on back barrier basin characteristics. Key note in 7th International conference on Coastal Dynamics 2013, Arcachon, France.

De Swart, H.E. and Zimmerman, J.T.F., 2009. Morphodynamics of tidal inlet systems. Annual review Fluid Mechanic, 41: 223-229.

Di Silvio, G., 1989. Modeling of morphological evolution of tidal lagoons and their equilibrium configurations. XXII Congress of the IAHR, Ottawa, Canada: 169-175.

Dibajnia, M. and Watanabe, A., 1992. Sheet flow under nonlinear waves and currents. Proceedings of 23rd International Conference on Coastal Engineering, Venice, Italy: 2015-2028.

Dibajnia, M. and Watanabe, A., 1996. A transport rate formula for mixed-size sands. ASCE American Society of Civil Engineers: 3791-3804.

Dieckmann, R., Osterhun, M. and Partenscky, H.W., 1988. A comparison between German and North American tidal inlets, Proceedings of the 21st International Conference on Coastal Engineering. ASCE, Torremolinos, Spain, pp. 2681-2691.

DiLorenzo, J.L., 1988. The overtide and filtering response of small inlet-bay systems. In: D.G. Aubrey and L. Weishar (Editors), Hydrodynamics and sediment dynamics of tidal inlets. Lecture Notes on Coastal and Estuarine Studies. Springer-Verlag, New York: 24-53.

Dimas, A.A. and Kolokythas, G.A., 2011. Flow Dynamics and Bed Resistance of Wave Propagation over Bed Ripples J. Waterway, Port, Coastal, Ocean Eng, 137(2) (ASCE): 64-74.

Dissanayake, D.M.P.K., Ranasinghe, R. and Roelvink, J.A., 2012. The morphological response of large tidal inlet/basin system to relative sea level rise. Climatic Change, 113(2): 253-276.

Dissanayake, D.M.P.K., Roelvink, J.A. and Van der Wegen, M., 2009. Modelled channel patterns in a schematized tidal inlet. Coastal Engineering, 56 (11-12): 1069-1083.

Dronkers, J.J., 1968. Discussion of the paper "Water level fluctuations and flow in tidal inlets" by J. van de Kreeke. Journal of the Waterways and Harbors Division, 94 (WW3): 375-377.

Duck, R.W. and da Silva, J.F., 2012. Coastal lagoons and their evolution: A hydromorphological perspective. Estuarine, Coastal and Shelf Science, 110: 2-14.

Duijts, R.W., 2002. Tidal asymmetry in the Dutch Wadden Sea. A model study of morphodynamic equilibrium of tidal basins. MSc thesis, Delft University of Technology, The Netherlands.

Elias, E.P.L., Cleveringa, J., Buijsman, M.C., Roelvink, J.A. and Stive, M.J.F., 2006. Field and model data analysis of sand transport patterns in Texel Tidal inlet (the Netherlands). Coastal Engineering, 53 (5-6): 505-529.

Elliott, D.O., 1932. The improvement of the lower Mississippi River for flood control and navigation Waterways Experiment Station, U.S . Army Corps of Engineers, Vicksburg, Miss ., U.S., 345 pp.

Erickson, M.K., Kraus, N.C. and Carr, E.E., 2003. Circulation change and ebb shoal development following relocation of Mason inlet, North Carolina. Proc. Coastal Sediments'03. World Science, CD-ROM: 13 pp.

Escoffier, F.F., 1940. Stability of Tidal Inlets Shore and Beach, 3 (4): 114-115.

Escoffier, F.F., 1977. Hydraulics and Stability of Tidal Inlets. GITI Report-13, CERC, U.S. Army Engineer Waterways Experiment Station, Vicksburg, MS., 72pp.

Escoffier, F.F. and Walton, T.L., 1980. Inlet Stability Solutions for Tributary Inflow. Journal of Waterways, Harbors and Coastal Engineering Division, 105(WW4): 341-356.

Eysink, W.D., 1990. Morphological response to tidal basins to change. Proc. 22nd International Conference on Coastal Engineering, Delft. ASCE, 2: 1948-1962.

Eysink, W.D., 1991. Impact of sea level rise on the morphology of the. Wadden Sea in the scope of its ecological function. ISOS*2 Project, Phase 1: Inventory of available data and literature and recommendations on aspects to be studied. Report H1300, WL | Delft Hydraulics, Delft.

Ferguson, R.I. and Church, M., 2004. A simple universal equation for grain settling velocity. Journal of Sedimentary Research, 74 (6): 933-937.

FitzGerald, D.M., 1982. Sediment bypassing at mixed energy tidal inlets. Proceedings of the 18th Int. Conference on Coastal Engineering, Cape Town. ASCE: 1094-1118.

FitzGerald, D.M., 1988. Shoreline erosional-depositional processes associated with tidal inlets. In: D.G. Aubrey and L. Weishar (Editors), Hydrodynamics and sediment dynamics of tidal inlets. Lecture Notes on Coastal and Estuarine Studies. Springer-Verlag, New York: 269-283.

FitzGerald, D.M., 2005. Tidal inlets. In: M. Schwartz (Editor), Encyclopedia of Coastal Science. Encyclopedia of Earth Sciences Series. Elsevier, Dordrecht: 958-964.

FitzGerald, D.M., Hubbard, D.K. and Nummedal, D., 1978. Shoreline changes associated with tidal inlets along the South Carolina coast. Coastal Zone ’78, Symposium on Technical, Environmental, Socioeconomic, and Regulatory Aspects of C.Z.M, San Francisco, America. ASCE: 1973-1994.

Foreman, M.G.G., 1977. Manual for tidal heights analysis and prediction. Report 77-10, Pacific Marine Science, 101 pp.

Friedrichs, C.T., 1995. Stability shear stress and equilibrium cross-sectional geometry of sheltered tidal channels. Journal of Coastal Research, 11 (4): 1062-1074.

Friedrichs, C.T. and Aubrey, D.G., 1994. Tidal propagation in strongly convergent channels. Geophysical Research 99(C2): 3321–3336.

Fritz, H.M. et al., 2007. Hurricane Katrina storm surge distribution and field observations on the Mississippi Barrier Islands. Estuarine, Coastal and Shelf Science 74: 12-20.

Gallagher, E.L., Boyd, W., Elgar, S., Guza, R.T. and Woodward, B., 1996. Performance of a sonar altimeter in the nearshore. J. of Marine Geology, 133: 241– 248.

Gao, S. and Collins, M., 1994. Tidal Inlet Equilibrium, in Relation to Cross-sectional Area and Sediment Transport Patterns. Estuarine, Coastal and Shelf Science, 38 (2): 157-172.

Gaudiano, D.J. and Kana, T.W., 2001. Shoal bypassing in mixed energy inlets: Geomorphic variables and empirical predictions for nine South Carolina inlets. J. of Coastal Res., 17 (2): 280-291.

Gerritsen, F., Dunsbergen, D.W. and Israel, C.G., 2003. A relational stability approach for tidal inlets, including analysis of the effect of wave action. Journal of Coastal Research, 19 (4): 1066-1081.

GHD, 2012. Lake Conjola Interim Entrance Management Policy, Shoalhaven City Council, 47 pp.

Goda, Y., 1970. A synthesis of breaker indices. Transaction of Japan Society of Civil Engineering 13: 227-230 (in Japanese).

Godin, G., 1985. Modification of River Tides by the Discharge. J. Waterways, Port, Coastal, and Ocean Eng., ASCE, 111: 259-274.

Gonzalez-Rodriguez, D. and Madsen, O.S., 2007. Seabed shear stress and bedload transport due to asymmetric and skewed waves. Coastal Engineering, 54 (12): 914-929.

Gosford City Council, 1995. Gosford Coastal lagoons processes study: Volume 1. City Council 1995, Coastal lagoons management plan: Wamberal, Terrigal, Avoca and Cockrone (Minute No 815/95), 51pp.

Guard, P.A. and Baldock, T.E., 2007. The influence of seaward boundary conditions on swash zone hydrodynamics. Coastal Engineering, 54: 321-331.

Haines, P. and Vienot, P., 2007. Lake Conjola Flood Study. R.N0758.004.05, BMT WBM, 159 pp.

Hale, J. and Butcher, R., 2008. Summary and review of approaches to the bioregionalisation and classification of aquatic ecosystems within Australia and internationally, 73 pp.

Hands, E.B. and Shepsis, V., 1999. Cyclic channel movement at the entrance to Willapa bay, Washington, USA. Proc. Coastal Sediments (1999), Hauppauge, New York, Reston, VA. ASCE, 2: 1522-1536.

Hanslow, D.J. and Nielsen, P., 1993. Shoreline setup on natural beaches. Coastal Research (Special issue): 1-10.

Hanslow, D.J., Nielsen, P. and Hibbert, K., 1996. Wave set up at river entrances, Chapter 174. Coastal Engineering Proc. 1996, Orlando, Florida: 2244-2257.

Hanson, H., Aarninkhof, S., Capobianco, M., Jiménez, J.A., Larson, M., Nicholls, R.J., Plant, N.G., Southgate, H.N., Steetzel, H.J., Stive, M.J.F. and de Vriend, H.J., 2003. Modelling of coastal evolution on yearly to decadal time scales. Journal of Coastal Research, 19(4): 790-811.

Hapke, C.J. and Christiano, M., 2007. Long-term and Storm-related Shoreline Change Trends in the Florida Gulf Islands National Seashore. US Geological Survey Open-file Report 2007-1392, 18 pp.

Hardisty, J. (Editor), 1990. Beaches form and process. Academic Division of Unwin Hyman Ltd, 297 pp.

Hayes, M.O., 1979. Barrier Island Morphology as a Function of Tidal and Wave Regime. In: S.P. Leatherman (Editor), Barrier Islands from the Gulf of St. Lawrence to the Gulf of Mexico. Academic Press, New York: 1-27.

Heap, A. et al., 2001. Australian estuaries & coastal waterways: a geoscience perspective for improved and integrated resource management. report to the National Land and Water Resources Audit, Theme 7: ecosystem health, Australian Geological Survey Organisation, 188 pp.

Hedges, T.S. and Reis, M.T., 1998. Random wave overtopping of simple sea walls: a new regression model. Proceedings of the Institution of Civil Engineers. Water, maritime and energy, 130 (1): 1-10.

Hibma, A., Schuttelaars, H.M. and Wang, Z.B., 2003a. Comparison of longitudinal equilibrium profiles of estuaries in idealised and process-based models. Ocean Dynamics, 53: 252-269.

Hibma, A., de Vriend, H.J. and Stive, M.J.F., 2003b. Numerical modelling of shoal pattern formation in well-mixed elongated estuaries. Estuarine, Coastal and Shelf Science, 57 (5-6): 981-991.

Hibma, A., Stive, M.J.F. and Wang, Z.B., 2004. Estuarine morphodynamics. Coastal Engineering, 51(8-9): 765-778.

Hicks, D.M. and Hume, T.M., 1996. Morphology and size of ebb tidal deltas at natural inlets on open-sea and pocket bays coasts, North Island, New Zealand. Journal of Coastal Research, 12 (1): 47-63.

Hinwood, J. and Aoki, S.I., 2013. Effects of entrance constriction and ocean forcing on waterlevels in an unregulated tidal inlet. Coastal Engineering Journal, 55 (2): 1350005 (30 pp).

Hinwood, J.B. and McLean, E.J., 2001. Monitoring and modelling tidal regime changes following inlet scour. Journal of Coastal Research (SI 34): 449-458.

Hinwood, J.B., McLean, E.J. and Wilson, B.C., 2012. Non-linear dynamics and attractors for the entrance state of a tidal estuary. Coastal Engineering, 61: 20-26.

Hoan, L.X., Hanson, H., Larson, M. and Kato, S., 2011. A mathematical model of spit growth and barrier elongation: Application to Fire Island Inlet (USA) and Badreveln Spit (Sweden). Estuarine, Coastal and Shelf Science, 93 (4): 468-477.

Hogg, A.J., Baldock., T.E. and Pritchard, D., 2011. Overtopping a truncated planar beach. Journal of Fluid Mechanics, 666, 521-553.

Horrevoets, A.C., Savenije, H.H.G., Schuurman, J.N. and Graas, S., 2004. The influence of river discharge on tidal damping in alluvial estuaries. Journal of Hydrology, 294 (4): 213-228.

Houser, C. and Hamilton, S., 2009. Sensitivity of post-hurricane beach and dune recovery to event frequency. Earth Surface Processes and Landforms, 34 (5): 613-628.

Houser, C., Hamilton, S., Meyer-Arendt, K. and Oravetz, J., 2007. EOF analysis of morphological response to Hurricane Ivan. Coastal Sediment'07, New Orleans, Louisiana. ASCE: 10.

Hsu, T.J. and Yu, X., 2008. Sand transport under near shore wave and current and its implication to sand bar migration. Nonlinear wave dynamics. Selected papers of the symposium held in Honor of Philip L-F Liu's 60th Birthday: 247-266.

Hughes, S.A., 2002. Equilibrium cross sectional area at tidal inlets. Journal of Coastal Research, 18 (1): 160-174.

Hume, T.M. and Herdendorf, C.E., 1993. On the use of empirical stability relationships for characterizing estuaries. Journal of Coastal Research, 9 (1): 413-422.

Hunt, I.A., 1956. Design of seawalls and breakwaters. J. of Waterways and Harbors Division, 85: 123-152.

Hurther, D. and Thorne, P.D., 2011. Suspension and near-bed load sediment transport processes above a migrating, sand- rippled bed under shoaling wave. Geophys. Res., 116 (C07001): 1-17.

Inman, D.L. and Bowen, A.J., 1963. Flume experiments on sand transport by waves and currents. Proceeding 8th International Conference Coastal Engineering. ASCE: 137-150.

Ippen, A.T., 1966. Estuary and coastline hydrodynamics. McGraw-Hill Book company, US, 744 pp.

Isla, F.I., 1995. Coastal lagoons In: G.M.E. Periloo (Editor), Geomorphology and sedimentology of estuaries. Elsevier, Amsterdam: 241-272.

Jarrett, J.T., 1976. Tidal Prism - Inlet Area Relationships GITI Report 3, CERC, U.S. Army Engineer Waterways Experiment Station, Vicksburg, MS, 60 pp.

Jay, D.A., 1991. Green's Law Revisited: Tidal Long-Wave Propagation in Channels With Strong Topography. J. Geophys. Res., 96 (C11): 20585-20598.

Jay, D.A. and Flinchem, E.P., 1999. A comparison of methods for analysis of tidal records containing multi-scale non-tidal background energy. Continental Shelf Research, 19 (13): 1695-1732.

Johnson, H.K. and Zyserman, J.A., 2002. Controlling spatial oscillations in bed level update schemes. Coastal Engineering, 46 (2): 109-126.

Kana, T.W., Williams, M.L. and Stevens, D., 1985. Managing shoreline changes in the presence of nearshore shoal migration and attachment. Proceedings of the 4th Symposium on Coastal and Ocean Management (Coastal Zone '85), Baltimore, MD. New York. ASCE, 2: 1277-1294.

Keulegan, G.H., 1967. Tidal Flow in Entrances: Water-Level Fluctuations of Basins in Communication with Seas Technical Bulletin Number 14, U.S. Army Engineer Waterways Experiment Station, Committee on Tidal Hydraulics, Vicksburg, MS, 113 pp.

Keulegan, G.H. and Hall, J.V., 1950. A Formula for the Calculation of Tidal Discharge Through an Inlet. U.S. Army Corps of Engineer, Beach Erosion Board Bulletin, 4, 15-29.

King, D.B., 1974. The Dynamics of Inlets and Bays. Technical Report No. 22, Coastal and Oceanographic Engineering Laboratory, University of Florida, Gainesville, 94 pp.

Kjerfve, B., 1994. Coastal lagoon processes. Elsevier Oceanography Series, 60. Elsevier, Amsterdam, 576 pp.

Klopman, G., 1994. Vertical structure of the flow due to waves and currents - Laser-doppler flow measurements for waves following or opposing a current 38 pp.

Knudsen, S.B., Ingvardsen, S.M., Madsen, T.H., Sorensen, C. and Christensen, B.B., 2012. Increased water levels due to morphodynamic changes; the Limf Jord, Denmark, International Conference on Coastal Engineerng, ICCE 2012, Santander, Spain.

Kraus, N.C., 1998. Inlet cross-section area calculated by process based model. Proc. of 26th Int. Conf. on Coastal Eng. ASCE, 3: 3265-3278.

Kraus, N.C., 1999. Analytical model of spit evolution at inlets, In: Proceeding Of Coastal Sediments '99. ASCE, New York, pp. 1739-1754.

Kraus, N.C., 2000. Reservoir Model of Ebb-Tidal Shoal Evolution and Sand Bypassing Journal of Waterway, Port, Coastal and Ocean Engineering, 126 (6): 305-313

Kraus, N.C., 2010. Engineering of tidal inlets and morphologic consequences. In: Y.C. Kim (Editor), Handbook of coastal and ocean engineering. World Scientific, los Angeles, USA: 867-900.

Kraus, N.C. and Lin, L., 2002. Coastal processes study of San Bernard River Mouth, Texas: Stability and maintenance of the mouth. TR ERDC/CHL-02-10, U.S. Army Engineer Research and Develop Center, Coastal and Hydraulics Lab., Vicksburg, MS, 76 pp.

Kraus, N.C., Zarillo, G.A. and Tavolaro, J.F., 2003. Hypothetical relocation of Fire Island Inlet, New York. Coastal Sediments 2003: 14.

Krishnamurthy, M., 1977. Tidal prism of equilibrium inlets. J. of the Waterway, Ports, Coastal and Ocean Div. ASCE, 103 (WW4): 423-432.

Kulmar, M. and Hesse, S., 2008. New South Wales South Coast April 2006 storm surge MHL1618, Manly Hydraulics Laboratory, Department of Environment and Climate change NSW, 78 pp.

Lai, R.J., Long, S.R. and Huang, N.E., 1989. Laboratory studies of wave-current interaction: kinematic of strong interaction. J. Geophys. Res.Ocean, 94 (C11): 16201-16214.

Lam, N.T., 2009. Hydrodynamics and morphodynamics of a seasonally forced tidal inlet system. PhD Thesis, Delft University of Technology, Delft, 141 pp.

Landau, L.D. and Lifshitz, E.M., 1987. Course of Theoretical Physics, FluidMechanics 2nd Ed. Pergamon Press: 336-343.

Lanzoni, S. and Seminara, G., 1998. On tide propagation in convergent estuaries. J. Geophys. Res., 103 (C13): 30793-30812.

Lanzoni, S. and Seminara, G., 2002. Long-term evolution and morphodynamic equilibrium of tidal channels. Journal of Geophysical Research, 107 (C1): 1-13.

Larson, M., Hanson, H., Kraus, N.C. and Hoan, L.X., 2011. Analytical model for the Evolution of coastal inlet cross-sectional area. Coastal Sediment (CS'11): Bringing together theory and Practice, Miami, Florida, US.: 444-457.

Laudier, N.A., Thornton, E.B. and MacMahan, J., 2011. Measured and modeled wave overtopping on a natural beach. Coastal Engineering, 58: 815-825.

Le, A.T., 2004. Dac diem che do khi tuong - thuy van vung dong bang song Cuu Long. Can Tho University: 18.

Leblond, P.H., 1978. On Tidal Propagation in Shallow Rivers. Geophysical Research, 83: 4717-4721.

LeConte, L.J., 1905. Discussion of “Notes on the Improvement of River and Harbor Outlets in the United States”. Transactions, 55: 306-308.

Lesser, G.R., Roelvink, J.A., van Kester, J.A.T.M. and Stelling, G.S., 2004. Development and validation of a three-dimensional morphological model. Coastal Engineering, 51 (8-9): 883-915.

Lin, L., Rosati, J.D. and Kraus, N.C., 2009. Long-term simulation of channel infilling at Pensacola Pass, FL. 22nd Annual National Conference on Beach Preservation Technology, St. Petersburg Beach, FL: 35.

Longuet-Higgins, M.S., 1958. The mechanics of the boundary-layer near the bottom in a progressive wave. An Experimental Investigation of Drift Profiles in a Closed Channel. 6th

Conf. on Coastal Eng., Council of Wave Research, University of California, Berkeley: 171-193.

Lorentz, H.A., 1926. Verslag Staatscommissie Zuiderzee 1918-1926, Algemene Landsdrukkerij, 's-Gravenhage, 345 pp.

Ma, Y. et al., 2010. Laboratory observations of wave evolution, modulation and blocking due to spatially varying opposing currents. Fluid Mechanics: 1-22.

Madsen, O.S. and Grant, W.D., 1976. Sediment transport in the coastal environment. Ralph M. Parsons Laboratory for Water Resources and Hydrodynamics, Dept. of Civil Engineering, Massachusetts Institute of Technology, Cambridge, 105 pp.

Marciano, R., Wang, Z.B., Hibma, A., De Vriend, H.J. and Defina, A., 2005. Modelling of channel patterns in short tidal basins. J. Geophys. Res., 100 (F01001).

Marino, J.N. and Mehta, A.J., 1987. Inlet ebb tide shoals related to coastal parameters. Proc. Coastal Sediments '87. ASCE: 1608-1622.

Mase, H., 2001. Multi-directional random wave transformation model based on energy balance equation. Coastal Engineering Journal, 43 (4): 317-337.

Meyer-Peter, E. and Müller, R., 1948. Formulas for bed-load transport. Report on the 2nd Meeting International Association Hydraulic Structure Research, Stockholm, Sweden: 39–64.

Miche, A., 1944. Mouvements ondulatoire de lamer en protondeur croissaante ou decroissante. Forme limite de la houle lors de son deferlement.application aux digues maritimes. Troisieme partie.forme et proprieties des houles lors du deferlement.croissance des vitesses vers la vie. Ananales des ponts et chausses, Tome 114 (369-406).

Militello, A. and Kraus, N.C., 2001. Shinnecock inlet, New York, site investigation: Evaluation of flood and ebb shoal sediment source alternative for the west of Shinnecock interim project, New York. Report 4. TR CHL TR-98-32, Coastal Inlet Research Program, U.S. Army Research and Develop. Center, Coastal and Hydraulics Laboratory, Vicksburg, MS.

Mirfenderesk, H. and Tomlinson, R., 2008. Observation and Analysis of Hydrodynamic Parameters in Tidal Inlets in a Predominantly Semidiurnal Regime. Coastal Research, 24 (5): 1229–1239.

Nielsen, P., 1979. Some basic concepts of wave sediment transport. Series Paper 20. Institute of Hydrodynamic and Hydraulic Engineering (ISVA), Technical University of Denmark: 160.

Nielsen, P., 1981. Dynamics and geometry of wave generated ripples. J. Geophys. Res., 86(C7): 6467-6472.

Nielsen, P., 1988. Three simple model of wave sediment transport. Coastal Engineering, 12: 43-62.

Nielsen, P., 1992. Coastal bottom boundary layers and sediment transport. Advanced Series on Ocean Engineering, Vol. 4. World Scientific, Singapore.

Nielsen, P., 2006. Sheet flow sediment transport under waves with acceleration skewness and boundary layer streaming. Coastal Engineering, 53 (9): 749-758.

Nielsen, P., 2009. Coastal and estuarine processes. Advanced series on Ocean Engineering. World Scientific, 343 pp.

Nielsen, P., Brander, R.W. and Hughes, M.G., 2001. Rip currents: observations of hydraulic gradients, frictions factors and wave pump efficiency. Coastal Dynamics '01. ASCE, Lund: 483-492.

Nielsen, P. and Callaghan, D.P., 2003. Shear stress and sediment transport calculations for sheet flow under waves. Coastal Engineering, 47: 347-354.

Nielsen, P., Guard, P.A., Callaghan, D.P. and Baldock, T.E., 2008. Observations of wave pump efficiency. Coastal Engineering, 55 (1): 69-72.

Nielsen, P., Svendsen, I.A. and Staub, C., 1978. Onshore-offshore sediment transport on a beach. Proc.16th Int. Conf. Coastal Eng., Hamburg: 1475-1492.

Nielsen, P. and You, Z.-J., 1996. Eulerian mean velocities under non-breaking waves o n horizontal bottoms. 25th Coastal Engineering, Orlando , Florida. ASCE, 4: 4066-4078.

O'Brien, J.T., 1969. Discussions on Tan My Model Study with AOICC-Engineering-RVN and others by Program Manager and Director of Look Laboratory at Saigon RVN 20-24 January 1969, Look Laboratory of Oceanographic Engineering, University of Hawaii, Honolulu, Hawaii.

O'Brien, M.P., 1931. Estuary tidal Prisms related to entrance areas. Civil Engineering, 1 (8): 738-739.

O'Brien, M.P. and Clark, R.R., 1974. Hydraulic constants of tidal entrances. Proceeding of the 14th Coastal Engineering Conference: 1546-1565.

O'Cornner, B.A., Nicholson, J. and Rayner, R., 1990. Estuary geometry as a function of tidal range. In: B.L. Edge (ed.), Coastal Engineering New York. ASCE: 3050-3062.

O'Donoghue, T., Doucette, J.S., van der Werf, J.J. and Ribberink, J.S., 2006. The dimensions of sand ripples in full-scale oscillatory flows. Coastal Engineering, 53(12): 997-1012.

O'Donoghue, T. and Wright, S., 2004. Flow tunnel measurements of velocities and sand flux in oscillatory sheet flow for well-sorted and graded sands. Coastal Engineering, 51: 1163-1184.

Ojha, S.P. and Mazumder, B.S., 2010. Turbulence characteristics of flow over a series of 2-D bed forms in the presence of surface waves. Journal of Geophysical Research, 115 (F4).

Oliveira, A., Fortunato, A.B. and Rego, J.R.L., 2006. Effect of morphological changes on the hydrodynamics and flushing properties of the Obidos lagoon (Portugal). Continental Shelf Research, 26 (8): 917-942.

Özsoy, E., 1977. Flow and Mass Transport in the Vicinity of Tidal Inlets. Technical Report TR-306, Coastal and Oceanographic Engineering Department, University of Florida, Gainesville, 196 pp.

Pawlowicz, R., Beardsley, B. and Lentz, S., 2002. Classical tidal harmonic analysis including error estimates in MATLAB using T TIDE. Computers & Geosciences 28: 929-937.

Peregrine, D.H. and Williams, S.M., 2001. Swash overtopping a truncated plane beach. Fluid Mechanics, 440 (391-399): 391-399.

Powell, M., Thieke, R. and Mehta, A., 2006. Morphodynamic relationships for ebb and flood delta volumes at Florida's tidal entrances. Ocean Dynamics, 56 (3): 295-307.

Powell, M.A., 2003. Ebb shoal and flood shoal volume on the coast of Florida: St Marys entrance to Pensacola Pass. MS Thesis, University of Florida.

Press, W.H., Teukolsku, S.A., Vetterling, W.T. and Flannery, B.P. (Editors), 1992. Numerical Recipes in FORTRAN: The Art of Scientific Computing. University Press, Cambridge., 1486 pp.

Pullen, T. et al., 2007. EurOtop: Wave overtopping of Sea Defenses and Related Structures: Assessment Manual, 201 pp.

Ranasinghe, R., Pattiaratchi, C. and Masselink, G., 1999. A morphodynamic model to simulate the seasonal closure of tidal inlets. Coastal Engineering, 37 (1): 1-36.

Ribberink, J. and Al Salem, A., 1994. Sediment transport in oscillatory boundary layers in cases of rippled beds and sheet flow. Journal of Geophysical Research, 99 (C6): 707–727.

Ribberink, J. and Chen, Z., 1993. Sediment transport of fine sand under asymmetric oscillatory flow. Report H840, part VII, Delft Hydraulics, The Netherlands.

Ribberink, J.S., Dohmen-Janssen, C.M., Hanes, D.M., McLean, S.R. and Vincent, C., 2000. Near-bed sand transport mechanisms under waves. Proc 27th Int. Conf. Coastal Engineering, Sydney. ASCE, New York: 3263– 3276.

Roache, P.J. (Editor), 1972. Computational Fluid Dynamics. Hermosa Publishers, 434 pp.

Roelvink, J.A., 2006. Coastal morphodynamic evolution techniques. Coastal Engineering, 53 (2-3): 277-287.

Roelvink, D., Boutmy, A. and Stam, J.-M., 1998. A simple method to predict long-term morphological changes Proc. 26th Int. Conf. on Coastal Engineering. ASCE, New York, Copenhagen.

Roelvink, J.A. and Van Banning, G.K.F., 1994. Design and Development of Delft3D and Application to Coastal Morphodynamics. In: Verwey, Minns, Babovic and Masksimovic (Editors), Hydroinformatics'94. Balkema, Rotterdam, pp. 451-455.

Roos, A., 1997. Tides and Tidal Currents. Lecture Notes. IHE, Delft, 158 pp.

Roper, T. et al., 2011. Assessing the condition of estuaries and coastal lake ecosystems in NSW. Estuaries and coastal lakes, Office of Environment and Heritage, 270 pp.

Roy, P.S. et al., 2001. Structure and function of south-east Australian estuaries. Estuarine, Coastal and Shelf Science, 53: 351-384.

Ruessink, B.G., Ramaekers, G. and van Rijn, L.C., 2012. On the parameterization of the free-stream non-linear wave orbital motion in nearshore morphodynamic models. Coastal Engineering, 65(0): 56-63.

Saintilan, N., 2004. Relationships between estuarine geomorphology, wetland extent and fish landings in New South Wales estuaries. Estuarine, Coastal and Shelf Science, vol. 61: 591-601

Sanchez, A. and Wu, W., 2011. A Non-Equilibrium Sediment Transport Model for Coastal Inlets and Navigation Channels. Journal of Coastal Research, SI 59: 39-48.

Sato, S., 1986. Oscillatory boundary layer flow and sand movement over ripples. PhD Thesis, University of Tokyo, Tokyo.

Savenije, H.H.G., 1998. Analytical expression for tidal damping in alluvial estuaries. Hydraulic Engineering, 124: 615-618.

Savenije, H.H.G., 2001. A simple analytical expression to describe tidal damping or amplification. Journal of Hydrology, 243 (3-4): 205-215.

Savenije, H.H.G., Toffolon, M., Haas, J. and Veling, E.J.M., 2008. Analytical description of tidal dynamics in convergent estuaries. J. Geophys. Res., 113 (C10): C10025.

Sawamoto, M. and Yamashita, T., 1986. Sediment transport rate due to wave action. J. of Hydroscience and Hydraulic Engineering, 4 (1): 1-15.

Schepers, J.D., 1978. Zand transport onder invloed van golven en een eenparige stroom bij varierende korreldiameter. Master thesis Thesis, Delf University of Technology.

Schuttelaars, H.M. and de Swart, H.E., 1996. An idealized long-term morphodynamic model of a tidal embayment. Eur. J. Mech. B Fluids, 15: 55-80.

Schuttelaars, H.M. and de Swart, H.E., 2000. Multiple morphodynamic equilibria in tidal embayments. J. Geophys. Res., 105: 24105-24118.

Seabergh, W.C., 1979. Model testing of structures at a tidal inlet, Proc. Conf. Coastal Structures, 79. Amer. Soc. Civil Eng., pp. 690-709.

Seelig, W.N., Harris, D.L. and Herchenroder, B.E., 1977. A Spatially Integrated Numerical Model of Inlet Hydraulics, US Army Coastal Engineering Research Center, Fort Belvoir, VA., 105 pp.

Shand, T.D. et al., 2011. Long term trend in NSW coastal wave climate and derivation of extreme design storms: 12.

Shemdin, O.H. and Forney, R.M., 1970. Tidal Motion in Bays. Proc. of the 12nd Coastal Engr. Conf., Washington, D.C. ASCE, 3: 2224-2242.

Shen, M.C. and Meyer, R.E., 1963. Climb of a bore on a beach. Part 3 Run-up. Fluid Mechanic, 16: 113-125.

Shigemura, T., 1980. Tidal prism - throat area relationships of the bays of Japan. Shore and Beach, 48 (3): 30-35.

Shimamoto, T., Nielsen, P. and Baldock, T.E., 2013. Updated " Grap and Dump" model for sediment transport under acceleration skewed waves. Coastal Dynamics 2013- 7th International conference on Coastal Dynamics, Arcachon, France: 1495-1504.

Silva, P.A., Temperville, A. and Seabra Santos, F., 2006. Sand transport under combined current and wave conditions: a semi-unsteady, practical model. Coastal Engineering, 53: 897–913.

Sleath, J.F.A., 1999. Conditions for plug formation in oscillatory flow. Continental Shelf Research, 19 (13): 1643-1664.

Smith, D., 1984. The hydrology and geomorphology of tidal basins. In: W. van Aslst (Editor), The Closure of Tidal Basins. Delft University Press, Delft: 85-109.

Smith, P.B., Stelling, G.S. and al., e., 2011. Assessment of non-hydrostatic wave flow model SWASH for directionally spread waves propagating through a barred basin. Fifth International Conference on Advanced Computational Methods in Engineering: 10.

Stive, M., Wang, Z., Capobianco, M., Ruol, P. and Buijsman, M.C., 1998 Morphodynamics of a tidal lagoon and the adjacent coast. Physics of estuaries and coastal seas: proceedings of the 8th International Biennial Conference on physics of estuaries and coastal seas, The Hague, Netherlands: 397-407.

Stive, M.J.F., 2006. Coastal inlets and Tidal basins, Lecture Notes CT5303. Delft University of Technology, Delft.

Stive, M.J.F. and Rakhorst, R.D., 2008. Review of empirical relationships between inlet cross-section and tidal prism. Journal of Water Resources and Environment Engineering, 23: 89-95.

Stive, M.J.F., Tran, T.T. and Nghiem, T.L., 2012. Stable and unstable coastal inlet cross-sectional behaviour. In: Nguyen. Q.K. (Editor), The 4th International Conference on Estuaries and Coasts (ICEC), Hanoi, Vietnam. Science and Techniques Publishing House, 2: 479-488.

Stive, M.J.F., Van De Kreeke, J., Lam, N.T., Tung, T.T. and Ranasinghe, R., 2009. Empirical relationships between inlet cross- section and tidal prism: a review. Coastal Dynamics 2009, Impacts of human activities on dynamics coastal processes, Tokyo, Japan. World Scientific Publishing Co. Pte.Ltd: 10.

Stive, M.J.F. and Wang, Z.B., 2003. Morphodynamic modeling of tidal basins and coastal inlets. In: V.C. Lakhan (Editor), Advances in coastal modeling. Elsevier Oceanography Series, 67. Elsevier, Amsterdam, The Netherlands: 367-392.

Suprijo, T. and Mano, A., 2004. Dimensionless parameters to describe topographical equilibrium of coastal inlets. Proc. of 29th Int. Conf. on Coastal Eng, Lisbon, Portugal: 2531-2543.

Takeda, I. and Sunamura, T., 1982. Formation and height of berms. Transactions-Japanese Geomorphological Union 3: 145–157.

Tambroni, N. and Seminara, G., 2010. On the theoretical basic of O'Brien-Jarrett-Marchi law for tidal inlets and tidal channels. Proc. 6th IAHR Conference on River, Coastal and Estuarine morphodynamics (RCEM 2009) Taylor and Francis Group, London: 329-335.

Tanaka, H., 2012. Tsunami disasters in coastal and estuarine environments due to the 2011 Great East Japan Earthquake. The 4th International Conference on Estuaries and Coast (ICEC 2012), Hanoi, Vietnam. Science and Techniques Publishing House: 423-431.

Thuy, T.T.V., Nielsen, P. and Callaghan, D.P., 2013a. Inferring inlet morphodynamics and hydraulic parameters from tidal records: A case study of four closure events of Avoca Lake, Australia. International Journal of Earth Sciences and Engineering, 6 (2): 225-231.

Thuy, T.T.V., Nielsen, P. and Callaghan, D.P., 2013b. Inlet morphodynamics during a storm event inferred from tidal records: A case study of the Brunswick River, NSW, Australia. International Journal of Engineering Research, 2 (2): 38-43.

Thuy, T.T.V., Nielsen, P., Callaghan, D.P. and Hanslow, D.J., 2011. Application of the wave pump concept to simulate tidal anomalies in Conjolalake, NSW, Australia. Proceedings of the 6th International Conference on APAC 2011, HongKong. World Scientific, Singapore: 812-819.

Thuy, T.T.V., Nielsen, P., Callaghan, D.P. and Lam, T.N., 2012. Inferring inlet morphodynamics and hydraulic parameters from tidal records of Avoca Lake, NSW, Australia. The 4th International Conference on Estuaries and Coast (ICEC 2012), Hanoi, Vietnam: 74-80.

Toffolon, M. and Savenije, H.H.G., 2011. Revisiting linearized one-dimensional tidal propagation. Journal of Geophysical Research, 116 (C7).

Tonnon, P.K., van Rijn, L.C. and Walstra, D.J.R., 2007. The morphodynamic modelling of tidal sand waves on the shoreface. Coastal Engineering, 54 (4): 279-296.

Townend, I., 2005. An Examination of Empirical Stability Relationships for UK Estuaries. Journal of Coastal Research, 21 (5): 1042-1053.

Tracy, B.A. and Cialone, A., 1996. Wave information study Annual Summary Report, Gulf of Mexico 1995. WIS Report 37 November 1996, Waterways Experiment station, U.S. Army Corps of Engineers, Vicksburge, MS, 59 pp.

Tran, T.T., 2011. Morphodynamics of seasonally closed coastal inlets at the central coast of Vietnam. PhD Thesis, Delft University of Technology, Delft, 208 pp.

Tran, T.T. and Stive, M.J.F., 2009. Coastal inlets and estuaries along the central coast of Vietnam. 3rd Int. Conf. on Estuaries and Coasts (ICEC-2009), Sendai, Japan: 894-901.

Tran, T.T., Van de Kreeke, J. and Stive, M.J.F., 2011. Dynamic equilibrium and morphological stability of idealized tidal inlets using process-based modelling. Coastal Sediment (CS'11): Bringing together theory and Practice, Miami, Florida, US: 406-418.

Traykovski, P., Hay, A.E., Irish, J.D. and Lynch, J.F., 1999. Geometry, migration, and evolution of wave orbital ripples at LEO-15. Journal of Geophysical Research: Oceans, 104 (C1): 1505-1524.

Tung, T.T., Stive, M.J.F., van de Graaff, J. and Walstra, D.-J.R., 2007. Morphological Behaviour of Seasonal Closure of Tidal Inlets. Coastal Sediments '07, New Orleans, Louisiana. ASCE, 239: 123-123.

Turpin, F., Benmoussa, C. and Mei, C.C., 1983. Effects of slowly varying depth and current on the evolution of a Stokes wavepacket. J. Fluid Mech., 132: 1-23.

USACE, 2002. Hydrodynamics of tidal inlets, Coastal Engineering Manual: 79.

Van de Graaff, J. and Tilmans, W.M.K., 1980. Sand transport by waves. Proc. 17th Int. Conf. Coastal Engineering, Sydney: 1140-1157.

van de Kreeke, J., 1967. Water Level Fluctuations and Flow in Tidal Inlets. Journal of Waterways Harbors Division, 93 (WW4): 97-106.

Van de Kreeke, J., 1969. Closure of the paper "Water level fluctuations and flow in tidal inlets". Journal of the Waterways and Harbors Division., 95 (1): 106-107.

van de Kreeke, J., 1985. Stability of tidal inlets- Pass Cavallo, Texas. Estuarine, Coastal and Shelf Science, 21 (1): 33-43.

van de Kreeke, J., 1990a. Can multiple tidal inlets be stable? Estuarine, Coastal and Shelf Science, 30 (3): 261-273.

van de Kreeke, J., 1990b. Stability analysis of a two-inlet bay system. Coastal Engineering, 14 (6): 481-497.

van de Kreeke, J., 1992. Stability of Tidal Inlets; Escoffier's Analysis Shore and Beach, 60 (1): 9-12.

Van de Kreeke, J., 1998. Adaptation of the Frisian inlet to a reduction in basin area with special reference to the cross-sectional area of the inlet channel. In Dronkers, J. and Scheffers , M.B.A.M. (Eds). Proc. PECS conference: 355-362

van de Kreeke, J., 2004. Equilibrium and cross-sectional stability of tidal inlets: application to the Frisian Inlet before and after basin reduction. Coastal Engineering, 51 (5-6): 337-350.

Van de Meer, J.W. and Janssen, W., 1995. Wave run-up and wave overtopping at dikes. In: D. Kabayashi (Editor), Wave forces on inclined and vertical wall structures. American Society of Civil Engineers. ASCE, New York: 1-27.

van der A, D.A., O'Donoghue, T. and Ribberink, J.S., 2010a. Measurements of sheet flow transport in acceleration-skewed oscillatory flow and comparison with practical formulations. Coastal Engineering, 57 (3): 331-342.

van der A, D.A., Ribberink, J.S., van der Werf, J.J. and O'Donoghue, T., 2010b. New practical model for sand transport induced by non-breaking waves and currents. The 32nd International Conference on Coastal Engineering (ICCE 2010), Shanghai, China. The ICCE 2010 Local Organizing Committee: 1-14.

Van der Wegen, M., Dastgheib, A. and Roelvink, J.A., 2010. Morphodynamic modeling of tidal channel evolution in comparison to empirical PA relationship. Coastal Engineering, 57 (9): 827-837.

van der Werf, J.J., Ribberink, J.S., O'Donoghue, T. and Doucette, J.S., 2006. Modelling and measurement of sand transport processes over full-scale ripples in oscillatory flow. Coastal Engineering, 53 (8): 657-673.

Van Dongeren, A.D. and De Vriend, H.J., 1994. A model of morphological behaviour of tidal basins. Coastal Engineering, 22: 287-310.

van Doorn, T., 1981. Experimental investigation of near bottom velocities in water waves with and without a current. TOW Report M1423 part 1, Delft Hydraulics Laboratory, Delft, The Netherlands, 250 pp.

Van Goor, M.A., Zitman, T.J., Wang, Z.B. and Stive, M.J.F., 2003. Impact of sea-level rise on the morphological equilibrium state of tidal inlets. Marine Geology, 202 (3-4): 211-227.

Van Rijn, L.C., 1984. Sediment transport, Part II: Suspended Load Transport. Journal of Hydraulic Engineering, 110 (11): 1613-1641.

Van Rijn, L.C., 1993. Principles of Sediment Transport in Rivers, Estuaries and Coastal Seas. Aqua Publications, Amsterdam, 690 pp.

Van Rijn, L.C., 2007a. Unified view of sediment transport by currents and waves, I: Initiation of bed motion, bed roughness, and bed-load transport. J. Hydraulic Eng., 133 (6): 649-667.

Van Rijn, L.C., 2007b. Unified view of sediment transport by currents and waves, II: Suspended transport. J. Hydraulic Eng., 133 (6): 668-689.

Van Rijn, L.C. and al., e., 1993. Transport of fine sands by currents and waves. Journal of Waterway and Ocean Engineering, 119 (2): 123-143.

Vongvisessomjai, S. and Chatanantavet, P., 2006. Analytical model of interaction of tide and river flow. Songklanakarin J. Sci. Technol., 28 (6): 1149-1160.

Vongvisessomjai, S. and Rojanakamthorn, S., 1989. Interaction of Tide and River Flow. Journal of Waterway, Port, Coastal, and Ocean Engineering, 115 (1): 86-104.

Wainwright, D.J., 2012. Dynamic Modelling of Coastal Lagoon Opening Processes. PhD Thesis, University of Queensland, Brisbane, 298 pp.

Walton, T.L., 2004. Linear systems analysis approach to inlet–bay systems. Ocean Engineering, 31 (3-4): 513-522.

Walton, T.L. and Adams, W.D., 1976. Capacity of inlet outer bars to store sand. Proceedings of the 15th International Conference on Coastal Engineering, New York. ASCE: 1919–1937.

Walton, T.L. and Escoffier, F.F., 1981. Linearized Solution to the Inlet Equation with Inertia. Journal of the Waterway, Port, Coastal and Ocean Division, 107 (WW3): 191-195.

Wang, Z.B., De Vriend, H.J., Louters, T., 1991. A morphodynamic model for a tidal inlet. In: Arcilla, S., Pastor, M., Zienkiewicz, C., Schrefler, B., (Eds.), Computer Modelling in Ocean Engineering, vol. 91. Balkema, Rotterdam, pp. 235– 245.

Wang, Z.B., Louters, T., de Vriend, H.J., 1995. Morphodynamic modelling of a tidal inlet in the Wadden Sea. Journal of Marine Geology 126, 289– 300.

Watanabe, A., 1987. 3-dimensional numerical model of beach evolution. Proc. Coastal Sediments '87, N.C. Kraus (ed.), ASCE, Reston, VA: 802-817.

Watanabe, A. and Sato, S., 2004. A sheet-flow transport rate formula for asymmetric, forward-leaning waves and currents. Proceedings 29th International Conference on Coastal Engineering, Lisbon, Portugal. ASCE: 1703-1714.

Webb, M. and Associates, 1986. Brunswick River flood study, Byron Shine Council, 65 pp.

Webb, M. and Associates, 1995. Avoca Lake Estuary Processes Study: Part A, Gosford City Council, Sydney, 77 pp.

Weir, F.M., Hughes, M.G. and Baldock, T.E., 2006. Beach face and berm morphodynamics fronting a coastal lagoon. Geomorphology, 82 (3–4): 331-346.

Williams, B.G. and Pan, S., 2011. Storm-driven morphological evolution and sediment bypassing at a dynamic tidal inlet: A simulation-based analysis. J. of Coastal Research (SI 64 (Proceedings of the 11th International Coastal Symposium), Poland, ISSN 0749-0208): 1209 - 1213.

Winter, C. et al., 2006. The concept of "representative tides" in morphodynamic numerical modelling Geo-Marine Letters, 26 (3): 125-132.

Work, P.A., Charles, L. and Dean, R.G., 1991. Perdido Key Historical summary and interpretation of monitoring programs. UFL/COEL-91/009, Coastal and Oceanographic Engineering Department, University of Florida, Gainesville, FL, 49 pp.

Wright, L.D., 1977. Sediment transport and deposition at river mouths: A synthesis, Geological Society of America Bulletin. Doc. No.70614 857-868.

Wright, L.D., Coleman, J.M. and Thom, B.G., 1973. Processes of Channel Development in a High-Tide-Range Environment: Cambridge Gulf-Ord River Delta, Western Australia. The Journal of Geology, 81 (1): 15-41.

Wu, W., 2004. Depth-averaged two-dimensional numerical modeling of unsteady flow and non-uniform sediment transport in open Channels. Journal of Hydraulic Engineering, ASCE, 130(10): 1013-1024.

Wu, W. (Editor), 2007. Computational River Dynamics. London: Taylor & Francis, pp. 494 pp.

Wu, W., Sanchez, A. and Zhang, M., 2010. An implicit 2-D depth-averaged finite -volume model of flow and sediment transport in coastal waters. Coastal Engineering: 13.

Zarillo, G.A., Kraus, N.C. and Hoeke, R.K., 2003. Morphologic analysis of Sebastian inlet, Florida: Enhancements to the tidal inlet reservoir model. Proc. Coast. Sediments'03. World Sci.: 8pp.

Zhang, C., Zheng, J.H., Dong, X.W., Cao, K. and Zhang, J.S., 2013. Morphodynamic response of Xiaomiaohong tidal channel to a coastal reclamation project in Jiangsu Coast, China. Journal of Coastal Research (SI 65): 630-635.

Zhang, Q.M., 1987. Analysis of P-A correlationship of tidal inlets along the coast of south China. In COPEDEC, Beijing, China. China Ocean Press, 2: 412-422.

Zheng, J., Mase, H., Demirbileck, Z. and Lin, L., 2008. Implementation and evaluation of alternative wave breaking formulas in a coastal spectral wave model Ocean Engineering, 35: 1090-1101.

Zijlema, M., Stelling, G. and Smit, P., 2011. Simulating nearshore wave transformation with non-hydrostatic wave-flow modelling. 12th International Workshop on Wave Hindcasting and Forecasting & 3rd Coastal Hazard Symposium, Oct 30-Nov 4, 2011, Kohala Coast, Hawaii: 11.

APPENDICES

Appendix 1: Details of NSW estuaries in different groups presented using the classification of Roy et al. (2001) and Heap et al. (2001) and arranged from small to larger values of $Q_{tide}/\sqrt{gH^5}$.

Appendix 2: Details of the US estuaries from Powell (2006) and CIRP used for constructing equilibrium relationships in Figure 5.6, 5.7 and 5.19.

Appendix 3: Available data during closure events and their fitting curves for T_{morph} presented in Table 6.1 (Avoca 1 and Avoca cf. Section 4.1).

APPENDIX – 1

Details of NSW estuaries in different groups presented using the classification of Roy et al. (2001) and Heap et al. (2001) and arranged from small to larger values of $Q_{tide}/\sqrt{gH^5}$.

Appendix 1.1: Group of 35 Wave dominated estuaries (WDE) in NSW.

Nth	Estuary	Entrance location		A_b	P	Total annual flow	$\overline{H_s}$	Roy type	Heap type	Entrance condi-tion	SC	$\tilde{Q}_{tide}$	Q_f	$\sqrt{gH^3}$	$\frac{Q_f}{\sqrt{gH^3}}$	$\frac{\tilde{Q}_{tide}}{\sqrt{gH^3}}$	LGA(s)4
		Lat	Long	(Km^2)	(Ml)	(Ml)	(m)					m^3/s	m^3/s	m^3/s	[-]	[-]	water zone
136	Candlagan C	-35.84	150.18	0.13	49	6106	1.43	3D	WDD	O	BR	3.4	0.19	7.7	0.03	0.45	Eurobodalla
123	Tabourie L	-35.44	150.41	1.45	176	13715	1.58	4C	WDE	O(I)	LG	12.4	0.43	9.8	0.04	1.26	Shoalhaven
35	Deep C	-30.60	153.01	1.08	193	27405	1.58	4C	WDE	I/O	LG	13.6	0.87	9.8	0.09	1.38	Nambucca
44	Cathie C	-31.55	152.86	7.86	272	28776	1.61	4C	WDE	I/O	LG	19.1	0.91	10.3	0.09	1.86	Hastings
160	Murrah R	-36.53	150.06	0.68	302	41099	1.64	3D	WDE	O	BR	21.2	1.30	10.8	0.12	1.97	Bega V
122	Burrill L	-35.40	150.45	4.14	373	23601	1.58	3A	WDE	O(I)	L	26.2	0.75	9.8	0.08	2.67	Shoalhaven
164	Nelson LG	-36.69	149.99	1.19	427	3787	1.64	3C	WDE	O	BR	30.0	0.12	10.8	0.01	2.78	Bega V
180	Wonboyn R	-37.25	149.97	3.69	508	45542	1.64	3A	WDE	O	BR	35.7	1.44	10.8	0.13	3.31	Bega V
29	Boambee C	-30.35	153.11	0.96	488	20494	1.58	3D	WDE	O	BR	34.3	0.65	9.8	0.07	3.49	Coffs Harbour
70	Narrabeen LG	-33.70	151.31	2.31	546	13491	1.63	4B	WDE	I/O	L	38.3	0.43	10.6	0.04	3.61	Pittwater
2	Cudgen C	-28.26	153.58	2.1	575	34500	1.66	5A	WDE	O/T	BR	40.4	1.09	11.1	0.10	3.63	Tweed
118	Narrawallee inlet	-35.30	150.47	0.86	541	26445	1.58	3D	WDE	O(I)	BR	38.0	0.84	9.8	0.09	3.87	Shoalhaven
30	Bonville C	-30.38	153.10	1.5	620	74030	1.58	3D	WDE	O	BR	43.5	2.35	9.8	0.24	4.43	Coffs Harbor
156	Wallaga L	-36.37	150.08	9.14	726	56702	1.64	3B	WDE	O/I	L	51.0	1.80	10.8	0.17	4.73	Bega V
94	L Illawarra	-34.54	150.88	35.53	746	98643	1.58	3B	WDE	O/I	L	52.4	3.13	9.8	0.32	5.33	Shell harbour
175	Towamba R	-37.11	149.91	1.91	857	176194	1.64	3D	WDE	O	BR	60.2	5.59	10.8	0.52	5.58	Bega V
131	Cullendulla C	-35.70	150.21	1.12	683	6050	1.43	3D	TC	I(O)	B	48.0	0.19	7.7	0.03	6.27	Eurobodalla
165	Bega R	-36.70	149.98	3.31	1050	388109	1.64	3D	WDE	I/O	BR	73.7	12.31	10.8	1.14	6.84	Bega V
78	Cooks R	-33.95	151.17	1.2	1154	27760	1.63	2C	TC	O	BR	81.0	0.88	10.6	0.08	7.63	Botany bay
162	Wapengo LG	-36.63	150.02	3.17	1300	12148	1.64	3C	WDE	O	L	91.3	0.39	10.8	0.04	8.47	Bega V
17	Wooli Wooli R	-29.89	153.27	3.08	1185	28274	1.58	3D	WDE	O/T	BR	83.2	0.90	9.8	0.09	8.47	Clarence V
93	Port Kembla	-34.46	150.91	1.37	1385	2189	1.58	0	WDE	O	Bay	97.3	0.07	9.8	0.01	9.90	Wollongong
113	St Georges Basin'	-35.19	150.59	40.76	1570	108618	1.58	3B	WDE	O	L	110.3	3.44	9.8	0.35	11.2	Shoalhaven
169	Merimbula L	-36.90	149.92	4.99	1752	6322	1.64	3B	WDE	O	L	123.0	0.20	10.8	0.02	11.4	Bega V
117	Conjola L	-35.27	150.51	6.69	1641	45773	1.58	3B	WDE	O	L	115.2	1.45	9.8	0.15	11.7	Shoalhaven
61	Tuggerah L	-33.34	151.50	80.63	2227	124539	1.63	3B	WDE	I/O	L	156.4	3.95	10.6	0.37	14.7	Wyong
170	Pambula R	-36.95	149.92	4.36	2473	50520	1.64	3C	WDE	O	BR	173.7	1.60	10.8	0.15	16.1	Bega V

Appendix 1.1: (continue…)

Nth	Estuary	Entrance location		A_b	P	Tot annual flow	$\overline{H_s}$	Roy type	Heap type	Entrance condi-tion	SC	$\hat{Q}_{tide}$	Q_f	$\sqrt{gH^5}$	$\frac{Q_f}{\sqrt{gH^5}}$	$\frac{\bar{Q}_{tide}}{\sqrt{gH^5}}$	LGA(s)4
		Lat	Long	(Km^2)	(Ml)	(Ml)	(m)					m^3/s	m^3/s	m^3/s	[-]	[-]	water zone
75	Lane cove R	-33.84	151.18	2.98	3001	29099	1.63	2A		O	DV	210.8	0.92	10.6	0.09	19.9	Hunters Hill
46	Camden Haven R	-31.64	152.84	31.39	4854	198013	1.61	3B	WDE	O/T	L	340.9	6.28	10.3	0.61	33.1	Greater
149	Wagonga Inlet	-36.21	150.13	6.91	3810	23731	1.43	3A	WDE	O/T	L	267.6	0.75	7.7	0.10	35.0	Eurobodalla
143	Tuross R	-36.07	150.13	14.7	4783	448055	1.43	3C	WDE	O	BR	335.9	14.21	7.7	1.86	43.9	Eurobodalla
1	Tweed R	-28.17	153.56	21.95	7175	491730	1.66	3D	WDE	O/T	BR	503.9	15.59	11.1	1.40	45.3	Tweed
58	L Macquarie	-33.09	151.66	113.2	8888	113188	1.63	3A	WDE	O/T	L	624.2	3.59	10.6	0.34	58.8	L Macquarie
50	Wallis L	-32.17	152.51	92.8	9851	311525	1.61	3A	WDE	O/T	L	691.8	9.88	10.3	0.96	67.2	Great L
66	Brisbane water	-33.52	151.33	27.22	11780	40894	1.63	3A	WDE	O	L	827.3	1.30	10.6	0.12	77.9	Gosford

Note abbreviation:

SC:	subclass	BR:	Barrier river	L:	Lake
LG:	Lagoon	C:	Creek	R:	river
DV:	drowned Valley	V:	Valley	TC:	tidal channel

Roy type:

1: Bay	Four states of sediment in filling:
2: TDE	A: youthful
3: WDE	B: intermediate
4: ICOLLs	C: semi-mature
5: Fresh water body	D: mature

Entrance condition: O: open; I: intermittent; T: Trained; C: close;

Appendix 1.2: Group of 16 Wave dominated delta (WDD) in NSW.

Nth	Estuary	Entrance Location		A_b	P	Total annual flow	$\overline{H_s}$	Roy type	Heap type	Entrance condition	SC	$\bar{Q}_{tide}$	Q_f	$\sqrt{gH^5}$	$\frac{Q_f}{\sqrt{gH^5}}$	$\frac{\bar{Q}_{tide}}{\sqrt{gH^5}}$	LGA(s)[4]
		Lat	Long	(Km^2)	(Ml)	(Ml)	(m)					m^3/s	m^3/s	m^3/s	[-]	[-]	water zone
19	Corindi R	-29.98	153.23	1.32	512	32389	1.58	3D	WDD	O	BR	36.0	1.03	9.82	0.10	3.66	Coffs Harbour
107	Currambene C	-35.04	150.67	2.22	999	56853	1.58	4C	WDD	O	BR	70.2	1.80	9.82	0.18	7.14	Shoalhaven
96	Minnamurra R	-34.63	150.86	1.53	1041	56962	1.58	3D	WDD	O	BR	73.1	1.81	9.82	0.18	7.44	Kiama
135	Tomaga R	-35.84	150.19	1.35	881	24591	1.43	3D	WDD	O	BR	61.9	0.78	7.66	0.10	8.08	Eurobodalla
11	Evans R	-29.11	153.44	2.3	1494	20021	1.66	3A	WDD	O/T	BR	104.9	0.63	11.11	0.06	9.44	Richmond V
157	Bermagui R	-36.42	150.07	1.99	1753	16437	1.64	3C	WDD	O/T	BR	123.1	0.52	10.78	0.05	11.42	Bega Valle
5	Brunswick R	-28.54	153.56	3.28	1940	190003	1.66	3D	WDD	O/T	BR	136.2	6.02	11.11	0.54	12.26	Byron
16	Sandon R	-29.67	153.33	2.14	1936	19351	1.58	3D	WDD	O	BR	136.0	0.61	9.82	0.06	13.84	Clarence V
101	Shoalhaven R	-34.90	150.77	29.84	3802	1383177	1.58	3D	WDD	O	BR	267.0	43.86	9.82	4.46	27.18	Shoalhaven
36	Nambucca R	-30.65	153.01	11.37	4966	434704	1.58	3D	WDD	O/T	BR	348.7	13.78	9.82	1.40	35.50	Nambucca
138	Moruya R	-35.91	150.15	5.35	4329	389537	1.43	3D	WDD	O/T	BR	304.0	12.35	7.66	1.61	39.71	Eurobodalla
47	Manning R	-31.88	152.70	32.27	10463	2213954	1.61	3D	WDD	O/T	BR	734.8	70.20	10.30	6.82	71.36	Greater Taree
37	Macleay R	-30.87	153.03	27.39	10095	1721899	1.58	3D	WDD	O/T	BR	708.9	54.60	9.82	5.56	72.17	Kempsey
9	Richmond R	-28.88	153.59	37.78	14302	2097981	1.66	3D	WDD	O/T	BR	1004.0	66.53	11.11	5.99	90.37	Ballina
43	Hastings R	-31.43	152.92	28.09	14220	1371676	1.61	3D	WDD	O/T	BR	998.6	43.50	10.30	4.22	96.99	Hastings
56	Hunter R	-32.91	151.80	41.83	23060	2269672	1.61	3D	WDE	O/T	BR	1619.4	72.0	10.30	6.99	157.28	Dungog

Note: Yellow color for inlets belongs to River dominated group.

Appendix 1.3: Group of tide dominated estuaries (TDE) in NSW.

Nth	Estuary	Entrance Location		A_b	P	Total annual flow	$\overline{H_s}$	Roy type	Heap type	Entrance condition	SC	$\hat{Q}_{tide}$	Q_f	$\sqrt{gH^5}$	$\frac{Q_f}{\sqrt{gH^5}}$	$\frac{\bar{Q}_{tide}}{\sqrt{gH^5}}$	LGA(s)[4]
		Lat	Long	(Km^2)	(Ml)	(Ml)	(m)					m^3/s	m^3/s	m^3/s	[-]	[-]	water zone
74	Middle Harbour C	-33.82	151.26	6.11	6163	26720	1.63	2A		O	DV	433	0.8	10.6	0.08	40.8	Ku-Ring-Gai
81	Port Hacking	-34.07	151.16	11.57	11809	29301	1.63	2A	WDE	O	DV	829	0.9	10.6	0.09	78.1	Sutherland
53	Karuah R	-32.67	151.97	14.12	11680	358874	1.61	2C	TDD	O	BR	820	11.4	10.3	1.11	79.7	Great Lake
76	Parramatta R	-33.84	151.19	13.74	13846	49278	1.63	2B		O	DV	972	1.6	10.6	0.15	91.6	Ashfield
79	Georges R	-34.00	151.16	25.75	14913	157735	1.63	2B	EMB	O	DV	1047	5.0	10.6	0.47	98.6	Bankstown
69	Broken Bay	-33.56	151.34	17.14	17281	1639	1.63	2C		O	BR	1214	0.1	10.6	0.005	114.3	Gosford
68	Pittwater	-33.58	151.32	18.36	18423	6368	1.63	2C	WDE	O	DV	1294	0.2	10.6	0.02	121.8	Pittwater
132	Clyde R	-35.71	150.18	17.03	13408	511814	1.43	2B	WDE	O	BR	942	16.2	7.7	2.12	123.0	Eurobodalla
54	Tilligerry C	-32.73	152.05	20.45	20616	11580	1.61	3D	WDE	O	L	813	0.4	10.3	0.04	140.6	Port Stephens
77	Port Jackson	-33.83	151.29	28.97	28269	10746	1.63	2A	WDE	O	DV	1985	0.3	10.6	0.03	187.0	Leichhardt
13	Clarence R	-29.43	153.37	129.4	31028	3E+06	1.58	3D	WDE	O/T	BR	233832	105	9.8	10.75	221.8	Clarence V
52	Myall R	-32.67	152.15	112.5	49955	144708	1.61	5C	WDE	O	L	10162	4.6	10.3	0.45	340.7	Great Lake
67	Hawkesbury R	-33.56	151.31	111.6	107564	2E+06	1.63	2C	WDE	O	DV	7554	76.7	10.6	7.23	711.4	Baulkham Hills
Group of Embayment, bay																	Gosford
177	Twofold Bay	-37.08	149.95	30.73	30976	1044	1.64	1	EMB	O	Bay	2175	0.0	10.8	0.003	201.7	Bega V
80	Botany Bay	-34.00	151.23	38.79	37943	9122	1.63	1	WDE	O	Bay	2665	0.3	10.6	0.03	250.9	Botany
133	Batemans bay	-35.76	150.25	34.48	34758	9510	1.43	1	WDE	O	Bay	2441	0.3	7.7	0.04	318.9	Eurobodalla
55	Port Stephens	-32.71	152.20	123.8	115137	38796	1.61	2A	WDE	O	DV	8086	1.2	10.3	0.12	785.3	Great Lake
112	Jervis Bay	-35.10	150.79	122.4	122352	10923	1.58	1	EMB	O	Bay	8592	0.3	9.8	0.04	874.7	Shoalhaven

Appendix 1.4: 100 ICOLLs in NSW.

Nth	Estuary	Entrance Location		A_b	R_{ot}	Total Annual flow	$\overline{H_s}$	Roy type	Heap type	Entra-nce Condi-tion	SC	$\hat{Q}_{tide,pot}$	Q_f	$\sqrt{gH^5}$	$\frac{Q_f}{\sqrt{gH^5}}$	$\frac{\bar{Q}_{tide}}{\sqrt{gH^5}}$	LGA(s)4
		Lat	Long	(Km^2)	m	(Ml)	m					m^3/s	m^3/s	m^3/s	[-]	[-]	water zone
172	Shadrachs C	-37.08	149.88	0.01	1.15	1670	1.64	4C		I	C	0.8	0.05	10.8	0.005	0.08	Bega V
49	Black Head LG	-32.07	152.54	0.01	1.11	693	1.61	4D		I	C	0.8	0.02	10.3	0.002	0.08	Greater Taree
59	Middle Camp C	-33.15	151.64	0.01	1.28	851	1.63	4C		I	C	0.9	0.03	10.6	0.003	0.08	L Macquarie
106	Callala C	-35.01	150.72	0.01	1.25	4373	1.58	4D		I	C	0.9	0.14	9.8	0.014	0.09	Shoalhaven
109	Flat Rock C	-35.12	150.70	0.01	1.25	2623	1.58	4D		I	C	0.9	0.08	9.8	0.008	0.09	Shoalhaven
111	Telegraph C	-35.14	150.73	0.01	1.25	1469	1.58	4D		I	C	0.9	0.05	9.8	0.005	0.09	Commonwealth
119	Mollymook C	-35.34	150.47	0.01	1.25	1971	1.58	4D	CL	I	C	0.9	0.06	9.8	0.006	0.09	Shoalhaven
84	Stanwell C	-34.23	150.99	0.01	1.25	1759	1.58	4D		I	C	0.9	0.06	9.8	0.006	0.09	Wollongong
20	Pipe Clay C	-30.02	153.21	0.01	1.38	439	1.58	4D		I	C	1.0	0.01	9.8	0.001	0.10	Coffs Harbour
137	Bengello C	-35.87	150.16	0.01	1.12	2737	1.43	4D		I	C	0.8	0.09	7.7	0.011	0.10	Eurobodalla
45	Duchess Gully	-31.59	152.84	0.02	1.09	2432	1.61	4D		I	C	1.5	0.08	10.3	0.007	0.15	Hastings
174	Boydtown C	-37.10	149.88	0.02	1.15	548	1.64	4C		I	C	1.6	0.02	10.8	0.002	0.15	Bega V
88	Bellambi Gully	-34.37	150.92	0.02	1.25	4395	1.58	4D	CL	I	C	1.8	0.14	9.8	0.014	0.18	Wollongong
24	Flat Top Point C	-30.13	153.20	0.02	1.38	872	1.58	4D		I	C	1.9	0.03	9.8	0.003	0.20	Coffs Harbour
27	Pine Brush C	-30.25	153.14	0.02	1.38	2498	1.58	4D		I	C	1.9	0.08	9.8	0.008	0.20	Coffs Harbour
129	Durras C	-35.66	150.30	0.02	1.12	1108	1.43	4D		I	C	1.6	0.04	7.7	0.005	0.21	Eurobodalla
127	Butlers C	-35.55	150.38	0.03	1.12	1557	1.58	4D		I	C	2.4	0.05	9.8	0.005	0.24	Shoalhaven
82	Wattamolla C	-34.14	151.12	0.03	1.25	1322	1.63	4C		I	C	2.6	0.04	10.6	0.004	0.25	Sutherland
103	Currarong C	-35.01	150.82	0.03	1.25	3917	1.58	4C		I	C	2.6	0.12	9.8	0.013	0.27	Shoalhaven
89	Bellambi L	-34.38	150.92	0.03	1.25	976	1.58	4C	CL	I	C	2.6	0.03	9.8	0.003	0.27	Wollongong
130	Maloneys C	-35.71	150.24	0.03	1.12	1527	1.43	4D		I	C	2.4	0.05	7.7	0.006	0.31	Eurobodalla
90	Towradgi C	-34.38	150.92	0.04	1.25	5365	1.58	4C	CL	I	C	3.5	0.17	9.8	0.017	0.36	Wollongong
8	Broken Head C	-28.70	153.61	0.05	1.18	502	1.66	4B		I	LG	4.1	0.02	11.1	0.001	0.37	Byron
176	Fisheries C	-37.11	149.93	0.05	1.15	856	1.64	4D		I	LG	4.0	0.03	10.8	0.003	0.38	Bega V
179	Woodburn R	-37.17	150.01	0.05	1.15	1744	1.64	4C		I	C	4.0	0.06	10.8	0.005	0.38	Bega V
57	Glenrock LG	-32.96	151.74	0.05	1.28	1762	1.63	4B		I	C	4.5	0.06	10.6	0.005	0.42	L Macquarie

Appendix 1.4: (continued…)

Nth	Estuary	Entrance Location		A_b	R_{ot}	Total Annual flow	$\overline{H_s}$	Roy type	Heap type	Entrance Condition	SC	$\hat{Q}_{tide,pot}$	Q_f	$\sqrt{gH^5}$	$\frac{Q_f}{\sqrt{gH^5}}$	$\frac{\bar{Q}_{tide}}{\sqrt{gH^5}}$	LGA(s)4
		Lat	Long	(Km^2)	m	(Ml)	m					m^3/s	m^3/s	m^3/s	[-]	[-]	water zone
97	Spring C	-34.66	150.85	0.05	1.25	2088	1.58	4C		I	C	4.4	0.07	9.8	0.007	0.45	Kiama
110	Captains beach LG	-35.13	150.71	0.05	1.25	1403	1.58	4C		I	C	4.4	0.04	9.8	0.005	0.45	Commonwealth
178	Saltwater C	-37.17	150.00	0.06	1.15	2386	1.64	4C		I	C	4.9	0.08	10.8	0.007	0.45	Bega V
182	Table C	-37.41	149.95	0.06	1.15	2018	1.64	4B		I	C	4.9	0.06	10.8	0.006	0.45	Bega V
72	Curl Curl LG	-33.77	151.30	0.07	1.25	956	1.63	4C	CL	I		6.2	0.03	10.6	0.003	0.58	Warringah
22	Darkum C	-30.10	153.20	0.06	1.38	2180	1.58	4D		I	C	5.8	0.07	9.8	0.007	0.59	Coffs Harbour
167	Bourda LG	-36.82	149.94	0.08	1.15	4925	1.64	4B		I	C	6.5	0.16	10.8	0.014	0.60	Bega V
141	Kellys L	-36.01	150.16	0.06	1.12	820	1.43	4B		I	LG	4.7	0.03	7.7	0.003	0.62	Eurobodalla
116	Nerrindillah C	-35.23	150.53	0.07	1.25	6501	1.58	4C	CL	I	C	6.1	0.21	9.8	0.021	0.63	Shoalhaven
33	Dalhousie C	-30.52	153.03	0.07	1.38	1448	1.58	4C	CL	I	LG	6.8	0.05	9.8	0.005	0.69	Bellingen
95	Elliott L	-34.56	150.87	0.08	1.25	4033	1.58	4C		I	C	7.0	0.13	9.8	0.013	0.71	Shellharbour
140	Meringo C	-35.98	150.15	0.07	1.12	1574	1.43	4B	CL	I	LG	5.5	0.05	7.7	0.007	0.72	Eurobodalla
121	Ulladulla	-35.36	150.48	0.09	1.12	0.59	1.58	0	CL	O	Bay	7.1	0.00	9.8	0.000	0.72	Shoalhaven
161	Bunga LG	-36.54	150.06	0.11	1.10	2182	1.64	4C	WDE	I	LG	8.5	0.07	10.8	0.006	0.79	Bega V
73	Manly LG	-33.79	151.29	0.10	1.25	5225	1.63	4C	CL	I	C	8.8	0.17	10.6	0.016	0.83	Manly
155	Liitle L	-36.34	150.10	0.12	1.10	423	1.64	4C		I	LG	9.3	0.01	10.8	0.001	0.86	Eurobodalla
181	Merrica River	-37.30	149.95	0.12	1.15	9737	1.64	4B	CL	I	C	9.7	0.31	10.8	0.029	0.90	Bega V
7	Tallow C	-28.67	153.62	0.12	1.25	3347	1.66	4B	CL	I	LG	10.6	0.11	11.1	0.010	0.95	Byron
91	Fairy C	-34.41	150.90	0.11	1.25	12050	1.58	4D	CL	I	C	9.7	0.38	9.8	0.039	0.99	Wollongong
25	Hearns L	-30.13	153.20	0.10	1.38	1792	1.58	4B	CL	I	LG	9.7	0.06	9.8	0.006	0.99	Coffs Harbour
42	Goolawah LG	-31.21	152.97	0.13	1.09	872	1.58	5C		I	LG	9.9	0.03	9.8	0.003	1.01	Kempsey
150	Little L	-36.22	150.14	0.10	1.10	542	1.43	4B		I	LG	7.8	0.02	7.7	0.002	1.01	Eurobodalla
151	Bullengella L	-36.24	150.14	0.15	1.10	109	1.64	4B		I	L	11.6	0.00	10.8	0.000	1.08	Eurobodalla
21	Arrawarra C	-30.06	153.20	0.11	1.38	3552	1.58	4D	CL	I	LG	10.7	0.11	9.8	0.011	1.09	Coffs Harbour
10	Salty LG	-29.08	153.44	0.16	1.18	1071	1.66	4C		I	LG	13.3	0.03	11.1	0.003	1.19	Richmond V

Appendix 1.4: (continued…)

Nth	Estuary	Entrance Location		A_b	R_{ot}	Total Annual flow	$\overline{H_s}$	Roy type	Heap type	Entra-nce Condi-tion	SC	$\hat{Q}_{tide,pot}$	Q_f	$\sqrt{gH^5}$	$\frac{Q_f}{\sqrt{gH^5}}$	$\frac{\bar{Q}_{tide}}{\sqrt{gH^5}}$	LGA(s)4
		Lat	Long	(Km^2)	m	(Ml)	m					m^3/s	m^3/s	m^3/s	[-]	[-]	water zone
139	Congo C	-35.95	150.16	0.12	1.12	14146	1.43	4D	CL	I	C	9.4	0.45	7.7	0.059	1.23	Eurobodalla
99	Werri LG	-34.73	150.84	0.14	1.25	9441	1.58	4B	WDE	I	C	12.3	0.30	9.8	0.030	1.25	Kiama
108	Moona Moona C	-35.05	150.68	0.14	1.25	9004	1.58	4C		I	C	12.3	0.29	9.8	0.029	1.25	Shoalhaven
34	Oyster C	-30.56	153.02	0.14	1.38	4665	1.58	4D	CL	I	LG	13.6	0.15	9.8	0.015	1.38	Bellingen,
183	Nadgee River	-37.44	149.97	0.19	1.15	11747	1.64	4D		I	C	15.4	0.37	10.8	0.035	1.43	Bega V
105	Wowly Gully	-35.00	150.73	0.16	1.25	1759	1.58	4D		I	LG	14.0	0.06	9.8	0.006	1.43	Shoalhaven
6	Belongil C	-28.63	153.59	0.19	1.25	18304	1.66	4B	CL	I	C	16.7	0.58	11.1	0.052	1.50	Byron
23	Woolgoolga L	-30.10	153.20	0.16	1.38	6514	1.58	4B	WDE	I	LG	15.5	0.21	9.8	0.021	1.58	Coffs Harbour
148	Kianga L	-36.19	150.13	0.17	1.10	2044	1.43	4C	CL	I	LG	13.2	0.06	7.7	0.008	1.72	Eurobodalla
144	L Brunderee	-36.09	150.14	0.19	1.12	1727	1.43	4C	CL	I	LG	14.9	0.05	7.7	0.007	1.95	Eurobodalla
15	Cakora LG	-29.60	153.33	0.23	1.21	2074	1.58	4D	CL	I	LG	19.5	0.07	9.8	0.007	1.99	Clarence V
71	Dee Why LG	-33.75	151.30	0.24	1.25	3825	1.63	4C	CL	I	C	21.1	0.12	10.6	0.011	1.99	Warringah
39	Saltwater C	-30.88	153.04	0.28	1.09	2867	1.58	5C	WDE	I	LG	21.3	0.09	9.8	0.009	2.17	Kempsey
41	Killick C	-31.19	152.98	0.28	1.09	1205	1.58	4B	CL	I	LG	21.3	0.04	9.8	0.004	2.17	Kempsey
63	Terrigal LG	-33.44	151.44	0.28	1.25	3238	1.63	4B	CL	I	LG	24.6	0.10	10.6	0.010	2.32	Gosford
115	Berrara C	-35.21	150.55	0.26	1.25	9400	1.58	4B	CL	I	LG	22.8	0.30	9.8	0.030	2.32	Shoalhaven
173	Nullica river	-37.09	149.87	0.32	1.15	7121	1.64	4C	WDE	I	LG	25.9	0.23	10.8	0.021	2.40	Bega V
18	Station C	-29.95	153.26	0.25	1.38	3597	1.58	4D	WDE	I	LG	24.2	0.11	9.8	0.012	2.47	Coffs Harbour
126	Willinga L	-35.50	150.39	0.31	1.12	3830	1.58	4D		I	LG	24.4	0.12	9.8	0.012	2.48	Shoalhaven
168	Back LG	-36.88	149.93	0.36	1.15	4724	1.64	4C	CL	I	LG	29.1	0.15	10.8	0.014	2.70	Bega V
65	Cockrone L	-33.49	151.43	0.33	1.25	1762	1.63	4B	CL	I	LG	29.0	0.06	10.6	0.005	2.73	Gosford
12	Jerusalem C	-29.21	153.39	0.32	1.21	8762	1.58	3B	CL	I	LG	27.1	0.28	9.8	0.028	2.76	Clarence V
3	Cudgera C	-28.36	153.58	0.41	1.17	29174	1.66	4C	CL	O	BR	33.6	0.93	11.1	0.083	3.02	Tweed
145	L Tarourga	-36.11	150.14	0.33	1.10	1493	1.43	4B	WDE	I	LG	25.6	0.05	7.7	0.006	3.34	Eurobodalla
158	Baragoot L	-36.46	150.07	0.47	1.10	2403	1.64	4C	CL	I	LG	36.4	0.08	10.8	0.007	3.38	Bega V

Appendix 1.4: (continued…)

Nth	Estuary	Entrance Location		A_b	R_{ot}	Total Annual flow	$\overline{H_s}$	Roy type	Heap type	Entra-nce Condi-tion	SC	$\hat{Q}_{tide,pot}$	Q_f	$\sqrt{gH^5}$	$\frac{Q_f}{\sqrt{gH^5}}$	$\frac{\hat{Q}_{tide}}{\sqrt{gH^5}}$	LGA(s)4
		Lat	Long	(Km^2)	m	(Ml)	m					m^3/s	m^3/s	m^3/s	[-]	[-]	water zone
70	Narrabeen LG	-33.70	151.31	2.31	546	13491	1.63	4B	WDE	I/O	L	38.3	0.43	10.6	0.04	3.61	Pittwater
163	Middle LG	-36.65	150.01	0.51	1.10	4862	1.64	4D	WDE	I	LG	39.5	0.15	10.8	0.014	3.67	Bega V
152	Nangudga L	-36.25	150.14	0.60	1.10	2964	1.64	4C	WDE	I	LG	46.5	0.09	10.8	0.009	4.31	Eurobodalla
62	Wamberal LG	-33.43	151.45	0.52	1.28	1882	1.63	4B	CL	I	L	46.6	0.06	10.6	0.006	4.39	Gosford
124	Termeil L	-35.46	150.39	0.57	1.12	4157	1.58	4C	WDE	I	LG	44.8	0.13	9.8	0.013	4.56	Shoalhaven
171	Curalo LG	-37.05	149.92	0.71	1.15	4385	1.64	4C	WDE	I	LG	57.5	0.14	10.8	0.013	5.33	Bega V
64	Avoca L	-33.46	151.44	0.67	1.25	3199	1.63	4A	CL	I	LG	59.0	0.10	10.6	0.010	5.55	Gosford
154	Tilba Tilba L	-36.33	150.12	1.02	1.10	3634	1.64	4C	WDE	I	LG	79.1	0.12	10.8	0.011	7.33	Eurobodalla
14	L Arragan	-29.57	153.34	0.97	1.21	1278	1.58	4B	CL	I	L	82.3	0.04	9.8	0.004	8.38	Clarence V
159	Cuttagee L	-36.49	150.06	1.24	1.10	9468	1.64	4B	WDE	I	LG	96.1	0.30	10.8	0.028	8.92	Bega V
184	Nadgee L	-37.47	149.97	1.20	1.15	1307	1.64	4C	CL	I	L	97.2	0.04	10.8	0.004	9.01	Bega V
48	Khappinghat C	-32.01	152.57	1.03	1.33	25604	1.61	4D	WDD	I	LG	95.9	0.81	10.3	0.079	9.32	Greater Taree
125	Meroo L	-35.48	150.39	1.37	1.12	5670	1.58	4C	WDE	I	LG	107.7	0.18	9.8	0.018	10.96	Shoalhaven
117	Conjola L	-35.27	150.51	6.69	1641	45773	1.58	3B	WDE	O	L	115.2	1.45	9.8	0.150	11.70	Shoalhaven
153	Corunna L	-36.29	150.13	2.08	1.10	8785	1.64	4B	WDE	I	LG	161.3	0.28	10.8	0.026	14.96	Eurobodalla
147	L Mummuga	-36.16	150.13	1.63	1.10	6887	1.43	4B	WDE	I	LG	126.4	0.22	7.7	0.029	16.51	Eurobodalla
104	Caranna C	-35.00	150.78	2.39	1.25	2716	1.58	4C		O	L	209.6	0.09	9.8	0.009	21.34	Shoalhaven
146	L Brou	-36.13	150.13	2.37	1.10	10823	1.43	4C	WDE	I	LG	183.7	0.34	7.7	0.045	24.00	Eurobodalla
166	Wallagoot L	-36.79	149.96	3.87	1.15	3513	1.64	4B	WDE	I	L	313.4	0.11	10.8	0.010	29.06	Bega V
128	Durras L	-35.64	150.31	3.60	1.12	14377	1.43	4B	WDE	I	L	282.9	0.46	7.7	0.060	36.96	Eurobodalla
114	Swan L	-35.20	150.56	4.68	1.25	7506	1.58	4A	WDE	I	L	410.5	0.24	9.8	0.024	41.79	Shoalhaven
102	Wollumboola L	-34.94	150.78	6.33	1.25	10358	1.58	4B	WDE	I	L	555.2	0.33	9.8	0.033	56.52	Shoalhaven
142	Coila L	-36.05	150.14	6.77	1.12	13687	1.43	4A	WDE	I	L	532.0	0.43	7.7	0.057	69.50	Eurobodalla
51	Smiths L	-32.40	152.52	10.01	1.11	6461	1.61	4A	CL	I	L	781.0	0.20	10.3	0.020	75.85	Great L

APPENDIX – 2

Details of the US estuaries from Powell (2006) and CIRP used for constructing equilibrium relationships in Figure 5.6, 5.7 and 5.19.

Appendix 2.1: Details of the US estuaries from Powell (2006)

No.	Entrance	County	Lat.	Long.	R_{to}	T_t	d_{50}	$\overline{H_s}$	T_w	A_c	P	V_{Ebb}	V_{Flood}	$\hat{Q}_{tide}$	$\frac{\bar{Q}_{tide}}{\sqrt{gH^5}}$	A_c/H^2
			(°)	(°)	(m)	(s)	(mm)	(m)	(s)	(m^2)	($10^7 m^3$)	($10^6 m^3$)	($10^6 m^3$)	(m^3/s)	[-]	[-]
2	Nassau Sound	Nassau	30.5	-81.42	1.8	44700	0.4	1.1	7	6800	6.80	41.000	NA	4779.2	1202.4	5619.8
6	Matanzas	St. Johns	29.72	-81.22	1.5	44700	0.2	1.1	7	910	1.40	4.800	0.13	983.9	247.5	752.1
22	Sands Cut	Dade	25.5	-80.18	0.8	44700	0.7	0.9	5	210	0.22	NS	1.66	154.6	64.2	259.3
23	Caesar Creek	Dade	25.38	-80.23	0.8	44700	0.7	0.9	5	1600	2.50	15.000	1.40	1757.0	730.0	1975.3
27	Snake Creek	Monroe	24.95	-80.58	0.7	44700	0.7	0.9	5	380	1.60	NS	1.51	1124.5	467.2	469.1
29	Caxambas Pass	Collier	25.9	-81.72	0.9	44700	0.3	0.7	4	680	0.63	2.860	6.58	442.8	344.8	1387.8
30	Big Marco Pass	Collier	25.97	-81.73	0.9	44700	0.3	0.7	4	1500	4.40	10.600	4.26	3092.4	2408.3	3061.2
31	Capri Pass	Collier	25.98	-81.75	0.9	44700	0.3	0.7	4	2600	4.10	1.570	1.57	2881.6	2244.1	5306.1
32	Hurricane Pass	Collier	26	-81.75	0.9	44700	0.3	0.7	4	590	0.52	1.640	1.61	365.5	284.6	1204.1
35	Clam Pass	Collier	26.22	-81.82	0.9	44700	0.2	0.7	4	26	0.03	0.149	0.03	23.2	18.1	53.1
36	Wiggins Pass	Collier	26.3	-81.83	0.9	44700	0.2	0.7	4	130	0.14	0.596	0.46	98.4	76.6	265.3
37	Big Hickory Pass	Lee	26.37	-81.87	0.8	44700	0.2	0.7	4	59	0.12	0.474	0.67	84.3	65.7	120.4
38	New Pass	Lee	26.38	-81.87	0.8	44700	0.2	0.7	4	410	0.76	0.887	0.82	534.1	416.0	836.7
40	San Carlos Pass	Lee	26.47	-81.97	0.8	44700	0.4	0.7	4	24000	59.00	35.500	35.50	41466.2	32293.5	48979.6
41	Blind Pass (Lee)	Lee	26.47	-82.18	0.8	44700	0.4	0.7	4	64	0.12	Minor	0.05	84.3	65.7	130.6
42	Redfish Pass	Lee	26.55	-82.2	0.7	44700	0.4	0.7	4	1600	1.40	3.310	2.17	983.9	766.3	3265.3
43	Captiva Pass	Lee	26.6	-82.23	0.7	44700	0.5	0.7	4	2200	5.40	7.890	11.30	3795.2	2955.7	4489.8
44	Boca Grande Pass	Charlotte	26.72	-82.27	0.7	44700	0.4	0.7	4	9300	36.00	74.100	9.77	25301.4	19704.5	18979.6
45	Gasparilla Pass	Charlotte	26.82	-82.28	0.7	44700	0.3	0.6	4	410	1.30	6.290	18.60	913.7	1046.1	1138.9
46	Stump Pass	Sarasota	26.9	-82.35	0.7	44700	0.5	0.7	4	240	0.42	0.573	2.21	295.2	229.9	489.8
48	Big Sarasota Pass	Sarasota	27.28	-82.57	0.7	44700	0.1	0.8	4	1500	3.50	3.800	11.80	2459.9	1372.0	2343.8
54	Bunces Pass	Manatee	27.65	-82.73	0.7	44700	0.3	0.7	4	1400	1.20	9.180	3.42	843.4	656.8	2857.1
59	Willys Cut(*)	Pinellas	28.05	-82.82	0.9	44700	0.2	0.8	4	570	0.39		NA	274.1	152.9	890.6
64	West Pass	Franklin	29.63	-85.1	0.5	89400	0.3	0.8	4	3900	7.60	14.100	14.30	2670.7	1489.6	6093.8
67	Pensacola Pass	Santa Rosa	30.34	-87.32	0.4	89400	0.3	1	5	10000	27.00	1.130	3.50	9488.0	3029.3	10000.0

Note: NS: No significant ebb delta volume due to deep entrance channel or other features, NA data not available

Appendix 2.2: Details of the US estuaries from CIRP

No.	Entrance	State	Lat.	Long.	R_{to}	T_t	$\overline{H_s}$	T_w	A_c	P	$\hat{Q}_{tide}$	$\frac{\hat{Q}_{tide}}{\sqrt{gH^5}}$	A_c/H^2
			(°)	(°)	(m)	(s)	(m)	(s)	(m^2)	($10^7 m^3$)	(m^3/s)	[-]	[-]
34	Hereford (Stone Harbor)	New Jersey	39.50	-74.45	1.31	44700	1.0	6.6	1320	3.37	2367.29	756.20	1319.7
59	Stono River Inlet	South Carolina	32.30	-80.00	1.61	44700	0.9	6.5	5045	8.10	5689.93	2365.31	6228.34
47	Beaufort Inlet	North Carolina	34.71	-76.65	1.11	44700	1.2	6.3	8048	14.40	10115.4	2048.42	5589.1
45	Ocracoke Inlet	North Carolina	35.06	-76.01	0.30	44700	1.0	6.0	8996	14.80	10396.4	3321.01	8996.3
62	St. Simon Sound / Brunswick	Georgia	31.06	-81.19		44700	0.9	7.0	23327	38.20	26834	11154.91	28798.9
86	Mobile Bay	Alabama	30.15	-88.00	0.36	89400	1.1	5.5	29275	56.70	19914.8	5012.80	24194.3
126	Willapa Bay	Washington	46.69	-123.83	2.08	44700	2.0	10.0	46004	70.80	49734.2	2808.45	11500.9
60	Port Royal Sound	South Carolina	32.37	-80.70	1.86	44700	0.9	5.9	50279	41.30	29011.6	12060.15	62072.6
37	Alsea Bay Inlet	Oregon	43.50	-130.50	1.77	44700	3.3	12.0	744	1.42	994.574	16.06	68.3196
12	San Francisco Inlet	California	36.50	-126.50	1.25	44700	3.1	12.0	87175	144.42	101447	1915.23	9071.28
89	Caminada Pass	Louisiana	29.10	-90.03		89400	0.9	5.0	1171	1.80	632.215	303.18	1620.76

T_t: Tidal period; (44700s corresponds to semi-diurnal and 89400s corresponds to diurnal tidal regime)
T_w: wave period.

- Almost data from CIRP was down-loaded from data base in http://chl.erdc.usace.army.mil/ in 2002, except data of 2 inlets Alsea Bay and San Francisco was from unpublished data table in CIRP.

APPENDIX – 3

Available data during closure events and their fitting curves for T_{morph} presented in Table 6.1 (Avoca 1 and Avoca cf. Section 4.1)

Avoca Lake closure event 2

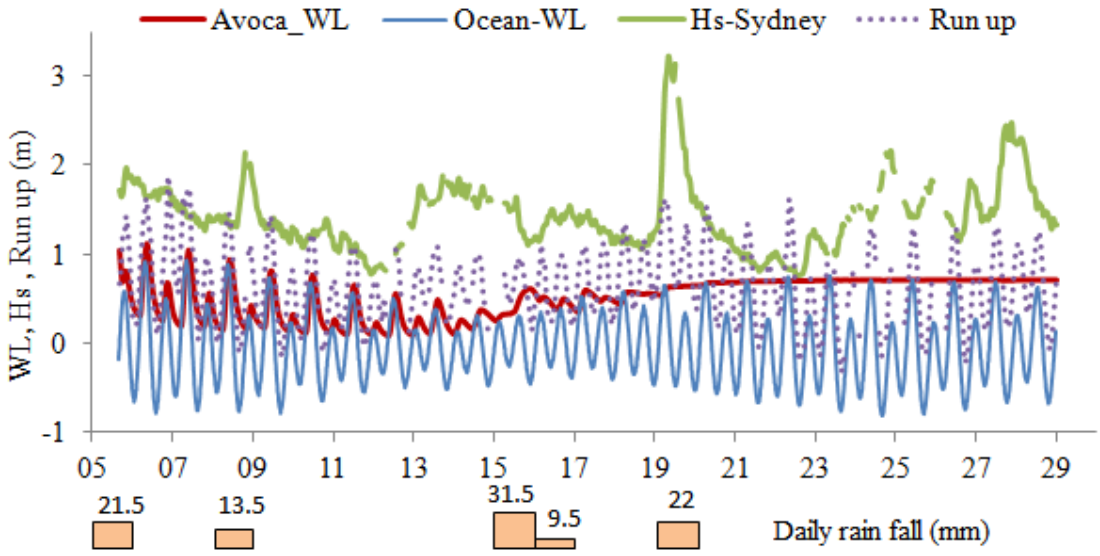

Figure A3.1: Water levels, wave height, daily rain fall and wave run up for closure event 2 at Avoca Lake from 5/11/2010 to 28/11/2010.

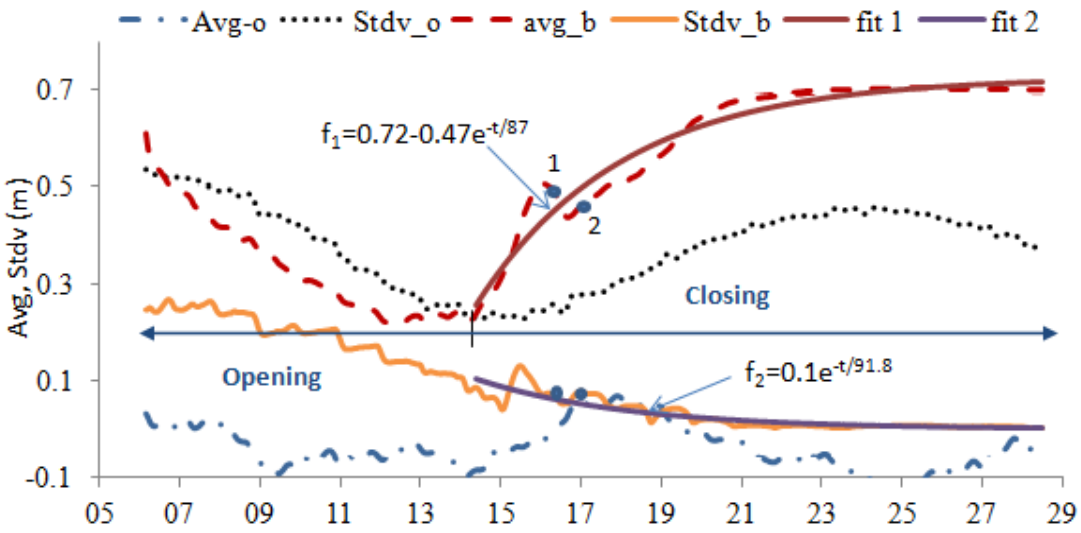

Figure A3.2: Results of $\overline{\eta_{24.5}}(t)$ and $Stdv_{24.5}(t)$ with fitting curves for event 2

T_{morph} =87h from fitting $\overline{\eta_{24.5\,b}}(t)$ and T_{morph} =91.8h from fitting $Stdv_{24.5b}(t)$.

Avoca Lake closure event 5

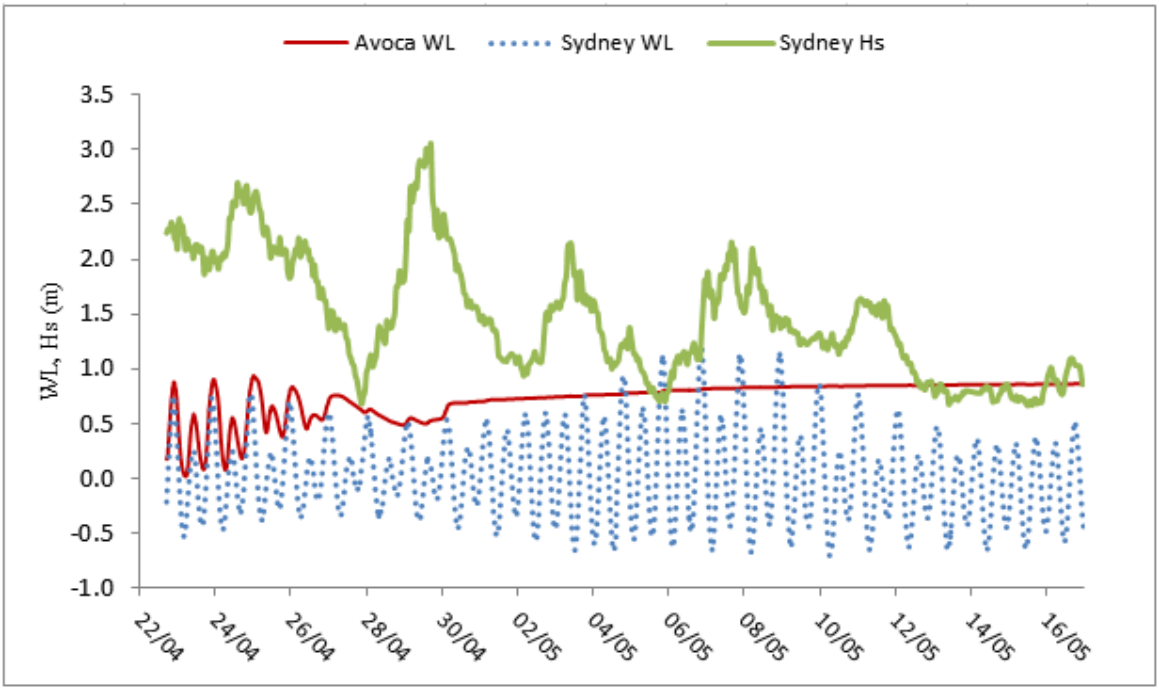

Figure A3.3: Water levels, wave height, for closure event 5 at Avoca Lake from 24/04/2008 to 30/04/2008.

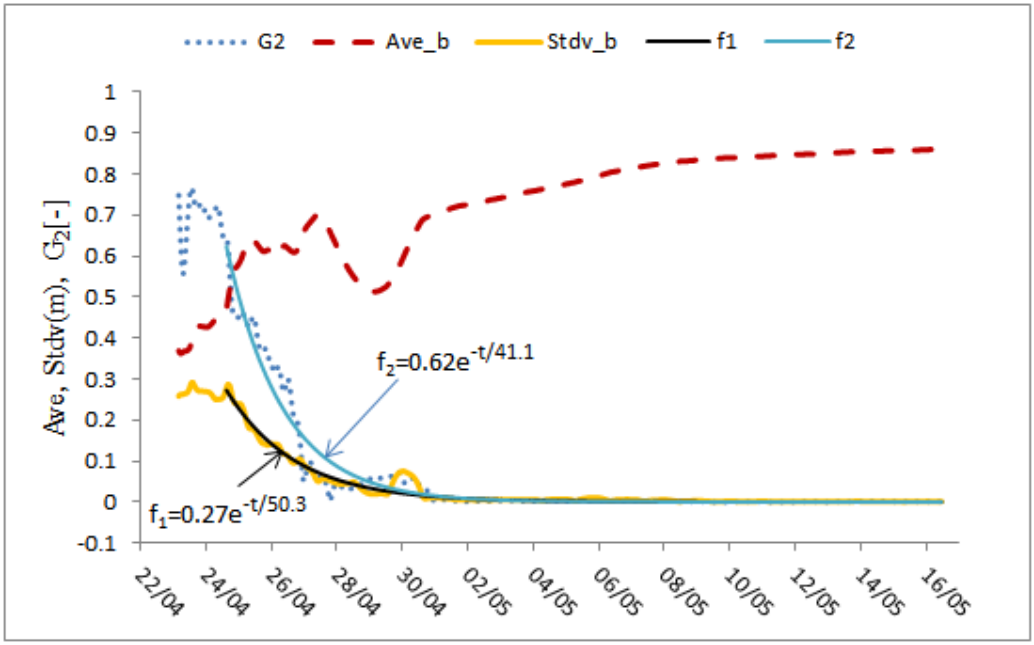

Figure A3.4: Results of $\overline{\eta_{24.5\,b}}(t)$, $Stdv_{24.5\text{-}b}(t)$ and $G_2$with fitting curves for event 5 T_{morph} =50.3h from fitting $Stdv_{24.5b}(t)$ and T_{morph} =41.1h from fitting G_2.

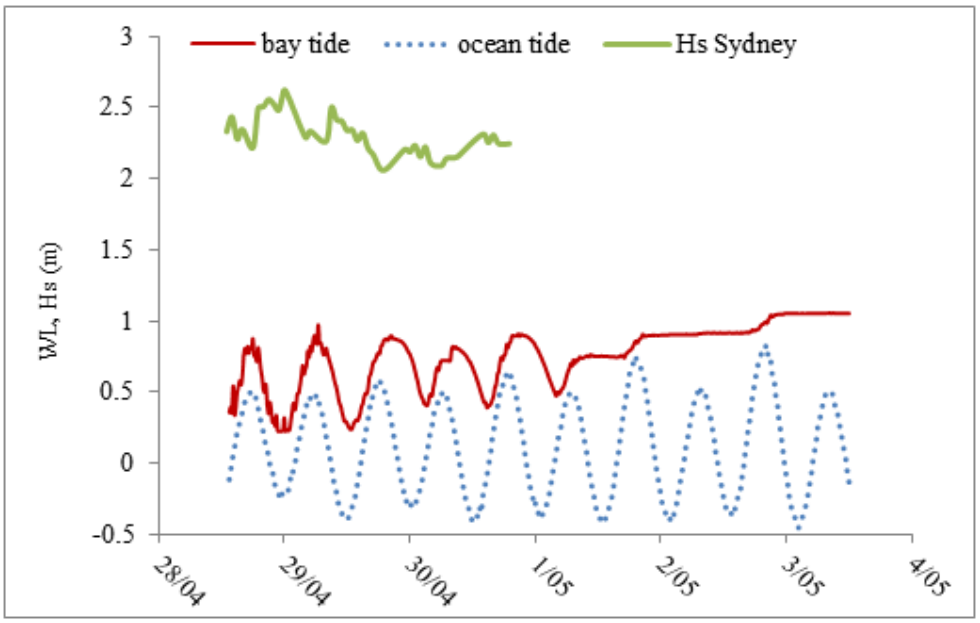

Figure A3.5: Water levels and wave height for closure event at Wamberal from 29/04/2011 to 3/05/2011.

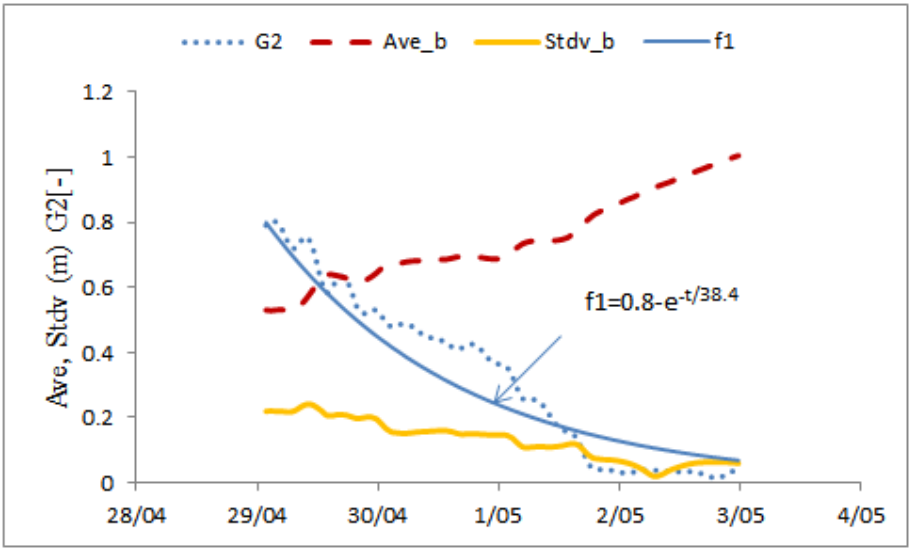

Figure A3.6: Results of $\overline{\eta_{24.5\,b}}(t)$, $Stdv_{24.5\text{-b}}(t)$ and $G_2$with fitting curves for G_2 T_{morph} =38.4h from fitting G_2.

Werri closure event 1

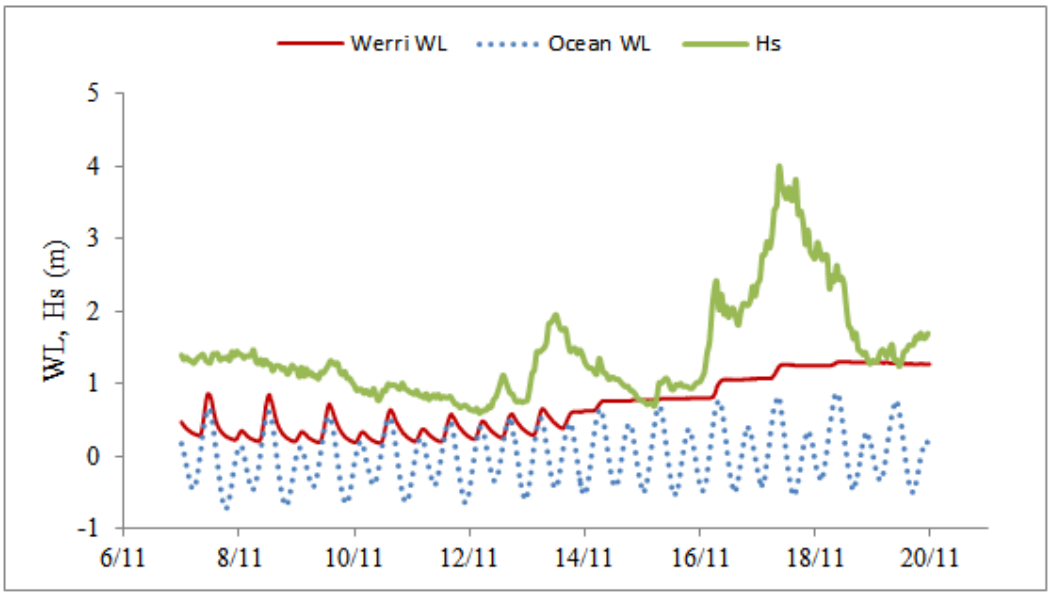

Figure A3.7: Water levels and wave height at Port Kembla for closure event1 at Werri from 07/11/2009 to 19/11/2009.

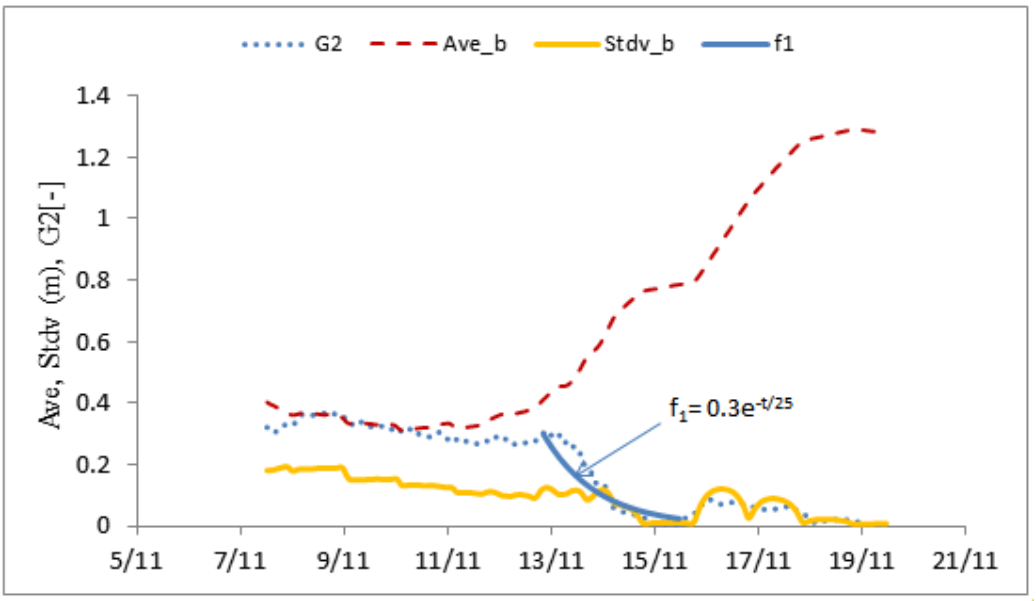

Figure A3.8: Results of $\overline{\eta_{24.5\,b}}(t)$, $Stdv_{24.5\text{-b}}(t)$ and $G_2$with fitting curves for G_2 T_{morph} =25h from fitting G_2.

Werri closure event 2 from 1/4-13/5/2010

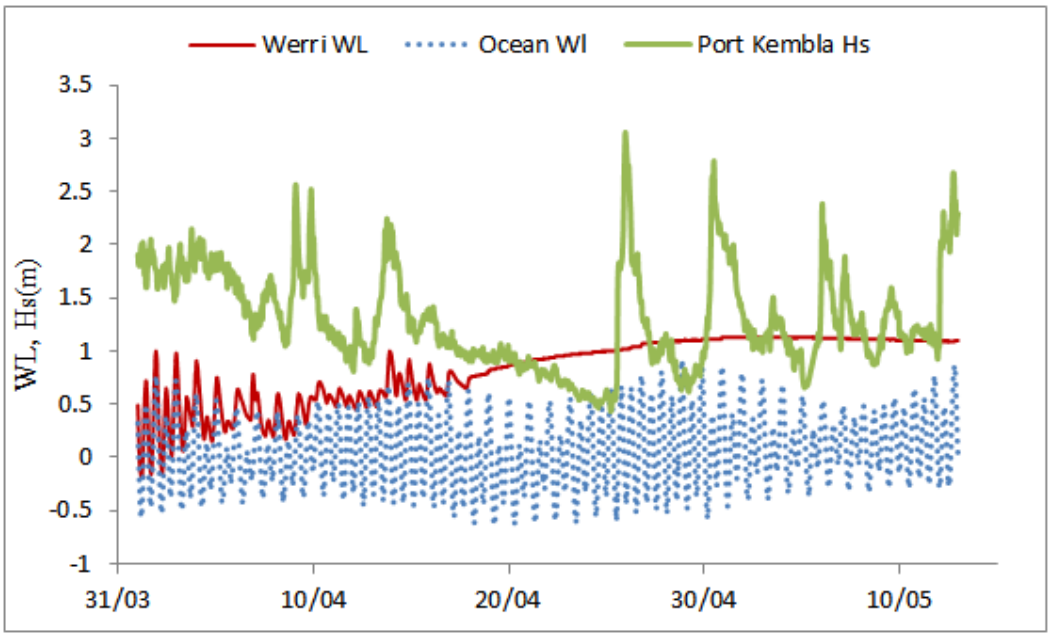

Figure A3.9: Water levels and wave height at Port Kembla for closure event 2 at Werri from 01/04/2010 to 13/5/2010.

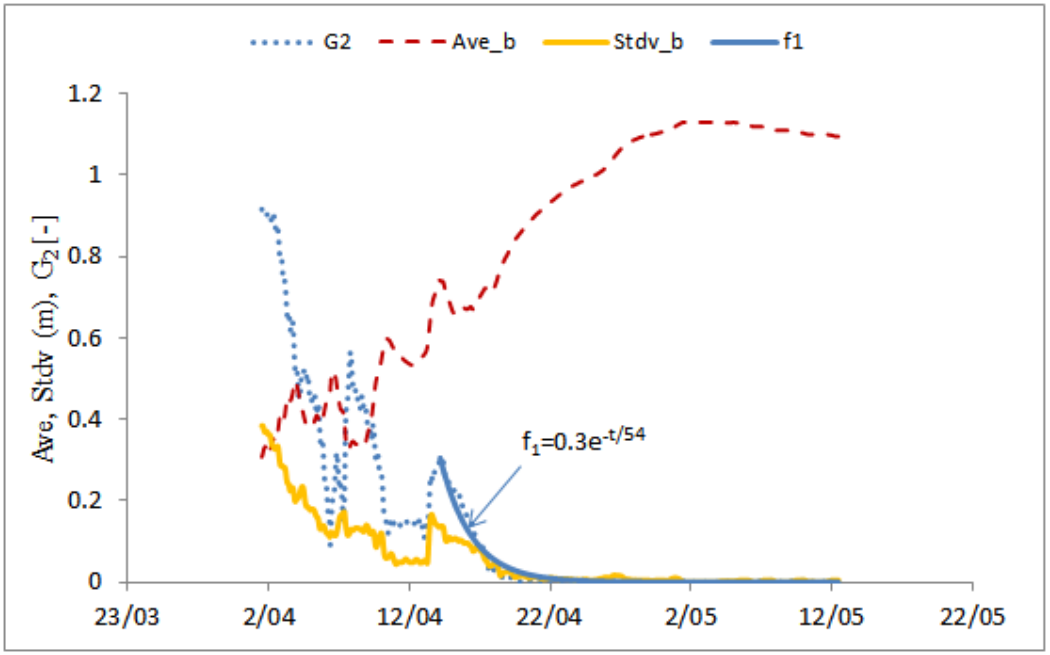

Figure A3.10: Results of $\overline{\eta_{24.5\,b}}(t)$, $Stdv_{24.5\text{-}b}(t)$ and $G_2$with fitting curves for G_2 T_{morph} =54h from fitting G_2.

Dee Why lagoon closure 1

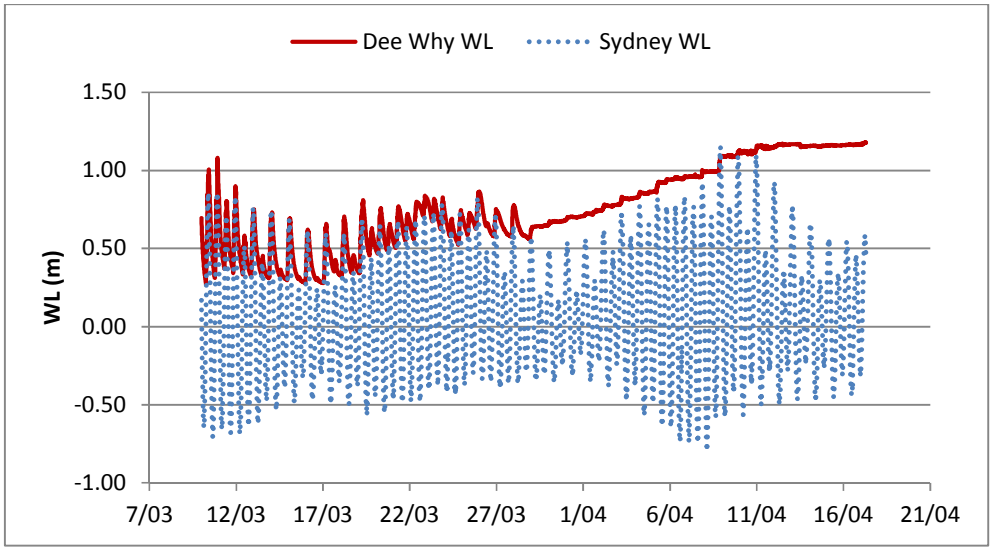

Figure A3.11: Water levels for closure event 1 at Dee Why lagoon 17/03/2012 to 16/4/2012.

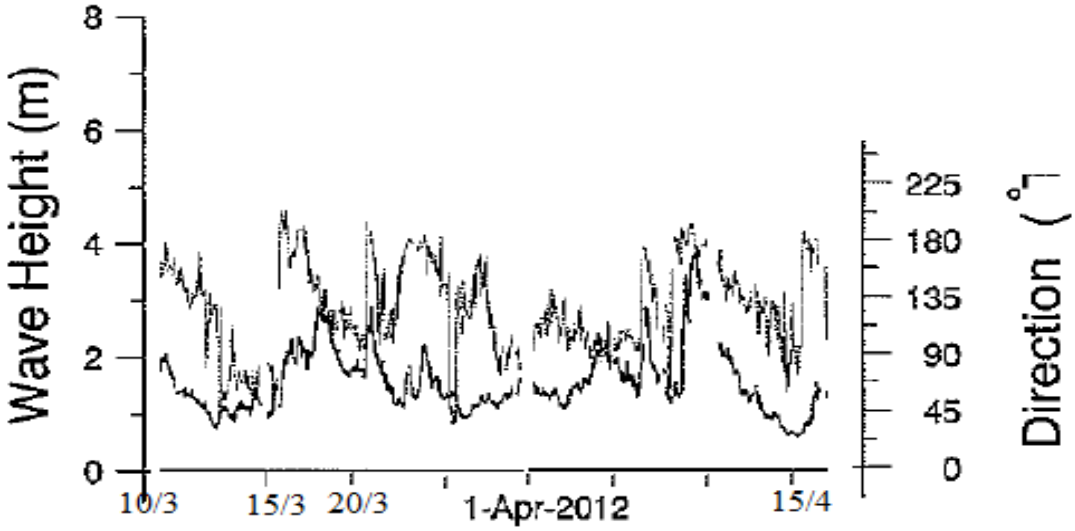

Figure A3.12: Wave height and wave direction offshore Sydney for closure event 1 at Dee Why lagoon from 17/03/2012 to 16/4/2012.

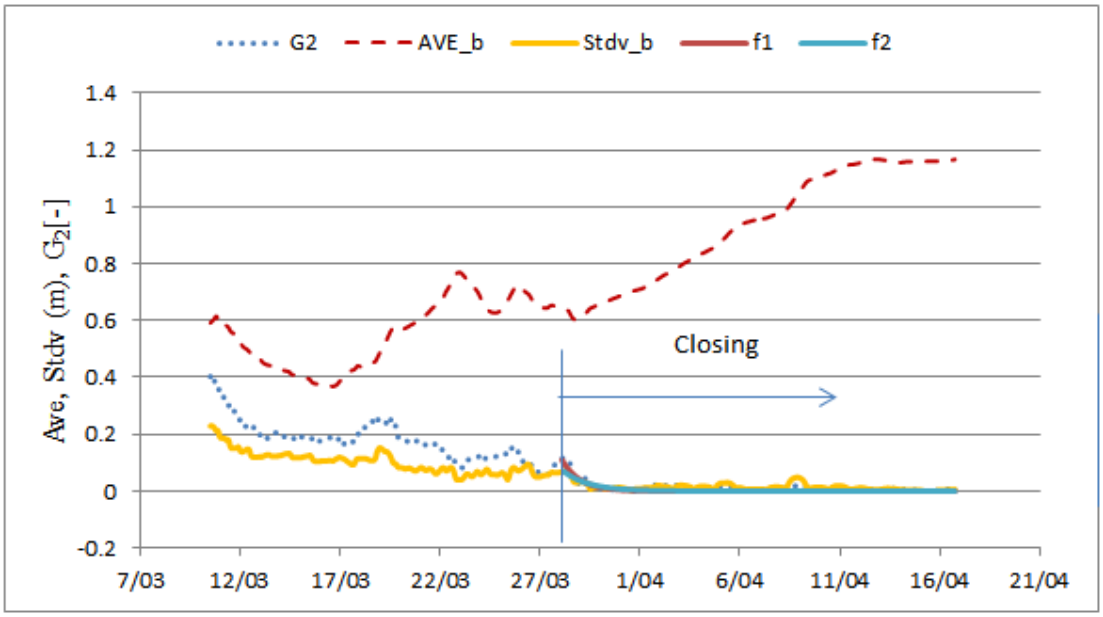

Figure A3.13: Results of $\overline{\eta_{24.5\,b}}(t)$, $Stdv_{24.5\text{-b}}(t)$ and $G_2$with fitting curves for G_2 and $Stdv_{24.5\text{-b}}(t)$.

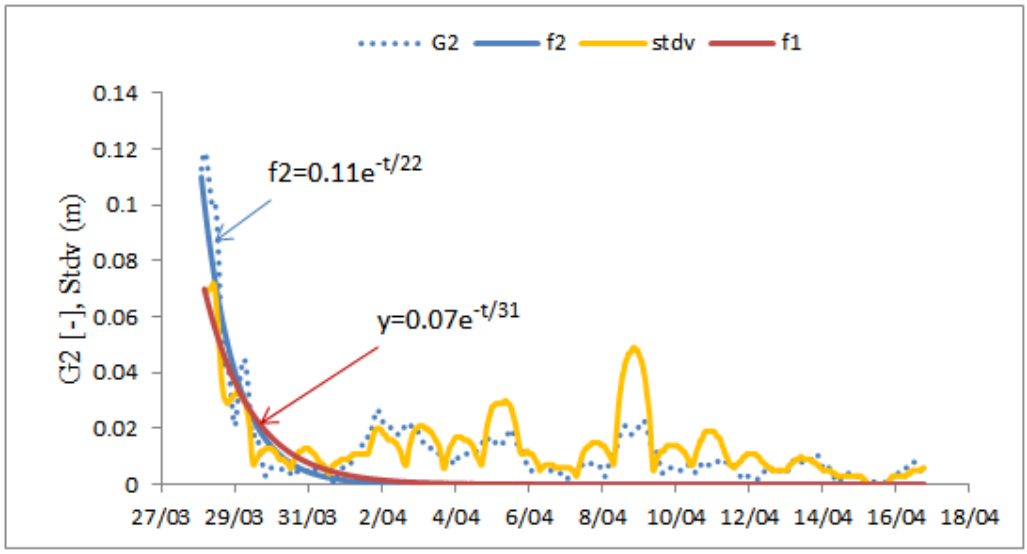

Figure A3.14: Results of G_2 and $Stdv_{24.5\text{-b}}(t)$ with fitting curves closer in closing process for event 1 at Dee Why lagoon.
T_{morph} =22h from fitting G_2 and T_{morph} =31h from fitting $Stdv_{24.5\text{-b}}(t)$.

Dee Why lagoon Closure event 2

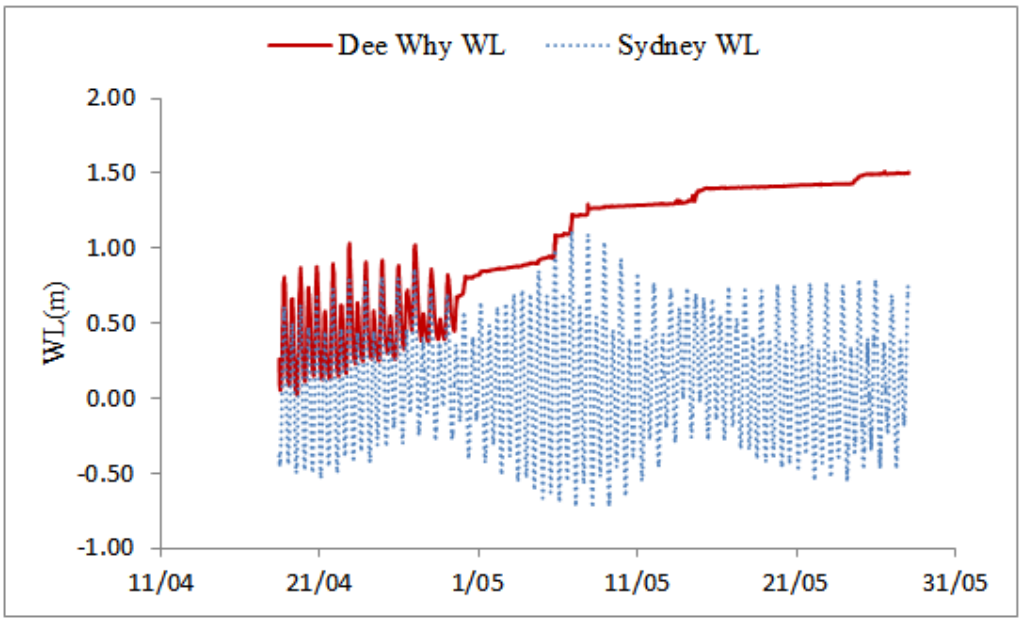

Figure A3.15: Water levels for closure event 1 at Dee Why lagoon from 18/4/2012 to 28/5/2012.

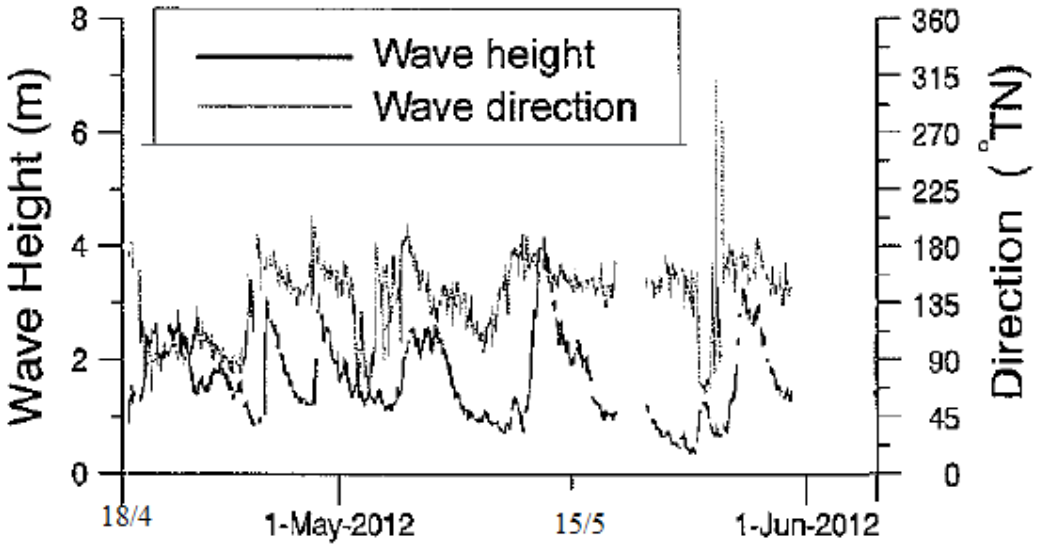

Figure A3.16: Wave height and wave direction offshore Sydney for closure event 2 at Dee Why lagoon from 18/4/2012 to 28/5/2012.

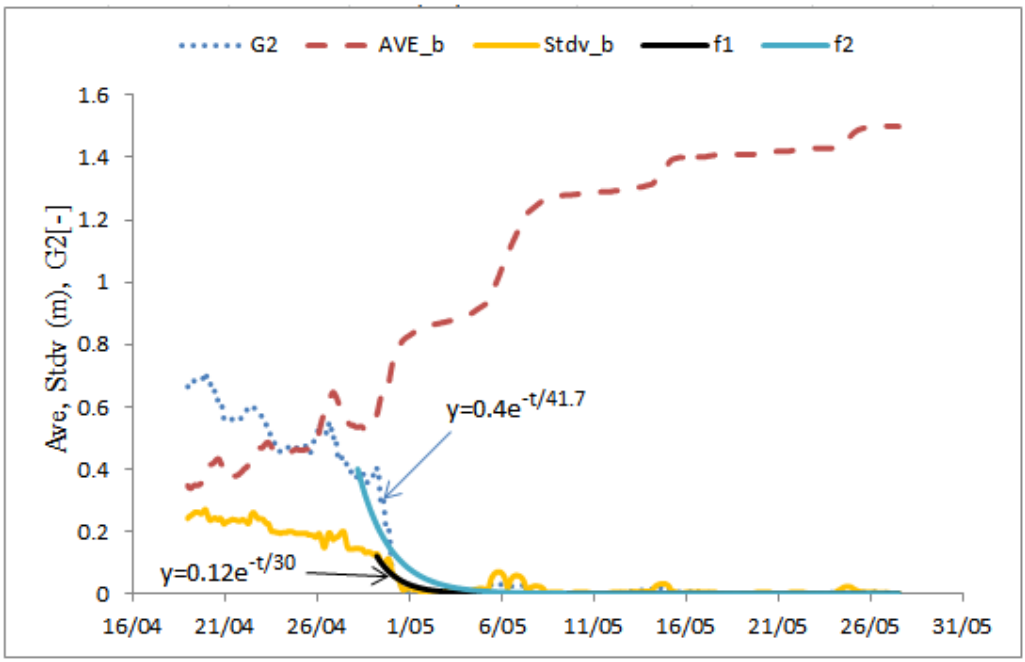

Figure A3.17: Results of $\overline{\eta_{24.5\,b}}(t)$, G_2 and $Stdv_{24.5\text{-b}}(t)$ with fitting curves for closure event 2 at Dee Why lagoon.
T_{morph} =41.7h from fitting G_2 and T_{morph} =30h from fitting $Stdv_{24.5\text{-b}}(t)$.

Terrigal closure event1

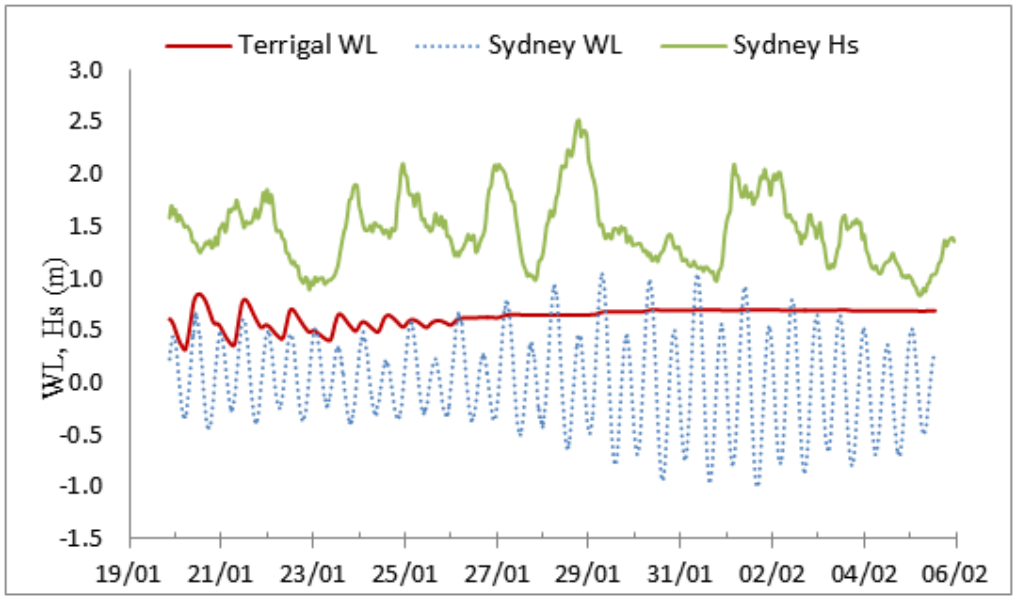

Figure A3.18: Water levels and wave height at Sydney for closure event 1 at Terrigal from 18/1/2011 to 5/2/2011.

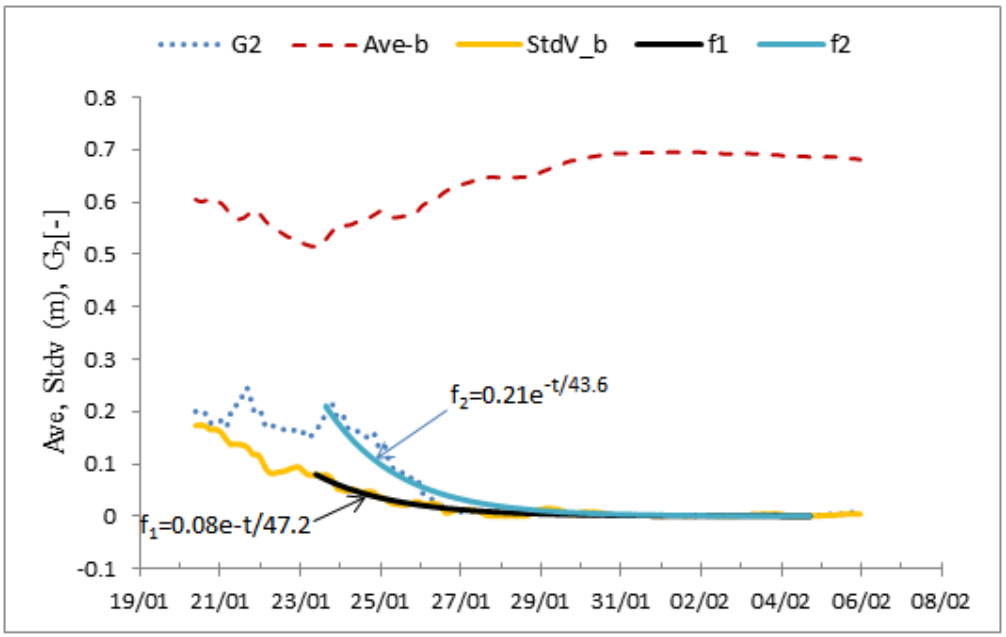

Figure A3.19: Results of $\overline{\eta_{24.5\,b}}(t)$, G_2 and $Stdv_{24.5\text{-b}}(t)$ with fitting curves for closure event 1 at Terrigal.
T_{morph} =43.6h from fitting G_2 and T_{morph} =47.2h from fitting $Stdv_{24.5\text{-b}}(t)$

Terrigal closure event 2

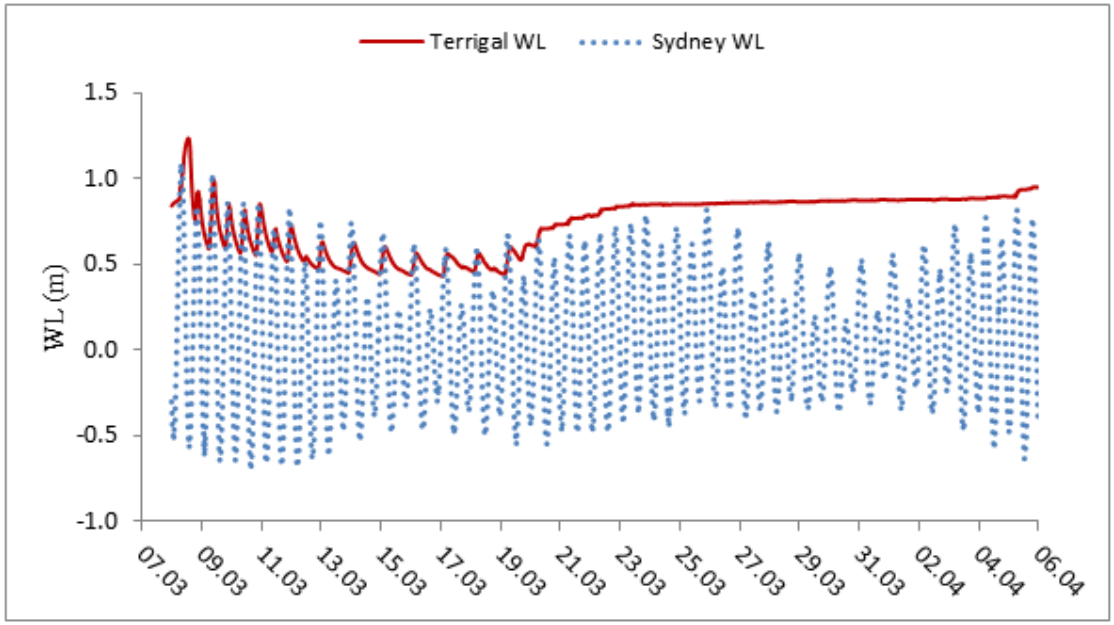

Figure A3.20: Water levels for closure event 2 at Terrigal from 13/3/2012 to 24/3/2012.

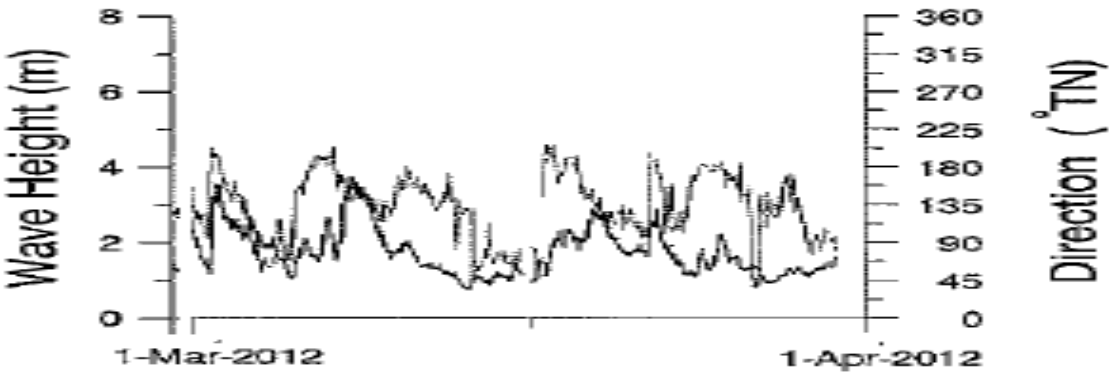

Figure A3.21: Wave height and wave direction offshore Sydney for closure event 2 at Terrigal from 13/3/2012 to 24/3/2012.

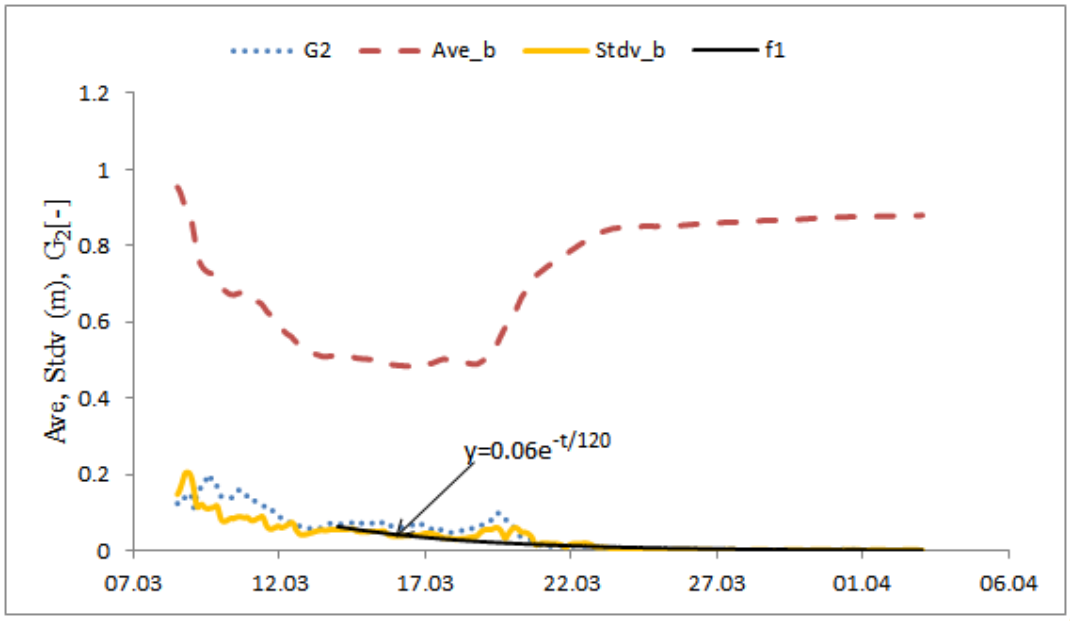

Figure A3.22: Results of $\overline{\eta_{24.5\,b}}(t)$, G_2 and $Stdv_{24.5\text{-}b}(t)$ with fitting curves for closure event 2 at Terrigal.
T_{morph} =120h from fitting $Stdv_{24.5\text{-}b}(t)$.

Cockrone closure event from 21/6-25/6/2008

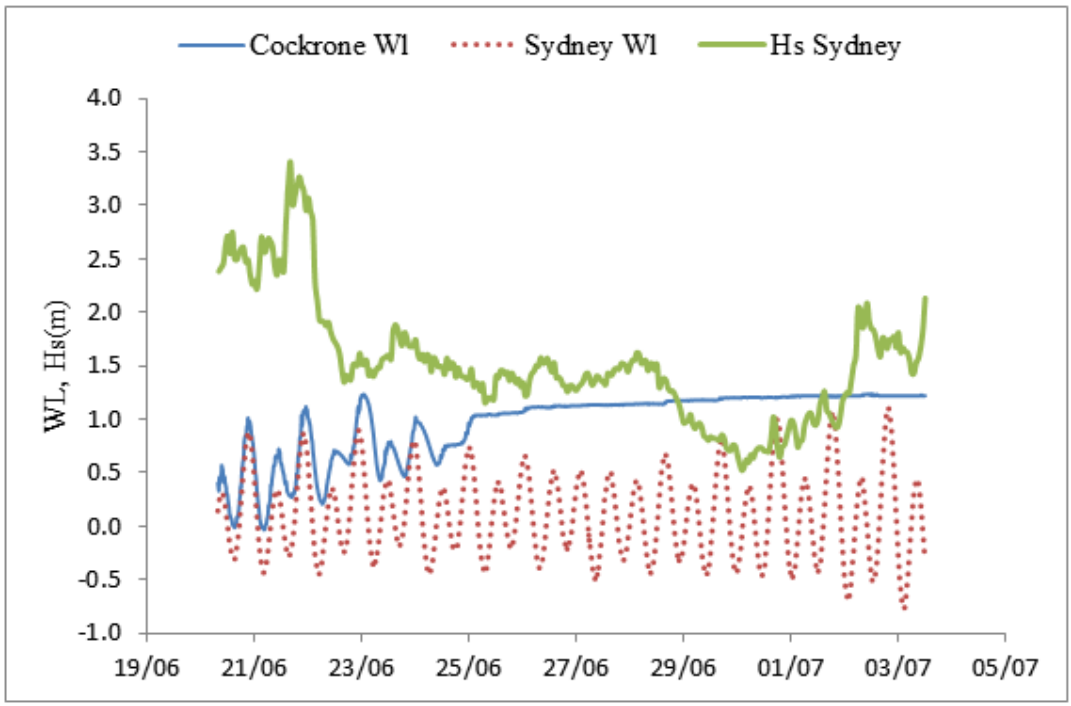

Figure A3.23: Water levels and wave height at Sydney for closure event at Cockrone from 21/6/2008-25/6/2008.

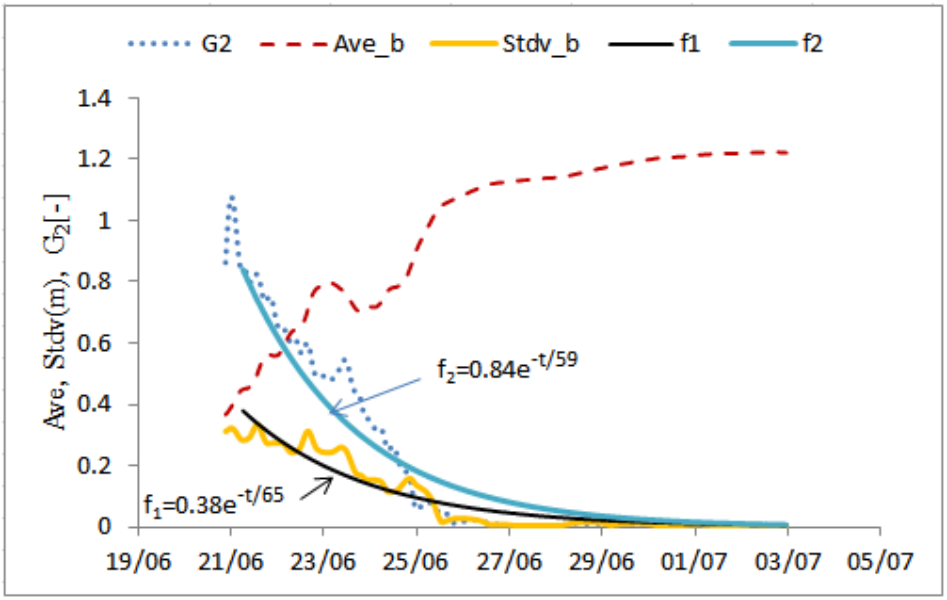

Figure A3.24: Results of $\overline{\eta_{24.5\,b}}(t)$, G_2 and $Stdv_{24.5\text{-}b}(t)$ with fitting curves for closure event at Cockrone.

T_{morph} =59h from fitting G_2 and T_{morph} =65h from fitting $Stdv_{24.5\text{-}b}(t)$.

Back Lagoon closure event

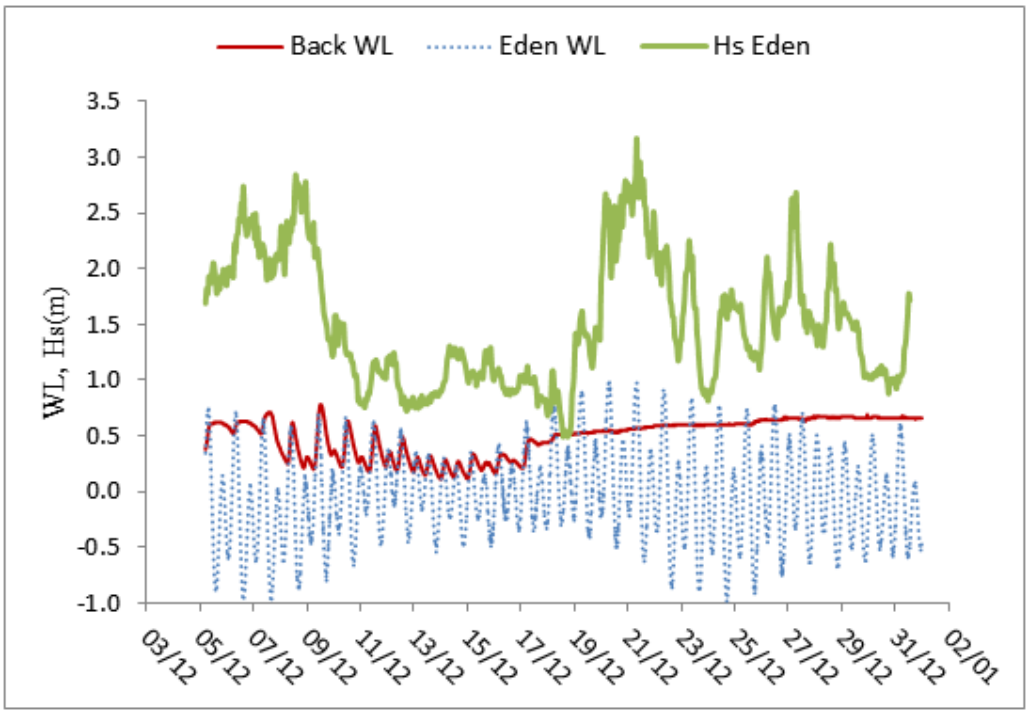

Figure A3.25: Water levels and wave height at Eden for closure event at Back lagoon from 14/12/2010-18/12/2010.

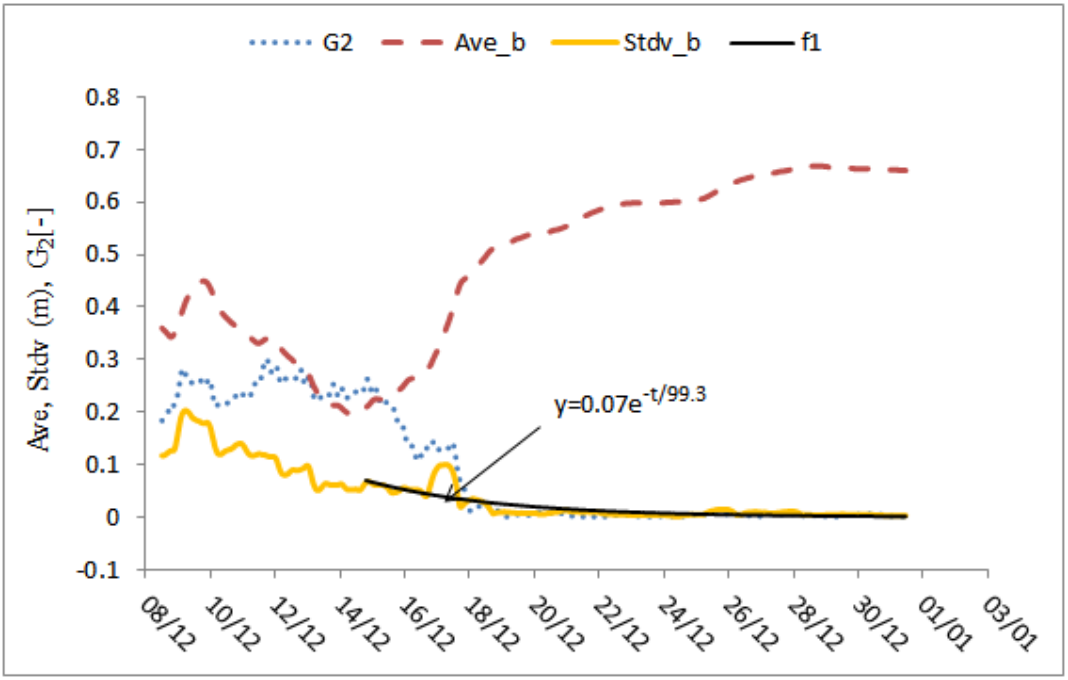

Figure A3.26: Results of $\overline{\eta_{24.5\,b}}(t)$, G_2 and $Stdv_{24.5\text{-}b}(t)$ with fitting curves for closure at Back lagoon.
T_{morph} =99.3h from fitting $Stdv_{24.5\text{-}b}(t)$.